frontiers
RESEARCH TOPICS

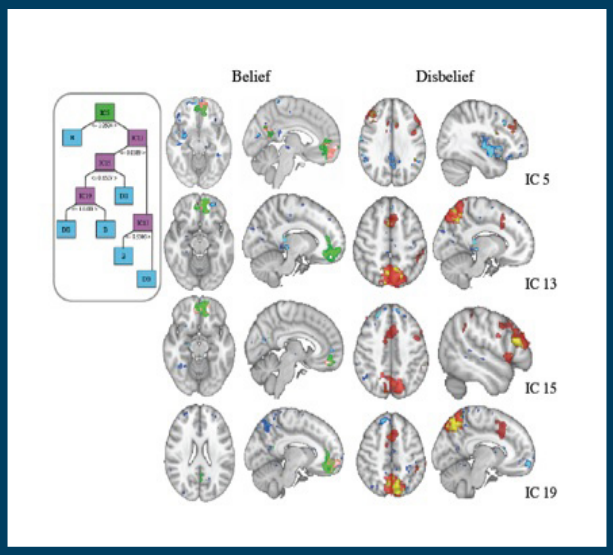

ICA OF fMRI STUDIES: NEW APPROACHES AND CUTTING EDGE APPLICATIONS

Topic Editors
Veronika Schöpf and Simon D. Robinson

frontiers in
HUMAN NEUROSCIENCE

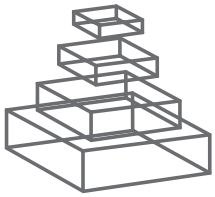

frontiers

ISSN 1664-8714
ISBN 978-2-88919-200-7
DOI 10.3389/978-2-88919-200-7

ABOUT FRONTIERS

Frontiers is more than just an open-access publisher of scholarly articles: it is a pioneering approach to the world of academia, radically improving the way scholarly research is managed. The grand vision of Frontiers is a world where all people have an equal opportunity to seek, share and generate knowledge. Frontiers provides immediate and permanent online open access to all its publications, but this alone is not enough to realize our grand goals.

FRONTIERS JOURNAL SERIES

The Frontiers Journal Series is a multi-tier and interdisciplinary set of open-access, online journals, promising a paradigm shift from the current review, selection and dissemination processes in academic publishing.
All Frontiers journals are driven by researchers for researchers; therefore, they constitute a service to the scholarly community. At the same time, the Frontiers Journal Series operates on a revolutionary invention, the tiered publishing system, initially addressing specific communities of scholars, and gradually climbing up to broader public understanding, thus serving the interests of the lay society, too.

DEDICATION TO QUALITY

Each Frontiers article is a landmark of the highest quality, thanks to genuinely collaborative interactions between authors and review editors, who include some of the world's best academicians. Research must be certified by peers before entering a stream of knowledge that may eventually reach the public - and shape society; therefore, Frontiers only applies the most rigorous and unbiased reviews.
Frontiers revolutionizes research publishing by freely delivering the most outstanding research, evaluated with no bias from both the academic and social point of view.
By applying the most advanced information technologies, Frontiers is catapulting scholarly publishing into a new generation.

WHAT ARE FRONTIERS RESEARCH TOPICS?

Frontiers Research Topics are very popular trademarks of the Frontiers Journals Series: they are collections of at least ten articles, all centered on a particular subject. With their unique mix of varied contributions from Original Research to Review Articles, Frontiers Research Topics unify the most influential researchers, the latest key findings and historical advances in a hot research area!
Find out more on how to host your own Frontiers Research Topic or contribute to one as an author by contacting the Frontiers Editorial Office: researchtopics@frontiersin.org

ICA OF fMRI STUDIES: NEW APPROACHES AND CUTTING EDGE APPLICATIONS

Topic Editors:
Veronika Schöpf, Medical University of Vienna, Austria
Simon D. Robinson, Medical University of Vienna, Austria

Table of Contents

frontiers in
HUMAN NEUROSCIENCE

EDITORIAL
published: 28 October 2013
doi: 10.3389/fnhum.2013.00724

ICA of fMRI studies: new approaches and cutting edge applications

Simon Daniel Robinson*[1] *and* ***Veronika Schöpf*[2]**

[1] *High Field MR Centre, Department of Biomedical Imaging and Image-guided Therapy, Medical University of Vienna, Vienna, Austria*
[2] *Department of Biomedical Imaging and Image-guided Therapy, Medical University of Vienna, Vienna, Austria*
**Correspondence: simon.robinson@meduniwien.ac.at*

Edited by:
Hauke R. Heekeren, Freie Universität Berlin, Germany

Keywords: independent component analysis, functional magnetic resonance imaging, resting-state networks, schizophrenia, presurgical planning, real-time fMRI, ultra-high field, multiband EPI

Independent component analysis (ICA) is the most commonly used and most diversely applicable exploratory method for the analysis of functional magnetic resonance imaging (fMRI) data. Over the last 10 years it has offered a wealth of insights into brain function during task execution and in the resting state.

Independent component analysis is a blind source separation method that was originally applied to identify technical and physiological artifacts in fMRI, and to allow their removal prior to analysis with model-based approaches. It has matured into a method capable of offering a stand-alone assessment of activation on a sound statistical footing. Recent innovations have taken on the challenges of how components should be combined over subjects to allow group inferences, and how activation identified with ICA might be compared between groups – of patients and controls – for instance. Its reputation having been bolstered by multiple successes in the investigation of resting-state networks, ICA is being applied in other cutting edge uses of fMRI; in multivariate pattern analysis, real-time fMRI, *in utero* studies, with a wide variety of paradigms and stimulus types and with challenging tasks with patients at ultra-high field. These are testament both to ICA's flexibility and its evolving role both in basic neuroscience and clinical applications of fMRI.

This Research Topic has attracted 19 contributions from the most renowned researchers in the field, including the inventor of Fast ICA, Aapo Hyvärinen (Hyvärinen and Ramkumar, 2013), and the authors of the most widely used ICA software for fMRI – Christian Beckmann (FSL's MELODIC) and Vince Calhoun (GIFT). The capacity of ICA to find common patterns of activation in huge cohorts of subjects is demonstrated by the parallel computing approach described by Kalcher et al. (2012) and the use of ICA with cutting edge MR methods are presented by the groups of Stefan Posse [Echo Volume Imaging (Posse et al., 2013)], Markus Barth [EEG-fMRI (Meyer et al., 2013) and Ultra-Fast Generalized Inverse Imaging (Boyacioglu et al., 2013)], and Jorge Jovicich [real-time fMRI (Soldati et al., 2013a,b)].

Two articles in this research topic reflect the continued use of ICA to identify artifacts, using the temporal characteristics of components (Rummel et al., 2013) or both temporal and spatial features (Bhaganagarapu et al., 2013). In addition to using frequency signatures to identify noise, the frequencies of signal fluctuations during rest have been studied using temporal ICA (Boubela et al., 2013) and in ultra-fast generalized imaging (Boyacioglu et al., 2013), while Di et al. (2013) examine the influence of amplitude on resting-state connectivity and Balsters et al. (2013) assess the correlation between BOLD spectral power and working memory performance.

The ICA applications featured in this Research Topic range from clinical resting-state studies with patients suffering from schizophrenia (Manoliu et al., 2013; Sui et al., 2013) and neurological patients performing chin and hand motor tasks (Robinson et al., 2013) to the investigation of processing streams using chemosensory stimuli (Frasnelli et al., 2012). Combined methodological approaches are used to study belief decision making with fMRI and EEG (Douglas et al., 2013), to discriminate schizophrenia using data from fMRI, DTI, and sMRI (Sui et al., 2013), to identify amyotrophic lateral sclerosis diseased brains (Welsh et al., 2013) and to examine the microvascular specificity of the BOLD effect at 3 and 7 T using SWI (Geissler et al., 2013).

We hope this collection of original research articles illustrates the extent to which ICA is becoming an increasingly flexible and potent analysis method – particularly through innovations such as real-time ICA, temporal ICA, and parallel processing implementations – and that the capacity of ICA to isolate the underlying signal sources in fMRI data is being enhanced by multimodal and ultra-fast imaging. These innovations are leading to an increase in the utility of ICA and the richness of information it can provide in both basic research work and clinical applications.

REFERENCES

Balsters, J. H., Robertson, I. H., and Calhoun, V. D. (2013). BOLD frequency power indexes working memory performance. *Front. Hum. Neurosci.* 7:207. doi: 10.3389/fnhum.2013.00207

Bhaganagarapu, K., Jackson, G. D., and Abbott, D. F. (2013). An automated method for identifying artifact in independent component analysis of resting-state fMRI. *Front. Hum. Neurosci.* 7:343. doi: 10.3389/fnhum.2013.00343

Boubela, R. N., Kalcher, K., Huf, W., Kronnerwetter, C., Filzmoser, P., and Moser, E. (2013). Beyond noise: using temporal ICA to extract meaningful information from high-frequency fMRI signal fluctuations during rest. *Front. Hum. Neurosci.* 7:168. doi: 10.3389/fnhum.2013.00168

Boyacioglu, R., Beckmann, C. F., and Barth, M. (2013). An investigation of RSN frequency spectra using ultra-fast generalized inverse imaging. *Front. Hum. Neurosci.* 7:156. doi: 10.3389/fnhum.2013.00156

Di, X., Kim, E. H., Huang, C.-C., Tsai, S.-J., Lin, C.-P., and Biswal, B. B. (2013). The influence of the amplitude of low-frequency fluctuations on resting-state functional connectivity. *Front. Hum. Neurosci.* 7:118. doi: 10.3389/fnhum.2013.00118

Douglas, P. K., Lau, E., Anderson, A., Head, A., Kerr, W., Wollner, M., et al. (2013). Single trial decoding of belief decision making from EEG and fMRI data using independent components features. *Front. Hum. Neurosci.* 7:392. doi: 10.3389/fnhum.2013.00392

Frasnelli, J., Lundström, J. N., Schöpf, V., Negoias, S., Hummel, T., and Lepore, F. (2012). Dual processing streams in chemosensory perception. *Front. Hum. Neurosci.* 6:288. doi: 10.3389/fnhum.2012.00288

Geißler, A., Fischmeister, F. PhS., Grabner, G., Wurnig, M., Rath, J., Foki, T., et al. (2013). Comparing the microvascular specificity of the 3- and 7-T BOLD response using ICA and susceptibility-weighted imaging. *Front. Hum. Neurosci.* 7:474. doi: 10.3389/fnhum.2013.00474

Hyvärinen, A., and Ramkumar, P. (2013). Testing independent component patterns by inter-subject or inter-session consistency. *Front. Hum. Neurosci.* 7:94. doi: 10.3389/fnhum.2013.00094

Kalcher, K., Huf, W., Boubela, R. N., Filzmoser, P., Pezawas, L., Biswal, B., et al. (2012). Fully exploratory network independent component analysis of the 1000 functional connectomes database. *Front. Hum. Neurosci.* 6:301. doi: 10.3389/fnhum.2012.00301

Manoliu, A., Riedl, V., Doll, A., Bäuml, J. G., Mühlau, M., Schwerthöffer, D., et al. (2013). Insular dysfunction reflects altered between-network connectivity and severity of negative symptoms in schizophrenia during psychotic remission. *Front. Hum. Neurosci.* 7:216. doi: 10.3389/fnhum.2013.00216

Meyer, M. C., Janssen, R. J., Van Oort, E. S. B., Beckmann, C. F., and Barth, M. (2013). The quest for EEG power band correlation with ICA derived fMRI resting state networks. *Front. Hum. Neurosci.* 7:315. doi: 10.3389/fnhum.2013.00315

Posse, S., Ackley, E., Mutihac, R., Zhang, T., Hummatov, R., Akhtari, M., et al. (2013). High-speed real-time resting-state fMRI using multi-slab echo-volumar imaging. *Front. Hum. Neurosci.* 7:479. doi: 10.3389/fnhum.2013.00479

Robinson, S. D., Schöpf, V., Cardoso, P., Geissler, A., Fischmeister, F. PhS., Wurnig, M., et al. (2013). Applying independent component analysis to clinical fMRI at 7 T. *Front. Hum. Neurosci.* 7:496. doi: 10.3389/fnhum.2013.00496

Rummel, C., Verma, R. K., Schöpf, V., Abela, E., Hauf, M., Berruecos, J. F. Z., et al. (2013). Time course based artifact identification for independent components of resting-state fMRI. *Front. Hum. Neurosci.* 7:214. doi: 10.3389/fnhum.2013.00214

Soldati, N., Calhoun, V. D., Bruzzone, L., and Jovicich, J. (2013a). ICA analysis of fMRI with real-time constraints: an evaluation of fast detection performance as function of algorithms, parameters and *a priori* conditions. *Front. Hum. Neurosci.* 7:19. doi: 10.3389/fnhum.2013.00019

Soldati, N., Calhoun, V. D., Bruzzone, L., and Jovicich, J. (2013b). The use of a priori information in ICA-based techniques for real-time fMRI: an evaluation of static/dynamic and spatial/temporal characteristics. *Front. Hum. Neurosci.* 7:64. doi: 10.3389/fnhum.2013.00064

Sui, J., He, H., Yu, Q., Chen, J., Rogers, J., Pearlson, G. D., et al. (2013). Combination of resting state fMRI. *Front. Hum. Neurosci.* 7:235. doi: 10.3389/fnhum.2013.00235

Welsh, R. C., Jelsone-Swain, L. M., and Foerster, B. R. (2013). The utility of independent component analysis and machine learning in the identification of the amyotrophic lateral sclerosis diseased brain. *Front. Hum. Neurosci.* 7:251. doi: 10.3389/fnhum.2013.00251

Received: 26 September 2013; accepted: 11 October 2013; published online: 28 October 2013.
Citation: Robinson SD and Schöpf V (2013) ICA of fMRI studies: new approaches and cutting edge applications. Front. Hum. Neurosci. ***7****:724. doi: 10.3389/fnhum.2013.00724*
This article was submitted to the journal Frontiers in Human Neuroscience.

frontiers in
HUMAN NEUROSCIENCE

ORIGINAL RESEARCH ARTICLE
published: 26 August 2013
doi: 10.3389/fnhum.2013.00479

High-speed real-time resting-state fMRI using multi-slab echo-volumar imaging

Stefan Posse[1,2,3]*, Elena Ackley[1], Radu Mutihac[4,5], Tongsheng Zhang[1], Ruslan Hummatov[3], Massoud Akhtari[6], Muhammad Chohan[7], Bruce Fisch[1] and Howard Yonas[7]

[1] Department of Neurology, School of Medicine, The University of New Mexico, Albuquerque, NM, USA
[2] Department of Electrical and Computer Engineering, The University of New Mexico, Albuquerque, NM, USA
[3] Department of Physics and Astronomy, The University of New Mexico, Albuquerque, NM, USA
[4] Department of Physics, University of Bucharest, Bucharest, Romania
[5] Division of Psychiatry and Neuroscience, Walter Reed Army Institute of Research, Silver Spring, MD, USA
[6] Semel Institute for Neuroscience and Human Behavior, University of California Los Angeles, Los Angeles, CA, USA
[7] Department of Neurosurgery, School of Medicine, The University of New Mexico, Albuquerque, NM, USA

Edited by:
Simon D. Robinson, Medical University of Vienna, Austria

Reviewed by:
Rasim Boyacioglu, Radboud University, Netherlands
Erik Van Oort, University of Twente, Netherlands

***Correspondence:**
Stefan Posse, Department of Neurology, School of Medicine, The University of New Mexico, 1 University of New Mexico, MSC 105620, Albuquerque, NM 87131, USA
e-mail: sposse@unm.edu

We recently demonstrated that ultra-high-speed real-time fMRI using multi-slab echo-volumar imaging (MEVI) significantly increases sensitivity for mapping task-related activation and resting-state networks (RSNs) compared to echo-planar imaging (Posse et al., 2012). In the present study we characterize the sensitivity of MEVI for mapping RSN connectivity dynamics, comparing independent component analysis (ICA) and a novel seed-based connectivity analysis (SBCA) that combines sliding-window correlation analysis with meta-statistics. This SBCA approach is shown to minimize the effects of confounds, such as movement, and CSF and white matter signal changes, and enables real-time monitoring of RSN dynamics at time scales of tens of seconds. We demonstrate highly sensitive mapping of eloquent cortex in the vicinity of brain tumors and arterio-venous malformations, and detection of abnormal resting-state connectivity in epilepsy. In patients with motor impairment, resting-state fMRI provided focal localization of sensorimotor cortex compared with more diffuse activation in task-based fMRI. The fast acquisition speed of MEVI enabled segregation of cardiac-related signal pulsation using ICA, which revealed distinct regional differences in pulsation amplitude and waveform, elevated signal pulsation in patients with arterio-venous malformations and a trend toward reduced pulsatility in gray matter of patients compared with healthy controls. Mapping cardiac pulsation in cortical gray matter may carry important functional information that distinguishes healthy from diseased tissue vasculature. This novel fMRI methodology is particularly promising for mapping eloquent cortex in patients with neurological disease, having variable degree of cooperation in task-based fMRI. In conclusion, ultra-high-real-time speed fMRI enhances the sensitivity of mapping the dynamics of resting-state connectivity and cerebro-vascular pulsatility for clinical and neuroscience research applications.

Keywords: real-time resting state fMRI, multi-slab echo-volumar imaging, independent component analysis (ICA), seed-based functional connectivity, cerebrovascular pulsatility, epilepsy, brain tumor, arteriovenous malformation

INTRODUCTION

Mapping of intrinsic signal variation mostly in the low-frequency band <0.1 Hz has emerged as a powerful tool and adjunct to task-related fMRI and fiber tracking based in diffusion tensor imaging (DTI) for mapping functional connectivity within and between resting-state networks (RSNs) (Fox et al., 2005; De Luca et al., 2006; Raichle and Snyder, 2007; Schopf et al., 2010; Li et al., 2011). Recent studies have shown that dozens of different RSNs can be measured across groups of subjects (Abou-Elseoud et al., 2010; Allen et al., 2011). Anti-correlations between the default mode network (DMN) and task-positive networks provide insights into competitive mechanisms that control resting-state fluctuations (Fox et al., 2005; Uddin et al., 2009). There is increasing evidence that RSNs are not stationary (Hou et al., 2006; Kang et al., 2011) and that correlations with fluctuations in other measurements, such as α-power in EEG (Wu et al., 2010) and transient (∼100 ms) topographies of EEG current source densities (microstates) (Britz et al., 2010; Laufs, 2010; Lehmann, 2010; Musso et al., 2010; Van de Ville et al., 2010) exist. Variations in ongoing activity have been shown to predict changes in task performance and alertness, highlighting their importance for understanding the connection between brain activity and behavior (Eichele et al., 2008; Sadaghiani et al., 2010). Resting-state correlation mapping has been shown to be a promising tool for reliable functional localization of eloquent cortex in healthy controls, and patients with brain tumors and epilepsy (Liu et al., 2009; Zhang et al., 2009; Mannfolk et al., 2011; Stufflebeam et al., 2011). It has been suggested that this task-free paradigm may provide a powerful approach to map functional anatomy in

patients without task compliance, which allows multiple brain systems to be determined in a single scanning session (Liu et al., 2009). Recent studies have investigated non-stationarity, which is prominent in the resting state, and demonstrated dynamic changes in network connectivity (Chang and Glover, 2010; Sakoglu et al., 2010; Kiviniemi et al., 2011). There is now emerging evidence that these fluctuations differ in clinical populations compared to healthy controls. However, the mechanisms that govern the dynamics of resting-state connectivity at different time scales are still poorly understood. Monitoring these dynamics in real-time enables assessment of data quality and sensitivity as intra-scan non-stationarity of connectivity can compromise the detection of RSNs in single subjects. Real-time monitoring of these dynamics is not only expected to improve consistency of data quality in clinical research studies, but will also contribute to our understanding of the neurophysiological mechanisms underlying the resting-state dynamics.

Seed-based correlation analysis (Van Dijk et al., 2010) and spatial independent component analysis (ICA) (Calhoun et al., 2001) are the principal tools to map functional connectivity, which have been shown to provide similar results (Van Dijk et al., 2010; Erhardt et al., 2011). Seed-based connectivity measures have been shown to be the sum of ICA-derived within- and between-network connectivities (Joel et al., 2011). ICA also performs spatial filtering, which enables segregation of spatially overlapping components. Seed-based techniques are sensitive to the choice of the seed regions (Cole et al., 2010a). On the other hand, source separation with ICA is sensitive to the selection of the model order, which is *a priori* unknown and necessitates dimensionality estimation approaches, such as the minimum description length (MDL), Bayesian information criterion (BIC), and Akaike's information criterion (AIC) (Calhoun et al., 2001; Li et al., 2007). Furthermore, automated ordering of ICA components to enable consistent identification of RSNs is not yet feasible and source separation with ICA in individual subject data is limited by the contrast-to-noise ratio of the signal fluctuations and aliasing of cardiac- and respiration-related signal fluctuations. Seed-based correlation analysis surpasses ICA in detecting resting-state connectivity, but it requires regression of confounding signals, which typically include the six parameters of motion correction and their derivatives, and the average signal from up to three brain regions (whole brain over a fixed region in atlas space, ventricles, and white matter in the centrum semiovale). Regression of these signals is computationally intensive and may remove RSN signal changes that are temporally correlated with confounding signals.

The measurement of functional connectivity in the resting state has been limited, in part, by sensitivity and specificity constraints of current fMRI data acquisition methods. Echo-planar imaging (EPI) methods necessitate long scan times and detection of resting-state signal fluctuation suffers from temporally aliased physiological signal fluctuation, despite ongoing efforts to develop post-acquisition correction methods (Glover et al., 2000; Deckers et al., 2006; Beall and Lowe, 2007; Behzadi et al., 2007). Movement during the fMRI acquisition is a major confound for resting-state connectivity studies obscuring networks as well as creating false-positive connections (Satterthwaite et al., 2012; Van Dijk et al., 2012) despite state-of-the-art motion "correction" in post-processing. Distinction of BOLD contrast-based resting-state activity and of confounding physiological signal fluctuations has been shown to benefit from multi-echo acquisition. This approach not only increases BOLD sensitivity (Posse et al., 1999), but was also found to enable differentiation of BOLD contrast-based resting-state activity and of confounding physiological signal fluctuations (Kundu et al., 2012; Wu et al., 2012). However, multiple echo acquisition reduces temporal resolution and/or volume coverage, which have limited practical applications (Posse, 2012).

Recent advances in high-speed fMRI method development that enable un-aliased sampling of physiological signal fluctuation have considerably increased sensitivity for mapping task-based activation and functional connectivity, as well as for detecting dynamic changes in connectivity over time (Feinberg et al., 2010; Posse et al., 2012; Smith et al., 2012). High temporal resolution fMRI improves separation of RSNs using data driven analysis approaches (Smith et al., 2012) and may facilitate detecting the temporal dynamics of RSNs at much higher frequencies (up to 5 Hz) than detectable with traditional resting-state fMRI (Boubela et al., 2013; Boyacioglu et al., 2013; Chu et al., 2013; Lee et al., 2013). The development of ultra-high-speed fMRI methods with temporal resolution on the order of 100 ms or less has focused on echo-volumar imaging (EVI) (Rabrait et al., 2008; Witzel et al., 2008; van der Zwaag et al., 2009), inverse imaging (InI) (Lin et al., 2006, 2008, 2010), and MR encephalography (MREG) using highly undersampled projection imaging (Grotz et al., 2009), and fast volumetric imaging based on single-shot 3D rosette trajectories (Zahneisen et al., 2011). However, these single-shot methods are associated with degradation of spatial resolution and image uniformity. The recent development of simultaneous multi-slice (SMS) EPI using parallel imaging with blipped CAIPI acquisition increases temporal resolution without the $\sqrt{R}$ penalty incurred when using conventional parallel imaging methods, while maintaining acceptable image quality (Setsompop et al., 2012). Typical acceleration factors of eightfold are achievable using a 32 channel coil and faster acceleration has been shown in combination with in-plane parallel imaging (Moeller et al., 2010) and simultaneous echo refocusing (Feinberg et al., 2010; Chen et al., 2012). Recent advances in SMS-EPI enable up to 16-fold acceleration. Although acceleration is limited by RF power deposition (SAR), necessitating small flip angles, and image degradation at high acceleration factors due to increasing slice cross-talk and worsening g-factor (Moeller et al., 2010, 2012), SMS-EPI currently enables much higher spatial resolution compared to EVI. Furthermore, recent advances in RF pulse design, such as spatially periodic pulses, mitigate the RF power requirement for SMS EPI (Norris et al., 2011; Koopmans et al., 2013). We have recently introduced parallel imaging accelerated sequential multi-slab echo-volumar imaging (MEVI), which shortens the long EVI readout to achieve an image quality approaching that of EPI, and have demonstrated significant increases in BOLD sensitivity compared to EPI (Posse et al., 2012). This methodology enables ultra-high-speed real-time fMRI on conventional clinical 3 T scanners with 276 ms temporal resolution for whole brain acquisition and 136 ms temporal resolution for partial brain acquisition.

In the present study the *primary goals* were to characterize the sensitivity of MEVI for mapping major RSNs, comparing ICA and a novel real-time seed-based connectivity method that

combines sliding-window correlation analysis with meta-statistics, and to map dynamic changes in resting-state connectivity at short time scales. The hypotheses for this novel seed-based connectivity approach are that: (a) resting-state connectivity can be measured at short time scales (seconds) and (b) averaging across short-term connectivity maps avoids the conventional artifact prone correlation across the entire scan. The *secondary goals* were to: (a) compare resting state and task-based fMRI in patients with neurological disorders for localizing sensorimotor and visual cortex in the vicinity of brain tumors and arterio-venous malformations, and to (b) to assess the feasibility of monitoring disease-related changes in functional connectivity in epilepsy. Localization of eloquent cortex adjacent to brain lesions is of critical value in presurgical planning and decision-making. Mapping of RSNs using fMRI has been suggested as an alternative to task-based fMRI, however, the utility for presurgical planning is still under investigation (Liu et al., 2009; Zhang et al., 2009; Mannfolk et al., 2011; Stufflebeam et al., 2011). The *tertiary goal* was to characterize regional differences in the cardiac-related cerebro-vascular pulsation in the healthy controls and in the patients with brain tumors, arterio-venous malformations, and epilepsy. Virtually all fMRI studies so far have sought to remove physiological signal fluctuations due to cardiac and respiration using model-based retrospective deconvolution methods (Glover et al., 2000). Ultra-high-speed fMRI enables direct observation of cardiac pulsation and its harmonics, which may carry important functional information that distinguishes healthy from diseased tissue vasculature.

MATERIALS AND METHODS

EQUIPMENT

Data were collected on a clinical 3 T scanner, MAGNETOM Trio, A Tim System (Siemens Healthcare, Erlangen, Germany) equipped with MAGNETOM Avanto gradient system and 12-channel array receive-only head coil. A 32 channel coil became available during the last months of the study. Pulse and respiration waveforms were recorded with 1 kHz sampling rate using an MP150 data acquisition system and Acknowledge software 4.3 (Biopac Inc., Goleta, CA, USA). Reconstructed 2D images were exported from the scanner reconstruction computer via the scanner host computer to an external Intel Xeon E5530, six core, 2.4 GHz workstation for reconstruction of the third spatial dimension and real-time fMRI analysis, which were integrated into our custom TurboFIRE real-time fMRI software version V5.12.3.11.4.2 (Posse et al., 2001, 2012).

SUBJECTS

Nine healthy male and female subjects aged 21–50 years and eight patients with neurological disorders participated after giving institutionally reviewed informed consent.

Brain tumor

Patient 1 was a 30-year old male with a low-grade right frontal lobe lesion associated with epilepsy and motor impairment, which was radiologically diagnosed as a low-grade glioma. The routine EEG demonstrated C4 (right central) epileptiform spikes. His seizures consist of an initial numbness and tingling sensation in the left arm and leg, followed by stiffening and jerking movements of the left side of the body. He failed treatment with oxcarbazepine, phenytoin, topiramate, and lorazepam. There was no obvious involvement of the primary motor cortex, based on the MEG motor and somatosensory responses, and the structural MRI. High-speed 3D short TE MR spectroscopic imaging (MRSI) using proton-echo-planar-spectroscopic-imaging (PEPSI) (Posse et al., 2007) showed increased Choline, reduced *N*-acetyl-aspartate (NAA), and strong lipid resonances, suggesting an oligodendroglioma (Posse et al., 2013). Intraoperative assessment confirmed a high lipid content. Postsurgical histology classified the tumor as an oligodendroglioma.

Patient 2 was a 38-year old female with a 1.5-year history of headaches. The clinical MRI showed loss of gray-white matter differentiation with multiple areas of gyral expansion in the left superior frontal gyrus and in the left parietal lobe, which were suspected to be a primary glial tumor, such as multiple oligodendroglioma or multiple astrocytic tumors. High-speed 3D short TE MRSI using PEPSI (Posse et al., 2007) showed only a slight increase in Choline and slight reduction of *N*-acetyl-aspartate (NAA). The patient remained under observation. A biopsy performed a year later in the T_2 hyperintense left parietal lesion revealed disease progression. The histological interpretation was infiltrating grade 2 astrocytoma.

Arterio-venous malformation

Patient 3 was a 44-year old male with a two and a half year history of complex partial seizures and progressive right lower extremity weakness, who on imaging studies was found to have a Spetzler–Martin grade III arterio-venous malformation in the left fronto-parietal area. Cerebral angiography demonstrated a dense nidus with feeders from anterior, middle, and posterior cerebral arteries with early drainage into the superior sagittal sinus without significant deep drainage. Because of its location in the eloquent cortex, definitive treatment, either by surgery or endovascular means was not recommended. His seizures followed a Jacksonian-March pattern: starting from his right foot and marching up. The frequency of seizures at the time of testing was variable, ranging from daily to weekly, despite treatment with multiple anti-epileptic medications. The patient's interictal EEG did not contain epileptiform abnormalities. He is on multiple anti-epileptic medications and his seizure control remains a challenge.

Patient 4 was a 24-year old male with new onset of seizures with vivid visual aura who on workup was found to have a vascular lesion in the right occipital region. He described his aura as colors of rainbow that started in the center of the visual field and quickly shifted to the left hemifield followed by a generalized tonic-clonic seizure. Cerebral angiography demonstrated a clear hypervascular nidus without early venous drainage to qualify for an AVM. He underwent a surgical resection, which showed an arterial venous malformation with multiple thrombosed cortical veins. He is currently been weaned off his anti-epileptic medications and remains seizure free.

Temporal lobe epilepsy

Patient 5 was a 53-year old male who had temporal lobe epilepsy with right mesial temporal lobe sclerosis and complex partial seizures preceded by deja vu, sometimes progressing to a secondarily generalized seizure. Epilepsy monitoring during

withdrawal of anti-epileptic medication demonstrated seizures electrographically localized to the right anterior temporal area, and all interictal epileptiform activity similarly arising from the right anterior temporal area (F8 maximal). FDG-PET scanning demonstrated right mesial temporal hypometabolism and MEG interictal epileptiform activity localized to the left anterior temporal lobe in a distribution typical for mesial temporal epilepsy. He underwent temporal lobe resection and remains seizure free.

Patient 6 was a 12-year old female who had had complex partial seizures with left temporal FDG-PET hypometabolism and seizures lateralized to the left hemisphere on non-invasive epilepsy monitoring. Invasive monitoring demonstrated seizure onset in the left temporal mesial area.

Cortical epilepsy

Patient 7 was a 27-year old female with right posterior temporal lobe epilepsy. She suffered simple and complex partial seizures. FDG-PET demonstrated right posterior temporal hypometabolism and EEG and MEG localized interictal epileptiform spikes to the right occipital area. MRI demonstrated a right occipital area of cortical dysplasia, consistent with the patient's left homonymous hemianopia.

Patient 8 was a 50-year old male who had a left hemispheric localized cortical dysplasia associated with epilepsy and a prior history of stroke and transient ischemic attack. The MRI showed gyral expansion in the left frontal lobe with abnormal T_2 signal extension through the cortical mantle to the ventricular margin. The morphology suggests focal transmantle cortical dysplasia with balloon cells. Single voxel MR spectroscopy and MRSI demonstrated elevated choline, consistent with focal cortical dysplasia. At the time of testing he had failed to gain complete seizure control despite trying multiple anti-epileptic medications.

DATA ACQUISITION

Resting-state fMRI data were acquired using a MEVI pulse sequence with flyback along the k_z-direction, which was described in Posse et al. (2012). Briefly, multiple adjacent slabs were excited sequentially in a single TR and encoded using repeated EPI modules with interleaved phase encoding gradients, fourfold acceleration using partial parallel imaging (GRAPPA), 6/8 partial Fourier encoding, and oversampling along the slab-direction. The reconstruction pipeline used distributed computing across the scanner using the ICE environment for in-plane (k_x, k_y) reconstruction and the external workstation using TurboFIRE (Posse et al., 2001) for reconstruction of the third dimension (k_z) as described in Posse et al. (2012). The time delay from acquisition to display of reconstructed images was less than a TR. MEVI data were acquired using the following parameters:

- Four-slab EVI/MEVI4: TR: 276 ms, TE_{eff}: 28 ms, α: 10°, four slabs in AC/PC orientation, interleaved acquisition order, slab thickness: 24 mm, inter-slab gap: 10%, matrix per slab: $64 \times 64 \times 8$, Field of View (FOV) per slab: $256 \times 256 \times 32\,mm^3$, reconstructed isotropic voxel dimensions: 4 mm, 27 slices, scan time: 5 min and 15 s using 1100 scan repetitions.
- Two-slab EVI/MEVI2: TR: 136 ms, TE_{eff}: 28 ms, α: 10°, two slabs in AC/PC orientation, slab thickness: 42 mm, inter-slab gap: 10%, matrix per slab: $64 \times 64 \times 8$, FOV per slab: $256 \times 256 \times 48\,mm^3$, reconstructed voxel dimensions: $4 \times 4 \times 6\,mm^3$, 13 slices, scan time: 5 min and 16 s using 2200 scan repetitions.

The 32 channel coil was used in one healthy control studied with MEVI2, in two of the five patients studied with MEVI2, and in two of the three patients studied with MEVI4, where one patient was scanned using both methods. *Patient 7* was studied using MEVI2 with the 12-channel coil and eight repetitions of 2.5 min scan time.

For comparison, resting-state scans in one healthy control was performed with multi-echo EPI using six TEs ranging from 5.8 to 49 ms, TR: 2 s, FOV 256 mm, spatial matrix, threefold GRAPPA acceleration, 6/8 partial Fourier encoding, 3.6 mm slice thickness, 10% slice gap, 168 scan repetitions, and 5 min 55 s scan time. Multi-echo data were combined using weighted echo averaging (Posse et al., 1999).

Task-based fMRI in patients was performed with multi-echo EPI using 10 TEs ranging from 5.8 to 82 ms, TR: 3 s, FOV 256 mm, spatial matrix, threefold GRAPPA acceleration, 6/8 partial Fourier encoding, 3.6 mm slice thickness, 10% slice gap, 56 scan repetitions, scan time: 3 min 12 s. Multi-echo data were combined using weighted echo averaging (Posse et al., 1999).

Structural imaging was performed using high-resolution Turbo-Spin-Echo and multi-echo MP-RAGE scans. Diffusion tensor MRI was performed using TR/TE: 9 s/84 ms, 35 gradient directions, *b*-values: 0 and 800 s/mm^2, voxel size: $2 \times 2 \times 2\,mm^3$, and scan time: 5 min 42 s.

RESTING STATE AND ACTIVATION TASKS

Resting-state scans were performed during eyes open condition. Subjects were instructed to relax, clear their minds, and fixate on a crosshair presented on a computer screen.

The block-design auditory-gated visual-motor activation task consisted of eyes open in the lit scanner environment versus eyes closed, and simultaneous 2 Hz right hand index finger tapping versus rest. Subjects were asked to tap with maximum extension of the index finger. Covert word generation was performed in response to presentation of single letters. The task duration was 12 s and the interstimulus interval was 18 s. Five blocks of task activation were performed. Subjects were instructed to attend to each task with a constant effort across scans. Paradigm presentation was programed using ePrime software (Psychology Software Tools, Inc., Pittsburgh, PA, USA). Visual stimulation was provided using an in-house built MR compatible projection system. Auditory stimulation was delivered using an MR compatible headset (Avotek Inc., Stuart, FL, USA). An in-house developed button-response device (MIND Research Network, Albuquerque, NM, USA) was employed to monitor motor task execution.

DATA ANALYSIS

Retrospective ICA analysis

Spatial ICA was performed using the GIFT software package v1.3i[1]. Preprocessing using SPM8[2] consisted of motion correction, coregistration with the EPI.mni template and spatial

[1]http://mialab.mrn.org/software/gift/
[2]http://www.fil.ion.ucl.ac.uk/spm/

normalization to ensure consistent multi-session and/or multi-subject analysis. Spatial interpolation and Gaussian smoothing ($6 \times 6 \times 6\,mm^3$) was applied. The ICA algorithm used throughout was FastICA introduced by Hyvarinen and Oja (1997), since it had previously been shown to be more robust and computationally efficient compared with the competing alternative approaches for fMRI data analysis (Mutihac and Van Hulle, 2004). The settings used for all data sets were the following: epsilon: 10^{-6}, maximum number of iterations: 1024, maximum number of fine-tuning sessions: 64, using tanh as the non-linear transfer function, sample size: 1, deflation mode, stabilization: on, and pow3 as "g" function. In order to estimate the data subspace (model selection), MDL was applied to the raw data. Alternatively, heuristically settings of 64 and 128 estimated number of independent latent sources, respectively, were investigated in view of detecting as many as possible default networks irrespective of any data model selection criteria. The validation of ICA decomposition was carried out by running ICASSO[3] for each subject, so that the most stable directions were selected after statistical resampling (bootstrap) of the raw data. Principal component analysis (PCA) was used for prewhitening based on singular value decomposition. A Z-threshold of 1.2 was used to map independent components (ICs). The maximum Z-scores in each component was measured. ICs representing RSNs were identified by visual inspection in reference to the MNI brain atlas using spatial selection criteria described for 7 RSN categories and 28 components identified as RSNs in Allen et al. (2011). RSNs were further identified by slowly modulated signal time courses that were well above noise level. The power spectral density (PSD) estimate was computed by means of Welch's overlapped segment averaging estimator implemented in MATLAB.

A time-frequency analysis of the time courses of RSN identified in two-slab EVI data was performed using the `spectrogram` function in MATLAB with a 28.6-s window for the FFT and 24.3 s overlap. The high-frequency limit of the RSN spectrum was measured using an amplitude threshold that was set at the level of the peaks of the high-frequency noise level outside of the cardiac and the respiratory bands.

Online seed-based sliding-window correlation analysis with meta-statistics

Real-time fMRI analysis was performed using TurboFIRE (Posse et al., 2001). Data preprocessing included motion correction, spatial normalization into MNI space using the SPM99 EPI template (Gao and Posse, 2003), segmentation of the MNI atlas space into 144 brain regions in reference to the Talairach Daemon Database that segregated left and right hemispheric regions (Zheng et al., 2013), and spatial smoothing using an $8 \times 8 \times 8\,mm^3$ Gaussian filter. Signal fluctuation due to cardiac pulsation and respiration was suppressed using a 4-s time domain moving average filter (Lin et al., 2011). Detrending of confounding signal changes using weighted subtraction of multiple ROI time courses from white matter, CSF, and the entire brain was implemented as an option. Six single voxel seed locations were selected in reference to the MNI coordinates of the peak activations in six of the seven principal RSN categories reported in Allen et al. (2011):

- Auditory RSN (IC17): left superior temporal gyrus (BA22), coordinate: −51, −18, 7
- Sensorimotor RSN (IC7): left precentral gyrus (BA4), coordinate: −52, −9, 31
- Visual RSN (IC64): bilateral lingual gyrus (BA17, 18), coordinate: 1, −71, 13
- Default mode RSN (IC50): bilateral precuneus (BA7), coordinate: 1, −64, 43
- Attention RSN (IC34): left inferior parietal lobule (BA40), coordinate: −47, −57, 39
- Frontal RSN (IC42): right inferior frontal gyrus (BA45), coordinate: 50, 23, 2

The signal time course within each seed region was used as input to dynamic reference vector modeling (Gao and Posse, 2004), which was adapted to bypass convolution with the hemodynamic response function. Seed-based sliding-window correlation analysis was combined with a meta-statistics approach that employs an efficient running variance algorithm (Welford, 1962) across dynamically updated correlation maps to generate cumulative meta-statistics maps of the mean and the standard deviation. The sliding-window width (N_w) was 4, 8, 28, 52, 105, 210, or 420 scans, i.e., 1, 2, 4, 8, 15, 30, or 60 s, respectively. The initial 50 scans were discarded (N_d). Correlation values were threshold with correction for degrees of freedom as described in eq. 13 in Bandettini et al. (1993) using a cross-correlation threshold of 0.52. Meta-statistics were computed at each TR starting at ($N_d + N_w$) and the final meta-statistics maps were used for individual and group analysis. The final meta-statistics maps were segmented into 144 brain regions based on the modified Talairach Daemon database. Cross-correlation coefficients between the six seed ROI time courses were computed at each TR.

Offline processing of seed-based connectivity results

A metric of functional network connectivity (FNC) was created by spatially averaging the meta-statistics maps within each brain region. The group average across nine subjects of the *intra-network* FNC within each of six major seeded RSNs was computed using the following subset of brain regions (Allen et al., 2011):

- Auditory RSN: left and right BA22, BA24
- Sensorimotor RSN: left and right BA2, BA4, BA6
- Visual RSN: left and right BA17, BA18
- Default mode RSN: left and right BA7, BA10, BA23, BA31, BA32, BA39
- Attention RSN: left and right BA8, BA40
- Frontal RSN: left and right BA22, BA44, BA45

Signal time courses from the six seed regions were extracted at each TR to represent RSN time courses. A matrix of cross-correlation coefficients between the different RSN time courses was computed as a metric of *inter-network* FNC at 4 s intervals. Time averaged matrices were computed across entire scans. The rows of the inter-network FNC matrix were averaged to obtain a metric of *global* FNC for each seed region. Group averages of the inter-network and global FNC across nine subjects were computed.

[3]http://www.cis.hut.fi/projects/ica/icasso/

Cardiac pulsatility

The time course of ICs with cardiac-related signal pulsation, measured in nine healthy controls and in seven patients who underwent resting-state fMRI using MEVI2, was analyzed in a beat-by-beat manner using an automatic delineator method that identifies fiducial points of the pulsation waveform (Li et al., 2010) to enable coherent time averaging of the pulsation waveforms in the presence of heart rate variability. The averaged waveforms were replicated 128 times and Fourier transformed to create power spectra of cardiac-related pulsation. The peak amplitudes at the cardiac frequency, the first harmonic, and the second harmonic were measured. The ratio R of the amplitude of the peak at the cardiac frequency with respect to the amplitude of the first harmonic was computed.

Diffusion tensor imaging

DICOM images were converted to NIFTI format using the MATLAB toolbox MRIconvert. Eddy current correction was performed in FSL using the FDT Diffusion toolbox. Brain masking was applied to exclude artifacts outside the brain. DTI analysis with tractography was performed using MedINRIA software[4]. Manually defined seed ROIs in the motor pathways were used for fiber tracking.

Statistical analysis

The TurboFIRE data output was post-processed using custom PERL scripts and spreadsheets, and standard MATLAB toolboxes. Statistical analysis was performed using a two-tailed heteroscedastic Student's t-test.

RESULTS

RESTING-STATE fMRI IN HEALTHY CONTROLS USING ICA

Independent component analysis analysis of MEVI2 and MEVI4 data showed clear delineation of major RSNs (**Figure 1A**) described in Allen et al. (2011), and separation of multiple ICs showing cardiac- and respiration-related signal pulsation. ICs with RSNs were characterized by slowly varying signal time courses with high contrast-to-noise-ratio well above noise level (**Figure 1B**) and small contamination from cardiac- and respiration-related signal pulsation (**Figure 1C**). Cardiac-related signal pulsation was resolved on a beat-by-beat basis in synchrony with peripheral pulse recording (**Figure 1D**). The corresponding ICs mapped cardiac signal pulsation in insular cortex, cortical gray matter, brain stem, sagittal sinus, and ventricles. Respiration-related signal changes were detected at the edges of the imaging slabs. Brief head movements were clearly detected as separate ICs with spatial components located in orbital frontal cortex and at the edges of the brain.

Independent component analysis of 5 min 25 s scans collected in eight subjects using MEVI2 and the 12-channel coil separated on average 28.4 ± 7.2 ICs, which consisted on average of 11.5 ± 5.7 ICs corresponding to the major RSNs described in Allen et al. (2011). In some subjects multiple RSNs belonging to a particular category (e.g., some of the six sensorimotor RSNs described in Allen et al., 2011) were mapped into different ICs, but co-localized with RSNs belonging to other categories (e.g., the auditory RSN) within single ICs. As a consequence, the sum of RSN, cardiac, respiratory, and artifact ICs exceeded the number of total ICs. On average, 12.8 ± 4.9 RSNs were identified in these ICs with some of the ICs containing up to three different RSNs. In addition, 6.6 ± 3.3 ICs corresponded to cardiac pulsation, 4.6 ± 2.9 ICs corresponded to respiration-related signal changes, and 7.8 ± 4.9 ICs corresponded to artifacts related to head movement and to 1 Hz signal oscillations, predominantly at the edges of the slabs (**Table 1**). Maximum Z-scores ranged from 5.2 to 20.2 for attentional RSNs with other RSNs having maximum Z-score within this range. The average Z-score across all RSNs was 11.8 ± 0.7. ICA analysis of data collected in one subject using the 32 channel coil separated 42 ICs, of which 20 were related to RSNs, 10 were related to cardiac pulsation, 5 were related to respiration related signal changes, and 13 were related to head movement and artifacts, including coherent constant amplitude 1 Hz signal oscillation at the edges of the brain and in parietal cortex. Z-scores reached up to 32.2 for sensorimotor and attentional RSNs, and the average Z-score across all RSNs was 18.4. These results are consistent with the data collected in the patients (see below). **Table 1** shows the results averaged across all nine subjects.

The time-frequency analysis of signal fluctuations in RSNs measured with MEVI2 was performed in five subjects. The spectrograms (**Figures 1C,D**) displayed low-frequency components that had maximum power around 0.1 Hz and extended on average to a maximum frequency of 0.27 Hz (**Table 2**). Short-term fluctuations of this frequency range at short times scales (i.e., individual 24.3 s segments) were up to ± 0.1 Hz. The range of measurable RSN frequencies was also limited by residual signal fluctuation due to respiration, which in some cases overlapped with RSN frequency components.

SENSITIVITY COMPARISON MEVI2, MEVI4, AND MEPI

In one healthy subject a sensitivity comparison was performed between MEVI2, MEVI4, and weighted averaged multi-echo EPI using the 12-channel coil and identical isotropic resolution ($4 \times 4 \times 4\,mm^3$). ICA analysis of the multi-echo EPI data separated 33 ICs, which were related to 16 RSNs (**Table 1**). RSNs measured with multi-echo EPI were mixed with aliased cardiac- and respiration-related signal pulsation and displayed spurious connectivity in white matter. ICs with predominantly cardiac (2) and respiratory (3) signal changes in these data were only identifiable based on their spatial localization in reference to the EVI results. The MEVI4 data in this subject displayed improved separation of cardiac- and respiration-related signal contamination, but smaller number of separated ICs (21), with 14 identifiable RSNs. The corresponding MEVI2 data showed further reduction of spurious connectivity in white matter, larger number of ICs (34) comparable to multi-echo EPI and larger number of identified RSNs (21).

In patients a corresponding trend was found: MEVI2 separated more ICs on average than MEVI4 (38.6 ± 13.4 versus 26.0 ± 12.1) with more ICs corresponding to RSNs (16.6 ± 7.8 versus 7.0 ± 5.3, $p = 0.09$). MEVI2 enabled identification of a

[4]http://www-sop.inria.fr/asclepios/software/MedINRIA/

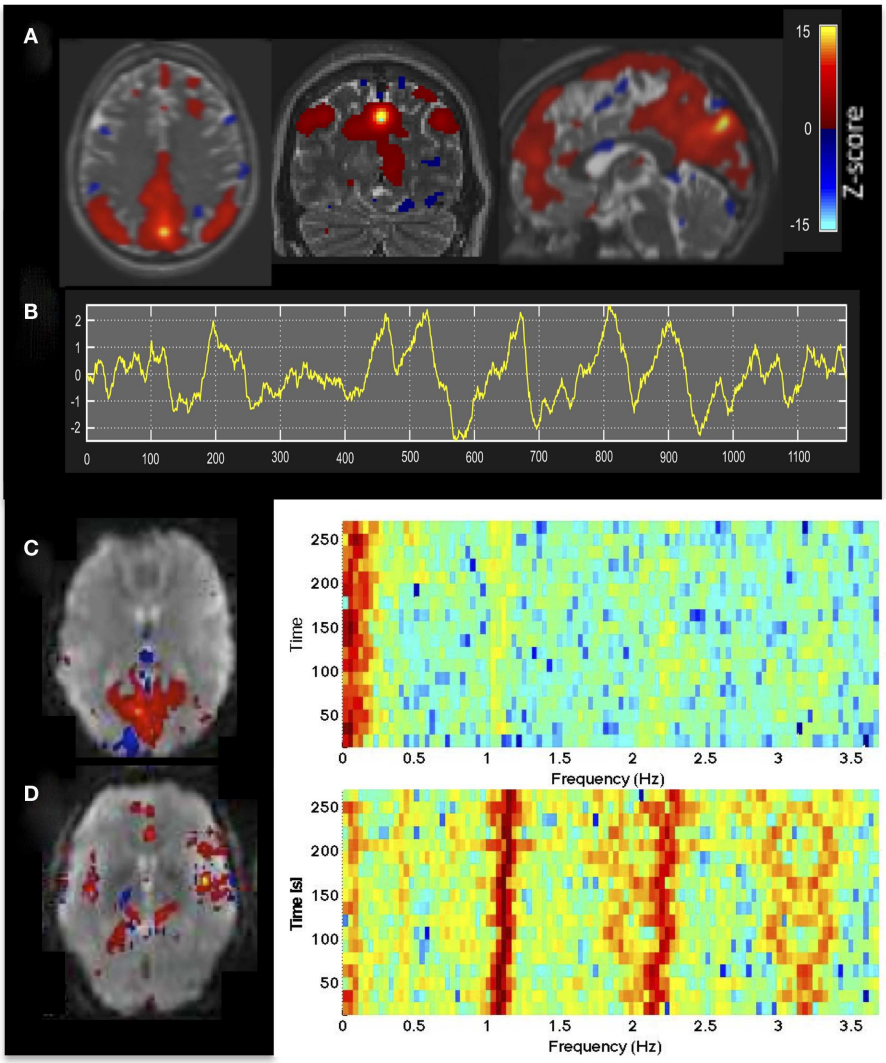

FIGURE 1 | (A) Resting-state fMRI in a healthy control using whole brain MEVI4 with TR: 276 ms. The spatial ICA map with *Z*-scores up to 15 shows a clearly delineated default mode RSN. **(B–D)** ICA-based mapping of RSNs and cardiac pulsatility using MEVI2 with TR: 136 ms. **(B)** Slowly varying signal changes well above noise level ($z_{max} > 10$) distinguish **(C)** RSNs from **(D)** cardiac-related signal pulsation. The corresponding spectrograms display **(C)** the dynamically fluctuating low-frequency power spectrum of the RSN and **(D)** the first and second harmonics of the cardiac pulsation.

larger number of RSNs (19.6 ± 9.1 versus 13.0 ± 8.9) and cardiac components (7.6 ± 4.4 versus 4.0 ± 1.7, $p = 0.16$) compared to MEVI4 (**Table 1**).

Using seed-based connectivity with meta-statistics (see below) MEVI2 yielded larger peak correlation coefficients and larger extent of connectivity across the two-slab volume compared with MEVI4 across a wide range of time scales from 4 to 60 s (**Figure 2**).

RESTING-STATE DYNAMICS USING SEED-BASED CONNECTIVITY WITH META-STATISTICS

The meta-statistics approach provided strong rejection of confounding signals from head movement, respiration, cardiac pulsation, and signal drifts (**Figures 3A,B**), without using regression of movement parameters and signals from white matter and CSF. The degree of rejection of confounding signals increased with decreasing sliding-window width, while mean correlation coefficients decreased only slightly. A window width of 60 s often provided considerable artifact suppression, but a 15-s window was preferred due to even more robust artifact suppression. The correlation coefficients in white matter and CSF using this approach were small, typically <0.2 (**Figure 3B**). Weighted subtraction of signals from white matter, CSF, and the entire brain did not result in consistent improvement of mapping the major RSNs.

Our data show high sensitivity for mapping intra- and inter-network connectivity at time scales as short as 4 s, which is consistent with the upper frequency range of signal fluctuation in major RSNs shown in **Table 2**. Interestingly, the auditory network displayed connectivity at time scales as short as 1 s with little decrease in mean correlation coefficient (**Figures 3C–F**). Using this meta-statistics approach RSNs were detected in tens of seconds. Some

Table 1 | Source separation using ICA in healthy controls and patients.

# Components		Total IC	RSN IC	Basal ganglia RSN	Auditory RSN	Sensori-motor RSN	Visual RSN	Default mode RSN	Attentional RSN	Frontal RSN	Lesion RSN	Sum/mean RSN	Cardiac IC	Respiratory IC	Artifact IC
CONTROLS															
MEVI2	Mean	29.9	11.8	0.0	0.8	2.4	2.3	2.0	4.6	1.4		13.6	7.0	4.7	8.3
($n=9$)	SD	8.1	5.4	0.0	0.4	2.6	1.3	0.9	2.4	0.9		5.2	3.3	2.7	4.9
*MEVI2**	$n=1$	34.0	19.0	0.0	0.0	9.0	1.0	4.0	6.0	1.0		21.0	3.0	6.0	6.0
*MEVI4**	$n=1$	21.0	8.0	1.0	1.0	1.0	4.0	1.0	5.0	1.0		14.0	2.0	1.0	8.0
*MEPI**	$n=1$	33.0	14.0	0.0	1.0	1.0	4.0	2.0	5.0	3.0		16.0	2.0	3.0	15.0
PATIENTS															
MEVI2	Mean	38.6	16.6	0.0	1.4	2.4	3.4	3.2	5.8	1.6	1.8	19.6	7.6	5.2	11.4
($n=5$)	SD	13.4	7.8	0.0	0.9	1.7	2.1	2.2	2.5	1.3	2.5	9.1	4.4	7.8	3.4
MEVI4	Mean	26.0	7.0	0.0	1.3	1.0	2.7	2.0	4.3	1.7	0.0	13.0	4.0	9.0	6.0
($n=3$)	SD	12.1	5.3	0.0	0.6	1.0	2.1	1.0	2.5	2.1	0.0	8.9	1.7	6.2	7.8
MEVI2**	Mean	18.3	6.9	0.1	1.1	1.1	2.4	1.4	2.6	1.0	1.1	10.9	3.3	1.0	7.9
	SD	1.0	1.8	0.4	0.4	0.4	0.9	0.5	0.7	0.0	0.8	2.0	0.5	0.9	1.4
MAXIMUM *Z*-SCORES: CONTROLS															
MEVI2	Mean				13.0	16.0	13.0	12.7	12.1	11.6		13.1	17.3	13.6	15.3
($n=5$)	SD				2.2	8.4	4.0	3.4	2.8	1.5		3.0	2.0	3.8	6.0

*Top: total number of ICs based on the MDL criterion, and number of detected ICs that correspond to RSNs, cardiac-related signal pulsation, respiration related signal changes, and artifacts (*same subject, **single subject, eight scan repetitions, 2.5 min per scan). Bottom: maximum Z-scores averaged across all ICs in a given category and across healthy controls. MEVI2 = partial brain two-slab EVI (TR: 136 ms), MEVI4 = whole brain four-slab EVI (TR: 276 ms), MEPI = multi-echo EPI (TR: 2 s).*

of the major RSNs, such as the DMN, the auditory network, and the visual network were often detectable in as little as 10–20 s. The localization and spatial extent of principal nodes of major RSNs using the seed-based analysis approach were comparable to the ICA results (**Figure 4**).

Mapping of dynamic changes in *intra-network* FNC revealed considerable differences in short-term fluctuations in different nodes of major RSNs. For example, the IPL region (BA39 + BA40) showed some of the strongest fluctuation within the DMN (**Figure 5**), consistent with a recent group ICA study (Allen et al., 2012). FNC between the 6 seeds and 144 brain regions averaged across an entire scan was predominantly positive and showed extensive connectivity across many brain areas. In general, major nodes of connectivity with higher short-term correlation were predominantly associated with lower standard deviation of short-term correlation as shown in **Figure 6**, which is an example of seed-based connectivity across 144 brain regions averaged across nine subjects using a 15-s sliding window. On the other hand, higher standard deviation was frequently measured in regions with lower short-term correlation. The default mode and the visual networks share a similar pattern of FNCs. There were notable right-left asymmetries in the meta-means maps: for example, FNC in the frontal network with BA45 showed the largest right side dominance (difference = 0.2), along with BA25, BA44, BA46, and BA47. The FNC in the attention network showed the largest asymmetry for BA39. The DMN showed the largest asymmetry in Medial Geniculum Body.

Table 2 | High-frequency cutoff of low-frequency resting-state signal fluctuations in healthy controls.

Subject	Mean (Hz)	SD (Hz)
1	0.29	0.02
2	0.25	0.02
3	0.32	0.09
4	0.26	0.02
5	0.22	0.02
Mean	0.27	0.03
SD	0.04	0.03

A group analysis in nine subjects demonstrated that *intra-network* FNC measured using this sliding-window based meta-statistics approach yielded intra-network correlation values that were comparable in amplitude with previous studies using ICA (**Figure 7**) (Allen et al., 2012). Intra-network FNC in major nodes of six principal RSNs decreases moderately at 4 s sliding-window width compared to 15 and 60 s sliding-window widths (**Figure 7A**). Some of the strongest intra-network FNC was measured within the DMN. Consistent with previous studies, temporal fluctuations in intra-network FNC increased with decreasing sliding-window width (**Figure 7B**).

A group analysis of *inter-network* FNC in nine subjects demonstrated mean correlation values comparable to previous studies

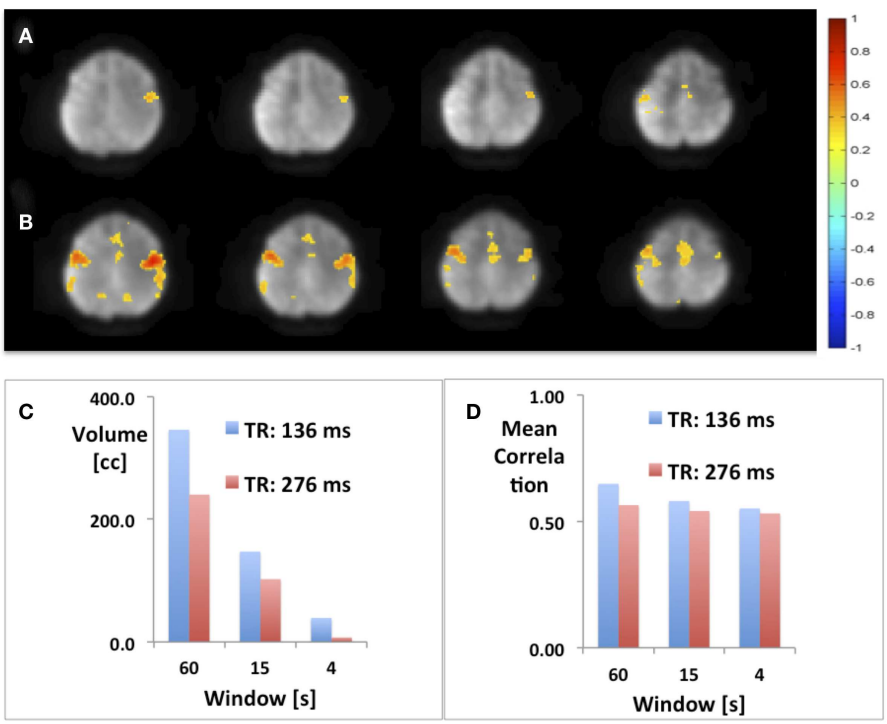

FIGURE 2 | Seed-based mapping with 4 s sliding window of the sensorimotor RSN comparing (A) MEVI4 (TR: 286 ms) and (B) MEVI2 (TR: 136 ms), which shows higher peak correlation and larger spatial extent of connectivity across the two-slab volume compared with MEVI4. (C) The spatial extent of connectivity decreases strongly with sliding-window width, but it is larger with MEVI2 compared to MEVI4 at all three time scales. **(D)** The mean correlation is comparable across the range of time scales.

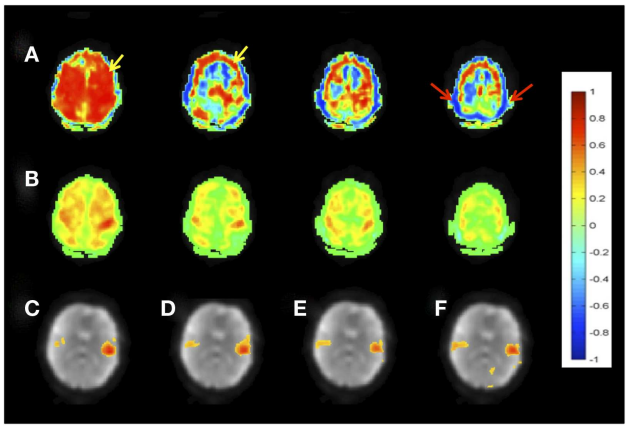

FIGURE 3 | Seed-based connectivity of the sensorimotor RSN measured with MEVI2 (TR: 136 ms). **(A)** Correlation across the entire 5 min scan without regression of confounding signal changes displays widespread artifacts (yellow arrow) and edge artifacts due to head movement (red arrows). **(B)** Sliding-window correlation analysis with meta-statistics using a 4-s sliding-window removes the artifacts and reveals the expected localization of the sensorimotor network in the mean meta-statistics map. **(C–F)** Seed-based connectivity of the auditory RSN shown as mean meta-statistics across the 5 min scan using sliding-window widths of **(C)** 15 s, **(D)** 4 s, **(E)** 2 s, and **(F)** 1 s.

using ICA (**Figures 8A–C**) (Allen et al., 2012). Some of the strongest inter-network FNC was measured between the DMN and the visual network, and between the DMN and the attention network. The inter-network connectivity increased moderately with increasing sliding-window width between 4 and 60 s. The *global* FNC averaged across nine subjects decreased moderately at 4 s sliding-window width compared to 15 and 60 s sliding-window widths (**Figure 8D**). Inline with the intra-network connectivity, temporal fluctuations in global FNC increased with decreasing sliding-window width (**Figure 8E**). The DMN displayed the strongest temporal fluctuation of global FNC at a time scale of 4 s.

Figure 8F shows a typical series of dynamic inter-network FNC matrices in a single subject for a seed in the DMN, which show both positive and negative FNC at short time scales (sliding-window width: 15 s) between the seed in the DMN and five seeds in task-positive RSNs. The corresponding five time courses of the short-term FNC within the sliding-window demonstrate rapidly changing correlations between positive and negative values (**Figure 8G**). The mean and the standard deviation across these correlation time courses show considerable fluctuation of inter-network coherence (**Figure 8H**). Similar short-term temporal dynamics of positive and negative FNC between the seed in the DMN and the five seeds in task-positive RSNs were observed in all subjects.

RESTING-STATE fMRI IN PATIENTS WITH NEUROLOGICAL DISORDERS

Patients exhibited a greater number of RSNs on average compared to healthy controls (**Table 1**) due in part to the transition to the 32 channel coil. Spatial displacement of major RSNs and reduced connectivity within RSNs was mapped in the vicinity of brain tumors and vascular malformations. Unanticipated connectivity was also found in some of the patients. The following cases demonstrated noteworthy changes in functional organization.

Patient 1 with a frontal lobe brain tumor showed much stronger activation of motor cortex and extensive activation of non-motor areas adjacent to the tumor during left hand index finger tapping compared to right hand index finger tapping (**Figure 9**). This may reflect the increased effort of left hand task execution, which the patient reported, and dysregulation of cerebro-vascular coupling within the edema around the tumor. By contrast, the sensorimotor RSNs measured in this patient showed comparable focal connectivity within both motor cortices. Interestingly, the sensorimotor RSN was separated into two lateralized subnets, which suggests reduced functional connectivity within the sensorimotor RSN due to the tumor. In this patient we also illustrate the integration of RSN maps into the StealthStation neuronavigation system (Medtronics, MN, USA) for presurgical planning using the sum of all RSNs in the vicinity of the tumor (**Figure 9H**).

Functional connectivity mapping in *patient 2* with a posterior temporal lobe tumor showed decreased connectivity in and adjacent to the lesion in DTI-based fiber tracking and in the default mode RSN. Interestingly, the sensorimotor RSN was not detected with ICA although the other major RSN were present and task-based fMRI clearly localized sensorimotor cortex. Seed-based connectivity using seed locations based on motor activation that was detected in task-based fMRI mapped the sensorimotor RSN.

Patient 3 with a temporal lobe AVM exhibited extensive recruitment of brain regions in the vicinity of the AVM during right finger tapping, which may reflect the considerably increased effort of task execution compared to left hand finger tapping and dysregulation of cerebro-vascular coupling in the vicinity of the AVM (**Figures 10A–K**). The resting-state sensorimotor network showed a complete disconnection on the side of the AVM, resulting in the detection of with three separate RSNs in the left and the right sensorimotor cortex and the supplementary motor area.

Patient 4 with an occipital lobe AVM displayed asymmetrical activation in visual cortex during visual stimulation that excluded the rims of the AVM (**Figures 10L–Q**). Interestingly, a visual imagery task that involved imagining the "aura" resulted in a complex activation pattern along the rims of the AVM, suggesting that these regions may be involved in the visual aura associated with the seizure. The major visual RSN, which was detected both with ICA and seed-based correlation analysis, excluded the rims of the AVM. However, a seed placed in the AVM revealed extensive connectivity with secondary visual cortex.

Patient 6 with temporal lobe epilepsy exhibited hyperplasia in anterior left frontal cortex (**Figures 11A–D**), which in DTI-based fiber tracking shows reduced connectivity and, uncharacteristically for epilepsy, hypermetabolism in this region in the FDG-PET scan. Cortical recordings using an implanted electrode grid (**Figure 11B**) showed that this region was not the source of epileptic activity. The default mode RSN showed asymmetric connectivity in the frontal cortex. The attention RSN displayed spatial asymmetry as well, whereas the visual RSN displayed connectivity with the hyperplasia lesion. The lesion itself was also connected to other cortical regions, which was mapped in a separate IC. In this patient we also illustrate the integration of RSN maps into the

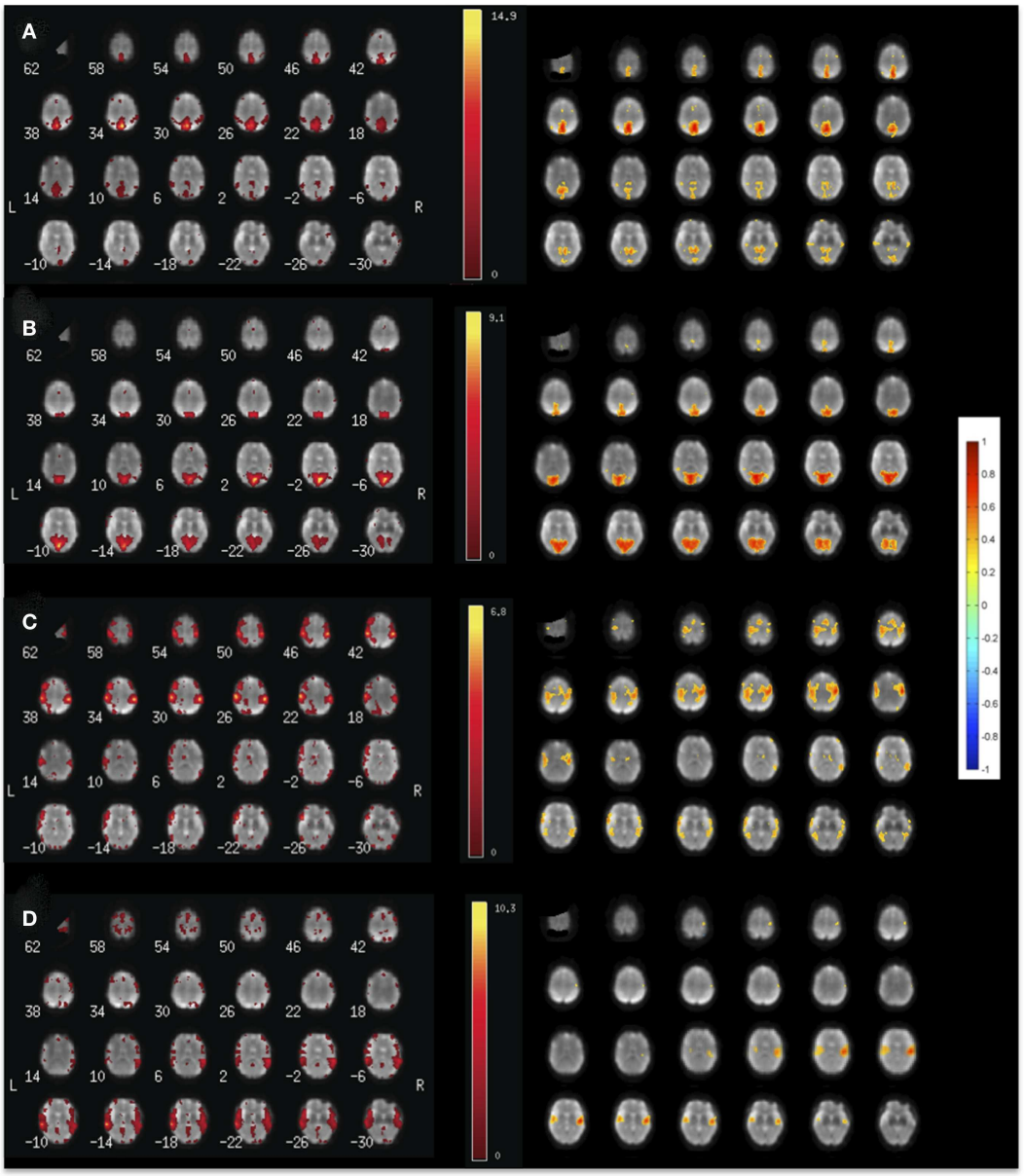

FIGURE 4 | Comparison of (left) ICA and (right) seed-based connectivity in a single subject for mapping (A) the default mode RSN, (B) the visual RSN, (C) the sensorimotor RSN, and (D) the auditory using MEVI2 at TR: 136 ms.

StealthStation neuronavigation system (Medtronics, MN, USA) for presurgical planning.

Functional connectivity mapping in *patient 7* with cortical epilepsy revealed progressive changes in functional connectivity during eight consecutive resting-state scans (**Figures 11E–J**). In the third scan the visual RSN became spatially asymmetric. In the fourth scan a new RSN was detected that encompassed right posterior parietal and temporal cortex, a region that showed interictal spike activity in EEG and MEG. The visual RSN was spatially asymmetric and the sensorimotor RSN was not detected. In the fifth scan a spatially asymmetric visual RSN was detected again. In scan 6 the spatial asymmetry of the visual RSN increased, excluding the right posterior temporal lobe, and negative correlation with the right motor and posterior parietal cortex was seen. In scan 8 the previously detected RSN in right posterior parietal and temporal cortex extended into more inferior brain regions.

CARDIAC-RELATED PULSATILITY

Cardiac-related physiological signal fluctuation in healthy controls was mapped into clearly separated ICs in insular cortex, cortex, sagittal sinus, brain stem, and CSF. Several cardiac-related ICs of vascular origin with Z-scores ranging from 8.1 to 20.7 were detected in insular cortex, cortex, sagittal sinus (**Figure 12**), in addition to pulsation in the brain stem ($Z = 22.2$) and in the

ventricles ($Z = 16.5$). This pulsation, which was detected on a beat-by-beat basis, was synchronous with peripheral pulse recording throughout the entire scan. Power spectra showed significant amplitude at the first harmonic and in some cases also at the second harmonic (**Figure 12C**). The waveform of the cardiac-related signal pulsation in insular cortex (**Figures 12D,E**) was inverted with respect to typical Transcranial Doppler Ultrasound (TDU) and phase contrast MRI waveforms obtained from the middle cerebral artery (e.g., Wagshul et al., 2011), which suggests that the cardiac-related signal pulsation in our MEVI data is dominated by BOLD contrast rather than in-flow effects as usually assumed for BOLD contrast fMRI (e.g., Kruger and Glover, 2001). The signal pulsation in our data is also consistent with the pulsation waveform measured in cingular cortex in one of the early studies using conventional EPI (Dagli et al., 1999). The first harmonic of the cardiac-related pulsation was stronger in components with vascular origin (insula, sagittal sinus) compared to components originating from the ventricles and the brain stem (**Figure 13**). Multiple ICs with strongly enhanced cardiac-related signal pulsation were measured in *patient 1* with a brain tumor and in *patient 3* with an arterio-venous malformation (**Figure 13B**). Distinct time shifts on the order of 100 ms were measured between cardiac-related ICs in and adjacent to the AVM, which reflect different phases of the cardiac-related pulse wave propagation. The statistical analysis showed a trend (t-test, $p = 0.14$) toward a larger amplitude ratio R in gray matter in patients compared with healthy controls (**Figure 13C**).

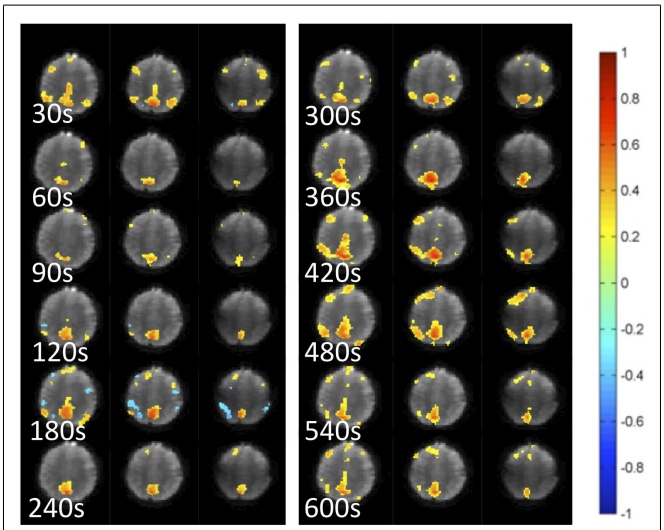

FIGURE 5 | Dynamic changes in temporal correlation within the default mode RSN measured at 30 s intervals using MEVI2 (TR: 136 ms) and sliding-window seed-based correlation analysis with 30 s window in a healthy control.

DISCUSSION

ICA AND SEED-BASED CONNECTIVITY

Mapping of intrinsic signal variation mostly in the low-frequency band <0.1 Hz has emerged as a powerful tool and adjunct to task-related fMRI and DTI-based fiber tracking for mapping functional connectivity within and between RSNs (Fox et al., 2005; De Luca et al., 2006; Raichle and Snyder, 2007; Schopf et al., 2010; Li et al., 2011). Recent studies have shown that dozens of different RSNs can be measured across groups of subjects (Abou-Elseoud et al., 2010; Allen et al., 2011). However, source separation with ICA in

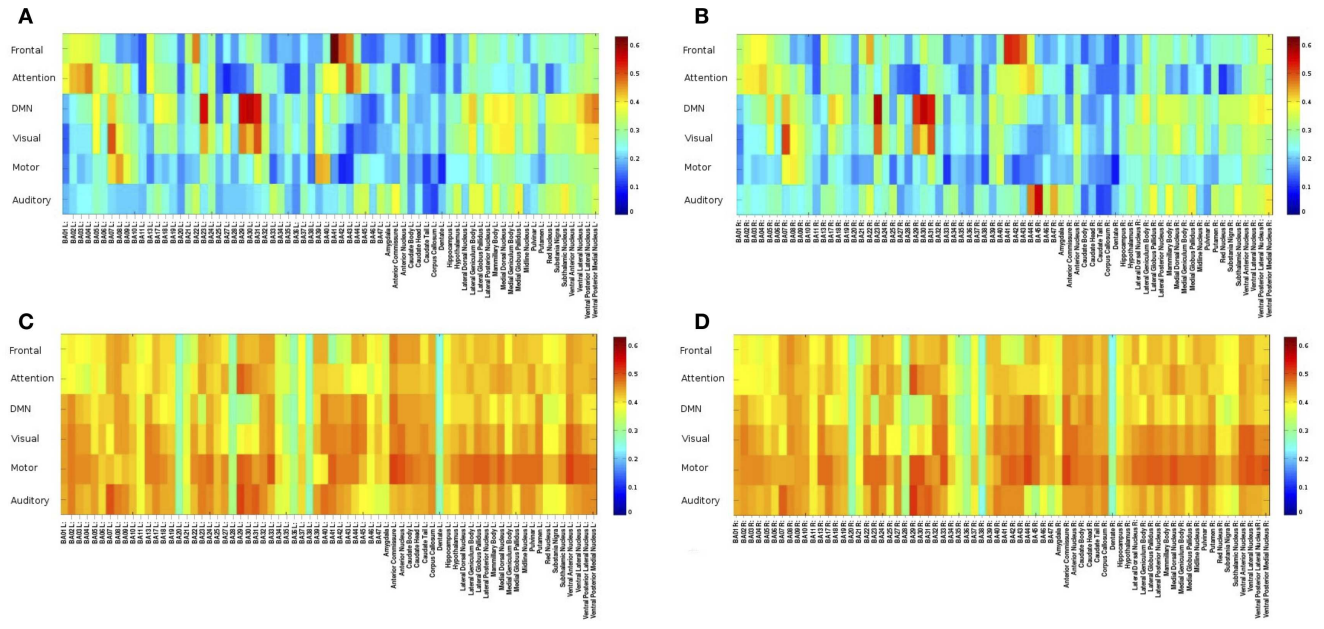

FIGURE 6 | Seed-based FNC between 6 seed regions and 144 brain regions using MEVI2 (TR: 136 ms) and meta-statistics averaged across nine healthy subjects at the end of the scan. Spatial means of **(A)** left hemisphere meta-statistics means, **(B)** right hemisphere meta-statistics means, **(C)** left hemisphere meta-statistics standard deviations, and **(D)** right hemisphere meta-statistics standard deviations.

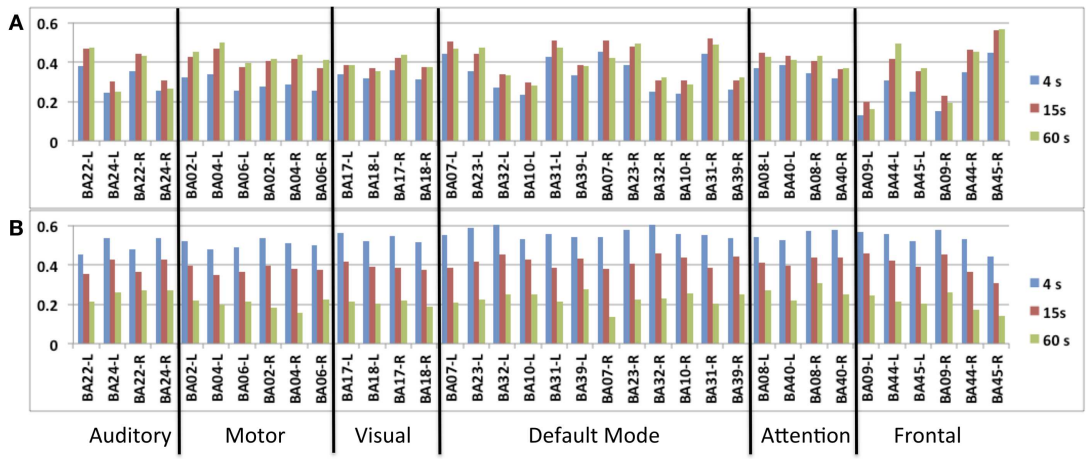

FIGURE 7 | Seed-based intra-network FNC at the end of the scan averaged across nine healthy subjects using MEVI2 (TR: 136 ms). Spatial means of the meta-statistics **(A)** means and **(B)** standard deviation in a subset of 18 selected Brodmann areas as a function of sliding-window width (4, 15, and 60 s).

individual subject data using conventional EPI is limited by the contrast-to-noise ratio of the signal fluctuations and aliasing of cardiac- and respiration-related signal fluctuations, which requires model-based retrospective deconvolution methods (Glover et al., 2000). Our data using MEVI and ICA show that a considerable number of RSNs that have been mapped in a recent group study (Allen et al., 2011) can be identified in single subjects. Our data also show that source separation in single subjects exhibits considerable inter-individual variability. This variability may reflect inter-individual differences in dynamic cycling between different FNC states, including hypersynchronization, drowsiness, and low synchronization (Allen et al., 2012), as well as in neurovascular coupling and physiological signal fluctuation. Physiological noise correction might further improve ICA analysis, in particular in data sets that exhibit low contrast-to-noise ratio in the RSN signal time courses. Given the spatial heterogeneity in cardiac-related signal pulsation shown in our study this approach will require a comprehensive analysis of ICA source separation as a function of contrast-to-noise ratio in the RSN, respiration, and cardiac frequency bands using regionally adaptive signal pulsation models. This approach will be explored in a future study. Movement during the fMRI acquisition is a major confound for resting-state connectivity studies obscuring networks as well as creating false-positive connections (Satterthwaite et al., 2012; Van Dijk et al., 2012) despite state-of-the-art motion "correction" in post-processing. Monitoring these dynamics in real-time to assess data quality is expected to improve consistency of data quality in clinical research studies and our understanding of the underlying neurophysiological mechanisms.

Seed-based correlation analysis (Van Dijk et al., 2010) and spatial ICA (Calhoun et al., 2001) are the principal tools to map functional connectivity, which have been shown to provide similar results (Van Dijk et al., 2010; Erhardt et al., 2011). Seed-based connectivity measures have been shown to be the sum of ICA-derived within- and between-network connectivities (Joel et al., 2011). Seed-based correlation analysis is suitable for real-time resting-state fMRI due to the high sensitivity of correlation analysis and straightforward interpretation of results (Cole et al., 2010a). In contrast, data driven approaches, such as ICA, in single subjects may require considerable user interaction to interpret resulting maps and time courses. Semi-automated data sorting routines for ICA are under development, but actual real-time applications have not yet been demonstrated (Soldati et al., 2013a,b). A model-based approach such as seed-based correlation analysis that uses prior knowledge is advantageous compared to ICA for detecting small signal changes. However, seed-based techniques are sensitive to the choice of the seed regions (Cole et al., 2010a). Furthermore, seed-based correlation analysis requires regression of confounding signals, which typically include the six parameters of motion correction and their derivatives, and the average signal from up to three brain regions (whole brain over a fixed region in atlas space, ventricles, and white matter in the centrum semiovale). Regression of these signals is computationally intensive and may remove RSN signal changes that are temporally correlated with confounding signals. Here we introduce the combination of seed-based sliding-window correlation analysis with a meta-statistics approach that employs a running mean and standard deviation (Welford, 1962) across dynamically updated correlation maps to generate cumulative meta-statistics maps. Our data show that this meta-statistics approach provides strong rejection of confounding signals from head movement, respiration, cardiac pulsation, and signal drifts (**Figure 3**) and high sensitivity for mapping inter- and intra-network connectivity dynamics at time scales as short as 1 s without the need for regression of confounding signals (**Figures 6** and **7**). Furthermore, this methodology is suitable for real-time mapping of FNC dynamics as shown in **Figures 5** and **8**.

Independent component analysis on the other hand is a powerful data driven approach that has been applied in many group studies and is suitable for single subject analysis (Koopmans et al., 2012). ICA also performs spatial filtering, which enables segregation of spatially overlapping components. However, source separation with ICA is sensitive to the selection of the model order,

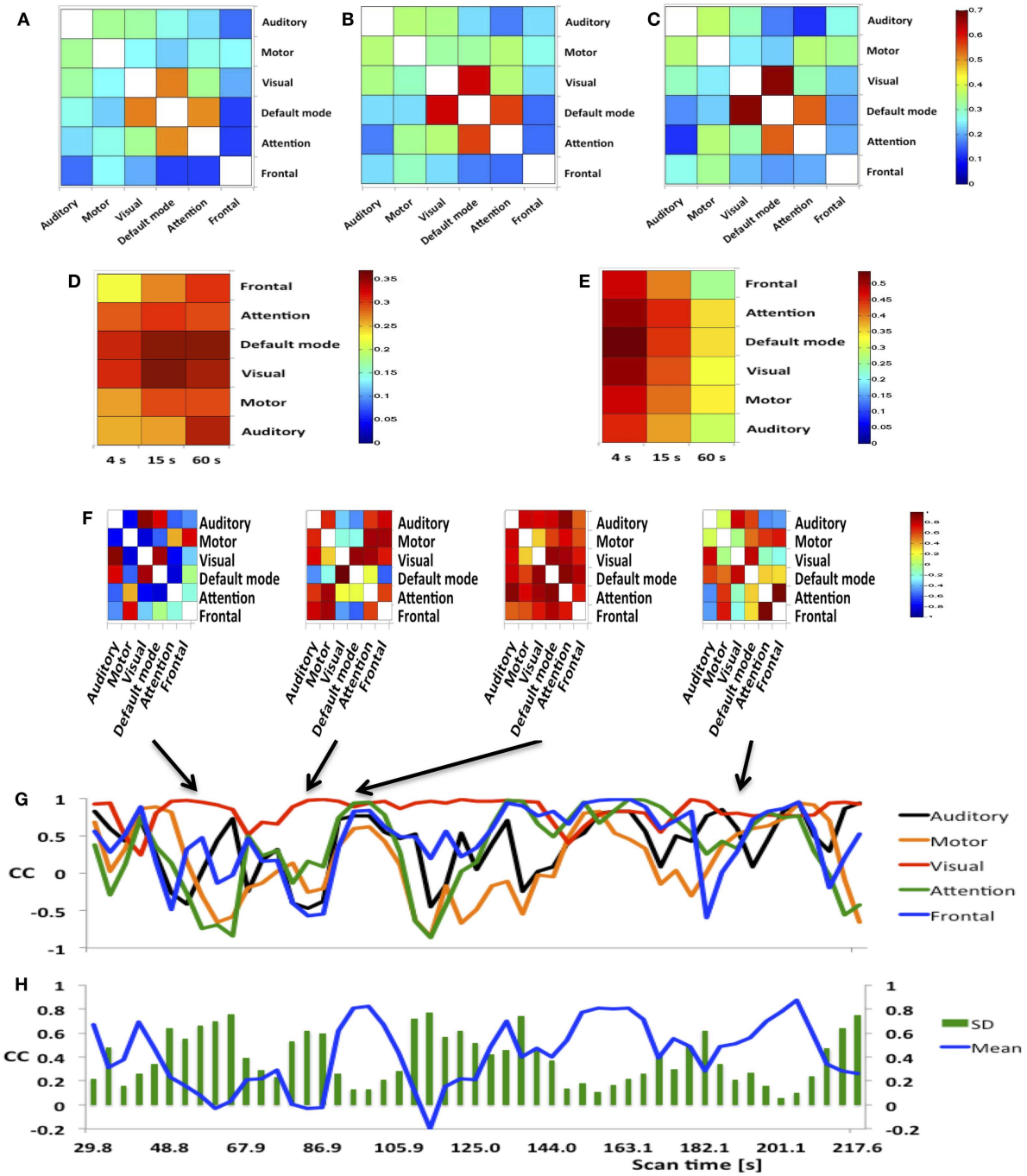

FIGURE 8 | (A–E) Seed-based inter-network FNC averaged across nine healthy subjects using MEVI2 (TR: 136 ms) and **(F–H)**. Simulated real-time monitoring of inter-network FNC in a single subject using MEVI2 (TR: 136 ms) with the 12-channel coil and a 15-s sliding window. Subject average of the meta-statistics correlation coefficient matrix for six seeds at a time scale of **(A)** 4 s **(B)** 15 s, and **(C)** 60 s at the end of the scan. Group-averaged **(D)** mean and **(E)** standard deviation of global FNC for six seeds at time scales of 4, 15, and 60 s at the end of the scan. **(F)** Selected connectivity matrices for 15 s sliding windows at time points of low (64, 83 s), high (95 s), and intermediate (190 s) synchronization in a single subject. **(G)** Corresponding time courses of the correlations between the cuneus seed time course of the DMN and the seed time courses of five major task-positive RSNs within the sliding window. **(H)** Corresponding time courses of the mean and standard deviation of the correlation time courses in **(G)** as a metric of inter-network FNC.

which is *a priori* unknown and necessitates dimensionality estimation approaches, such as the MDL, BIC, and AIC (Calhoun et al., 2001; Li et al., 2007). Furthermore, automated ordering of ICA components to enable consistent identification of RSNs is challenging. Using the MDL criterion to determine the model order resulted in a relatively small number of ICs relative to the

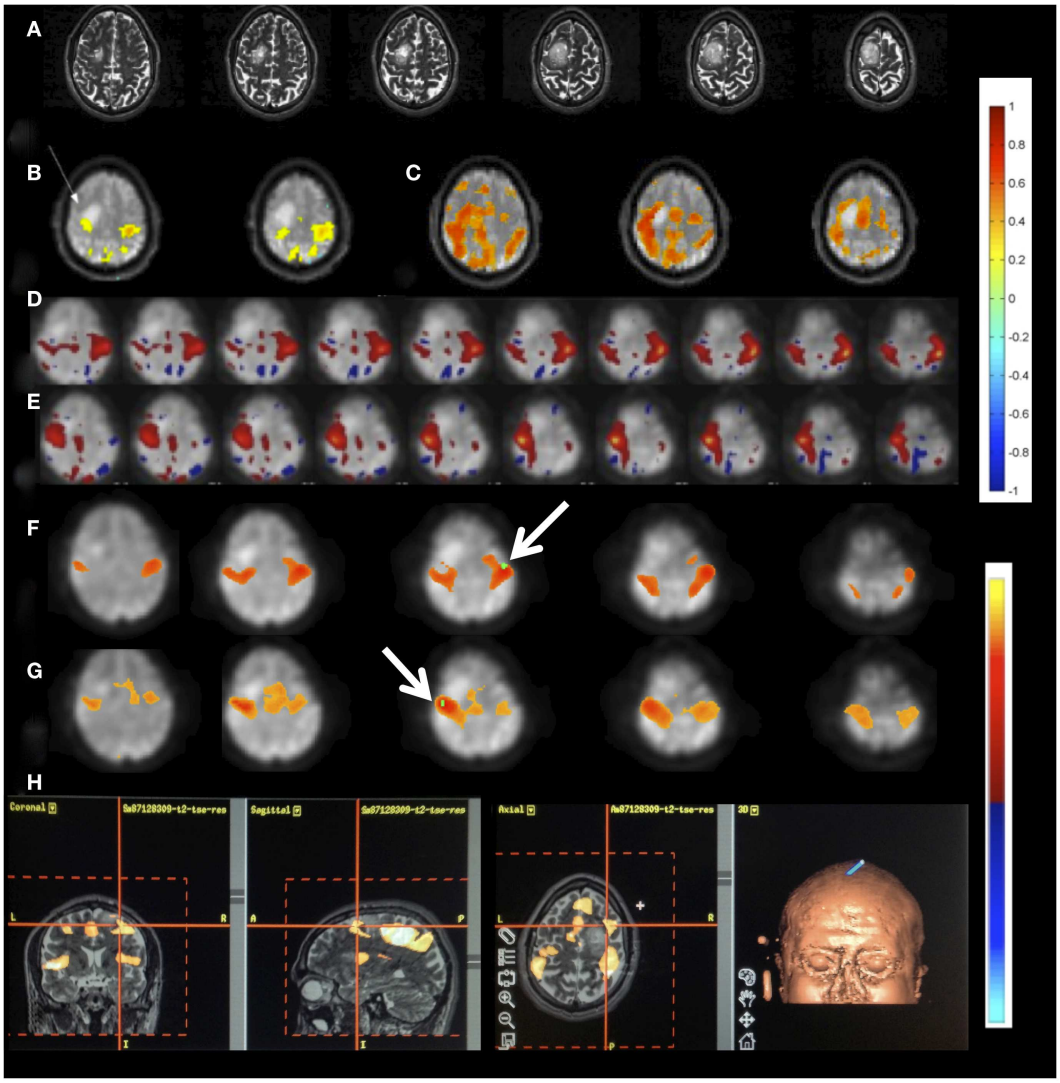

FIGURE 9 | Presurgical mapping in *patient 1 with right prefrontal low-grade oligodendroglioma*. **(A)** T2-weighted MRI. Task-based fMRI using MEPI (TR: 2 s). **(B)** Right hand finger tapping shows sharp delineation of eloquent cortex. **(C)** Left hand finger tapping shows diffuse activation in the vicinity of the tumor. Resting-state fMRI using MEVI2 (TR: 136 ms) and ICA shows **(D)** left sensorimotor cortex localization ICA ($z_{max} = 7.9$) consistent with task-activation in **(B,E)** right sensorimotor RSN mapping with showing more focal localization ($z_{max} = 12$). Seed-based analysis shows focal localization of the sensorimotor RSN consistent with ICA: **(F)** left motor seed and **(G)** right motor seed (arrows). **(H)** Sum of all seed-based resting-state networks in the vicinity of the tumor integrated into presurgical planning. Color scales for task-based correlation analysis and seed-based connectivity (top), and ICA (bottom) are shown on the right.

large number of time points in a MEVI scan. At shorter simulated scans times the ICA was less able to separate sources and we found that multiple RSNs were merged in single ICs. Our resting-state data also suggest that using a larger number of components than provided by the MDL criterion may be advantageous for separating RSNs that are co-localized in a single IC in some of our data. Interestingly, the number ICs detected by the MDL criterion increased considerably when spatially interpolating the data, which suggests that spatial dimensionality independent of spatial information content plays an important role in source separation with ICA. This dependence of ICA source separation on preprocessing warrants further investigation. The effects of increasing model order on the noise level and segregation of RSNs in individual subject data need to be addressed in a future study. Furthermore, it will be of interest to investigate the loss of MEVI information in the initial PCA-based data reduction step. The performance of ICA source separation with high-speed fMRI requires further investigation as sensitivity for detecting and for separating RSNs varied across subjects. For example, in some subjects the ICA time course displayed dynamic mixing and unmixing of different signal sources throughout the entire ICA time course. In other cases a separation of a steady signal pulsation time course into two complementary ICs with time courses that displayed decreasing and increasing pulsation amplitude was

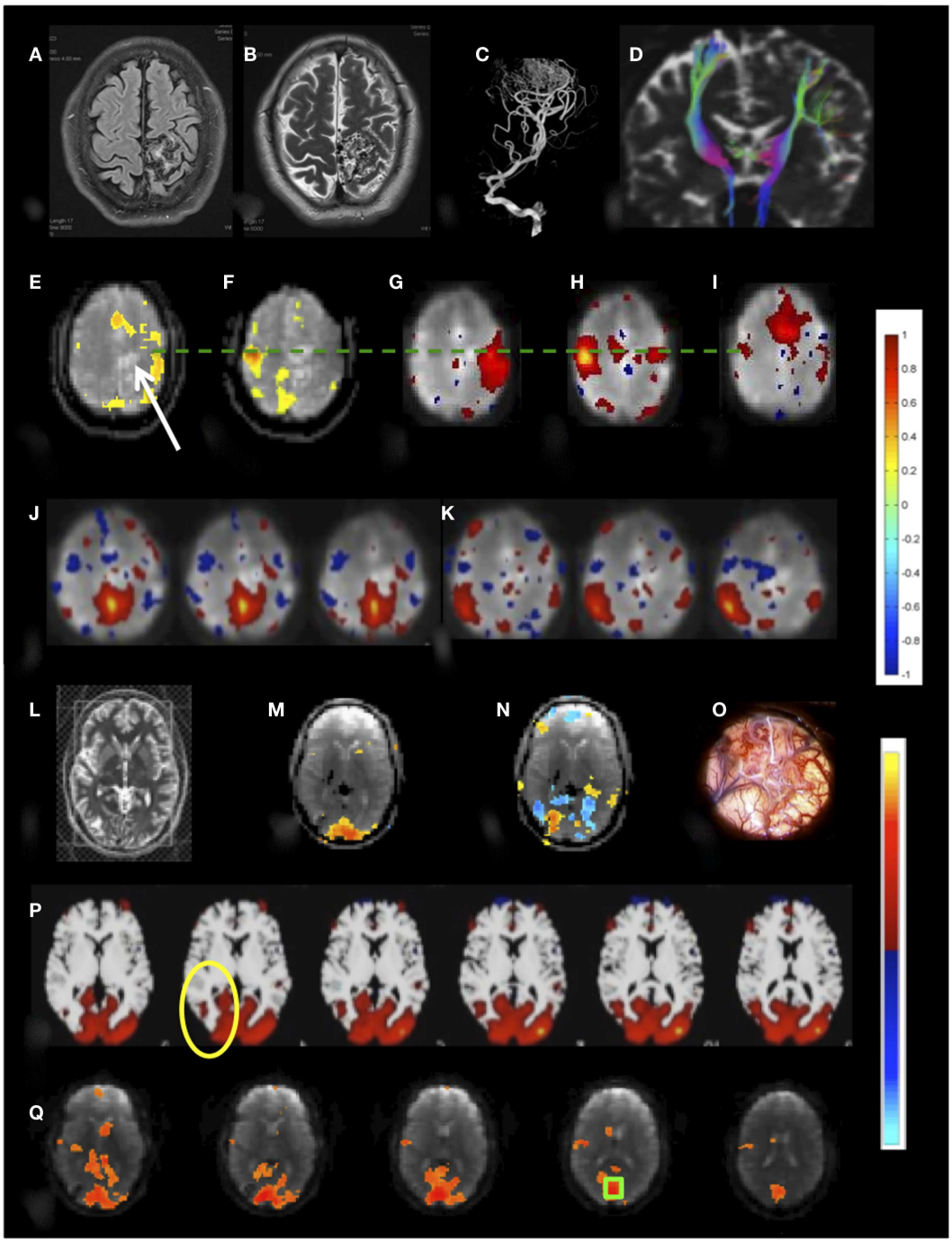

FIGURE 10 | Presurgical mapping in two patients with arterio-venous malformations (AVM). *Patient 3 with left parietal AVM*: **(A)** T1-weighted MRI, **(B)** T2-weighted MRI, **(C)** MR-angiogram, **(D)** DTI-based fiber tracking show distortion of motor pathways. Task-based fMRI using MEPI (TR: 2 s): **(E)** right hand finger tapping shows distributed activation around the lesion (indicated by arrow) beyond the left motor cortex and in the supplementary motor area and **(F)** left hand finger tapping shows focal localization of right motor cortex. Resting-state fMRI using MEVI2 (TR: 136 ms) and ICA segregates the sensorimotor RSN into three subnetworks with focal localization of motor areas: **(G)** a right sensorimotor RSN ($z_{max} = 7.9$), **(H)** a left sensorimotor RSN ($z_{max} = 8.9$), and **(I)** a supplementary motor area RSN ($z_{max} = 9.4$). ICA also segregates the default mode RSN into two subnetworks **(J,K)** that do not extend into the left parietal cortex ($z_{max} = 6.2$ and 8.5, respectively). *Patient 4 with right occipital AVM*: **(L)** T2-weighted MRI. Task-based fMRI using MEPI (TR: 2 s). **(M)** Visual stimulation does not activate the lesion and **(N)** imagination of the experience of the "aura" associated with epilepsy activates and deactivates areas at the rim of the lesion. **(O)** Intraoperative image. **(P)** Resting-state fMRI using MEVI2 (TR: 136 ms) and ICA shows a visual RSN that does not extend into the AVM consistent with visual stimulation ($z_{max} = 12.6$). **(Q)** Seed-based functional connectivity of the visual RSN with a seed in BA 17 (green box) does not show visual eloquence within the AVM. Color scales for task-based correlation analysis and seed-based connectivity (top), and ICA (bottom) are shown on the right.

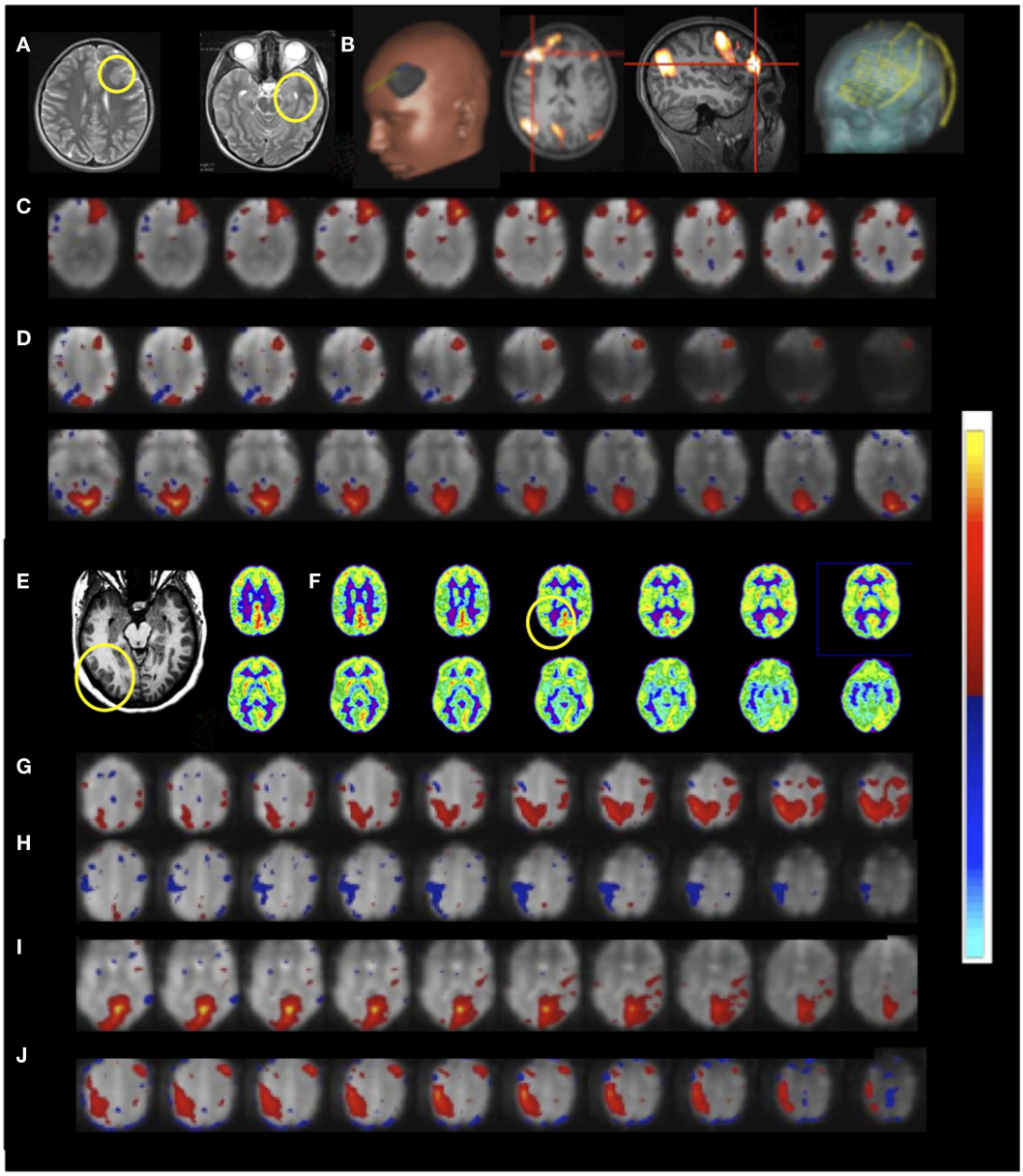

FIGURE 11 | Presurgical mapping in two patients with epilepsy Resting-state fMRI using MEVI2 (TR: 136 ms) and ICA. *Patient 6 with temporal lobe epilepsy*. **(A)** The T_2-weighted MRI shows hyperplasia in anterior left frontal cortex and left mesial temporal lobe sclerosis. **(B)** Presurgical planning using resting-state networks encompassing language areas and the area of dysplasia. ICA shows **(C)** a resting-state network encompassing the area of dysplasia ($z_{max} = 15.6$) and **(D)** abnormal connectivity between the area of dysplasia and the visual RSN ($z_{max} = 9.0$). *Patient 7 with cortical epilepsy*. **(E)** The T_1-weighted MRI shows cortical thickening in the right posterior temporal lobe (yellow circle) **(F)** FDG-PET shows hypometabolism in this region (yellow circle). ICA shows dynamic RSN changes in consecutive scans. **(G)** An unanticipated RSN emerges in right posterior parietal and temporal cortex during scan 4 ($z_{max} = 15.0$). **(H,I)** In scan 6 the visual RSN displays spatial asymmetry that excludes the right posterior temporal lobe and exhibits negative correlation with the right motor and posterior parietal cortex ($z_{max} = 17.3$). **(J)** The unanticipated RSN in right posterior parietal and temporal cortex extends into inferior regions during scan 8 ($z_{max} = 16.3$). The color scale for ICA is shown on the right.

observed. Several studies have shown that optimization of the data analysis methodology, such as using back-projection methods, reduces inter-session variability (Smith et al., 2005; Chen et al., 2008). Further work across larger groups of subjects is thus necessary to assess the reproducibility of source separation in single subjects.

There is now increasing evidence that RSNs are not stationary (Hou et al., 2006; Kang et al., 2011), which has attracted considerable interest in recent studies (Chang and Glover, 2010; Scholvinck et al., 2010; Allen et al., 2012). However, the neural correlates of resting-state fluctuations in fMRI are not well understood and are a focus of current research (Morcom and Fletcher, 2007; Shmueli

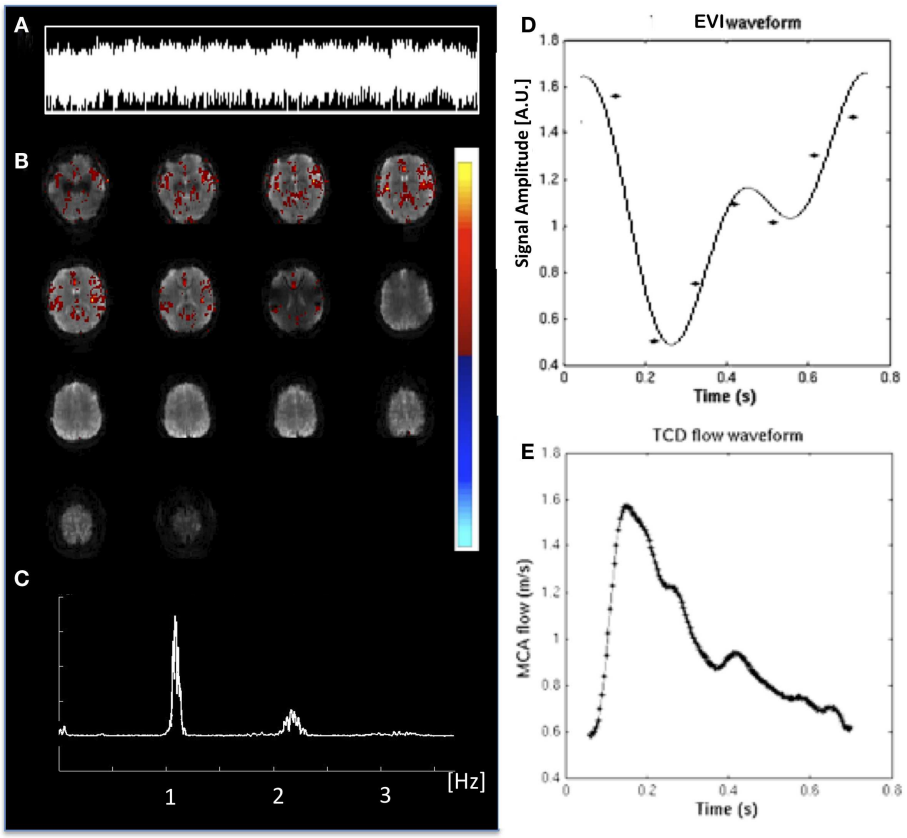

FIGURE 12 | Cardiac-related signal pulsation measured in a healthy control using MEVI2 (TR: 136 ms). (A) ICA time course of the pulsation. **(B)** ICA spatial map shows pulsation predominantly in insular cortex and medial gray matter ($z_{max} = 12.5$). The color scale for ICA is shown on the right. **(C)** Corresponding raw power spectrum shows the cardiac frequency and its first harmonic. **(D)** Fitted MEVI2 signal time course, which is inverted with respect to **(E)** a typical Transcranial Doppler Ultrasound waveform from the middle cerebral artery (from Wagshul et al., 2011).

et al., 2007; Pizoli et al., 2011; Wong et al., 2011). The seed-based real-time sliding-window correlation analysis with meta-statistics developed in this study enables sensitive analysis of fluctuations in resting-state connectivity at much shorter time scales compared to ICA and hypothesis-driven analysis of connectivity between specific nodes of RSNs. The decreases in connectivity fluctuation with increasing sliding-window width measured in our data highlights the advantage of ultra-high-speed fMRI for characterizing the temporal dynamics of resting-state connectivity and for monitoring transitions between resting states. It also emphasizes that averaging across several minutes of a resting-state scan may underestimate the maximum strength of functional connectivity between regions that exhibit strongly fluctuating connectivity.

Our seed-based sliding-window correlation analysis combined with meta-statistics revealed considerable short-term temporal fluctuation of intra- and inter-network FNC between positive and negative values at short time scales. FNC averaged across an entire 5 min scan was predominantly positive across subjects as shown in **Figure 8**, which is consistent with previous studies demonstrating positive overall correlation between RSN time courses before regression of the global mean (Fox et al., 2009; Murphy et al., 2009). A recent study demonstrated that correlation coefficients between the PCC and its anti-correlated regions without global regression were substantially weaker than those of the positive correlations within regions of the DMN, consistent with previous studies (Chang and Glover, 2010). That study also showed considerable fluctuation in signal correlation at time scales of 2 and 4 min. The observed anti-correlation between the DMN and task-positive networks remains a topic of ongoing investigation and intense debate with regards to the validity of global signal regression (Fox et al., 2009; Murphy et al., 2009; Uddin et al., 2009; Cole et al., 2010b; Chai et al., 2012). With seed-based connectivity the observation of correlations and anti-correlations is highly dependent on the choice of seed locations. Future studies will have to more thoroughly investigate correlations with a wider range of seed locations. In summary, the measurement of short-term correlations and anti-correlations at time scales much shorter than those reported in previous studies, using high-speed fMRI without global signal regression, will facilitate the characterization of the neurobiological basis of the observed anti-correlations.

Monitoring RSN fluctuations online in correlation with other observables of subject behavior and state would provide a new approach for studying the physiological and cognitive correlates of resting-state fluctuations. Our real-time methodology enables

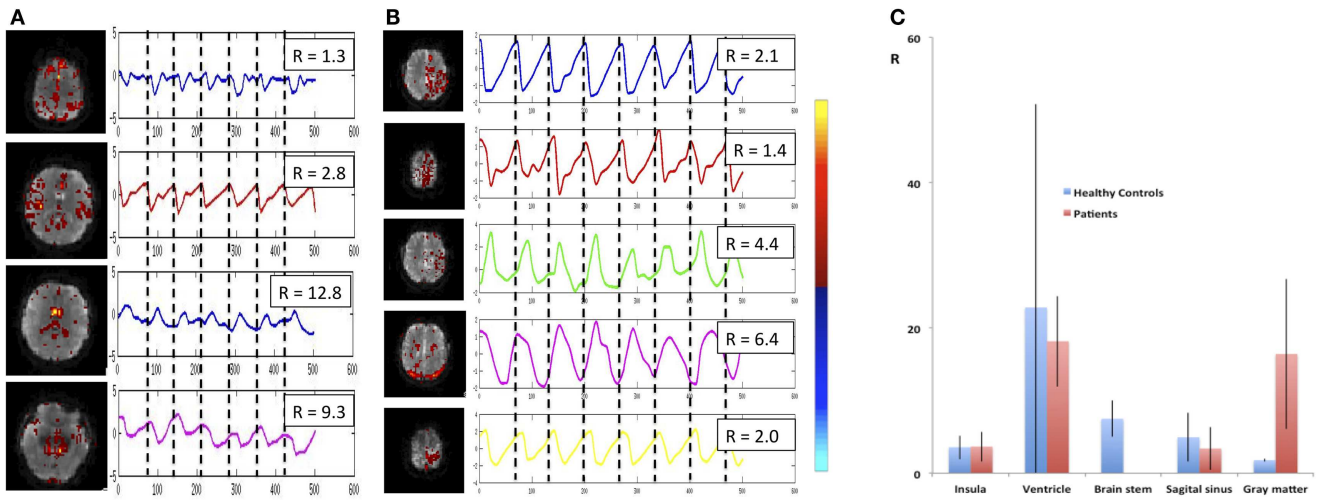

FIGURE 13 | Cardiac-related signal pulsation in different brain areas measured using MEVI2 (TR: 136 ms) in (A) a healthy control and (B) patient 3 with an AVM. Selected slices from the spatial ICA show regions with cardiac-related signal pulsation [z_{max} ranging from 7.7 to 14.4 in **(A)** and from 5.3 to 14.4 in **(B)**]. Interpolated ICA time courses within a 6.8-s window showing remarkable morphological waveform differences and shifts in phase in the AVM and in adjacent gray matter regions. The ratio R of the power spectrum amplitudes at the cardiac frequency versus the first harmonic is shown in the insets. **(C)** Group analysis across healthy controls ($n = 9$) and patients ($n = 6$) shows regional differences in R (ratio of the power spectrum amplitudes at the cardiac frequency versus the first harmonic). The color scale for ICA is shown between **(B)** and **(C)**.

experimental neurofeedback based on intra- and inter-network connectivity, which may provide a means for self-controlling the temporal dynamics of resting-state fluctuations. For example, by controlling activation of task-positive networks it may be possible to modulate the anti-correlated default mode RSN, which may have implications for cognitive behavioral therapy.

SENSITIVITY OF MEVI

Inline with recent studies, we show that the detection of major RSNs and separation of physiological signal fluctuation in single subjects is facilitated by the high temporal resolution MEVI, which avoids aliasing of cardiac- and respiration-related signal fluctuations, and by the high BOLD sensitivity of MEVI (Posse et al., 2012). As recent studies have shown high temporal resolution improves separation of RSNs using ICA (Smith et al., 2012) and may facilitate detecting the temporal dynamics of RSNs at frequencies above 0.1 Hz (Boubela et al., 2013; Boyacioglu et al., 2013; Chu et al., 2013; Lee et al., 2013), which as a recent study suggests may exhibit greater spatial and temporal stability than low-frequency connectivity (Lee et al., 2013). Consistent with these studies our data show that MEVI improves separation of RSNs and facilitates detecting the higher frequency ranges of resting-state signal fluctuation, which as our data show extend up to 0.27 Hz.

High-speed fMRI reveals respiration-related signal changes at the edges of the MEVI slabs, which may be due to movement, B_0-shifts, or a combination of both, whereas the center of the slabs was free of these signal changes. This spatial separation of respiration-related artifacts represents a distinct advantage of 3D encoding with MEVI compared to multi-slice EPI, where these signal changes are not spatially separable and may thus be more difficult to remove.

CLINICAL FEASIBILITY STUDIES

There is now increasing evidence that alterations in functional connectivity are detectable in neurologic (Bettus et al., 2010; Pereira et al., 2010; Luo et al., 2011; Negishi et al., 2011) and psychiatric (Greicius, 2008; Broyd et al., 2009) disorders, which may have diagnostic value. The clinical cases in this study demonstrate that high-speed fMRI has high sensitivity for mapping major RSNs and disease-related changes in functional connectivity in individual patients. Spatial displacement of major RSNs and reduced connectivity within RSNs was mapped in the vicinity of brain tumors and vascular malformations. Resting-state fMRI is particularly advantageous for mapping the sensorimotor cortex in patients with motor impairment, which may be challenging with task-based fMRI due to attention-related unspecific activation and dysregulation of cerebro-vascular coupling in the vicinity of brain lesions. Localization of sensorimotor cortex in patients with motor disability and in the vicinity of brain lesions with impaired cerebro-vascular coupling was more focal in resting-state fMRI compared with task-based fMRI. Segregation of the sensorimotor RSN into laterality-specific subnetworks in patients with brain tumors and AVMs in this study suggests disruption of functional connectivity in the sensorimotor cortex. This dynamic measure of functional integration is complementary to the static connectivity metric obtained with fiber tracking in DTI. Our data show that disease-related changes in resting-state connectivity in the vicinity of brain lesions may manifest as decreases or increases in connectivity between nodes of major RSNs, or even as separate lesion-specific RSNs. Anti-correlations between the DMN and task-positive networks that may be affected by brain lesions provide insights into competitive mechanisms that control resting-state fluctuations (Fox et al., 2005; Uddin et al., 2009).

Inter-individual variability in connectivity may be elevated by certain disease conditions, in particular in the vicinity of brain lesions known to impair neurovascular coupling and in brain regions with inflammation. For example, gliomas may be associated with mass effect that can distort anatomy, and may affect eloquent cortex function by tumor infiltration and abnormal neurovascular coupling, generally greater with higher grade, potentially compromising detection of BOLD fMRI signal (Holodny et al., 2000; Hou et al., 2006; Jiang et al., 2010). While resting-state fMRI may provide a sensitive approach for studying neurovascular correlates of disease processes that is complementary to structural MRI and DTI, further studies are required to characterize the specificity of this connectivity information and to quantitatively assess the impact of altered cerebro-vascular reactivity in the vicinity of brain lesions on resting-state connectivity. As a range of pathological tissue changes, such as hyperplasia, inflammation, and edema, may impact apparent resting-state connectivity, it is necessary to investigate whether these changes are indeed indicative of true changes in functional connectivity or whether they are a side-effect of changes in regional cerebro-vascular reactivity.

In two of our patients with epilepsy it was feasible to monitor dynamic changes in major RSNs and the emergence of a separate RSN associated with cortical dysplasia. In *patient 7* with cortical epilepsy a separate RSN emerged dynamically in right posterior parietal and temporal cortex, a region that exhibited interictal spike activity. While these findings may be related to interictal spike activity during the scans, a more definitive assessment requires concurrent EEG-fMRI, which is under development in our laboratory. The high sensitivity of high-speed fMRI is expected to be advantageous for studying the infrequent hemodynamic responses to interictal spike activity in patients with epilepsy compared to conventional EPI. MEVI is compatible with the standard 12-channel head array coil that accommodates an EEG cap. It employs small flip angle excitation resulting in low RF power levels, which minimizes saturation of the EEG amplifiers.

CARDIAC-RELATED PULSATILITY

Only recently was arterial pulse wave propagation mapped with fMRI (Tong and Frederick, 2012). There is increasing evidence that aging, hypertension, dementia, and Alzheimer disease may have a common microvascular origin and that traumatic brain injury is associated with microvascular damage (Wagshul et al., 2011). However, lack of a non-invasive method capable of assessing pulsatile blood volume in small resistance arteries proves to be the limitation to investigate cerebral microvessels (Wszedybyl-Winklewska et al., 2011).

Our data show that cardiac-related signal pulsation has region specific waveforms and may carry clinically relevant functional information about cerebro-vascular pulsatility in cortex and in vascularized brain lesions. The high temporal resolution of MEVI enables measurement of the pulsation waveform on a beat-by-beat basis using spatial ICA. Increasing the temporal resolution of MEVI to 50 ms is desirable to more fully resolve regional differences in the pulsation waveform and in the phase of the pulse wave propagation. This real-time approach is complementary to phase contrast MRI and TDU as it extends the measurement of cardiac-related pulsatility into gray matter and enables monitoring of dynamic changes in pulsatility waveform.

CONCLUSION

We have shown that ultra-high-speed resting-state fMRI is a sensitive tool for presurgical mapping of connectivity within the sensorimotor network, which is complementary to task-based fMRI. Preliminary results in patients with neurological disease demonstrate high sensitivity for monitoring altered resting-state connectivity in the vicinity of brain lesion. Localization of sensorimotor cortex in patients with motor disability and in the vicinity of brain lesions with impaired cerebro-vascular coupling is more focal in resting-state fMRI compared with task-based fMRI, which is advantageous for presurgical mapping. Resting-state fMRI thus provides unique insights into altered functional connectivity associated with brain lesions, which is advantageous for presurgical mapping. Ultra-high-speed fMRI also enables whole brain online monitoring of vascular pulsation and may be useful to assess alterations in arterial pulse wave propagation and vascular compliance in patients with neurological diseases.

The multi-slab EVI pulse sequence and the TurboFIRE software tool are available for research use. Please contact the corresponding author for additional information.

ACKNOWLEDGMENTS

We gratefully acknowledge our patients for their participation. We thank Mona Chaney and Brittany Mead for assisting with patient recruitment and consenting. We gratefully acknowledge Diana South and Catherine Smith for assistance with scanner operations. Vineeth Yeruva assisted with operating the stimulus presentation. We thank Abhishek Reddy Yeruva, James Thrasher, and Daniel Allen McKearney for assistance with data analysis. We thank Eswar Damaraju (Mind Research Network) for advice on seed-based analysis using AFNI. The MEVI pulse sequence was developed in collaboration with Maxim Zaitsev and Jochen Rick (U. Freiburg, Germany), and Oliver Speck (U. Magdeburg, Germany). This project was supported in part by grants from the National Center for Research Resources (5P20RR021938-05) and the National Institute of General Medical Sciences (8 P20 GM103472-05) from the National Institutes of Health, and by the Department of Neurosurgery at UNM. We also thank the reviewers for their insightful comments.

REFERENCES

Abou-Elseoud, A., Starck, T., Remes, J., Nikkinen, J., Tervonen, O., and Kiviniemi, V. (2010). The effect of model order selection in group PICA. *Hum. Brain Mapp.* 31, 1207–1216.

Allen, E. A., Damaraju, E., Plis, S. M., Erhardt, E. B., Eichele, T., and Calhoun, V. D. (2012). Tracking whole-brain connectivity dynamics in the resting state. *Cereb. Cortex.* doi:10.1093/cercor/bhs352. [Epub ahead of print].

Allen, E. A., Erhardt, E. B., Damaraju, E., Gruner, W., Segall, J. M., Silva, R. F., et al. (2011). A baseline for the multivariate comparison of resting-state networks. *Front. Syst. Neurosci.* 5:2. doi:10.3389/fnsys.2011.00002

Bandettini, P. A., Jesmanowicz, A., Wong, E. C., and Hyde, J. S. (1993). Processing strategies for time-course data sets in functional MRI of the human brain. *Magn. Reson. Med.* 30, 161–173. doi:10.1002/mrm.1910300204

Beall, E. B., and Lowe, M. J. (2007). Isolating physiologic noise sources with independently determined spatial measures. *Neuroimage* 37, 1286–1300. doi:10.1016/j.neuroimage.2007.07.004

Behzadi, Y., Restom, K., Liau, J., and Liu, T. T. (2007). A component based noise correction method (CompCor) for BOLD and perfusion based fMRI. *Neuroimage* 37, 90–101. doi:10.1016/j.neuroimage.2007.04.042

Bettus, G., Bartolomei, F., Confort-Gouny, S., Guedj, E., Chauvel, P., Cozzone, P. J., et al. (2010). Role of resting state functional connectivity MRI in presurgical investigation of mesial temporal lobe epilepsy. *J. Neurol. Neurosurg. Psychiatr.* 81, 1147–1154. doi:10.1136/jnnp.2009.191460

Boubela, R. N., Kalcher, K., Huf, W., Kronnerwetter, C., Filzmoser, P., and Moser, E. (2013). Beyond noise: using temporal ICA to extract meaningful information from high-frequency fMRI signal fluctuations during rest. *Front. Hum. Neurosci.* 7:168. doi:10.3389/fnhum.2013.00168

Boyacioglu, R., Beckmann, C. F., and Barth, M. (2013). An investigation of RSN frequency spectra using ultra-fast generalized inverse imaging. *Front. Hum. Neurosci.* 7:156. doi:10.3389/fnhum.2013.00156

Britz, J., Van De Ville, D., and Michel, C. M. (2010). BOLD correlates of EEG topography reveal rapid resting-state network dynamics. *Neuroimage* 52, 1162–1170. doi:10.1016/j.neuroimage.2010.02.052

Broyd, S. J., Demanuele, C., Debener, S., Helps, S. K., James, C. J., and Sonuga-Barke, E. J. (2009). Default-mode brain dysfunction in mental disorders: a systematic review. *Neurosci. Biobehav. Rev.* 33, 279–296. doi:10.1016/j.neubiorev.2008.09.002

Calhoun, V. D., Adali, T., Pearlson, G. D., and Pekar, J. J. (2001). A method for making group inferences from functional MRI data using independent component analysis. *Hum. Brain Mapp.* 14, 140–151. doi:10.1002/hbm.1048

Chai, X. J., Castanon, A. N., Ongur, D., and Whitfield-Gabrieli, S. (2012). Anticorrelations in resting state networks without global signal regression. *Neuroimage* 59, 1420–1428. doi:10.1016/j.neuroimage.2011.08.048

Chang, C., and Glover, G. H. (2010). Time-frequency dynamics of resting-state brain connectivity measured with fMRI. *Neuroimage* 50, 81–98. doi:10.1016/j.neuroimage.2009.12.011

Chen, L., Chang, A., Xu, J., Moeller, S., Auerbach, E. J., Vu, A. T., et al. (2012). "Comparison of simultaneous multiband whole brain imaging with multiplexed-EPI," in *Proceedings of the Annual Meeting of the International Society of Magnetic Resonance in Medicine* (Melbourne: International Society for Magnetic Resonance in Medicine), 2860.

Chen, S., Ross, T. J., Zhan, W., Myers, C. S., Chuang, K. S., Heishman, S. J., et al. (2008). Group independent component analysis reveals consistent resting-state networks across multiple sessions. *Brain Res.* 1239, 141–151. doi:10.1016/j.brainres.2008.08.028

Chu, Y.-H., Ahveninen, J., Tommi, R., Kuo, W.-J., Belliveau, J. W., and Lin, F.-H. (2013). Resting-state fMRI at 4 Hz. *Annual Meeting of the ISMRM*, Salt Lake City, 41.

Cole, D. M., Smith, S. M., and Beckmann, C. F. (2010a). Advances and pitfalls in the analysis and interpretation of resting-state FMRI data. *Front. Syst. Neurosci.* 4:8. doi:10.3389/fnsys.2010.00008

Cole, M. W., Pathak, S., and Schneider, W. (2010b). Identifying the brain's most globally connected regions. *Neuroimage* 49, 3132–3148. doi:10.1016/j.neuroimage.2009.11.001

Dagli, M. S., Ingeholm, J. E., and Haxby, J. V. (1999). Localization of cardiac-induced signal change in fMRI. *Neuroimage* 9, 407–415. doi:10.1006/nimg.1998.0424

De Luca, M., Beckmann, C. F., De Stefano, N., Matthews, P. M., and Smith, S. M. (2006). fMRI resting state networks define distinct modes of long-distance interactions in the human brain. *Neuroimage* 29, 1359–1367. doi:10.1016/j.neuroimage.2005.08.035

Deckers, R. H., van Gelderen, P., Ries, M., Barret, O., Duyn, J. H., Ikonomidou, V. N., et al. (2006). An adaptive filter for suppression of cardiac and respiratory noise in MRI time series data. *Neuroimage* 33, 1072–1081. doi:10.1016/j.neuroimage.2006.08.006

Eichele, T., Debener, S., Calhoun, V. D., Specht, K., Engel, A. K., Hugdahl, K., et al. (2008). Prediction of human errors by maladaptive changes in event-related brain networks. *Proc. Natl. Acad. Sci. U.S.A.* 105, 6173–6178. doi:10.1073/pnas.0708965105

Erhardt, E. B., Allen, E. A., Damaraju, E., and Calhoun, V. D. (2011). On network derivation, classification, and visualization: a response to Habeck and Moeller. *Brain Connect.* 1, 1–19. doi:10.1089/brain.2011.0022

Feinberg, D. A., Moeller, S., Smith, S. M., Auerbach, E., Ramanna, S., Gunther, M., et al. (2010). Multiplexed echo planar imaging for sub-second whole brain FMRI and fast diffusion imaging. *PLoS ONE* 5:e15710. doi:10.1371/journal.pone.0015710

Fox, M. D., Snyder, A. Z., Vincent, J. L., Corbetta, M., Van Essen, D. C., and Raichle, M. E. (2005). The human brain is intrinsically organized into dynamic, anticorrelated functional networks. *Proc. Natl. Acad. Sci. U.S.A.* 102, 9673–9678. doi:10.1073/pnas.0504136102

Fox, M. D., Zhang, D., Snyder, A. Z., and Raichle, M. E. (2009). The global signal and observed anticorrelated resting state brain networks. *J. Neurophysiol.* 101, 3270–3283. doi:10.1152/jn.90777.2008

Gao, K., and Posse, S. (2003). "TurboFire: real-time fMRI with automated spatial normalization and Talairach daemon database," in *Proceedings of the 9th Annual Meeting of the Organization of Human Brain Mapping* (New York: Organization for Human Brain Mapping), 838.

Gao, K., and Posse, S. (2004). "TurboFIRE: real-time fMRI with online generation of reference vectors," in *Proceedings of the 10th Annual Meeting of the Organization of Human Brain Mapping* (Budapest: Organization for Human Brain Mapping), WE177.

Glover, G. H., Li, T. Q., and Ress, D. (2000). Image-based method for retrospective correction of physiological motion effects in fMRI: RETROICOR. *Magn. Reson. Med.* 44, 162–167. doi:10.1002/1522-2594(200007)44:1<162::AID-MRM23>3.3.CO;2-5

Greicius, M. (2008). Resting-state functional connectivity in neuropsychiatric disorders. *Curr. Opin. Neurol.* 21, 424–430. doi:10.1097/WCO.0b013e328306f2c5

Grotz, T., Zahneisen, B., Ella, A., Zaitsev, M., and Hennig, J. (2009). Fast functional brain imaging using constrained reconstruction based on regularization using arbitrary projections. *Magn. Reson. Med.* 62, 394–405. doi:10.1002/mrm.22009

Holodny, A. I., Schulder, M., Liu, W. C., Wolko, J., Maldjian, J. A., and Kalnin, A. J. (2000). The effect of brain tumors on BOLD functional MR imaging activation in the adjacent motor cortex: implications for image-guided neurosurgery. *AJNR Am. J. Neuroradiol.* 21, 1415–1422.

Hou, B. L., Bradbury, M., Peck, K. K., Petrovich, N. M., Gutin, P. H., and Holodny, A. I. (2006). Effect of brain tumor neovasculature defined by rCBV on BOLD fMRI activation volume in the primary motor cortex. *Neuroimage* 32, 489–497. doi:10.1016/j.neuroimage.2006.04.188

Hyvarinen, A., and Oja, E. (1997). Fast fixed-point algorithm for independent component analysis. *Neural Comput.* 9, 1483–1492. doi:10.1162/neco.1997.9.7.1483

Jiang, Z., Krainik, A., David, O., Salon, C., Tropres, I., Hoffmann, D., et al. (2010). Impaired fMRI activation in patients with primary brain tumors. *Neuroimage* 52, 538–548. doi:10.1016/j.neuroimage.2010.04.194

Joel, S. E., Caffo, B. S., van Zijl, P. C., and Pekar, J. J. (2011). On the relationship between seed-based and ICA-based measures of functional connectivity. *Magn. Reson. Med.* 66, 644–657. doi:10.1002/mrm.22818

Kang, J., Wang, L., Yan, C., Wang, J., Liang, X., and He, Y. (2011). Characterizing dynamic functional connectivity in the resting brain using variable parameter regression and Kalman filtering approaches. *Neuroimage* 56, 1222–1234. doi:10.1016/j.neuroimage.2011.03.033

Kiviniemi, V., Vire, T., Remes, J., Elseoud, A. A., Starck, T., Tervonen, O., et al. (2011). A sliding time-window ICA reveals spatial variability of the default mode network in time. *Brain Connect.* 1, 339–347. doi:10.1089/brain.2011.0036

Koopmans, P. J., Boyacioglu, R., Barth, M., and Norris, D. G. (2012). Whole brain, high resolution spin-echo resting state fMRI using PINS multiplexing at 7 T. *Neuroimage* 62, 1939–1946. doi:10.1016/j.neuroimage.2012.05.080

Koopmans, P. J., Boyacioglu, R., Barth, M., and Norris, D. G. (2013). Simultaneous multislice inversion contrast imaging using power independent of the number of slices (PINS) and delays alternating with nutation for tailored excitation (DANTE) radio frequency pulses. *Magn. Reson. Med.* 69, 1670–1676. doi:10.1002/mrm.24402

Kruger, G., and Glover, G. H. (2001). Physiological noise in oxygenation-sensitive magnetic resonance imaging. *Magn. Reson. Med.* 46, 631–637. doi:10.1002/mrm.1240

Kundu, P., Inati, S. J., Evans, J. W., Luh, W. M., and Bandettini, P. A. (2012). Differentiating BOLD and non-BOLD signals in fMRI time series using multi-echo EPI.

Neuroimage 60, 1759–1770. doi:10.1016/j.neuroimage.2011.12.028

Laufs, H. (2010). Multimodal analysis of resting state cortical activity: what does EEG add to our knowledge of resting state BOLD networks? *Neuroimage* 52, 1171–1172. doi:10.1016/j.neuroimage.2010.05.034

Lee, H. L., Zahneisen, B., Hugger, T., LeVan, P., and Hennig, J. (2013). Tracking dynamic resting-state networks at higher frequencies using MR-encephalography. *Neuroimage* 65, 216–222. doi:10.1016/j.neuroimage.2012.10.015

Lehmann, D. (2010). Multimodal analysis of resting state cortical activity: what does fMRI add to our knowledge of microstates in resting state EEG activity? Commentary to the papers by Britz et al. and Musso et al. in the current issue of neuroimage. *Neuroimage* 52, 1173–1174. doi:10.1016/j.neuroimage.2010.05.033

Li, B. N., Dong, M. C., and Vai, M. I. (2010). On an automatic delineator for arterial blood pressure waveforms. *Biomed. Signal Process. Control* 5, 76–81. doi:10.1016/j.bspc.2009.06.002

Li, R., Chen, K., Fleisher, A. S., Reiman, E. M., Yao, L., and Wu, X. (2011). Large-scale directional connections among multi resting-state neural networks in human brain: a functional MRI and Bayesian network modeling study. *Neuroimage* 56, 1035–1042. doi:10.1016/j.neuroimage.2011.03.010

Li, Y. O., Adali, T., and Calhoun, V. D. (2007). Estimating the number of independent components for functional magnetic resonance imaging data. *Hum. Brain Mapp.* 28, 1251–1266. doi:10.1002/hbm.20359

Lin, F. H., Nummenmaa, A., Witzel, T., Polimeni, J. R., Zeffiro, T. A., Wang, F. N., et al. (2011). Physiological noise reduction using volumetric functional magnetic resonance inverse imaging. *Hum. Brain Mapp.* 33, 2815–2830. doi:10.1002/hbm.21403

Lin, F. H., Wald, L. L., Ahlfors, S. P., Hamalainen, M. S., Kwong, K. K., and Belliveau, J. W. (2006). Dynamic magnetic resonance inverse imaging of human brain function. *Magn. Reson. Med.* 56, 787–802. doi:10.1002/mrm.20997

Lin, F. H., Witzel, T., Chang, W. T., Wen-Kai Tsai, K., Wang, Y. H., Kuo, W. J., et al. (2010). K-space reconstruction of magnetic resonance inverse imaging (K-InI) of human visuomotor systems. *Neuroimage* 49, 3086–3098. doi:10.1016/j.neuroimage.2009.11.016

Lin, F. H., Witzel, T., Mandeville, J. B., Polimeni, J. R., Zeffiro, T. A., Greve, D. N., et al. (2008). Event-related single-shot volumetric functional magnetic resonance inverse imaging of visual processing. *Neuroimage* 42, 230–247. doi:10.1016/j.neuroimage.2008.04.179

Liu, H., Buckner, R. L., Talukdar, T., Tanaka, N., Madsen, J. R., and Stufflebeam, S. M. (2009). Task-free presurgical mapping using functional magnetic resonance imaging intrinsic activity. *J. Neurosurg.* 111, 746–754. doi:10.3171/2008.10.JNS08846

Luo, C., Li, Q., Lai, Y., Xia, Y., Qin, Y., Liao, W., et al. (2011). Altered functional connectivity in default mode network in absence epilepsy: a resting-state fMRI study. *Hum. Brain Mapp.* 32, 438–449. doi:10.1002/hbm.21034

Mannfolk, P., Nilsson, M., Hansson, H., Stahlberg, F., Fransson, P., Weibull, A., et al. (2011). Can resting-state functional MRI serve as a complement to task-based mapping of sensorimotor function? A test-retest reliability study in healthy volunteers. *J. Magn. Reson. Imaging* 34, 511–517. doi:10.1002/jmri.22654

Moeller, S., Xu, J., Auerbach, E. J., Yacoub, E., and Ugurbil, K. (2012). "Signal leakage (L-factor) as a measure for parallel imaging performance among simultaneously multi-slice (SMS) excited and acquired signals," in *Proceedings of the Annual Meeting of the International Society of Magnetic Resonance in Medicine* (Melbourne: International Society for Magnetic Resonance in Medicine), 519.

Moeller, S., Yacoub, E., Olman, C. A., Auerbach, E., Strupp, J., Harel, N., et al. (2010). Multiband multislice GE-EPI at 7 tesla, with 16-fold acceleration using partial parallel imaging with application to high spatial and temporal whole-brain fMRI. *Magn. Reson. Med.* 63, 1144–1153. doi:10.1002/mrm.22361

Morcom, A. M., and Fletcher, P. C. (2007). Does the brain have a baseline? Why we should be resisting a rest. *Neuroimage* 37, 1073–1082. doi:10.1016/j.neuroimage.2006.09.013

Murphy, K., Birn, R. M., Handwerker, D. A., Jones, T. B., and Bandettini, P. A. (2009). The impact of global signal regression on resting state correlations: are anti-correlated networks introduced? *Neuroimage* 44, 893–905. doi:10.1016/j.neuroimage.2008.09.036

Musso, F., Brinkmeyer, J., Mobascher, A., Warbrick, T., and Winterer, G. (2010). Spontaneous brain activity and EEG microstates. A novel EEG/fMRI analysis approach to explore resting-state networks. *Neuroimage* 52, 1149–1161. doi:10.1016/j.neuroimage.2010.01.093

Mutihac, R., and Van Hulle, M. M. (2004). Comparison of PCA and ICA for BSS. *Rom. Rep. Phys.* 56, 20–32.

Negishi, M., Martuzzi, R., Novotny, E. J., Spencer, D. D., and Constable, R. T. (2011). Functional MRI connectivity as a predictor of the surgical outcome of epilepsy. *Epilepsia* 52, 1733–1740. doi:10.1111/j.1528-1167.2011.03191.x

Norris, D. G., Koopmans, P. J., Boyacioglu, R., and Barth, M. (2011). Power independent of number of slices (PINS) radiofrequency pulses for low-power simultaneous multislice excitation. *Magn. Reson. Med.* 66, 1234–1240. doi:10.1002/mrm.23152

Pereira, F. R., Alessio, A., Sercheli, M. S., Pedro, T., Bilevicius, E., Rondina, J. M., et al. (2010). Asymmetrical hippocampal connectivity in mesial temporal lobe epilepsy: evidence from resting state fMRI. *BMC Neurosci.* 11:66. doi:10.1186/1471-2202-11-66

Pizoli, C. E., Shah, M. N., Snyder, A. Z., Shimony, J. S., Limbrick, D. D., Raichle, M. E., et al. (2011). Resting-state activity in development and maintenance of normal brain function. *Proc. Natl. Acad. Sci. U.S.A.* 108, 11638–11643. doi:10.1073/pnas.1109144108

Posse, S. (2012). Multi-echo acquisition. *Neuroimage* 62, 665–671. doi:10.1016/j.neuroimage.2011.10.057

Posse, S., Ackley, E., Mutihac, R., Rick, J., Shane, M., Murray-Krezan, C., et al. (2012). Enhancement of temporal resolution and BOLD sensitivity in real-time fMRI using multi-slab echo-volumar imaging. *Neuroimage* 61, 115–130. doi:10.1016/j.neuroimage.2012.02.059

Posse, S., Otazo, R., Dager, S. R., and Alger, J. (2013). MR spectroscopic imaging: principles and recent advances. *J. Magn. Reson. Imaging* 37, 1301–1325. doi:10.1002/jmri.23945

Posse, S., Binkofski, F., Schneider, F., Gembris, D., Frings, W., Habel, U., et al. (2001). A new approach to measure single-event related brain activity using real-time fMRI: feasibility of sensory, motor, and higher cognitive tasks. *Hum. Brain Mapp.* 12, 25–41. doi:10.1002/1097-0193(200101)12:1<25::AID-HBM30>3.0.CO;2-H

Posse, S., Otazo, R., Caprihan, A., Bustillo, J., Chen, H., Henry, P. G., et al. (2007). Proton echo-planar spectroscopic imaging of J-coupled resonances in human brain at 3 and 4 tesla. *Magn. Reson. Med.* 58, 236–244. doi:10.1002/mrm.21287

Posse, S., Wiese, S., Gembris, D., Mathiak, K., Kessler, C., Grosse-Ruyken, M. L., et al. (1999). Enhancement of BOLD-contrast sensitivity by single-shot multi-echo functional MR imaging. *Magn. Reson. Med.* 42, 87–97. doi:10.1002/(SICI)1522-2594(199907)42:1<87::AID-MRM13>3.0.CO;2-O

Rabrait, C., Ciuciu, P., Ribes, A., Poupon, C., Le Roux, P., Dehaine-Lambertz, G., et al. (2008). High temporal resolution functional MRI using parallel echo volumar imaging. *J. Magn. Reson. Imaging* 27, 744–753. doi:10.1002/jmri.21329

Raichle, M. E., and Snyder, A. Z. (2007). A default mode of brain function: a brief history of an evolving idea. *Neuroimage* 37, 1083–1090; discussion 1097–1089. doi:10.1016/j.neuroimage.2007.02.041

Sadaghiani, S., Scheeringa, R., Lehongre, K., Morillon, B., Giraud, A. L., and Kleinschmidt, A. (2010). Intrinsic connectivity networks, alpha oscillations, and tonic alertness: a simultaneous electroencephalography/functional magnetic resonance imaging study. *J. Neurosci.* 30, 10243–10250. doi:10.1523/JNEUROSCI.1004-10.2010

Sakoglu, U., Pearlson, G. D., Kiehl, K. A., Wang, Y., Michael, A., and Calhoun, V. D. (2010). A method for evaluating dynamic functional network connectivity and task-modulation: application to schizophrenia. *MAGMA* 23, 351–366. doi:10.1007/s10334-010-0197-8

Satterthwaite, T. D., Wolf, D. H., Loughead, J., Ruparel, K., Elliott, M. A., Hakonarson, H., et al. (2012). Impact of in-scanner head motion on multiple measures of functional connectivity: relevance for studies of neurodevelopment in youth. *Neuroimage* 60, 623–632. doi:10.1016/j.neuroimage.2011.12.063

Scholvinck, M. L., Maier, A., Ye, F. Q., Duyn, J. H., and Leopold, D. A. (2010). Neural basis of global resting-state fMRI activity. *Proc. Natl. Acad. Sci. U.S.A.* 107, 10238–10243. doi:10.1073/pnas.0913110107

Schopf, V., Windischberger, C., Kasess, C. H., Lanzenberger, R., and Moser, E. (2010). Group ICA of resting-state data: a comparison. *MAGMA*

23, 317–325. doi:10.1007/s10334-010-0212-0

Setsompop, K., Gagoski, B. A., Polimeni, J. R., Witzel, T., Wedeen, V. J., and Wald, L. L. (2012). Blipped-controlled aliasing in parallel imaging for simultaneous multislice echo planar imaging with reduced g-factor penalty. *Magn. Reson. Med.* 67, 1210–1224. doi:10.1002/mrm.23097

Shmueli, K., van Gelderen, P., de Zwart, J. A., Horovitz, S. G., Fukunaga, M., Jansma, J. M., et al. (2007). Low-frequency fluctuations in the cardiac rate as a source of variance in the resting-state fMRI BOLD signal. *Neuroimage* 38, 306–320. doi:10.1016/j.neuroimage.2007.07.037

Smith, S. M., Beckmann, C. F., Ramnani, N., Woolrich, M. W., Bannister, P. R., Jenkinson, M., et al. (2005). Variability in fMRI: a re-examination of inter-session differences. *Hum. Brain Mapp.* 24, 248–257. doi:10.1002/hbm.20080

Smith, S. M., Miller, K. L., Moeller, S., Xu, J., Auerbach, E. J., Woolrich, M. W., et al. (2012). Temporally-independent functional modes of spontaneous brain activity. *Proc. Natl. Acad. Sci. U.S.A.* 109, 3131–3136. doi:10.1073/pnas.1121329109

Soldati, N., Calhoun, V. D., Bruzzone, L., and Jovicich, J. (2013a). ICA analysis of fMRI with real-time constraints: an evaluation of fast detection performance as function of algorithms, parameters and a priori conditions. *Front. Hum. Neurosci.* 7:19. doi:10.3389/fnhum.2013.00019

Soldati, N., Calhoun, V. D., Bruzzone, L., and Jovicich, J. (2013b). The use of a priori information in ICA-based techniques for real-time fMRI: an evaluation of static/dynamic and spatial/temporal characteristics. *Front. Hum. Neurosci.* 7:64. doi:10.3389/fnhum.2013.00064

Stufflebeam, S. M., Liu, H., Sepulcre, J., Tanaka, N., Buckner, R. L., and Madsen, J. R. (2011). Localization of focal epileptic discharges using functional connectivity magnetic resonance imaging. *J. Neurosurg.* 114, 1693–1697. doi:10.3171/2011.1.JNS10482

Tong, Y., and Frederick, B. (2012). Concurrent fNIRS and fMRI processing allows independent visualization of the propagation of pressure waves and bulk blood flow in the cerebral vasculature. *Neuroimage* 61, 1419–1427. doi:10.1016/j.neuroimage.2012.03.009

Uddin, L. Q., Kelly, A. M., Biswal, B. B., Xavier Castellanos, F., and Milham, M. P. (2009). Functional connectivity of default mode network components: correlation, anticorrelation, and causality. *Hum. Brain Mapp.* 30, 625–637. doi:10.1002/hbm.20531

Van de Ville, D., Britz, J., and Michel, C. M. (2010). EEG microstate sequences in healthy humans at rest reveal scale-free dynamics. *Proc. Natl. Acad. Sci. U.S.A.* 107, 18179–18184. doi:10.1073/pnas.1007841107

van der Zwaag, W., Kober, T., Marques, J. P., Glover, G., Gruetter, R., and Krueger, G. (2009). Comparison of single-shot 2D EPI and segmented 3D EVI acquisition for fMRI at 7T. *Annual Meeting of the International Society of Magnetic Resonance in Medicine*, Honolulu, HI, 1550.

Van Dijk, K. R., Hedden, T., Venkataraman, A., Evans, K. C., Lazar, S. W., and Buckner, R. L. (2010). Intrinsic functional connectivity as a tool for human connectomics: theory, properties, and optimization. *J. Neurophysiol.* 103, 297–321. doi:10.1152/jn.00783.2009

Van Dijk, K. R., Sabuncu, M. R., and Buckner, R. L. (2012). The influence of head motion on intrinsic functional connectivity MRI. *Neuroimage* 59, 431–438. doi:10.1016/j.neuroimage.2011.07.044

Wagshul, M. E., Eide, P. K., and Madsen, J. R. (2011). The pulsating brain: a review of experimental and clinical studies of intracranial pulsatility. *Fluids Barriers CNS* 8, 5. doi:10.1186/2045-8118-8-5

Welford, B. P. (1962). Note on a method for calculating corrected sums of squares and products. *Technometrics* 4, 419–420. doi:10.1080/00401706.1962.10490022

Witzel, T., Polimeni, J. R., Wiggins, G. C., Lin, F., Biber, S., Hamm, M., et al. (2008). Single-shot echo-volumar imaging using highly parallel detection. *Annual Meeting of the International Society of Magnetic Resonance in Medicine*, Toronto, CA, 1387.

Wong, C. W., Olaffson, V., He, H., and Liu, T. (2011). "Resting state networks and EEG-fMRI," in *Proceedings of the Annual Meeting of the Society of Magnetic Resonance in Medicine* (Montréal: ISMRM), 359.

Wszedybyl-Winklewska, M., Frydrychowski, A. F., Michalska, B. M., and Winklewski, P. J. (2011). Effects of the Valsalva maneuver on pial artery pulsation and subarachnoid width in healthy adults. *Microvasc. Res.* 82, 369–373. doi:10.1016/j.mvr.2011.08.003

Wu, C. W., Gu, H., Zou, Q., Lu, H., Stein, E. A., and Yang, Y. (2012). TE-dependent spatial and spectral specificity of functional connectivity. *Neuroimage* 59, 3075–3084. doi:10.1016/j.neuroimage.2011.11.030

Wu, L., Eichele, T., and Calhoun, V. D. (2010). Reactivity of hemodynamic responses and functional connectivity to different states of alpha synchrony: a concurrent EEG-fMRI study. *Neuroimage* 52, 1252–1260. doi:10.1016/j.neuroimage.2010.05.053

Zahneisen, B., Grotz, T., Lee, K. J., Ohlendorf, S., Reisert, M., Zaitsev, M., et al. (2011). Three-dimensional MR-encephalography: fast volumetric brain imaging using rosette trajectories. *Magn. Reson. Med.* 65, 1260–1268. doi:10.1002/mrm.22711

Zhang, D., Johnston, J. M., Fox, M. D., Leuthardt, E. C., Grubb, R. L., Chicoine, M. R., et al. (2009). Preoperative sensorimotor mapping in brain tumor patients using spontaneous fluctuations in neuronal activity imaged with functional magnetic resonance imaging: initial experience. *Neurosurgery* 65, 226–236. doi:10.1227/01.NEU.0000350868.95634.CA

Zheng, W., Ackley, E. S., Martínez-Ramón, M., and Posse, S. (2013). Spatially aggregated multiclass pattern classification in functional MRI using optimally selected functional brain areas. *Magn. Reson. Imaging* 31, 247–261. doi:10.1016/j.mri.2012.07.010

Conflict of Interest Statement: The authors declare that the research was conducted in the absence of any commercial or financial relationships that could be construed as a potential conflict of interest.

Received: 18 February 2013; accepted: 29 July 2013; published online: 26 August 2013.

Citation: Posse S, Ackley E, Mutihac R, Zhang T, Hummatov R, Akhtari M, Chohan M, Fisch B and Yonas H (2013) High-speed real-time resting-state fMRI using multi-slab echo-volumar imaging. Front. Hum. Neurosci. ***7****:479. doi: 10.3389/fnhum.2013.00479*

This article was submitted to the journal Frontiers in Human Neuroscience.

frontiers in
HUMAN NEUROSCIENCE

ORIGINAL RESEARCH ARTICLE
published: 10 June 2013
doi: 10.3389/fnhum.2013.00251

The utility of independent component analysis and machine learning in the identification of the amyotrophic lateral sclerosis diseased brain

Robert C. Welsh[1,2]*, Laura M. Jelsone-Swain[1] and Bradley R. Foerster[1,3]

[1] *Department of Radiology, University of Michigan, Ann Arbor, MI, USA*
[2] *Department of Psychiatry, University of Michigan, Ann Arbor, MI, USA*
[3] *Ann Arbor VA Healthcare System, Ann Arbor, MI, USA*

Edited by:
Veronika Schöpf, Medical University Vienna, Austria

Reviewed by:
Federica Agosta, Vita-Salute San Raffaele University, Italy
Christian Rummel, University Institute for Diagnostic and Interventional Neuroradiology, Switzerland

****Correspondence:***
Robert C. Welsh, Department of Radiology, University of Michigan, Medical Science I, Room 3208C, 1301 Catherine Street, Ann Arbor, MI 48109, USA
e-mail: rcwelsh@med.umich.edu

Amyotrophic lateral sclerosis (ALS) is a devastating disease with a lifetime risk of ∼1 in 2000. Presently, diagnosis of ALS relies on clinical assessments for upper motor neuron and lower motor neuron deficits in multiple body segments together with a history of progression of symptoms. In addition, it is common to evaluate lower motor neuron pathology in ALS by electromyography. However, upper motor neuron pathology is solely assessed on clinical grounds, thus hindering diagnosis. In the past decade magnetic resonance methods have been shown to be sensitive to the ALS disease process, namely: resting-state connectivity measured with functional MRI, cortical thickness measured by high-resolution imaging, diffusion tensor imaging (DTI) metrics such as fractional anisotropy and radial diffusivity, and more recently magnetic resonance spectroscopy (MRS) measures of gamma-aminobutyric acid concentration. In this present work we utilize independent component analysis to derive brain networks based on resting-state functional magnetic resonance imaging and use those derived networks to build a disease state classifier using machine learning (support-vector machine). We show that it is possible to achieve over 71% accuracy for disease state classification. These results are promising for the development of a clinically relevant disease state classifier. Future inclusion of other MR modalities such as high-resolution structural imaging, DTI and MRS should improve this overall accuracy.

Keywords: independent component analysis, support vector machine, resting-state functional connectivity, amyotrophic lateral sclerosis, machine learning, disease-state classification

INTRODUCTION

Amyotrophic lateral sclerosis (ALS) is a progressive neurodegenerative disease involving the motor cortex, corpus callosum, cortical spinal tract, and spinal anterior horn neurons, and presents with upper motor neuron and lower motor neuron signs (Ghadge et al., 2003; Turner et al., 2009). The disease can have a highly variable presentation and can be challenging to diagnose, which can have significant implications for the patients as the median survival time is between 2 and 4 years (Beghi et al., 2006). There is no definitive diagnostic test for ALS. The diagnosis relies on the clinical examination to detect upper and lower motor neuron signs in multiple body segments (Brooks et al., 2000) along with symptom progression. Unfortunately, there is on average a 1-year delay between onset of symptoms and diagnosis for this rapidly progressive disease (Zoccolella et al., 2006), which precludes timely intervention with emerging disease-modifying treatments. The development of reliable diagnostic and prognostic biomarkers would represent a significant advance in the clinical work-up of ALS (Karitzky and Ludolph, 2001; Cudkowicz et al., 2004; Turner et al., 2009).

Conventional magnetic resonance imaging provides limited and potentially inconsistent information describing ALS patients (Cheung et al., 1995; Hofmann et al., 1998; Comi et al., 1999; Chan et al., 2003). Therefore, there has been great interest in using advanced neuroimaging modalities to establish markers of ALS. Although techniques such as voxel-based morphometry (Roccatagliata et al., 2009), resting-state functional connectivity (Mohammadi et al., 2009; Jelsone-Swain et al., 2010; Verstraete et al., 2011; Agosta et al., 2013), magnetic resonance spectroscopy (Foerster et al., 2012a), and diffusion tensor imaging (Filippini et al., 2010) have demonstrated differences between groups of ALS patients and healthy controls (HC), few studies have investigated diagnostic test accuracy measures (Turner and Modo, 2010; Foerster et al., 2012b).

Functional connectivity is a relatively new and powerful advanced neuroimaging method to evaluate regional brain interactions (establishing neural networks) that occur when a subject is not performing an explicit task (Biswal et al., 1997; Lowe et al., 1998; Jelsone-Swain et al., 2010). Alterations of brain networks have been seen in diseases such as Alzheimer's disease (Greicius et al., 2004), schizophrenia (Welsh et al., 2010), depression (Zeng et al., 2012), obsessive compulsive disorder (Stern et al., 2011), as well as ALS (Mohammadi et al., 2009; Jelsone-Swain et al., 2010; Verstraete et al., 2010, 2011; Douaud et al., 2011; Agosta et al., 2013). In particular, there is evidence of extensive brain network alterations due to the ALS disease process, such as those affecting

the default-mode network (Mohammadi et al., 2009), motor networks (Douaud et al., 2011), and fronto-parietal networks (Agosta et al., 2013).

Statistical image analysis that can incorporate the entirety of a brain image can have an advantage over massively parallel univariate techniques (Wang and Summers, 2012). Machine-learning methods integrate a potentially large number of observables (that is, variables or features, and in the example of functional connectivity the feature space spans the number of connection strengths/edges derived from each resting-state time-series) into a coherent analysis that leverages the combined space of the features into an increase of detection power (Chen et al., 2008). Machine-learning methods using functional connectivity data have been applied to classify disease state such as in Alzheimer's disease (Magnin et al., 2008; Orrù et al., 2012), depression (Craddock et al., 2009), and other psychiatric diseases (Orrù et al., 2012), and therefore could also be applied to ALS. To meet this important unmet need, we have explored the utility of machine-learning methodology to analyze resting-state functional magnetic resonance imaging (fMRI) data for ALS disease classification.

MATERIALS AND METHODS

PARTICIPANTS

We recruited 32 patients diagnosed with ALS and 31 age and gender matched healthy controls (HCs). The ALS patients were recruited through the University of Michigan Motor Neuron Disease Clinic in the Department of Neurology at the University of Michigan. HC participants were recruited through local advertising and web portals. This study was approved by the University of Michigan Institutional Review Board. The participants gave informed consent prior to the MRI examination. All participants in this cohort underwent MRI examination, which included resting-state fMRI. All ALS participants had date of symptom onset recorded as well as disease severity at time of scan assessed by the ALS Functional Rating Scale, revised version (ALSFRS-R) (Cedarbaum et al., 1999). The maximum score of the ALSFRS-R is 48, with lower scores indicating increased physical disability.

MAGNETIC RESONANCE ACQUISITION

Image acquisition

All scanning took place on a GE 3T Excite 2 magnet (General Electric, Milwaukee, WI, USA). All participants had high-resolution anatomic T_1-weighted imaging (spoiled-gradient-recall, SPGR). High-resolution images were collected with a 256^2 matrix, 220 mm FOV, and 1.0 mm slice thickness) and resting-state fMRI. T_2*-time-series data were acquired parallel to the AC-PC axis using a reverse-spiral *k*-space readout. A total of 240 T_2*-weighted volumes were collected during each scanning session (repetition time, TR = 2 s; 40-slice volumes; 3 mm slice thickness, no skip; echo time, TE = 30 ms; 64 × 64 matrix; field-of-view FOV = 220 mm).

Functional connectivity

Resting-state time-series data were pre-processed similarly to Welsh et al. (2010). We used an in-house pre-preprocessing method which uses both FSL 4.1.9 (Jenkinson et al., 2012) and SPM8 (release 4667). Time-series data were preprocessed in the following steps: slice-time corrected (FSL), motion corrected (FSL), and normalized to MNI space (SPM8/VBM8). Time-series data were resampled to 3 mm voxel resolution and isotropically smoothed with a 5-mm Gaussian kernel. A mask of white-matter was derived from the SPGR during the spatial normalization step using VBM8. To minimize partial volume effects, the resulting mask was eroded three times over with FSL. A similarly derived cerebral spinal fluid (CSF) mask was also created, however, due to variance in ventricular size across subjects the CSF mask was only eroded once. Prior to independent components analysis (ICA) data were further filtered: (1) global signal normalization was performed (Chang and Glover, 2009; Fox et al., 2009); (2) motion parameters (translation and rotation) were regressed from the time-series data; (3) voxel time-courses were then extracted from white-matter and CSF masks and analyzed with principle components analysis (PCA), following Behzadi et al. (2007) the top five PCA components were then used to regress out systematic variance due to physiological noise; (4) data were then band-pass filtered (fast-Fourier transform) in the 0.01–0.10-Hz range (Cordes et al., 2001).

The resulting time-series data for each subject was then independently analyzed with ICA using FSL/Melodic (Beckmann and Smith, 2004). The number of components was not specified as the number was best determined by Melodic (Beckmann and Smith, 2004) using the Minimum Description Length algorithm (Rissanen, 1978). The ICA analysis produced between 15 and 40 ICA spatial components and corresponding temporal modes[1].

Next, we used the spatial templates from the networks defined in Smith et al. (2009). We took the top 10 templates defined from their BrainMap analysis[2] in the 20-component ICA scheme, thresholding each map at (component magnitude) >3.0. These template network maps were then used to identify the corresponding resting-state network (RSN) in our analysis. Assignment of a particular network to a component was done by maximizing the overall match for all 10 RSNs following the procedure of Greicius et al. (2004). A score was calculated for each network for the best matching ICA spatial component by taking the average of the in-map spatial component weight minus the average out-of-map spatial component weight. We required that a component could only be used once and if there was one component best matched to two or more RSNs, then all possible combinations were searched to get an overall best RSNs match for that subject.

In order to provide properly scaled data to the support vector machine, a correlation map for any particular RSN was created by calculating the correlation coefficient for each voxel in the RSN with the associate ICA time-course, after all other ICA time-courses had been regressed from the voxel time-series.

For this work we explored the utility of disease state classification based upon the networks that have been shown to be altered in ALS: DMN, Motor, and Fronto-Parietal. Additionally, given the observed ∼35% cognitive impairment in ALS (Jelsone-Swain et al., 2012) we also included the frontal executive network. In the Smith et al. (2009) nomenclature these are RSNs: RSN04,

[1]Mean number of components for ALS was 27 +/−7 and the mean number of components for HC was 24 +/- 4.

[2]http://www.fmrib.ox.ac.uk/analysis/brainmap+rsns/

RSN06, RSN07[3], RSN08, RSN09, RSN10. The selected networks are shown in **Figure 1**.

SUPPORT VECTOR MACHINE

Current implementations of support vector machines were first formulated by Cortes and Vapnik (1995). Briefly, a support vector machine is a supervised learning formalism that allows for complex solutions of discrimination classification. Typically an array of measures is carried out for each instance of a class. In our study measures of connectivity (the array of measures) are determined for each participant (each participant being an instance/observation) in the study. Unlike a massively parallel univariate analysis carried out between two groups, support vector machine formalism examines all measures simultaneously to determine a hyperplane in the space defined by the array of measures that may separate the two groups. Using the notation of Guyon and Elisseeff (2003):

$$D(\mathbf{x}) = \mathbf{w}\mathbf{x} + b$$

using a training data set, the decision boundary is optimized to give the weights $\boldsymbol{w}$. At the testing phase the decision solution for a given observation $\mathbf{x}$ of the array of measures can be calculated with the weight vector $\boldsymbol{w}$ determined by the SVM, and b is a bias value also determined by the SVM. When $D(\mathbf{x}) < 0$, then $\mathbf{x}$ belongs to the first class, while $D(\mathbf{x}) > 0$ indicates membership in the second class. *Inherently, the decision is a binary one.* Further formalism of the SVM methodology can be found in Cortes and Vapnik (1995).

As a simple example we illustrate this concept with **Figure 2**. In both examples each observation is characterized by two metrics. The boundary of the first is easily derived, but the boundary of the second that maximally discriminates between the two groups can take a highly complex form, even in this two-dimensional example.

We utilized the support vector machine (*libsvm version 3.17*) implementation of Chang and Lin (2011) and we opted to use

[3]We visually inspected each RSN template prior to selection. By using the "atlas" tool in FSL we determined that RSN07 also included portions of the motor system (pre-central gyrus), therefore we included it as a relevant network.

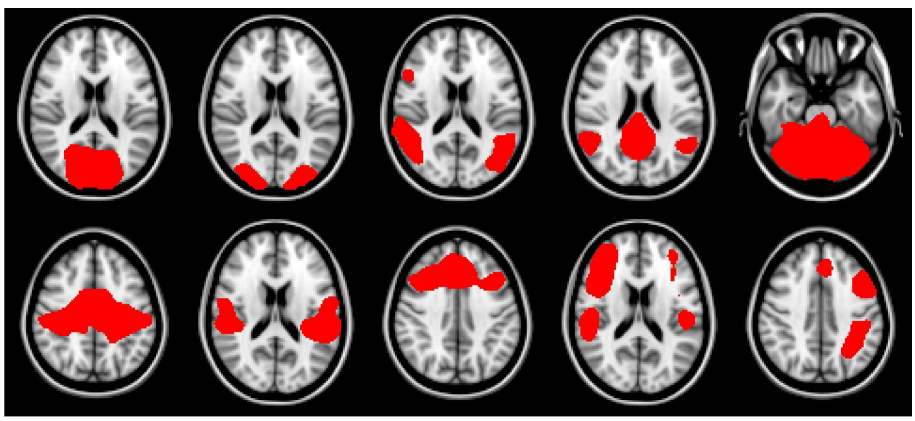

FIGURE 1 | Resting-state network templates corresponding to networks 1 through 10 from Smith et al. (2009). RSNs are numbered 1 through 10, with upper left being 1, and lower right be number 10. As in Smith et al. (2009) networks are as follows: 1–3: visual, 4: default mode, 5: cerebellum, 6: sensorimotor, 7: auditory, 8: executive, 9–10: fronto-parietal.

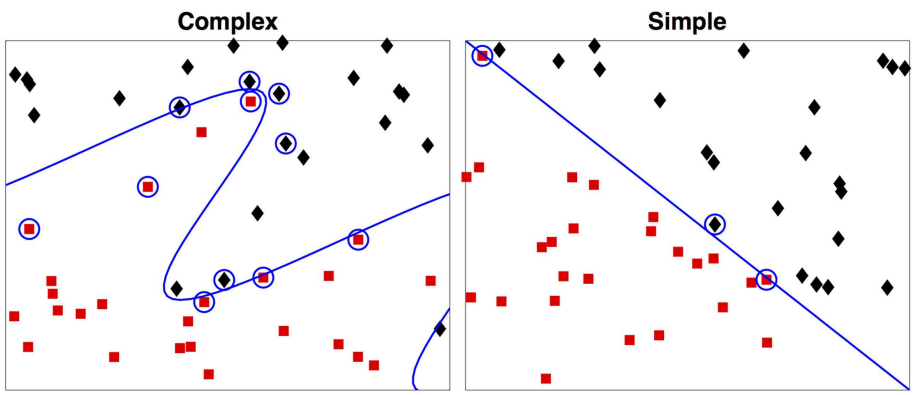

FIGURE 2 | Two-dimensional examples of a simple and a complex support vector machine solution. The two-class membership is indicated by color. The support vectors are indicated by the circles with the boundary defined by $D(\mathbf{x}) = 0$. During testing only the support vectors are used in determination of the class for the test case.

the linear kernel. Given the observations in the literature for compromises related to ALS in a variety of resting-state networks, we built feature-vectors of correlation coefficients from the following RSNs: default mode (Mohammadi et al., 2009), motor areas (Verstraete et al., 2010, 2011; Douaud et al., 2011), and left and right frontal-parietal regions (Agosta et al., 2013).

We used leave-one-out-cross-validation (LOOCV) (Burges, 1998) for calculation of SVM accuracy. The overall scheme is shown in **Figure 3**. We also examined the efficacy of simple feature filtering by including those features from a network that passed a two-tailed liberal statistically significant group difference of $p \leq 0.05$ (uncorrected) (Craddock et al., 2009). We performed a bootstrap (Jiang and Simon, 2007) on the LOOCV (100 bootstraps) and calculated the class prediction for each test case in the LOOCV as a continuous variable by averaging the 100 binary decision results. This average class prediction then allowed for the calculation of a receiver-operator curve (ROC). To estimate the variance on the area-under-the-curve (AUC) of the ROC we performed a bootstrap ROC.

Final classification accuracy was defined as the:

$$\frac{N^{\mathrm{ALS}}_{\mathrm{Correct}} + N^{\mathrm{HC}}_{\mathrm{Correct}}}{N^{\mathrm{ALS}}_{\mathrm{Total}} + N^{\mathrm{HC}}_{\mathrm{Total}}}$$

with $N^{\mathrm{ALS}}_{\mathrm{Total}} = 32$ and $N^{\mathrm{HC}}_{\mathrm{Total}} = 31$. $N^{\mathrm{ALS}}_{\mathrm{Correct}}$ and $N^{\mathrm{ALS}}_{\mathrm{Correct}}$ being the number of correctly SVM classified ALS and HC participants. To assess performance of the SVM against a typical univariate method, we followed methods by Fair et al. (2007) and calculated the number of nodes (Sporns, 2009) (voxels) present for a subject in the given network surpassing a Z-score of 0.10, 0.15, 0.20, 0.25, and 0.30. The number of nodes by subject was then used to calculate a univariate ROC.

RESULTS

DEMOGRAPHICS

A total of 32 individuals with ALS were enrolled in our study. Our main objective for HCs was to match for age. Mean ALS age was 58.4 ± 6.6 years and our HCs were aged 56.9 ± 5.0 and there was no significant difference in age (two-sample t-test $p = 0.319$). We did have a slight imbalance in gender matching, with ALS male/female = 21/11, and HC male/female = 16/15. However there was no age by gender bias, $p > 0.05$. Mean time since onset of symptoms for ALS was 1.8 ± 1.4 years with a range of 0.4–6.0 years. ALSFRS-R average score was 38.2 ± 5.7 with a range of 25–46. The ALSFRS-R score and time of scan since symptom onset distributions are show in **Figure 4**.

ICA GROUP VALIDATION

To demonstrate that the template matching succeeded, we calculated typical resting-state group analyses: subject correlation maps for each RSN were converted to Z-scores and entered into random effects analyses by group. Statistical images for the default mode (RSN04) and the primary motor network (RSN06) are shown in **Figure 5**.

SUPPORT VECTOR MACHINE RESULTS

In this survey of classification performance the SVM achieved 71.5% accuracy for determination of disease state as either ALS or healthy. This maximal classification accuracy came from a combined use of the default-mode network (RSN04) and the primary motor network (RSN06). For this combination the fraction of correctly classified ALS and HC was $N^{\mathrm{ALS}}_{\mathrm{Correct}} = 23$ and $N^{\mathrm{HC}}_{\mathrm{Correct}} = 22$. The SVM classification and univariate classification ROCs are shown in **Figure 6**. The bootstrap calculated AUC and variance was AUC = 0.716 ± 0.047. The univariate AUC was AUC = 0.544 ± 0.008. To test for a classification bias due to

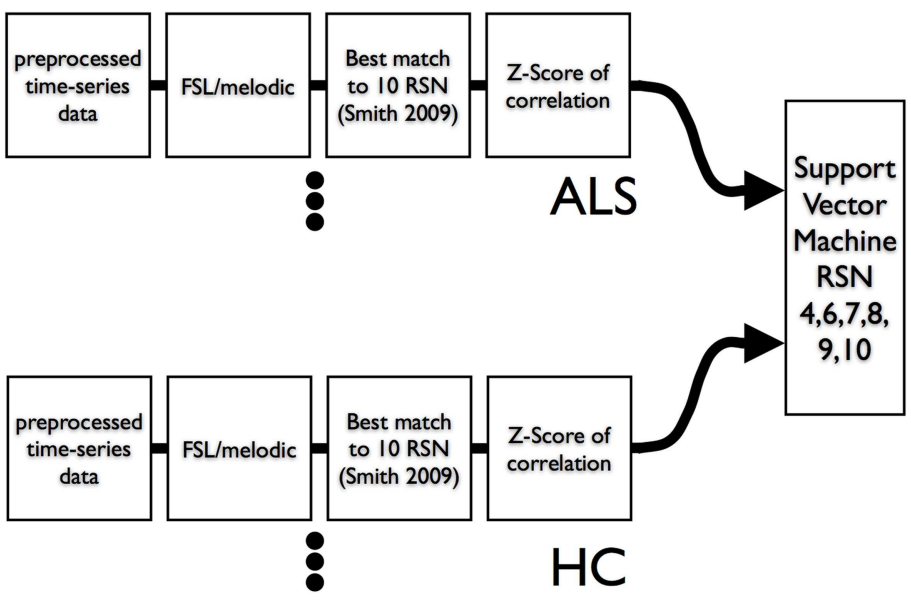

FIGURE 3 | Data flow of resting-state times series into ICA and then into SVM. A leave-one-out-cross-validation was utilized to assess SVM classification accuracy.

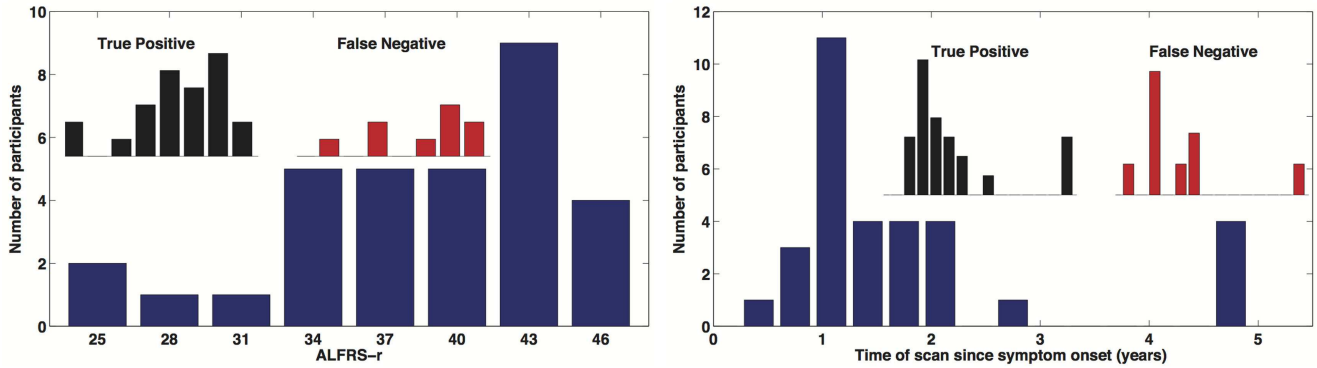

FIGURE 4 | Distribution of time of scan since symptom onset and observed distribution of ALSFRS-r in our ALS participant cohort. Inserted distributions are for the true-positive and false-negative classified groups.

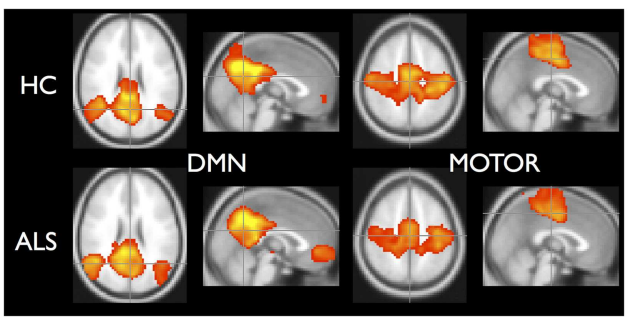

FIGURE 5 | Random effects analysis for default-mode network and motor network. Healthy controls are in top row and ALS are in bottom row. Statistical maps thresholded for $t \geq 3.5$ for illustrative purposes.

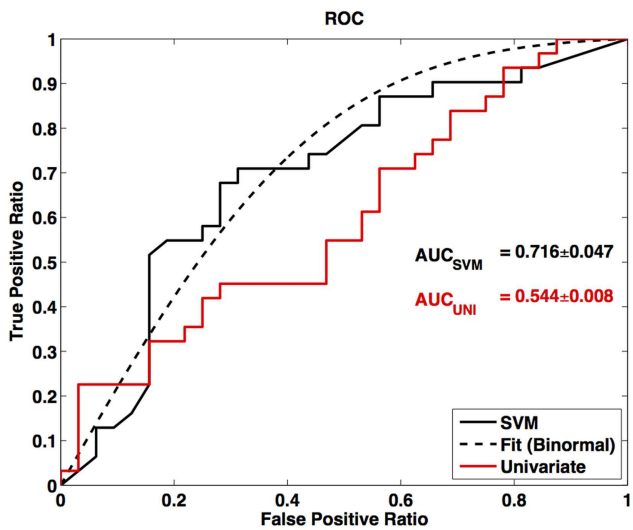

FIGURE 6 | Receiver-operator curve for LOOCV SVM and ROC for univariate node counting. Smooth curve is a binormal (Cai and Moskowitz, 2004) fit to the LOOCV SVM ROC. AUC is calculated from binormal fit.

ALSFRS-R or time-of-scan-since-symptom-onset (ONSET) we did a *post hoc* examination of the ALSFRS-R score and ONSET for those ALS participants that were accurately classified as ALS and those incorrectly classified as healthy. We also tested disease progression rate [defined as (48-ALSFRS-R)/ONSET] between these groups. We performed a non-parametric Kolmogorov–Smirnov (Chakravarti et al., 1967) test to assess if these values were drawn from the same or different parent distribution. Comparison of ALSFRS-R, ONSET, and progression rate between true-positive and false-negative groups revealed no significant differences ($p = 0.306$, $p = 0.744$, and $p = 0.372$ respectively). The ALSFRS-R and ONSET distributions for true positives and false negatives are shown in **Figure 4**.

DISCUSSION

Our work combined resting-state connectivity [derived from ICA (Beckmann and Smith, 2004)] and machine learning (Chang and Lin, 2011) to explore their utility for ALS disease-state prediction. ICA reliably identified well established (Damoiseaux et al., 2006; Smith et al., 2009) RSNs in our ALS and HC cohorts. By using a subset of these networks that have been shown to be altered by the ALS disease process (Mohammadi et al., 2009; Jelsone-Swain et al., 2010; Verstraete et al., 2010; Douaud et al., 2011; Agosta et al., 2013), in conjunction with machine learning (as implemented with a support vector machine), we have shown that machine learning has modest disease classification accuracy using resting-state fMRI data. The AUC of the SVM indicates better performance than the univariate classifier. In schizophrenia SVM derived classifications have been found to be between ∼62 and ∼85% (Tang et al., 2012; Yu et al., 2013) using whole brain connectivity. Using a specific and more finite number of network nodes Craddock et al. (2009) achieved 62% classification accuracy in depression with comparable *t*-test filtering.

Although extra motor regions have been implicated in ALS using other advanced neuroimaging methods such as diffusion tensor imaging (DTI), it is important to note that the motor networks had significant contribution to the SVM state classification. Though not presently recognized as a resting-state network showing alteration, the executive control network also contributes to

the disease state classification. The classification sensitivity to the executive network could be due to the ∼35% observed cognitive impairment seen in ALS (Rippon et al., 2006; Jelsone-Swain et al., 2012). Our findings demonstrate the power of multivariate techniques such as machine learning. We have shown there can exist significant systematic differences when the network is considered as a whole even though there can be a lack of statistically significant differences in specific node or edge-wise comparisons, such as in counting of significant nodes in a network (Sporns, 2009).

Seeley et al. (2009) suggested that disease state can be classified by functional network metrics derived from resting-state measurements using fMRI. Until recently the vast majority of the resting-state fMRI literature tested for statistically significant group differences with a voxel-wise approach (Smith, 2012). Much of that work was done with either seed based analysis or ICA (Fox et al., 2005; Damoiseaux et al., 2006) to determine these brain networks. The voxel-wise approach requires a spatial coherence in change due to the disease process, but also requires an observable change that meets statistical significance after correction for multiple comparisons (Marchini and Presanis, 2004). Although in our previous approach of investigating group differences, we relaxed this condition of spatially coherent change in the network by examining distribution differences of network metrics (correlation coefficient) (Jelsone-Swain et al., 2010). More recent group comparison approaches have taken on graph theoretical methodology (Cabral et al., 2011) to address questions of group differences.

In a multivariate approach, the data are used coherently to assess significance between groups. This approach is readily extended to build a decision algorithm to determine group membership based on the full suite of variables under consideration. The decision algorithm can be trained with an independent dataset and then assessed for accuracy through the use of an independent testing dataset. Indeed this is the operational approach of machine learning (Vatolkin et al., 2012). Essentially a mathematical decision boundary can be derived in the space of the suite of variables. This boundary is derived to maximize the separation of the groups to be classified [though due to noise in real systems one would not expect 100% separation (Wang and Summers, 2012)].

Discovering differences in brain metrics between two cohorts leads to a better understanding of the effect that a disease process has on a brain (Bandettini, 2012), such as an aberration in the motor network in ALS (Jelsone-Swain et al., 2010; Verstraete et al., 2010, 2011; Douaud et al., 2011). However, with increased understanding of observed changes, patterns can be revealed. These group differences can manifest patterns that can then be identified through machine-learning algorithms, more specifically in regard to identifying group membership. Eventually this can lead to the use of brain metrics to classify between two brain activity states (Laconte et al., 2005; De Martino et al., 2008; LaConte, 2011), or between states of diseased and healthy (Orrù et al., 2012). Thus, invoking multivariate techniques can lead to better state differentiation than differentiation based on voxel-wise or edge-wise univariate comparisons.

Advanced neuroimaging techniques, specifically resting-state fMRI, DTI and voxel-based morphometry, generate a large number of potentially useful data points. It is becoming increasingly clear that more conventional univariate brain analysis techniques used in concert with single modality imaging techniques do not provide sufficient disease discrimination in ALS. For example, a meta-analysis of DTI data results indicates only modest diagnostic test accuracy in ALS (Foerster et al., 2012b). As a result there is increased interest in applying more advanced brain mapping statistical techniques in ALS, including the implementation of machine-learning methods to analyze advanced MRI data in an effort to develop an imaging "fingerprint" of disease. The results presented here point to the potential utility of machine-learning methods to classify disease status in ALS using imaging data sets with a large number of variables. Additional research efforts are required to further explore this approach including combining different advanced neuroimaging approaches using machine-learning methods. In addition to resting-state fMRI the modalities to be included should be: DTI (Chapman et al., 2013), high-resolution structural imaging (Grosskreutz et al., 2006), and magnetic resonance spectroscopy (Foerster et al., 2012a) as put forth by Turner et al. (2009). Furthermore, given the heterogenous presentation of ALS, which can lead to clinical diagnostic uncertainly, it would be warranted to apply SVM classification methods and advanced neuroimaging techniques to a cohort of individuals at first presentation with neurological symptoms. The imaging should occur prior to a definitive diagnosis of ALS and follow the individuals longitudinally. Given the differential nature of disease diagnosis, future studies should also include ALS mimics, that is, other neurodegenerative diseases with overlapping symptom presentation, to fully explore the power of classification schemes (Turner and Modo, 2010). The true diagnostic utility of such a classifier would be in providing input into the clinical process with the resulting goal of shortening the duration between symptom presentation and final diagnosis of ALS.

LIMITATIONS

There are of course limitations to our study. First, ALS is a highly divergent disease process with highly varying progression paths. Certainly, utilizing a larger cohort of individuals with ALS and a larger cohort of HCs would lead to a better definition of classifiers. Though the ALS disease process has a quite divergent nature we have built our classifier decision from two classes. Another approach would be to build a single state (one-class) classifier (Manevitz and Yousef, 2002). Under those conditions, the question would be, "*Does the test case belong to the one-class classifier?*" Our approach has also only included a single category of metrics, namely resting-state derived brain networks. Other MRI modalities have also been shown to be sensitive to the ALS disease process, such as cortex thinning (Roccatagliata et al., 2009; Turner et al., 2009), increased radial diffusivity (RD) and decreased fractional anisotropy (FA) (Wang and Melhem, 2005; Schimrigk et al., 2007; Filippini et al., 2010; Foerster et al., 2012b), and more recently decreased gamma-aminobutyric acid (GABA) concentration in the motor cortex (Foerster et al., 2012a). We do note that this is the first application of machine learning for the classification of disease status in ALS using MRI data[4]. Construction of a complex

[4]A pubmed.org search of the title/abstract terms [("ALS" or "amyotrophic lateral sclerosis") and ("support vector machine" or "SVM")] yields no imaging literature.

differential diagnosis classification scheme first has to demonstrate distinction between well-defined classes such as definite ALS and HCs. As such, this current work is exploratory in nature but demonstrates the clear promise of such techniques to continue in the near future.

CONCLUSION

Resting-state functional connectivity reveals intrinsic networks in the human brain. These networks can be viewed as patterns that are a manifestation of the state of the brain including altered network patterns present in disease (Seeley et al., 2009). By applying multivariate pattern classification methodology we have demonstrated that machine-learning methodology (support vector machine) in conjunction with brain networks derived from resting-state fMRI can be used to classify a diseased brain (ALS) from a healthy brain. Additional research efforts are required to validate our findings as well as to investigate the added diagnostic utility of including other MR modalities in the setting of ALS using machine-learning methods.

ACKNOWLEDGMENTS

We would like to thank Dr. Kirsten Gruis and the ALS Clinic/Motor Neuron Clinic at the University of Michigan for their invaluable assistance in recruitment of ALS patients. We would like to thank Rebecca Hovatter and Nick Rademacher for study coordination. We thank MR research technologist Keith Newnham for assisting in collection of the MR data. This work has been supported by Basic Radiological Sciences Seed Grant (Robert C. Welsh) and NIH/NINDS R01-NS052514 (Robert C. Welsh).

REFERENCES

Agosta, F., Canu, E., Valsasina, P., Riva, N., Prelle, A., Comi, G., et al. (2013). Divergent brain network connectivity in amyotrophic lateral sclerosis. *Neurobiol. Aging* 34, 419–427. doi:10.1016/j.neurobiolaging.2012.04.015

Bandettini, P. A. (2012). Twenty years of functional MRI: the science and the stories. *Neuroimage* 62, 575–588. doi:10.1016/j.neuroimage.2012.04.026

Beckmann, C. F., and Smith, S. M. (2004). Probabilistic independent component analysis for functional magnetic resonance imaging. *IEEE Trans. Med. Imaging* 23, 137–152. doi:10.1109/TMI.2003.822821

Beghi, E., Logroscino, G., Chiò, A., Hardiman, O., Mitchell, D., Swingler, R., et al. (2006). The epidemiology of ALS and the role of population-based registries. *Biochim. Biophys. Acta* 1762, 1150–1157. doi:10.1016/j.bbadis.2006.09.008

Behzadi, Y., Restom, K., Liau, J., and Liu, T. T. (2007). A component based noise correction method (CompCor) for BOLD and perfusion based fMRI. *Neuroimage* 37, 90–101. doi:10.1016/j.neuroimage.2007.04.042

Biswal, B. B., Van Kylen, J., and Hyde, J. S. (1997). Simultaneous assessment of flow and BOLD signals in resting-state functional connectivity maps. *NMR Biomed.* 10, 165–170. doi:10.1002/(SICI)1099-1492(199706/08)10:4/5<165::AID-NBM454>3.0.CO;2-7

Brooks, B. R., Miller, R. G., Swash, M., and Munsat, T. L. (2000). El Escorial revisited: revised criteria for the diagnosis of amyotrophic lateral sclerosis. *Amyotroph. Lateral Scler. Other Motor Neuron Disord.* 1, 293–299. doi:10.1080/146608200300079536

Burges, C. (1998). A tutorial on support vector machines for pattern recognition. *Data Min. Knowl. Discov.* 2, 121–167. doi:10.1023/A:1009715923555

Cabral, J., Hugues, E., Sporns, O., and Deco, G. (2011). Role of local network oscillations in resting-state functional connectivity. *Neuroimage* 57, 130–139. doi:10.1016/j.neuroimage.2011.04.010

Cai, T., and Moskowitz, C. S. (2004). Semi-parametric estimation of the binormal ROC curve for a continuous diagnostic test. *Biostatistics* 5, 573–586. doi:10.1093/biostatistics/kxh009

Cedarbaum, J. M., Stambler, N., Malta, E., Fuller, C., Hilt, D., Thurmond, B., et al. (1999). The ALSFRS-R: a revised ALS functional rating scale that incorporates assessments of respiratory function. BDNF ALS Study Group (Phase III). *J. Neurol. Sci.* 169, 13–21. doi:10.1016/S0022-510X(99)00210-5

Chakravarti, I. M., Laha, R. G., and Roy, J. (1967). *Handbook of Methods of Applied Statistics*, Vol. 1. New York: John Wiley and Sons. 392–394.

Chan, S., Kaufmann, P., Shungu, D. C., and Mitsumoto, H. (2003). Amyotrophic lateral sclerosis and primary lateral sclerosis: evidence-based diagnostic evaluation of the upper motor neuron. *Neuroimaging Clin. N. Am.* 13, 307–326. doi:10.1016/S1052-5149(03)00018-2

Chang, C., and Glover, G. H. (2009). Effects of model-based physiological noise correction on default mode network anti-correlations and correlations. *Neuroimage* 47, 1448–1459. doi:10.1016/j.neuroimage.2009.05.012

Chang, C.-C., and Lin, C.-J. (2011). LIBSVM. *ACM Trans. Intell. Syst. Technol.* 2, 1–27. doi:10.1145/1961189.1961199

Chapman, M. C., Jelsone-Swain, L., Johnson, T. D., Gruis, K. L., and Welsh, R. C. (2013). Diffusion tensor MRI of the corpus callosum in amyotrophic lateral sclerosis. *J. Magn. Reson. Med.* (in press).

Chen, S.-H., Sun, J., Dimitrov, L., Turner, A. R., Adams, T. S., Meyers, D. A., et al. (2008). A support vector machine approach for detecting gene-gene interaction. *Genet. Epidemiol.* 32, 152–167. doi:10.1002/gepi.20272

Cheung, G., Gawel, M. J., Cooper, P. W., Farb, R. I., Ang, L. C., and Gawal, M. J. (1995). Amyotrophic lateral sclerosis: correlation of clinical and MR imaging findings. *Radiology* 194, 263–270.

Comi, G., Rovaris, M., and Leocani, L. (1999). Review neuroimaging in amyotrophic lateral sclerosis. *Eur. J. Neurol.* 6, 629–637. doi:10.1046/j.1468-1331.1999.660629.x

Cordes, D., Haughton, V. M., Arfanakis, K., Carew, J. D., Turski, P. A., Moritz, C. H., et al. (2001). Frequencies contributing to functional connectivity in the cerebral cortex in "resting-state" data. *AJNR Am. J. Neuroradiol.* 22, 1326–1333.

Cortes, C., and Vapnik, V. (1995). Support vector machine. *Mach. Learn.* 20, 273–297. doi:10.1023/A:1022627411411

Craddock, R. C., Holtzheimer, P. E. III, Hu, X. P., and Mayberg, H. S. (2009). Disease state prediction from resting state functional connectivity. *Magn. Reson. Med.* 62, 1619–1628. doi:10.1002/mrm.22159

Cudkowicz, M., Qureshi, M., and Shefner, J. (2004). Measures and markers in amyotrophic lateral sclerosis. *NeuroRx* 1, 273–283. doi:10.1602/neurorx.1.2.273

Damoiseaux, J. S., Rombouts, S. A. R. B., Barkhof, F., Scheltens, P., Stam, C. J., Smith, S. M., et al. (2006). Consistent resting-state networks across healthy subjects. *Proc. Natl. Acad. Sci. U.S.A.* 103, 13848–13853. doi:10.1073/pnas.0601417103

De Martino, F., Valente, G., Staeren, N., Ashburner, J., Goebel, R., and Formisano, E. (2008). Combining multivariate voxel selection and support vector machines for mapping and classification of fMRI spatial patterns. *Neuroimage* 43, 44–58. doi:10.1016/j.neuroimage.2008.06.037

Douaud, G., Filippini, N., Knight, S., Talbot, K., and Turner, M. R. (2011). Integration of structural and functional magnetic resonance imaging in amyotrophic lateral sclerosis. *Brain* 134, 3470–3479. doi:10.1093/brain/awr279

Fair, D. A., Dosenbach, N. U. F., Church, J. A., Cohen, A. L., Brahmbhatt, S., Miezin, F. M., et al. (2007). Development of distinct control networks through segregation and integration. *Proc. Natl. Acad. Sci. U.S.A.* 104, 13507–13512. doi:10.1073/pnas.0705843104

Filippini, N., Douaud, G., Mackay, C. E., Knight, S., Talbot, K., and Turner, M. R. (2010). Corpus callosum involvement is a consistent feature of amyotrophic lateral sclerosis. *Neurology* 75, 1645–1652. doi:10.1212/WNL.0b013e3181fb84d1

Foerster, B. R., Callaghan, B. C., Petrou, M., Edden, R. A. E., Chenevert, T. L., and Feldman, E. L. (2012a). Decreased motor cortex-aminobutyric acid in amyotrophic lateral sclerosis. *Neurology* 78, 1596–1600. doi:10.1212/WNL.0b013e3182563b57

Foerster, B. R., Dwamena, B. A., Petrou, M., Carlos, R. C., Callaghan, B. C., and Pomper, M. G. (2012b). Diagnostic accuracy using diffusion tensor imaging in the diagnosis of ALS: a meta-analysis. *Acad. Radiol.* 19, 1075–1086. doi:10.1016/j.acra.2012.04.012

Fox, M. D., Snyder, A. Z., Vincent, J. L., Corbetta, M., Van Essen, D. C., and Raichle, M. E. (2005). The human brain is intrinsically organized into dynamic, anticorrelated functional networks. *Proc. Natl. Acad. Sci. U.S.A.* 102, 9673–9678. doi:10.1073/pnas.0504136102

Fox, M. D., Zhang, D., Snyder, A. Z., and Raichle, M. E. (2009). The global signal and observed anticorrelated resting state brain networks. *J. Neurophysiol.* 101, 3270–3283. doi:10.1152/jn.90777.2008

Ghadge, G. D., Slusher, B. S., Bodner, A., Canto, M. D., Wozniak, K., Thomas, A. G., et al. (2003). Glutamate carboxypeptidase II inhibition protects motor neurons from death in familial amyotrophic lateral sclerosis models. *Proc. Natl. Acad. Sci. U.S.A.* 100, 9554–9559. doi:10.1073/pnas.1530168100

Greicius, M. D., Srivastava, G., Reiss, A. L., and Menon, V. (2004). Default-mode network activity distinguishes Alzheimer's disease from healthy aging: evidence from functional MRI. *Proc. Natl. Acad. Sci. U.S.A.* 101, 4637–4642. doi:10.1073/pnas.0308627101

Grosskreutz, J., Kaufmann, J., Frädrich, J., Dengler, R., Heinze, H.-J., and Peschel, T. (2006). Widespread sensorimotor and frontal cortical atrophy in amyotrophic lateral sclerosis. *BMC Neurol.* 6:17. doi:10.1186/1471-2377-6-17

Guyon, I., and Elisseeff, A. (2003). An introduction to variable and feature selection. *J. Mach. Learn. Res.* 3, 1157–1182.

Hofmann, E., Ochs, G., Pelzl, A., and Warmuth-Metz, M. (1998). The corticospinal tract in amyotrophic lateral sclerosis: an MRI study. *Neuroradiology* 40, 71–75. doi:10.1007/s002340050543

Jelsone-Swain, L., Persad, C., Votruba, K. L., Weisenbach, S. L., Johnson, T. D., Gruis, K. L., et al. (2012). The relationship between depressive symptoms, disease state, and cognition in amyotrophic lateral sclerosis. *Front. Psychol.* 3:542. doi:10.3389/fpsyg.2012.00542

Jelsone-Swain, L. M., Fling, B. W., Seidler, R. D., Hovatter, R., Gruis, K., and Welsh, R. C. (2010). Reduced interhemispheric functional connectivity in the motor cortex during rest in limb-onset amyotrophic lateral sclerosis. *Front. Syst. Neurosci.* 4:158. doi:10.3389/fnsys.2010.00158

Jenkinson, M., Beckmann, C. F., Behrens, T. E. J., Woolrich, M. W., and Smith, S. M. (2012). FSL. *Neuroimage* 62, 782–790. doi:10.1016/j

Jiang, W., and Simon, R. (2007). A comparison of bootstrap methods and an adjusted bootstrap approach for estimating the prediction error in microarray classification. *Stat. Med.* 26, 5320–5334. doi:10.1002/sim.2968

Karitzky, J., and Ludolph, A. C. (2001). Imaging and neurochemical markers for diagnosis and disease progression in ALS. *J. Neurol. Sci.* 191, 35–41. doi:10.1016/S0022-510X(01)00628-1

Laconte, S., Strother, S., Cherkassky, V., Anderson, J., and Hu, X. (2005). Support vector machines for temporal classification of block design fMRI data. *Neuroimage* 26, 317–329. doi:10.1016/j.neuroimage.2005.01.048

LaConte, S. M. (2011). Decoding fMRI brain states in real-time. *Neuroimage* 56, 440–454. doi:10.1016/j.neuroimage.2010.06.052

Lowe, M. J., Mock, B. J., and Sorenson, J. A. (1998). Functional connectivity in single and multislice echoplanar imaging using resting-state fluctuations. *Neuroimage* 7, 119–132. doi:10.1006/nimg.1997.0315

Magnin, B., Mesrob, L., Kinkingnéhun, S., Pélégrini-Issac, M., Colliot, O., Sarazin, M., et al. (2008). Support vector machine-based classification of Alzheimer's disease from whole-brain anatomical MRI. *Neuroradiology* 51, 73–83. doi:10.1007/s00234-008-0463-x

Manevitz, L. M., and Yousef, M. (2002). One-class SVMs for document classification. *J. Mach. Learn. Res.* 2, 139–154.

Marchini, J., and Presanis, A. (2004). Comparing methods of analyzing fMRI statistical parametric maps. *Neuroimage* 22, 1203–1213. doi:10.1016/j.neuroimage.2004.03.030

Mohammadi, B., Kollewe, K., Samii, A., Krampfl, K., Dengler, R., and Münte, T. F. (2009). Changes of resting state brain networks in amyotrophic lateral sclerosis. *Exp. Neurol.* 217, 147–153.

Orrù, G., Pettersson-Yeo, W., Marquand, A. F., Sartori, G., and Mechelli, A. (2012). Using support vector machine to identify imaging biomarkers of neurological and psychiatric disease: a critical review. *Neurosci. Biobehav. Rev.* 36, 1140–1152. doi:10.1016/j.neubiorev.2012.01.004

Rippon, G. A., Scarmeas, N., Gordon, P. H., Murphy, P. L., Albert, S. M., Mitsumoto, H., et al. (2006). An observational study of cognitive impairment in amyotrophic lateral sclerosis. *Arch. Neurol.* 63, 345–352. doi:10.1001/archneur.63.3.345

Rissanen, J. (1978). Modeling by shortest data description. *Automatica* 14, 465–471. doi:10.1016/0005-1098(78)90005-5

Roccatagliata, L., Bonzano, L., Mancardi, G., Canepa, C., and Caponnetto, C. (2009). Detection of motor cortex thinning and corticospinal tract involvement by quantitative MRI in amyotrophic lateral sclerosis. *Amyotroph. Lateral Scler.* 10, 47–52. doi:10.1080/17482960802267530

Schimrigk, S. K., Bellenberg, B., Schlüter, M., Stieltjes, B., Drescher, R., Rexilius, J., et al. (2007). Diffusion tensor imaging-based fractional anisotropy quantification in the corticospinal tract of patients with amyotrophic lateral sclerosis using a probabilistic mixture model. *AJNR Am. J. Neuroradiol.* 28, 724–730.

Seeley, W. W., Crawford, R. K., Zhou, J., Miller, B. L., and Greicius, M. D. (2009). Neurodegenerative diseases target large-scale human brain networks. *Neuron* 62, 42–52. doi:10.1016/j.neuron.2009.03.024

Smith, S. M. (2012). The future of FMRI connectivity. *Neuroimage* 62, 1257–1266. doi:10.1016/j.neuroimage.2012.01.022

Smith, S. M., Fox, P. T., Miller, K. L., Glahn, D. C., Fox, P. M., Mackay, C. E., et al. (2009). Correspondence of the brain's functional architecture during activation and rest. *Proc. Natl. Acad. Sci. U.S.A.* 106, 13040–13045. doi:10.1073/pnas.0905267106

Sporns, O. (2009). "The human connectome: linking structure and function in the human brain," in *Diffusion MRI*, eds H. Johansen-Berg and T. Behrens (San Diego: Elsevier), 309–332.

Stern, E. R., Welsh, R. C., Fitzgerald, K. D., Gehring, W. J., Lister, J. J., Himle, J. A., et al. (2011). Hyperactive error responses and altered connectivity in ventromedial and frontoinsular cortices in obsessive-compulsive disorder. *Biol. Psychiatry* 69, 583–591. doi:10.1016/j.biopsych.2010.09.048

Tang, Y., Wang, L., Cao, F., and Tan, L. (2012). Identify schizophrenia using resting-state functional connectivity: an exploratory research and analysis. *Biomed. Eng. Online* 11, 1–1. doi:10.1186/1475-925X-11-50

Turner, M. R., Kiernan, M. C., Leigh, P. N., and Talbot, K. (2009). Biomarkers in amyotrophic lateral sclerosis. *Lancet Neurol.* 8, 94–109. doi:10.1016/S1474-4422(08)70293-X

Turner, M. R., and Modo, M. (2010). Advances in the application of MRI to amyotrophic lateral sclerosis. *Expert Opin. Med. Diagn.* 4, 483–496. doi:10.1517/17530059.2010.536836

Vatolkin, I., Theimer, W., and Botteck, M. (2012). "Partition based feature processing for improved music classification," in *Studies in Classification, Data Analysis, and Knowledge Organization*, eds W. A. Gaul, A. Geyer-Schulz, L. Schmidt-Thieme, and J. Kunze (Berlin: Springer), 411–419.

Verstraete, E., van den Heuvel, M. P., Veldink, J. H., Blanken, N., Mandl, R. C., Hulshoff Pol, H. E., et al. (2010). Motor network degeneration in amyotrophic lateral sclerosis: a structural and functional connectivity study. *PLoS ONE* 2012:e13664. doi:10.1371/journal.pone.0013664

Verstraete, E., Veldink, J. H., Mandl, R. C. W., van den Berg, L. H., and van den Heuvel, M. P. (2011). Impaired structural motor connectome in amyotrophic lateral sclerosis. *PLoS ONE* 6:e24239. doi:10.1371/journal.pone.0024239

Wang, S., and Melhem, E. R. (2005). Amyotrophic lateral sclerosis and primary lateral sclerosis: the role of diffusion tensor imaging and other advanced MR-based techniques as objective upper motor neuron markers. *Ann. N. Y. Acad. Sci.* 1064, 61–77. doi:10.1196/annals.1340.013

Wang, S., and Summers, R. M. (2012). Machine learning and radiology. *Med. Image Anal.* 16, 933–951. doi:10.1016/j.media.2012.02.005

Welsh, R. C., Chen, A. C., and Taylor, S. F. (2010). Low-frequency BOLD fluctuations demonstrate altered thalamocortical connectivity in schizophrenia. *Schizophr. Bull.* 36, 713–722. doi:10.1093/schbul/sbn145

Yu, Y., Shen, H., Zhang, H., Zeng, L.-L., Xue, Z., and Hu, D. (2013). Functional connectivity-based signatures of schizophrenia revealed by multiclass pattern analysis of resting-state fMRI from schizophrenic patients and their healthy siblings. *Biomed. Eng. Online* 12, 1–1. doi:10.1186/1475-925X-12-10

Zeng, L. L., Shen, H., Liu, L., Wang, L., Li, B., Fang, P., et al. (2012). Identifying major depression using whole-brain functional connectivity: a multivariate pattern analysis. *Brain* 135, 1498–1507. doi:10.1093/brain/aws059

Zoccolella, S., Beghi, E., Palagano, G., Fraddosio, A., Samarelli, V., Lamberti, P., et al. (2006). Predictors of delayin the diagnosis and clinical trial entry of amyotrophic lateral sclerosis patients: a population-based study. *J. Neurol. Sci.* 250, 45–49. doi:10.1016/j.jns.2006.06.027

Conflict of Interest Statement: The authors declare that the research was conducted in the absence of any commercial or financial relationships that could be construed as a potential conflict of interest.

Received: 25 January 2013; accepted: 20 May 2013; published online: 10 June 2013.

*Citation: Welsh RC, Jelsone-Swain LM and Foerster BR (2013) The utility of independent component analysis and machine learning in the identification of the amyotrophic lateral sclerosis diseased brain. Front. Hum. Neurosci. **7**:251. doi: 10.3389/fnhum.2013.00251*

frontiers in
HUMAN NEUROSCIENCE

ORIGINAL RESEARCH ARTICLE
published: 22 March 2013
doi: 10.3389/fnhum.2013.00094

Testing independent component patterns by inter-subject or inter-session consistency

***Aapo Hyvärinen*[1,2]* and *Pavan Ramkumar*[3]**

[1] *Department of Computer Science and Helsinki Institute for Information Technology, University of Helsinki, Helsinki, Finland*
[2] *Department of Mathematics and Statistics, University of Helsinki, Helsinki, Finland*
[3] *Brain Research Unit, O. V. Lounasmaa Laboratory, Advanced Magnetic Imaging Centre, Aalto University, Espoo, Finland*

Edited by:
Veronika Schöpf, Medical University Vienna, Austria

Reviewed by:
Robert C. Welsh, University of Michigan, USA
Jorge Jovicich, University of Trento, Italy

***Correspondence:**
Aapo Hyvärinen, Department of Computer Science, Gustaf Hällströmin katu 2b, 00560 Helsinki, Finland.
e-mail: aapo.hyvarinen@helsinki.fi

Independent component analysis (ICA) is increasingly used to analyze patterns of spontaneous activity in brain imaging. However, there are hardly any methods for answering the fundamental question: are the obtained components statistically significant? Most methods considering the significance of components either consider group-differences or use arbitrary thresholds with weak statistical justification. In previous work, we proposed a statistically principled method for testing if the coefficients in the mixing matrix are similar in different subjects or sessions. In many applications of ICA, however, we would like to test the reliability of the independent components themselves and not the mixing coefficients. Here, we develop a test for such an inter-subject consistency by extending our previous theory. The test is applicable, for example, to the spatial activity patterns obtained by spatial ICA in resting-state fMRI. We further improve both this and the previously proposed testing method by introducing a new way of correcting for multiple testing, new variants of the clustering method, and a computational approximation which greatly reduces the memory and computation required.

Keywords: independent component analysis, inter-subject consistency, resting-state fMRI, significance testing, group analysis

1. INTRODUCTION

After estimating the parameters of any statistical model, it would be reasonable to test them in some way for statistical significance, also called reliability in some contexts. In the case of independent component analysis (ICA), methods for such testing have not been widely used, nor do many exist in the first place. Methods for group-difference testing (Calhoun et al., 2009) are widely used, but the fundamental question of which components are reliable in a single group or even a single subject is rarely considered using principled statistical testing methods.

In previous work, we proposed a framework which develops such testing methods based on the concept of inter-subject consistency. The basic idea is to perform ICA separately for each subject, and define that an estimated component can be considered significant if it appears in sufficiently similar form in more than one subject (Hyvärinen, 2011). A rigorous formula for what is "sufficiently" similar was derived based on the definition of a null hypothesis and application of statistical testing theory. This provided a quantitative theoretical basis for the self-organizing group ICA method originally proposed by Esposito et al. (2005). Thus, the testing method provided, at the same time, a solution to the problem of how to do ICA simultaneously on data from many subjects, or in general, many data matrices (Calhoun et al., 2001, 2009). In fact, data from a single subject can also be tested by doing ICA separately for data from several sessions recorded from the same subject, and considering similarities between the sessions in the same way.

However, the theory by Hyvärinen (2011) was only developed for the case where the inter-subject consistency was seen in the columns of the mixing matrices. This is relevant in particular to the case of temporal ICA, typically applied on EEG and MEG, where the mixing matrix gives the spatial patterns of activity. Yet, the most common application of ICA in brain imaging is the spatial ICA of fMRI data, often measured at rest (Kiviniemi et al., 2003; van de Ven et al., 2004; Beckmann et al., 2005). A related spatial ICA method was recently proposed on MEG as well by Ramkumar et al. (2012). For such spatial ICA, inter-subject consistency is usually measured between the spatial patterns which are the independent components themselves, and not the columns of the mixing matrix.

Here, we adapt the theory by Hyvärinen (2011) for the case where the inter-subject consistency is sought among the independent components, as in spatial ICA of resting-state fMRI. We propose a generalization of the null hypothesis by Hyvärinen (2011) to accommodate the case of testing the independent components. We take an empirical approach to modeling the null distributions since a purely analytical approach like in Hyvärinen (2011) does not seem feasible. We also propose a number of improvements and generalizations to the general framework, which can be used in the case of testing the mixing matrix as well. Like the method in Hyvärinen (2011), the current method can be directly applied on data from different recording sessions of the same subject as well.

2. MATHEMATICAL THEORY

2.1. CLUSTERING OF COMPONENTS BY INTER-SUBJECT CONSISTENCY

Assume we have measurements of r subjects or sessions. Denote by $\mathbf{X}_k$, $k = 1, \ldots, r$ the data matrix for the k-th subject or session. For simplicity of terminology, we assume in the following that the data comes from different subjects and not sessions. If the data matrix comes from fMRI recordings, and we are to perform spatial ICA, each row is one time point (one volume) and each column a voxel. Assume we have performed ICA separately for all the subjects, obtaining the estimated decompositions.

$$\hat{\mathbf{S}}_k = \hat{\mathbf{W}}_k \mathbf{X}_k, \text{ or } \mathbf{X}_k = \hat{\mathbf{A}}_k \hat{\mathbf{S}}_k, \tag{1}$$

where $\hat{\mathbf{A}}_k$ is the pseudoinverse of $\hat{\mathbf{W}}_k$. In the following we only analyze $\hat{\mathbf{S}}_k$, so it is immaterial whether any dimension reduction is done by PCA, and whether the $\hat{\mathbf{W}}_k$ and $\hat{\mathbf{A}}_k$ are in the whitened space or in the original.

Now, following Esposito et al. (2005), we want to combine the ICA results for the different subjects by clustering. That is, we try to find components which are similar enough in different subjects, so that we can consider them to correspond to the same underlying component. Each such cluster of sufficiently similar components (i.e., components with sufficient inter-subject consistency) is then considered a single group-level component in subsequent analysis. The key challenges in such a method are to find principled and practical definitions for similarity, and to define the thresholds regarding when the components are similar enough to be considered the same.

Our goal here is to devise a statistical test to determine if some of the rows of $\hat{\mathbf{S}}_k$ are sufficiently similar for different k in the sense that the similarity cannot be due to chance. We assume here that the rows of $\hat{\mathbf{S}}_k$ model the phenomena of interest (e.g., spatial patterns of brain activity in fMRI) whose inter-subject consistency we want to test. In contrast, we do not assume that the $\mathbf{A}_k$ have any inter-subject consistency. For example, in spatial ICA of fMRI, the $\mathbf{A}_k$ give the time courses which hardly have any inter-subject consistency in the case of resting-state activity.

The key to a principled statistical test is the definition of a null hypothesis, H_0. The null hypothesis should model the case where the ICA results for different subjects are completely independent of each other in the sense that the components in different subjects have no similarity at all, other than what would be expected by chance. As argued by Hyvärinen (2011), the randomness can in fact come from two different sources:

1. It could be that the ICA algorithm fails completely, or
2. It could be that the underlying data are completely different for each subject in the sense that the brain networks are completely different from each other.

We will begin by introducing a null distribution which embodies these two sources of randomness.

2.2. DEFINITION OF NULL DISTRIBUTION

In order to model the randomness in the ICA estimation procedure, we define a null hypothesis as follows. We assume, following Hyvärinen (2011), that the estimated $\hat{\mathbf{A}}_k$ are random orthogonal transformations of the actual mixing matrices. Denote by $\mathbf{U}_k$ random orthogonal matrices (more precisely, matrices uniformly distributed in the set of orthogonal matrices). Under the null hypothesis we have, for the estimated decompositions:

$$\hat{\mathbf{A}}_k = \mathbf{A}_k \mathbf{U}_k \text{ or } \hat{\mathbf{W}}_\mathbf{k} = \mathbf{U}_\mathbf{k}^\mathbf{T} \mathbf{W}_\mathbf{k} \tag{2}$$

where $\mathbf{A}_k$ and $\mathbf{S}_k$ below denote the actual underlying values of those parameters or random variables, as opposed to the estimates $\hat{\mathbf{A}}_k$ and $\hat{\mathbf{S}}_k$. This randomness due to the $\mathbf{U}_k$ models errors in the ICA estimation procedure. The idea is to assume that the prewhitening step in ICA was successfully performed, but the ICA algorithm returned a random result, i.e., a random orthogonal transformation in the whitened space. This is equivalent to assuming that the estimates of the $\mathbf{S}_k$ are random orthogonal rotations of the actual $\mathbf{S}_k$:

$$\hat{\mathbf{S}}_k = \mathbf{U}_k^T \mathbf{S}_k \tag{3}$$

since $\mathbf{X}_k = \hat{\mathbf{A}}_k \hat{\mathbf{S}}_k = \mathbf{A}_k \mathbf{S}_k$.

We have to further model randomness in the actual independent components, due to individual differences in brain anatomy and physiology. In our previous model (Hyvärinen, 2011), the randomness relating to the actual individual differences of the brains was assumed to be reflected in this same orthogonal rotation, since the spatial patterns corresponded to the columns of $\mathbf{A}_k$. This assumption was justified in the case of testing the mixing matrix, e.g., in the case of temporal ICA of EEG or MEG. However, when testing for similarities of the independent components, that assumption does not seem to be adequate. This is because if the individual differences of the brains were modeled by a random rotation of the spatial patterns as in equation (3), we would be violating the ICA model, since such a random rotation would make the components dependent. Therefore, we need to model the individual variability of the brains by a separate random model. The random model should give random spatial patterns which still follow the ICA model, i.e., are independent for each subject.

The approach we take here is to assume that under the null hypothesis H_0, the rows of the $\mathbf{S}_k$, denoted by $\mathbf{S}_{ki}$, follow the same multivariate distribution $p_s(\mathbf{S}_{ki})$. In general, this is a stochastic (spatial) process which models the hypothetical generation of spatial patterns given by the independent components. Drawing each $\mathbf{S}_{ki}$ randomly and independently of each other from p_s does give us a number of components which are, by construction, independent, and thus respect the assumptions of the ICA model.

In the case of spatial ICA, the distribution p_s essentially models the spatial regularities of the patterns, including patterns of brain activity or artifacts on the one hand, and measurement noise on the other. We cannot assume, for example, that the voxels are all independent of each other, since this would grossly overestimate the degree of randomness, and thus underestimate the similarities obtained by chance.

Here, we do not attempt to construct an explicit model of p_s. Instead, we construct an empirical model of the null distribution of the similarities between the components, which is the relevant quantity for the construction of tests, as will be discussed next.

2.3. EMPIRICAL MODEL OF NULL DISTRIBUTION OF SIMILARITIES

We define the similarities of the components of two subjects $k \neq 1$ as the entries of the following matrix:

$$\mathbf{\Gamma}_{kl} = \hat{\mathbf{S}}_k \hat{\mathbf{S}}_l^T \tag{4}$$

This simple definition assumes that the estimated rows $\hat{\mathbf{S}}_k$ are zero mean, and constrained to unit norm. The $\hat{\mathbf{S}}_{ki}$ are further assumed orthogonal for each subject, i.e., for $i \neq j$ for fixed k. For example, components estimated by FastICA always fulfill the orthogonality and norm constraint after the means have been subtracted from the estimated components.

The central problem is how to model the distribution of the matrix $\mathbf{\Gamma}$ under the null hypothesis. For simplicity, we only attempt to model the marginal distributions of the entries in this matrix and approximate the joint distribution by assuming independence of the entries. Denote this marginal distribution by p_γ. We take here an empirical approach and fit a parametric model to the statistics of the measured similarities to model p_γ.

Under H_0, we have

$$\mathbf{\Gamma}_{kl} = \mathbf{U}_k^T \mathbf{S}_k \mathbf{S}_l^T \mathbf{U}_l^T \tag{5}$$

where $\mathbf{U}_k$ and $\mathbf{U}_l$ are random orthogonal matrices independent of each other, and the rows of $\mathbf{S}_k$ and $\mathbf{S}_l$ are obtained from the prior distribution p_s. It is, in fact, possible to obtain an empirical sample of p_γ by the following procedure: take the matrices of the estimated independent components $\hat{\mathbf{S}}_k$, make a number of random rotations as $\mathbf{V}_k \hat{\mathbf{S}}_k$, and compute the similarities

$$\widetilde{\mathbf{\Gamma}}_{kl} = \mathbf{V}_k \hat{\mathbf{S}}_k \hat{\mathbf{S}}_l^T \mathbf{V}_l^T. \tag{6}$$

This has the distribution of $\overline{\mathbf{U}}_k \mathbf{S}_k \mathbf{S}_l \overline{\mathbf{U}}_l$ where $\overline{\mathbf{U}}_k = \mathbf{V}_k \mathbf{U}_k^T$ is again a random orthogonal matrix (and likewise for the index l). Thus, the constructed matrix follows the same distribution as the similarity matrix $\widetilde{\mathbf{\Gamma}}_{kl}$ under H_0. In principle, we could obtain a Monte Carlo sample of this distribution by generating random orthogonal matrices, but we will show next that this is not necessary.

It was pointed out by Hyvärinen (2011) that the distribution of the square of each entry of $\mathbf{U}_k^T \mathbf{U}_l$ follows a beta distribution Beta(α, β) with parameters $\alpha = 1/2$ and $\beta = (n-1)/2$ where n is the dimension of the data $\mathbf{X}_k$ (after a possible dimension reduction by PCA). So, we decide to fit a Beta($1/2$, β) distribution to the entries of the random matrix $\widetilde{\mathbf{\Gamma}}_{kl}$, with β being the free parameter. This should provide a reasonable approximation, and as we will see next, this approximation leads to a particularly simple method.

A basic way of estimating the parameters in a beta distribution is given by the moment method. A well-known formula gives the expectation of a beta-distributed random variable u^2 as

$$E\left\{u^2\right\} = \frac{\alpha}{\alpha + \beta} \tag{7}$$

from which we can derive, using the method of moments, the estimator of β with known $\alpha = 1/2$ as

$$\hat{\beta} = \alpha \left(\left[E\left\{u^2\right\} \right]^{-1} - 1 \right) = \frac{1}{2} \left(\left[E\left\{u^2\right\} \right]^{-1} - 1 \right) \tag{8}$$

Thus, we see that parameter β can be estimated based on the expectation of the squares of the matrix of similarities after random rotations.

Using the expectation of squares leads to a dramatic simplification of the method. Since the expectation of squares is taken over all the elements of the matrix, we can think of it being first taken over all the elements of the similarity matrix for each subject pair $\mathbf{\Gamma}_{kl}$, and then over different subject pairs k, l, $k \neq l$. Now, the orthogonal transformations in equation (6) do not change the sum of the squares of the elements of the matrix, so they can be omitted. Thus, we do not need to take the random rotations into account in the estimation of β, and no Monte Carlo simulation of the distribution is necessary. We can simply estimate β using the sum of squares of the computed similarity matrices $\mathbf{\Gamma}_{kl}$ as

$$\hat{\beta} = \frac{1}{2}(\tilde{n} - 1) \tag{9}$$

with

$$\tilde{n} = \left[E\left\{\gamma^2\right\} \right]^{-1} = \frac{n^2 r\,(r-1)}{\sum\limits_{ij,k\neq l} \gamma_{kl,ij}^2} \tag{10}$$

where $\gamma_{kl,ij}^2$ is the i, j-th entry in the matrix $\mathbf{\Gamma}_{kl}$. Here, the quantity $\tilde{n}$ can be considered as measure of the "randomness," i.e., lack of structure, of the independent components. If the independent components are very random in the sense of having no spatial structure (e.g., white noise), the similarities in the denominator will be small and this quantity will be large; however, $\tilde{n}$ depends on the data dimension as well. In fact, $\tilde{n}$ coincides with a parameter which gives the "effective" data dimension in the original framework by Hyvärinen (2011).

Thus, to test the hypothesis, we only need to estimate β as $\hat{\beta}$ in equation (9) and then compute the p-values based on the beta distribution.

2.4. NEW CORRECTIONS FOR MULTIPLE TESTING

The p-values for the connections (similarities) computed above can be used in a hierarchical clustering procedure to create clusters which contain one component from as many subjects as possible using only significant connections. Since we will be testing many possible candidates to be included in the clusters, we need some corrections for multiple testing.

As proposed by Hyvärinen (2011), we control here the false positive rate (FPR) for the formation of clusters, and the false discovery rate (FDR) for adding new elements to clusters. This is because claiming the existence of a cluster which does not actually exist can be considered a more serious error than adding an extra component to the cluster, and thus we want to be more conservative in forming new clusters.

For controlling the number of falsely formed clusters, we thus use Bonferroni correction like in Hyvärinen (2011). Denoting by α_{FP} the uncorrected false positive level, we obtain the corrected level as

$$\alpha_{FP}^{corr} = \frac{\alpha_{FP}}{m} \tag{11}$$

where the number of tests is

$$m = \frac{nr\,(r-1)}{2} \tag{12}$$

with r, the number of subjects, and n, the dimension of the data. The goal here is to make the probability of inferring even one wrong cluster smaller than α_{FP}. This is essentially the same as the family wise error rate.

Regarding the process of adding further components to the cluster after it has been formed, we develop here a method related to FDR. The problem with using ordinary FDR as in Hyvärinen (2011) is that in computing the true and false positives, it uses the number of connections which are considered true, while we are interested in the number of components which are added to the clusters. To see why these may not be closely related, consider a true cluster of 10 components. It contains 45 connections within itself, and thus the number of true connections within the cluster should be taken as 45. Now, if we falsely infer one of the outgoing connections to be true, we would calculate the FDR to be 1/46. However, since this means that we will have 11 components, one of which is falsely added to the cluster, it would make more sense to say we have an FDR of 1/11. The relationship between the FDR of connections and the FDR of components is thus quite complicated.

Since it is not straightforward to define the number of false discoveries in this problem, it is not clear how generic FDR methods, such as Simes' procedure (Simes, 1986; Benjamini and Hochberg, 1995) should be applied, as already pointed out by Hyvärinen (2011). Next, we provide one possible definition of false discoveries (and their rate) which attempts to optimally adapt the concept to the problem at hand. The number of false discoveries is basically the number of components falsely added to any of the clusters.

Consider a cluster which actually has c components, all of them true ones. There are $c(r-c)$ connections which go out of that cluster (we are considering maximal connections only as explained below in Section 2.5), each of which can give rise to a false positive. Given a corrected $\alpha_{\mathrm{FD}}^{\mathrm{corr}}$ level used in the test, and considering the tests independent, we would have an FDR which is smaller than

$$\frac{\alpha_{\mathrm{FD}}^{\mathrm{corr}}\, c\,(r-c)}{c} = (r-c)\,\alpha_{\mathrm{FD}}^{\mathrm{corr}} \tag{13}$$

where we omit the false positives in the denominator to obtain a simple upper bound. To guarantee that this is smaller than a given FDR rate α_{FD}, we can simply choose

$$\alpha_{\mathrm{FD}}^{\mathrm{corr}} = \frac{\alpha_{\mathrm{FD}}}{r-2} \tag{14}$$

which makes (13) less than or equal to α_{FD} for any $c > 2$ (in the case $r = 2$, i.e., only two subjects, the FDR is not used anyway). Thus, we propose to use the correction in equation (14) in the testing. It controls the FDR in the sense of the number of falsely added components.

2.5. COMPUTATIONAL SIMPLIFICATION

Next, we propose to reduce the computational resources (both memory and CPU time) by a simple approximation. After computing the similarities of the components of two subjects in matrix $\mathbf{\Gamma}_{kl}$, we only store the maximum similarities of each component with the components of the other subject. In other words, we only store the maxima of the rows and columns of $\mathbf{\Gamma}_{kl}$, as well as the indices obtaining those maxima. This is justified because a component can belong to only one cluster anyway, and it is most likely to be the one with the most significant similarity.

This reduces the amount of memory needed by a factor of $n/2$, and the computation time is reduced by a similar amount although its exact computation is not straightforward. Hyvärinen (2011) found that the computational bottleneck of the method is in the memory needed for storing all the similarities, so this reduction in memory storage is what perhaps most matters in practice.

We need to find the distribution for these maxima. We propose a simple approximation assuming the elements of the similarity matrix are independent, and by applying basic probability calculus, which gives

$$P\left(\max_i s_i \leq \alpha\right) = \prod_{i=1}^{n} P\left(s_i \leq \alpha\right) \tag{15}$$

for independent variables s_i.

2.6. DIFFERENT CLUSTERING STRATEGIES

We further propose that the clustering can use different strategies. The method proposed by Hyvärinen (2011) is related to the single-linkage strategy in hierarchical clustering, and adds a new component to a cluster by finding the largest similarity (which here means minimum p-value) among the similarities from the cluster to components not yet clustered (belonging to subjects not yet in the cluster). The classical alternatives to such a single-linkage are average-linkage and complete-linkage.

We propose to use complete-linkage as an alternative strategy in our testing method. Adapted to our specific clustering scheme, the idea is that we add a component to a cluster by considering the *maximum* of the p-values of the similarities from within the cluster to components in the remaining subjects (who do not have components in that cluster). The component with the smallest maximum of p-values will be added to the cluster. In particular, this means that a candidate component can be added to the cluster only if the connections from *all* the components inside the cluster are significant, because otherwise the maximum p-value would not be significant. (Since we store only the strongest connections between subjects, we have to also check that all the maximizing links stored point to the same component. If they don't, the component will not be considered for inclusion.)

Using complete-linkage alleviates the well-known drawback of the single-linkage strategy, which is that when components are added one-by-one to the cluster, they can be more and more different from the two components which started the cluster. The last component to be added can be so different that the cluster cannot be considered very meaningful anymore. On the other hand, complete-linkage has the drawback of sometimes leading to conservative cluster formation.

The average-linkage strategy is often considered a useful compromise between the single-linkage and complete-linkage strategies. As an implementation of the principle of average-linkage, we further propose here a method called median-linkage. The idea is that the median of the p-values of the connections to the new component has to be significant, which means half of the connection from the cluster have to be significant[1]. This should provide an interesting compromise between single-linkage and complete-linkage.

3. EXPERIMENTAL METHODS

Next, we validated the testing method proposed above by simulations and experiments on real data.

3.1. SIMULATION 1: DATA RESEMBLING fMRI

As a basic test for the validity of our method, we created independent components which resemble those obtained in a (resting-state) fMRI experiment. The number of subjects was fixed to 12, and the number of independent components (or PCA dimension) was fixed to 40.

The consistent spatial patterns were small blobs in a grid. The size of the grid was 25×25 because this seems to be statistically the closest to real fMRI data in terms of giving a similar effective dimension $\tilde{n}$. FMRI data of course has more voxels, but the correlations between the voxels are strong, and thus the statistics of similarities are more similar to our simulations on such a small grid[2].

Various amounts of Gaussian white noise were added to the blob-like patterns to simulate measurement noise. The signal-to-noise ratio was quantified as the z-score of the activity blobs: the noise always had standard deviation equal to one, whereas the maxima of the blobs were varied in the range of 1–5, and this we called the z-level of the pattern. Some examples are shown in **Figure 1**.

In the basic setting, half of the subjects (the "consistent subjects") had 20 consistent components (half of the components). In the consistent components, the underlying spatial patterns were equal for all subjects, but the measurement noises were independent for different subjects. The rest of the subjects (the "non-consistent subjects") had patterns consisting of Laplacian white noise, generated independently of each other. Laplacian white noise is a simple model for components which are sparse and reasonably independent, thus having properties similar to blobs in fMRI data[3]. The measurement noise added to the non-consistent subjects had the same variance as the spatial patterns. After adding the noise, all the patterns were normalized to unit variance.

We created data from four different scenarios. In Scenario 1, the measurement noise was Gaussian, the single-linkage strategy was used for clustering, and as already mentioned, the proportion of consistent subjects and components was one half. We varied these basic settings one at a time to produce the other scenarios. In Scenario 2, we investigated the effect of more consistency in the data, and thus set the number of consistent subjects and consistent components to be 3/4 instead of 1/2 as in Scenario 1. In Scenario 3, we applied the complete-linkage strategy for clustering, while the data was like in Scenario 1. In Scenario 4, we investigated the effect of non-Gaussian noise: the noise was Laplacian, while other parameters were like in Scenario 1. The Laplacian distribution is not meant as a physically realistic noise model (Wink and Roerdink, 2004); its purpose is to model heavy-tailed noise possibly consisting of outliers and other deviations from the model.

[1]In our implementation, we handle ties inherent in median calculation by requiring that more than one half of the connections must be significant.

[2]For a grid of this size, the effective dimension is at most 625, and typically of the order of hundreds. In the fMRI experiments reported below, the $\tilde{n}$ was in the range of 100 . . . 500, depending mainly on the PCA dimension.

[3]While we could have created the inconsistent patterns to contain activity blobs as well, this would have created the problem that some of the supposedly inconsistent patterns would have been strongly correlated by chance. Then, the validation of the method would have failed since the distinction between consistent and inconsistent patterns would not have been well-defined.

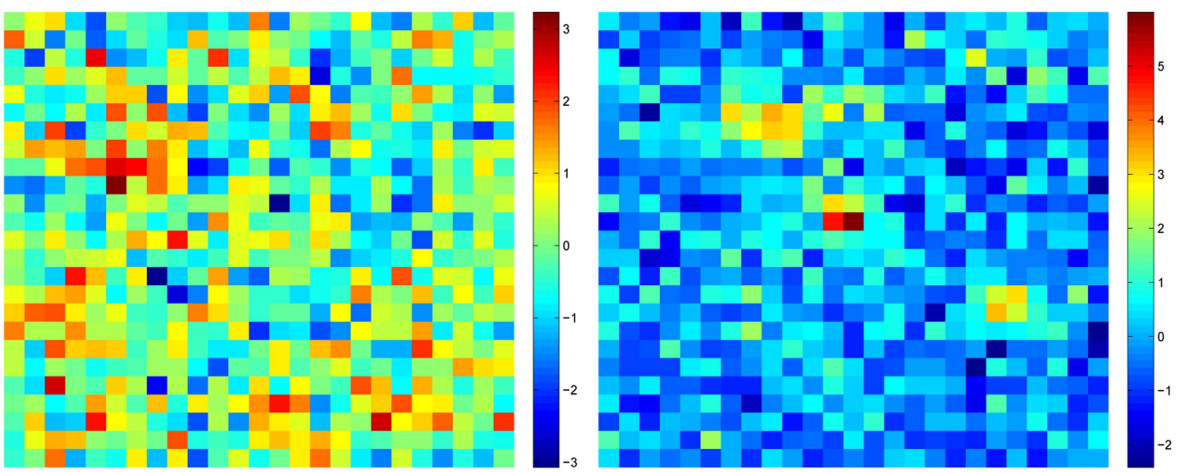

FIGURE 1 | Two patterns of activity used in Simulation 1. Left: z-level 1.5; Right, z-level 4. Z-level means the ratio of maximum of activity blob to noise standard deviation, i.e., maximum z-score of the signal.

For comparison, we applied the method by Hyvärinen (2011) on the same spatial patterns. While the method by Hyvärinen (2011) was not really conceived for this purpose, it is possible to input the obtained spatial patterns to that algorithm to obtain a useful baseline.

We ran 250 trials with $\alpha_{FP} = \alpha_{FD} = 10\%$ and computed a number of quantities to characterize the clustering results:

- the false positive rate for clusters. A cluster was considered false positive if it didn't include the same consistent component from at least two different consistent subjects. We ignored the actual number of false positive clusters and simply computed if there was at least one such cluster for each trial. Averaging this over trials, we computed the probability of having at least one false positive cluster, which is then compared to the FPR defined above.
- the false discovery rate of further connections. First we determined for each cluster the component which was most often present among the consistent subjects. False discoveries were then defined as components which either came from the non-consistent subjects, or came from consistent subjects but were not the same component as the one most often present (if the cluster was false positive, all the components were considered false discoveries). Their number was divided by the total number of components clustered to give the FDR. We took the median of FDR over the trials since taking a mean of rates is not very meaningful.
- The number of "perfect" clusters found. As in Hyvärinen (2011), we defined a perfect cluster as one which contains the same component from all consistent subjects, and no components from the non-consistent subjects. This is basically a rather stringent measure of true positives found by the methods. The number was averaged over trials.
- Finally, we computed the total number of clusters found (including false positives), and averaged it over trials.

3.2. SIMULATION 2: NEW VARIANT FOR TESTING THE MIXING MATRIX

While the theory presented in this paper is primarily intended to extend our earlier theory to testing the independent components, we have also proposed two ideas which can be used to improve the testing of the mixing matrix. In particular, our explicit FDR control formula in Section 2.4 and the computational simplification in Section 2.5 should improve the method in Hyvärinen (2011). Also, the new linkage strategy in Section 2.6 could be used as an option. To investigate this possibility, we provide here a simulation in which we use the present theory for testing the mixing matrix.

Here, we replicate Simulation 1 in Hyvärinen (2011) with the new FDR formula and the computational simplification. (We do not consider the alternative linkage strategies here.) The simulation consists of artificial data of five different scenarios in which FPR and FDR are explicitly defined, see Hyvärinen (2011) for details.

The goal of the simulation is to see if both α_{FP} and α_{FD} are still well controlled if use the introduced modification to test the mixing matrix. We set both to error rates to 0.05 in the testing method.

3.3. SIMULATION 3: COMPUTATIONAL COMPLEXITY

Next, we investigated the computational complexity of the method, using the same framework as in our earlier work (Hyvärinen, 2011).

First, to allow straightforward comparison with Hyvärinen (2011), we took the procedure of Simulation 4 from that paper without any changes, except for trying out larger dimensions. In particular, we applied the testing on the columns of the mixing matrix (which is possible as pointed out above).

Here, no ICA was done, instead we randomly generated data which models the mixing matrices obtained by ICA. We took the number of subjects to be equal to the number of independent components, using the values 8, 16, 32, 64, 128, 256, and 512 for those parameters. We generated the data so that for half of the subjects, half of the components were consistent (in fact, equal). For half of the subjects, the mixing coefficients were pure noise, and for those subjects with half consistent components, the other half of the mixing matrix was noise. The actual data generation procedure does not have a lot of influence on the computational complexity, but what is important here is that the data contains significant clusters whose number is proportional to the data dimension, and their size is proportional to the number of subjects.

We set $\alpha_{FP} = \alpha_{FD} = 0.05$. The computations were done using Matlab on a rather ordinary Linux desktop computer system with two cores of 2.66 GHz each, and 2.4 GB of memory available.

To assess the complexity, we computed the CPU time needed as well as the memory needed. The memory usage considered only the memory needed for storing the explicit variables, i.e., the final values of any Matlab operations neglecting any intermediate results, and thus clearly provides a lower bound only.

Second, we did the same simulations for testing the independent components in a more fMRI-like setting. We generated the independent component matrices $\mathbf{S}_k$ randomly with the same idea of half the components being consistent for half the subjects. The number of voxels (data points) was taken to be 10,000. The same settings for the number of subjects and independent components were used.

3.4. EXPERIMENTS ON REAL fMRI DATA

Finally, we applied the method on real fMRI data from Malinen et al. (2010). The data consisted of 10-min resting-state 3 T fMRI data obtained from 10 healthy subjects (37–64 years; mean 50 years; 8 males, 2 females). The statistical parametric mapping software SPM2[4] was used to preprocess the fMRI data, including realignment, skull-stripping, normalization into the Montreal Neurological Institute (MNI) standard space, and smoothing with a 6-mm (full-width at half-maximum) Gaussian filter. For further details about fMRI data acquisition and preprocessing, see Malinen et al. (2010).

From each individual subject's data, we reduced the dimensionality to 48 using principal component analysis (PCA) and subsequently extracted 48 spatial independent components (ICs) using FastICA (Hyvärinen, 1999). While methods have been proposed for automatically estimating the PCA dimension (Beckmann and Smith, 2004), their application is not without problems

[4]http://www.fil.ion.ucl.ac.uk/spm/

(Abou-Elseoud et al., 2010), which is why we simply fix the PCA dimension here. Our testing framework further assumes that the PCA dimension is the same for different subjects, while it would, in principle, be possible to estimate it separately for different subjects (Beckmann and Smith, 2004).

We applied the method using two different false positive rates and false discovery rates, set to either $\alpha_{FP} = \alpha_{FD} = 0.05$ or $\alpha_{FP} = \alpha_{FD} = 0.01$. In addition, we also investigated the effect of the two different linkage strategies during hierarchical clustering: single and complete-linkage. Finally, we applied the method for two further PCA dimensions, 25 and 75, where we fixed $\alpha_{FP} = \alpha_{FD} = 0.05$, and adopted the complete-linkage strategy.

4. RESULTS

4.1. SIMULATION 1: DATA RESEMBLING fMRI

The results are shown in **Figure 2**. Basically, our new method has quite well controlled error rates (less than the set $\alpha_{FP} = \alpha_{FD} = 10\%$) in most cases (green curves on the left).

The FPR rates reach 10% in many cases, and go to 15% in the case of non-Gaussian noise (scenario 4). The case of non-Gaussian noise makes the distributions have heavier tails and therefore our method seems to slightly underestimate the probability of false positives. On the other hand, Laplacian noise is quite non-Gaussian and presumably more non-Gaussian than typical fMRI measurement noise.

The FDR are always clearly lower than the desired 10%. This may not be surprising since our corrected FDR threshold was constructed to be conservative.

On the other hand, for our previous test proposed in Hyvärinen (2011), the FPR rates are not properly controlled, and sometimes exceed 10%, while the FDR are extremely small (so close to zero that they are not clearly visible). The fact that the error rates are not controlled is not very surprising considering that the test in Hyvärinen (2011) was designed for a different kind of test. Thus, this result merely confirms that we cannot directly use our earlier theory for testing independent components themselves, and the present developments are necessary.

Furthermore, the proposed test has clearly more power than the one in Hyvärinen (2011), which is seen in that fact that it finds more perfect clusters, as well as clusters in general (right-hand side panels in **Figure 2**).

Overall, there is surprisingly little variation between the four different scenarios.

4.2. SIMULATION 2: NEW VARIANT FOR TESTING THE MIXING MATRIX

The false positive rates and false discovery rates, as defined in Hyvärinen (2011) are shown in **Figure 3** for the different data-generating scenarios of Hyvärinen (2011). We can see that they are all less than the required 5%, and thus well controlled in spite of the further approximations done in developing our method in addition to the ones in Hyvärinen (2011). In fact, the approximation made in the computation of the p-values seem to lead to conservative testing, so the FPR and FDR do not need to be chosen particularly small.

4.3. SIMULATION 3: COMPUTATIONAL COMPLEXITY

The results are shown in **Figure 4**. Regarding the testing of the mixing matrix, we see a clear improvement with respect to Hyvärinen (2011). Both the memory and the CPU time needed are decreased approximately by a factor of 20 for the largest data set[5]. Thus, the optimized method greatly expands the applicability of the method, for example to the case of databases with hundreds of subjects.

In the case of testing the independent components, both the memory and the CPU time requirements are larger than in the case of testing the mixing matrix, approximately by a factor of five in the case of the largest data set. This is understandable since the independent components have much larger dimensions than the columns of the mixing matrix. In fact, we ran into a problem unrelated to our testing method, which is that just storing the independent components in memory takes a lot of space and ultimately seems to limit the dimensions we can use[6]. Thus, the poorer performance is rather related to the size of the data being analyzed and not the testing method itself.

Based on the computed graphs of memory and CPU time consumption, it is possible to extrapolate and approximate what amount of computational resources are sufficient for a given $n = r$, knowing that our computer was sufficient for the cases mentioned above. The results are of course a very rough approximation since they depend on implementation details, and because the number of values of $n = r$ we used was limited. We set the target at $n = r = 512$ which would correspond to rather long recordings of hundreds of subjects collected in a database. Simple linear extrapolations indicate 7 GB of memory is sufficient for testing the mixing matrix, and 150 GB for testing the components. Thus, while testing the mixing matrix is not a problem even for many computer systems at the time of this writing, the testing of components is more challenging. The number of voxels might also be larger than the 10,000 we used above, which would further increase the memory requirements. Likewise, we can extrapolate the computation times needed in the case $n = r = 512$: whether testing the mixing matrix or components, the computations would take some 30 h on our modest computer system, so the computation time is really not the bottleneck here.

4.4. EXPERIMENTS ON REAL fMRI DATA

Table 1 shows the number of clusters found, the average number of components per cluster, and the total number of components clustered for the 5 different parameter settings.

Typically, the method assigned a bit more than 30% of the independent components to one of the clusters. Interestingly, the percentage of components clustered was much higher, almost 50%, when the PCA dimension was increased, which indicates that 48 principal components may not be enough. A larger PCA dimension may be necessary to be able to find more corresponding components in different subjects.

[5]To characterize the significance of the improvement on a more anecdotal basis, let us point out that in Hyvärinen (2011) we could do $n = r = 64$ on an ordinary computer (the very same computer as in the current experiments), while $n = r = 128$ was impossible because we ran out of memory. With the new optimized method which stores maximal connections only, we were able to compute $n = r = 128$ as well as $n = r = 256$. The case $n = r = 512$ was not feasible because the system ran out of memory.

[6]Again, considering the performance of our particular computer system: We were able to do only $n = r = 64$ since simply storing the independent components in memory took 37% of it.

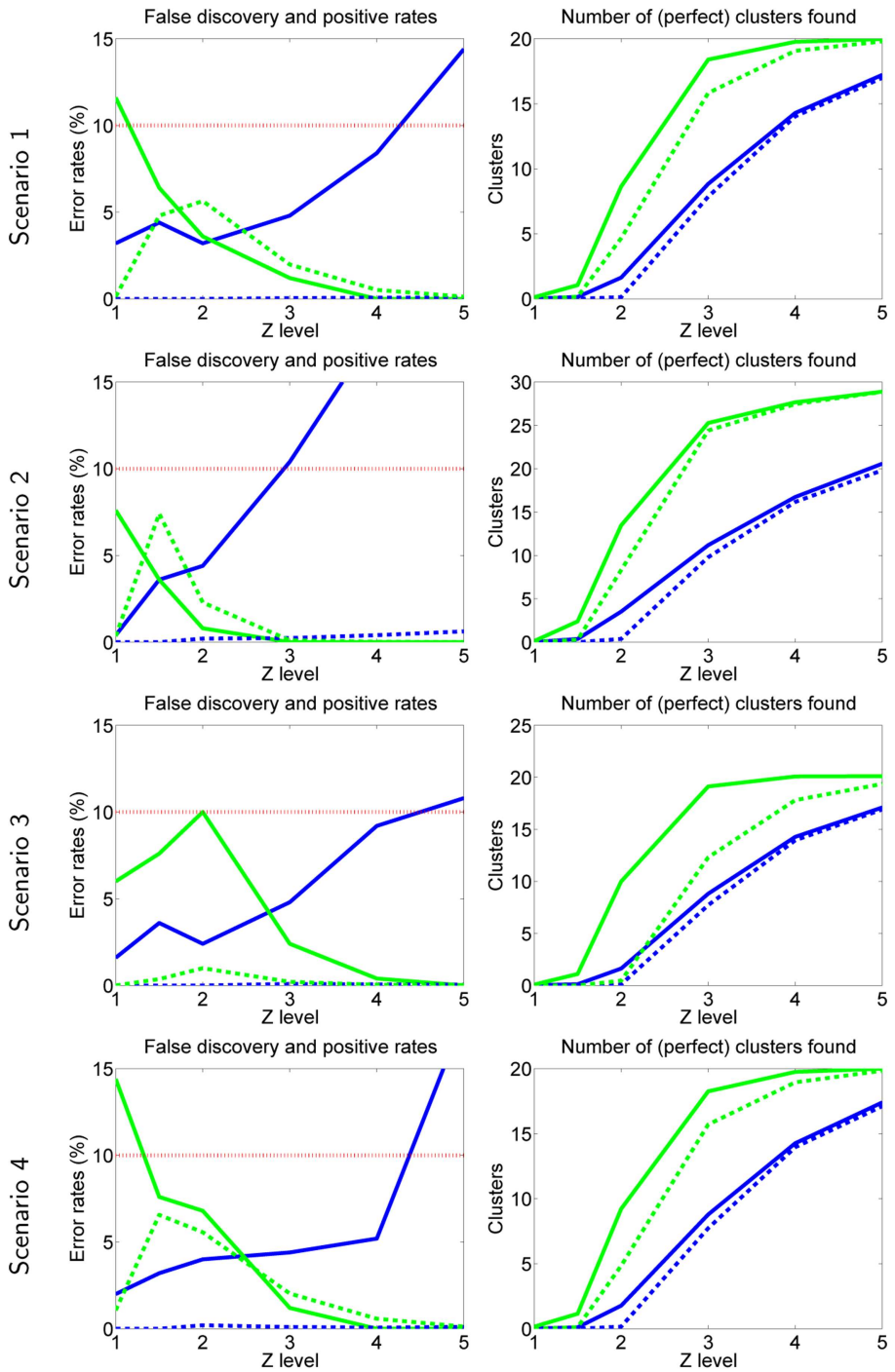

FIGURE 2 | Simulation 1: data resembling fMRI. Each row is one scenario, briefly: scenario 1 is basic setting, scenario 2 has more inter-subject consistency, scenario 3 uses complete-linkage, scenario 4 has non-Gaussian noise. In all plots, green curves are obtained by the method proposed here, and blue curves by the method proposed by Hyvärinen (2011), given for comparison. In error rates (left), solid line is FPR and dashed line FDR. In number of clusters (right), dashed line gives the number of perfect clusters, solid line gives the total number of clusters (including false ones). The desired rates $\alpha_{FD} = \alpha_{FP} = 0.10$ are shown by the dotted red line.

We also see the well-known phenomenon where complete-linkage clustering leads to smaller clusters, but produces more of them. We found that single-linkage in fact produced clusters which were sometimes quite heterogeneous (results not shown), so complete-linkage may be preferred on this data. On the other hand, the total number of component clustered is smaller for

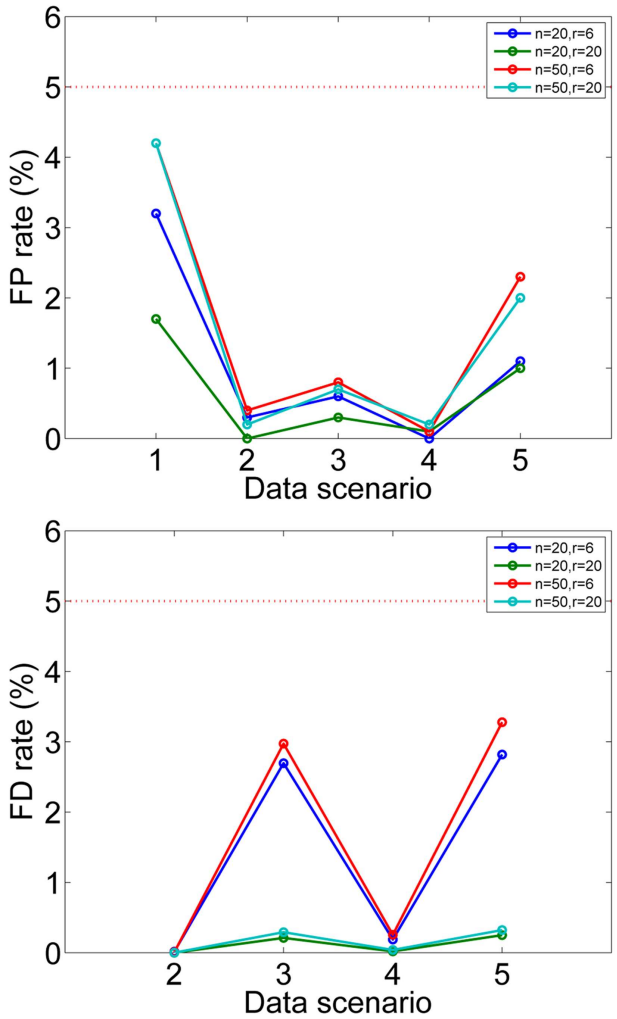

FIGURE 3 | Simulation 2: testing the mixing matrix. False positive rates and false discovery rates are shown for simulated data. Different settings of data dimension *n* and number of subjects *r* are given in different colors. The data scenarios are explained in detail in Hyvärinen (2011), briefly: 1: no consistent components, 2: half of components consistent for all subjects, 3: all components consistent for half of the subjects, 4: for half the subjects, all components consistent and half of the components consistent for the rest of the subjects, 5: for half of the subjects, half of the components were consistent. The desired false positive and discovery rates $\alpha_{FP} = \alpha_{FD} = 0.05$ are shown by the dotted red line. For scenario 1, FDR cannot be meaningfully computed since the number of true positives is zero.

complete-linkage, because it requires all the connections from the cluster to be significant, which is a more conservative criterion.

Obviously, a smaller α leads to fewer clusters and fewer components in the clusters, but the difference between 0.01 and 0.05 is rather small.

Some examples of the clusters are shown in **Figures 5–7**. These were obtained in the basic setting where PCA dimension was 48, complete-linkage was used, and the α levels were 0.05. The first cluster in **Figure 5** seems to consist of a part of the default-mode network, the second in **Figure 6** seems to be a motor network, and the third in **Figure 7** is an auditory area. The clusters contain components from 5 to 6 subjects. The clusters were manually selected to reflect some well-known resting-state networks.

5. DISCUSSION

In this paper, we extended our previous work (Hyvärinen, 2011) on testing the ICA mixing matrix to testing the values of the independent component patterns. An important application for the present method is spatial ICA of fMRI, especially in resting-state. We proposed an empirical model of the null distribution, whose parameters can be directly estimated from the observed data. We further proposed improvements to the general framework, applicable to both our present and earlier testing methods; they simplify the theory of FDR computation, reduce the computational requirements, and provide alternative clustering strategies.

While the idea of doing a separate ICA on each subject, followed by clustering, is not new (Esposito et al., 2005), the method proposed here is, to the best of our knowledge, the first one which associates statistically principled p-values to each cluster. Thus, the method indicates which clusters should be included in any further analysis and which should be discarded, with a principled computation of the similarity thresholds.

Matlab code for computing the tests proposed in this paper is freely available at www.cs.helsinki.fi/u/ahyvarin/code/isctest/.

5.1. UTILITY IN fMRI ANALYSIS

Results on real fMRI group data showed reasonable clustering of components to clusters similar to well-known resting-state ICA networks.

Some well-known networks may also be split into more than one cluster. The splitting may be due to individual variability of the spatial patterns. The probability of such splitting depends on the α value as well as the clustering strategy. It is well-known in the theory of hierarchical clustering that complete-linkage tends to create clusters which are smaller, but at the same gives more clusters than single-linkage.

Another factor which has a strong effect on the splitting of clusters, independently of individual variability or our testing method, is the PCA dimension. Its effect was systematically investigated by Abou-Elseoud et al. (2010), who found that with a PCA dimension of 10, a single default-mode network is found. For larger dimensions, it is often split into at least two components, and at a PCA dimension of 50 (very close to 48 used above), even four components.

These factors should largely explain why, for example, the cluster related to the default-mode network in **Figure 5** contained only the precuneus and only from six subjects. In fact, other clusters containing parts of the default-mode network were found as well (but not shown). Increasing the false positive and false discovery rates and using single-linkage would prevent such splitting of clusters to some degree but at the risk of too permissive clustering of components which may not be related enough. Even so, simply due to the effect of our relatively large PCA dimension, it seems unlikely that we could capture the whole default-mode network in a single cluster. This problem might possibly be alleviated by estimating the number of independent components separately for each subject (Beckmann and Smith, 2004), but determining the dimension automatically is not easy as discussed by Abou-Elseoud

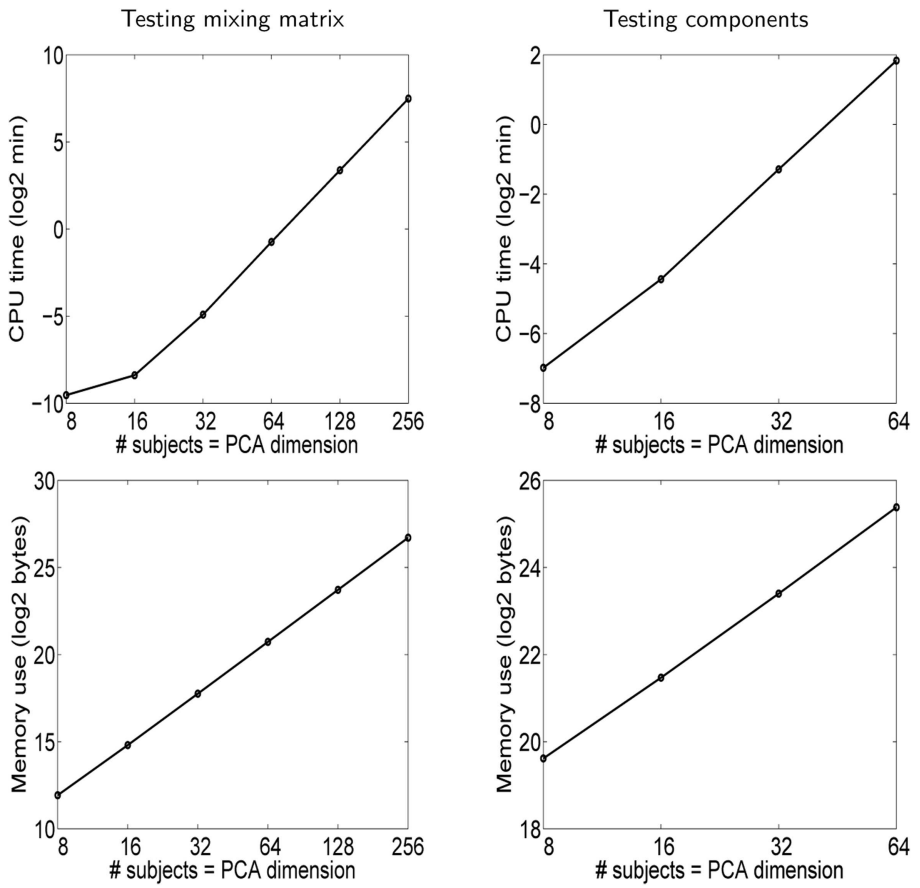

FIGURE 4 | Simulation 3: computational complexity. The results are shown in each case as far as our computer was able to perform the computations, i.e., in the case of the mixing matrix, $n = r = 512$ was infeasible because it would have required more memory than was available, and likewise for $n = r = 128$ in the case of testing independent components.

Table 1 | Results on real resting-state fMRI data.

PCA dim	α	Linkage strategy	Clusters found	Avg. comps per cluster	# Comps clustered	% Comps clustered
48	0.05	Single	25	6.92	173	36.1
48	0.05	Complete	36	4.14	149	31.0
48	0.01	Complete	34	3.88	132	27.5
75	0.05	Complete	93	3.92	365	48.7
25	0.05	Complete	18	4.22	76	30.4

The testing and clustering method was applied by varying the PCA dimension, the false positive rate $\alpha = \alpha_{FP} = \alpha_{FD}$, and the linkage strategy during hierarchical clustering.

et al. (2010). Another factor that might be relevant is the large age range of the subjects; age was shown to change resting-state networks by Dosenbach et al. (2010), so our group might have particularly small inter-subject consistency.

Our method does not by any means discard artifacts, which sometimes form consistent clusters as well, although we only showed resting-state networks above. In fact, the testing method does not seem to contain anything which would prefer components of real brain activity over any kind of artifacts (whether physiological or technical). ICA is well-known to find many artifacts, and the present method just considers all components on an equal footing. Of course, it might be possible that some artifacts are either more or less consistent than brain activity, but we are not aware of results showing any such systematic differences. An automatic method for detecting which components are artifacts was proposed by Tohka et al. (2008).

5.2. RELATIONSHIP TO OTHER METHODS

Related testing methods were proposed by Perlbarg et al. (2008); Varoquaux et al. (2010); Schöpf et al. (2010). Schöpf et al. (2010)

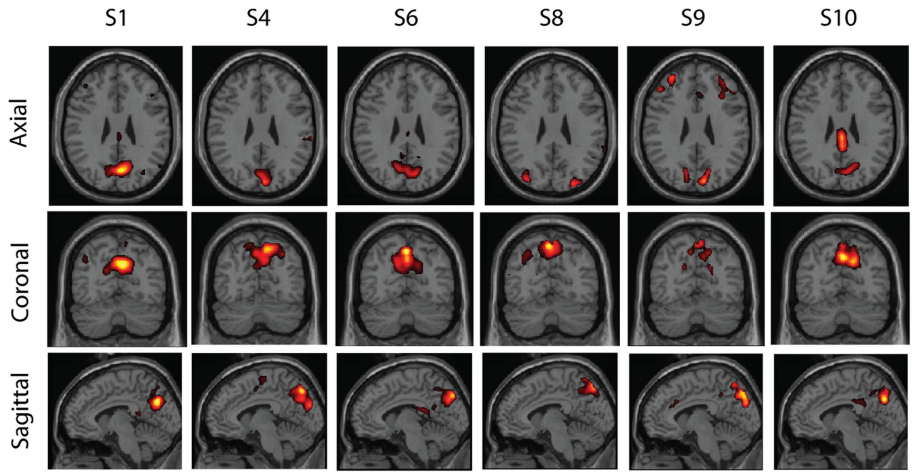

FIGURE 5 | One cluster found in real resting-state fMRI data. The component was found in sufficiently similar form in six subjects (out of 10). The cluster seems to correspond to a part of the default-mode network, centered in the precuneus.

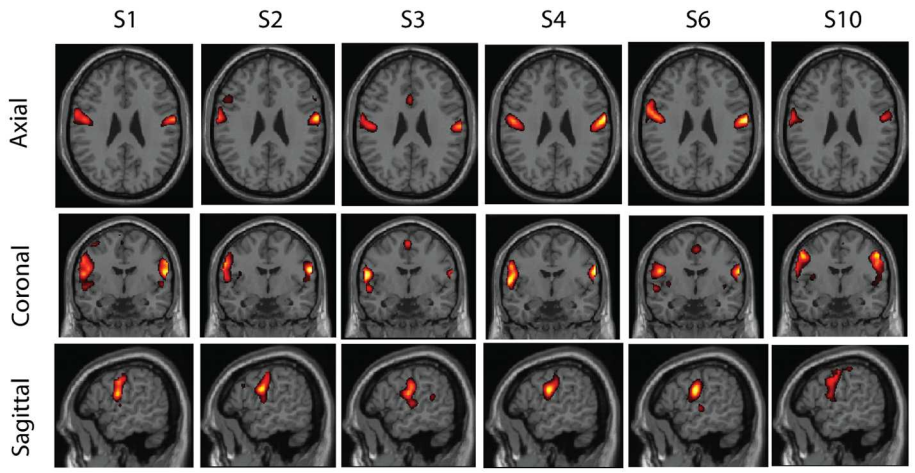

FIGURE 6 | A second cluster found in real resting-state fMRI data. This cluster also has components from six subjects, and seems to correspond to bilateral motor areas.

used principled statistical methods based on GLM to quantify the similarities between the components, and to rank them in order of consistency. Perlbarg et al. (2008) applied bootstrapping to test the consistency of inter-subject consistency grouping, but the grouping itself used similarity thresholds which were not statistically principled. Varoquaux et al. (2010) applied the idea of random orthogonal rotations like Hyvärinen (2011), but not over different subjects. While all the work cited above used statistical methods to quantify the similarity and/or significance of components, none of them directly addressed the problem we are concerned with: obtaining principled p-values for each component.

An alternative utility of single subject ICA was proposed by Yang et al. (2012), who did ICA on individual subjects and then clustered the *subjects* instead of components based on the inter-subject consistencies of the components.

5.3. RELATIONSHIP TO OUR PREVIOUS TESTING METHOD

Our empirical approach introduced above is closely related to the original testing method by Hyvärinen (2011). Thus, we need to understand the differences between the two methods.

5.3.1. Which testing method should be applied?

First we would like to clarify when the different testing methods should be applied. While both methods are applicable in the myriad of application fields where ICA can be applied, we consider only brain imaging data in the following discussion.

The choice of testing method really depends on the combination of two factors: whether we do temporal or spatial ICA, and what the experimental paradigm is. (The imaging modality *per se* plays a smaller role here, but it affects the choice of temporal vs. spatial ICA.) The discussion of whether temporal or spatial ICA is

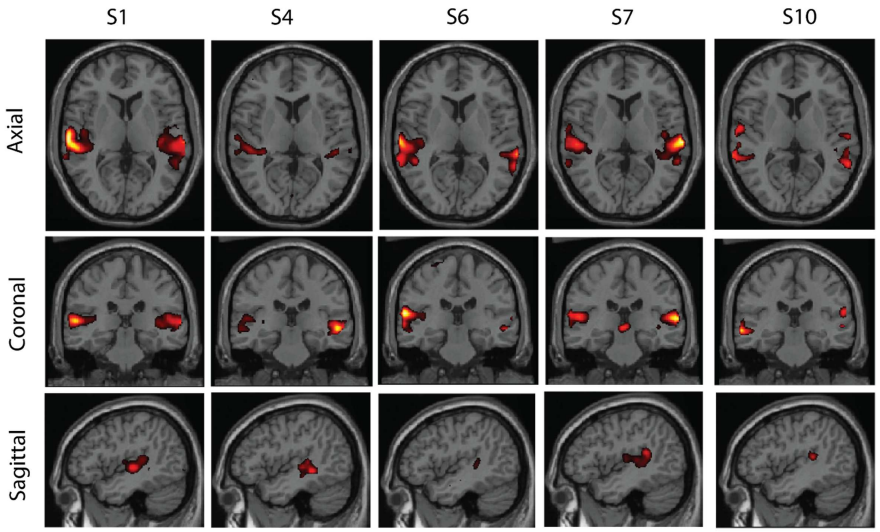

FIGURE 7 | A third cluster found in real resting-state fMRI data. The cluster has components from five subjects and seems to correspond to auditory areas.

to be performed for a given data set is a completely separate one (see, e.g., Calhoun et al., 2009). First one should decide which type of ICA is the right one, and only then choose the testing method.

ICA is typically applied on data on which we can only perform one of the tests. This is the case when the data come from a resting-state study, from a study where the responses are induced but not time-locked to stimuli and hence not correlated (e.g., event-related suppression in EEG/MEG), or any non-resting study with no systematically evoked responses. For such data, we can assume the spatial patterns to be similar, but not the time courses.

Basically, in the case of *temporal* ICA for such data, we would typically assume that the mixing matrix is approximately the same over subjects, since the mixing matrix gives the spatial patterns of activity. This is the case whether we analyze EEG, MEG, or fMRI. (Temporal ICA on fMRI is very rare, however.) So, we should test the mixing matrix using the method by Hyvärinen (2011). Testing the independent component patterns would not be meaningful since they correspond to the activity time courses which cannot be assumed to be correlated here.

Next we consider the cases where the data comes from *spatial* ICA, and from the experimental paradigms mentioned above (resting-state or similar). Then, it is typically the independent components ($\mathbf{s}_k$) which are approximately the same over subjects, since they correspond to the spatial patterns. So, we should test the independent components themselves, using the method in this paper. Testing the mixing matrix would not meaningful here, since again, the time courses cannot be assumed to be correlated over subjects in the above-mentioned cases. In particular, the popular spatial ICA of resting-state fMRI needs our new testing method proposed in this paper, and cannot be done with our previous method.

However, in some cases it may be possible to apply either of the two tests. This is the case when the data comes from an evoked response study in which the responses for different subjects are similar enough in the sense of being strongly correlated. This is because then both the spatial patterns and the time courses can be tested for inter-subject consistency. The choice of testing method then depends on which of the inter-subject consistencies is stronger, or more interesting from the viewpoint of the study. For example, in an evoked response study with fMRI, after applying spatial ICA, it may be particularly interesting to apply the testing on the mixing matrix to see if the responses themselves (and not just the spatial patterns) have inter-subject consistency.

5.3.2. Similarity measures and effective dimensions

Next, we consider the connections between our two testing methods from the viewpoint of the theory.

In both testing methods, we compute similarities between the components. One important difference is that Hyvärinen (2011) used a weighted Mahalanobis similarity, whereas here we use simple correlations. Related to this, it was assumed by Hyvärinen (2011) that the covariances of the subjects are equal. These two assumptions made it possible to analytically derive the null distribution in Hyvärinen (2011), while here we used an empirical model of the null distribution.

However, these two differences may not be as large as they seem. In fact, let us first consider what happens if we use our empirical model of the similarities when testing the mixing matrix. Suppose that we are testing the similarities of mixing matrices like Hyvärinen (2011), and the covariances of the subjects are equal. Theorem 1 by Hyvärinen (2011) shows that the Mahalanobis similarity matrix is a random orthogonal matrix under the null hypothesis. Thus, its sum of squares equals the data dimension, and the estimate $\hat{n}$ of the effective dimension we would get from equation (10) is equal to the data dimension. This means that the empirical model of the null distribution would be equal to the one used by Hyvärinen (2011). Thus, if we use our empirical approach to modeling the similarity matrix in testing the mixing matrix, we recover exactly the same null distribution which was analytically derived by Hyvärinen (2011), provided that the assumption

of equal covariances holds. In this sense, the present empirical method is a generalization of our earlier method.

On the other hand, one may ask if we could or should we use the Mahalanobis distance in testing independent components like in this paper. This does not seem necessary because if we adapt the assumptions in Hyvärinen (2011) to the present case, we in fact obtain the simple similarity measure used here. Since the $\mathbf{S}_k$ have orthogonal rows of unit variance, as assumed above, the weighting matrix in the Mahalanobis similarity is equal to identity in the subspace spanned by the rows of $\mathbf{S}_k$. Thus, any weighting in the distance measure would disappear. In this sense, our present method is rather a special case of the framework by Hyvärinen (2011).

The two points above show that the apparent differences in the definition of the similarities and effective dimensions are much smaller than it seems. Rather, one might see our earlier method and the method proposed here as two instances of the same method, adapted to the parameters inherent to the testing of the mixing matrix or the independent components, respectively.

There is one practical difference, however. In the empirical method proposed here, we do not re-estimate the effective dimension after deflating away components, as was done by Hyvärinen (2011). This makes the present test less conservative. The effect of such re-estimation of the dimension would probably be much smaller here because the effective dimension $\tilde{n}$ is higher (typically of the order of hundreds), so reducing it by the number which is of the same order as the number of components (typically not more than one hundred) as in our earlier method would not change much. Moreover, it may not be necessary even on theoretical grounds because it is closely related to the assumption of equal covariances. If the covariances are not equal over subjects, the vectors are much less constrained and such reduction of degrees of freedom does not happen. There is some the risk that this makes the test too permissive and creates false positives. However, according to the simulations presented, this does not seem to be the case in reasonably realistic scenarios.

5.3.3. Modeling of the independent components

Any modeling of the independent components using a distribution p_s was not necessary in our earlier method (Hyvärinen, 2011), since the analysis was exclusively concentrated on the estimated mixing matrices. Introduction of p_s in this paper basically means that we admit that there is some additional source of uncertainty. Taking the empirical approach means that we further admit we cannot explicitly model the independent components, i.e., p_s, because of their complexity. This uncertainty is then implicitly modeled by fitting the parameter $\tilde{n}$ (or β) to the data. Thus, the present method is a generalization of our earlier method in this sense as well: we allow for more uncertainty under H_0, and adapt to it empirically.

In addition to modeling individual differences, another practical meaning of p_s is modeling measurement noise. Any measurement noise is still present in the independent components, and its effect on the similarities has to be modeled. This is in contrast to similarities of columns of the mixing matrix: since measurement noise is basically averaged out in the estimates of the mixing matrix, it can largely be ignored.

5.4. APPLICABILITY TO DIFFERENT ICA ALGORITHMS

In the simulations above, we used FastICA. However, no part of the derivation of the testing method assumed that we would use FastICA instead of other ICA algorithms. The only assumption related to ICA estimation was that the estimation is divided into two parts: whitening and finding an orthogonal mixing matrix. Most ICA and blind source separation algorithms, including SOBI (Belouchrani et al., 1997), AMUSE (Tong et al., 1991), and JADE (Cardoso and Souloumiac, 1993), use the same division of estimation into two stages, so our method is just as applicable to them as it is for FastICA.

The notable exception among the ICA algorithms is the infomax algorithm (Bell and Sejnowski, 1995; Amari et al., 1996), which does not require such a division into two stages. However, most implementations of the infomax algorithm do use a preliminary whitening to speed up the algorithm, effectively using two estimation stages as above. Yet, there is usually no constraint of orthogonality of the mixing matrix in the infomax algorithm. This means that our method may not be fully justified for the infomax algorithm. On the other hand, by the definition of the ICA model, even the infomax algorithm should asymptotically give an orthogonal mixing matrix for whitened data, under the theoretical assumption that the ICA model holds. Thus, the assumptions of our method are approximately correct even for the infomax algorithm. Whether this approximation is good enough in practice is an empirical question that we leave for future research.

5.5. COMPUTATIONAL IMPLEMENTATION DETAILS

We proposed a simple way of speeding up computation by storing only the maximal similarities in memory. This is not exactly equivalent to using all of them as in our earlier method (Hyvärinen, 2011) but the difference is likely to be very small. This improvement can be used with the testing method in Hyvärinen (2011) as well, and, indeed, with many related methods (Himberg et al., 2004; Esposito et al., 2005).

In Simulation 3, the bottleneck of the computations was seen to be in the large size of the spatial patterns themselves, which we stored in the memory. Thus, the bottleneck is essentially in the database implementation, and not in our testing method *per se*. A further computational improvement would presumably be obtained if we didn't try to hold all the independent components in the memory at the same time. This would require some relatively simple programing solutions in which only part of the ICA outputs are loaded into memory at the same time for computation of the similarities. Such methods might be quite slow because of the disk access needed but they would expand the possibilities of the testing method. However, we leave such database technicalities for future research.

5.6. GROUP ICA AND TESTING

The method developed here can also be viewed as a method for group ICA, if the datasets come from different subjects, as originally proposed by Esposito et al. (2005) and further developed, among others, by Wang and Peterson (2008) and Schöpf et al. (2010). The approach is quite different from conventional group ICA methods (Calhoun et al., 2009) in which the primary goal is to obtain a set of group-average components which characterize

the whole group. Such a set of average components can then be used to compute the corresponding components in each subject. Malinen et al. (2010) originally applied such a method (GIFT) on the data we re-analyze here, so comparing the present results to theirs will give a general idea on the differences and commonalities of the two analyses.

Estimating group-level component has been further advanced by Beckmann and Smith (2005), whose tensorial ICA method allows some inter-subject variability in both the independent components and the mixing matrix; however, tensorial ICA assumes the component time courses to be similar for all the subjects in whom the component is present, so it is hardly applicable to spatial ICA of resting-state fMRI. Guo and Pagnoni (2008) further proposed a principled expectation-maximization approach for estimating group components.

A possible problem with estimating group-level components is that there is no guarantee that the component "exists" in each subject, since the subject-wise components are computed by simple formulas without any checking that the obtained component matches the data of the subject in question. The question of whether the components obtained by group-level ICA are present in single subjects was considered by Erhardt et al. (2011) and Allen et al. (2012). The main advantage of computing a separate ICA for each subject is that there is more certainty that the subject-wise components really correspond to the statistical properties of the subject (Esposito et al., 2005).

On the other hand, computing a separate ICA for each subject may have the disadvantage that the estimation of the components does not use all the information available, in particular the information that the components are likely to be similar in the different subjects. In fact, in the fMRI results above, the components were hardly ever found in more than half of the subjects. While this may be an accurate description of the underlying individual differences in neurophysiology and anatomy, it is also possible that this is a conservative estimate. For example, due to the algorithmic randomness of ICA algorithms (Himberg et al., 2004), the components obtained are just a subset of the larger set of all the possible components. In ICA estimation, there is thus an aspect of random sampling from this pool of components, which reduces the number of matches that can be found by a clustering algorithm like the one proposed here.

A possible compromise would be to use a framework similar to Varoquaux et al. (2011), which develops an explicit model of the components, and in particular their individual differences. This is an interesting direction for future research. However, such models cannot be straightforwardly used for the testing of the components because the components are not estimated independently in different subjects. Another important question for future research is how comparison between groups can be done in the present testing framework. Any methods applicable for the original framework by Esposito et al. (2005) are likely to be applicable for our method as well.

ACKNOWLEDGMENTS

The fMRI data were derived from the healthy person data by Malinen et al. (2010), a collaboration between the Brain Research Unit, O. V. Lounasmaa Laboratory, Aalto University and the Department of Clinical Neurosciences and the Department of Anesthesia and Intensive Care Medicine, Helsinki University Central Hospital, Finland. We are grateful to the authors of that study for the possibility of using the data here. Aapo Hyvärinen was supported by the Academy of Finland (CoE in Inverse Problems, CoE in Algorithmic Data Analysis, Computational Sciences Program). Pavan Ramkumar was supported by the Academy of Finland, Brain2Brain ERC Advanced Grant #232946 (to R. Hari), and the Finnish Graduate School of Neuroscience.

REFERENCES

Abou-Elseoud, A., Starck, T., Remes, J., Nikkinen, J., Tervonen, O., and Kiviniemi, V. (2010). The effect of model order selection in group PICA. *Hum. Brain Mapp.* 31, 1207–1216.

Allen, E. A., Erhardt, E. B., Wei, Y., Eichele, T., and Calhoun, V. D. (2012). Capturing inter-subject variability with group independent component analysis of fMRI data: a simulation study. *Neuroimage* 59, 4141–4159.

Amari, S.-I., Cichocki, A., and Yang, H. (1996). "A new learning algorithm for blind source separation," in *Advances in Neural Information Processing Systems 8*, eds D. S. Touretzky, M. C. Mozer, and M. E. Hasselmo (Cambridge, MA: MIT Press), 757–763.

Beckmann, C. F., DeLuca, M., Devlin, J. T., and Smith, S. M. (2005). Investigations into resting-state connectivity using independent component analysis. *Philos. Trans. R. Soc. Lond. B Biol. Sci.* 360, 1001–1013.

Beckmann, C. F., and Smith, S. M. (2004). Probabilistic independent component analysis for functional magnetic resonance imaging. *IEEE Trans. Med. Imaging* 23, 137–152.

Beckmann, C. F., and Smith, S. M. (2005). Tensorial extensions of independent component analysis for group fMRI data analysis. *Neuroimage* 25, 294–311.

Bell, A. J., and Sejnowski, T. J. (1995). An information-maximization approach to blind separation and blind deconvolution. *Neural. Comput.* 7, 1129–1159.

Belouchrani, A., Meraim, K. A., Cardoso, J.-F., and Moulines, E. (1997). A blind source separation technique based on second order statistics. *IEEE Trans. Signal Process.* 45, 434–444.

Benjamini, Y., and Hochberg, Y. (1995). Controlling the false discovery rate: a practical and powerful approach to multiple testing. *J. R. Stat. Soc. Ser.* 57, 289–300.

Calhoun, V., Adali, T., Pearlson, G., and Pekar, J. (2001). A method for making group inferences from functional MRI data using independent component analysis. *Hum. Brain Mapp.* 14, 140–151.

Calhoun, V. D., Liu, J., and Adali, T. (2009). A review of group ICA for fMRI data and ICA for joint inference of imaging, genetic, and ERP data. *Neuroimage* 45, S163–S172.

Cardoso, J.-F., and Souloumiac, A. (1993). Blind beamforming for non Gaussian signals. *IEE Proceedings-F* 140, 362–370.

Dosenbach, N. U. F., Nardos, B., Cohen, A. L., Fair, D. A., Power, J. D., Church, J. A., et al. (2010). Prediction of individual brain maturity using fMRI. *Science* 329, 1358–1361.

Erhardt, E. B., Rachakonda, S., Bedrick, E. J., Allen, E. A., Adali, T., and Calhoun, V. D. (2011). Comparison of multi-subject ICA methods for analysis of fMRI data. *Hum. Brain Mapp.* 32, 20752095.

Esposito, F., Scarabino, T., Hyvärinen, A., Himberg, J., Formisano, E., Comani, S., et al. (2005). Independent component analysis of fMRI group studies by self-organizing clustering. *Neuroimage* 25, 193–205.

Guo, Y., and Pagnoni, G. (2008). A unified framework for group independent component analysis for multi-subject fMRI data. *Neuroimage* 42, 1078–1093.

Himberg, J., Hyvärinen, A., and Esposito, F. (2004). Validating the independent components of neuroimaging time-series via clustering and visualization. *Neuroimage* 22, 1214–1222.

Hyvärinen, A. (1999). Fast and robust fixed-point algorithms for independent component analysis. *IEEE Trans. Neural Netw.* 10, 626–634.

Hyvärinen, A. (2011). Testing the ICA mixing matrix based on inter-subject or inter-session consistency. *Neuroimage* 58, 122–136.

Kiviniemi, V., Kantola, J.-H., Jauhiainen, J., Hyvärinen, A., and Tervonen, O. (2003). Independent component analysis of nondeterministic fMRI signal sources. *Neuroimage* 19, 253–260.

Malinen, S., Vartiainen, N., Hlushchuk, Y., Koskinen, M., Ramkumar, P., Forss, N., et al. (2010). Aberrant temporal and spatial brain activity during rest in patients with chronic pain. *Proc. Natl. Acad. Sci. U.S.A.* 107, 6493–6497.

Perlbarg, V., Marrelec, G., Doyon, J., Pelegrini-Issac, M., Lehericy, S., and Benali, H. (2008). "NEDICA: detection of group functional networks in FMRI using spatial independent component analysis," in *IEEE International Symposium on Biomedical Imaging* (Paris: IEEE Press), 1247–1250.

Ramkumar, P., Parkkonen, L., Hari, R., and Hyvärinen, A. (2012). Characterization of neuromagnetic brain rhythms over time scales of minutes using spatial independent component analysis. *Hum. Brain Mapp.* 33, 1648–1662.

Schöpf, V., Kasess, C., Lanzenberger, R., Fischmeister, F., Windischberger, C., and Moser, E. (2010). Fully exploratory network ICA (FENICA) on resting-state fMRI data. *J. Neurosci. Methods* 192, 207–213.

Simes, R. J. (1986). An improved Bonferroni procedure for multiple tests of significance. *Biometrika* 73, 751–754.

Tohka, J., Foerde, K., Aron, A. R., Tom, S. M., Toga, A. W., and Poldrack, R. A. (2008). Automatic independent component labeling for artifact removal in fMRI. *Neuroimage* 39, 1227–1245.

Tong, L., Liu, R.-W., Soon, V. C., and Huang, Y.-F. (1991). Indeterminacy and identifiability of blind identification. *IEEE Trans. Circuits Syst.* 38, 499–509.

van de Ven, V. G., Formisano, E., Prvulovic, D., Roeder, C. H., and Linden, D. E. (2004). Functional connectivity as revealed by spatial independent component analysis of fMRI measurements during rest. *Hum. Brain Mapp.* 22, 165–178.

Varoquaux, G., Gramfort, A., Pedregosa, F., Michel, V., and Thirion, B. (2011). "Multi-subject dictionary learning to segment an atlas of brain spontaneous activity," in *Information Processing in Medical Imaging*, eds G. Székely and H. K. Hahn (Kaufbeuren: Springer), 562–573.

Varoquaux, G., Keller, M., Poline, J. B., Ciuciu, P., and Thirion, B. (2010). "ICA-based sparse features recovery from fMRI datasets," in *IEEE International Symposium on Biomedical Imaging* (Rotterdam: IEEE Press), 1177–1180.

Wang, Z., and Peterson, B. S. (2008). Partner-matching for the automated identification of reproducible ICA components from fMRI datasets: algorithm and validation. *Hum. Brain Mapp.* 29, 875–893.

Wink, A. M., and Roerdink, J. B. T. M. (2004). Denoising functional MR images: a comparison of wavelet denoising and Gaussian smoothing. *IEEE Trans. Med. Imaging* 23, 374–387.

Yang, Z., Zuo, X., Wang, P., Li, Z., LaConte, S., Bandettini, P., et al. (2012). Generalized RAICAR: discover homogeneous subject (sub)groups by reproducibility of their intrinsic connectivity networks. *Neuroimage* 63, 403–414.

Conflict of Interest Statement: The authors declare that the research was conducted in the absence of any commercial or financial relationships that could be construed as a potential conflict of interest.

Received: 30 November 2012; accepted: 05 March 2013; published online: 22 March 2013.

*Citation: Hyvärinen A and Ramkumar P (2013) Testing independent component patterns by inter-subject or inter-session consistency. Front. Hum. Neurosci. **7**:94. doi: 10.3389/fnhum.2013.00094*

frontiers in
HUMAN NEUROSCIENCE

METHODS ARTICLE
published: 01 February 2013
doi: 10.3389/fnhum.2013.00019

ICA analysis of fMRI with real-time constraints: an evaluation of fast detection performance as function of algorithms, parameters and *a priori* conditions

Nicola Soldati[1]*, Vince D. Calhoun[2], Lorenzo Bruzzone[3] and Jorge Jovicich[1,4]

[1] *CIMeC, Interdipartimental Center for Mind/Brain Sciences, University of Trento, Trento, Italy*
[2] *MIAlab, Department of Electrical and Computer Engineering, The Mind Research Network, University of New Mexico, Albuquerque, NM, USA*
[3] *RSlab, Department of Information Engineering and Computer Science, Faculty of Engineering, University of Trento, Trento, Italy*
[4] *Department of Cognitive and Education Sciences, University of Trento, Trento, Italy*

Edited by:
Simon D. Robinson, Medical University of Vienna, Austria

Reviewed by:
Andrea Caria, University of Tuebingen, Germany
Nikolaus Weiskopf, University College London, UK

****Correspondence:***
Nicola Soldati, CIMeC, Interdipartimental Center for Mind/Brain Sciences, University of Trento, Trento I-38068, Italy.
e-mail: nicola.soldati@unitn.it

Independent component analysis (ICA) techniques offer a data-driven possibility to analyze brain functional MRI data in real-time. Typical ICA methods used in functional magnetic resonance imaging (fMRI), however, have been until now mostly developed and optimized for the off-line case in which all data is available. Real-time experiments are ill-posed for ICA in that several constraints are added: limited data, limited analysis time and dynamic changes in the data and computational speed. Previous studies have shown that particular choices of ICA parameters can be used to monitor real-time fMRI (rt-fMRI) brain activation, but it is unknown how other choices would perform. In this rt-fMRI simulation study we investigate and compare the performance of 14 different publicly available ICA algorithms systematically sampling different growing window lengths (WLs), model order (MO) as well as *a priori* conditions (none, spatial or temporal). Performance is evaluated by computing the spatial and temporal correlation to a target component as well as computation time. Four algorithms are identified as best performing (constrained ICA, fastICA, amuse, and evd), with their corresponding parameter choices. Both spatial and temporal priors are found to provide equal or improved performances in similarity to the target compared with their off-line counterpart, with greatly reduced computation costs. This study suggests parameter choices that can be further investigated in a sliding-window approach for a rt-fMRI experiment.

Keywords: independent component analysis, whole-brain fMRI, ill-posed problems, real-time

1. INTRODUCTION

Independent component analysis (ICA) is a data-driven blind source separation (BSS) method widely used in brain functional magnetic resonance imaging (fMRI) data analysis (McKeown et al., 1998; Calhoun and Adali, 2006). The basic idea underlying ICA is to disentangle in a multivariate way all the independent components (ICs) whose combination gives the actual measured signal. The generic procedure is thus to fix an arbitrary number of ICs, i.e., the model order (MO), and let the algorithm exploit a criterion of independence to compute the decomposition that optimizes the criterion given that MO. Several algorithms have been proposed to measure independence of the sources in order to separate them into ICs. The most popular criteria have been based on information theory principles, such as the Infomax algorithm (Bell and Sejnowski, 1995) or higher order statistics (second, third, and fourth order cumulants), such as kurtosis fastICA (Hyvärinen and Oja, 2000). Given the nature of data-driven BSS algorithms which try to deal with and take advantage of an enormous amount of data, ICA found an optimal field of application in the analysis of fMRI data. Its canonical use has been that of analyzing data off-line, that is, once all experimental data has been already acquired. For this paper the use of ICA off-line can be defined as analyzing data in well-posed conditions, as we have usually a great amount of time available for computation and a complete dataset with all the relevant information.

A very different situation arises if ICA is to be considered for dynamic studies such as real-time fMRI (rt-fMRI), in which there is an interest in the dynamic characterization of brain states during the experiment (deCharms, 2008; Weiskopf, 2012). Recently rt-fMRI received a great deal of attention since it makes it possible to perform experiments characterized by novel paradigms (LaConte, 2011; Caria et al., 2012). The most investigated novel paradigm with rt-fMRI is neurofeedback (Shibata et al., 2011; Subramanian et al., 2011). In such experiments subjects receive stimulation that is derived from their ongoing fMRI activity and the task can be to develop mental strategies to regulate the activation. ICA methods could be of interest in such studies for their data-driven nature, particularly when considering experimental designs in which hemodynamic response models will be difficult to use for predicting the brain states under investigation, such as resting state. In a rt-fMRI context ICA will work under ill-posed conditions because the data need to be analyzed under critical time constraints and with a reduced dataset. In addition, since the data changes dynamically whereas the algorithm is usually

fixed, the choice of the algorithm can drastically affect computation time and quality of the results. The first implementation of ICA algorithms for rt-fMRI demonstrated successful use of the fastICA algorithm (Esposito et al., 2003). In that work the authors adopted several specific choices for real-time ICA analysis, including a specific ICA algorithm, the choice of a sliding window with a defined temporal window length (WL) and a MO. This study gave two main results. Firstly, it demonstrated in both real and simulated data that the expected task-related activity was equally detected by ICA and by the standard general linear model (GLM) approach. Secondly, ICA was able to detect transient or unexpected neural activity which had not been originally included in the hemodynamic response model. Together these results support the motivation of the evaluation and use of ICA in a rt-fMRI experiments. Real-time ICA has been recently implemented as a plug-in of Turbo Brain Voyager software (Goebel, 2012).

However, there are many possible choices for ICA algorithms, differing mostly in the mathematical criteria used to establish source independence, and it is not obvious which of these algorithms could best characterize neural activity as captured by the BOLD contrast. In addition to which particular algorithm is used, there is also freedom for parameter setting and it is not clear how these might affect the performance of an ICA-based rt-fMRI analysis. Indeed, performance comparisons among different ICA algorithms applied to fMRI data have historically been reported only for the well-posed off-line fMRI case in which the full acquired time-series data was available after the experiment (Esposito et al., 2002; Correa et al., 2005, 2007). Further, from off-line ICA experiments it is known that *a priori* conditions may help the identification of a particular IC most congruent with a predefined target, such as a spatial map (Lin et al., 2010). This *a priori* knowledge can be implemented in different ways depending on the characteristics of the algorithms. It can be as low invasive as a simple tailoring in the nature of the statistical distribution to be extracted, i.e., weighting more super-Gaussian or sub-Gaussian distributions, or as constrained as targeting a specific time course or spatial map. This approach is known as semi-blind decomposition, and its main property is to fuse the positive principles of data-driven algorithms with some kind of *a priori* knowledge on the problem of interest. The introduction of *a priori* knowledge can be done in several ways, e.g., by orienting the decomposition of data into sources with some specific properties. An example of a semi-blind approach is presented in Lin et al. (2010), in which a spatial *a priori* constraint has been introduced in the decomposition algorithm with the aim of extracting the source most congruent with a predefined spatial target. The motivation of considering priors includes reduced computational time (as *a priori* information suggests shortcuts in the decomposition to the algorithm), and improved quality of the sources obtained (given that the results are closer to what is expected). In general not all ICA implementations foresee the possibility of introducing prior knowledge at spatial or temporal level. In this context, and given the noisy data of rt-fMRI experiments from the limited data available for analysis, it is of interest to extend the evaluation of real-time ICA strategies with the consideration of temporal and spatial priors.

In this study we investigated and compared the performance of various ICA algorithms under the ill-posed conditions imposed by rt-fMRI. We used fMRI data of healthy subjects performing a visual-motor task in a framework that simulated a real-time acquisition for each subject separately. Four brain networks were extracted from the full time course of an independent randomly chosen subject not included in further analysis and used as target networks for the performance evaluations: the right and left visual motor networks, the default mode network (DMN), and a noise (NOISE) network associated with physiological noise. In each network we tested 10 out of 14 different publicly available ICA algorithms, and for each algorithm we investigated how the length of the time window (i.e., the number of time points) used for the analysis, the MO (i.e., the number of computed ICs) and the type of *a priori* information (none, spatial or temporal) affected performance. The evaluation of performance was done by considering computation time together with the spatial and temporal correlations of the dynamic ICs with the network reference target. The goal was thus to find, for each network, the ICA implementation that gave the fastest and highest spatial and temporal similarity to the target, but using only a fraction of the time series.

2. MATERIALS AND METHODS

2.1. fMRI EXPERIMENT

This simulation study was based on data acquired in a real fMRI experiment (Calhoun et al., 2003). This data set (7 male, 1 female, average age 24 years) has been chosen because it activates a variety of well-known networks (including Default Mode, right visual/motor, and left visual/motor areas) and it has been extensively studied with ICA since part of the dataset is included in the public distribution of the Group ICA fMRI toolbox (GIFT: http://mialab.mrn.org/software/gift/index.html). The dataset is fully described in the original publication and here we outline only the main aspects related to the cognitive tasks, data acquisition and preprocessing.

2.1.1. Cognitive tasks

The visual-motor paradigm contains two identical but spatially offset, periodic, visual stimuli, shifted by 20 s from one another (**Figure 1**). The visual stimuli were projected via an LCD projector onto a rear-projection screen subtending approximately 25° of

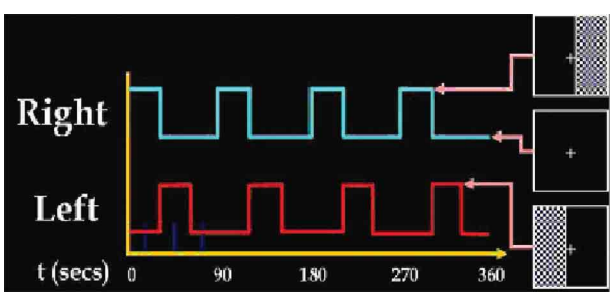

FIGURE 1 | Summary of the stimulus set-up presented to the subject during experiment data acquisition.

visual field, visible via a mirror attached to the MRI head coil. The stimuli consisted of an 8 Hz reversing checker-board pattern presented for 15 s in the right visual hemi-field, followed by 5 s of an asterisk fixation, followed by 15 s of checker-board presented to the left visual hemi-field, followed by 20 s of a central asterisk fixation. The 55 s event set was repeated four times for a total of 220 s. The motor stimuli consisted of participants touching their right thumb to each of their four fingers sequentially, back and forth, at a self-paced rate using the hand on the same side on which the visual stimulus is presented. fMRI data from this paradigm, when analyzed with standard ICA (Calhoun et al., 2003), separated activation network results into two different task-related components, one in left visual and motor cortex, the other in right visual and motor cortex.

2.1.2. Imaging parameters

Scans were acquired by a Philips NT 1.5-Tesla MRI scanner. A sagittal localizer scan was performed first, followed by a T1-weighted anatomic scan [repeat time (TR) = 500 ms, echo time (TE) = 30 ms, field of view = 24 cm, matrix = 256 × 256, slice thickness = 5 mm, and gap = 0.5 mm] consisting of 18 slices through the entire brain including most of the cerebellum. Functional scans were acquired over the same 18 slices consisting of a single-shot, EPI scan (TR = 1 s, TE = 39 ms, field of view = 24 cm, matrix = 64 × 64, slice thickness = 5 mm, gap = 0.5 mm, and flip angle = 90°) obtained consistently over a 3 min, 40 s period for a total of 220 scans. Ten dummy scans were performed at the beginning to allow for longitudinal equilibrium, after which the paradigm was automatically triggered to start by the scanner.

2.1.3. Preprocessing

The data used in this study were previously preprocessed. The fMRI data were first corrected for timing differences between the slices using windowed Fourier interpolation to minimize the dependence upon the reference slice chosen. Next, the data were imported into the statistical parametric mapping software package, SPM99. Data were motion corrected, spatially smoothed with a 6 × 6 × 10 mm Gaussian kernel, and spatially normalized into the standard Talairach space. The data (originally collected at 3.75 × 3.75 × 5 mm) were slightly sub-sampled to 3 × 3 × 5 mm, resulting in 53 × 63 × 28 voxels.

2.2. SOFTWARE AND COMPUTER FOR ICA SIMULATIONS

The entire simulation work was based on an in-house MATLAB (The MathWorks Inc., Natick, Massachusetts) implementation (http://www.mathworks.com/products/matlab) (MATLAB, 2010) that exploits the code available with the GIFT toolbox (GIFT,http://mialab.mrn.org/software/gift). Given the ICA algorithms code present in the toolbox, all the data analysis steps were implemented in an automatic fashion to permit a testing routine to be run on ICA algorithms varying their parameters (i.e., varying the WL, the MO, the *a priori* knowledge, and the subjects). The PC adopted to run the simulations was an Intel(R) Core(TM) i5 CPU M460 @2.53 GHz equipped with 6 GB of RAM and running a Windows 7 64-bit OS.

2.3. ICA ALGORITHMS

From a total of 14 different ICA algorithms a subset of 10 was considered (see **Table 1**). Among the algorithms not selected were those based on Infomax criterion, which has been used as reference algorithm, thus it and all the ICA methods based on it (semi-blind infomax, radical ICA, and SDD ICA) were eliminated from the analysis. The algorithms were available from the GIFT toolbox and most of them were discussed in a recent comparative study (Correa et al., 2005). The list included algorithms already used in rt-fMRI experiments, like the fastICA algorithm (Esposito et al., 2003). These algorithms, which are public and were taken as in their original distributions, differ in their data reduction preprocessing steps (e.g., centering, whitening, and dimensionality reduction) and independence criteria for source separation (e.g., minimization of mutual information and maximization of non-Gaussianity) (Cichocki and Amari, 2002).

In the following we outline key aspects of the adopted ICA algorithms. A detailed description of each technique is beyond the scope of this study and we refer the reader to the cited works. The selected algorithms cover the major approaches known in the ICA literature for defining independence of sources: information maximization, maximization of non-Gaussianity, joint diagonalization of cross-cumulant matrices and second-order correlation-based methods.

Infomax is a stochastic method which uses a non-linear function to maximize the information mapped between input and output of a network. The implementation adopted here was extended infomax, which improves the ability to disentangle sub and super-Gaussian sources using natural gradient descend method (Bell and Sejnowski, 1995; Lee et al., 1999).

FastICA is a stochastic method that uses a fixed-point iterative approach to extract maximally non-Gaussian sources. The

Table 1 | List of tested ICA algorithms and their possibility to accept as parameters arbitrary *a priori* knowledge (both spatial and temporal) and a varying number of ICs.

ICA algorithm	*a priori* knowledge	Arbitrary number of ICs
Infomax	Yes	Yes
FastICA	Yes	Yes
ERICA	No	Yes
SIMBEC	No	Yes
EVD	No	Yes
JADEOPAC	No	No
AMUSE	No	No
SDD ICA	No	No
Semi-blind infomax	Yes	Yes
Constrained ICA	Yes	No
Radical ICA	No	No
COMBI	No	No
ICA-EBM	Yes	Yes
FBSS	Yes	No

Those algorithms which cannot accept an arbitrary number of ICs extract a number of ICs equal to the time window length. These algorithms references are contained in GIFT toolbox (GIFT: http://mialab.mrn.org/software/gift/index.html).

independence criterion adopted can be higher order statistics or the negentropy of the output (Hyvärinen and Oja, 2000).

ERICA (equivariant robust ICA) is an algorithm that minimizes the amount of signal and noise interference on the estimated sources. It is also asymptotically equivariant for sufficient number of samples (Cruces et al., 2000).

SIMBEC (simultaneous blind extraction using cumulants) is a deterministic algorithm that exploits natural gradient ascent in a Stiefel manifold with the aim of jointly identify sources using as contrast function higher order cumulants (Amari, 1999; Cruces et al., 2001).

EVD (eigen value decomposition) is an algorithm that separates sources exploiting both second-order statistics and higher-order correlation functions. It creates and sums a set of shifted cross variance matrices, after this it applies singular-value decomposition to achieve source separation. The EVD approach is fast and useful when the spectra of the components are different (Georgiev and Cichocki, 2002).

JADEOPAC (joint approximate diagonalization of eigenmatrices) is another deterministic algorithm which diagonalizes fourth order cumulant matrices using the Jacobi technique to obtain spatially independent sources (Cardoso and Souloumiac, 1993).

AMUSE (algorithm for multiple unknown sources extraction) is a second order method based on the EVD algorithm. The difference is that it applies EVD on a single time-delayed covariance matrix for pre-whitened data. The shift of the cross-variance matrix is chosen here to obtain sources with non-zero autocorrelation of sources at that shift, with auto-correlations as different as possible from each other (Cichocki and Amari, 2002).

Constrained ICA is an algorithm that exploits a reference signal to perform ICA. The extracted source is forced to be as close as possible to the reference adopted (Lin et al., 2007, 2010).

COMBI is an algorithm which is the result of a combination of two different methods (Combination and Multi-combination of WASOBI and EFICA). SOBI (second order blind identification) was developed with the aim of dealing with sources which could be temporally correlated. It exploits second order statistic to get rid of temporal correlation and maximize the separability of sources (Belouchrani et al., 1993). WASOBI is an asymptotically optimal algorithm for autoregressive sources (Yeredor, 2000), while EFICA is an asymptotically efficient version of the FastICA algorithm (Koldovsky et al., 2006).

ICA-EBM (entropy bound minimization) is based on an entropy numerical estimation. The estimated bound of entropy is minimized to find the ICAs. The algorithm adopts a line search procedure initially constraining the demixing matrix to be orthogonal (Li and Adali, 2010b).

FBSS (full BSS) is an algorithm that exploits an entropy rate estimator to model second and higher-order correlated sources. This estimator is the adopted to separate sources minimizing their entropy rate (Li and Adali, 2010a).

2.4. USE OF *a priori* INFORMATION

As previously mentioned, the exploitation of *a priori* knowledge permits an improvement in the performance of analysis run in ill-posed conditions. However, it is worth noting that the use of *a priori* knowledge can also address another practical challenge of ICA decomposition, which is particularly relevant in ill-posed conditions. In fact a critical choice in ICA algorithms implementation is the ranking or selection of ICs. A practical challenge is to select and track the ICs of interest against the background of non-relevant (or noise) ICs. To address this problem the concept of either spatial (Lin et al., 2010) or temporal (Esposito et al., 2003) *a priori* information has been explored in literature. Other ways to solve the problem of ranking ICs could be represented by exploitation of characteristic expected features of the ICs of interest via a classifier (DeMartino et al., 2007; Soldati et al., 2009).

In the context of rt-fMRI *a priori* information may be available from a localizer scan that elicits aspects of activation that are then to be tracked dynamically in a subsequent experiment. The priors can make the mathematical computation of ICA easier, driving the algorithm initial conditions closer to the basin of attraction of the target IC. In this simulation study the temporal and spatial IC priors were determined from the ICA analysis of the full time series of an independent subject taken from the same group. This *a priori* information was incorporated into the ICA algorithms as an initial estimation of the weighted matrix or as a final constraint of the shape of the target IC. Due to the intrinsic characteristics of the ICA algorithms, only a subset of them allowed us to incorporate spatial and/or temporal *a priori* knowledge in the analysis (see **Table 1**).

Given the general model of ICA (Calhoun et al., 2001), it is possible to describe an fMRI ICA problem as $\mathbf{Y} = \mathbf{AX}$, where $\mathbf{Y}$ is the data matrix of dimension equal to the number of time points by the number of voxels; $\mathbf{A}$ is a mixing matrix of dimension equal to the number of time points by the number of ICs; and $\mathbf{X}$ is the matrix of the sources of dimension equal to the number of ICs by the number of voxels. If we denote with $\mathbf{W} = \mathbf{A}^{-1}$ the weighting matrix (i.e., unmixing matrix), it is then possible to insert *a priori* information in the rows of the matrix $\mathbf{W}$ directly, if the information is temporal (i.e., a time course). In case the expected or known behavior is spatial (i.e., spatial map) it is possible to construct the $\mathbf{W}$ matrix as $\mathbf{W} = \mathbf{Y}\text{pinv}\mathbf{X}$ where the rows of $\mathbf{X}$, i.e., the expected spatial maps of the independent sources are known. In one case [spatially constrained ICA algorithm (Lin et al., 2010)] the *a priori* knowledge is not given as initialization of the weighted matrix but, following the implementation, it is imposed as final target of the decomposition. In this last case instead of starting from a point close to the basin of attraction, the constraint means that the ending point will be close to the basin of attraction. In the context of rt-fMRI *a priori* information may be available from the functional localizer scan that is typically acquired at the beginning of neurofeedback experiments to define the networks that will be of interest to track dynamically.

2.5. PARAMETERS ANALYSED IN THE ICA SIMULATIONS

The main purpose of this rt-fMRI simulation study was to investigate a number of ICA algorithms to find the one that performed best across subjects using a trade-off of the following parameters:

1. Window length (WL) (i.e., time length of data acquisition)
2. Model order (MO) (i.e., number of ICs)
3. Type of *a priori* information (none, spatial, or temporal)

These choices for these parameters are discussed in more details in the following sections.

2.6. WINDOW LENGTH AND MODEL ORDER

The amount of data that an ICA algorithm uses depends directly on the number of brain volumes available in the growing time window, which in turn defines a limit to the maximum number of ICs that may be computed. As the time WL becomes longer there may be a more accurate representation of the averaged dynamic responses of the brain because more data is available. However, this may come at a cost related to both reducing temporal resolution of the dynamics characterized and increasing the computation time. Conversely, with shorter windows the characterizations may be faster yet less accurate. In this study we focused on a growing window approach because we were interested in finding an optimal WL. For the simulation of each ICA algorithm the WL was varied between 3 and 12 brain volumes (the full time series consisted of 220 brain volumes, and 12 TRs approximated to the hemodynamic delay). For each time WL the number of ICs was varied between 2 (minimum meaningful value of MO in BSS) and the actual WL. Moreover, since for computational reasons the MO must be less than or equal to the WL, the WL minimum value was set to 3. Thus while increasing the WL all possible MOs between 2 and WL were evaluated to find the best performing pair of parameters (WL and MO). Not all the ICA algorithms considered permitted an arbitrary selection of the number of desired ICs. Some of them (jade-opac, amuse, Radical ICA, combi, ICA-ebm, and FBSS) allowed extraction of only the number of ICs that was fixed for each run and was equal to the number of available data points. In our case, this means that for these algorithms the spanned parameter space was represented by a line identified by the points in the space with equal number of ICs and time WL.

2.7. COMPUTATION TEMPLATE ICs FOR PERFORMANCE EVALUATIONS

Four template ICs were identified on a single subject not included in further analysis by applying the Infomax ICA algorithm with 20 components on the full time series. Infomax is well known to fMRI studies as it has been commonly applied and its performances shown to be stable and reliable (Calhoun et al., 2004). Moreover, when applied on task-related datasets, it furnishes results completely similar to those obtained via application of SPM (Calhoun et al., 2001; Correa et al., 2007). For this reason, although an absolute accuracy as gold standard cannot be defined for ICA results, we opted to use it as a relative reference against which to compare results computed by other algorithms. In addition, to further reduce bias we decided to eliminate from the on-line test analysis Infomax itself and all the other ICA algorithms based on the same criteria (semi-blind infomax, radical ICA, and SDD ICA).

The spatial maps and associated time courses of these networks were later used as reference and as *a priori* knowledge options for the performance evaluation of different ICA implementations, in particular shorter time series to simulate rt-fMRI conditions.

The task-related networks were the right visuo-motor task (RVMT) and left visuo-motor task (LVMT), which were selected by visual inspection using as reference the originally published results (Calhoun et al., 2003). In addition, the DMN and a NOISE network were also identified and used as templates for networks typically present in resting state studies (Robinson et al., 2009; Soldati et al., 2009). **Figure 2** shows sample spatial representations of the four template networks in a subject.

In our simulation study there could be a potential bias favoring the performance of algorithms that use *a priori* information given that the priors are derived in the same way as the reference templates used for performance estimation: spatial and temporal ICA for the networks of interest using the Infomax ICA algorithm on the full time series. Two considerations were made to reduce this bias. Firstly, a random subject was chosen from the

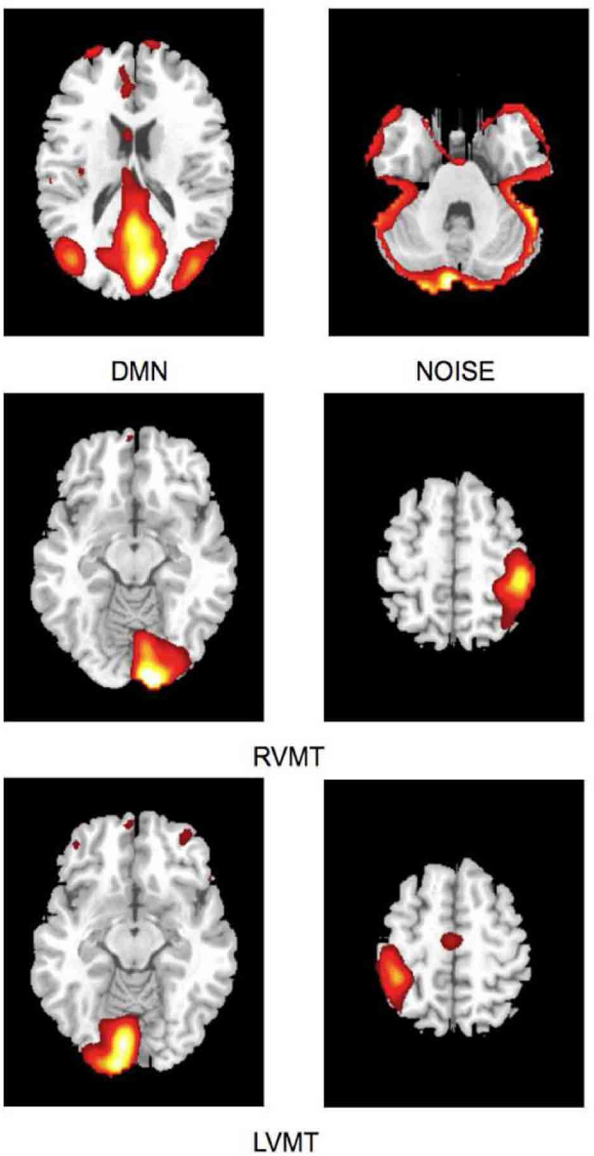

FIGURE 2 | Spatial maps of ICs considered in the simulation obtained from Group ICA 20 ICs. For ease of visualization only the relevant slices are reported here. First row depicts default mode network (DMN) and residual motion artifact (Noise). Second and third rows depict the two task-related ICs, right visuo-motor task (RVMT) and left visuo-motor task (LVMT).

group of 8, the spatial and temporal priors were derived from this subject and used as priors for the other seven subjects. In this way the priors and reference templates are not identical, because the latter ones continue to be calculated for each subject separately. Secondly, the real-time simulation did not use the Infomax algorithm nor other algorithms based on similar principles (semi-blind infomax, radical ICA, and SDD ICA)for performance evaluations.

2.8. EVALUATION OF PERFORMANCE FOR DIFFERENT ICA IMPLEMENTATIONS

The performance of each ICA algorithm was assessed separately for each subject (7 out of 8) and network (RVMT, LVMT, DMN, and NOISE) by systematically sampling the space of algorithm variables, finding for each variable set the targeted network ICs and comparing them with the corresponding template networks.

The ICA implementations for each subject and network were manipulated through the following variables:

- ICA algorithm: 10 out of 14 algorithms listed in **Table 1**.
- Prior: all 10 algorithms were tested without priors. A subgroup of four algorithms (fastICA, Constrained ICA, ICA-EBM, and FBSS) allowed the additional implementation of either spatial or temporal priors taken from the template ICs.
- Window length (WL): for each algorithm the WL varied from 3 TRs to 12 TRs in a growing window scheme. The lower limit of 3 TRs was chosen as the minimum time course length for which an ICA can be computed. The upper limit of 12 TRs was chosen because it is approximate to the hemodynamic response.
- Model Order (MO): for each WL the MO was varied between 2 and WL.

These parameters were manipulated according to an iterative automatic procedure (Soldati et al., 2010), as schematically shown in **Figure 3**. This meant that for each subject (a total of 7 out of 8), network (a total of 4), and ICA algorithm (a total of 18: 10 with no priors, 4 with spatial, and 4 with temporal priors), 66 ICA computations were made given that WL spans from 3 to 12 and for each WL, MO spans from 2 to WL. At each iteration the extracted IC results were compared with the templates to estimate the performance of the iteration's parameters.

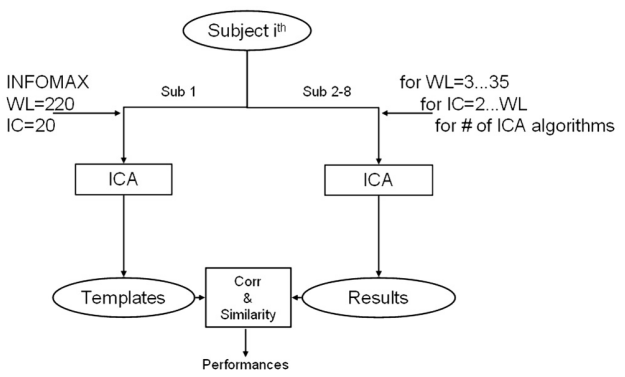

FIGURE 3 | Diagram of adopted method for ICA algorithm comparison. For one separated subject data are exploited for creating templates using INFOMAX with model order (ICs) of 20 and window length (WL) equal to the entire available time course. The ICA algorithms are then tested iteratively on all the other subjects for each combination of IC and WL. Results of each computation are compared with templates and evaluated in terms of spatial similarity and temporal correlation.

The performance of each algorithm was characterized from the following three parameters:

1. Spatial similarity with template network: the target network IC was selected automatically by choosing the one with the highest spatial similarity (i.e., spatial overlap) between the ICs extracted and the template IC for the corresponding network. The spatial similarity metric was computed as the absolute value of

$$\text{Similarity} = \frac{a * b}{\text{norm}(a) * \text{norm}(b)} \quad (1)$$

   where a and b are the vectors representing the spatial map (reshaped to 1D) of extracted and the template IC of interest, respectively.
2. Temporal correlation with template network: the temporal correlation between the IC extracted and the template IC derived was computed, with its statistical significance ($p < 0.05$).
3. Computation time: the computation time to extract the ICs was recorded.

Considering a fixed subject, brain network and ICA algorithm (with or without prior), the best performing ICA implementation (choice of WL and MO) was considered the one that gave the highest spatial similarity with a significant temporal correlation to the reference network and a computational time below the 12 s threshold.

3. RESULTS

The proposed method has been applied to characterize the behavior of different ICA algorithms in ill-posed conditions simulating rt-fMRI manipulating MO, WL, and *a priori* conditions. The goal was to find the implementations that would give the best compromise between computational time and similarity between the detected IC and the reference IC at minimal computation time.

The obtained group performance results are reported in **Figures 4–6**. These figures report the optimal values of the parameters obtained without exploiting *a priori* knowledge (**Figure 4**), exploiting spatial *a priori* knowledge (**Figure 5**), or temporal *a priori* knowledge (**Figure 6**). From the results it can be clearly seen how the selected ICA algorithms differed in performance in these extreme conditions. A trade-off of these results must be obtained to evaluate the winners. In the case of no *a priori* knowledge exploitation (**Figure 4**) erica, evd, amuse, and partially fastICA seemed to be the more suitable algorithms given their particularly low computational time, with fastICA and evd being the best performing also with respect to spatial and temporal similarity to the reference template.

When considering spatial (**Figure 5**) and temporal (**Figure 6**) *a priori* knowledge only 4 of the 10 considered ICA algorithms

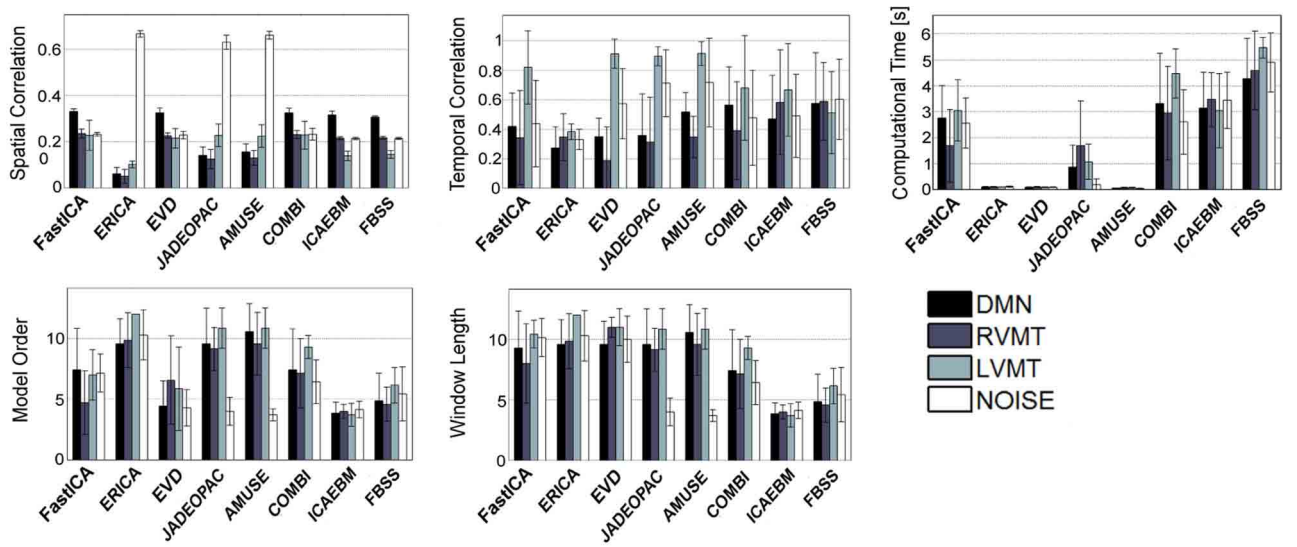

FIGURE 4 | Results of the best performing runs (mean across subjects) for all available ICA algorithms for a growing length of time window up to 12 TRs and no *a priori* information considered. For each ICA algorithm the values of similarity (Sim), computational time (CT), temporal correlation (TC), model order (MO), and window length (WL) w.r.t. four reference ICs representing brain activities of interest (**Figure 3**), are reported for the same optimal condition identified. It is worth noting that here is reported a total of 8 algorithms out of 14 given that Infomax and all those algorithms based on it (semi-blind infomax, radical ICA, and SDD ICA) are excluded from the on-line simulations. Moreover constrained ICA has been excluded since it cannot work without *a priori* knowledge. Finally SIMBEC proved itself to not respect the constraints on computational time, thus it has not been included.

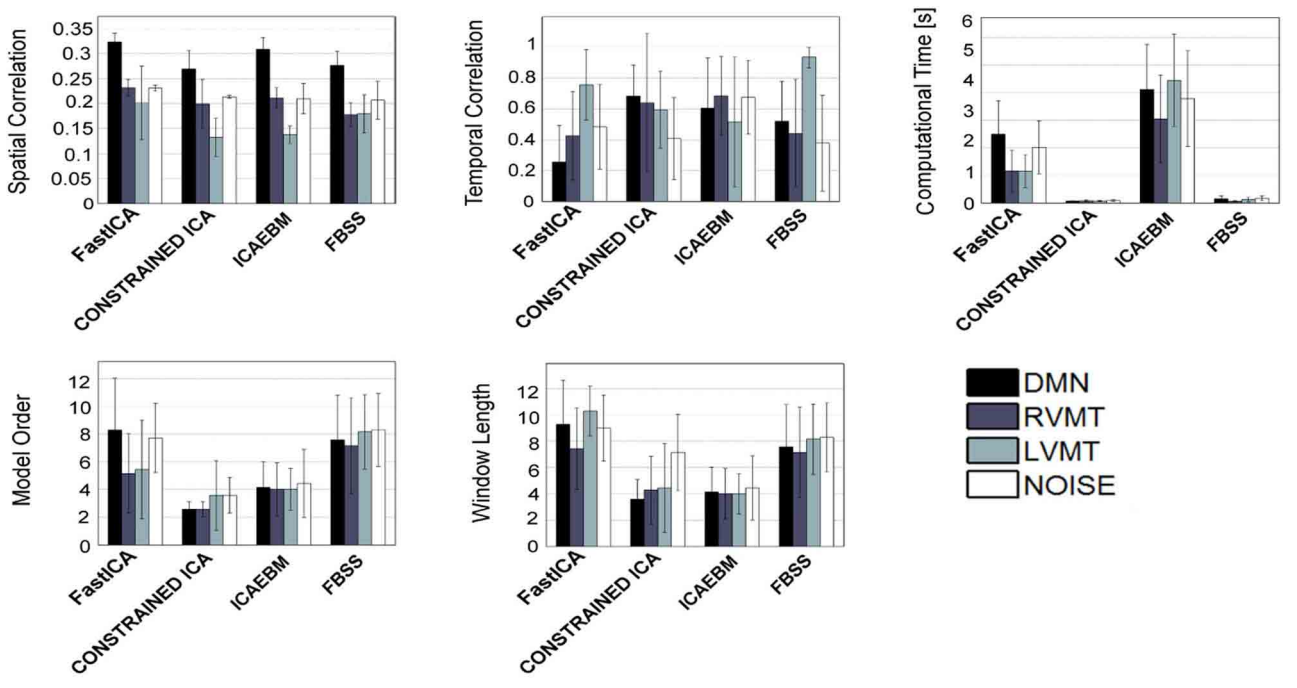

FIGURE 5 | Similar to Figure 4, but considering only the algorithms which permit the inclusion of spatial *a priori* knowledge.

allowed the evaluation of *a priori* information. Constrained ICA and FBSS were the fastest algorithms, while fastICA, though slower, obtained a slightly higher overall performance in computing similarity metrics. A comparison between **Figures 4** and **6** shows the advantages of using prior information with some of the tested algorithms. In particular, for FBSS the computational time improved by a factor of more than two with either spatial or temporal *a priori* information keeping the same performance

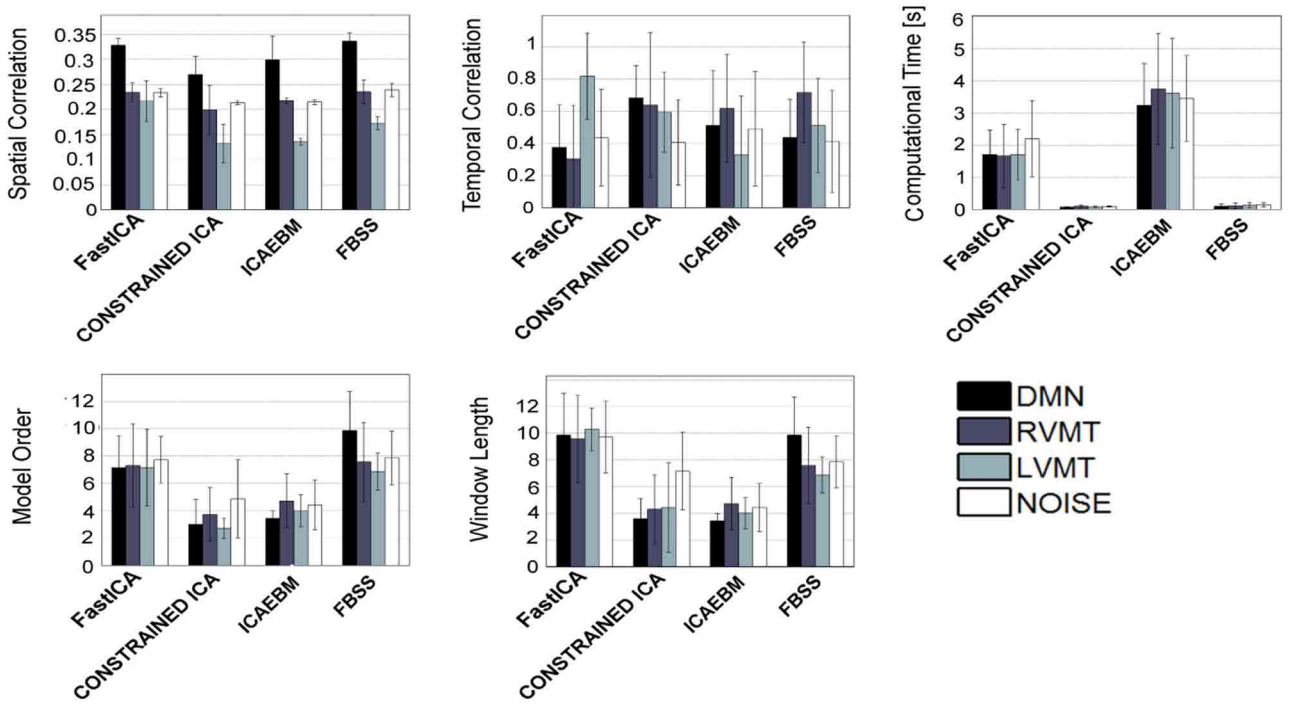

FIGURE 6 | Similar to Figure 4, but considering only the algorithms which permit the inclusion of temporal *a priori* knowledge.

in terms of spatial and temporal correlation. Also, with the use of *a priori* information the fastest algorithm (constrained ICA, computation time < 0.15 s) was about two orders of magnitude faster than those giving comparable spatial similarities without priors. It is worth noting that the results varied across different monitored networks, i.e., tasks.

4. DISCUSSION

The aim of the present study was to evaluate the performance of ICA algorithms in ill-posed conditions, i.e., with a small amount of data availability and constraints on computational time. The issue here was to understand if it is possible to adapt an ICA algorithm to a non-ideal environment, as presented in Esposito et al. (2003). Moreover the analysis was extended to investigate which ICA algorithm was more suitable to this kind of conditions from the perspectives of monitoring a brain activity of interest.

Our goal was to explore the performance in terms of ability to reach the spatial and temporal network characteristics that could be derived from the full dataset in a standard off-line analysis. Thus, we assumed as reference template the optimal results obtained via a single subject ICA with all time-points available, a MO of 20 and using the infomax algorithm, considering stochastic differences not critical. Another intrinsic issue is that the differences in results between off-line and ill-posed conditions can be related not only to computation, but also to the extraction of dynamic behavior with respect to the stationary behavior typically extracted by off-line ICA.

One issue that deserves special consideration is circularity. The use of a validating reference template obtained from the same data used in the simulations did not introduce circularity issues since we are in principle just checking that the same information can be extracted in different ways, with only differences due to noise.

A practical issue to consider is that the high dimensionality of the parameter space results in a high computational load for running simulations spanning the entire multidimensional parameter space. The best performance can be evaluated in a trade-o perspective, since different combinations of parameters can give similar results. The consequence is that performance optimization is heavily connected to the practical application and conditions in which the ICA algorithm is adopted.

Relying on these elements, we performed a direct comparison of different algorithms, defining a cluster of algorithms on the basis of the manipulability of the parameters that they offer (**Table 1**). In fact the tested ICA algorithms can be divided into three groups: those which accept setting of MO and *a priori* knowledge (i.e., infomax, fastICA, and semi-blind infomax), those which accept neither setting of MO nor *a priori* knowledge (i.e., jade-opac, amuse, radical ICA, and combi), and those which accept only one of the two (i.e., erica, simbec, evd, constrained ICA, ICA-ebm, and FBSS). These constraints are intrinsic to the publicly distributed algorithms. It is beyond the scope of this work to try to change any of the algorithms to eventually make them more flexible. The more flexible algorithms (i.e., those accepting full manipulability of parameters) will, however, not necessarily

be better, since the most rigid could be the most adaptable for specific circumstances. Putting everything in a rt-fMRI experiment perspective, it is possible to distinguish the algorithms on the basis of the tasks and conditions they must face. Those algorithms which do not accept any *a priori* knowledge could work very well to define the target networks from the functional localizer step that usually precedes a rt-fMRI acquisition, a step in which *a priori* knowledge may not be necessary or even available. For this use it is possible to permit a higher computational load, since usually the localizer part of an experiment can have more time allocated. The algorithms that tended to be more suitable for this use were evd and amuse, which resulted in particularly fast computation, with evd performing slightly better. The jade-opac and fastICA algorithms also performed well but at the cost of a higher computational time (**Figure 5**). The results showed that the use of *a priori* knowledge can drastically improve computation time and spatial similarity to a target IC. This suggests that use of priors may be crucial in the dynamic analysis part of the rt-fMRI experiment, where any information from the localizer can be exploited to speed up the process and increase accuracy. From this point of view the flexibility of the ICA algorithm is essential. Thus among the algorithms which accept *a priori* knowledge, constrained ICA provided the optimal solution, followed by fastICA (**Figures 5** and **6**).

For completeness, it is important to analyze the values of the two parameters growing WL and MO for the previously reported best performing algorithms. In an on-line perspective these values are related to the time needed to elapse before obtaining the first real-time result or step updating. This means that the longer the window and the higher the MO, the more time will pass before the availability of results. This is critical for the on-line computation, since the scale of the resolution in monitoring the brain dynamics will be directly associated to that.

Another observation is related to the type of brain activity monitored (i.e., if it represents a resting state brain activity, a task-related activity or physiological noise). Monitoring ICs with different origins conveys different information. Cross-task variability can be due to the fact that the less the variance of data is explained by the IC, the more difficult it is to extract, especially with a decreased amount of data available. For this reason ICs whose rank is low in a full-data ICA decomposition are critical to identify in the ill-posed conditions. Nonetheless, as the simulations showed, they can still be at least partially captured.

The periodicity of the ICs of interest affects the choice of optimal parameters. The DMN deserves particular considerations due to the low frequency nature of its sources (Damoiseaux et al., 2006). Its identification, despite being easily done by data-driven algorithm, is dramatically harder in ill-posed conditions given that its periodicity is significantly longer than the WL. This results in difficulties in observing its full dynamic. Given these new dimensions (type of brain activity and periodicity) it was possible to see that different algorithms had different effectiveness in adequately identifying brain activity coming from different kinds of sources. It can be seen that the same algorithm could outperform all the others in detecting task-related activity, while suffering in dealing with non-structured noise or, vice versa, as for example it happened in the case of evd and jade-opac, or evd and combi with no *a priori* knowledge. The same reasoning holds for the use of *a priori* knowledge. Even if in this case not all algorithms permitted the introduction of *a priori* knowledge in performing the ICA decomposition, for those which accepted this input the performance varied considering different target sources. Indeed fastICA and constrained ICA alternated best performance, with constrained ICA performing slightly better overall.

Additional ambiguity comes from the stochastic nature of most ICA algorithms, resulting in different runs of ICA delivering slightly different results. This is due to the search procedure of final results optimization, which could result in the algorithm being trapped in a local minima. Another observation can be related to the computational time of ICA decomposition: in general it grows linearly with the increase of the WL, and this can be easily justified by the fact that the more data are to be processed the more time it takes. But as the data become more descriptive of the source to be extracted, the algorithm is able to extract the source more easily, thus reducing the computational time needed, independently of the data length.

One limitation of this study is that the adopted implementations of ICA algorithms are not directly optimized for ill-posed conditions. This opens the door to further development oriented toward their methodological and algorithmic optimization, which would make them more efficient and flexible. Nonetheless, this work demonstrates a methodology for evaluating different ICA implementations for the purpose of finding the ICA algorithms and analysis parameters for the optimal detection of a target brain network under ill-posed conditions. Further experiments are needed to evaluate the performance of ICA implementations on larger datasets and also other networks.

Another element to be taken into account is the relatively small number of subjects adopted in the simulations (8) and reduced number of brain networks studied (visual, motor, and default mode). These constraints result from the use of a dataset whose behavior is well known in the ICA domain and which could confirm the stability and validity of obtained results. Nonetheless, this work demonstrated a methodology for evaluating different ICA implementations for the purpose of finding the ICA algorithms and analysis parameters for the optimal detection of a target brain network under ill-posed conditions. Further experiments are needed to evaluate the performance of ICA implementations on larger datasets, other brain networks and experimental conditions.

The results of this study can be used to evaluate ICA implementations for the dynamic analysis of fMRI data. In particular, in a potential rt-fMRI perspective, the best performing ICA algorithm without the use of *a priori* knowledge can be adopted to analyze the functional localizer data in a data-driven way. In this approach the target ICs to be then followed dynamically in the real-time experiment are defined without considering spatial or temporal constraints. The sources defined by the functional localizer can then be used in different algorithms that include *a priori* spatial, temporal or spatio-temporal knowledge for the dynamic monitoring of target ICs in a rt-fMRI experiment, such as for neurofeedback.

5. CONCLUSION

In this paper we presented an extensive comparison of ICA algorithms under the constraints to have a fast decomposition with a small amount of data available (ill-posed condition). The aim of ICA is to exploit the multivariate nature of data-driven methods to perform a whole-brain analysis. Here we have shown that ICA can satisfactory work in ill-posed conditions with results which are similar and thus acceptable with respect to the off-line implementation. In our comparison we found that several ICA algorithms (evd, amuse, fastICA , and constrained ICA) can be adopted in ill-posed conditions and thus can be exploited for dynamic analysis of fMRI data. The best performing algorithms (evd and constrained ICA) were also shown to be useful in terms of robustness against errors in parameters, and fast in terms of computational time. this opens the door to their exploitation in applications such as rt-fMRI, both as functional localizers and for on-line dynamic analysis. Adoption of these methods would be useful for experimental designs such those known as neurofeedback experiments, although further work is needed to implement a fully real-time ICA method for fMRI data analysis.

ACKNOWLEDGMENTS

This work has been realized thanks to the support from the Provincia autonoma di Trento and the Fondazione Cassa di Risparmio di Trento e Rovereto, Italy. Jorge Jovicich was supported by a PRIN grant (Prot. 2008HETS3W_002) from MIUR (Italy). The authors would also like to specially thank James Hartzell.

REFERENCES

Amari, S.-I. (1999). Natural gradient learning for over-and under-complete bases in ICA. *Neural Comput.* 11, 1875–1883.

Bell, A. J., and Sejnowski, T. J. (1995). An information-maximization approach to blind separation and blind deconvolution. *Neural Comput.* 7, 1129–1159.

Belouchrani, A., Abed Meraim, K., Cardoso, J., and Moulines, E. (1993). "Second-order blind separation of correlated sources," in *Proceedings of the International Conference on Digital Signal Processing* (Nicosia), 346–351.

Calhoun, V. D., and Adali, T. (2006). Unmixing fMRI with independent component analysis. *IEEE Eng. Med. Biol. Mag.* 25, 79–90.

Calhoun, V. D., Adali, T., Pearlson, G. D., and Pekar, J. J. (2001). Spatial and temporal independent component analysis of functional MRI data containing a pair of task-related waveforms. *Hum. Brain Mapp.* 13, 43–53.

Calhoun, V. D., Adali, T., Pekar, J. J., and Pearlson, G. D. (2003). Latency (in)sensitive ICA. Group independent component analysis of fMRI data in the temporal frequency domain. *Neuroimage* 20, 1661–1669.

Calhoun, V., Pearlson, G., and Adali, T. (2004). Independent component analysis applied to fMRI data: a generative model for validating results. *J. VLSI Signal Process. Syst.* 37, 281–291.

Cardoso, J.-F., and Souloumiac, A. (1993). Blind beamforming for non Gaussian signals. *IEE Proceedings-F* 140, 362–370.

Caria, A., Sitaram, R., and Birbaumer, N. (2012). Real-time fMRI: a tool for local brain regulation. *Neuroscientist* 18, 487–501.

Cichocki, A., and Amari, S.-I. (2002). *Adaptive Blind Signal and Image Processing: Learning Algorithms and Applications*. New York, NY: John Wiley & Sons Inc.

Correa, N., Adali, T., and Calhoun, V. D. (2007). Performance of blind source separation algorithms for fMRI analysis using a group ICA method. *Magn. Reson. Imaging* 25, 684–694.

Correa, N., Adali, T., Li, Y.-O., and Calhoun, V. D. (2005). "Comparison of blind source separation algorithms for fMRI using a new matlab toolbox: GIFT," in *Proceedings of the IEEE International Conference on Acoustics, Speech, and Signal Processing (ICASSP '05), Vol. 5*. (Philadelphia, PA), 401–404.

Cruces, S., Cichocki, A., and Amari, S.-I. (2001). "Criteria for the simultaneous extraction of arbitrary groups of sources," in *Proceedings of the International Conference on Independent Component Analysis and Blind Signal Separation* (San Diego, CA).

Cruces, S., Cichocki, A., and Castedo, L. (2000). "Blind source extraction in gaussian noise," in *Proceedings of the 2nd International Workshop on Independent Component Analysis and Blind Signal Separation (ICA'2000)* (Helsinki), 63–68.

Damoiseaux, J. S., Rombouts, S. A. R. B., Barkhof, F., Scheltens, P., Stam, C. J., Smith, S. M., et al. (2006). Consistent resting-state networks across healthy subjects. *Proc. Natl. Acad. Sci. U.S.A.* 103, 13848–13853.

deCharms, R. C. (2008). Applications of real-time fMRI. *Nat. Rev. Neurosci.* 9, 720–729.

DeMartino, F., Gentile, F., Esposito, F., Balsi, M., Salle, F. D., Goebel, R., et al. (2007). Classification of fMRI independent components using IC-fingerprints and support vector machine classifiers. *Neuroimage* 34, 177–194.

Esposito, F., Formisano, E., Seifritz, E., Goebel, R., Morrone, R., Tedeschi, G., et al. (2002). Spatial independent component analysis of functional MRI time-series: to what extent do results depend on the algorithm used? *Hum. Brain Mapp.* 16, 146–157.

Esposito, F., Seifritz, E., Formisano, E., Morrone, R., Scarabino, T., Tedeschi, G., et al. (2003). Real-time independent component analysis of fMRI time-series. *Neuroimage* 20, 2209–2224.

Georgiev, P., and Cichocki, A. (2002). "Blind source separation via symmetric eigenvalue decomposition," in *Proceeding of the Sixth International Symposium on Signal Processing and Its Applications* (Kuala Lumpur), 17–20.

Goebel, R. (2012). Brainvoyager – past, present, future. *Neuroimage* 62, 748–756.

Hyvärinen, A., and Oja, E. (2000). Independent component analysis: algorithms and applications. *Neural Netw.* 13, 411–430.

Koldovsky, Z., Tichavsky, P., and Oja, E. (2006). Efficient variant of algorithm fastICA for independent component analysis attaining the Cram amp; 201;r-Rao lower bound. *IEEE Trans. Neural Netw.* 17, 1265–1277.

LaConte, S. M. (2011). Decoding fMRI brain states in real-time. *Neuroimage* 56, 440–454.

Lee, T.-W., Girolami, M., and Sejnowski, T. J. (1999). Independent component analysis using an extended infomax algorithm for mixed subgaussian and supergaussian sources. *Neural Comput.* 11, 417–441.

Li, X.-L., and Adali, T. (2010a). "Blind spatiotemporal separation of second and/or higher-order correlated sources by entropy rate minimization," in *International Conference on Acoustics, Speech, and Signal Processing (ICASSP '10)*. (Dallas, TX), 1934–1937.

Li, X.-L., and Adali, T. (2010b). Independent component analysis by entropy bound minimization. *IEEE Trans. Signal Proc.* 58, 5151–5164.

Lin, Q.-H., Liu, J., Zheng, Y.-R., Liang, H., and Calhoun, V. D. (2010). Semiblind spatial ICA of fMRI using spatial constraints. *Hum. Brain Mapp.* 31, 1076–1088.

Lin, Q.-H., Zheng, Y.-R., Yin, F.-L., Liang, H., and Calhoun, V. D. (2007). A fast algorithm for one-unit ICA-R. *Inf. Sci.* 177, 1265–1275.

MATLAB. (2010). *Version 7.10.0 (R2010a)*. Natick, MA: The MathWorks Inc.

McKeown, M. J., Makeig, S., Brown, G. G., Jung, T. P., Kindermann, S. S., Bell, A. J., et al. (1998). Analysis of fMRI data by blind separation into independent spatial components. *Hum. Brain Mapp.* 6, 160–188.

Robinson, S., Basso, G., Soldati, N., Sailer, U., Jovicich, J., Bruzzone, L., et al. (2009). A resting state network in the motor control circuit of the basal ganglia. *BMC Neurosci.* 10:137. doi: 10.1186/1471-2202-10-137

Shibata, K., Watanabe, T., Sasaki, Y., and Kawato, M. (2011). Perceptual learning incepted by decoded fMRI neurofeedback without stimulus presentation. *Science* 334, 1413–1415.

Soldati, N., Hinds, O., Triantafyllou, C., and Jovicich, J. (2010). "Preliminary investigation of RSN dynamics for rt-fMRI analysis," in *Proceedings of the HBM International Conferences Human Brain Mapping (HBM '10)* (Barcelona).

Soldati, N., Robinson, S., Persello, C., Jovicich, J., and Bruzzone, L. (2009). Automatic classification of brain resting states using fMRI temporal signals. *Electron. Lett.* 45, 19–21.

Subramanian, L., Hindle, J. V., Johnston, S., Roberts, M. V., Husain, M., Goebel, R., et al. (2011). Real-time functional magnetic resonance imaging neurofeedback for treatment of Parkinson's disease. *J. Neurosci.* 31, 16309–16317.

Weiskopf, N. (2012). Real-time fMRI and its application to neurofeedback. *Neuroimage* 62, 682–692.

Yeredor, A. (2000). Blind separation of Gaussian sources via second-order statistics with asymptotically optimal weighting. *IEEE Signal Proc. Lett.* 7, 197–200.

Conflict of Interest Statement: The authors declare that the research was conducted in the absence of any commercial or financial relationships that could be construed as a potential conflict of interest.

Received: 25 September 2012; accepted: 16 January 2013; published online: 01 February 2013.

Citation: Soldati N, Calhoun VD, Bruzzone L and Jovicich J (2013) ICA analysis of fMRI with real-time constraints: an evaluation of fast detection performance as function of algorithms, parameters and a priori conditions. Front. Hum. Neurosci. 7:19. doi: 10.3389/fnhum.2013.00019

frontiers in
HUMAN NEUROSCIENCE

METHODS ARTICLE
published: 11 March 2013
doi: 10.3389/fnhum.2013.00064

The use of *a priori* information in ICA-based techniques for real-time fMRI: an evaluation of static/dynamic and spatial/temporal characteristics

Nicola Soldati[1]*, Vince D. Calhoun[2,3], Lorenzo Bruzzone[4] and Jorge Jovicich[1,5]

[1] *Center for Mind/Brain Sciences, University of Trento, Trento, Italy*
[2] *Department of Electrical and Computer Engineering, University of New Mexico, Albuquerque, NM, USA*
[3] *The Mind Research Network, Albuquerque, NM, USA*
[4] *Department of Information Engineering and Computer Science, Faculty of Engineering, University of Trento, Trento, Italy*
[5] *Department of Cognitive and Education Sciences, University of Trento, Trento, Italy*

Edited by:
Veronika Schöpf, Medical University Vienna, Austria

Reviewed by:
Jim Voyvodic, Duke University, USA
Ariana Anderson, University of California Los Angeles, USA

****Correspondence:***
Nicola Soldati, CIMeC, Interdipartimental Center for Mind/Brain Sciences, University of Trento, Trento I-38068, Italy.
e-mail: nicola.soldati@unitn.it

Real-time brain functional MRI (rt-fMRI) allows *in vivo* non-invasive monitoring of neural networks. The use of multivariate data-driven analysis methods such as independent component analysis (ICA) offers an attractive trade-off between data interpretability and information extraction, and can be used during both task-based and rest experiments. The purpose of this study was to assess the effectiveness of different ICA-based procedures to monitor in real-time a target IC defined from a functional localizer which also used ICA. Four novel methods were implemented to monitor ongoing brain activity in a sliding window approach. The methods differed in the ways in which *a priori* information, derived from ICA algorithms, was used to monitor a target independent component (IC). We implemented four different algorithms, all based on ICA. One Back-projection method used ICA to derive static spatial information from the functional localizer, off-line, which was then back-projected dynamically during the real-time acquisition. The other three methods used real-time ICA algorithms that dynamically exploited temporal, spatial, or spatial-temporal priors during the real-time acquisition. The methods were evaluated by simulating a rt-fMRI experiment that used real fMRI data. The performance of each method was characterized by the spatial and/or temporal correlation with the target IC component monitored, computation time, and intrinsic stochastic variability of the algorithms. In this study the Back-projection method, which could monitor more than one IC of interest, outperformed the other methods. These results are consistent with a functional task that gives stable target ICs over time. The dynamic adaptation possibilities offered by the other ICA methods proposed may offer better performance than the Back-projection in conditions where the functional activation shows higher spatial and/or temporal variability.

Keywords: real-time fMRI, ICA, *a priori* knowledge, dynamic monitoring, adaptive algorithms

INTRODUCTION

Real-time fMRI (rt-fMRI) is an emerging neuroimaging tool based on the estimation of brain activity in real-time (typically around 1–2 s; Weiskopf et al., 2004, 2007; deCharms, 2008; LaConte, 2011). This tool can be used not only for overall monitoring of fMRI data quality (Weiskopf et al., 2007) but also for manipulating the cognitive state of the subject based on their own brain activity (Shibata et al., 2011). The neurofeedback approach has been used in various fields of cognitive neuroscience such as attention (Thompson et al., 2009) and emotion (Posse et al., 2003). Neurofeedback approaches have also been used with rt-fMRI in clinical research, such as the study of control of chronic pain (deCharms et al., 2005) and the control of craving (Chiu et al., 2010; Anderson et al., 2011).

Since its advent, rt-fMRI has had to face a number of technical challenges, mainly due to the computational load of the data analysis which directly competes against the goal of providing real-time feedback (i.e., <1 TR). However, recent technological advancements have provided a way to overcome this issue by making large scale computations possible even on standard platforms (Weiskopf et al., 2007; Weiskopf, 2012). These technical advances have enabled us to shift our focus of attention from technical issues to data analysis aspects.

The usual goal of a real-time system is to permit the identification and monitoring of an activity of interest during its ongoing development and actuation. The identification is defined as an initialization phase where the real-time analysis and derived spatial-temporal features to be monitored are defined, usually with a functional localizer (FL) or a classification training step (LaConte et al., 2007). The monitoring represents the execution of the online analysis of the event of interest and the real-time delivery of results that can eventually operate on the stimulation paradigm. From a conceptual point of view, it is thus possible to discriminate the identification and monitoring phases and to develop different algorithms and strategies to deal with them.

The initial and still most common analysis framework for rt-fMRI is based on univariate hypothesis-driven approaches, with adaptation of standard algorithms, such as the general linear model family (GLM), to the real-time domain (Cox et al., 1995; Gembris et al., 2000; Hinds et al., 2011). These methods are common mostly because they are associated with ease of interpretability and fast computation. In these approaches both the identification and monitoring phases are typically implemented using hemodynamic response-based models of the expected cognitive tasks and eventual nuisance variables taking place during the rt-fMRI experiment.

Another family of data analysis techniques is represented by the multivariate data-driven algorithms, which have shown a great capability of exploiting the full information content intrinsically present in the data to be analyzed without assuming the explicit shape or timing of the hemodynamic response to a stimulus (McKeown et al., 1998; Mouro-Miranda et al., 2005; Norman et al., 2006). The driving motivation behind these methods is that they allow characterizing functions that may not be detectable without exploiting both second order (variance) and higher-order statistics, thus relying on a greater amount of information. These properties make the multivariate data-driven techniques very appealing for use in the real-time domain. Within this concept several machine learning algorithms have been successfully adopted and exploited in the real-time data analysis framework. The most successful implementations are based on support vector machines (SVM; LaConte et al., 2007; Magland et al., 2011; Sitaram et al., 2011). SVM provides a powerful solution to a number of applications that are subject specific, at the cost of training the classifier and imposing some interpretability issues on the results. In this context, the two phases of the canonical rt-fMRI framework are represented by the two steps of a classifier, i.e., the first phase is the training of the classifier, and the second phase is the test or execution of the classifier (i.e., the classification itself).

In addition to SVM, independent component analysis (ICA), another multivariate data-driven technique, has proven to be very effective in fully exploiting the complete amount of information which is present in the data. ICA enables the extraction of knowledge other than that merely modeled in a classical univariate approach (Hyvrinen and Oja, 2000; Calhoun et al., 2001; Beckmann and Smith, 2004). Furthermore, ICA methods can also be applied in a series of problems for which univariate inference cannot offer a solution, i.e., in experiments that lack a regressor model to be adopted in the univariate analysis. This is the case for resting data analysis or also experiments with particular patient populations (Calhoun et al., 2009).

The idea of translating ICA properties to a real-time implementation was firstly proposed by Esposito et al. (2003) in a seminal paper and implemented as a plug-in in Turbo Brain Voyager software (Goebel, 2012). In this initial work the authors presented a FastICA based rt-fMRI analysis tool exploiting precise design choices and including an identification phase and a monitoring phase. The first identification phase solved the problem of ranking ICs of interest, i.e., a canonical univariate functional localizer step was implemented to define areas of interest. Other ways to solve the problem of ICs ranking could be represented by exploitation of expected characteristic features of the ICs of interest via a classifier (DeMartino et al., 2007). The second monitoring phase used on-line execution of FastICA (implemented in a sliding window fashion) for extracting different ICs. The ICs were ordered on the basis of their spatial overlap with the IC of interest, which in this case consisted of single-slice representation of motor activity derived from a finger tapping localizer.

The work presented by Esposito et al. (2003) was recently extended to evaluate the performance of 14 different ICA algorithms considering as additional variables the model order and different types of *a priori* knowledge (spatial/temporal; Soldati et al., 2013). This work showed that ICA algorithms such as EVD, amuse, jadeopac, and FastICA were suitable when implemented in the identification phase via a functional localizer since they performed well even without extensive use of *a priori* knowledge. It is interesting to note that FastICA algorithm represented a good trade-off and its performance was valid in both functional localizer and dynamic monitoring phases. Other algorithms like constrained ICA performed worse without *a priori* knowledge and may thus be more suited for the dynamic monitoring phase due to their ability to incorporate *a priori* knowledge. Such *a priori* knowledge may help guiding the algorithm to detect a specific target IC with higher priority over the other ICs present in the data. However, there are several types of prior information that are available including spatial domain, the temporal domain, or both, and any of these could be used in different ways (as constant references from a localizer or derived dynamically). It is however not clear how these various ways of using priors may affect the performance of the results both in terms of computation time and correlation to a reference optimal ICA. Moreover, the ICA algorithm (FastICA) is stochastic, which means that multiple repetitions of the analysis on the same dataset can give slightly different results, both in the spatial and temporal domains. The problem has been extensively discussed in the literature, with one of the main proposed solutions being based on multiple ICA runs and clustering of the obtained components, with the aim of reducing the issue of stochastic variability (Himberg et al., 2004). Such instabilities can be characterized by the standard deviation of the derived (STD) results (spatial and/or temporal) when the analysis is repeated multiple times on the same dataset. The STD can be considered as a stability performance parameter of the algorithm, lower STD algorithms corresponding to more stable ones. This parameter may be particularly relevant if different ICA-based algorithms are to be considered and compared for real-time fMRI, where the analysis is repeated dynamically during data acquisition.

This study extends previous work (Esposito et al., 2003) in two ways. Firstly, the target IC to be monitored dynamically is identified from a functional localizer using an ICA-based method instead of using a GLM of the hemodynamic response. This approach allows the full analysis pipeline to be multivariate and data-driven. Secondly, novel ICA-based algorithms are proposed that introduce different types of *a priori* knowledge for the dynamic monitoring of ongoing fMRI activity. The main goal of this study was to evaluate how these algorithms perform with respect to an off-line ICA analysis after the acquisition is complete. The *a priori* information considered was either temporal, spatial, or both spatial and temporal. In addition, the *a priori* information was considered both in its static version when derived from the functional localizer, as

well as dynamic when estimated recursively as the sliding window progresses over the time course throughout the run. The different ICA-based analysis methods proposed here were tested by artificially simulating a real-time fMRI experiment using real fMRI data from a visual motor study (Calhoun et al., 2001). The original data used is unrelated to a real-time fMRI experiment, but was adopted because it is public and offers robust functional activation in well-known anatomical areas. The measures of performance to compare the various real-time methods were based on the following three metrics: (i) spatial and/or temporal correlation between the independent component (IC) estimated dynamically and the target IC derived from the localizer, (ii) computation time, and (iii) intrinsic stochastic variability of the algorithms as estimated from multiple analysis runs.

MATERIALS AND METHODS

DATASET

One of the aims of this work was to test a variety of ICA implementations in a fashion which can be directly applied to real world conditions. For the simulation of the rt-fMRI experiment we used a dataset coming from a real publicly available fMRI experiment, with tasks that show robust activation in well-known brain networks. We chose to use the data that comes as part of the GIFT package (Calhoun and Adali, 2006) because the ICA characterization of the task-induced activation networks was extensively tested. The dataset is thus publicly available and in the release it is stated that The Johns Hopkins Institutional Review Board approved the protocol and all participants provided written informed consent.

Imaging parameters

Scans were acquired on a Philips NT 1.5-T scanner. A sagittal localizer scan was performed first, followed by a T1-weighted anatomic scan [repeat time (TR) = 500 ms, echo time (TE) = 30 ms, field of view = 24 cm, matrix = 256 × 256, slice thickness = 5 mm, gap = 0.5 mm] consisting of 18 slices through the entire brain including most of the cerebellum. Next, we acquired functional scans over the same 18 slices consisting of a single-shot, echoplanar scan (TR = 1 s, TE = 39 ms, field of view = 24 cm, matrix = 64 × 64, slice thickness = 5 mm, gap = 0.5 mm, flip angle = 90°) obtained consistently over a 3-min, 40-s period for a total of 220 scans. Ten "dummy" scans were performed at the beginning to allow for longitudinal equilibrium, after which the paradigm was automatically triggered to start by the scanner.

Experiment setup

The GIFT package contains three subjects example data-sets that employ a visuo-motor paradigm derived from other studies (Calhoun et al., 2001). The paradigm contains two identical but spatially offset, periodic, visual stimuli, shifted by 20 s from one another. The stimuli consisted of an 8 Hz reversing checker-board pattern presented for 15 s in the right visual hemi-field, followed by 5 s of a central asterisk fixation, followed by 15 s of checker-board presented to the left visual hemi-field, followed by 20 s of a central asterisk fixation. The 55 s set of events was repeated four times for a total of 220 s. The motor stimuli consisted of participants touching their thumb to each of their four fingers sequentially, back and forth, at a self-paced rate using the hand on the same side on which the visual stimulus is presented.

Pre-processing

The images were first corrected for timing differences between the slices using windowed Fourier interpolation to minimize the dependence upon the reference slice chosen. Next, the data were imported into the statistical parametric mapping software package, SPM99. Data were motion corrected, spatially smoothed with a 6 mm × 6 mm × 10 mm Gaussian kernel, and spatially normalized into the standard Montreal Neurologic Institute space. The data were slightly subsampled to 3 mm × 3 mm × 5 mm, resulting in 53 × 63 × 28 voxels.

In this study the pre-processing steps were not included as part of the real-time fMRI simulations for several reasons: (i) the pre-processed and not the raw data are publicly available as part of the GIFT package (Calhoun et al., 2001) thereby being a reference starting point for various analysis tools, (ii) these pre-processing steps can be performed in real-time as several review studies describe (LaConte, 2011; Caria et al., 2012; Maclaren et al., 2013), (iii) the focus of this simulation study was on the data-driven network characterization through various real-time algorithms. For these reasons, and to keep a manageable number of variables in this study we limit our simulations to the manipulation of real-time analyses that follow the standard pre-processing steps.

TOOLBOX AND PC

The entire simulation work was based on an in-house implementation with MATLAB (2010) of the tested algorithm based on the code of GIFT toolbox (Calhoun and Adali, 2006). Given the ICA algorithms code present in the toolbox, all the data analysis steps (presented in Materials and Methods section) were implemented in an automatic fashion to permit a testing routine to be run by varying parameters, techniques, *a priori* knowledge, and different subjects. The PC adopted to run the simulations was an Intel(R) Core(TM) i5 CPU M460 @ 2.53 GHz equipped with 6 GB of RAM and running a Windows 7 64-bit OS.

ICA MATHEMATICAL PRELIMINARIES

Since all the methods share a common core based on ICA principles, we briefly recall the main concept associated with the ICA. Let's assume that we have a set of fMRI measurements Y_i where $i = 1, \ldots, v$ is the index of voxels and each Y_i is a vector of y_{ij} elements, where $j = 1, \ldots, t$ is the index of time points. The entire dataset can thus be represented as a matrix Y of dimensions time points by voxels. Now, let's assume that the signal measured in the dataset is generated by a subset of n underlying sources which are linearly mixed and summed up. This reflects in the following canonical formulation using the vector-matrix notation.

$$Y = AX \tag{1}$$

where Y is the acquired data matrix of dimension equal to the number of time points by the number of voxels, A is the mixing matrix of dimension equal to the number of time points by the number of sources to be recovered and X is the matrix of the sources (i.e., ICs) of dimension the number of sources by the number of voxels. Each *jth* row of Y is a vector $y_{ji=1:v}$ representing

an fMRI volume in a *jth* time point and is thus obtained by the linear weighted combination of hidden sources spatial maps $y_j = a_{j1}x_1 + \ldots + a_{jn}x_n \forall_j$. This means

$$Y = \sum_{j=1}^{n} a_j x_j \tag{2}$$

Given this definition and assuming that the sources x_n are mutually independent, it is possible to recover those hidden sources by computing an estimation of the unmixing matrix $W = A^{-1}$ such that

$$X = WY \tag{3}$$

is an estimate of the sources. The estimation of W can be obtained via different algorithms, leading to different ICA implementations with different properties and effectiveness (see Bell and Sejnowski, 1995 for details). In this paper the selection of FastICA (Hyvrinen and Oja, 2000) as the core ICA algorithm has been driven by a recent study that compared the performance of 14 different ICA algorithms, and found FastICA to be amongst the most stable ones (Soldati et al., 2013). The FastICA algorithm exploits the non-Gaussianity as a metric of independence of the sources. This means, in the simplified iterative algorithm for several units, that the estimation of W is obtained through the following steps

1. initialize randomly W
2. given $W = \frac{W}{\sqrt{\|WW^T\|}}$
3. repeat until convergence $W = \frac{2}{3}W - \frac{1}{2}WW^TW$ and step 1–3.

Other approximations of the solution can be obtained, but a detailed description of the methods to obtain FastICA decomposition is anyway beyond the scope of the present paper.

ANALYSIS FRAMEWORK

The purpose of our analysis was to perform an extensive comparison between the standard off-line ICA analysis and several novel on-line ICA methods. The main goals of this study were to evaluate the feasibility of on-line ICA and identify the best performing algorithm from those proposed. For the purpose of our rt-fMRI simulations we proceeded with three different stages: calculation of reference ICs for performance evaluation, calculation of the target ICs from a functional localizer, and estimation of a dynamic IC on real-time. The first stage used FastICA on the complete fMRI time series to identify spatial and temporal IC templates from the networks that were later monitored dynamically. These templates were derived from the full dataset so they were in this sense considered as gold standard references against which the dynamically extracted components were later compared for spatial-temporal accuracy evaluations. The second and third stages were more strictly related to the rt-fMRI simulations. The second stage simulated a functional localizer (FL) session by taking the first 60 TRs of the fMRI time series. FastICA was used on the simulated FL to extract target ICs that was later monitored dynamically. The third stage represented the real-time fMRI simulation, the on-line ICA decomposition that used the information coming from the simulated FL. This last stage of real-time ICA decomposition was performed using the different novel techniques proposed and described in the next subsections.

The proposed framework for performing rt-fMRI used a multivariate and data-driven approach schematically presented in **Figure 1**. The general structure and workflow can be outlined as follows: (1) The MR data acquired by the scanner was stored during acquisition and made available to the data analysis system as soon as the images were reconstructed. (2) At the beginning of the experiment a short period (typically about 5 min or less) was devoted to acquire data from a FL. In the proposed framework the FL data was analyzed using a blind (unconstrained) ICA algorithm to preserve the multivariate data-driven advantages. Others used univariate methods at this stage (Esposito et al., 2003). (3) An IC of interest was selected from the FL analysis, this IC became the data-informed multivariate ROI whose activity was meant to be monitored dynamically. (4) The IC of interest, along with possible *a priori* information, could be incorporated in the rt-ICA data analysis algorithm. The ICA algorithm used a sliding window approach and a blind source extraction (BSE) perspective to deliver results at each TR while updating the best match to the target component. This monitored component or other *a priori* knowledge was then provided recursively to the algorithm, which extracted the actual version of the monitored IC updated by the actual values of data. (5) The monitored IC could be used as in classical rt-fMRI paradigms for visualization, neurofeedback, or brain computer interfaces. The component selected in real-time was the one that has a spatial map which maximally correlates with the reference spatial map component identified during the Functional Localizer (FL) step. The spatial FL component corresponds in turn to the FL component whose temporal correlation with the timing of the paradigm was highest.

In this study two main different approaches were investigated to dynamically extract in real-time a target IC: static methods based on Back-projection and dynamic methods based on iteratively performed ICA. In particular, for the dynamic methods, FastICA, and constrained ICA were updated for a sliding window real-time fMRI implementation. The size of the sliding window was fixed and it was chosen based on previous work that systematically evaluated the performance of multiple ICA algorithms as function of window length amongst other variables (Soldati et al., 2013). This study showed that the sliding window length that gave the optimal trade-off between computational speed and spatial/temporal correlation with the results from the whole time course was approximately equal to the period of the behavioral task to be monitored. In our experiment this could be approximated to around 30 s, i.e., 15 TRs. It is worth noting that the size of this window, as pointed out in the discussion, was strongly related to the period of the behavior to be monitored.

Template creation and accuracy estimation

To estimate the accuracy of one technique in correctly describing a monitored IC at one arbitrary time point we generated task related network templates which represented the principal spatial and temporal characteristics of the ICs to be monitored during the simulation. These templates of task related ICs were thus taken into account as reference data to evaluate the quality

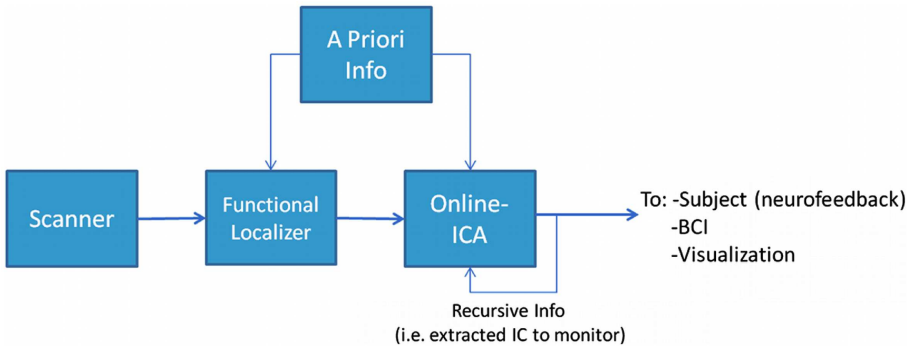

FIGURE 1 | The experimental design framework. In this structure it is possible to identify two main phases (or steps). The first step is to identify what to monitor, i.e., performing a Functional Localization. This can be done with or without incorporating some kind of *a priori* knowledge. The second step is to monitor the phenomenon we identified in the previous step using a suitable on-line analysis method.

of rt techniques. This evaluation was obtained via comparing the dynamically reconstructed ICs with these templates using temporal correlation and spatial overlap. To create the templates an ICA analysis was performed on the single subject level by considering all time points (i.e., 220 TR), but using FastICA with the same model order to be used in the on-line implementation (i.e., 5). Three different target ICs were manually selected to simulate their dynamic monitoring see **Figure 2**: two task related components (RVMT and LVMT) and the task-induced default mode network (DMN).

Functional localizer

In a rt-fMRI experiment the functional localizer could be used to identify the IC to be later dynamically monitored. For the analysis of the FL we considered the use of whole brain ICA to maintain a multivariate data-driven method. Previous simulations suggested that the ICA analysis of the FL data is most accurate when using algorithms such as evd, jadeopac, or FastICA (Soldati et al., 2013). We thus performed the FL applying the FastICA algorithm with a model order of 5, the same algorithm used in the template creation, to the first 60 TRs of the time series. With the application of FastICA as FL an unmixing matrix W was estimated of dimension 5 by number of time points. Each row of the matrix represented a time course of a hidden source, and the associated row of the X derived matrix represented the corresponding spatial map. The target IC to be monitored was then automatically selected as the one whose spatial map maximally correlated with the reference template and was monitored later dynamically with the on-line techniques. In this study three components were extracted from the FL for separate evaluations in the dynamic monitoring: the default mode network, the right, and left hemisphere visual motor networks activated by the cognitive task.

On-line techniques

In this section we present the main developed work, that is the methods implemented to perform the on-line monitoring of the sources. To simulate the on-line ICA analysis, coming after the FL, the rest of the time course (i.e., 220–60 TRs) was used to dynamically monitor the FL-derived target ICs using a sliding window approach. Given that the target was to properly exploit the *a priori* knowledge, different approaches to combine this knowledge and the ICA algorithms were developed. In a comprehensive perspective all the possible combinations were explored. Starting from the concept of sliding window ICA as it was presented by Esposito et al. (2003), more sophisticated and different methods were implemented. The target was to obtain an actual temporal value of the activation of interest and/or an actual spatial map of this component. Two main criteria were the guidelines in these implementations, that is the dynamic of the data and the type of *a priori* knowledge. The dynamic criterion means how much novel information is exploited and weighted into the on-line method, while the type of information exploited denote the nature of the *a priori* knowledge, i.e., temporal, spatial, or both. The implementation exploited state of the art ICA algorithms (FastICA, Constrained ICA) with the target of making the implementation easy to reply and distribute.

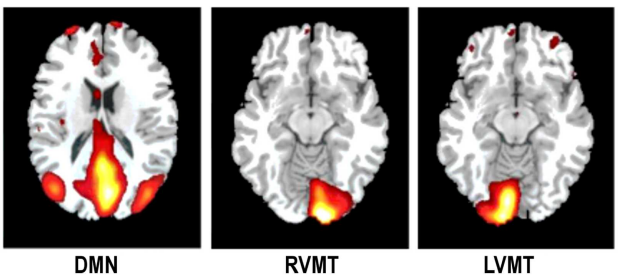

FIGURE 2 | The monitored ICs. An illustrative example of the monitored ICs is reported. Spatial maps of ICs considered in the simulation are obtained from Group ICA 20 ICs. For ease of visualization only the relevant slices are reported here. First column depicts Default Mode Network (DMN). Second and third columns depict the two task related ICs, Right Visuo-Motor Task (RVMT) and Left Visuo-Motor Task (LVMT).

The following subsections present the details of the different on-line monitoring techniques proposed.

Static method: back-projection. The basic assumption behind this static method was that the brain activation of interest maintains its basic characteristics, in particular its spatial map (SM),

relatively stable during the fMRI experiment. If this assumption holds, the spatial ICA performed in the FL step is enough to extract a precise representation of that spatial map that will be later tracked dynamically during the real-time experiment. ICA would be in fact able to create a space described by the directions of the extracted ICs that is fairly representative of the brain state during the performance of the task of interest. Given this assumption, the SM of an IC of interest obtained from the FL can be kept fixed and it should then be possible to simply back project each newly acquired volume of data into this space (i.e., onto the SM of the IC of interest) to be able to quantify the contribution of the new data to the brain activity of interest. This means that no ICA analysis must be performed in real-time, and the results will only depend on the ICA performed in the Functional Localizer session. This contribution will thus represent the time course of the IC. In more detail, the processing steps can be outlined as follows:

1. FastICA was used on the FL to estimate an unmixing matrix $W = A^{-1}$ and thus the associated SM of the sources $X_{nIC,v}$ with nIC equal to the number of extracted components (5 in this case) and v equal to the number of voxels.
2. The SM of the desired component was then chosen as the source whose associated time course was the most correlated to the task of the FL, that is we have $X_{nIC=sel,v}$. The chosen spatial map was therefore an independent component computed by the FastICA algorithm, which gives it unitary variance and null mean value characteristics.
3. At this point, for each newly acquired volume Y_{ith} of dimension one by number of voxels we could compute:

$$a_{ith} = Y_{ith} X^{\dagger}_{nIC=sel,v} \tag{4}$$

where a_{ith} is the actual single time value of the IC of interest and † denotes the pseudo-inverse. It is worth noting that this can be straightforwardly extended to cases in which multiple components are monitored simultaneously via parallelizing equation (4) for different SM or obtaining a meta-SM via combining different SM, i.e., X matrices.

Dynamic method: recursive temporally constrained. This algorithm is a direct extension of that used by Esposito et al. (2003). The main differences are that here it was applied to the whole brain and that the computation of *a priori* temporal knowledge was not model-driven, but it was rather data-driven and obtained with an approach based on the previously presented Back-projection method. The actual difference with the previously presented Back-projection method, in which the SM was static, was that we obtained an actual updated dynamic SM via iterative ICA computation. The details of the method are as follows:

1. From the FL a SM was obtained, which was used as in Back-projection method to obtain temporal *a priori* information in subsequent steps
2. During the experiment
   (a) using the Back-projection the time course of the brain activation was extracted
   (b) a FastICA algorithm with model order 5 and time window length 15 TR was applied to the data with a sliding window approach. The FastICA was temporally constrained using the *a priori* temporal constraint (obtained using the Back-projection) to initialize the mixing matrix A.

In practice a sliding window of dimension Δ was updated for each newly acquired volume n leading to a matrix $Y_{[n-\Delta,n],v}$ of dimension Δ by number of voxels. This matrix and the SM obtained in the FL step (i.e., $X_{nIC=sel,v}$) were used to extract a time course in a data-driven way in the same fashion as for the Back-projection algorithm, resulting in a time course a_n of dimension nTP by one. With the actual data matrix $Y_{[n-nTP,n+nTP],v}$ and the time course a_n it was then possible to apply FastICA to extract the actual SM of the component of interest. This was done by initializing the first entry of the W matrix with the inverse of a_n, given that $W = A^{-1}$, in the routine presented in the ICA mathematical preliminaries section. The result was the actual SM IC (i.e., *Xnew*) present in the data whose behavior was closest to the reference time course. In other words the extracted IC was constrained to be as close as possible to the reference one at the initial step, permitting a much more dynamic computation of the IC and thus update of the monitoring. In this approach the SM was dynamically updated each time a new volume was acquired.

Dynamic method: recursive spatially constrained. As in the previous method, also in this dynamic method, the on-line monitoring required a continuous update of the ICA decomposition matrix. There were two main differences with respect to the RTC method: (i) the ICA algorithm was a spatially constrained ICA (Lin et al., 2010), and (ii) the *a priori* knowledge was spatial instead of temporal. In this approach, the knowledge of an *a priori* SM of the IC of interest (obtained by the FL) permitted constraining the computation of the ICA algorithm. The constrained ICA algorithm was applied on time windows of data still of length 15 TR with a sliding window approach. The extracted IC, although based on newly acquired data, was forced to be spatially as close as possible to the spatial *a priori* given map (i.e., to the SM obtained during FL). This means that the dynamically extracted IC represented the SM of the brain activity of interest in the shape that was actually present in the novel data, thus dynamically updated. The associated time value was given by an approach similar to the Back-projection method but depending on the dynamically updated SM, i.e., given the new SM (i.e., *Xnew*), by computing $a_{ith} = Y_{ith} X^{\dagger}_{new}$.

Dynamic method: recursive spatio-temporal method. This algorithm implemented the possibility of obtaining actual dynamic values from both the time course and the spatial map with two concatenated steps. This was obtained by combining the previous methods to obtain a fully updated on-line method based on the following steps:

1. Back project the actual data on the SM of FL, obtaining the actual value of time course in the FL space $a_{FL} = Y_{ith} X^{\dagger}_{nIC=sel,v}$ (note that in the BP algorithm we assumed little or no difference between the template space and the actual subject space)

2. Apply the temporally constrained algorithm (i.e., initialize the W matrix exploiting the a_{FL}) to obtain the SM (i.e., X_{sub}) in the actual subject space (note that this is different from the FL space)
3. Apply the spatially constrained ICA with the SM in the actual subject space to obtain the actual time course value in the subject space, that is $a_{sub} = Y_{ith}X_{sub}^{\dagger}$.

Adopting the described steps it was thus possible to obtain temporal and spatial values of the brain activation of interest fully exploiting the actual data, thus adapting to the dynamic changes which could occur, but keeping as a target the characteristics defined in the FL session.

VARIABILITY EFFECTS FROM THE STOCHASTIC NATURE OF ICA

ICA methods (with some exceptions like the jade algorithm) are typically non-deterministic since there is a stochastic component in the analysis. This introduces variability each time the algorithm is run, which in turn can affect the computation time and the performance of the dynamic monitoring of a target IC. Such variability effects were investigated by repeating the analysis 10 times for each subject on the same data, and then computing the standard deviation across repeated trials for the mean correlation between dynamic and template spatial maps and temporal time course.

RESULTS

Using publicly available fMRI data from a previous experiment (Calhoun et al., 2001) we simulated a real-time acquisition in a sliding window approach to evaluate the performance of four implementations of ICA with different uses of *a priori* information: (i) Back-projection of constant spatial information derived from a functional localizer (BP), (ii) dynamic use of temporal (RTC), (iii) spatial (RSC), or (iv) spatio-temporal ICA constrained data (RSTC).

Given the stochastic nature of the ICA algorithms used, the variability of the spatial and temporal results was evaluated for each subject on each of the target networks (Default Mode Network (DMN), Right Visual Motor and Left Visual Motor Task related components (RVMT and LVMT respectively)) and for each of the four ICA implementations. The results showed in **Figure 3** point out that stochastic effects can introduce variability in the performance of the IC order ranking accuracy up to 10%, sometimes producing large fluctuations. This behavior suggested that none of the four ICA implementations gave consistently the lowest sensitivity to fluctuations due to stochastic effects, although the BP method tended to be the lowest in 15 out of 18 cases.

Proceeding with further analysis it was possible to focus on the evaluation of stability of results across subjects and across different monitored ICs, as presented in **Figure 4**. This figure reports the standard deviation across subjects of the mean (across trials, for each subject) spatial and temporal correlation for the monitored ICs.

Finally the performance evaluation numbers were reported in **Figure 5** and **Table 1**, in which one can see the spatial and temporal correlation between the reconstructed time courses and spatial maps of the monitored ICs and the reference templates of those ICs.

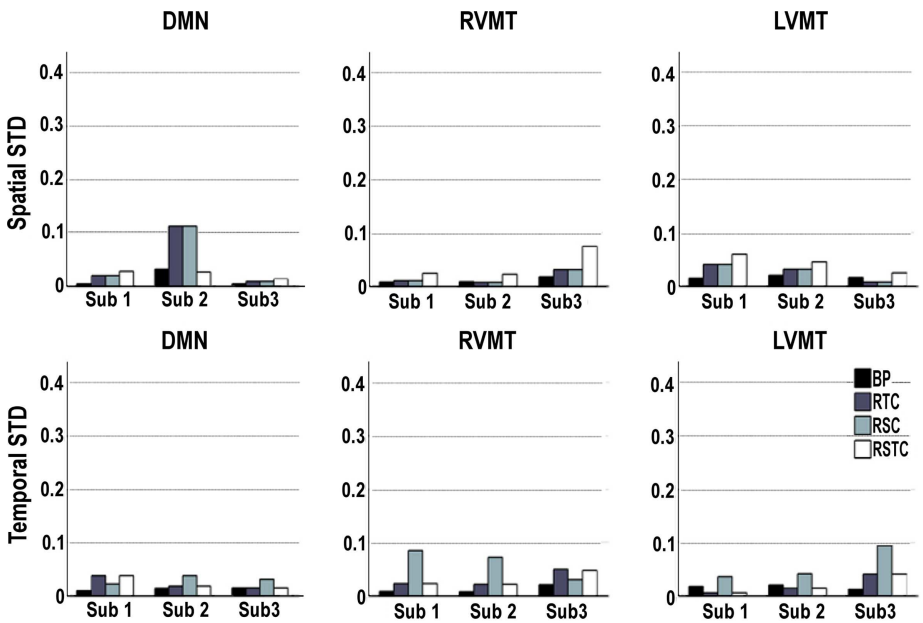

FIGURE 3 | Variability of dynamic tracking performance results due to the stochastic nature of ICA. Performance is here represented by two metrics: spatial or temporal correlation between the template and the dynamically tracked IC, averaged along the time course. The calculations were repeated 10 times for each subject, for each of the three networks evaluated (default mode or DMN, right visual motor or RVMT, and left visual motor or LVMT), and for each ICA implementation (Back-projection or BP, temporally constrained or TC, spatially constrained or SC, spatio-temporal constrained or STC). The variability of the dynamic tracking performance results is expressed as the standard deviation across trials, per subject, brain network, and ICA implementation.

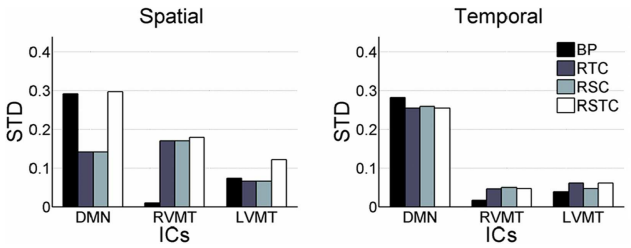

FIGURE 4 | Variability of dynamic tracking performance results due to subjects. Similar to **Figure 2**, but here mean results across trials are used to compute variability across subjects, expressed as standard deviation. The subject variability is shown for each of the three networks evaluated (default mode or DMN, right visual motor or RVMT, and left visual motor or LVMT) and for each of the four ICA implementations (Back-projection or BP, temporally constrained or TC, spatially constrained or SC, spatio-temporal constrained or STC).

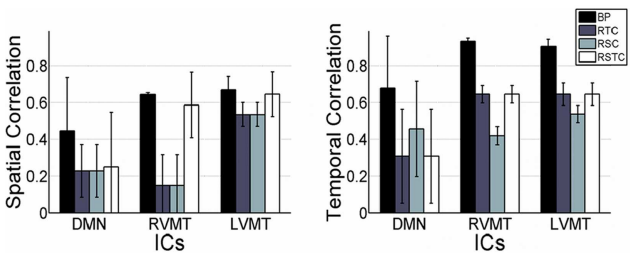

FIGURE 5 | Overall dynamic tracking performance in reconstructing ICs. The mean and standard deviation performance results are shown across subjects and trials in terms of both spatial and temporal correlation with the template ICs. The results are shown for each of the three networks evaluated (default mode or DMN, right visual motor or RVMT, and left visual motor or LVMT) and for each of the four ICA implementations (Back-projection or BP, temporally constrained or RTC, spatially constrained or RSC, and spatio-temporal constrained or RSTC).

The table reports the performances in terms of computational time necessary to update the actual value of time course or spatial maps for each new available data volume. This represents another critical issue of a real-time analysis.

The results show that the Back-projection method offered the highest performance both in terms of time course reconstruction (correlation value to the template time course was significant and quite high, around 0.9), and speed (computation of update value was far below the TR). This method was very fast and effective as long as the monitored IC had a strong and well defined behavior and/or it was well extracted in the FL, since it relied on an accurate description of the spatial behavior. The fluctuation reported in the figures represents error fluctuations in the FL phase which directly reflect in the Back-projection method. The dynamic methods offered comparable performances at cost of higher computational time (CT) (around 2 s for RTC). In particular the spatio-temporal method performed comparably in terms of CT to Back-projection, offering more variable performances in terms of reconstruction of spatial maps and time courses.

Table 1 | Performance.

On-line method	CT[s]		
	DMN	RVMT	LVMT
Back-projection	0.0056 (0.0002)	0.0054 (0.0004)	0.0054 (0.0007)
Temporally constrained	2.3 (0.4)	2.1 (0.1)	2.0 (0.3)
Spatially constrained	0.119 (0.003)	0.1167 (0.0002)	0.1169 (0.0003)
Spatio-temporally constrained	0.123 (0.003)	0.1207 (0.0002)	0.1208 (0.0002)

This table summarizes the performance results in terms of computational time (CT) from all the investigated rt-ICA techniques relative to the different monitored ICs. Mean values of updating CT are reported for simulations on three subjects and ten trials per subject. Standard deviations associated to mean values across subjects and trials are shown in parenthesis. The selected ICs to monitor were default mode network (DMN), right visuo-motor task (RVMT), and left visuo-motor task (LVMT).

DISCUSSION

In the present work we presented and evaluated different methods to combine ICA-based algorithms for real-time fMRI. The motivation for this work was to investigate how the advantages of such multivariate data-driven based methods can be adapted to real-time fMRI applications, extending previous work (Esposito et al., 2003). One goal of this work was to simulate a realistic scenario fully based on ICA consisting of two essential steps. The first step was dedicated to identifying brain networks of interest from the ICA of a functional localizer. The second step consisted in dynamically monitoring a target IC (derived from the first step) with the use of different types of *a priori* knowledge in the computations. The *a priori* information considered ranged from static to dynamic, where spatial maps and time courses can be updated separately or together to give more weight to the dynamic monitoring of data within a pre-established time window in the fMRI time course. The incorporation of *a priori* information was motivated to address the challenge of identifying and keeping track of a specific IC of interest, despite all the other ICs that might be present in the data. This work therefore focused on evaluating different ways of using prior information about the target IC to monitor such that during the dynamic monitoring phase the target IC could be effectively detected with higher priority relatively to other possible ICs.

The ICA-based techniques presented for the on-line monitoring were characterized by different advantages and disadvantages. Overall findings confirmed two general expected features: (i) the dynamic monitoring performance was directly related to the strength of activation of the target IC identified in the functional localizer, stressing the importance of this first step, and (ii) as algorithms became more adaptive in the use of spatial and/or temporal priors in the dynamic monitoring, they introduced less stability in the performance results compared to off-line results. This reflected the intrinsic differences between static off-line analysis and dynamic one.

Back-projection is the only method presented for which the ICA is computed only once in the FL session, and not updated

later during the on-line monitoring. This means that this method as implemented here is based on ICA since it depends on the quality of ICA performed in the FL session, but it is not a fundamentally ICA method. Back-projection could in principle also be used by defining a target brain network from the functional localizer with a standard general linear model that makes assumptions on the hemodynamic responses. The use of ICA, however, allowed the analysis to be fully data-driven (Esposito et al., 2003; Beckmann and Smith, 2004; Norman et al., 2006; Calhoun et al., 2009; Magland et al., 2011; Sitaram et al., 2011) and this represents an advantage in all those experimental designs where the classical ICA showed to be robust, as in all cases lacking a defined regressor. The Back-projection technique had the positive features of being stable in terms of lowest fluctuation across trial and subjects, very fast relative to the TR of fMRI data acquisition (since it just involves a matrix multiplication), conceptually simple, and being able to monitor more than one IC of interest. The main potential disadvantage of the Back-projection method was related to its non-adaptivity, since it assumed that the target IC of interest was always present with the same properties, i.e., a fixed spatial map was considered.

The temporally constrained ICA was more adaptive to data with respect to Back-projection. Even if similar to what was presented by Esposito et al. (2003) this method offered different characteristics. The main one was that the reference time course used as constraint was not obtained using a hemodynamic model, but it was extracted from the data in a multivariate data-driven way by the FL. Moreover in this method the reference time course was updated in a similar way to Back-projection, while the crucial difference was that the spatial map updates iteratively each time new data become available. A characteristic of the temporally constrained ICA was that the dynamic spatial map generated was derived from the time course used to initialize the ICA algorithm. This time course, being derived from the Back-projection of actual data on a static space (i.e., keeping the spatial map of the IC of interest fixed), was strictly related to the quality of the FL. For this reason the time course reconstructed was in the template space (i.e., FL space), while the spatial map was in the subject space, being obtained by exploiting the reconstructed time course as *a priori* knowledge during the application of the ICA algorithm. A limitation of the temporally constrained algorithm was that its mean computation time was more than one order of magnitude higher relative to all the other methods tested. This is due to the fact that the FastICA algorithm adopted in it, while performing generally lower than a TR, sometimes (around 2–3% of the times) got stuck in a local minimum thus increasing the time to perform the decomposition (in some cases from 1.5 upto 8 s). A possible solution to this would be to skip the updating of the information for those volumes which exceed a pre-determined temporal limit to update.

The spatially constrained ICA assumed a fixed spatial map of the IC of interest. This approach suffered from the small amount of data available for the decomposition. The main advantages included low computational time and low variability of the results, qualities that make it a good candidate for use in real-time experiments.

The combined implementation of spatial and temporal constrained ICA permitted a better description of the actual dynamic behavior of data, thus focusing on data characteristics which were strongly transient and for this reason probably not modeled in the off-line static analysis, which privileged extraction of static periodic or quasi-periodic behaviors. This method enabled us to obtain valuable results both in terms of accuracy and computational time. Its main disadvantage was that it was less able to characterize static aspects of the data.

A further consideration is needed related to the variability of monitoring performance. Three kinds of variability were investigated in the simulations. The first one was due to the stochastic nature of principal ICA algorithms, which caused different results to be obtained in different runs of the algorithm on the same data. Multiple repetitions of the analysis showed that this variability can affect computation time, but the obtained performance had a stability better than 10%. The second kind of variability identified was subject specific which caused about 20% of the variability. The third source of variability in the dynamic performance monitoring related to the specific target IC within a subject. Across different monitored ICs within the same subject, the results of **Table 1** and **Figure 2** confirm that the difference in behavior of different subjects was consistent across ICs. Indeed the performance improved for all the subjects when monitoring task related RVMT and LVMT (**Figure 1**) with respect to Resting State Network (RSN) related Default Mode Network (DMN) (**Figure 2**) thus proving that difference in the nature of monitored IC was the strongest source of variability (up to 30%) for these kind of presented methods. This may be due to the fact that different activations have particular statistical distribution properties, being more or less suitable to be extracted by ICA algorithms. In addition, a reason for the difficulty in extracting spatial characterization of the DMN is its low frequency relative to the sliding time window length, thus making it difficult for the algorithm to correctly follow it.

This work has some limitations. One limitation is related to the definition of dynamic monitoring performance, which depends on temporal or spatial correlations with a template reference derived from the whole time course. It is not necessarily correct to expect that spatial-temporal characteristics derived from the sliding window along the time course should match the ones derived from the whole time course. For this reason the performance measures are only indicative.

The possibility that the actual dynamic brain activation is correctly identified by these on-line methods opens the door to future definition of techniques and experiments. These experiments could exploit these methods to have a confirmation of transient activation identification independently of the off-line analysis, which represents a general reference for evaluation of results, but may also represent a bias.

Another limitation relates to the simulation nature of the work, which should be further evaluated on a real implementation in which the performance of the different methods can be studied, for example using a neurofeedback setup.

The comparison of ICA with non-ICA approaches in rt-fMRI setups was beyond the scope of this study. Given the known

potential advantages of data-driven analysis (Norman et al., 2006; Magland et al., 2011; Sitaram et al., 2011), and in particular ICA methods (Esposito et al., 2003; Beckmann and Smith, 2004; Calhoun et al., 2009), this simulation study is limited to the comparison of novel ICA-based methods for rt-fMRI using robust activation in well-known visual motor areas. Future studies will be needed to evaluate these ICA methods with brain activation that could be more challenging to identify.

This work proposed and evaluated several strategies for using *a priori* information for the monitoring of brain networks in real-time fMRI experiments. The performance of the methods was characterized by both computation speed and correlation between the spatial-temporal properties of a target independent component derived dynamically and a reference component. The method that gave the highest performance was based on the Back-projection of a constant target spatial map derived by the spatial localizer. In this method the use of ICA was exploited only in the Functional Localizer phase, while during the on-line monitoring the reference component was kept constant and not updated with any ICA algorithm. This combination of both ICA and non-ICA methods shows thus to be very helpful and promising. This method had the limitation that its reference was constant and this means that it may not be optimal to follow dynamic changes as it cannot adapt to changes in brain. The other tested methods were based on the use of adaptive spatial, temporal, or spatial-temporal priors and may have useful applications in studies where there is a need of higher flexibility to monitor variable activation.

CONCLUSION

This study proposed and evaluated several strategies for using spatial and/or temporal *a priori* information in ICA-based methods for the monitoring of brain networks in real-time fMRI experiments. The effectiveness of the novel real-time ICA-based method was evaluated against the off-line ICA analysis that is typically possible after all data has been acquired. The performance of the methods was characterized by both computation speed and correlation between the spatial-temporal properties of a target independent component derived dynamically and a reference component. In our testing conditions of relative low frequency task-induced activations (with a period of 20 s) we found that the Back-projection method outperformed the other methods giving the highest spatial-temporal correlations to the reference and the fastest computation time. The Back-projection method here investigated uses the ICA decomposition only in the functional localizer data, and not during the dynamic on-line analysis. It remains to be further investigated whether the spatial-temporal constrained methods can be better, as in principle expected, in situations where the networks to be monitored have higher frequency fluctuations in space and time.

ACKNOWLEDGMENTS

This work has been realized thanks to the support from the Provincia autonoma di Trento and the Fondazione Cassa di Risparmio di Trento e Rovereto, Italy. Jorge Jovicich was supported by a PRIN grant (Prot. 2008HETS3W _002) from MIUR (Italy). The authors would also like to specially thank James Hartzell.

REFERENCES

Anderson, A., Han, D., Douglas. P. K., Bramen, J., and Cohen, M. S. (2011). "Real-time functional MRI classification of brain states using markov-svm hybrid models: peering inside the rt-fMRI black box," in *MLINI. Machine Learning and Interpretation in Neuroimaging – International Workshop, MLINI 2011, Held at NIPS 2011*. Lecture Notes in Computer Science, Vol. 7263, eds G. Langs, I. Rish, M. Grosse-Wentrup, and B. Murphy (Sierra Nevada: Springer), 242–255. [December 16–17, 2011; Revised Selected and Invited Contributions].

Beckmann, C. F., and Smith, S. M. (2004). Probabilistic independent component analysis for functional magnetic resonance imaging. *IEEE Trans. Med. Imaging* 23, 137–152.

Bell, A. J., and Sejnowski, T. J. (1995). An information-maximization approach to blind separation and blind deconvolution. *Neural Comput.* 7, 1129–1159.

Calhoun, V., and Adali, T. (2006). Unmixing fMRI with independent component analysis. *IEEE Eng. Med. Biol. Mag.* 25, 79–90.

Calhoun, V. D., Adali, T., Pearlson, G. D., and Pekar, J. J. (2001). Spatial and temporal independent component analysis of functional MRI data containing a pair of task-related waveforms. *Hum. Brain Mapp.* 13, 43–53.

Calhoun, V. D., Eichele, T., and Pearlson, G. (2009). Functional brain networks in schizophrenia: a review. *Front. Hum. Neurosci.* 3:17. doi:10.3389/neuro.09.017.2009

Caria, A., Sitaram, R., and Birbaumer, N. (2012). Real-time fMRI: a tool for local brain regulation. *Neuroscientist* 18, 487–501.

Chiu, P., Lisinski, J., King-Casas, B., Sharp, J., Eagleman, D., Versace, F., et al. (2010). Modulating "crave" and "don't crave" brain states with real-time fMRI neurofeedback in smokers. *Paper Presented at the 16th Annual Meeting of the Organization for Human Brain Mapping*, Barcelona.

Cox, R. W., Jesmanowicz, A., and Hyde, J. S. (1995). Real-time functional magnetic resonance imaging. *Magn. Reson. Med.* 33, 230–236.

deCharms, R. C. (2008). Applications of real-time fMRI. *Nat. Rev. Neurosci.* 9, 720–729.

deCharms, R. C., Maeda, F., Glover, G. H., Ludlow, D., Pauly, J. M., Soneji, D., et al. (2005). Control over brain activation and pain learned by using real-time functional MRI. *Proc. Natl. Acad. Sci. U.S.A.* 102, 18626–18631.

DeMartino, F., Gentile, F., Esposito, F., Balsi, M., Salle, F. D., Goebel, R., et al. (2007). Classification of fMRI independent components using IC-fingerprints and support vector machine classifiers. *Neuroimage* 34, 177–194.

Esposito, F., Seifritz, E., Formisano, E., Morrone, R., Scarabino, T., Tedeschi, G., et al. (2003). Real-time independent component analysis of fMRI time-series. *Neuroimage* 20, 2209–2224.

Gembris, D., Taylor, J. G., Schor, S., Frings, W., Suter, D., and Posse, S. (2000). Functional magnetic resonance imaging in real time (fire): sliding-window correlation analysis and reference-vector optimization. *Magn. Reson. Med.* 43, 259–268.

Goebel, R. (2012). Brainvoyager – past, present, future. *Neuroimage* 62, 748–756.

Himberg, J., Hyvrinen, A., and Esposito, F. (2004). Validating the independent components of neuroimaging time series via clustering and visualization. *Neuroimage* 22, 1214–1222.

Hinds, O., Ghosh, S., Thompson, T. W., Yoo, J. J., Whitfield-Gabrieli, S., Triantafyllou, C., et al. (2011). Computing moment-to-moment bold activation for real-time neurofeedback. *Neuroimage* 54, 361–368.

Hyvrinen, A., and Oja, E. (2000). Independent component analysis: algorithms and applications. *Neural Netw.* 13, 411–430.

LaConte, S. M. (2011). Decoding fMRI brain states in real-time. *Neuroimage* 56, 440–454.

LaConte, S. M., Peltier, S. J., and Hu, X. P. (2007). Real-time fMRI using brain-state classification. *Hum. Brain Mapp.* 28, 1033–1044.

Lin, Q. H., Liu, J., Zheng, Y. R., Liang, H., and Calhoun, V. D. (2010). Semiblind spatial ICA of fMRI using spatial constraints. *Hum. Brain Mapp.* 31, 1076–1088.

Maclaren, J., Herbst, M., Speck, O., and Zaitsev, M. (2013). Prospective motion correction in brain imaging: a review. *Mag. Reson. Med.* 69, 621–636.

Magland, J. F., Tjoa, C. W., and Childress, A. R. (2011). Spatio-temporal activity in real time (star): optimization of regional fMRI feedback. *Neuroimage* 55, 1044–1053.

MATLAB. (2010). *Version 7.10.0 (R2010a)*. Natick, MA: The MathWorks Inc.

McKeown, M. J., Makeig, S., Brown, G. G., Jung, T. P., Kindermann, S. S., Bell, A. J., et al. (1998). Analysis of fMRI data by blind separation into independent spatial components. *Hum. Brain Mapp.* 6, 160–188.

Mouro-Miranda, J., Bokde, A. L. W., Born, C., Hampel, H., and Stetter, M. (2005). Classifying brain states and determining the discriminating activation patterns: support vector machine on functional MRI data. *Neuroimage* 28, 980–995.

Norman, K. A., Polyn, S. M., Detre, G. J., and Haxby, J. V. (2006). Beyond mind-reading: multi-voxel pattern analysis of fMRI data. *Trends Cogn. Sci. (Regul. Ed.)* 10, 424–430.

Posse, S., Fitzgerald, D., Gao, K., Habel, U., Rosenberg, D., Moore, G. J., et al. (2003). Real-time fMRI of temporolimbic regions detects amygdala activation during single-trial self-induced sadness. *Neuroimage* 18, 760–768.

Shibata, K., Watanabe, T., Sasaki, Y., and Kawato, M. (2011). Perceptual learning incepted by decoded fMRI neurofeedback without stimulus presentation. *Science* 334, 1413–1415.

Sitaram, R., Lee, S., Ruiz, S., Rana, M., Veit, R., and Birbaumer, N. (2011). Real-time support vector classification and feedback of multiple emotional brain states. *Neuroimage* 56, 753–765.

Soldati, N., Calhoun, V. D., Bruzzone, L., and Jovicich, J. (2013). ICA analysis of fMRI with real-time constraints: an evaluation of fast detection performance as function of algorithms, parameters and a priori conditions. *Front. Hum. Neurosci.* 7:19. doi:10.3389/fnhum.2013.00019

Thompson, T., Hinds, O., Ghosh, S., Lala, N., and Triantafyllou, C. (2009). Training selective auditory attention with real-time fMRI feedback. *Neuroimage* 47, S65.

Weiskopf, N. (2012). Real-time fMRI and its application to neurofeedback. *NeuroImage* 62, 682–692.

Weiskopf, N., Scharnowski, F., Veit, R., Goebel, R., Birbaumer, N., and Mathiak, K. (2004). Self-regulation of local brain activity using real-time functional magnetic resonance imaging (fMRI). *J. Physiol. Paris* 98, 357–373.

Weiskopf, N., Sitaram, R., Josephs, O., Veit, R., Scharnowski, F., Goebel, R., et al. (2007). Real-time functional magnetic resonance imaging: methods and applications. *Magn. Reson. Imaging* 25, 989–1003.

Conflict of Interest Statement: The authors declare that the research was conducted in the absence of any commercial or financial relationships that could be construed as a potential conflict of interest.

Received: 05 October 2012; accepted: 18 February 2013; published online: 11 March 2013.

Citation: Soldati N, Calhoun VD, Bruzzone L and Jovicich J (2013) The use of a priori information in ICA-based techniques for real-time fMRI: an evaluation of static/dynamic and spatial/temporal characteristics. Front. Hum. Neurosci. 7:64. doi: 10.3389/fnhum.2013.00064

frontiers in
HUMAN NEUROSCIENCE

ORIGINAL RESEARCH ARTICLE
published: 06 November 2012
doi: 10.3389/fnhum.2012.00301

Fully exploratory network independent component analysis of the 1000 functional connectomes database

Klaudius Kalcher[1,2]*†, Wolfgang Huf[1,2,3†], Roland N. Boubela[1,2], Peter Filzmoser[2], Lukas Pezawas[3], Bharat Biswal[4], Siegfried Kasper[3], Ewald Moser[1] and Christian Windischberger[1]*

[1] MR Centre of Excellence, Center for Medical Physics and Biomedical Engineering, Medical University of Vienna, Vienna, Austria
[2] Department of Statistics and Probability Theory, Vienna University of Technology, Vienna, Austria
[3] Department of Psychiatry and Psychotherapy, Medical University of Vienna, Vienna, Austria
[4] Department of Radiology, University of Medicine and Dentistry of New Jersey, New Jersey Medical School, Newark, NJ, USA

Edited by:
Simon Daniel Robinson, Medical University of Vienna, Austria

Reviewed by:
Lars Nyberg, Umeå University, Sweden
Tom Eichele, University of Bergen, Norway

***Correspondence:**
Klaudius Kalcher and Christian Windischberger, MR Centre of Excellence, Center for Medical Physics and Biomedical Engineering, Medical University of Vienna, Währinger Gürtel 18-20, 1090 Vienna, Austria.
e-mail: klaudius.kalcher@meduniwien.ac.at; christian.windischberger@meduniwien.ac.at

† These authors have equally contributed to this work.

The 1000 Functional Connectomes Project is a collection of resting-state fMRI datasets from more than 1000 subjects acquired in more than 30 independent studies from around the globe. This large, heterogeneous sample of resting-state data offers the unique opportunity to study the consistencies of resting-state networks at both subject and study level. In extension to the seminal paper by Biswal et al. (2010), where a repeated temporal concatenation group independent component analysis (ICA) approach on reduced subsets (using 20 as a pre-specified number of components) was used due to computational resource limitations, we herein apply Fully Exploratory Network ICA (FENICA) to 1000 single-subject independent component analyses. This, along with the possibility of using datasets of different lengths without truncation, enabled us to benefit from the full dataset available, thereby obtaining 16 networks consistent over the whole group of 1000 subjects. Furthermore, we demonstrated that the most consistent among these networks at both subject and study level matched networks most often reported in the literature, and found additional components emerging in prefrontal and parietal areas. Finally, we identified the influence of scan duration on the number of components as a source of heterogeneity between studies.

Keywords: magnetic resonance imaging, fMRI, resting-state, ICA, default-mode network

INTRODUCTION

Since the seminal report by Biswal et al. (1995), low-frequency spontaneous fluctuations (in the range of 0.01–0.1 Hz) of blood oxygen level dependent (BOLD) signal in the brain have consistently been found in the absence of task-induced activity. Research in this area has increasingly gained momentum during the last years, from both a methodological perspective (Margulies et al., 2010) and a neuroscientific point of view (Raichle and Snyder, 2007). Even beyond the original finding of the motor network by Biswal et al. (1995), an increasing number of other networks have consistently been reported, and these are now referred to as resting state networks (Fox and Raichle, 2007). Most commonly, networks related to motor function, visual processing, executive function, auditory processing, memory, as well as the default-mode network have been named in this context (Damoiseaux et al., 2006; Robinson et al., 2009; Schöpf et al., 2010). However, variability in the exact extent of networks reported as well as the total number of resting-state networks and their possible subdivisions still exist today (Leech et al., 2011), and a quantification of variability of number and type of resting-state networks identified in the data of different centers has not yet been performed.

In the most general terms, the concept of brain networks is based on the measure of functional connectivity, defined as temporal coherence between the low-frequency (< 0.1 Hz) BOLD signal of spatially remote brain regions (Richiardi et al., 2011). This functional connectivity is commonly calculated using a seed-based analysis approach, where temporal correlation is calculated with respect to a seed voxel or region. Consequently, a clear-cut distinction of the networks is limited by the fact that a single brain region can be involved in several networks (Joel et al., 2011), e.g., the lateral parts of the parietal lobes that are associated with both the default-mode network and the frontoparietal (working memory) network (Corbetta and Shulman, 2002). Additionally, the detection of previously unknown networks and the identification of unexpected properties are hampered by the inherent necessity for *a priori* selection of seed regions rendering seed-based functional connectivity an inherently parametric approach.

Non-parametric methods have been used to overcome this limitation, among them clustering and pattern-recognition algorithms, but it is independent component analysis (ICA)—or, more specifically, spatial ICA, as opposed to temporal ICA—that has emerged as the most successful method to identify spatially independent brain networks, as witnessed by a large number of influential studies (Damoiseaux et al., 2006; Smith et al., 2009; Biswal et al., 2010; Allen et al., 2011). The capability of ICA to identify neuroscientifically meaningful effects is corroborated by the similarity of results from ICA of resting state fMRI data and from ICA of electrophysiology data acquired using magnetoencephalography (MEG) (Brookes et al., 2011). In contrast

to seed-based analysis, though, ICA offers no canonical method for group comparison, and multiple solutions have been put forward to address this question, including, among others, time-concatenated ICA (Calhoun et al., 2001), i.e., time concatenation of individual-subject time series before ICA analysis, tensor-based ICA, tensor-based probabilistic ICA (Damoiseaux et al., 2006), probabilistic ICA (PICA) (Luca et al., 2006), and self-organizing group ICA (sogICA) (van de Ven et al., 2008). Earlier studies relying on these methods have found varying numbers of independent components based on automated dimension estimation, ranging from 5 (Luca et al., 2006) to about 12 (Damoiseaux et al., 2006; Robinson et al., 2009), while more recently, the use of a prespecified number of components has become more widespread, using either a low model order with about 20 components (Smith et al., 2009; Biswal et al., 2010) or a high model order with about 75 components (Allen et al., 2011), different choices of model order of course leading to the identification of different networks or subdivisions of networks.

The variability of results depending on model order has been investigated by Abou-Elseoud et al. (2010), who found that low model order ICA results had highest repeatability, while higher model orders lead to the identification of finer subdivisions of the networks, up to a model order of about 100—beyond that value, repeatability only declined without any additional benefits. Model order is not the only source of variability in the results of ICA studies, though. A certain amount of inconsistency between studies is due to random variability between samples, which, due to practical limitations, often comprise only 20–30 subjects. Finally, some divergence between results can be attributed to methodological issues: for once, there is the inherent stochasticity of the fastICA algorithm, the basis for most ICA implementations currently employed (Himberg et al., 2004) and additional variability may be introduced by the heterogeneity of preprocessing strategies (Weissenbacher et al., 2009).

Evaluation of between-subject variability of group components can be undertaken from two directions. Back reconstruction algorithms (Biswal et al., 2010; Allen et al., 2011, 2012) start with group components and evaluate how consistent the connectivity of these group components is on the single-subject level. In this study, we opted for the opposite direction—starting with individual-subject components and evaluating the variability of components between subjects—and chose fully exploratory network ICA (FENICA), proposed by Schöpf et al. (2010), as a means for combining single-subject results at group level. FENICA is a group ICA method that, based on single-subject ICA, calculates each group component as the mean of the most similar components, one of each individual-subject ICA. This in turn allows for the group components to be directly related to single-subject ICA components and thus to gain a more immediate view on the differences of ICA components across subjects. In addition, the averaging of components from multiple ICA runs in FENICA helps to increase stability of group results and limits the effects of the stochasticity of fastICA (Himberg et al., 2004), though some caution in this respect is still advisable when interpreting individual single-subject components.

It must be noted, though, that the heterogeneity of populations investigated by different studies leads to inter-study variability near-impossible to overcome within the scope of a single study. A comprehensive exploratory analysis should therefore neither take into account only a single population nor a single setup of scanner hardware but rather combine a large number of different datasets from different studies. A meta-analytic approach using individual-subject data therefore seems most promising to summarize available evidence about resting-state networks and to assess heterogeneity between datasets of different origin (Huf et al., 2011). The 1000 Functional Connectomes Project (Biswal et al., 2010), a collection of resting-state fMRI datasets from over 30 international centers encompassing more than 1000 different subjects, provided us with the opportunity to perform precisely this kind of analysis on a suitably broad basis for approaching the question of consistent networks on a large scale.

METHODS

The entirety of the dataset of the 1000 Functional Connectomes Project (Biswal et al., 2010) directly available at its webpage was downloaded (see http://www.nitrc.org/projects/fcon_1000). To avoid the most important sources of heterogeneity as well as complications due to non-independence, subjects with more than one run in the dataset were excluded from the analysis. The final sample consisted of 1000 subjects (age 28 ± 13, 561 females; see **Table 1**) randomly sampled from the remainder of the dataset consisting of 33 independent samples originating from 26 centers in North America (15), Europe (8), Asia (2), and Australia (1). The original scans were performed using echo planar imaging (EPI) during resting-state with variable scanning parameters and brain coverage at 1.5 T, 3 T, and 4 T, with a duration between 216 and 590 s.

Due to the *post-hoc* nature of the 1000 Functional Connectomes dataset's formation by merging independent, non-coordinated individual studies, between-study heterogeneity is an important issue to clarify before analyzing this dataset. The original analysis by Biswal et al. (2010) has, as one of its main results, established the feasibility of using the dataset as a whole with a reasonable expectation to obtain homogeneous results, even for studies using scanners with different magnetic field strength. Further attempts to include estimated study quality, e.g., for weighting purposes, are discouraged in the meta-analytic setting due to possible bias introduced by such procedures (Huf et al., 2011), and are thus not part of our analysis.

Preprocessing of the resting-state fMRI data was performed according to Weissenbacher et al. (2009) by first applying motion correction and spatial smoothing using an 8 mm FWHM Gaussian kernel followed by correction for mean cerebro-spinal fluid (CSF), white matter (WM) and gray matter signals as well as motion parameters. Subsequently, time series were filtered using a bandpass of the interval 0.01–0.1 Hz, and ICA was calculated on the resulting time series using FSL MELODIC (Smith et al., 2004) with the dimension estimation criterion LAP, yielding a number of components in the range of typical low model order studies. Automated model order estimation rather than fixed model order was chosen to allow for a comparison of model order estimates between subjects and between the datasets of the individual studies, as well as for an estimation of the variability of these

Table 1 | Demographic statistics of the sample analyzed.

	Study	N	% Male	Mean age	SD age	Voxel size	TR	Volumes	Duration	Components
1	AnnArbor_a	25	88.0	21.0	7.4	35.4	1.00	295	295.0	17
2	AnnArbor_b	36	47.2	NA	NA	37.8	1.00	395	395.0	19
3	Atlanta	28	46.4	30.9	9.9	47.3	2.02	205	414.1	16
4	Baltimore	23	34.8	29.3	5.5	21.3	2.50	123	307.5	15
5	Bangor	20	100.0	23.4	5.3	27.0	2.00	265	530.0	20
6	Beijing	198	38.4	21.2	1.8	35.2	2.00	225	450.0	17
7	Berlin	26	50.0	29.8	5.2	36.0	2.30	195	448.5	19
8	Cambridge	198	37.9	21.0	2.3	27.0	3.00	119	357.0	17
9	Cleveland	31	35.5	43.5	11.1	16.0	2.80	127	355.6	17
10	Dallas	24	50.0	42.6	20.1	47.3	2.00	115	230.0	13
11	ICBM	86	47.7	44.2	17.9	27.0	2.00	192	384.0	12
12	Leiden_2180	12	100.0	23.0	2.5	40.7	2.18	215	468.7	19
13	Leiden_2200	19	57.9	21.7	2.6	40.7	2.20	215	473.0	19
14	Leipzig	37	43.2	26.2	5.0	36.0	2.30	195	448.5	20
15	Milwaukee_a	18	NA	NA	NA	84.4	2.00	175	350.0	22
16	Milwaukee_b	46	32.6	53.6	5.8	56.2	2.00	175	350.0	16
17	Munchen	16	62.5	68.4	4.0	43.0	3.00	72	216.0	11
18	Newark	19	47.4	24.1	3.9	59.1	2.00	135	270.0	14
19	NewHaven_a	19	52.6	31.0	10.3	70.9	1.00	249	249.0	13
20	NewHaven_b	16	50.0	26.9	6.3	65.0	1.50	181	271.5	18
21	NewYork_a	25	80.0	35.0	9.6	27.0	2.00	192	384.0	13
22	NewYork_a	84	51.2	24.4	10.1	27.0	2.00	192	384.0	13
23	NewYork_b	20	40.0	29.8	9.9	36.0	2.00	175	350.0	13
24	Ontario	9	NA	NA	NA	64.0	3.00	105	315.0	15
25	Orangeburg	20	75.0	40.6	11.0	61.2	2.00	165	330.0	12
26	Oulu	103	35.9	21.5	0.6	70.4	1.80	245	441.0	15
27	Oxford	22	54.5	29.0	3.8	31.5	2.00	175	350.0	17
28	PaloAlto	17	11.8	32.5	8.1	57.9	2.00	235	470.0	20
29	Pittsburgh	17	58.8	37.9	9.0	31.3	1.50	275	412.5	13
30	Queensland	19	57.9	25.9	3.9	46.5	2.10	190	399.0	17
31	SaintLouis	31	45.2	25.1	2.3	64.0	2.50	127	317.5	17
32	Taipei_a	13	NA	NA	NA	56.3	2.00	295	590.0	25
33	Taipei_b	8	NA	NA	NA	47.3	2.00	175	350.0	17

Mean and standard deviation of age are given in years, voxel size in mm^3, TR in seconds; the column Volumes lists the number of volumes (or time points) scanned for every subject in the study, the column Duration lists scan duration in seconds and the column Components contains the median number of ICA components identified for the subjects of this study.

estimates. Finally, preprocessing was concluded by normalization to MNI 152 standard space and re-sampling to 3 mm isotropic voxels to enable group level analyses. All preprocessing steps were computed using AFNI (Cox, 1996), second-level analyses were performed in R 2.13.1 (R Development Core Team, 2012), using specialized packages for fMRI analysis, parallelization, and handling of large data (Tabelow et al., 2011; Boubela et al., 2012).

Following this preprocessing, individual-subject ICA results—one z-map for each component—were combined using the FENICA algorithm proposed by Schöpf et al. (2010). Briefly, the algorithm aims at exploratorily finding components consistent over a population of subjects and is composed of three stages: (1) identification of pairs of matching maps, (2) building of candidate average maps, and (3) selection of final average maps.

To allow for automated and thus reproducible exploratory selection of parameters of the algorithm, two modifications to the algorithm as originally described (Schöpf et al., 2010) have been made to adapt it to the necessities of the large dataset while minimizing the influence of observer bias (Boubela et al., 2012). First, identification of eligible pairs was set to match the number of original components. Second, the similarity threshold (Schöpf et al., 2010) to discard average components similar to at least one other component with a higher t-sum was chosen as the lowest value that produced a number of final components corresponding to the median number of components of the individual-subject results. Related groups of final components were defined by spatially clustering the components using hierarchical clustering with centroid distance between clusters (Mangiameli et al., 1996) using Kolmogorov–Smirnov distance (Kolmogorov, 1933) between z-values of components as the distance between maps.

Consistency across subjects was assessed for each resulting component by calculating the correlation of the original pairwise

average map that was used as the candidate for the generation of the group map with each subject's respective best matching component. The distribution of these correlation coefficients was then used to evaluate the consistency of each component.

An assessment of spectral characteristics of group networks was performed by computing individual-subject power spectra for each group network using a back reconstruction algorithm. The individual-subject spectra were averaged to determine power spectra at group level. From these, the dynamic range (i.e., the difference between the power at the peak of the spectrum and the minimum power of frequencies higher than this peak) and the power ratio (i.e., the ratio between the integral of the power of the frequencies below 0.1 Hz and the integral of the power of the frequencies higher than 0.15 Hz) are computed for each of the group components identified (Robinson et al., 2009).

In addition, the whole computation was performed separately for the subset of subjects of each individual study to determine consistency of components across studies. Group components were considered to be present in an individual study sample if and only if there was a component in the individual study results that could be partner-matched (Wang and Peterson, 2008) to that group component, i.e., if the group component had highest spatial correlation among all group components to the individual-study component in question and vice versa.

To assess the relationship between scan duration and number of components found at individual-subject level, a least-squares regression as well as a robust MM-estimator (Koller and Stahel, 2011) were fitted.

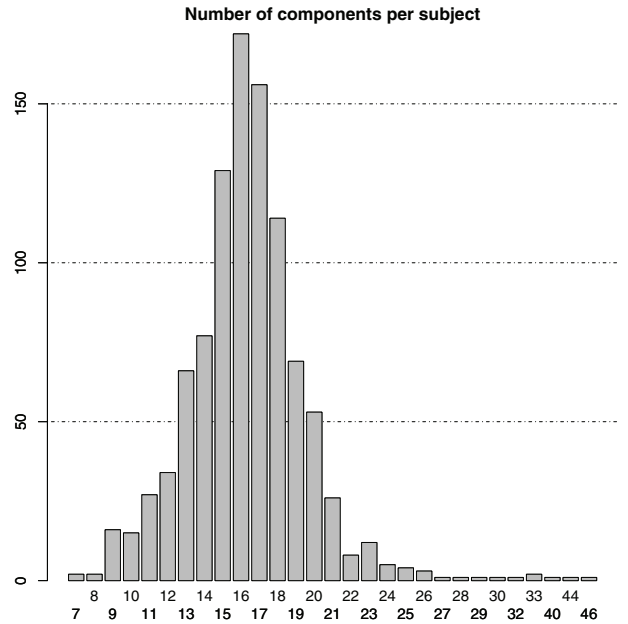

FIGURE 1 | Bar plot of the distribution of the number of components in the individual-subject ICA results.

RESULTS

At single-subject level, the number of ICA components was symmetrically distributed with a mean and median number of components both equal to 16 ± 3.5 (SD) (cf. the bar plot in **Figure 1**). In total, there were 16,365 individual-subject components from which the same number of candidate pairs of components were selected for calculation of average maps.

At group level, 16 group components were identified for a similarity threshold of 0.75, chosen to produce a number of components corresponding to the median number of individual-subject components as detailed above. Of these components, 13 can be described as gray matter networks (shown in **Figure 2**, using an arbitrary thresholded at $t_{999} = 18$, $p = 1.6 \cdot 10^{-57}$ FWE corrected for displaying purposes), and 3 show consistent activity mainly located in voxels outside the gray matter (components C.05, C.15 and C.16, see **Figure 3**) and will therefore be referred to as (consistent) artifact components from here on.

Gray matter networks, designated C.01 to C.16 in descending order of their voxelwise sum of t-values, can be described as follows (for correspondence to known resting-state networks cf. Discussion). Component C.01 corresponds mainly to the occipital lobe. Component C.02 includes the posterior cingulate cortex and precuneus. Component C.03 shows activation in ventral medial prefrontal, posterior cingulate, and lateral parietal cortex as well as hippocampus and, to a lesser extent, the inferior temporal lobe. Component C.06 is situated in ventral and dorsal medial prefrontal cortex, posterior cingulate cortex and, to a lesser extent, lateral parietal cortex. Thus, these two components correspond to regions commonly identified as part of the default-mode network, with component C.03 more focused in the posterior, and component C.06 in the anterior parts. C.04 is centered on the posterior cingulate cortex and precuneus, with co-activations in the dorsolateral prefrontal cortex. Components C.07 and C.09 are strongly lateralized, situated in the ventral and dorsal lateral prefrontal cortex, lateral parietal cortex and superior temporal lobe—predominantly right for component C.07, and left for component C.09—as well as the respective contralateral part of the cerebellum. Component C.10 and C.12 encompass dorsal parietal, precentral, as well as occipitotemporal (BA 37) areas, with C.10 being more focused on the ventral parts and C.12 more strongly involved in the dorsal parts of these areas, in particular the precentral areas. Component C.08 covers the pre- and postcentral gyri and can be described as a sensory-motor network, C.11 is focused on the anterior cingulate cortex, with co-activations in the dorsolateral prefrotal, orbitofrontal as well as posterior cingulate cortex. Finally, components C.13 and C.14 are located on the temporal lobes.

Clustering results of the networks are presented as a dendrogram in **Figure 4**, along with boxplots of the distribution of the correlation coefficients between candidate pairwise average maps and best matching components of each subject, showing inter-subject consistency of the final component maps. It can be noted that the gray matter components (shown in green), whose correlation coefficients are mostly around 0.3–0.4, are generally more consistent than the components identified as artifacts (shown in gray), with correlation coefficients of around 0.2. Still, there is also a number of gray matter components (C.06, C.12–C.14) which show lower consistency, comparable to that of the artifact components. In addition, on the left side of the

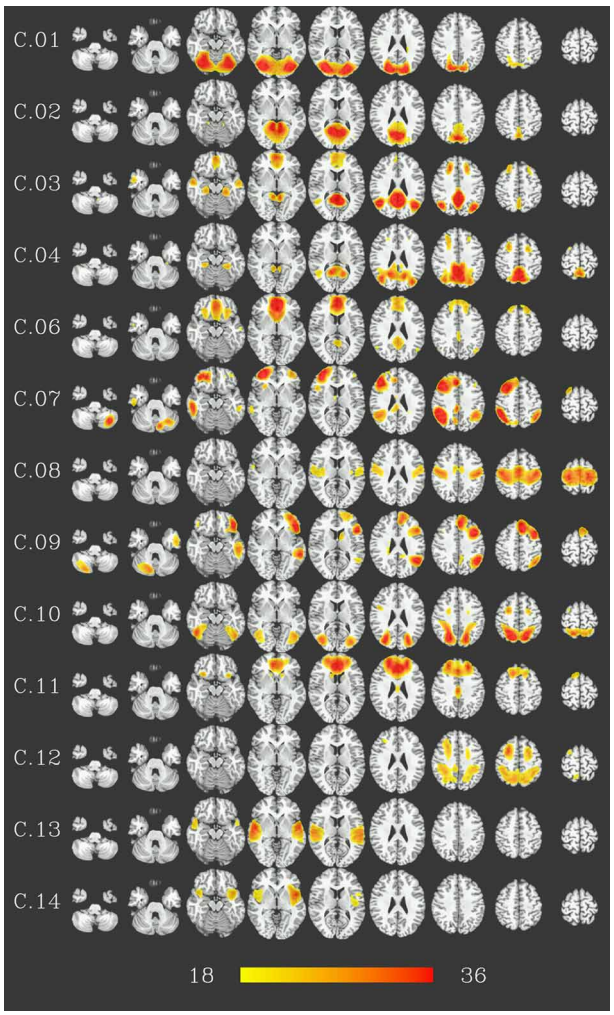

FIGURE 2 | Consistent gray-matter networks from 1000 resting-state datasets. Results are presented as *t*-values, thresholded at $t_{999} = 18$ ($p = 1.6 \cdot 10^{-57}$, FWE-corrected), each row corresponding to one network showing nine representative slices spaced 15 mm in z direction. Red color represents highest *t*-values, images are shown in radiological convention (the right side of the brain is displayed on the left). Color bar shown for *t*-values between 18 and 36 (bottom).

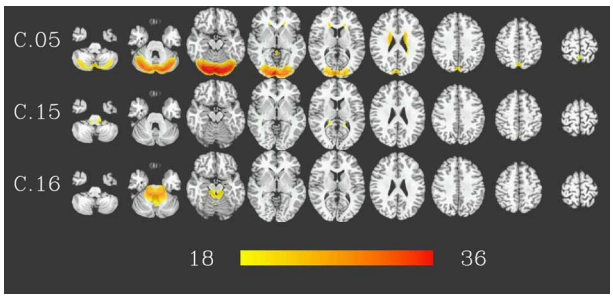

FIGURE 3 | Artifact components consistent in 1000 resting-state datasets. Results are presented as *t*-values, thresholded at $t_{999} = 18$ ($p = 1.6 \cdot 10^{-57}$, FWE-corrected), each row corresponding to one component showing nine representative slices spaced 15 mm in z direction. Red color represents highest *t*-values, images are shown in radiological convention (the right side of the brain is displayed on the left). Color bar shown for *t*-values between 18 and 36 (bottom).

dendrogram in **Figure 4**, one can find the least consistent components (C.12–C.16) situated quite apart from the components with higher consistency (including C.05, the most consistent of the three artifact components).

The spectral characteristics of the networks indicate that the artifact components have lower power ratio between high and low frequencies as well as lower dynamic range (see **Figure 5**): both values are lowest for components C.15 and C.16, while component C.05 shows higher values than the two least consistent gray matter components C.13 and C.14, but still lower than the other components. Indeed, the difference in the spectra for the components C.15 and C.16 is evident at the first glance (see **Figure 6**), while the spectrum of C.05 seems more similar to the spectra of the gray matter components. It is noteworthy here that the spectral characteristics of this occipital component can be related to an observation by Birn et al. (2008), where a medial occipital component was found to at least partly reflect respiratory-induced changes. One possible interpretation put forward by Birn et al. was that the component might be a mixture of gray matter and respiratory signal, which is consistent with our observation of the spectrum being more similar to gray matter component spectra than the other two artifact components.

At study level, **Figure 7** shows comparisons between the components in the individual FENICA component sets of all sites analyzed separately with the group components from the analysis of the whole sample presented in **Figures 2** and **3**. The most consistent components (i.e., C.01, C.03, C.07–C.09) are characterized by the existence of a successful match in almost all individual sites as well as high spatial correlation of the best matching components with the group component.

Of note, it can be seen that while on the one hand there are some components that can be found in almost all component sets of single studies analyzed separately (C.01, C.03, C.07–C.09), other components appear only in the single-study results of about half of the studies included in the 1000 Functional Connectomes dataset (C.02, C.12–C.16). Still, even the most consistent group components do not exhibit uniformly high spatial correlation with their matching components or fail to bidirectionally match with a component from each set of single-study components. Component C.08, for instance, has a partner-matched component in every single study, yet spatial correlations with its matched components are as low as 0.12 for the dataset Ann Arbor b, 0.39 for Milwaukee a and 0.46 for München. Conversely, there is a generally low consistency of some studies with all group results (the maximum correlations of a component of the three example studies mentioned above with a group component are 0.65, 0.7, and 0.62, respectively). On the other extreme, there are some group components which could not be unambiguously matched to only one component in a given study despite there being a component with high spatial correlation. This is an indication that there might be a second equally well matching component in this study's dataset, probably due to a division of the network into subcomponents.

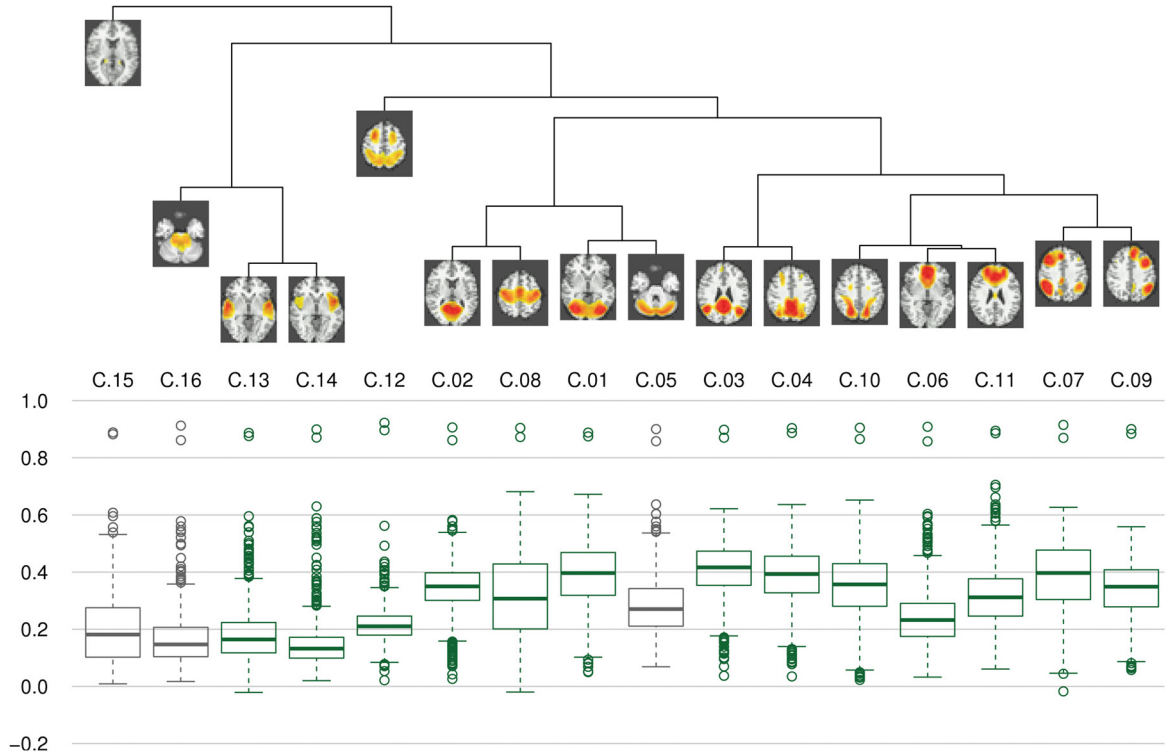

FIGURE 4 | Clustering and consistency of results. On top, a dendrogram represents results of hierarchical clustering using complete linkage distance between clusters. Below, boxplots of correlation coefficients illustrate the consistency of components between subjects. Boxes for gray matter components are drawn in green, artifacts are drawn in dark gray. It can be seen that the clusters with lower consistency (i.e., C.12–C.16) are quite distinct from a more homogeneous cluster of higher consistency components.

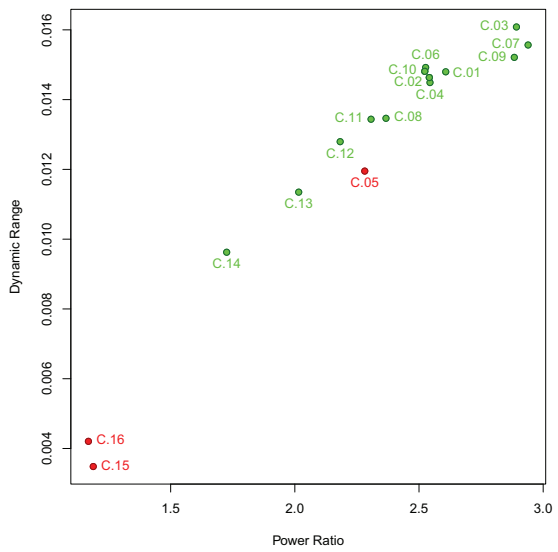

FIGURE 5 | Power ratio and dynamic range of the components identified. Gray matter components are shown in green, artifact components in red. Both power ratio and dynamic range are highest for gray matter networks and lower for artifactual components, though with some overlap since the most consistent of the artifact components, C.05, has higher power ratio and dynamic range than the two least consistent gray matter components, C.13 and C.14.

The components can thus be divided in three categories. First, there are components with high consistency at both single-subject and study level; these include C.01, C.03, C.04, and C.07–C.11. The second group of components can be characterized as those least consistent at both levels, notably C.12–C.16. As a third group, some components show differences in these two metrics: C.02 is about as consistent as other gray matter components at single-subject level, but can be found in only half of the single-study samples, C.05 and C.06 are among the less consistent components at single-subject level, but show average consistency at study-level. **Figure 8** illustrates this relationship between subject level and study level consistency.

Finally, single-subject results show systematic variation of the number of components, identified by MELODIC using the LAP criterion, depending on the study of origin of the individual-subject dataset (see **Figure 9**). In particular, there is a significant correlation between the median number of components found in the subjects of a study with the duration of the scans of that study, with longer scans being associated with larger number of components. The robustness of this finding is corroborated by the observation that the application of a robust methods of moments regression leads to the same result.

DISCUSSION

In this study we analyzed a publicly available dataset of 1000 subjects' resting-state scans using the exploratory analysis method

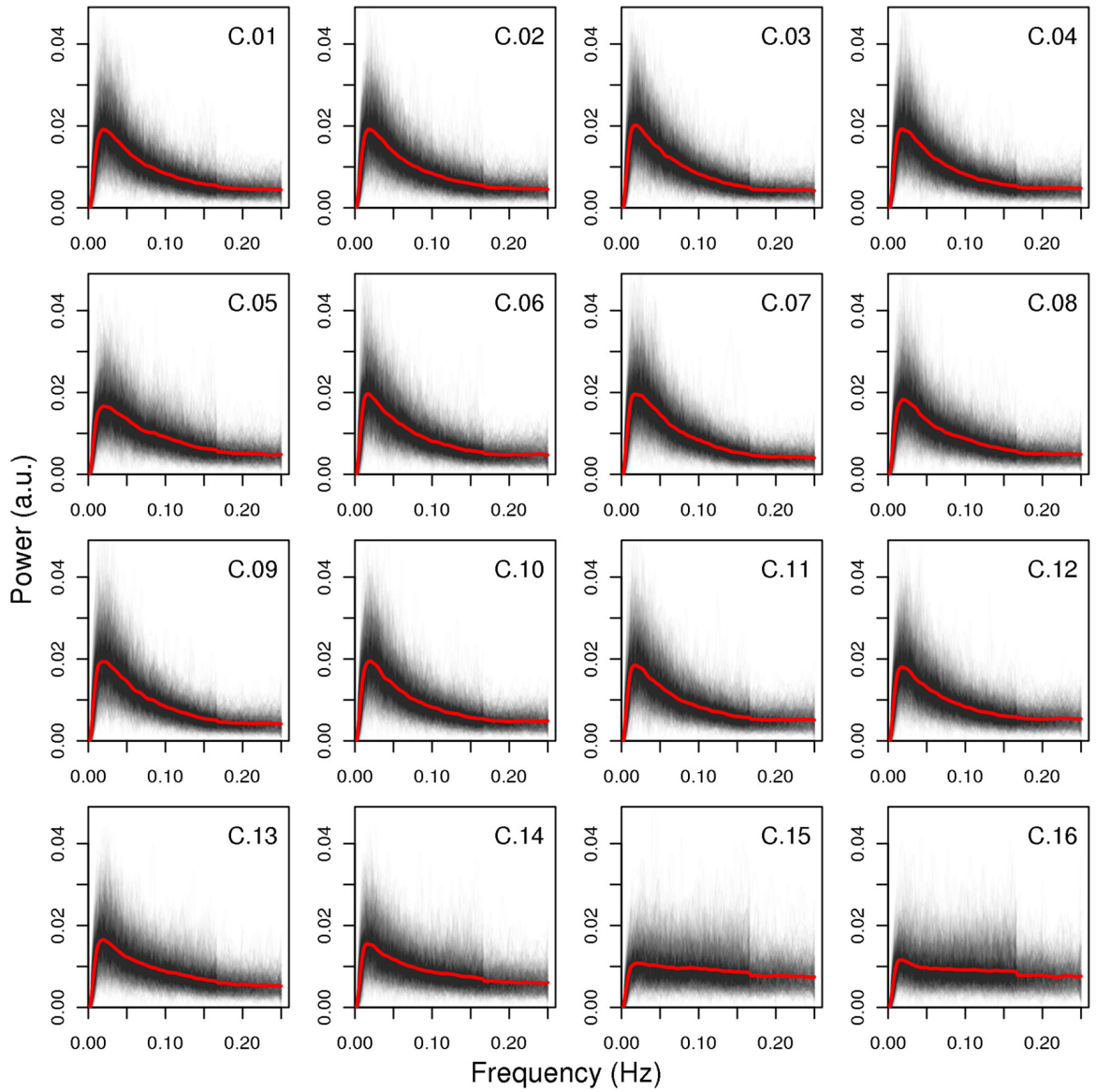

FIGURE 6 | Spectra of all components. All single-subject spectra were drawn as black lines, and the mean spectrum of each component is displayed as a red line. The artifact components C.15 and C.16 have markedly different spectra than the other components, the third artifact C.05 is more similar to the gray matter components in that it has higher power in lower frequency bands, but its decline in power after the peak is less steep.

FENICA (Schöpf et al., 2010; Boubela et al., 2012). Our goal was to examine the consistency of resting-state networks identified in previous, smaller studies in a very large sample originating from multiple, international centers, and to assess heterogeneity of results between studies.

Altogether, we identified 16 consistent components. Among them, 13 can be regarded as neuroscientifically meaningful gray matter components, while the remaining three may be attributed to consistent artifacts. The latter mostly correspond to ventricular/CSF regions, the most consistent of the three components being situated mainly in the occipital CSF. The consistency values of these artifacts, in particular the inter-subject spatial correlation coefficient of these component maps of around 0.2, can be seen as a reference to which the consistency of gray matter components can then be related.

Indeed, the consistency values of most gray matter networks are markedly higher than those of all artifact components. Many of the gray matter networks identified in this study correspond to networks as previously published (Damoiseaux et al., 2006; Smith et al., 2009; Biswal et al., 2010; Allen et al., 2011). The occipital visual network (C.01), the sensory-motor network (C.08) as well as the dorsal parietal network (C.10) have been reported in most fMRI studies on the resting brain. This study adds a quantification of the consistency of these networks, showing that the visual (C.01) and the sensory-motor networks (C.08) can be found in almost all single-study samples (85% for C.01

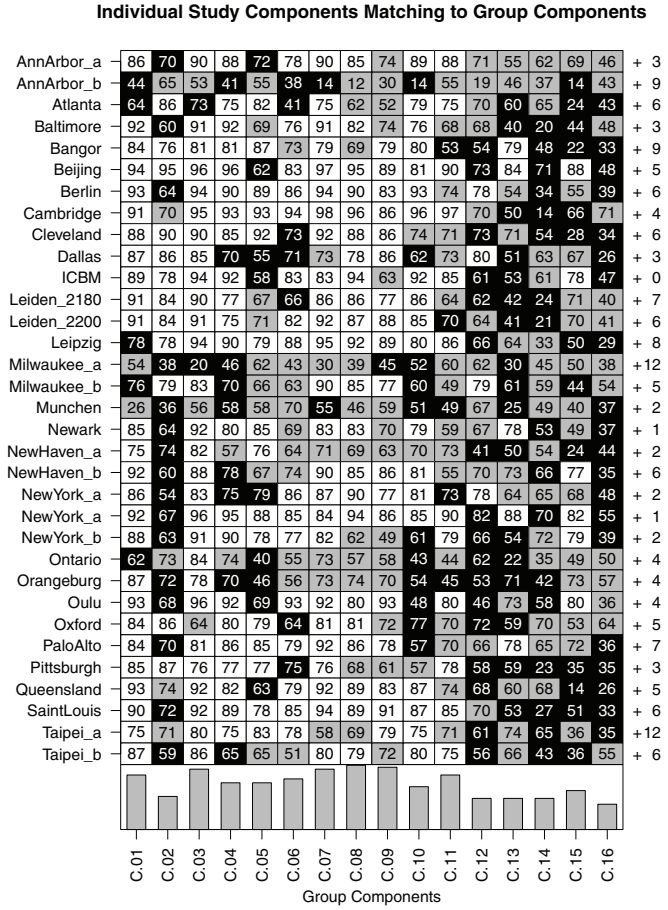

FIGURE 7 | Matrix of bidirectional 1-to-1 matching of components in individual-study analyses compared to group results from the whole dataset comprising 1000 subjects. Each field contains the spatial correlation coefficient (multiplied by 100 for readability) between the group component and the best matching individual-study component. White fields indicate a bidirectional match with a spatial correlation of at least 0.75, gray fields indicate bidirectional matches with lower spatial correlation, and black fields indicate the absence of a bidirectional match (note that the spatial correlation to the best matching component can nonetheless be high in some cases). To the right of each row, the number of other components found in the individual-study analysis which do not bidirectionally match any of the group components is listed. At the bottom of each column, a bar plot indicates the study-level consistency of each component, counting the number of studies in which a bidirectional match was found.

and 100% for C.08), and the dorsal parietal network (C.10) appears in two-thirds of these samples. The components C.07 and C.09, encompassing the regions associated with memory function in dorsolateral prefrontal and lateral parietal cortex, are both also among the most consistent networks identified (94% and 97%, respectively), highlighting the lateralized subdivision of the working memory network.

We found two networks associated with regions of the default-mode network of the brain (C.03 and C.06), with the posterior of the two (C.03) being one of the most consistent networks identified, appearing in 94% of single study results, and the anterior (C.06) being found in 79% of the study samples. The anterior default mode component, however, exhibits lower spatial correlation both between the group component map and study-level components as well as between the group component map and single-subject component maps. This supports the hypothesis of a functional segregation of the default-mode network (Kim and Lee, 2011), with one part particularly involved in the prefrontal regions, and the other part dominating in the posterior cingulate cortex, the parietal cortex, and the hippocampus. This division into anterior and posterior parts of the default-mode network, although not a novel concept, is not yet fully embraced in the literature (Buckner et al., 2008).

In contrast to the high consistency in the subdivision of the working memory networks in a left and right part, there are subtle differences in the results relating to the division of the default-mode network between Biswal et al. (2010) and this paper: here, the subcomponent focused on the medial prefrontal cortex (C.06) shows less activation in the posterior cingulate and parietal parts of the network than the corresponding component found by Biswal et al., while the posterior component with the main activation in the posterior cingulate cortex shows a marked coactivation in the medial prefrontal cortex, where the corresponding component found by Biswal et al. has very little coactivation. This variation in the spatial segregation of overlapping networks by spatial ICA can be attributed to methodological differences, in

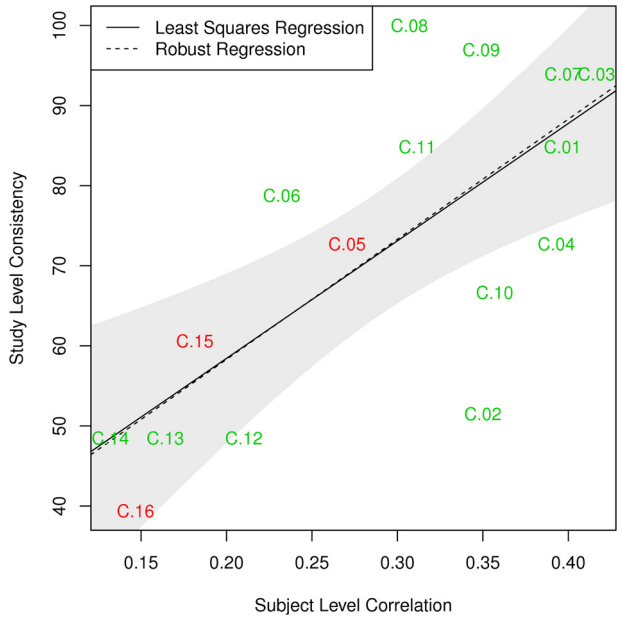

FIGURE 8 | Comparison of subject level consistency based on spatial correlation of single subject component maps with study level consistency based on identification of maps in individual-study results. Ordinary least squares (OLS; $p = 0.002$) and robust MM-estimator ($p < 10^{-4}$) illustrate the relationship between the two measures. The shaded area corresponds to a 95% confidence interval for the OLS estimator.

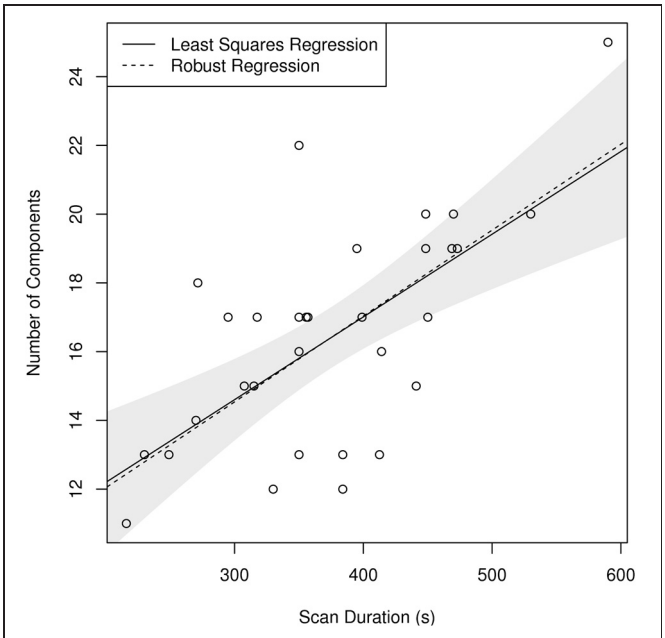

FIGURE 9 | Scatterplot showing a linear relationship between scan duration in seconds and median number of components per subject identified in each individual study using LAP criterion in FSL MELODIC. Note that both ordinary least squares (OLS) and the robust MM-estimator identify the same relationship, highlighting the robustness of this ratio ($p < 10^{-4}$ for both estimators). The shaded area corresponds to a 95% confidence interval for the OLS estimator.

particular due to the fact that spatial ICA intrinsically guarantees spatial independence of components and thus enforces a more or less arbitrary delineation of borders between possibly intermingled networks. Temporal ICA might resolve this issue but, due to its computational demands and the low number of time points in most experiments, is not yet widely used in fMRI research. With current multi-band acquisition protocols and their high temporal resolution, resulting in more time points without increasing scan duration, temporal ICA becomes an increasingly viable approach (Smith et al., 2012).

Altogether, the networks identified in this study correspond well to networks already found in the literature. For example, in Damoiseaux et al. (2006), network A corresponds well to our network C.01, B to C.03, C to C.09, D to C.07, H to C.10, I to C.13, and K to C.06. Note in particular that, despite the low model order of 10, Damoiseaux et al. found a segregation of both the default-mode network and the auditory network into two subcomponents, though their split of the auditory network was different than the one identified in our study, highlighting the apparent heterogeneity in this area. As another example, Smith et al. (2009) also found components matching our components rather closely: their component 1_{20} corresponds to C.02, 2_{20} to C.01, 3_{20} to C.10, 4_{20} to C.03, 6_{20} to C.08, 7_{20} to C.13, 8_{20} to C.11, 9_{20} to C.07 and 10_{20} to C.09. Networks C.04 and C.12 have no immediate counterparts in these two studies, though component C.04 can at least to some extent be related to components in high model order studies, e.g., to component 50 in Allen et al. (2011). C.12, being among the less consistent components in our sample, might be regarded as spurious unless it can be corroborated in future studies.

On the other hand, our study did not find some components otherwise typically found in resting-state ICA studies. First, we found fewer artifactual components than most previous studies, with the lack of a WM component being the most obvious; this might be due to different preprocessing strategies. Second, we found no basal ganglia component, which has been found in many (e.g., Robinson et al., 2009; Smith et al., 2009; Biswal et al., 2010), but not all (e.g., Damoiseaux et al., 2006) resting state ICA studies. Finally, our results did not include a separate cerebellar component, and instead included some cerebellar activity into the lateralized fronto-parietal components. One reason for this might lie in the differences in field of view between studies, with different coverage of the cerebellum, but other aspects of data quality (scanner performance, noise, motion, physiological effects) also introduce variability between the data of different studies.

This between-study variability leads to one of the main limitations of the FENICA method. Since it implicitly assumes that the group components appear in every subject (the assumption lies in the fact that the best matching component of every subject is averaged for the final group component maps), the algorithm is less likely to detect components that are not present in every subject, for example a cerebellar component if the cerebellum is not wholly within the field of view of all studies included in the analysis. This is corroborated by Biswal et al. (2010) who, using a different method

for the group ICA, identified a cerebellar network on data from the 1000 Functional Connectomes database. On a related note, in the short duration of a typical fMRI resting-state scan, it is possible that not all networks show a distinguishable activity pattern in all subjects to be discerned by ICA methods, which might also account for some between-subject variability in the networks identified. This fact is also a useful reminder that there are limits in the interpretability of individual ICA components (Moser and Ranjeva, 2010).

Another confounding effect could be the influence of motion on the component map estimation, as highlighted by Power et al. (2012), which could also generate some between-subject and even between-study heterogeneity if subjects of different studies differed in their head motion in the scanner. However, as Power et al. (2012) also pointed out, the motion effects they described are only of limited magnitude in adults, and a specific correction for these effects seems only necessary in studies with children or adolescents.

This work presents the largest exploratory fMRI study to date, including 1000 single subjects simultaneously, made possible due to new computational methods implemented in an R framework (R Development Core Team, 2012; Boubela et al., 2012). In Biswal et al. (2010), group ICA as the most complex of the computational tasks involved was performed separately on multiple subsets of 306 subjects due to computational limitations preventing simultaneous analysis of the whole sample. The extensive work of the R community in the handling of large datasets and parallel computing, including computation on graphics processing units (GPUs), provides the tools for analyses previously prohibitive from a computational point of view and accelerates the emergence of data driven discovery science in the field of neuroimaging. For instance, the exploratory approach used in this work allows for the unbiased drawing of an overall picture of the substantial amount of data acquired in 33 studies performed by 26 centers worldwide, while still keeping the total processing time under a week. The most important addition to the current knowledge made possible by the computational techniques employed, however, is the assessment of heterogeneity of resulting components with respect to the entire sample, both at the level of single subjects and of individual studies. As a result, an overview on networks more commonly found in individual studies as well as an assessment of divergence between the sets of networks intrinsically emerging from the data of different centers has been presented, possibly providing some guidance for the interpretation of variability in resting-state networks obtained in past and future studies. This paper shows the richness of evidence present in the 1000 Functional Connectomes dataset, but ultimately only scratches the surface of what can be examined and opens a host of new questions to be answered in future analyses.

ACKNOWLEDGMENTS

We want to thank all investigators contributing data to the 1000 Functional Connectomes project, without whom this analysis could not have been performed. This study has been supported by funds of the Oesterreichische Nationalbank (Anniversary Fund, project numbers: 13890, 13903, and 12982), by the Austrian Science Fund (FWF) as part of the Special Research Program 35 (SFB-35) and by the Institute for the Study of Affective Neuroscience (ISAN).

REFERENCES

Abou-Elseoud, A., Starck, T., Remes, J., Nikkinen, J., Tervonen, O., and Kiviniemi, V. (2010). The effect of model order selection in group PICA. *Hum. Brain Mapp.* 31, 1207–1216.

Allen, E. A., Erhardt, E. B., Damaraju, E., Gruner, W., Segall, J. M., Silva, R. F., et al. (2011). A baseline for the multivariate comparison of resting-state networks. *Front. Syst. Neurosci.* 5:2. doi: 10.3389/fnsys.2011.00002

Allen, E. A., Erhardt, E. B., Wei, Y., Eichele, T., and Calhoun, V. D. (2012). Capturing inter-subject variability with group independent component analysis of fMRI data: a simulation study. *Neuroimage* 59, 4141–4159.

Birn, R. M., Murphy, K., and Bandettini, P. A. (2008). The effect of respiration variations on independent component analysis results of resting state functional connectivity. *Hum. Brain Mapp.* 29, 740–750.

Biswal, B., Yetkin, F. Z., Haughton, V. M., and Hyde, J. S. (1995). Functional connectivity in the motor cortex of resting human brain using echo-planar MRI. *Magn. Reson. Med.* 34, 537–541.

Biswal, B. B., Mennes, M., Zuo, X.-N., Gohel, S., Kelly, C., Smith, S. M., et al. (2010). Toward discovery science of human brain function. *Proc. Natl. Acad. Sci. U.S.A.* 107, 4734–4739.

Boubela, R. N., Huf, W., Kalcher, K., Sladky, R., Filzmoser, P., Pezawas, L., et al. (2012). A highly parallelized framework for computationally intensive MR data analysis. *MAGMA* 25, 313–320.

Brookes, M. J., Woolrich, M., Luckhoo, H., Price, D., Hale, J. R., Stephenson, M. C., et al. (2011). Investigating the electrophysiological basis of resting state networks using magnetoencephalography. *Proc. Natl. Acad. Sci. U.S.A.* 108, 16783–16788.

Buckner, R. L., Andrews-Hanna, J. R., and Schacter, D. L. (2008). The brain's default network: anatomy, function, and relevance to disease. *Ann. N.Y. Acad. Sci.* 1124, 1–38.

Calhoun, V. D., Adali, T., Pearlson, G. D., and Pekar, J. J. (2001). A method for making group inferences from functional MRI data using independent component analysis. *Hum. Brain Mapp.* 14, 140–151.

Corbetta, M., and Shulman, G. L. (2002). Control of goal-directed and stimulus-driven attention in the brain. *Nat. Rev. Neurosci.* 3, 201–215.

Cox, R. W. (1996). AFNI: software for analysis and visualization of functional magnetic resonance neuroimages. *Comput. Biomed. Res.* 29, 162–173.

Damoiseaux, J. S., Rombouts, S. A. R. B., Barkhof, F., Scheltens, P., Stam, C. J., Smith, S. M., et al. (2006). Consistent resting-state networks across healthy subjects. *Proc. Natl. Acad. Sci. U.S.A.* 103, 13848–13853.

Fox, M. D., and Raichle, M. E. (2007). Spontaneous fluctuations in brain activity observed with functional magnetic resonance imaging. *Nat. Rev. Neurosci.* 8, 700–711.

Himberg, J., Hyvärinen, A., and Esposito, F. (2004). Validating the independent components of neuroimaging time series via clustering and visualization. *Neuroimage* 22, 1214–1222.

Huf, W., Kalcher, K., Pail, G., Friedrich, M.-E., Filzmoser, P., and Kasper, S. (2011). Meta-analysis: fact or fiction? How to interpret meta-analyses. *World J. Biol. Psychiatry* 12, 188–200.

Joel, S. E., Caffo, B. S., van Zijl, P. C. M., and Pekar, J. J. (2011). On the relationship between seed-based and ICA-based measures of functional connectivity. *Magn. Reson. Med.* 66, 644–657.

Kim, D.-Y., and Lee, J.-H. (2011). Are posterior default-mode networks more robust than anterior default-mode networks? Evidence from resting-state fMRI data analysis. *Neurosci. Lett.* 498, 57–62.

Koller, M., and Stahel, W. (2011). Sharpening wald-type inference in robust regression for small samples. *Comput. Stat. Data Anal.* 55, 2504–2515.

Kolmogorov, A. N. (1933). Sulla determinazione empirica di una legge di distribuzione. *Giorn. Ist. Ital. Attuar.* 4, 83–91.

Leech, R., Kamourieh, S., Beckmann, C. F., and Sharp, D. J. (2011). Fractionating the default mode

network: distinct contributions of the ventral and dorsal posterior cingulate cortex to cognitive control. *J. Neurosci.* 31, 3217–3224.

Luca, M. D., Beckmann, C. F., Stefano, N. D., Matthews, P. M., and Smith, S. M. (2006). fMRI resting state networks define distinct modes of long-distance interactions in the human brain. *Neuroimage* 29, 1359–1367.

Mangiameli, P., Chen, S. K., and West, D. (1996). A comparison of SOM neural network and hierarchical clustering networks. *Eur. J. Oper. Res.* 93, 402–417.

Margulies, D. S., Böttger, J., Long, X., Lv, Y., Kelly, C., Schäfer, A., et al. (2010). Resting developments: a review of fMRI post-processing methodologies for spontaneous brain activity. *MAGMA* 23, 289–307.

Moser, E., and Ranjeva, J.-P. (2010). *In vivo* MR imaging of brain networks: illusion or revolution? *MAGMA* 23, 275–277.

Power, J. D., Barnes, K. A., Snyder, A. Z., Schlaggar, B. L., and Petersen, S. E. (2012). Spurious but systematic correlations in functional connectivity MRI networks arise from subject motion. *Neuroimage* 59, 2142–2154.

R Development Core Team. (2012). R: *A Language and Environment for Statistical Computing*. Vienna, Austria: R Foundation for Statistical Computing. ISBN: 3-900051-07-0.

Raichle, M. E., and Snyder, A. Z. (2007). A default mode of brain function: a brief history of an evolving idea. *Neuroimage* 37, 1083–1090. discussion: 1097–1099.

Richiardi, J., Eryilmaz, H., Schwartz, S., Vuilleumier, P., and Van De Ville, D. (2011). Decoding brain states from fMRI connectivity graphs. *Neuroimage* 56, 616–626.

Robinson, S., Basso, G., Soldati, N., Sailer, U., Jovicich, J., Bruzzone, L., et al. (2009). A resting state network in the motor control circuit of the basal ganglia. *BMC Neurosci.* 10:137. doi: 10.1186/1471-2202-10-137

Schöpf, V., Kasess, C. H., Lanzenberger, R., Fischmeister, F., Windischberger, C., and Moser, E. (2010). Fully exploratory network ICA (FENICA) on resting-state fMRI data. *J. Neurosci. Methods* 192, 207–213.

Smith, S. M., Fox, P. T., Miller, K. L., Glahn, D. C., Fox, P. M., Mackay, C. E., et al. (2009). Correspondence of the brain's functional architecture during activation and rest. *Proc. Natl. Acad. Sci. U.S.A.* 106, 13040–13045.

Smith, S. M., Jenkinson, M., Woolrich, M. W., Beckmann, C. F., Behrens, T. E. J., Johansen-Berg, H., et al. (2004). Advances in functional and structural MR image analysis and implementation as FSL. *Neuroimage* 23(Suppl. 1), S208–S219.

Smith, S. M., Miller, K. L., Moeller, S., Xu, J., Auerbach, E. J., Woolrich, M. W., et al. (2012). Temporally-independent functional modes of spontaneous brain activity. *Proc. Natl. Acad. Sci. U.S.A.* 109, 3131–3136.

Tabelow, K., Clayden, J. D., de Micheaux, P. L., Polzehl, J., Schmid, V. J., and Whitcher, B. (2011). Image analysis and statistical inference in neuroimaging with R. *Neuroimage* 55, 1686–1693.

van de Ven, V., Bledowski, C., Prvulovic, D., Goebel, R., Formisano, E., Salle, F. D., et al. (2008). Visual target modulation of functional connectivity networks revealed by self-organizing group ica. *Hum. Brain Mapp.* 29, 1450–1461.

Wang, Z., and Peterson, B. S. (2008). Partner-matching for the automated identification of reproducible ICA components from fMRI datasets: algorithm and validation. *Hum. Brain Mapp.* 29, 875–893.

Weissenbacher, A., Kasess, C., Gerstl, F., Lanzenberger, R., Moser, E., and Windischberger, C. (2009). Correlations and anticorrelations in resting-state functional connectivity MRI: a quantitative comparison of preprocessing strategies. *Neuroimage* 47, 1408–1416.

Conflict of Interest Statement: Siegfried Kasper has received grant/research support from Eli Lilly, Lundbeck, Bristol-Myers Squibb, GlaxoSmithKline, Organon, Sepracor, and Servier; has served as a consultant or on advisory boards for AstraZeneca, Bristol-Myers Squibb, GlaxoSmithKline, Eli Lilly, Lundbeck, MSD, Pfizer, Organon, Schwabe, Sepracor, Servier, Janssen, and Novartis; and has served on speakers' bureaus for AstraZeneca, BMS, Angelini, Eli Lily, Lundbeck, Schwabe, Sepracor, Servier, Pfizer, Pierre Fabre, and Janssen. All other authors declare that their research was conducted in the absence of any commercial or financial relationships that could be construed as a potential conflict of interest.

Received: 20 July 2012; accepted: 19 October 2012; published online: 06 November 2012.

*Citation: Kalcher K, Huf W, Boubela RN, Filzmoser P, Pezawas L, Biswal B, Kasper S, Moser E and Windischberger C (2012) Fully exploratory network independent component analysis of the 1000 functional connectomes database. Front. Hum. Neurosci. **6**:301. doi: 10.3389/fnhum.2012.00301*

frontiers in
HUMAN NEUROSCIENCE

ORIGINAL RESEARCH ARTICLE
published: 25 June 2013
doi: 10.3389/fnhum.2013.00315

The quest for EEG power band correlation with ICA derived fMRI resting state networks

***Matthias Christoph Meyer*[1]*, *Ronald Johannes Janssen*[1], *Erik Sophius Bartus Van Oort*[1,2], *Christian F. Beckmann*[1,2] *and Markus Barth*[1,3]**

[1] *Radboud University Nijmegen, Donders Institute for Brain, Cognition and Behaviour, Nijmegen, Netherlands*
[2] *MIRA Institute for Biomedical Technology and Technical Medicine, University of Twente, Twente, Netherlands*
[3] *Erwin L. Hahn Institute for Magnetic Resonance Imaging, University Duisburg-Essen, Essen, Netherlands*

Edited by:
Simon Daniel Robinson, Medical University of Vienna, Austria

Reviewed by:
Andrew P. Bagshaw, University of Birmingham, UK
Marco Buiatti, INSERM, France

***Correspondence:**
Matthias Christoph Meyer, Radboud University Nijmegen, Donders Institute for Brain, Cognition and Behaviour, Kapittelweg 29, 6525EN Nijmegen, Netherlands
e-mail: matthias.meyer@donders.ru.nl

The neuronal underpinnings of blood oxygen level dependent (BOLD) functional magnetic resonance imaging (fMRI) resting state networks (RSNs) are still unclear. To investigate the underlying mechanisms, specifically the relation to the electrophysiological signal, we used simultaneous recordings of electroencephalography (EEG) and fMRI during eyes open resting state (RS). Earlier studies using the EEG signal as independent variable show inconclusive results, possibly due to variability in the temporal correlations between RSNs and power in the low EEG frequency bands, as recently reported (Goncalves et al., 2006, 2008; Meyer et al., 2013). In this study we use three different methods including one that uses RSN timelines as independent variable to explore the temporal relationship of RSNs and EEG frequency power in eyes open RS in detail. The results of these three distinct analysis approaches support the hypothesis that the correlation between low EEG frequency power and BOLD RSNs is instable over time, at least in eyes open RS.

Keywords: combined EEG-fMRI, resting state, source modeling, RSN, ICA, ECP, IHM

INTRODUCTION

Blood oxygen level dependent (BOLD) functional magnetic resonance imaging (fMRI) resting state networks (RSNs) have increasingly generated interest in the neuroscientific community, but the neuronal underpinnings remain unclear so far. Early studies, which examine correlations between the electroencephalography (EEG) theta, alpha, or beta band power and BOLD signal fluctuations using EEG derived regressors (Goldman et al., 2002; Laufs et al., 2003a,b, 2006; Moosmann et al., 2003; Feige et al., 2005; Goncalves et al., 2006; Scheeringa et al., 2008), report rather mixed and inconclusive BOLD correlation maps. The discovery and further analysis of RSNs (Biswal et al., 1995; Lowe et al., 2000; Cordes et al., 2001; Greicius et al., 2003; Fox et al., 2005; Damoiseaux et al., 2006; De Luca et al., 2006; Smith et al., 2009), together with the above mentioned early combined EEG-fMRI studies gave rise to the assumption that several frequency bands might be involved in distinct functional networks (Laufs et al., 2006; Mantini et al., 2007). The replication of this finding on subject level would fundamentally improve our understanding of the link with electrophysiology.

Simultaneous recordings of EEG and fMRI during resting state (RS), enables the investigation of the electrophysiological correlates of BOLD RSNs. Using simultaneous recordings, Mantini et al. (2007) reported a specific EEG frequency band power signature for RSNs on group level in eyes closed RS. However, further studies show large inter-subject variations of distinct brain areas correlated with EEG alpha band power (Goncalves et al., 2006, 2008) in RS. In a recent study by Meyer et al. (2013) electrophysiological correlation patterns (ECPs) between RSN BOLD time courses and EEG frequency band power showed large inter-subject and within subject variability. While RSNs by themselves exhibit a high reproducibility of their spatial characteristics across subjects, these studies point to less stable temporal correlations between RSNs seen in BOLD fMRI and EEG frequency band power.

Based on this evidence we hypothesize that the relationship between EEG frequency band power and RSN BOLD time courses is not stable over time. In order to assess this temporal variance in the correlation of the EEG signal and RSNs within a subject in this study, a dataset with a long RS of 34 min was split up into 15 segments and each was analyzed using the following three analysis approaches:

(1) Global frequency power correlation (GFPC) (Meyer et al., 2013) resulting in ECPs an approach that is similar to the one used by Mantini et al. (2007) who found stable correlation patterns on group level.
(2) An extended version of this method, including an anatomically informed analysis (Dale et al., 2000; Ou et al., 2010; Janssen et al., 2012) to separate the EEG based on RSN Z-maps within a subject, to obtain source frequency power correlation (SFPC), which should reduce the effect of volume conduction in the EEG.
(3) A channel wise frequency power fit (CFPF) with minimal assumptions, using the BOLD RSN time courses as the independent variable, which further reduces methodological bias.

We then calculated the temporal variance over the 15 segments for each of the three methods to estimate the temporal stability of the correlation between the two modalities.

MATERIALS AND METHODS

DATA ACQUISITION AND PRE-PROCESSING

In this study we performed a new analysis of the data sets acquired in Meyer et al. (2013). We briefly summarize the acquisition protocol and the pre-processing steps (for details, see Meyer et al., 2013): 34 min of eyes open RS were recorded from 12 healthy subjects, using combined EEG-fMRI, with approval of the local ethical committee. MR data were acquired on a 3 T Magnetom TIM Trio system (Siemens Healthcare, Erlangen, Germany) using the product 32 channel head coil. Functional data were recorded using a multi echo EPI sequence (Poser et al., 2006) (1030 Vol., TR = 2000 ms, 3.5 mm isotropic voxel size). A T1-weighted structural scan (MPRAGE) at 1 mm isotropic voxel size was also obtained (with EEG cap), to register the functional data to Montreal neurological institute (MNI) space. Five of the subjects (subjects 1, 2, 4, 10, and 11) were invited back to acquire a second T1-weighted structural scan without the EEG cap to enable the head model based analysis.

Simultaneous EEG data were recorded with a 32 channel cap (ANT WaveGuard MRI), using a BrainAmp MR plus amplifier (250 Hz low-pass analog hardware filter, 10 s time constant, 5 kHz sampling rate, 0.5 μV resolution, reference electrode: FCz) and BrainVision Recorder (BrainVision, Gilching, Germany). Two of the subjects were recorded with a 64 channel cap (BrainVision) using two BrainAmp MR plus amplifier; the same 30 channels (10–20 system) were used for all subjects in the analysis. The subjects were asked to relax, keep their eyes open, stay awake, and not think of anything specific. The room was darkened during the scan and an infrared eye tracker was used to confirm that the subject did not fall asleep. All subjects managed to stay awake for the complete duration of the experiment.

Functional magnetic resonance imaging pre-processing was performed using functions from the SPM5 software package (Welcome Department of Imaging Neuroscience, University College London, UK). The five echoes acquired at every time point were combined after SPM5 motion correction (Poser et al., 2006).

Electroencephalography pre-processing: MR related artifacts in the EEG signal were removed using Analyzer 2 (BrainVision). Trigger based average subtraction (Allen et al., 2000), as implemented in Analyzer 2, was applied to correct for gradient artifacts. The data were filtered using a Butterworth zero phase filter, 48 dB/oct, with a low cutoff at 0.8 Hz, to remove slow fluctuations from respiration, and a high cutoff at 50 Hz. Additionally, a notch filter at 50 Hz was used to remove residual mains frequency noise. Cardiac related MR artifacts were removed using the adaptive average subtraction (AAS) method of Analyzer 2 in semiautomatic mode (Allen et al., 1998). Further, eye blink related artifacts were removed using ICA and the EEG data were re-referenced to a common average.

ANALYSIS

As motivated in the introduction, three distinct methods (see **Figure 1**) were used to infer whether the relationship between EEG frequency band power and RSN BOLD time courses is temporally instable. For all these methods, the preprocessed fMRI data were spatially smoothed by 5 mm and transformed to MNI space using FMRIB's Software Library's (FSL) Feat (version 4.1[1]; Smith et al., 2004; Woolrich et al., 2009; Jenkinson et al., 2012). Group independent component analysis (ICA, as implemented in the FSL tool Melodic version 3.1) was performed on the fMRI data to obtain 30 ICs and 12 task related RSNs were selected according to Smith et al. (2009), see **Figure 2** for a depiction of the RSNs. A dual regression approach was used to derive subject specific RSN maps and time courses (Filippini et al., 2009). The further analysis is described for each method separately below.

GLOBAL FREQUENCY POWER CORRELATION

The datasets were split into 15 sections of equal length, each still longer than 2 min. For every section the EEG signal was split into 2 s segments corresponding to the TR used in the MR-acquisition. Within each section, for every segment, the mean frequency power over all channels for four frequency bands, i.e., delta: (2–4) Hz, theta: (4–8) Hz, alpha: (8–12) Hz, and beta: (12–30) Hz, was calculated, using a fast Fourier transformation (FFT), resulting in one time series for each frequency band. Motion related artifacts in the frequency power time courses were corrected. The frequency power time series were convolved with the standard SPM5 hemodynamic response function (HRF) and correlated with the RSN time courses taking into account common variance (partial correlation) between frequency bands. The correlation values were Z-transformed, using the mean over all correlation values across subjects as global mean, which resulted in time series of 15 Z-scores for every frequency band (see **Figure 3**). The temporal variance for each RSN and frequency band over the 15 time points was calculated and averaged over subjects (see **Table 1**). To estimate the temporal stability of ECPs within and across subjects, for each RSN and frequency band the Z-scores of the 15 sections were ranked from high to low, and averaged over subjects to visualize inter-subject variance.

SOURCE FREQUENCY POWER CORRELATION

In order to get an indication for the effect of volume conduction and obtain more specific correlation patterns, in five subjects an in-house developed fMRI-informed source model was applied. In combination with a four layer realistic head model it enables to separate the EEG according to the fMRI-RSNs. This new method was tested in a separate study that employs a simple visual stimulation and is further referred to as Integrative Head Model (IHM). It merges FSL analysis, Freesurfer mesh generation (Freesurfer image analysis suite[2]), and a Neuroelectromagnetic Forward Head Modeling Toolbox (NFT) based head model (VER 2.0[3]; Acar and Makeig, 2010), to combine fMRI and EEG in an integrative way (see **Figure 1**). Tissue surface meshes (TSMs) from the individual T1 images are derived using Freesurfer and NFT. The scalp, inner and outer skull as well as brain TSMs are used in the Boundary Element Method (BEM) based forward model as implemented in NFT (Brain/scalp conductivity = 0.33 S/m, Skull conductivity = 0.0132 S/m, CSF conductivity = 1.79 S/m). The source space

[1] www.fmrib.ox.ac.uk/fsl
[2] http://surfer.nmr.mgh.harvard.edu/
[3] http://sccn.ucsd.edu/nft/

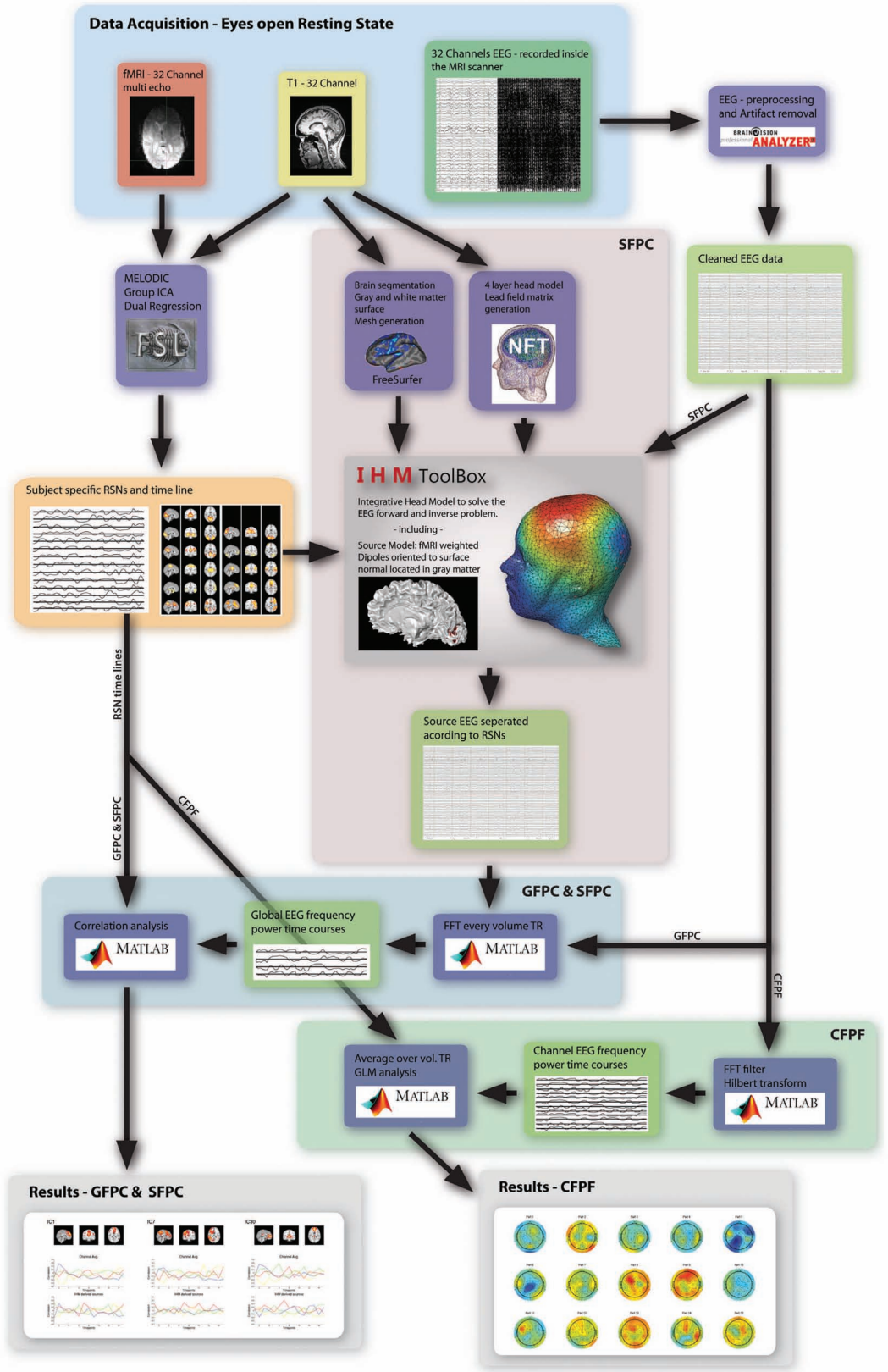

FIGURE 1 | Overview of the three analysis methods used in this study. The highlighted regions and arrows are labeled accordingly.

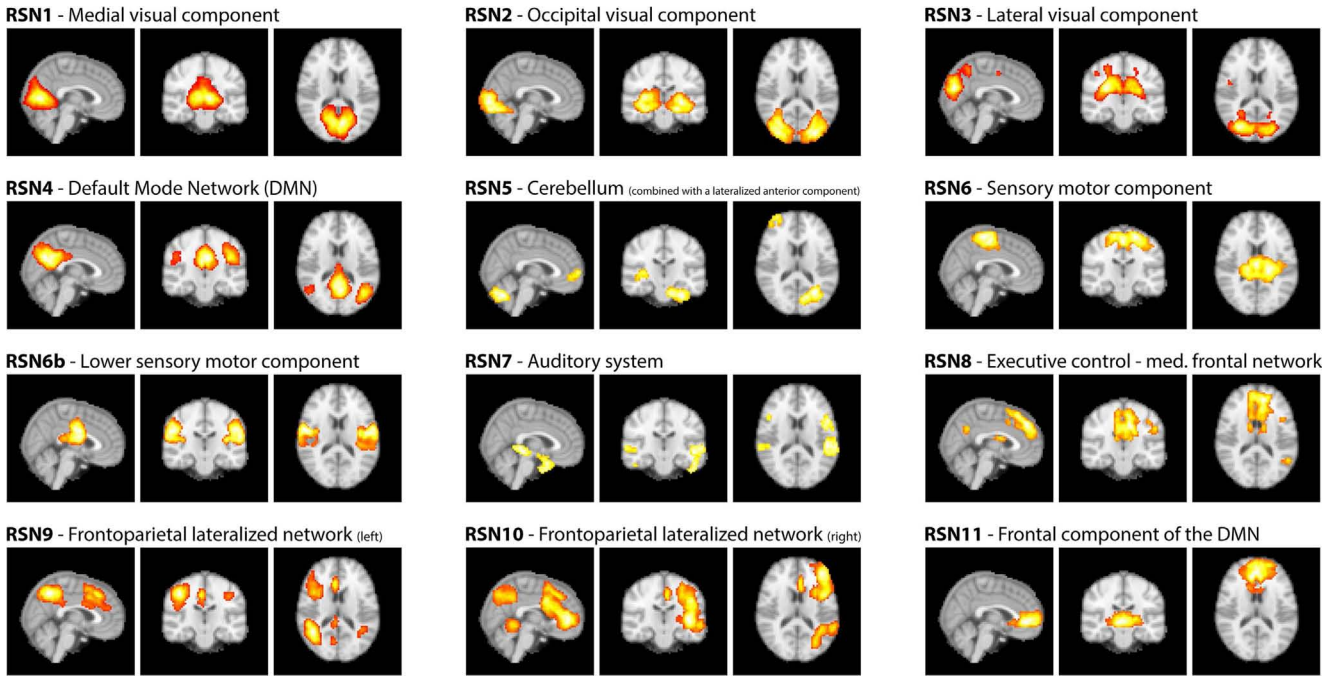

FIGURE 2 | RSNs on group level as maximum intensity projection on the central slices and their classification according to Smith et al. (2009).

is constructed by seeding the cortical sheet with dipoles, the location, and orientation of which is derived from the pial and white matter TSMs. Sources are defined by selecting dipoles according to fMRI RSNs, mapped to the cortical sheet. A source is defined as the weighted vector sum of its active dipoles, where the weights are equal to the Z values of the fMRI activation map at dipole location, and normalized subsequently so that the sum of all weights within one source equals one. These fMRI derived sources are fed into the forward model (in NFT) to calculate the specific lead field matrix (LFM) using an electrode template, which was manually transformed to each subjects head. This specific LFM has a low dimensionality given by the number of sources times number of channel. It is inverted using a Moore–Penrose pseudo inverse and the inverted LFM is used to transform the EEG data to source specific time courses. This results in an EEG time course for each RSN. Furthermore, the same analysis steps as described in Method 1 were applied to the transformed EEG signal. For each of the 15 sections and each frequency band the fMRI derived source frequency power time courses were convolved with the standard SPM5 HRF, partial correlated with their associated RSN time course, and the correlation values were Z-transformed. The variance over the 15 sections was calculated and the Z-scores of the sections were ranked from high to low, to obtain an estimate of the temporal stability.

CHANNEL WISE FREQUENCY POWER FIT

After pre-processing, each channel of the EEG data was band pass filtered in four frequency bands [delta: (2–4) Hz, theta: (4–8) Hz, alpha: (8–12) Hz, and beta: (12–30) Hz] using an FFT-filter (EEGlab). Power time courses were obtained from the filtered data by applying a Hilbert transform and taking the squared magnitude of the resulting signal. To correct for movement, time points where the power estimate exceeded a threshold (seven times the mean of the time course) were set to the average of the time points immediately before and after. Power time courses were segmented in to 2 s segments, according to the TR used in the fMRI acquisition; subsequently each segment was averaged over time and the resulting frequency power time course for each channel were convolved with an HRF (SPM 5). Finally the HRF convolved frequency power time course and the RSN time courses were normalized to have zero mean and a standard deviation of one. Time courses of all ICs (including noise related components) were fitted to each frequency power time course in a separate GLM for every channel. This resulted in an estimate of signal contribution for each RSN to each electrode and EEG frequency band. Plotting these contribution estimates on a scalp plot, here termed independent component expression pattern (ICEP), gives a visual representation of the electrophysiological expression of the RSN for each frequency band. Applying this approach to each of the 15 sections resulted in 15 subsequent ICEPs representing their evolution over time.

In order to obtain a comparable estimate for this method, which gives a spatial distribution as opposed to a point estimate of the other two methods, the temporal stability of the ICEPs was assessed by calculating the spatial correlation between subsequent sections within one subject, RSN and EEG frequency band. For each of those, the correlation values were Z-transformed using bootstrap statistics and the Z-scores were averaged to obtain the mean over all combinations of sections.

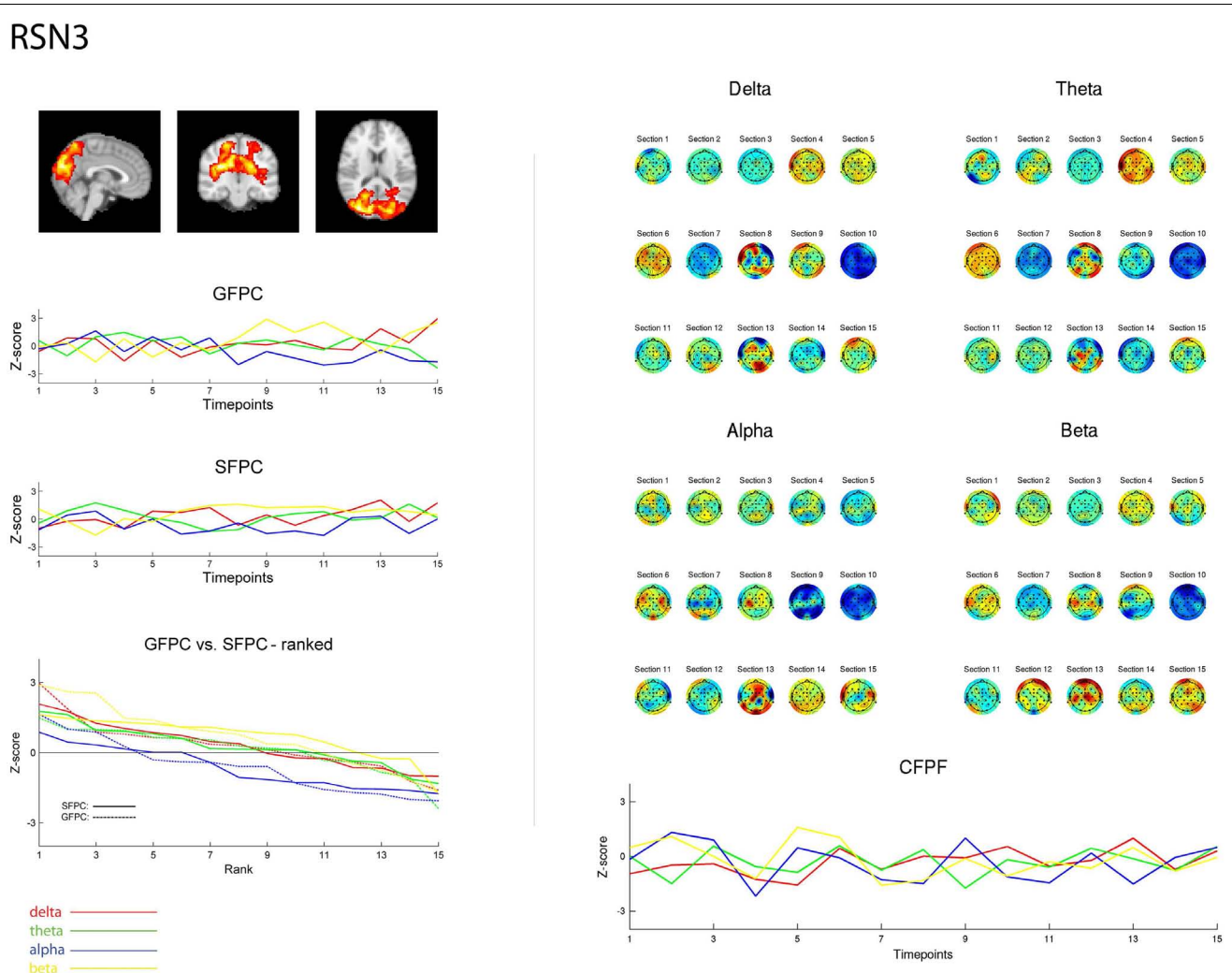

FIGURE 3 | Exemplary representation of data for the three methods used, depicting the results for RSN3 (lateral visual component) of subject 1. On the upper left hand side the subject specific map of RSN3 is plotted as maximum intensity projection on the central slices. The two graphs in the middle show the ECP time courses for each frequency band for GSPC and SFPC, illustrating the temporal variance. In the rank graph below the two methods are plotted on top of each other, depicting the similar variance of SFPC (solid line) and GFPC (dot-dashed line); for both methods alpha shows more negative correlation with BOLD in this visual component. On the upper right hand side the temporal sequence of ICEPs as calculated by CFPF for the four frequency bands is shown. Below the results of the spatial correlation of the subsequent ICEPs are depicted, showing no stable temporal signature.

For the bootstrapped Z-transformation a distribution was generated by repeatedly ($n = 10{,}000$) selecting 15 ICEPs at random from the entire set of ICEPs for that subject applying the same spatial correlation analysis. For each RSN and frequency band the Z-scores of the 15 sections were ranked from high to low, and for group analysis averaged over subjects. Additionally the variance over the 15 sections as well as the average variance over subjects for each RSN and frequency band was calculated.

RESULTS

As reported in Meyer et al. (2013) we found reproducible fMRI RSNs across subjects (see **Figure 2** for a depiction of the RSNs). In this study we observed very large inter-subject and intra-subject variability in the EEG frequency power correlations across all applied analysis methods. **Figure 3** depicts the output of the different methods for one network (RSN3) of subject 1. It is clearly visible that GFPC and SFPC are not stable in time regarding their EEG frequency power correlation with the RSN time courses for all frequency bands. **Figure 4** shows the results of the group analysis for GFPC and **Figure 5** the results for the five subjects analyzed with SFPC. In both figures the group rank plots for four different RSNs show a large temporal variance within a subject – as reflected in the variance of the ranked Z-scores – in the depicted RSNs for all frequency bands. The error bars, indicating the standard deviation across subjects, show the considerable inter-subject variability. The error bars in **Figure 5** are larger compared to those in **Figure 4** which cannot be explained by the smaller number of analyzed subjects as controlled by performing GFPC on the same five subjects as for SFPC. Also note

Table 1 | Group mean temporal variance values (variance across the 15 sections) for GFPC and CFPF, as well as the mean temporal variance values of the same five subjects analyzed with SFPC and GFPC, for each RSN and frequency band.

Freq band	RSN1	RSN2	RSN3	RSN4	RSN5	RSN6	RSN6b	RSN7	RSN8	RSN9	RSN10	RSN11	Average
GFPC MEAN VARIANCE ACROSS ALL SUBJECTS													
delta	1.029	1.080	0.985	1.036	0.857	1.081	1.050	0.805	1.031	0.882	1.091	0.936	**0.989**
theta	0.953	0.913	0.906	0.988	0.871	0.973	0.983	0.825	1.031	0.791	0.877	0.828	**0.912**
alpha	1.186	1.124	1.171	1.121	0.980	1.063	1.148	1.248	1.031	0.995	1.116	1.172	**1.113**
beta	1.193	1.219	0.981	0.961	0.855	1.060	1.124	0.994	1.031	0.943	1.102	1.136	**1.050**
Average	**1.090**	**1.084**	**1.011**	**1.026**	**0.891**	**1.044**	**1.076**	**0.968**	**1.031**	**0.903**	**1.046**	**1.018**	
CFPF MEAN VARIANCE ACROSS ALL SUBJECTS													
delta	0.620	0.501	0.695	0.566	0.667	0.658	0.590	0.731	0.685	0.650	0.635	0.669	**0.639**
theta	0.690	0.751	0.737	0.799	0.660	0.643	0.749	0.717	0.685	0.809	0.693	0.666	**0.717**
alpha	0.897	0.876	0.833	0.819	0.780	0.702	0.702	0.864	0.685	0.698	0.756	0.677	**0.774**
beta	0.798	0.842	0.856	0.759	0.767	0.763	0.808	0.827	0.685	0.743	0.839	0.755	**0.787**
Average	**0.751**	**0.742**	**0.780**	**0.736**	**0.719**	**0.691**	**0.712**	**0.785**	**0.685**	**0.725**	**0.731**	**0.692**	
SFPC VARIANCE FOR FIVE SUBJECTS													
delta	1.077	0.763	1.306	0.884	1.327	1.230	1.140	1.097	0.708	1.067	1.125	0.698	**1.035**
theta	0.587	0.829	1.004	0.791	1.241	1.330	1.018	0.840	0.708	0.889	0.882	0.965	**0.924**
alpha	1.658	1.582	1.366	1.550	0.671	1.508	1.511	1.763	0.708	1.081	1.491	1.095	**1.332**
beta	1.534	1.994	1.933	1.909	0.678	1.331	0.919	1.759	0.708	2.228	2.225	1.493	**1.559**
												Mean variance five subjects	**0.902**
GFPC VARIANCE FOR FIVE SUBJECTS													
delta	1.152	1.124	1.219	1.189	0.972	1.342	1.513	0.849	1.161	0.917	1.242	0.959	**0.987**
theta	0.812	0.944	0.923	1.121	0.923	1.190	1.135	0.867	1.161	0.734	0.949	0.860	**0.838**
alpha	1.448	1.315	1.325	1.253	0.885	1.323	1.503	1.317	1.161	0.990	1.336	1.109	**1.056**
beta	1.209	1.168	1.091	1.137	0.843	1.071	1.049	1.109	1.161	1.064	1.483	1.149	**0.994**
												Mean variance five subjects	**0.968**

The variance values of GFPC and SFPC are comparable since both show the temporal variance of ECPs which represents the direct correlation between frequency power and RSNs. For CFPF the variance values represent the variance of the subsequent spatial correlation of the ICEPs, which is an indirect measure and not directly comparable to the other methods. However the overall huge temporal variance across all methods depicts the temporal instable relation between both modalities.

that, using SFPC the overall observed Z-scores are lower compared to GFPC. Strikingly, one can see in the ranking plots that for the visual components (see RSN2 and RSN3 in **Figures 4** and **5**) alpha power shows a more negative correlation with the BOLD signal whereas delta power shows a more positive correlation. This is also the case for the third visual component (not shown).

On the right hand side of **Figure 3** the temporal sequence of ICEPs as calculated by CFPF for the four frequency bands as well as the results of the spatial correlation of the subsequent ICEPs is depicted. Clearly there is no temporally stable signature in the scalp maps for different sections of the dataset. This can be also observed in the group rank plot in **Figure 6**. The data shown in **Figure 3** as well as the rank plots in **Figures 4**, **5**, and **6** are typical examples for all analyzed subjects, all RSNs, and the four frequency bands examined, respectively. **Table 1** summarizes the results containing the group mean temporal variance across the 15 sections, for each RSN and frequency band for GFPC and CFPF, respectively, as well as for the same five subjects analyzed with SFPC and GFPC.

DISCUSSION

The three methods used in this study were chosen to examine the temporal variability of ECPs from different perspectives with the aim to minimize methodological bias. GFPC is a very conservative approach with fairly little assumptions, taking the global EEG frequency power as independent parameter. However, due to the mixed nature of the EEG signal, volume conduction cannot be excluded, which might cause several sources contributing to a certain correlation and might explain temporally unstable ECPs. SFPC addresses this shortcoming by separating the EEG signal according to the fMRI-RSNs to correlate with, but this also did not result in temporally stable ECPs.

To test for possible methodological bias of GFPC and SFPC as source for the observed variance, we analyzed the data sets using a third approach. CFPF uses the RSN timelines as independent parameters and only uses the HRF to model the relation between the two modalities. Also this approach did not result in temporally stable correlation patterns. While the human HRF itself shows quite complex spatial dependencies (de Munck et al., 2007, 2009), in our correlation analysis it mainly causes a constant time shift and temporal smoothing, therefore it cannot be the reason for temporally instable correlation. Together with the findings of GFPC and SFPC, this leads to the suggestion that the analyzed low dimensional RSNs do not have a temporally stable relationship with EEG frequency band power fluctuations. However, the observed negative correlation of alpha power with the BOLD time courses for the visual components reaches statistical significance within three

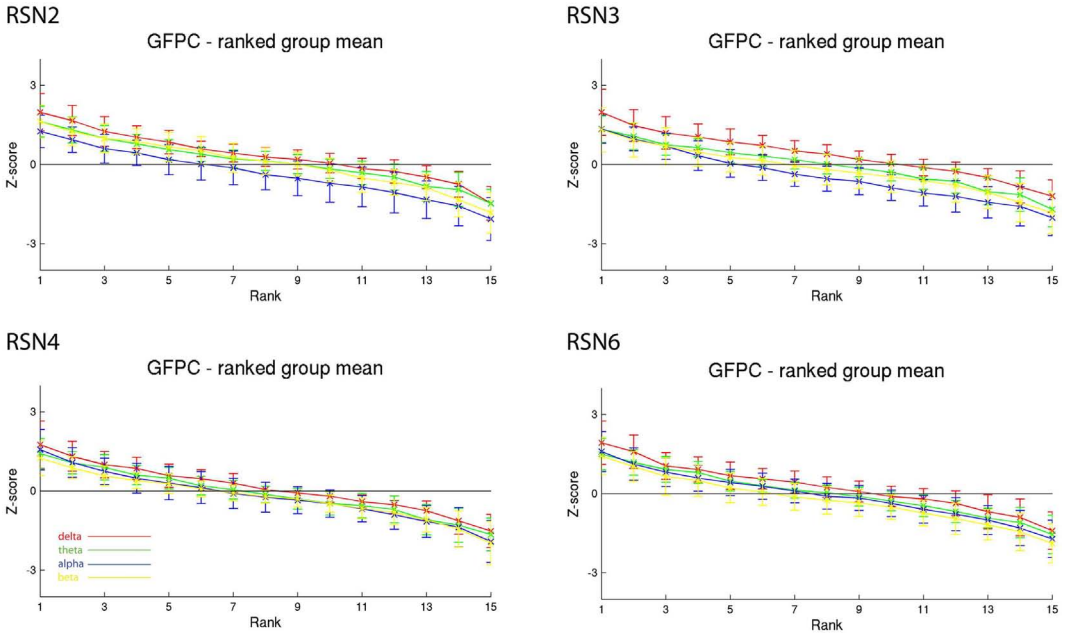

FIGURE 4 | Exemplary group results of RSN2 (occipital visual component), RSN3 (lateral visual component), RSN4 (DMN), and RSN6 (sensory motor component) for GFPC as rank graph showing large temporal variance within a subject. The error bars (standard deviation across subjects) show the considerable inter-subject variability. Clearly alpha power shows a more negative correlation with the BOLD signal whereas delta power shows a more positive correlation for the visual components. Note that the connecting lines are only for visualization purposes.

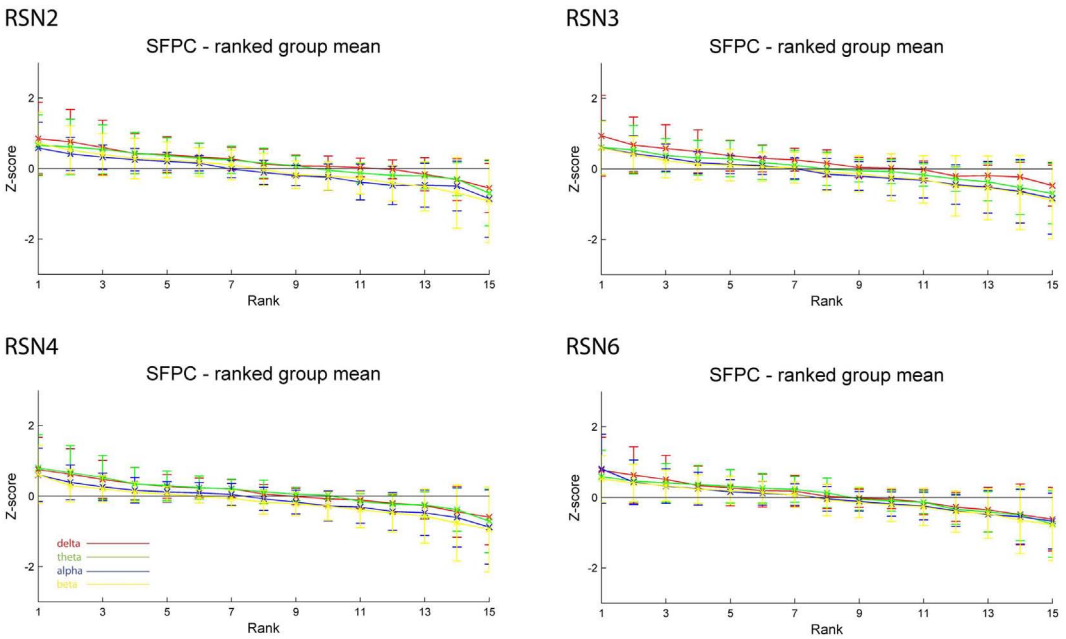

FIGURE 5 | Exemplary results of RSN2 (occipital visual component), RSN3 (lateral visual component), RSN4 (DMN), and RSN6 (sensory motor component) for the five analyzed subjects using SFPC comparable to Figure 4. The error bars (standard deviation across subjects) show the considerable inter-subject variability, which is higher compared to GFPC; note that the *Z*-scores are smaller compared to GFPC. Despite these differences, also when using SFPC, alpha power shows a more negative correlation with the BOLD signal whereas delta power shows a more positive correlation for the visual components. The connecting lines are only for visualization purposes.

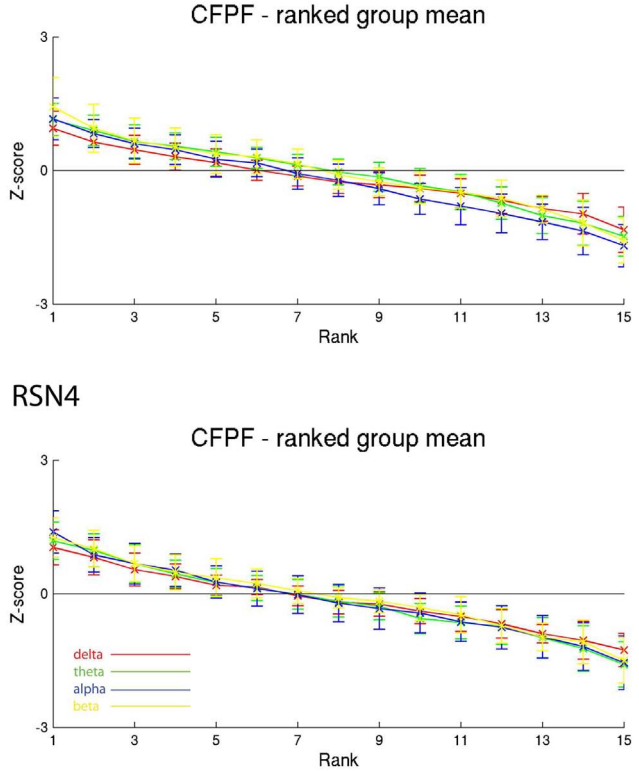

FIGURE 6 | Exemplary group results of RSN2 (occipital visual component) and RSN4 (DMN) for CFPF as rank graph showing no stable temporal signature. The connecting lines are only for visualization purposes.

subjects for GFPC in agreement with previous literature (Goldman et al., 2002; Laufs et al., 2003a, 2006; Goncalves et al., 2006, 2008; Meyer et al., 2013), but does not reach statistical significance for either method on the group level.

One possible explanation for our observation of temporally instable ECPs might be given by Smith et al. (2012), who applied temporal ICA on high dimensional (200 spatial IC components) fMRI-RSNs and reported vast temporal dynamics within the lower dimensional (20–30 spatial IC components) RSNs. As such, there still might be a direct relation between RSNs and EEG frequency band power, but on a smaller spatial scale. However, one would expect a certain temporal stability in the results of SFPC and CFPF even if just a subcomponent of the low dimensional RSN expresses itself in a given EEG frequency band, which was not observed in our study.

An alternative explanation of our results would be, that during RS, frequency-specific power in the lower frequency bands of the EEG is not linked to changes in neuronal activity, reflected in changed oxygen consumption as measured by BOLD fMRI. This would also be supported by recent animal studies, e.g., Schölvinck et al. (2010), that show no stable correlation for the lower frequency bands in EEG with BOLD fMRI particularly in eyes open RS.

The observation that using SFPC reduced the overall observed Z-scores compared to GFPC gives rise to the assumption that the studied RSN characteristics are not related. However, one has to consider the potential limitation of the head model as used in our study; (a) the spatial resolution of the head model is limited by the relatively low number of electrodes and (b) its reduced spatial specificity in the context of spatially extended sources like RSNs, as we assume a concurrent temporal behavior within the whole source.

We therefore conclude that the correlation between lower frequency band power in EEG and BOLD RSNs time courses is at least temporally instable or even absent in eyes open RS.

ACKNOWLEDGMENTS

Financial support from Provincie Gelderland and Overijssel, as well as from the ministry of economical affairs in the framework of the project "Pieken in de Delta – ViP Brainnetworks" is acknowledged. We gratefully acknowledge technical support from ANT.

REFERENCES

Acar, Z., and Makeig, S. (2010). Neuroelectromagnetic forward head modeling toolbox. *J. Neurosci. Methods* 190, 258–270. doi:10.1016/j.jneumeth.2010.04.031

Allen, P. J., Josephs, O., and Turner, R. (2000). A method for removing imaging artifact from continuous EEG recorded during functional MRI. *Neuroimage* 12, 230–239. doi:10.1006/nimg.2000.0599

Allen, P. J., Polizzi, G., Krakow, K., Fish, D. R., and Lemieux, L. (1998). Identification of EEG events in the MR scanner: the problem of pulse artifact and a method for its subtraction. *Neuroimage* 8, 229–239. doi:10.1006/nimg.1998.0361

Biswal, B., Yetkin, F. Z., Haughton, V. M., and Hyde, J. S. (1995). Functional connectivity in the motor cortex of resting human brain using echo-planar MRI. *Magn. Reson. Med.* 34, 537–541. doi:10.1002/mrm.1910340409

Cordes, D., Haughton, V. M., Arfanakis, K., Carew, J. D., Turski, P. A., Moritz, C. H., et al. (2001). Frequencies contributing to functional connectivity in the cerebral cortex in "resting-state" data. *AJNR Am. J. Neuroradiol.* 22, 1326–1333.

Dale, A. M., Liu, A. K., Fischl, B. R., Buckner, R. L., Belliveau, J. W., Lewine, J. D., et al. (2000). Dynamic statistical parametric mapping: combining fMRI and MEG for high-resolution imaging of cortical activity. *Neuron* 26, 55–67. doi:10.1016/S0896-6273(00)81138-1

Damoiseaux, J. S., Rombouts, S. A., Barkhof, F., Scheltens, P., Stam, C. J., Smith, S. M., et al. (2006). Consistent resting-state networks across healthy subjects. *Proc. Natl. Acad. Sci. U.S.A.* 103, 13848–13853. doi:10.1073/pnas.0601417103

De Luca, M., Beckmann, C. F., De Stefano, N., Matthews, P. M., and Smith, S. M. (2006). fMRI resting state networks define distinct modes of long-distance interactions in the human brain. *Neuroimage* 29, 1359–1367. doi:10.1016/j.neuroimage.2005.08.035

de Munck, J. C., Gonçalves, S. I., Huijboom, L., Kuijer, J. P., Pouwels, P. J., Heethaar, R. M., et al. (2007). The hemodynamic response of the alpha rhythm: an EEG/fMRI study. *Neuroimage* 35, 1142–1151. doi:10.1016/j.neuroimage.2007.01.022

de Munck, J. C., Gonçalves, S. I., Mammoliti, R., Heethaar, R. M., and Lopes da Silva, F. H. (2009). Interactions between different EEG frequency bands and their effect on alpha-fMRI correlations. *Neuroimage* 47, 69–76. doi:10.1016/j.neuroimage.2009.04.029

Feige, B., Scheffler, K., Esposito, F., Di Salle, F., Hennig, J., and Seifritz, E. (2005). Cortical and subcortical correlates of electroencephalographic alpha rhythm modulation. *J. Neurophysiol.* 93, 2864–2872. doi:10.1152/jn.00721.2004

Filippini, N., MacIntosh, B. J., Hough, M. G., Goodwin, G. M., Frisoni, G. B., Smith, S. M., et al. (2009). Distinct patterns of brain activity in young carriers of the APOE-epsilon4 allele. *Proc. Natl. Acad. Sci. U.S.A.* 106, 7209–7214. doi:10.1073/pnas.0811879106

Fox, M. D., Snyder, A. Z., Vincent, J. L., Corbetta, M., Van Essen, D. C., and Raichle, M. E. (2005). The human brain is intrinsically organized into dynamic, anticorrelated functional networks. *Proc. Natl. Acad. Sci. U.S.A.* 102, 9673–9678. doi:10.1073/pnas.0504136102

Goldman, R. I., Stern, J. M., Engel, J. Jr., and Cohen, M. S. (2002). Simultaneous EEG and fMRI of the alpha rhythm. *Neuroreport* 13, 2487–2492. doi:10.1097/00001756-200212200-00022

Goncalves, S. I., Bijma, F., Pouwels, P. J., Jonker, M., Kuijer, J. P., Heethaar, R. M., et al. (2008). A data and model-driven approach to explore inter-subject variability of resting-state brain activity using EEG-fMRI. *IEEE J. Sel. Top. Signal Process.* 2, 944–953. doi:10.1109/JSTSP.2008.2009082

Goncalves, S. I., de Munck, J. C., Pouwels, P. J., Schoonhoven, R., Kuijer, J. P. A., Maurits, N. M., et al. (2006). Correlating the alpha rhythm to BOLD using simultaneous EEG/fMRI: inter-subject variability. *Neuroimage* 30, 203–213. doi: 10.1016/j.neuroimage.2005.09.062

Greicius, M. D., Krasnow, B., Reiss, A. L., and Menon, V. (2003). Functional connectivity in the resting brain: a network analysis of the default mode hypothesis. *Proc. Natl. Acad. Sci. U.S.A.* 100, 253–258. doi:10.1073/pnas.0135058100

Janssen, R. J., Meyer, M. C., Beckmann, C. F., and Barth, M. (2012). "A framework to estimate electrophysiological dynamics of fMRI derived sources," in *Third Biennial Conference on Resting State Brain Connectivity*, Magdeburg, Poster 46.

Jenkinson, M., Beckmann, C. F., Behrens, T. E., Woolrich, M. W., and Smith, S. M. (2012). FSL. *Neuroimage* 62, 782–790. doi:10.1016/j

Laufs, H., Holt, J. L., Elfont, R., Krams, M., Paul, J. S., Krakow, K., et al. (2006). Where the BOLD signal goes when alpha EEG leaves. *Neuroimage* 31, 1408–1418. doi:10.1016/j.neuroimage.2006.02.002

Laufs, H., Kleinschmidt, A., Beyerle, A., Eger, E., Salek-Haddadi, A., Preibisch, C., et al. (2003a). EEG-correlated fMRI of human alpha activity. *Neuroimage* 19, 1463–1476. doi:10.1016/S1053-8119(03)00286-6

Laufs, H., Krakow, K., Sterzer, P., Eger, E., Beyerle, A., Salek-Haddadi, A., et al. (2003b). Electroencephalographic signatures of attentional and cognitive default modes in spontaneous brain activity fluctuations at rest. *Proc. Natl. Acad. Sci. U.S.A.* 100, 11053–11058. doi:10.1073/pnas.1831638100

Lowe, M. J., Dzemidzic, M., Lurito, J. T., Mathews, V. P., and Phillips, M. D. (2000). Correlations in low-frequency BOLD fluctuations reflect cortico-cortical connections. *Neuroimage* 12, 582–587. doi:10.1006/nimg.2000.0654

Mantini, D., Perrucci, M. G., Del Gratta, C., Romani, G. L., and Corbetta, M. (2007). Electrophysiological signatures of resting state networks in the human brain. *Proc. Natl. Acad. Sci. U.S.A.* 104, 13170–13175. doi:10.1073/pnas.0700668104

Meyer, M. C., van Oort, E. S., and Barth, M. (2013). Electrophysiological correlation patterns of resting state networks in single subjects: a combined EEG-fMRI study. *Brain Topogr.* 26, 98–109. doi:10.1007/s10548-012-0235-0

Moosmann, M., Ritter, P., Krastel, I., Brink, A., Thees, S., Blankenburg, F., et al. (2003). Correlates of alpha rhythm in functional magnetic resonance imaging and near infrared spectroscopy. *Neuroimage* 20, 145–158. doi:10.1016/S1053-8119(03)00344-6

Ou, W., Nummenmaa, A., Ahveninen, J., Belliveau, J. W., Hämäläinen, M. S., and Golland, P. (2010). Multimodal functional imaging using fMRI-informed regional EEG/MEG source estimation. *Neuroimage* 52, 97–108. doi:10.1016/j.neuroimage.2010.03.001

Poser, B. A., Versluis, M. J., Hoogduin, J. M., and Norris, D. G. (2006). BOLD contrast sensitivity enhancement and artifact reduction with multiecho EPI: Parallel-acquired inhomogeneity-desensitized fMRI. *Magn. Reson. Med.* 55, 1227–1235. doi:10.1002/mrm.20900

Scheeringa, R., Bastiaansen, M. C., Petersson, K. M., Oostenveld, R., Norris, D. G., and Hagoort, P. (2008). Frontal theta EEG activity correlates negatively with the default mode network in resting state. *Int. J. Psychophysiol.* 67, 242–251. doi:10.1016/j.ijpsycho.2007.05.017

Schölvinck, M. L., Maier, A., Ye, F. Q., Duyn, J. H., and Leopold, D. A. (2010). Neural basis of global resting-state fMRI activity. *Proc. Natl. Acad. Sci. U.S.A.* 107, 10238–10243. doi:10.1073/pnas.0913110107

Smith, S. M., Fox, P. T., Miller, K. L., Glahn, D. C., Fox, P. M., Mackay, C. E., et al. (2009). Correspondence of the brain's functional architecture during activation and rest. *Proc. Natl. Acad. Sci. U.S.A.* 106, 13040–13045. doi:10.1073/pnas.0905267106

Smith, S. M., Jenkinson, M., Woolrich, M. W., Beckmann, C. F., Behrens, T. E., Johansen-Berg, H., et al. (2004). Advances in functional and structural MR image analysis and implementation as FSL. *Neuroimage* 23, 208–219. doi:10.1016/j.neuroimage.2004.07.051

Smith, S. M., Miller, K. L., Moeller, S., Xu, J., Auerbach, E. J., Woolrich, M. W., et al. (2012). Temporally-independent functional modes of spontaneous brain activity. *Proc. Natl. Acad. Sci. U.S.A.* 109, 3131–3136. doi:10.1073/pnas.1121329109

Woolrich, M. W., Jbabdi, S., Patenaude, B., Chappell, M., Makni, S., Behrens, T., et al. (2009). Bayesian analysis of neuroimaging data in FSL. *Neuroimage* 45, 173–186. doi:10.1016/j.neuroimage.2008.10.055

Conflict of Interest Statement: The authors declare that the research was conducted in the absence of any commercial or financial relationships that could be construed as a potential conflict of interest.

Received: 20 January 2013; accepted: 10 June 2013; published online: 25 June 2013.

Citation: Meyer MC, Janssen RJ, Van Oort ESB, Beckmann CF and Barth M (2013) The quest for EEG power band correlation with ICA derived fMRI resting state networks. Front. Hum. Neurosci. 7:315. doi: 10.3389/fnhum.2013.00315

frontiers in
HUMAN NEUROSCIENCE

METHODS ARTICLE
published: 23 May 2013
doi: 10.3389/fnhum.2013.00214

Time course based artifact identification for independent components of resting-state fMRI

Christian Rummel[1]*†, Rajeev Kumar Verma[1†], Veronika Schöpf[2], Eugenio Abela[1,3], Martinus Hauf[1,4], José Fernando Zapata Berruecos[5,6] and Roland Wiest[1]

[1] Support Center for Advanced Neuroimaging, University Institute for Diagnostic and Interventional Neuroradiology, Inselspital – Bern University Hospital, University of Bern, Switzerland
[2] Division of Neuro- and Musculoskeletal Radiology, Department of Radiology, Medical University of Vienna, Vienna, Austria
[3] Department of Neurology, Inselspital – Bern University Hospital, University of Bern, Switzerland
[4] Klinik Bethesda Tschugg, Bern, Switzerland
[5] Universidad Pontificia Bolivariana, Medellín, Columbia
[6] Instituto Neurologico de Antioquia, Medellín, Columbia

Edited by:
Simon D. Robinson, Medical University of Vienna, Austria

Reviewed by:
Aapo Hyvärinen, University of Helsinki, Finland
Pamela Douglas, University of California Los Angeles, USA

***Correspondence:**
Christian Rummel, Support Center for Advanced Neuroimaging, University Institute for Diagnostic and Interventional Neuroradiology, Inselspital – Bern University Hospital, University of Bern, Freiburgstrasse 4, 3010 Bern, Switzerland.
e-mail: crummel@web.de

†Christian Rummel and Rajeev Kumar Verma have contributed equally to this work.

In functional magnetic resonance imaging (fMRI) coherent oscillations of the blood oxygen level-dependent (BOLD) signal can be detected. These arise when brain regions respond to external stimuli or are activated by tasks. The same networks have been characterized during wakeful rest when functional connectivity of the human brain is organized in generic resting-state networks (RSN). Alterations of RSN emerge as neurobiological markers of pathological conditions such as altered mental state. In single-subject fMRI data the coherent components can be identified by blind source separation of the pre-processed BOLD data using spatial independent component analysis (ICA) and related approaches. The resulting maps may represent physiological RSNs or may be due to various artifacts. In this methodological study, we propose a conceptually simple and fully automatic time course based filtering procedure to detect obvious artifacts in the ICA output for resting-state fMRI. The filter is trained on six and tested on 29 healthy subjects, yielding mean filter accuracy, sensitivity and specificity of 0.80, 0.82, and 0.75 in out-of-sample tests. To estimate the impact of clearly artifactual single-subject components on group resting-state studies we analyze unfiltered and filtered output with a second level ICA procedure. Although the automated filter does not reach performance values of visual analysis by human raters, we propose that resting-state compatible analysis of ICA time courses could be very useful to complement the existing map or task/event oriented artifact classification algorithms.

Keywords: ICA, resting-state networks, fMRI, BOLD, artifacts, group studies

1. INTRODUCTION

Functional magnetic resonance imaging (fMRI) technologies have nowadays been implemented into various clinical applications, e.g., pre-surgical mapping of eloquent areas of the brain before resective surgery in brain tumors and epilepsy (Gutbrod et al., 2012; Kollndorfer et al., 2013). The basic principle of fMRI lies in the statistical testing of changes in the blood oxygen level-dependent (BOLD) signal induced by either a given task or correlations with endogenous stimuli in the brain, as interictal epileptiform discharges (Hauf et al., 2012). Whilst the analysis of fMRI data is most frequently univariate, i.e., by paired categorical analysis using statistical parametric mapping, recent attempts have shifted toward understanding how multiple brain regions interact with one another. From a theoretical point of view, distributed networks are obscured by categorical analysis because subtraction methods are univariate, i.e., image voxels are analyzed independently. Categorical analysis thus has several limitations. It may overlook parts of a network that do not attain the defined level of significance, or vice versa, may resemble activations incidental to the studied phenomenon. Covariance analysis, in contrast, determines voxels of the brain that exhibit BOLD signal fluctuations correlated in time at low frequencies ($\lesssim 0.1$ Hz). This type of functional connectivity resembles networks of brain areas that reveal synchronized neural activity among topographically distinct regions.

Recently, a set of 23 independent networks has been identified in a sample of 180 healthy subjects (Doucet et al., 2011). They correspond to the so-called intrinsic and extrinsic systems, which are associated with internal- and external-oriented processing, respectively. The most frequently reported intrinsic module is the default mode network (DMN). These brain areas are typically active during rest and deactivated during tasks requiring attention such as visuo-spatial tasks (Greicius et al., 2003). The extrinsic modules include parietal the sensori-motor network (SMN), the frontal attention network (FAN), the visual (VIN), and auditory networks (AUN) as well as the working memory network (WMN).

The analysis of covariance in the BOLD signal is nowadays most frequently performed by independent component analysis (ICA). While region of interest (ROI) based approaches have focused on *a priori* assumptions, i.e., the presence of functional connectivity

is assumed from previous hypotheses, data-driven approaches as ICA offer the advantage to analyze coherent physiological signals on the whole brain level. Several implementations, most frequently based on the FastICA algorithm (Hyvärinen and Oja, 1997; Hyvärinen, 1999), have been provided to disentangle mixed signals into mutually least dependent spatial source signals that represent different networks following a similar temporal pattern. A frequent assumption is that N^{src} spatial "sources" $\mathbf{s}$ are linearly mixed by a constant $N^{\mathrm{obs}} \times N^{\mathrm{src}}$ matrix $\mathbf{A}$ to yield the N^{obs} "observations" $\mathbf{x}$ in the following way:

$$\mathbf{x} = \mathbf{A} \cdot \mathbf{s} \tag{1}$$

both, $\mathbf{A}$ and $\mathbf{s}$ are *a priori* unknown. Here and in the sequel $\mathbf{s}$ and $\mathbf{x}$ are matrix notations for s_{li} with $l = 1, \ldots, N^{\mathrm{src}}$ and x_{ti} with $t = 1, \ldots, N^{\mathrm{obs}}$, respectively. The index $i = 1, \ldots, N^{\mathrm{spc}}$ with $N^{\mathrm{spc}} \gg N^{\mathrm{src}}$, N^{obs} numbers the spatial degrees of freedom and will be omitted from now on to ease the notation. In ICA and related techniques the mixing matrix $\mathbf{A}$ is estimated by the requirement that the s_l become as independent as possible.

In spatial single-subject ICA the columns of the "mixing matrix" $\mathbf{A}$ of equation (1) represent the time courses of the independent components (IC) and the matrix elements A_{tl} inform how strongly and with which sign the source s_l contributes to the observation x_t. At a group level different approaches to ICA have been developed, either performing a secondary analysis on preselected single-subject ICs or methods in which raw single-subject data is integrated before analysis (for reviews, see Guo and Pagnoni, 2008; Calhoun et al., 2009). This includes group ICA approaches in which single-subject data is concatenated in time (Calhoun et al., 2001; Beckmann et al., 2005; Schöpf et al., 2010b) or space (Svensén et al., 2002; Schmithorst and Holland, 2004) or by using a three-dimensional tensor representing spatial, temporal, and subject-specific loadings for each group component (Beckmann and Smith, 2005). Group ICA methods after single-subject ICA have been introduced by selecting the single-subject ICs by visual inspection (Harrison et al., 2008), based on a spatial template (Calhoun et al., 2008), or based on the spatial correlation of the single-subject maps (Esposito et al., 2005; De Luca et al., 2006; Schöpf et al., 2010a, 2011; Varoquaux et al., 2010). A different technique that deserves mentioning in this context is "IC dictionary" creation using "bagged clustering" over a large number of single-subject ICs (Anderson et al., 2011). This approach first reduces dimensionality by projection onto anatomical ROIs and subsequently pools the data by k-means clustering.

By construction the ICs of fMRI data are not necessarily related to the BOLD effect. Rather, all kinds of physiological or non-physiological artifacts may appear in ICs. As their removal reduces the noise level in the data, several attempts to automated artifact classification of ICs have been undertaken. In McKeown (2000) a hybrid approach was proposed that combined data-driven spatial ICA with task-related a priory hypotheses that could be analyzed by the general linear model (GLM). IC maps explained by task-related head motion were identified in Kochiyama et al. (2005) by statistically examining task-related intensity and variance changes of the BOLD signals. Both methods require the presence of tasks to enable classification. In contrast, the method proposed by Thomas et al. (2002) used the power spectrum of IC time courses to classify them as candidates for white or structured noise (physiological fluctuations). Perlbarg et al. (2007) used manually defined regions of interest (ROIs) to define typical time courses of structured noise in fMRI data, which were used as regressors for the BOLD signals.

Also spatial features have been employed for artifact identification. A combination of six temporal and spatial features was used in Tohka et al. (2008) to classify ICs from fMRI data in event related and block design. Motivated by typical "IC fingerprints" (De Martino et al., 2007) in Sui et al. (2009) spatial correlation with tissue class templates as well as spatial structure and information content was used to identify artifactual IC maps.

So far, most attempts to automated IC classification were either designed for task/event related fMRI data or rely on spatial information. To our knowledge, automated time course based artifact identification suitable for resting-state fMRI data has not yet been undertaken. In the present contribution we propose a conceptually simple algorithm for unsupervised identification (and potentially removal) of artifactual single-subject ICs, which is entirely based on the time courses. After training on six datasets the algorithm is tested in 29 data sets and classification accuracy is compared to visual rating. Thereafter, the filtered data is subjected to a secondary ICA analysis to illustrate the impact of artifactual ICs on group studies.

2. MATERIALS AND METHODS

2.1. SUBJECTS AND DATA ACQUISITION

The data used in the present study consisted of 35 subjects that participated as healthy volunteers in a multiple sclerosis study. The study was approved by the ethics commission of the Canton of Bern. Demographics were chosen to match those of multiple sclerosis patients presenting at the neurological outpatient clinic of the Inselspital in Bern, see **Table 1**.

All subjects underwent T2*-weighted functional and T1-weighted high resolution structural MR imaging. Imaging was performed at the University Institute of Diagnostic and Interventional Neuroradiology, Inselspital, Bern (Rajeev Kumar Verma) on a 3-T Siemens Scanner (Magnetom Verio®, Siemens Medical Solutions, Erlangen, Germany) using a 32-channel head coil. Head motion was minimized by fitting foam pads between head and coil. Scanner noise was reduced by using ear plugs.

Resting-state functional images were acquired with a standard EPI sequence and analyzed in detail. In two groups BOLD data were registered with the same MR parameters: repetition time (TR) 1980 ms; echo time (TE) 30 ms; flip angle 90°; inversion time(TI) 910 ms; slice thickness 4 mm; field of view (FOV) 192 mm (matrix size 192 × 192); voxel size 3.0 mm × 3.0 mm × 4.0 mm. The "training data set" and "test data set" consisted of $N^{\mathrm{subj}} = 6$ and $N^{\mathrm{subj}} = 29$ subjects, respectively, where $N^{\mathrm{obs}} = 270$ and $N^{\mathrm{obs}} = 300$ volumes were registered. The shorter data sets were acquired earlier than the longer ones, i.e., the groups are not randomized. Notwithstanding, age, gender, and handedness distributions were not significantly different between the groups, see **Table 1**.

For anatomical co-registration three-dimensional T1-weighted images were obtained using the Modified Driven Equilibrium Fourier Transformation (MDEFT) sequence. The acquisition

Table 1 | Demography of subject groups.

		Training set $N^{subj} = 6$ $N^{obs} = 270$	Test set $N^{subj} = 29$ $N^{obs} = 300$	Difference between sets
Age (years)	Range	26–42	21–61	$p_U = 0.69$
	M	32.3	35.3	
	SD	6.7	11.0	
Gender	Male/female	1/5	8/21	$p_\chi = 0.72$
Handedness	Right/ ambidexter/left	6/0/0	27/2/0	$p_\chi = 0.36$

Test for equal median age: Mann-Whitney-Wilcoxon U-test. Test for equal gender and handedness distribution: χ^2-test with one (gender) and two (handedness) degrees of freedom.

was performed with the following parameters: TR = 7.92 ms; TE = 2.48 ms; flip angle = 16°; slices per slab = 176; slice thickness 1 mm; FOV = 256 mm (matrix size = 256 × 256), with a resulting voxel size of 1.0 mm × 1.0 mm × 1.0 mm.

2.2. DATA PRE-PROCESSING

Pre-processing and analysis of resting-state fMRI data was performed independently for each subject using the freely available FMRIB's Software Library FSL (http://www.fmrib.ox.ac.uk/fsl/), version 4.1.7. Analysis was done on a Quadcore computer with Intel Xenon®CPU at 2.4 GHz and 12 GB memory under the 64-bit version of Ubuntu Linux 12.04 LTS.

The pre-processing stream was as follows: Motion correction was carried out using the MCFLIRT tool and slice timing was corrected. The BET tool was used for brain extraction in structural and functional MR data and spatial smoothing with a 6-mm FWHM kernel was performed for functional data. The time constant for the high pass filter was set to 111 s, leaving only frequencies $f > 0.009$ Hz in the pre-processed BOLD time course.

fMRI data were first registered to each subject's high resolution structural images (MDEFT). Subsequently, the BOLD data were registered to the standard MNI space. For both registration steps linear transformations with 12 degrees of freedom (translation, rotation, scaling, sheering) were used.

2.3. SINGLE-SUBJECT ICA

Least dependent components in the BOLD maps were estimated for each subject separately. The number of single-subject sources N_n^{src} was estimated from the data for each subject by maximizing the Laplacian estimate to the Bayesian evidence of the model order (Minka, 2000; Beckmann and Smith, 2004). After dimensionality reduction by principal component analysis (PCA) single-subject ICA was performed using probabilistic ICA (Beckmann and Smith, 2004) as implemented in version 3.10 of FSL's MELODIC toolbox.

2.3.1. Supervised post-processing

The MELODIC output includes a collection of spatial maps, some of which represent physiological RSNs and some of which represent artifacts. For visual artifact identification the following criteria were applied by three raters independently (Christian Rummel, Eugenio Abela, and José Fernando Zapata Berruecos), both in the training as well as in the test data set. Maps were marked as obvious artifacts if the activations were confined:

(a) to the boundaries of the brain,
(b) to the cerebral ventricles,
(c) to the inter-hemispheric scission, or
(d) to less than three slices.

In addition, maps were marked as artifacts:

(e) if the activations were distributed irregularly over the whole parenchyma without clear regions of accumulation,
(f) if the time course resembled one or several motion correction parameters, or
(g) if the power spectrum of the time course was extraordinarily broad or narrow.

After independent rating the raters agreed on obvious artifact ICs and potential RSNs in a discussion session. The rating sensitivities:

$$\mathrm{sens}_n = \frac{\mathrm{TP}_n}{\mathrm{TP}_n + \mathrm{FN}_n}\,, \tag{2}$$

specificities

$$\mathrm{spec}_n = \frac{\mathrm{TN}_n}{\mathrm{FP}_n + \mathrm{TN}_n} \tag{3}$$

and accuracies

$$\mathrm{acc}_n = \frac{\mathrm{TP}_n + \mathrm{TN}_n}{\mathrm{TP}_n + \mathrm{FN}_n + \mathrm{FP}_n + \mathrm{TN}_n} = \frac{\mathrm{TP}_n + \mathrm{TN}_n}{N_n^{\mathrm{src}}} \tag{4}$$

were calculated subject-wise. In equations (2–4) TP_n and TN_n denote the numbers of true positives and true negatives in subject $n = 1, \ldots, N^{\mathrm{subj}}$ (i.e., the number of single-subject ICs rated the same way by an individual rater and in the agreement of all raters). Similarly, FP_n and FN_n are the numbers of false positives and false negatives (i.e., the number of single-subject ICs with disagreement).

2.3.2. Automated post-processing

The problem of automatic classification of ICs has been approached in De Martino et al. (2007), Tohka et al. (2008) by subjecting multi-dimensional feature vectors to support vector machines or global decision trees, respectively. Here, we do not aim at full IC classification. Rather, our objective is automated identification of single-subject ICs that are obviously artifacts. To this end we implemented two simple time course based criteria in an automatic filtering process:

(I) A GLM was fitted to the time course s_l of each single-subject IC with the motion correction parameters as regressors (three translations, three rotations). If the significance p_{moco} of Pearson's correlation coefficient between s_l and the GLM prediction was smaller than a threshold $p_{\mathrm{moco}}^{\mathrm{crit}} \in [0, 1]$ the component was discarded as probable artifact of residual subject motion.

(II) The spectral power density of the IC time courses s_l was estimated and filtered in the frequency band $0.009 < f < 0.08$ Hz, where RSN associated spontaneous BOLD fluctuations are expected (Biswal et al., 1995; Weissenbacher et al., 2009; Schöpf et al., 2010a). If the null hypothesis that the original and the filtered power distribution are compatible was rejected on a significance threshold $p_{\text{pow}}^{\text{crit}} \in [0, 1]$ by a Kolmogorov-Smirnov test (Siegel, 1956) the corresponding components were also interpreted as artifacts.

The criteria (I) and (II) of the automated filter represent a quantitative formulation of the time course based visual criteria (f) and (g) above. No information about the spatial distribution of activations was used.

Both thresholds $p_{\text{moco}}^{\text{crit}}$ and $p_{\text{pow}}^{\text{crit}}$ were chosen in a data driven way by optimizing the agreement between automated and visual analysis of single-subject IC maps in the training set. To this end the parameter space was systematically scanned in $10^{-50} \leq p_{\text{moco}}$, $p_{\text{pow}} \leq 10^{-1}$ and subject-wise agreement between automatic and visual rating (agreement of all raters) was assessed by the accuracy of the discriminator as defined in equation (4). The mean $\langle \text{acc}_n \rangle$ over the single-subject accuracies of the filter defined in equation (4) was maximized. As opposed to maximization of the global accuracy:

$$\text{acc}_{\text{glob}} = \frac{\sum_n \text{TP}_n + \sum_n \text{TN}_n}{\sum_n N_n^{\text{src}}} \tag{5}$$

of all single-subject ICs from all subjects this prevents over-tuning the parameters for training subjects with large N_n^{src}. The same thresholds $p_{\text{moco}}^{\text{crit}}$ and $p_{\text{pow}}^{\text{crit}}$ were subsequently used in the test set.

2.4. SIMPLE APPROACH TO GROUP ICA

Group ICA was performed by concatenating single-subject IC maps from all N^{subj} subjects in time and performing a secondary ICA on the joint data set using MELODIC. As in the single-subject case we estimated the number of group ICs using the Laplacian approximation to the model order (Minka, 2000; Beckmann and Smith, 2004). Comparing results for filtered and unfiltered single-subject ICs we briefly illustrate the potential impact of artifactual ICs on group ICA studies.

2.5. STATISTICAL EVALUATION

Statistical analysis was performed using Matlab 7.0.4 (MathWorks, Natick, MA, USA). As for our group sizes most often at least one distribution is small ($N < 10$) significance of different medians between k distributions was tested non-parametrically by the Mann-Whitney-Wilcoxon U-test for $k = 2$ and by the Kruskal-Wallis test for $k > 2$ (Siegel, 1956). Difference in discrete distributions was tested by the χ^2-test (Siegel, 1956). As significance level we chose $\alpha = 0.01$ for all tests. Results were interpreted as "marginally significant" or "trends" if $p < 0.05$.

3. RESULTS

3.1. SINGLE-SUBJECT ICA

In **Figure 1** we illustrate the results for the DMN exemplarily in two subjects. **Figures 1A,E** give an overview of the typical between-subject variability of the representation of the functional IC maps on the individual anatomies. The corresponding time courses s_l are displayed in **Figures 1B,F** and the best fit of a GLM with the six motion correction parameters as regressors in **Figures 1C,G**. Correlation is significant in both subjects. **Figures 1D,H** show the power spectra of the DMN time courses. Filtering in the range $0.009 < f < 0.08$ Hz (shaded in light blue) leads to significant changes of the power distribution.

Two obviously artifactual ICs are shown in **Figure 2**. Data was taken from the same subject as the right column in **Figure 1**. The IC of the left column is clearly related to residual subject motion, leading to a much smaller value p_{moco} than observed in **Figure 1B**. The activations of the IC map were mainly confined to the brain boundaries (**Figure 1A**). Other examples of this artifact type are characterized by typical activation "halos" in axial slices. In contrast to p_{moco} the power related p_{pow} is in the same range as for the DMNs in **Figure 1**. A typical power related artifact IC is displayed in the right column. Correlation between the time course and the GLM of the motion correction parameters is the same as in **Figure 1**. However, the time course has much more power in large frequencies (see **Figures 1F,H**), leading to a much smaller value of p_{pow}. In contrast to the motion related artifact here the IC map is much less suspicious on its own (**Figure 1E**). However, the asymmetry and the strong involvement of the cerebellum confirm this IC as artifact in visual inspection.

The large separation of p-values between obviously artifact related ICs and ICs that might represent RSNs allowed the construction of the proposed time course based automated artifact filter. In **Figure 3** the objective function $\langle \text{acc}_n \rangle$ is displayed for the training set as a function of the two thresholds p_{moco} and p_{pow} (logarithmic scale). The mean of the accuracies defined in equation (4) is maximized by the choice $p_{\text{moco}}^{\text{crit}} = 10^{-17}$ and $p_{\text{pow}}^{\text{crit}} = 10^{-8}$, where $\langle \text{acc}_n \rangle = 0.88$. Note that in the range $10^{-25} < p_{\text{moco}} < 10^{-15}$ and $10^{-15} < p_{\text{pow}} < 10^{-5}$ the mean accuracy is rather insensitive to the precise choice of the thresholds.

In **Table 2** the number of single-subject ICs are compiled. Neither the MELODIC estimate N_n^{src} nor the number of potential RSNs that passed the visual rating or the automatic filtering process (i.e., ICs that were not automatically rated as obvious artifacts) were significantly different between the training and the test data set. Starting from the Laplacian estimator for N_n^{src}, approximately 2/3 of the single-subject ICs were concordantly rated as obvious artifacts in both groups by the raters and the filter.

Neither the visual rating accuracies (i.e., single rater opinion as compared to inter-rater agreement) nor the filter accuracies were significantly different between the data sets, see **Table 3**. However, the smallest obtained accuracies were much smaller in the test set than in the training set, especially for the filter. Although the overall accuracy of the proposed time course based filter was rather high (mean accuracy 0.80 in out-of-sample tests) it did not reach the performance of human raters. The difference was much more significant in the test set than in the training set. Rating sensitivities and specificities are compiled in **Tables 4** and **5**. The only difference between the data sets was a trend toward smaller specificity of the automated filter in the test set ($p_U = 0.03$). While in the training data set sensitivity and specificity of the filter were only marginally smaller than for human raters the differences were significant in the test set.

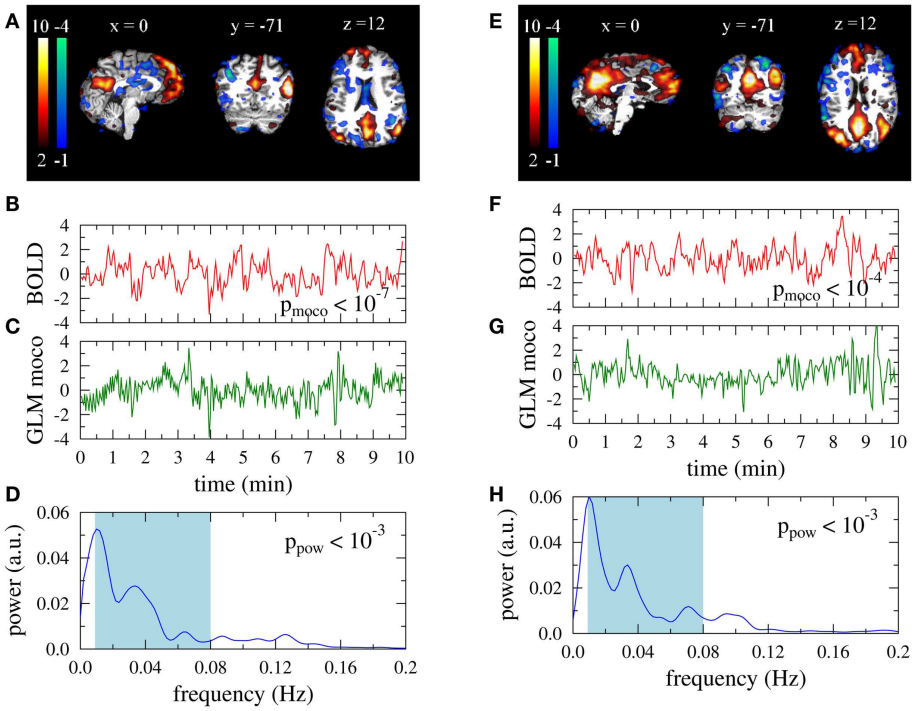

FIGURE 1 | Default mode networks for two subjects. Left: 37 year old male, right: 35 year old female participant. **(A,E)** Activation maps. Colorbars represent z-scores of IC weights per voxel. Data are presented in native space. **(B,F)** Associated BOLD time courses (normalized to zero mean and unit variance). **(C,G)** Best fit of a GLM with motion correction parameters as regressors to the BOLD data. **(D,H)** Power spectra of the BOLD time courses.

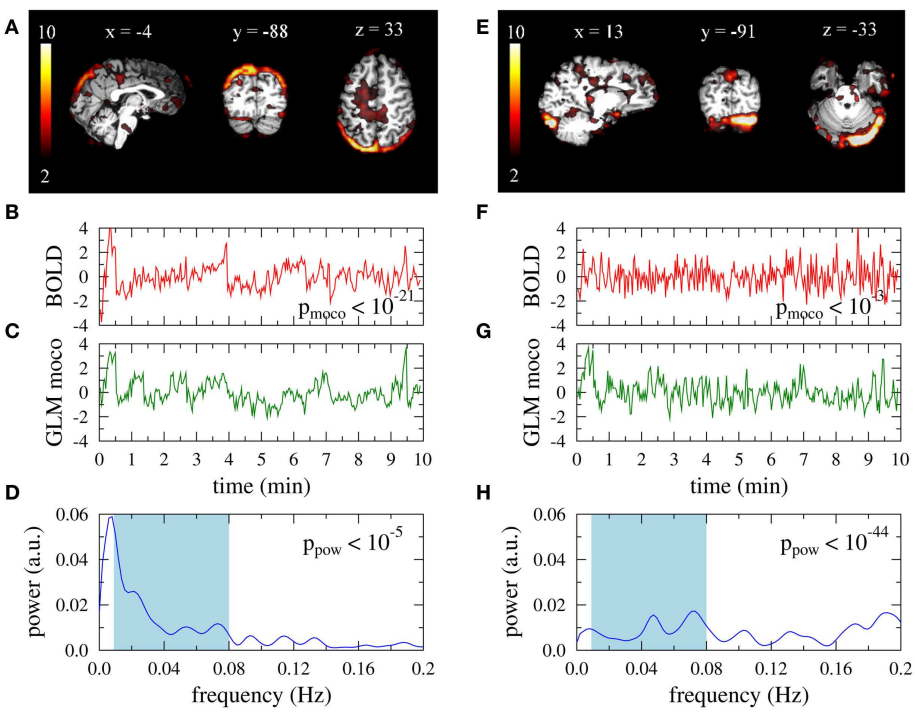

FIGURE 2 | Artifact related single-subject ICs that are excluded by the automatic filter. Data is taken from a 35-year old female participant. Right: typical type I artifact (residual subject motion), left: typical type II artifact (too much power in high frequencies). **(A,E)** Activation maps. Colorbars represent z-scores of IC weights per voxel. Data are presented in native space. **(B,F)** Associated BOLD time courses (normalized to zero mean and unit variance). **(C,G)** Best fit of a GLM with motion correction parameters as regressors to the BOLD data. **(D,H)** Power spectra of the BOLD time courses.

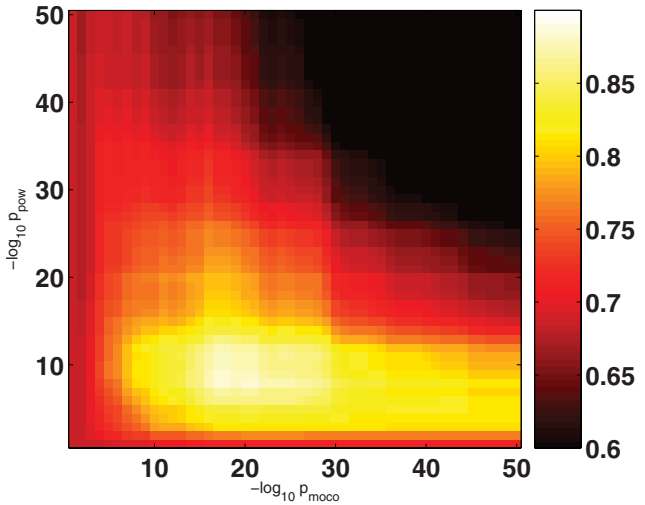

FIGURE 3 | Average filter accuracy in the training set as a function of $-\log_{10}(p_{moco})$ and $-\log_{10}(p_{pow})$.

Table 2 | Number of single-subject ICs as proposed by MELODIC and number of potential RSNs (i.e., ICs that were not rated as obvious artifacts by visual inspection or the automated filter).

		Training set	Test set	Difference between sets
N_n^{src}	Range	35–48	29–84	$p_U = 0.57$
	M	42.3	45.4	
	SD	6.0	9.1	
N_n^{RSN} (visual insp.)	Range	11–17	3–30	$p_U = 0.77$
	M	13.2	13.9	
	SD	2.1	4.7	
N_n^{RSN} (filter)	Range	8–24	5–26	$p_U = 0.28$
	M	13.3	15.6	
	SD	5.8	5.5	
Difference visual vs. filter		$p_U = 0.78$	$p_U = 0.18$	

Test for equal medians: Mann-Whitney-Wilcoxon U-test.

3.2. GROUP ICA

Concatenating all single-subject IC maps from all subjects in time (254 in the training set and 1356 in the test set) and performing a secondary ICA the MELODIC toolbox respectively estimated 29 and 581 group ICs (Laplacian method). Especially the number obtained for the test data set is of course much too large. In consequence, the vast majority of obtained group ICs were obviously artifactual and none of the typical RSNs was obtained. Rather, some ICs seemed to resemble fragments of known RSNs. After automated removal of the artifact ICs by the proposed filter, the secondary ICA revealed 14 and 59 group ICs in the training and test data sets, respectively. Many of the established RSNs were found as, e.g., the DMN, the SMN, the AUN, the VIN, and the WMN. Examples are compiled in **Figure 4**.

Table 3 | Rating accuracies of individual raters and automated filter as compared to the raters' agreement.

		Training set	Test set	Difference between sets
acc_n (visual insp.)	Range	0.95–1.00	0.82–1.00	$p_U = 0.23$
	M	0.98	0.96	
	SD	0.02	0.04	
acc_n (filter)	Range	0.76–0.94	0.41–0.96	$p_U = 0.12$
	M	0.88	0.80	
	SD	0.07	0.11	
Difference visual vs. filter		$p_U < 10^{-3}$	$p_U < 10^{-11}$	

Test for equal medians: Mann-Whitney-Wilcoxon U-test.

Table 4 | Rating sensitivities of individual raters and automated filter as compared to the raters' agreement.

		Training set	Test set	Difference between sets
$sens_n$ (visual insp.)	Range	0.94–1.00	0.83–1.00	$p_U = 0.79$
	M	0.97	0.97	
	SD	0.02	0.04	
$sens_n$ (filter)	Range	0.62–1.00	0.58–1.00	$p_U = 0.17$
	M	0.89	0.82	
	SD	0.14	0.11	
Difference visual vs. filter		$p_U = 0.03$	$p_U < 10^{-10}$	

Test for equal medians: Mann-Whitney-Wilcoxon U-test.

Table 5 | Rating specificities of individual raters and automated filter as compared to the raters' agreement.

		Training set	Test set	Difference between sets
$spec_n$ (visual insp.)	Range	0.92–1.00	0.67–1.00	$p_U = 0.81$
	M	0.97	0.94	
	SD	0.04	0.09	
$spec_n$ (filter)	Range	0.67–1.00	0.10–1.00	$p_U = 0.03$
	M	0.81	0.75	
	SD	0.14	0.23	
Difference visual vs. filter		$p_U = 0.02$	$p_U < 10^{-6}$	

Test for equal medians: Mann-Whitney-Wilcoxon U-test.

4. DISCUSSION

In this contribution we proposed a simple filter for automated identification of obviously artifactual single-subject ICs. The filter relies on only two features of the associated IC time courses: (I) correlation with motion correction parameters and (II) power outside the expected range $0.009 < f < 0.08$ Hz. Thresholds were deduced from a training data set of six subjects. The maximum of the mean subject-wise in-sample accuracy was found unique and broad (**Figure 3**) and thus smaller variations of the threshold parameters are not expected to influence our results sizably. In

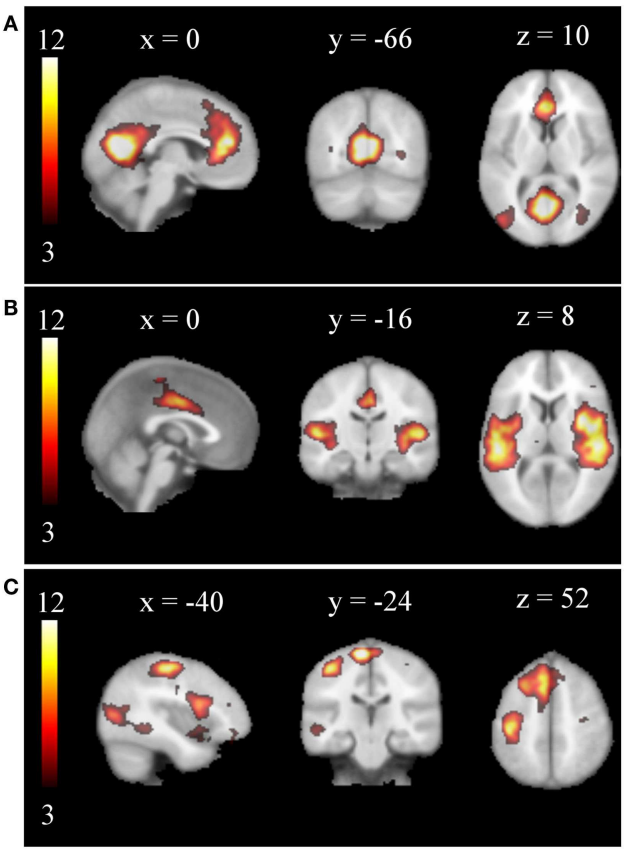

FIGURE 4 | Examples of group RSNs obtained from the test data set by a secondary ICA procedure: (A) DMN, (B) AUN, (C) WMN. Obvious artifacts were automatically removed before concatenation of the single-subject maps. The networks are displayed on a standard brain in MNI space.

addition, alternative implementations of the rules (I) and (II) are conceivable. For example, the *p*-value of the KS-test for the original and filtered power spectra could be replaced by a criterion on the spectral width or a threshold for the fraction of power found outside the allowed region.

The filter was applied to an out-of-sample test data set of 29 subjects. Neither the group demographics (see **Table 1**) nor the rater and filter performance were significantly different between the training and test data set (see **Tables 3–5**). We take these findings as a confirmation that the non-random selection of training and test data did not induce a bias.

Although our results for the test data set indicate that the automated artifact filter does not reach the performance of visual inspection by human raters, we consider the mean out-of-sample accuracy of 0.80 (mean sensitivity 0.82, mean specificity 0.75) high enough to considerably aid or replace user intervention in large data sets. As expected, performance differences between human raters and the filter were much more significant in the test than in the training data set. Besides the fact that in-sample performance is optimized whereas out-of-sample performance is not, the better statistics due to five times larger number of subjects may be the main explanation for this finding. As filters will almost always be trained on limited data and applied to larger sets, we consider this a realistic setting.

In contrast to the proposal by Sui et al. (2009), where only spatial information of IC maps was used, our artifact detector is entirely based on properties of the IC related BOLD time courses. However, as can be seen in **Figures 2A,E**, these are reflected by suspicious visual appearance of the IC maps. This suggests that map based identification of head movement related artifacts affecting mainly the brain boundaries (Tohka et al., 2008) could probably be replaced by our conceptually simpler criteria. Inclusion of our criteria (I) and (II) in a combination of non-related temporal and spatial features similar to the classification approaches by De Martino et al. (2007), Tohka et al. (2008) could possibly help to improve filter performances considerably.

Our rule (II) has similarity with the power spectrum based classification into structured or white noise time courses in Thomas et al. (2002) and the two signal power dependent features of Tohka et al. (2008). The criterion (I) is related to the methods by McKeown (2000), Kochiyama et al. (2005). However, these methods rely on the presence of tasks and are consequently not applicable to resting-state fMRI. In contrast, our proposal of using motion correction parameters in a GLM may also be suitable to distinguish task-related activations from task-related movement artifacts. The approach by Perlbarg et al. (2007) uses physiological noise time courses as regressors. Here, an important difference is that our proposal does not require manual user intervention for ROI definition.

Also the recent publication by Kundu et al. (2012) deserves discussion. Measuring at three echo times (TE) a differentiation between BOLD and non-BOLD signals in fMRI data was possible. However, this method requires acquisition of multi-echo echo planar imaging (EPI) sequences and can of course not be applied retrospectively to standard EPI data.

To illustrate the impact of artifact ICs on group studies we used a secondary ICA on top of full and artifact corrected single-subject ICA output. Considerable improvement was found in the sense that typical RSNs were obtained only after exclusion of artifacts. We used a simple group analysis strategy, which is similar to the approach implemented in GIFT (Calhoun et al., 2001, 2009). Spatial maps from all N^{subj} subjects are processed jointly by an arbitrary ICA algorithm. An important difference is that in our approach the number N_n^{src} of single-subject ICs is estimated individually for each subject $n = 1, \ldots, N^{\text{subj}}$, while in GIFT a PCA based dimensionality reduction is performed to the *same* predefined number $N_{\text{fix}}^{\text{src}}$ in all subjects. This bears the risk of subjecting noise ICs to the second level analysis in some subjects, while potentially eliminating ICs of interest in others. A common advantage of GIFT and the secondary ICA procedure is that the respective data dimensions $N^{(2)} = N^{\text{subj}} \cdot N_{\text{fix}}^{\text{src}}$ and $N^{(2)} = \sum_n N_n^{\text{src}}$ are usually much smaller than for straight forward temporal concatenation, where $N^{(2)} = N^{\text{subj}} \cdot N^{\text{obs}}$.

ACKNOWLEDGMENTS

This project was funded by the Swiss National Science Foundation (grants 33CM30-140332 and 33CM30-124089) and supported by the Swiss Multiple Sclerosis Society.

REFERENCES

Anderson, A., Bramen, J., Douglas, P., Lenartowicz, A., Cho, A., Culbertson, C., et al. (2011). Large sample group independent component analysis of functional magnetic resonance imaging using anatomical atlas-based reduction and bootstrapped clustering. *Int. J. Imaging Syst. Technol.* 21, 223–231.

Beckmann, C. F., DeLuca, M., Devlin, J. T., and Smith, S. M. (2005). Investigations into resting-state connectivity using independent component analysis. *Philos. Trans. R. Soc. Lond. B Biol. Sci.* 360, 1001–1013.

Beckmann, C. F., and Smith, S. M. (2004). Probabilistic independent component analysis for functional magnetic resonance imaging. *IEEE Trans. Med. Imaging* 23, 137–152.

Beckmann, C. F., and Smith, S. M. (2005). Tensorial extensions of independent component analysis for multisubject fMRI analysis. *Neuroimage* 25, 294–311.

Biswal, B., Yetkin, F. Z., Haughton, V. M., and Hyde, J. S. (1995). Functional connectivity in the motor cortex of resting human brain using echo-planar MRI. *Magn. Reson. Med.* 34, 537–541.

Calhoun, V., Adali, T., Pearlson, G., and Pekar, J. (2001). A method for making group inferences from functional MRI data using independent component analysis. *Hum. Brain Mapp.* 14, 140–151.

Calhoun, V., Liu, J., and Adali, T. (2009). A review of group ICA for fMRI data and ICA for joint inference of imaging, genetic, and ERP data. *Neuroimage* 45, S163–S172.

Calhoun, V. D., Kiehl, K. A., and Pearlson, G. D. (2008). Modulation of temporally coherent brain networks estimated using ICA at rest and during cognitive tasks. *Hum. Brain Mapp.* 29, 828–838.

De Luca, M., Beckmann, C. F., De Stefano, N., Matthews, P. M., and Smith, S. M. (2006). fMRI resting state networks define distinct modes of long-distance interactions in the human brain. *Neuroimage* 29, 1359–1367.

De Martino, F., Gentile, F., Esposito, F., Balsic, M., Di Salle, F., Goebel, R., et al. (2007). Classification of fMRI independent components using IC-fingerprints and support vector machine classifiers. *Neuroimage* 34, 177–194.

Doucet, G., Naveau, M., Petit, L., Delcroix, N., Zago, L., Crivello, F., et al. (2011). Brain activity at rest: a multiscale hierarchical functional organization. *J. Neurophysiol.* 105, 2753–2763.

Esposito, F., Scarabino, T., Hyvarinen, A., Himberg, J., Formisano, E., Comani, S., et al. (2005). Independent component analysis of fMRI group studies by self-organizing clustering. *Neuroimage* 25, 193–205.

Greicius, M. D., Krasnow, B., Reiss, A. L., and Menon, V. (2003). Functional connectivity in the resting brain: a network analysis of the default mode hypothesis. *Proc. Natl. Acad. Sci. U.S.A.* 100, 253–258.

Guo, Y., and Pagnoni, G. (2008). A unified framework for group independent component analysis for multi-subject fMRI data. *Neuroimage* 42, 1078–1093.

Gutbrod, K., Spring, D., Degonda, N., Heinemann, D., Nirkko, A., Hauf, M., et al. (2012). Determination of language dominance: Wada test and fMRI compared using a novel sentence task. *J. Neuroimag.* 22, 266–274.

Harrison, B. J., Pujol, J., Ortiz, H., Fornito, A., Pantelis, C., and Yücel, M. (2008). Modulation of brain resting-state networks by sad mood induction. *PLoS ONE* 3:e1794. doi:10.1371/journal.pone.0001794

Hauf, M., Jann, K., Schindler, K., Scheidegger, O., Meyer, K., Rummel, C., et al. (2012). Localizing seizure-onset zones in presurgical evaluation of drug-resistant epilepsy by electroencephalography/fMRI: effectiveness of alternative thresholding strategies. *Am. J. Neuroradiol.* 33, 1818–1824.

Hyvärinen, A. (1999). Fast and robust fixed-point algorithms for independent component analysis. *IEEE Trans. Neural Netw.* 10, 626–634.

Hyvärinen, A., and Oja, E. (1997). A fast fixed-point algorithm for independent component analysis. *Neural Comput.* 9, 1483–1492.

Kochiyama, T., Morita, T., Okada, T., Yonekura, Y., Matsumura, M., and Sadato, N. (2005). Removing the effects of task-related motion using independent-component analysis. *Neuroimage* 25, 802–814.

Kollndorfer, K., Fischmeister, F., Kasprian, G., Prayer, D., and Schöpf, V. (2013). A systematic investigation of the invariance of resting-state network patterns: is resting-state fMRI ready for pre-surgical planning? *Front. Hum. Neurosci.* 7:95. doi:10.3389/fnhum.2013.00095

Kundu, P., Inati, S. J., Evans, J. W., Luh, W.-M., and Bandettini, P. A. (2012). Differentiating BOLD and non-BOLD signals in fMRI time series using multi-echo EPI. *Neuroimage* 60, 1759–1770.

McKeown, M. J. (2000). Detection of consistently task-related activations in fMRI data with hybrid independent component analysis. *Neuroimage* 11, 24–35.

Minka, T. (2000). "Automatic Choice of Dimensionality for PCA," in *Advances in Neural Information Processing Systems 13*, eds T. K. Leen, T. G. Dietterich, and V. Tresp (Cambridge: MIT Press).

Perlbarg, V., Bellec, P., Anton, J., Pélégrini-Issac, M., Doyon, J., and Benali, H. (2007). CORSICA: correction of structured noise in fMRI by automatic identification of ICA components. *Magn. Reson. Imaging* 25, 35–46.

Schmithorst, V. J., and Holland, S. K. (2004). Comparison of three methods for generating group statistical inferences from independent component analysis of functional magnetic resonance imaging data. *J. Magn. Reson. Imaging* 19, 365–368.

Schöpf, V., Kasess, C., Lanzenberger, R., Fischmeister, F., Windischberger, C., and Moser, E. (2010a). Fully exploratory network ICA (FENICA) on resting-state fMRI data. *J. Neurosci. Methods* 192, 207–213.

Schöpf, V., Windischberger, C., Kasess, C. H., Lanzenberger, R., and Moser, E. (2010b). Group ICA of resting-state data: a comparison. *MAGMA* 23, 317–325.

Schöpf, V., Windischberger, C., Robinson, S., Kasess, C., Fischmeister, F. P., Lanzenberger, R., et al. (2011). Model-free fMRI group analysis using FENICA. *Neuroimage* 55, 185–193.

Siegel, S. (1956). *Non-Parametric Statistics for the Behavioral Sciences.* New York: McGraw-Hill.

Sui, J., Adali, T., Pearlson, G. D., and Calhoun, V. D. (2009). An ICA-based method for the identification of optimal fMRI features and components using combined group-discriminative techniques. *Neuroimage* 46, 73–86.

Svensén, M., Kruggel, F., and Benali, H. (2002). ICA of fMRI group study data. *Neuroimage* 16, 551–563.

Thomas, C. G., Harshman, R. A., and Menon, R. S. (2002). Noise reduction in BOLD-based fMRI using component analysis. *Neuroimage* 17, 1521–1537.

Tohka, J., Foerde, K., Aron, A. R., Tom, S. M., Toga, A. W., and Poldrack, R. A. (2008). Automatic independent component labeling for artifact removal in fMRI. *Neuroimage* 39, 1227–1245.

Varoquaux, G., Sadaghiani, S., Pinel, P., Kleinschmidt, A., Poline, J. B., and Thirion, B. (2010). A group model for stable multi-subject ICA on fMRI datasets. *Neuroimage* 51, 288–299.

Weissenbacher, A., Kasess, C., Gerstl, F., Lanzenberger, R., Moser, E., and Windischberger, C. (2009). Correlations and anticorrelations in resting-state functional connectivity MRI: a quantitative comparison of preprocessing strategies. *Neuroimage* 47, 1408–1416.

Conflict of Interest Statement: The authors declare that the research was conducted in the absence of any commercial or financial relationships that could be construed as a potential conflict of interest.

Received: 24 January 2013; accepted: 06 May 2013; published online: 23 May 2013.

Citation: Rummel C, Verma RK, Schöpf V, Abela E, Hauf M, Berruecos JFZ and Wiest R (2013) Time course based artifact identification for independent components of resting-state fMRI. Front. Hum. Neurosci. 7:214. doi: 10.3389/fnhum.2013.00214

frontiers in
HUMAN NEUROSCIENCE

METHODS ARTICLE
published: 10 July 2013
doi: 10.3389/fnhum.2013.00343

An automated method for identifying artifact in independent component analysis of resting-state fMRI

Kaushik Bhaganagarapu*[1,2], *Graeme D. Jackson*[1,2,3] *and David F. Abbott*[1,2]

[1] The Florey Institute of Neuroscience and Mental Health, The University of Melbourne, Austin Hospital, Melbourne, VIC, Australia
[2] Department of Medicine, The University of Melbourne, Melbourne, VIC, Australia
[3] Department of Radiology, The University of Melbourne, Melbourne, VIC, Australia

Edited by:
Simon Daniel Robinson, Medical University of Vienna, Austria

Reviewed by:
Prantik Kundu, University of Cambridge/National Institutes of Health, USA
Roland N. Boubela, Medical University of Vienna, Austria

***Correspondence:**
David F. Abbott, The Florey Institute of Neuroscience and Mental Health, The University of Melbourne, Austin Campus, 245 Burgundy Street, Heidelberg, Melbourne, VIC 3084, Australia
e-mail: bri@brain.org.au

An enduring issue with data-driven analysis and filtering methods is the interpretation of results. To assist, we present an automatic method for identification of artifact in independent components (ICs) derived from functional MRI (fMRI). The method was designed with the following features: does not require temporal information about an fMRI paradigm; does not require the user to train the algorithm; requires only the fMRI images (additional acquisition of anatomical imaging not required); is able to identify a high proportion of artifact-related ICs without removing components that are likely to be of neuronal origin; can be applied to resting-state fMRI; is automated, requiring minimal or no human intervention. We applied the method to a MELODIC probabilistic ICA of resting-state functional connectivity data acquired in 50 healthy control subjects, and compared the results to a blinded expert manual classification. The method identified between 26 and 72% of the components as artifact (mean 55%). About 0.3% of components identified as artifact were discordant with the manual classification; retrospective examination of these ICs suggested the automated method had correctly identified these as artifact. We have developed an effective automated method which removes a substantial number of unwanted noisy components in ICA analyses of resting-state fMRI data. Source code of our implementation of the method is available.

Keywords: functional magnetic resonance imaging, fMRI, independent component analysis, ICA, automated classification, automatic, artifacts, independent component labeling

1. INTRODUCTION

Functional magnetic resonance imaging (fMRI) is a non-invasive technique that uses the blood oxygen level dependent (BOLD) effect to explore neural activity (Ogawa et al., 1990). However, BOLD fMRI suffers from numerous sources of structured noise (Biswal et al., 1996; Friston et al., 1996; Glover et al., 2000) which compromises the fMRI signal. These include rapid and slow head movements, physiological activity (breathing and heartbeat), and potential acquisition artifacts. Even after traditional pre-processing steps, such as slice-timing correction, motion correction, high-pass filtering, and spatial smoothing, some of these artifacts still remain (Grootoonk et al., 2000; Lund et al., 2006). To overcome this, the use of data-driven techniques are increasingly being employed to generate potentially valuable information on the nature of signal and noise in fMRI data. In particular, spatial Independent Component Analysis (ICA), has been proposed (McKeown et al., 1998). Spatial ICA is a blind source separation (BSS) technique, that decomposes fMRI data into components which are maximally independent (Hyvärinen, 1999). Each Independent Component (IC) contains a 3D spatial map and a 1D time-course. When compared to traditional fMRI analysis approaches, where a design paradigm and assumptions about the hemodynamic processes in the brain are required to obtain spatial activation maps (Buxton et al., 2004), ICA offers a hypothesis free model to gain further insights in identifying the spatial location of brain activity. However, such an approach, due to its hypothesis free nature begs the question of interpretation of the results. In particular, how does one distinguish between ICs which are signal (i.e., components of neuronal origin) and noise (i.e., due to movement, cardiac pulsations etc.)? Typically, this has been done by visually inspecting each IC and manually categorizing them (McKeown et al., 1998; Moritz et al., 2003; Kelly Jr. et al., 2010). This is however, a very time consuming and subjective procedure which is dependent on the experience of the researcher. For example, Kelly Jr. et al. (2010) provide a detailed description of the criteria to manually classify ICs via visual inspection. They estimate approximately 37 min for classifying 100 ICs which can be a typical yield from lengthy resting-state ICA (Rodionov et al., 2007; LeVan et al., 2010).

Other methods have classified ICs by using paradigm information (Thomas et al., 2002; Calhoun et al., 2005; Kochiyama et al., 2005). Specifically, Calhoun et al. (2005) present an approach for semi-blind ICA analysis of event-related fMRI data by imposing regularization on certain estimated time courses using the paradigm information. This approach, however, is limited to studies where temporal information is available. In some applications it may not be desirable to use temporal information in the classifier. Resting-state functional connectivity is one such application. Another, which is a particular interest of ours, is the data-driven exploration of fMRI prior to an epileptic seizure (Federico et al.,

2005), where we have no prior model of expected signal change or event timing (apart from the seizure itself at which point the data acquisition usually ends).

More recently, several automatic techniques have been developed to assist in classifying ICs into categories of noise and signal (Perlbarg et al., 2007; Stevens et al., 2007; Calhoun et al., 2008; Sui et al., 2009; Kundu et al., 2012). Perlbarg et al. (2007) uses both spatial and temporal patterns to categorize ICs into noise and signal. However, their automatic classifier, CORSICA, is limited to identifying physiological noise. Calhoun et al. (2008) utilize a brain atlas to aid sorting ICs. However, atlas based sorting requires strong *a priori* assumptions on the spatial layout of the activation which is not always available. Sui et al. (2009) employ spatial only criterion to automatically classify ICs as they use contrast images that contain no time-domain information. Their method relies on generating cerebrospinal fluid (CSF) red and gray-matter (GM) masks. It can be difficult to obtain an accurate GM mask with fMRI images, especially at higher magnetic field strengths (e.g., 3 T) where image distortions and signal dropout can result in blurred boundaries between gray matter and white matter. Kundu et al. (2012) differentiate BOLD-like functional network components from non-BOLD-like components related to motion, pulsatility, and other nuisance effects based on TE-dependence. While this was found to be a robust method compared to conventional techniques for classifying artifacts, the technique requires a multi-echo acquisition sequence and cannot be applied to conventional single-echo fMRI data.

Other automatic techniques based on machine learning algorithms have been applied to identify artifactual ICs (De Martino et al., 2007; Tohka et al., 2008). De Martino et al. (2007) represents each IC in a multidimensional space, called an IC-fingerprint. Using these IC-fingerprints, they classify ICs into various categories of signal and noise. Tohka et al. (2008) uses a combination of spatial and temporal criteria to aid in classifying signal and noise via global decision trees. However, their classifier overlooks physiological noise. Moreover these two techniques are primarily dependent on a training data set.

We sought to overcome some of the limitations of existing classifiers by developing an artifact identification method that:

- Does not require temporal information about the fMRI paradigm.
- Does not require the user to train the algorithm.
- Requires only the EPI images (additional acquisition of anatomical images is not required).
- Is able to identify a high proportion of artifact-related ICs without removing components that are likely to be of neuronal origin.
- Can be applied to resting-state fMRI.
- Is automated, requiring minimal or no human intervention.

We are not aware of any existing IC artifact identification method that contains all of the above features. We have dubbed our method the Spatially Organized Component Klassifikator (SOCK). In the context of this paper, we mean by "Klassifikator" (a German word meaning classifier) the ability to distinguish between ICs dominated by artifact and those containing possible neuronal signal. We note from the outset that our approach is designed to complement rather than replace existing approaches. A limitation in some applications can be a strength in others. We designed SOCK for particular applications where the features listed above are the highest priorities.

2. METHODS

2.1. METHODS OVERVIEW

The overview of the automatic IC classification process is given below (see also **Figure 1**).

1. ICA was applied to the pre-processed fMRI data (see Section 2.5) using MELODIC (Beckmann and Smith, 2004), yielding both thresholded ($P < 0.05$) and unthresholded ICs and associated time courses and power spectra[1].
2. Calculation of features (smoothness measure, edge, CSF, and temporal frequency power) for each IC was computed via the SOCK algorithm.
3. Based on the above features, ICs dominated by artifact are classified into an Artifact category and all other ICs (i.e., those containing possible neuronal signal) into an Unlikely Artifact category.

Source code of our implementation of the method is available at http://www.brain.org.au/software.

2.2. ICA DECOMPOSITION

The idea behind ICA is to decompose the 4D fMRI time series into a linear combination of spatially independent component maps with an associated time-course (McKeown et al., 1998; Hyvärinen, 1999). This is expressed mathematically as follows:

$$X = \sum_{i=1}^{N} T_i S_i \tag{1}$$

where X is a $K \times M$ matrix ($K =$ number of samples and $M =$ number of time courses) of the fMRI time series, S the $N \times M$ matrix whose rows S_i ($i = 1, \ldots, N$) represent the i^{th} spatial component ($K \leq T$) and T is the $K \times N$ mixing matrix (unknown), whose columns T_i ($i = 1, \ldots, N$) contain the time courses of the N sources. Estimating the number of sources, N is done in the pre-processing step, usually via PCA (Beckmann and Smith, 2004).

The only constraint enforced in this decomposition is that each of the component maps, S_i's are spatially independent. This is equivalent to saying that all S_i's, with the exception of one have to be non-Gaussian. Structured non-Gaussian noise (head motion and physiological noise) in the fMRI data series is not explicitly modeled, but is treated as an independent source in the ICA decomposition (McKeown et al., 1998; Hyvärinen, 1999).

The ICA decomposition is done by estimating the mixing matrix, T, by minimizing redundancy in the spatial maps of the components, S. This can be mathematically expressed as:

$$S = \sum_{i=1}^{N} W_i X_i \tag{2}$$

[1]Temporal information expressed in the frequency domain. This is done mathematically by taking the discrete Fourier Transform of the time course.

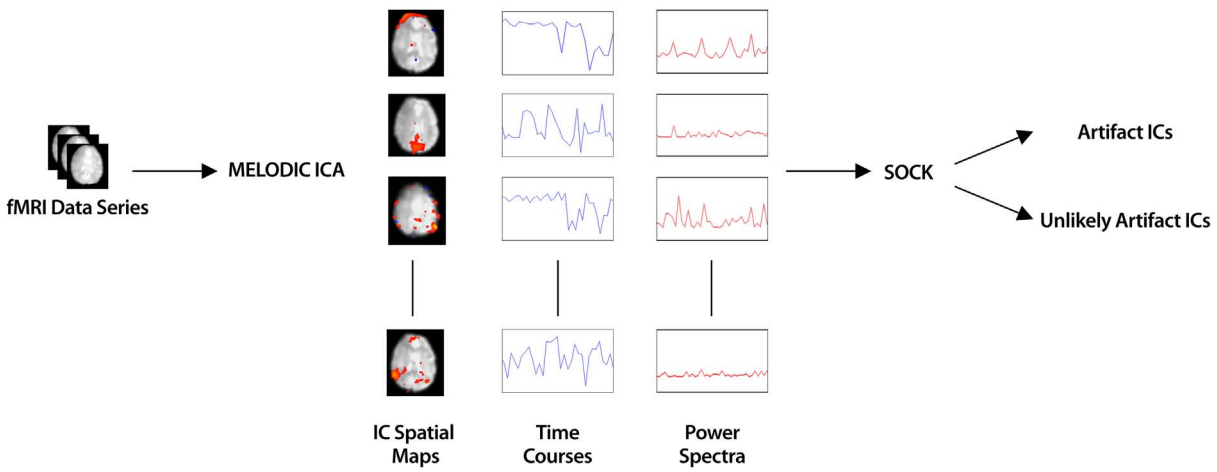

FIGURE 1 | ICA was applied to pre-processed fMRI data yielding spatial component maps with associated time courses and power spectra. SOCK automatically distinguishes between ICs dominated by artifact (Artifact category) and those containing possible neuronal signal (Unlikely Artifact category) by calculating IC features (smoothness measure, edge, CSF, and temporal frequency power).

where matrix W, called the "un-mixing" matrix, is the inverse of T. Several freely available software packages are available to perform this decomposition; we used MELODIC which is part of the FSL package (Beckmann and Smith, 2004). The output is a set of spatial maps (S_i) with associated time courses (T_i) and power spectra (PS_i). These then form the input for the automatic classifier, SOCK.

2.3. CALCULATION OF IC FEATURES

SOCK automatically identifies artifact in each IC using features likely to indicate motion, physiological noise, or machine or undetermined noise. To achieve this, each IC is assessed for the presence of substantial edge-only activity, activity in the ventricles, or a large number of isolated very small clusters or isolated voxels (i.e., a "spotty" appearance), respectively. Specifically, we use four measures:

1. Smoothness measure. This assesses the contributions of low and high *spatial* frequency content for each IC (Section 2.3.1).
2. Edge activity measure. This assesses the extent of activity in peripheral areas of the brain, via an edge mask (Section 2.3.2).
3. CSF activity measure. This assesses the extent of activity in ventricular areas of the brain, via a CSF mask (Section 2.3.3).
4. Temporal Frequency Noise (TFN) measure. This assesses the power in *temporal* frequency beyond 0.08 Hz (Section 2.3.4).

2.3.1. Smoothness measure

The spotty appearance of an IC, which reflects the degree of smoothness, is identified by observing spatial frequencies via a Fourier Transform. We assume components that are likely to be of neuronal origin will be relatively smooth and that by observing contributions in spatial frequency, we can distinguish between ICs that are smooth and unsmooth. The framework for the smoothness criterion is as follows.

Let $F^i(K_x, K_y, K_z)$ be the 3D Discrete Fourier Transform of IC, *i*. That is,

$$F^i\left(K_x, K_y, K_z\right) = \sum_X \sum_Y \sum_Z S^i (X, Y, Z)\, e^{-2\pi j\left(K_x \cdot X \cdot X_0 + K_y \cdot Y \cdot Y_0 + K_Z \cdot Z \cdot Z_0\right)} \quad (3)$$

where j is an imaginary unit, X, Y, and Z are vectors corresponding to the fMRI image dimensions and X_0, Y_0, and Z_0 are the step sizes between consecutive samples in the X, Y, and Z directions respectively. K_x, K_y, and K_z are vectors in the Fourier space and S is the intensity in the image space. A typical Fourier Transform for a *single slice* is illustrated in 2A. While a 3D Discrete Fourier Transform is implemented in SOCK, we show a 2D illustration for simplicity. Data in the center of this figure contains low spatial frequency information about the image, while data near the periphery represents high spatial frequencies. We apply the above Discrete Fourier Transform to *unthresholded* ICs, thus capturing all spatial frequency modes to assess whether or not an IC is smooth. To classify the extent of spatial smoothness of a particular IC, we calculate a ratio of low to high frequency information.

Let L^i be the low frequency information contained within volume, $V1$ (see **Figure 2A**) for IC, *i*. That is,

$$L^i = \sum_{V1_x} \sum_{V1_y} \sum_{V1_z} F^i\left(K_x, K_y, K_z\right) \quad (4)$$

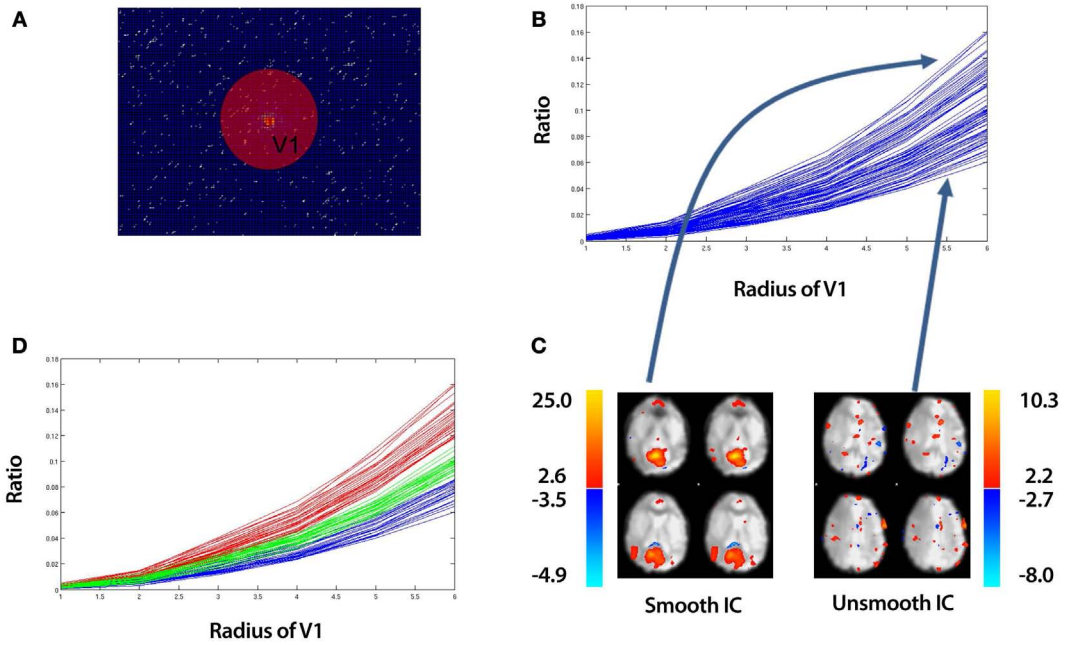

FIGURE 2 | An overview of identifying "spotty" artifact. The example data is taken from an ICA of a control that underwent a 10 min resting-state fMRI study (see Section 2.5). **(A)** Discrete Fourier Transform of a *single slice* of an IC. While a 3D Discrete Fourier Transform is implemented in SOCK, we show a 2D illustration for simplicity. Data in the center of figure contains low spatial frequency information about the image, while data near the periphery represents high spatial frequencies. The sphere with volume $V1$ is an arbitrary region which contains low spatial frequency information. **(B)** A plot of the ratio of low to high frequency information [equation (6)] vs. the radius of sphere $V1$ for all ICs. **(C)** A spatial map of the top and bottom curves corresponding to the smoothest and least smooth IC respectively. **(D)** Applying k-means clustering to split the ICs into a set of "smooth" (red curves), "subsmooth" (green curves), and "unsmooth" (blue curves) ICs. Each line in **(B,D)** represents the ratio for a particular IC calculated over all slices, not just the slice shown in **(A)**.

where $V1_x$, $V1_y$, and $V1_z$ are vectors corresponding to the dimensions in Fourier space of volume, $V1$. Let H^i be the high frequency information contained outside of volume, $V1$ for IC, *i*. That is,

$$H^i = \sum_{K_x - V1_x} \sum_{K_y - V1_y} \sum_{K_z - V1_z} F^i\left(K_x, K_y, K_z\right) \tag{5}$$

We then define, R^i as the ratio of low to high frequency information for IC, *i*. That is,

$$R^i = \frac{L^i}{H^i} \tag{6}$$

This ratio is a function of the radius of the volume, $V1$. As we increase the radius of $V1$, we increase the volume of low intensity frequencies contributing to the ratio. Plotting equation (6) as a function of different radius values, we obtain curves such as the example shown in **Figure 2B**. Each curve represents a different IC. These are referred to as *ratio curves* from here on in. These *ratio curves* naturally organize themselves from top to bottom representing the smoothest IC at the top to the least smooth IC at the bottom (**Figure 2C**).

To distinguish between smooth and unsmooth ICs, we apply a k-means clustering in a 2D feature space (Euclidean distance metric) implemented in MATLAB R2010b (The MathWorks Inc., Natick, MA, USA) to the *ratio curves*. Firstly, we split the *ratio curves* into two clusters:

$$(ClusterA,\ ClusterD) = kmeans\left(R^i, 2\right) \tag{7}$$

We further split the lower cluster into two clusters:

$$(ClusterB, ClusterC) = kmeans\left(ClusterD, 2\right) \tag{8}$$

This yields three sets of vectors (*ClusterA*, *ClusterB*, *ClusterC*), which contain *ratio curves*. We label these clusters (*Smooth*, *Subsmooth*, *Unsmooth*). An example of the clustering is shown in **Figure 2D**.

2.3.2. Edge activity measure

It has been demonstrated that in ICA of fMRI data, gross subject motion can result in artifactual activity at the edge of the brain (McKeown et al., 1998). We therefore assess the amount of activity within an edge mask, an example of which is shown in **Figure 3A** (single slice shown). For this we utilize the sub-routine, "New Segment" from the SPM8 software package (The Wellcome Trust Centre for Neuroimaging[2]), applied to the mean functional image. "New Segment" generates two edge masks covering the inner and

[2]www.fil.ion.ucl.ac.uk/spm

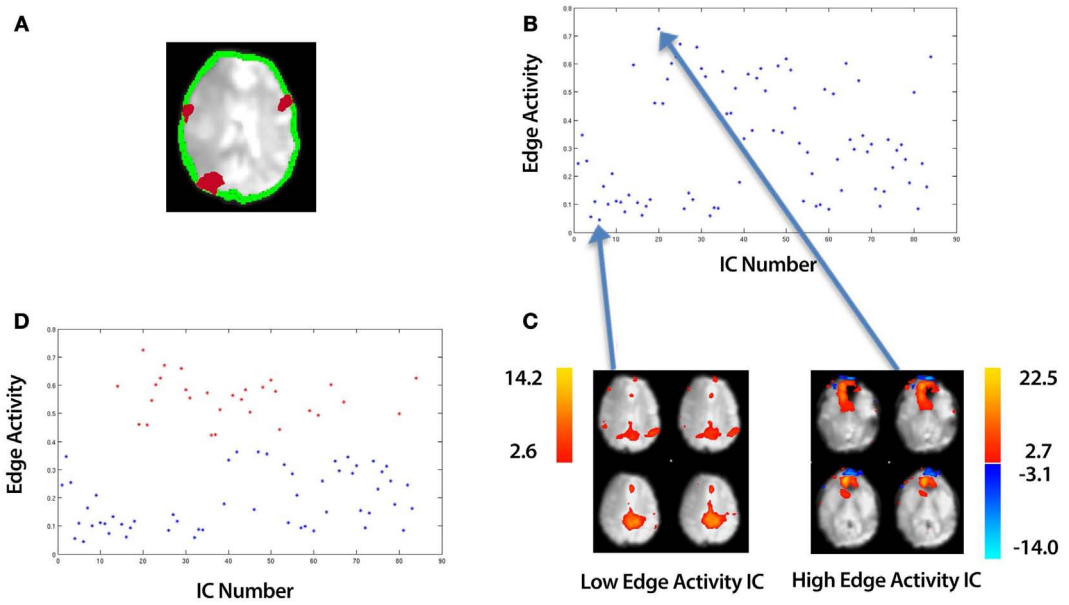

FIGURE 3 | An overview of identifying motion artifact. The example data is taken from an ICA of a control that underwent a 10 min resting-state fMRI study (see Section 2.5). **(A)** An edge mask (in green) automatically created by an SPM sub-routine, "New Segment" (single slice shown). This is overlaid onto a mean functional image. In red are an illustration of contiguous clusters which overlap the edge mask. **(B)** A plot of the edge activity for all ICs. **(C)** A spatial map of the top and bottom points corresponding to the highest and lowest edge activity ICs respectively. **(D)** Using k-means clustering, the ICs are automatically divided into a set of "High Edge Activity" components (points colored red in the scatter-plot) and "Low Edge Activity" components (points colored blue in the scatter-plot). Each point in the scatter-plot represents the edge activity for a particular IC summed over all slices.

outer brain boundary; we amalgamate these masks to produce a single edge mask. To identify ICs characterized by gross motion artifact, we define a variable, *edge activity*, which is a measure of the extent of activation overlapping the edge mask. The edge activity, EA^i for each IC, i is defined as follows:

$$EA^i = \frac{\sum_k OE_k}{E_v} \tag{9}$$

where E_v is the volume of the edge mask and $OE_k, \forall k = 1, 2, \ldots, n$ is the volume of those contiguous clusters which overlaps the edge mask with there being n of these clusters. An illustration of these clusters is shown in **Figure 3A** for a single slice. We used the "locmax.m" function within the FMRISTAT software (Worsley et al., 2002) to extract these contiguous clusters.

Plotting equation (9) for each IC, i produces a plot such as that shown in **Figure 3B**. Each point represents a different IC with the highest and lowest points corresponding to the ICs with the highest edge activity and lowest edge activity respectively (**Figure 3C**). Similar to the technique used in clustering the smooth and unsmooth ICs, we employ k-means clustering in a 2D feature space (Euclidean distance metric) to group edge activity into two clusters:

$$(ClusterA, ClusterB) = kmeans\left(EA^i, 2\right) \tag{10}$$

where (*ClusterA*, *ClusterB*) are two vectors which contain edge activities. We label these clusters (*Low Edge Activity*, *High Edge Activity*). An example of the clustering is shown in **Figure 3D**. In addition to the adaptive clustering we employ a fixed threshold rejecting ICs independent of any other criteria when they have a 50% or greater volume of activity overlapping the edge mask. This threshold was identified by testing combinations of thresholds on data independent from the data presented here (see Appendix B).

2.3.3. CSF activity measure

Physiological noise, due to breathing and heart-beat, is often most evident in or at the borders of CSF regions such as the ventricles (Weisskoff et al., 1993; Windischberger et al., 2002). To detect such noise we create a CSF mask, isolating the lateral ventricles. An example is shown in **Figure 4** (single slice shown). For this we utilize the sub-routine, "New Segment" from the SPM8 software package [The Wellcome Trust Centre for Neuroimaging (see text footnote 2)], applied to the mean functional image. To isolate the lateral ventricles, we manually defined this region on the Montreal Neurological Institute (MNI) templates included in SPM 8. To identify ICs characterized by CSF artifact, we define a variable, *CSF activity*, which is a measure of the extent of activation overlapping the CSF mask. The CSF activity, CA^i for each IC, i is defined as follows:

$$CA^i = \frac{\sum_k OC_k}{CSF_v} \tag{11}$$

where $OC_k, \forall k = 1, 2, \ldots, m$ is the volume of the contiguous clusters which overlaps the CSF mask with there being m of these clusters. An illustration of these clusters is shown in **Figure 4** for a single slice. CSF_v is the volume of the CSF mask.

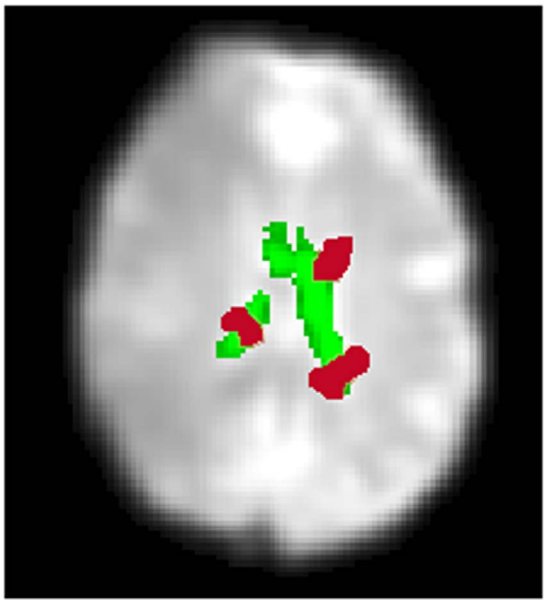

FIGURE 4 | An overview of identifying CSF artifact. A CSF mask automatically created by an SPM sub-routine, "New Segment" is shown in green (single slice shown). This is overlaid onto a mean functional image. In red are an illustration of contiguous clusters which overlap the CSF mask. If the volume of activity overlapping the CSF mask is 10% or greater, the IC is labeled *High CSF Activity* (*Low CSF Activity* otherwise). The CSF activity for a particular IC calculated over all slices, not just the slice shown above.

Unlike the smoothness and motion artifact measures, we do not employ a clustering technique to identify ICs characterized by CSF artifact. Instead, we employ a fixed threshold. If the volume of activity overlapping the CSF mask is 10% or greater, the IC is labeled *High CSF Activity* (*Low CSF Activity* otherwise). In addition, we reject ICs independent of any other criteria when they have a 30% or greater volume of activity overlapping the CSF mask. This threshold was identified by testing combinations of thresholds on data independent from the data presented here (see Appendix B).

2.3.4. Temporal frequency noise measure

The dominant period of the hemodynamic Response Function (HRF) is approximately 12 s (from onset to return to baseline, ignoring the post-stimulus undershoot) (Chapter 10, Huettel et al., 2009). Therefore we expect the dominant frequency for components which exhibit BOLD neuronal signal to be about 1/12 or 0.08 Hz. Hence to identify activity that is unlikely to come from the BOLD HRF, we quantify the temporal power beyond 0.08 Hz.

To identify ICs characterized by high frequency noise in the time series, we define a variable, Temporal Frequency Noise (TFN), which is a measure of the extent of temporal power beyond 0.08 Hz. The TFN, TFN^i for each IC, i, is defined as follows:

$$TFN^i = \sum_{0.08}^{f_{Nyquist}} PS^i \tag{12}$$

where PS^i, are the power spectrum values for each IC, i, which are provided by the MELODIC ICA (Beckmann and Smith, 2004) and $f_{Nyquist}$ is Nyquist frequency. This formula in essence calculates the sum of all power spectrum values from 0.08 Hz to the Nyquist frequency. Plotting equation (12) for each IC, i produces a plot, such as the example shown in **Figure 5A**. Each point represents a different IC. K-means clustering in a 2D feature space (Euclidean distance metric) is employed to cluster TFN values into two clusters:

$$(ClusterA,\ ClusterB) = kmeans\left(TFN^i,\ 2\right) \tag{13}$$

where (*ClusterA*, *ClusterB*) are two vectors which contain TFN values. We label these clusters (*High TFN*, *Low TFN*) which correspond to ICs with high and low TFN values respectively. An example of the clustering is shown in **Figure 5B**, with the spatial maps for the highest and lowest points shown in **Figure 5C**. The associated power spectra for these ICs are shown in **Figure 5D** with the blue and red curves representing the low and high TFN ICs respectively. This is a zoomed in view showing only frequencies beyond 0.08 Hz which is the region of interest.

2.4. CLASSIFICATION OF ICs

Based on the above features, ICs dominated by artifact are identified using the conditions given in **Table 1**. These were established by the authors based on their experience in visually classifying components from independent data (5 subjects scanned on the same scanner as data sets 1 and 2 in Section 2.5).

2.5. fMRI DATA

We validate SOCK for individual ICA analyses in 50 subjects, from three separate data sets. All were resting-state studies. See **Table 2** for a summary.

2.5.1. Data sets 1 and 2

The first two data sets consisted of resting-state data from thirty healthy control subjects that had participated in studies at our institute (Waites et al., 2005, 2006; Lillywhite et al., 2009; Abbott et al., 2010). Ethics approval was obtained from the Austin Health Human Research Ethics Committee or the Howard Florey Institute of Experimental Physiology and Medicine Human Research Ethics Committee and each subject gave informed consent.

Participants were instructed to close their eyes and relax without falling asleep and without focusing on anything in particular. A single run of fMRI data was collected for each of the participants; each run was 60 min in 9 of the participants and 10 min in 21 of the participants.

The fMRI studies were carried out with a 3 T GE Signa LX whole body scanner (General Electric, Milwaukee, WI, USA), using a standard birdcage quadrature head coil. Functional images were acquired as a series of gradient-recalled echo planar imaging (GR-EPI) volumes (TR/TE = 3,000/40 ms in 9 of the participants and TR/TE = 3,600/40 ms in 21 of the participants, 25 oblique slices 4 mm thick + 1-mm gap, voxel size = 1.875 mm × 1.875 mm × 5 mm, 24-cm field of view (FOV), 128 × 128 matrix). The first 14 volumes were discarded (to allow

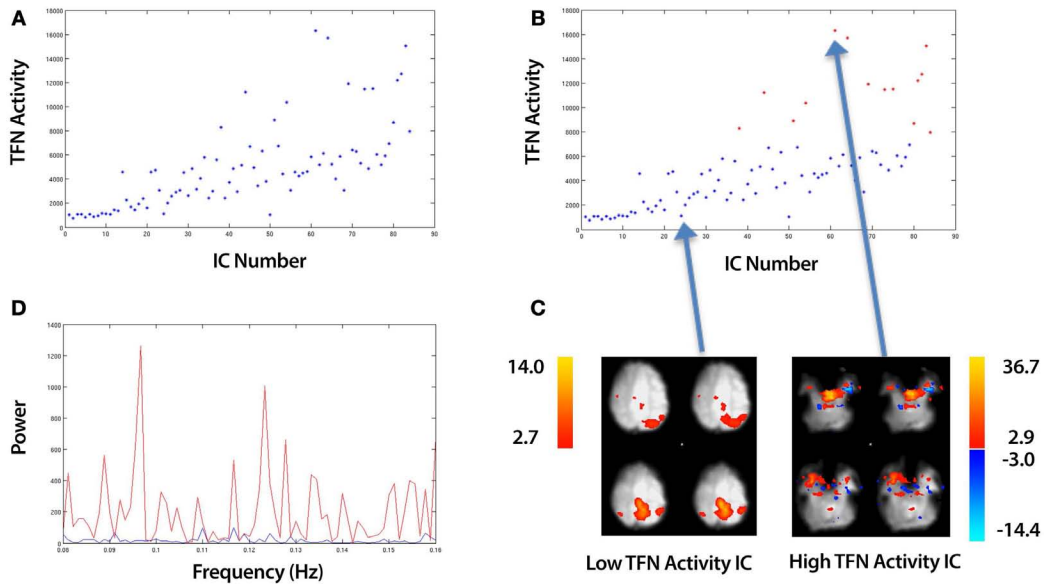

FIGURE 5 | An overview of identifying ICs with Temporal Frequency Noise (TFN). The example data is taken from an ICA of a control that underwent a 10 min resting-state fMRI study (see Section 2.5). **(A)** A plot of the TFN activity (sum of power spectrum values from 0.08 Hz to Nyquist frequency) for all ICs. **(B)** Applying k-means clustering to split the ICs into a set of Low and High TFN ICs. **(C)** A spatial map of the top and bottom points corresponding to the highest and lowest TFN activity ICs respectively. **(D)** The associated power spectra for these ICs with the blue and red curves representing the low and high TFN ICs respectively. This is a zoomed in view showing only frequencies beyond 0.08 Hz which is the region of interest.

Table 1 | The conditions used to automatically identify ICs dominated by artifact.

Smoothness	Edge activity	CSF activity	Temporal frequency noise
Unsmooth	–	–	–
Subsmooth	–	–	High
Smooth	High	High	–
–	High (above 50%)	–	–
–	–	High (above 30%)	–

Each row indicates a combination of conditions for which the IC is classified as artifact. For example an IC is classified as artifact if it is subsmooth and has high TFN activity.

Table 2 | A summary of the three different data sets used to verify SOCK.

Data set	No. of subjects	Length of study (min)	TR (s)	Pre-processed
1	9	60	3.0	Yes
2	21	10	3.6	Yes
3	20	9	2.0	No

In total, fMRI data of 50 healthy control subjects were used which had different: study lengths, TR's, and pre-processing pipelines.

the scanner time to reach steady-state and the subject to become settled to the procedure).

fMRI data were processed using SPM8 software (Wellcome Department of Imaging Neuroscience, London, UK[3]) with the aid of iBrain™ (Abbott and Jackson, 2001) and the iBrain™ Analysis Toolbox for SPM (Abbott et al., 2011)[4]. In brief, pre-processing included slice-timing correction, motion correction (realignment), and non-linear warping to a custom local template approximating that of the standard Montreal Neurological Institute (MNI) template supplied with SPM8. The spatially normalized image data were smoothed with an 8 mm isotropic Gaussian kernel and were written at a voxel size of 2 mm × 2 mm × 2 mm. No further pre-processing was carried out in FSL prior to ICA being performed using the MELODIC tool (Beckmann and Smith, 2004).

2.5.2. Data set 3 (functional connectomes data)

The third set of data consisted of resting-state fMRI data with a relatively short TR from twenty healthy controls obtained from the 1000 Functional Connectomes Project website (Biswal et al., 2010, data set 2 from Table S1 with TR = 2,000 ms, 34 slices and voxel size = 3 mm × 3 mm × 3 mm). Participants were instructed to open their eyes without focusing on anything in particular. fMRI data was collected for each of the participants in a 9 min study. The fMRI studies were carried out with a 3 T scanner (make of scanner not specified). Functional images were acquired using a sequential

[3]http://www.fil.ion.ucl.ac.uk/spm/software/spm8/
[4]www.brain.org.au/software

ascending sequence, discarding the first 5 time points of each time series.

No pre-processing [slice-timing correction, motion correction (realignment), normalization, or smoothing] was carried out on this data set.

Preforming ICA using the MELODIC tool, yielded both thresholded and unthresholded ICs and associated time courses and power spectra which were then inputs for SOCK (**Figure 1**).

In order to evaluate the performance of our algorithm, we assessed SOCK's classification against manual classification. An expert manual classification of components as either artifact or unlikely artifact was performed blinded to the SOCK classification. The manual classification used visual inspection criteria similar to that outlined in Kelly Jr. et al. (2010) and had previously been applied by consensus of all the authors on data independent from that presented here. In the present study, author KB manually classified all components, and author DA additionally manually classified all ICs in the 1000 Functional Connectomes Project dataset. For all 50 data sets, the number of discordant components [those which were identified as artifact by SOCK but as unlikely artifact by an expert (KB or DA)] were examined in an effort to understand the reason for discordance.

3. RESULTS

3.1. ICA ANALYSIS AND SOCK CLASSIFICATION

MELODIC ICA was applied to resting-state fMRI data acquired in 50 healthy control subjects across three data sets:

1. Data set 1: 7 male, 2 female; age range 7–11 years, mean = 8.8, SD = 1.6
2. Data set 2: 14 male, 7 female; age range 17–40 years, mean = 24.4, SD = 5.9
3. Data set 3: 20 male; age range 19–38 years, mean = 23.4, SD = 5.3

A total of 2,722 components (average of 54 components per subject) were obtained. SOCK classified between 26 and 72% of each subject's components as artifact (mean 55%). See **Table 3** for a summary. A comprehensive list of the ICA decomposition and the SOCK classification for all 50 subjects is also provided in the Appendix (see **Tables A1–A3** in Appendix A).

The time required for SOCK to run, including the automatic generation of the edge and CSF masks, was approximately 2 min per subject on a PC equipped with an Intel Quad-Core i7-2,600 3.4 GHz CPU.

We show below a case example of each of the SOCK criteria for ICs from a MELODIC ICA on one of the 50 subjects (**Table 4**; **Figure 6**). ICA yielded 87 components for this particular subject, out of which 44 (51%) ICs were classified as artifact. No discordant ICs were identified for this particular subject.

Figure 6 illustrates the spatial maps and the SOCK classification of a selected set of components from an ICA for this subject. The numbering of the ICs is based on the order of extraction in the ICA decomposition. For example, IC16 has been classified by SOCK as unlikely artifact as it has been clustered into the smooth category and has low edge and CSF activity and low TFN.

3.2. CLASSIFICATION PERFORMANCE

We assess the performance of SOCK by calculating the sensitivity, that is, the proportion of components SOCK classifies in the artifact category and the specificity, how many of these components are actually artifact. **Table 3** indicates that on average, 55% of ICs were classified in the artifact category. That is, SOCK was able to approximately halve the number of ICs we would otherwise need to look at.

We assessed the specificity by comparing SOCK's classification against manual classification done by an expert (KB or DA) blinded to the SOCK classification. An expert manually classified each IC into either an artifact or unlikely artifact category. All the ICs which SOCK classified as artifact were compared to ICs which the experts classified. Only 0.3% (7) of components identified as artifact by SOCK were discordant with the manual classification (last column of **Table 3**); retrospective examination of these ICs suggested SOCK had correctly identified these as artifact. All seven discordant components with their spatial maps and SOCK features are provided in **Figures 7** and **8**.

3.2.1. IC27 (subject 1)

IC27 in subject 1 (**Figure 7A**) was accepted by an expert because it contained smooth activity in regions of gray matter and was free from CSF artifact and high TFN. However, SOCK classified this IC as artifact as it contains greater than 50% of volume of activity overlapping the edge mask (see **Table 1**).

Table 3 | A summary of the SOCK classification for 50 subjects.

Data set	Number of subjects	SOCK classification			% of rejected ICs	Number of discordant ICs
		Total number of ICA components	Artifact	Unlikely artifact		
1	9	758	399	359	53 (39–71)	5
2	21	410	193	217	47 (26–61)	0
3	20	1,554	902	652	58 (42–72)	2
Total	50	2,722	1,494	1,228	55 (26–72)	7

The last column indicates the components which disagree with an experts classification (see Section 3.2).

3.2.2. IC7, IC23, and IC96 (subject 5)

IC7, IC23, and IC96 in subject 8 (**Figure 7B**) were accepted by an expert as they all appeared smooth and did not have gross edge or CSF activity. However, a closer look at the thresholded spatial maps of each IC overlaid on the edge mask (in green) reveals that a significant proportion of activation is overlapping the edge mask. Both axial and coronal views are shown to clearly indicate this. Hence, SOCK classified these ICs as artifact as they contain greater than 50% of volume of activity overlapping the edge mask (see **Table 1**).

3.2.3. IC90 (subject 5)

IC90 in subject 5 (**Figure 7C**) was accepted by an expert as it was smooth and did not have gross edge or CSF activity. However, a closer look at the unthresholded spatial map of IC90 (shown on the right of the thresholded map) reveals that the IC is not as smooth as it appears compared to viewing the thresholded spatial map. Hence, SOCK clustered it in the unsmooth category and subsequently classified it as artifact (see **Table 1**).

Table 4 | A summary of the SOCK classification for one (Subject 4) of the 30 subjects.

Total number of ICA components	SOCK classification		% of rejected ICs	Number of discordant ICs
	Artifact	Unlikely artifact		
87	44	43	51	0

ICA yielded 87 components for this particular subject, out of which 44 (51%) ICs were classified as artifact. No discordant ICs were identified.

3.2.4. IC70 and IC75 (subject 41)

IC70 and IC75 in subject 41 (**Figure 8**) were not rejected by an expert as they appeared to contain some possible neuronal activity. However these components were rejected by SOCK. SOCK determined IC70 was not sufficiently spatially smooth. Retrospective examination of the ICA decomposition revealed another IC (IC24, not rejected by SOCK) that had overlapping spatial regions (**Figure 8A**). Examination of the unthresholded component maps (not considered during manual classification) revealed the rejected component did indeed have a less smooth spatial pattern than the accepted component (**Figure 8A**). IC 75 was rejected by SOCK due to substantial temporal frequency noise. In this case, retrospective examination revealed two ICs (26 and 29) with spatial maps overlapping the apparent neuronal activity in the rejected component. These other components had less temporal frequency noise (as can seen in the shaded area of the power spectrum, **Figure 8B**) and were not rejected by SOCK.

4. DISCUSSION

We have illustrated a general approach for the identification of artifact in independent components derived from fMRI primarily using spatial criteria. The motivation for our algorithm was to automatically remove artifact without removing signal likely to be of neuronal origin from an ICA of resting-state fMRI. The algorithm assesses four types of artifacts; CSF, sparsely distributed noise, movement-related artifact, and high temporal frequency noise. The temporal feature of the IC is considered only after the initial clustering of ICs using spatial features because temporal

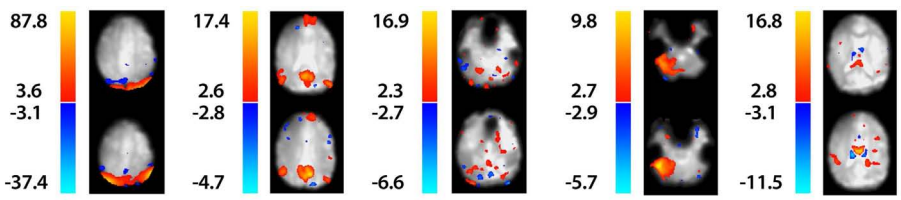

SOCK Features	IC3	IC16	IC46	IC57	IC76
Smoothness	Unsmooth	Smooth	Unsmooth	Smooth	Subsmooth
Edge Activity	High	Low	Low	High	Low
CSF Activity	Low	Low	Low	Low	High
Temporal Frequency Noise	High	Low	Low	Low	High
SOCK Classification	Artifact	Unlikely Artifact	Artifact	Unlikely Artifact	Artifact

FIGURE 6 | A selected set of spatial maps from an ICA and corresponding SOCK classification for Subject 4. The numbering of the ICs is based on the order of extraction in the ICA decomposition.

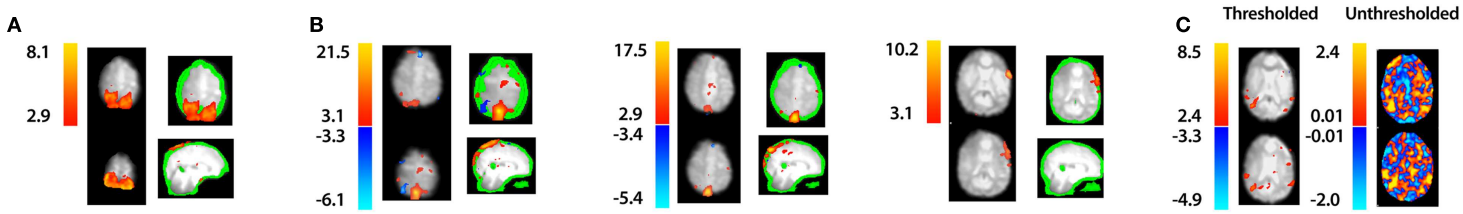

	Accepted by expert				
SOCK Features	IC27 (Subject 1)	IC7 (Subject 8)	IC23 (Subject 8)	IC96 (Subject 8)	IC90 (Subject 5)
Smoothness	Subsmooth	Smooth	Subsmooth	Subsmooth	Unsmooth
Edge Activity	High	High	High	High	Low
CSF	Low	Low	Low	Low	Low
TFN	Low	Low	Low	Low	High
SOCK Classification	Artifact	Artifact	Artifact	Artifact	Artifact

FIGURE 7 | Spatial maps from an ICA and corresponding SOCK classification for all discordant ICs among the first 30 subjects (data sets 1 and 2). All these ICs were classified by an expert as unlikely artifact, whereas SOCK classified them as artifact. The numbering of the ICs is based on the order of extraction in the ICA decomposition. **(A,B)** Subjects 1 and 8: thresholded spatial maps of IC27 for subject 1 and ICs 7, 23, and 96 for subject 8 overlaid on an edge mask (in green, single slice shown) reveals a significant proportion of activation overlapping the edge mask. **(C)** Subject 5: a closer look at the unthresholded spatial map of IC90 (shown on the right of the thresholded map), reveals that the IC is not as smooth as it appears; compared to viewing the thresholded spatial map.

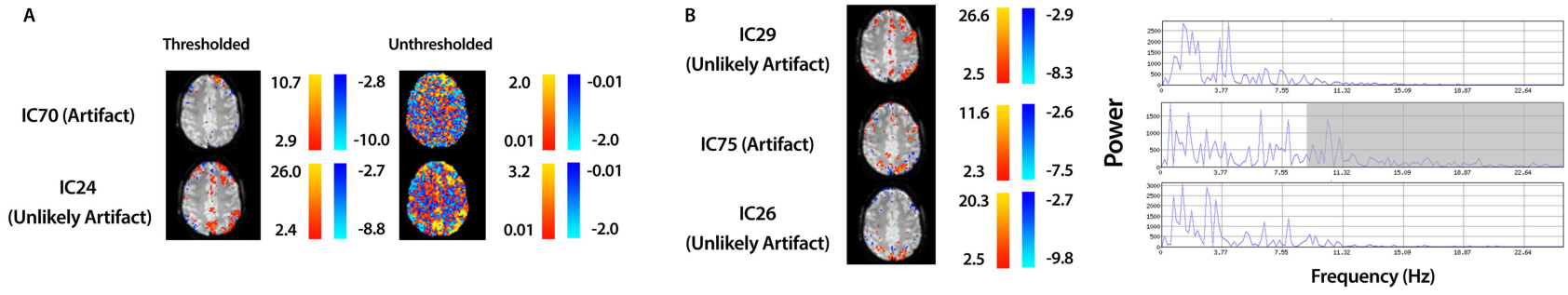

	Accepted by expert
SOCK Features	IC70 (Subject 41)
Smoothness	Unsmooth
Edge Activity	Low
CSF	Low
TFN	High
SOCK Classification	Artifact

	Accepted by expert
SOCK Features	IC75 (Subject 41)
Smoothness	Subsmooth
Edge Activity	Low
CSF	Low
TFN	High
SOCK Classification	Artifact

FIGURE 8 | Spatial maps from an ICA and corresponding SOCK classification for all discordant ICs among the last 20 subjects (data set 3). All these ICs were classified by an expert as unlikely artifact, whereas SOCK classified them as artifact. The numbering of the ICs is based on the order of extraction in the ICA decomposition. **(A)** Subject 41, IC70: SOCK rejected this IC as artifact as it was unsmooth. However, an IC with overlapping spatial regions, but with a greater degree of smoothness was observed in the ICA decomposition (compare unthresholded maps of IC70 vs. IC24). IC24 was not classified as artifact by SOCK. **(B)** Subject 41, IC75: SOCK rejected this IC as artifact as it had substantial temporal frequency noise (see shaded region of power spectrum). However, ICs with overlapping spatial regions, but with less temporal frequency noise were observed in the ICA decomposition (compare power spectra of IC75 vs. ICs 26 and 29). These ICs were not classified as artifact by SOCK.

frequency ranges of artifactual and neural activity sometimes overlap (Beckmann et al., 2005; Birn et al., 2006). Such overlap in frequencies complicates the determination of how much of component variance is due to artifacts vs. signal likely to be of neuronal origin.

We chose to use generic properties of the IC to categorize artifact, specifically limiting them to spatial features as we have particular interest in the application of SOCK to resting-state functional connectivity and to fMRI data collected prior to an epileptic seizure (Federico et al., 2005). In this case, we have no prior model of expected signal change or event timing (apart from the seizure itself at which point the data acquisition usually ends).

Despite the limited *a priori* information, SOCK was able to reduce the solution space by over 50% without rejecting any components that are likely to be of neuronal origin in our test group of 50 healthy controls. Only 0.3% (7) of components identified as artifact by SOCK were discordant with the manual classification and retrospective examination of these ICs suggested SOCK had correctly identified these as artifact. Thus, our method leads to a substantial reduction of the number of components to be inspected and interpreted.

There are other automatic classifier methods which like SOCK use a combination of spatial and temporal characteristics to inform IC classification (Thomas et al., 2002; Kochiyama et al., 2005; De Martino et al., 2007; Perlbarg et al., 2007; Tohka et al., 2008; Sui et al., 2009; Kundu et al., 2012), however, an important difference is that these methods either rely on training data (De Martino et al., 2007; Tohka et al., 2008) or task-related temporal or spatial information (Thomas et al., 2002; Kochiyama et al., 2005; Sui et al., 2009) or set thresholds (Perlbarg et al., 2007) or multi-echo acquisition sequences (Kundu et al., 2012). For example De Martino et al. (2007) used IC-fingerprints for characterizing independent components and in a support vector machines framework to classify them into six classes including activation and noise classes. However, the accuracy of their classifier was dependent on the training data. They found that automatic classification was less accurate in detecting residual motion signal effects due to small number of samples employed in the training. Other methods, such as Sui et al. (2009) classify ICs using contrast images that contain no time-domain information. Their method works on utilizing information concerning the proportion of active voxels overlapping ventricular CSF and gray-matter masks. From our experience, it is often difficult to obtain accurate gray-matter masks with EPI images at 3 T, as the boarders between GM and WM are often indistinct. Edge and CSF masks such as those used in SOCK can be more reliably extracted from EPI images than GM masks. The method of Sui et al. (2009) also requires a user-selected parameter (Z-score threshold) whereas SOCK uses the threshold automatically determined by the Gaussian mixture modeling approach implemented in MELODIC (Beckmann and Smith, 2004) when determining the edge and CSF activity and unthresholded maps when determining the degree of smoothness. Finally, the work of Kundu et al. (2012) offers a robust means for classifying components of interest vs. artifact based on TE-dependence. However, the applicability of this method is dependent on functional images being acquired with a multi-echo EPI sequence, which precludes it from use with data from studies not acquired in this fashion.

4.1. LIMITATIONS

The use of k-means clustering equips SOCK with objective and adaptive criteria, however it does require that at least some components are dominated by noise and others by signal of interest so that a meaningful clustering is achieved. This applies to clustering based upon degree of smoothness, edge activity, and temporal frequency noise. Even in the cases containing the fewest components in our study (subjects 25 and 27 in **Table A2** in Appendix), SOCK was still effective at correctly removing a substantial proportion artifactual components: ICA yielded 14 components out of which SOCK classified 43 and 50% as artifact respectively. Nevertheless we advise caution in applying SOCK as presently implemented to variations of ICA that are already effective in producing very few, if any, components that are dominated by noise. For example event-related ICA (eICA) typically yields very few components due to it only dealing with short time epochs time-locked to events of interest (Masterton et al., 2013a,b). When only a handful of components are generated there is less need for an automatic classifier as it is relatively easy to manually inspect the ICs.

The performance of the SOCK classification is dependent on the accuracy of the edge and CSF masks which are generated using SPM's New Segment tool. We found this tool robust in generating edge and CSF masks for the mean functional images used in this study. However, we did not test accuracy in cases where there exists gross pathology in subjects' brains or where insufficient contrast between CSF and gray-matter regions exists in the EPI images. In these situations where the automated edge or CSF segmentation fails, the user could either generate custom masks, or elect to ignore these criteria (in which case SOCK would be unable to reject as artifact components exhibiting these features).

We tested the SOCK algorithm successfully on data from two different 3 T MRI scanners. These data had TR's of 2.0, 3.0, and 3.6 s, voxel sizes of 2 mm × 2 mm × 2 mm and 3 mm × 3 mm × 3 mm and smoothing of 0 and 8 mm. The performance of SOCK was similar across all data sets. However, we only tested SOCK in conjunction with MELODIC (a popular ICA package). Other good ICA software exists [for example Egolf et al. (2004) and Himberg et al. (2004)] and we would therefore recommend a validation study if one were contemplating the use of SOCK with these or other packages.

A potential limitation of SOCK is that it may reject some neuronal activity if it is mixed with substantial noise in a single component. In the data we tested this may have occurred in two of the components we examined, as shown in **Figure 8**. In cases such as these it is not clear whether one should reject the component. One might argue that a conservative approach is rejection, because the potential activity of interest has the same time-course as noise. On the other hand, in clinical applications it may be considered conservative to retain the IC if any portion might be neuronal, even in the presence of noise. In the case of the two discordant components in this study, rejection would have had a minor impact on the possible neuronal activity, as there were other accepted components that contained substantially more activity in the same locations (see **Figure 8**).

In conclusion we have demonstrated a novel method for the automatic identification of artifactual ICs from resting-state fMRI data. SOCK proved to be effective in separating noise from signal in each of 50 healthy controls by identifying a high proportion of artifact-related ICs without removing components that are likely to be of neuronal origin. We tested the method with resting-state fMRI, however the method may also be effective for other study types and we therefore encourage validation studies in other contexts. SOCK does not require the user to train the algorithm and is able to adaptively determine variable threshold settings via use of k-means clustering. It does not require any temporal information about the fMRI paradigm or high-resolution anatomical scans. SOCK software is available at http://brain.org.au/software.

ACKNOWLEDGMENTS

This study was supported by the National Health and Medical Research Council of Australia (Project Grants 368650 and 318900, Program Grant 628952, and a practitioner fellowship 527800 to Graeme D. Jackson), the Austin Hospital Medical Research Foundation, and the Operational Infrastructure Support Program of the State Government of Victoria, Australia.

REFERENCES

Abbott, D., and Jackson, G. (2001). iBrain – software for analysis and visualisation of functional MR images. *Neuroimage* 13, S59. doi: 10.1016/S1053-8119(01)91402-8

Abbott, D., Masterton, R., Waites, A., Bhaganagarapu, K., Pell, G., Harvey, M., et al. (2011). "The iBrain^{TM} analysis toolbox for SPM," in *Proceedings of the 17th Annual Meeting of the Organisation for Human Brain Mapping*, Quebec City.

Abbott, D. F., Waites, A. B., Lillywhite, L. M., and Jackson, G. D. (2010). fMRI assessment of language lateralization: an objective approach. *Neuroimage* 50, 1446–1455. doi: 10.1016/j.neuroimage.2010.01.059

Beckmann, C., and Smith, S. (2004). Probabilistic independent component analysis for functional magnetic resonance imaging. *IEEE Trans. Med. Imaging* 23, 137–152. doi:10.1109/TMI.2003.822821

Beckmann, C. F., DeLuca, M., Devlin, J. T., and Smith, S. M. (2005). Investigations into resting-state connectivity using independent component analysis. *Philos. Trans. R. Soc. Lond. B Biol. Sci.* 360, 1001–1013. doi:10.1098/rstb.2005.1634

Birn, R. M., Diamond, J. B., Smith, M. A., and Bandettini, P. A. (2006). Separating respiratory-variation-related fluctuations from neuronal-activity-related fluctuations in fMRI. *Neuroimage* 31, 1536–1548. doi:10.1016/j.neuroimage.2006.02.048

Biswal, B., Deyoe, E. A., and Hyde, J. S. (1996). Reduction of physiological fluctuations in fMRI using digital filters. *Magn. Reson. Med.* 35, 107–113. doi:10.1002/mrm.1910350114

Biswal, B. B., Mennes, M., Zuo, X. N., Gohel, S., Kelly, C., Smith, S. M., et al. (2010). Toward discovery science of human brain function. *Proc. Natl. Acad. Sci. U.S.A.* 107, 4734–4739. doi:10.1073/pnas.0911855107

Buxton, R. B., Uluda, K., Dubowitz, D. J., and Liu, T. T. (2004). Modeling the hemodynamic response to brain activation. *Neuroimage* 23, 220–233. doi:10.1016/j.neuroimage.2004.07.013

Calhoun, V. D., Adali, T., Stevens, M. C., Kiehl, K. A., and Pekar, J. J. (2005). Semi-blind ICA of fMRI: a method for utilizing hypothesis-derived time courses in a spatial ICA analysis. *Neuroimage* 25, 527–538. doi:10.1016/j.neuroimage.2004.12.012

Calhoun, V. D., Maciejewski, P. K., Pearlson, G. D., and Kiehl, K. A. (2008). Temporal lobe and default hemodynamic brain modes discriminate between schizophrenia and bipolar disorder. *Hum. Brain Mapp.* 29, 1265–1275. doi:10.1002/hbm.20463

De Martino, F., Gentile, F., Esposito, F., Balsi, M., Di Salle, F., Goebel, R., et al. (2007). Classification of fMRI independent components using IC-fingerprints and support vector machine classifiers. *Neuroimage* 34, 177–194. doi:10.1016/j.neuroimage.2006.08.041

Egolf, E., Kiehl, K. A., and Calhoun, V. D. (2004). "Group ICA of fMRI toolbox (GIFT)," in *Proc. HBM*, Budapest.

Federico, P., Abbott, D. F., Briellmann, R. S., Harvey, A. S., and Jackson, G. D. (2005). Functional MRI of the preictal state. *Brain* 128, 1811–1817. doi:10.1093/brain/awh533

Friston, K. J., Williams, S., Howard, R., Frackowiak, R. S., and Turner, R. (1996). Movement-related effects in fMRI time-series. *Magn. Reson. Med.* 35, 346–355. doi:10.1002/mrm.1910350312

Glover, G. H., Li, T. Q., and Ress, D. (2000). Image-based method for retrospective correction of physiological motion effects in fMRI: RETROICOR. *Magn. Reson. Med.* 44, 162–167. doi:10.1002/1522-2594(200007)44:1<162::AID-MRM23>3.3.CO;2-5

Grootoonk, S., Hutton, C., Ashburner, J., Howseman, A., Josephs, O., Rees, G., et al. (2000). Characterization and correction of interpolation effects in the realignment of fMRI time series. *Neuroimage* 11, 49–57. doi:10.1006/nimg.1999.0515

Himberg, J., Hyvärinen, A., and Esposito, F. (2004). Validating the independent components of neuroimaging time series via clustering and visualization. *Neuroimage* 22, 1214–1222. doi:10.1016/j.neuroimage.2004.03.027

Huettel, S. A., Song, A. W., and McCarthy, G. (2009). *Functional Magnetic Resonance Imaging*. Sunderland: Sinauer Associates.

Hyvärinen, A. (1999). Fast and robust fixed-point algorithms for independent component analysis. *IEEE Trans. Neural Netw.* 10, 626–634. doi:10.1109/72.761722

Kelly, R. E. Jr., Alexopoulos, G. S., Wang, Z., Gunning, F. M., Murphy, C. F., Morimoto, S. S., et al. (2010). Visual inspection of independent components: defining a procedure for artifact removal from fMRI data. *J. Neurosci. Methods* 189, 233–245. doi:10.1016/j.jneumeth.2010.03.028

Kochiyama, T., Morita, T., Okada, T., Yonekura, Y., Matsumura, M., and Sadato, N. (2005). Removing the effects of task-related motion using independent-component analysis. *Neuroimage* 25, 802–814. doi:10.1016/j.neuroimage.2004.12.027

Kundu, P., Inati, S. J., Evans, J. W., Luh, W. M., and Bandettini, P. A. (2012). Differentiating bold and non-bold signals in fmri time series using multi-echo epi. *Neuroimage* 60, 1759–1770. doi:10.1016/j.neuroimage.2011.12.028

LeVan, P., Tyvaert, L., Moeller, F., and Gotman, J. (2010). Independent component analysis reveals dynamic ictal BOLD responses in EEG-fMRI data from focal epilepsy patients. *Neuroimage* 49, 366–378. doi:10.1016/j.neuroimage.2009.07.064

Lillywhite, L. M., Saling, M. M., Simon Harvey, A., Abbott, D. F., Archer, J. S., Vears, D. F., et al. (2009). Neuropsychological and functional MRI studies provide converging evidence of anterior language dysfunction in BECTS. *Epilepsia* 50, 2276–2284. doi:10.1111/j.1528-1167.2009.02065.x

Lund, T. E., Madsen, K. H., Sidaros, K., Luo, W. L., and Nichols, T. E. (2006). Non-white noise in fMRI: does modelling have an impact? *Neuroimage* 29, 54–66. doi:10.1016/j.neuroimage.2005.07.005

Masterton, R. A. J., Carney, P. W., Abbott, D. F., and Jackson, G. D. (2013a). Absence epilepsy subnetworks revealed by event-related independent components analysis of functional magnetic resonance imaging. *Epilepsia* 54, 801–808. doi:10.1111/epi.12163

Masterton, R. A. J., Jackson, G. D., and Abbott, D. F. (2013b). Mapping brain activity using event-related independent components analysis (eICA): specific advantages for EEG-fMRI. *NeuroImage* 70, 164–174. doi:10.1016/j.neuroimage.2012.12.025

McKeown, M. J., Makeig, S., Brown, G. G., Jung, T. P., Kindermann, S. S., Bell, A. J., et al. (1998). Analysis of fMRI data by blind separation into independent spatial components. *Hum. Brain Mapp.* 6, 160–188. doi:10.1002/(SICI)1097-0193(1998)6:5/6<368::AID-HBM7>3.3.CO;2-5

Moritz, C. H., Rogers, B. P., and Meyerand, M. E. (2003). Power spectrum ranked independent component analysis of a periodic fMRI complex motor paradigm. *Hum. Brain Mapp.* 18, 111–122. doi:10.1002/hbm.10081

Ogawa, S., Lee, T. M., Kay, A. R., and Tank, D. W. (1990). Brain magnetic resonance imaging with contrast dependent on blood oxygenation. *Proc. Natl. Acad. Sci. U.S.A.* 87, 9868–9872. doi:10.1073/pnas.87.24.9868

Perlbarg, V., Bellec, P., Anton, J. L., Plgrini-Issac, M., Doyon, J., and Benali, H. (2007). CORSICA: correction of structured noise in fMRI by automatic identification of ICA components. *Magn. Reson. Imaging* 25, 35–46. doi:10.1016/j.mri.2006.09.042

Rodionov, R., De Martino, F., Laufs, H., Carmichael, D. W., Formisano, E., Walker, M., et al. (2007). Independent component analysis of interictal fMRI in focal epilepsy: comparison with general linear model-based EEG-correlated fMRI. *Neuroimage* 38, 488–500. doi: 10.1016/j.neuroimage.2007.08.003

Stevens, M. C., Kiehl, K. A., Pearlson, G., and Calhoun, V. D. (2007). Functional neural circuits for mental timekeeping. *Hum. Brain Mapp.* 28, 394–408. doi:10.1002/hbm.20285

Sui, J., Adali, T., Pearlson, G. D., and Calhoun, V. D. (2009). An ICA-based method for the identification of optimal FMRI features and components using combined group-discriminative techniques. *Neuroimage* 46, 73–86. doi:10.1016/j.neuroimage.2009.01.026

Thomas, C. G., Harshman, R. A., and Menon, R. S. (2002). Noise reduction in BOLD-Based fMRI using component analysis. *Neuroimage* 17, 1521–1537. doi:10.1006/nimg.2002.1200

Tohka, J., Foerde, K., Aron, A. R., Tom, S. M., Toga, A. W., and Poldrack, R. A. (2008). Automatic independent component labeling for artifact removal in fMRI. *Neuroimage* 39, 1227–1245. doi:10.1016/j.neuroimage.2007.10.013

Waites, A. B., Briellmann, R. S., Saling, M. M., Abbott, D. F., and Jackson, G. D. (2006). Functional connectivity networks are disrupted in left temporal lobe epilepsy. *Ann. Neurol.* 59, 335–343. doi:10.1002/ana.20733

Waites, A. B., Stanislavsky, A., Abbott, D. F., and Jackson, G. D. (2005). Effect of prior cognitive state on resting state networks measured with functional connectivity. *Hum. Brain Mapp.* 24, 59–68. doi:10.1002/hbm.20069

Weisskoff, R., Baker, J., Belliveau, J., Davis, T., Kwong, K., Cohen, M., et al. (1993). Power spectrum analysis of functionally-weighted MR data: what's in the noise? *Proc. Int. Soc. Magn. Reson. Med.* 1993(Suppl. S1), 7.

Windischberger, C., Langenberger, H., Sycha, T., Tschernko, E. M., Fuchsjger-Mayerl, G., Schmetterer, L., et al. (2002). On the origin of respiratory artifacts in BOLD-EPI of the human brain. *Magn. Reson. Imaging* 20, 575–582. doi:10.1016/S0730-725X(02)00563-5

Worsley, K., Liao, C., Aston, J., Petre, V., Duncan, G., Morales, F., et al. (2002). A general statistical analysis for fMRI data. *Neuroimage* 15, 1–15. doi:10.1006/nimg.2001.0933

Conflict of Interest Statement: The authors declare that the research was conducted in the absence of any commercial or financial relationships that could be construed as a potential conflict of interest.

*Received: 20 December 2012; accepted: 17 June 2013; published online: 10 July 2013. Citation: Bhaganagarapu K, Jackson GD and Abbott DF (2013) An automated method for identifying artifact in independent component analysis of resting-state fMRI. Front. Hum. Neurosci. **7**:343. doi: 10.3389/fnhum.2013.00343*

APPENDIX A

Table A1 | ICA decomposition and the SOCK classification for 9 healthy controls who underwent a 60 min resting-state fMRI with TR of 3.0 s.

Length of study (min)	TR (s)	Subject	Number of ICA components	SOCK classification		% of rejected ICs	No. of discordant ICs
				Artifact	Unlikely artifact		
60	3.0	1	34	17	17	50	1
60	3.0	2	34	19	15	56	0
60	3.0	3	127	60	67	47	0
60	3.0	4	87	44	43	51	0
60	3.0	5	97	54	43	56	1
60	3.0	6	84	33	51	39	0
60	3.0	7	108	55	53	51	0
60	3.0	8	129	76	53	59	3
60	3.0	9	58	41	17	71	0

SOCK classified between 39 and 71% of each subject's components as artifact (mean 53%). Only 5 of the components identified as artifact by SOCK were discordant with the manual classification (last column); retrospective examination of these ICs suggested SOCK had correctly identified these as artifact.

Table A2 | ICA decomposition and the SOCK classification for 21 healthy controls who underwent a 10 min resting-state fMRI with TR of 3.6 s.

Length of study (min)	TR (s)	Subject	Number of ICA components	SOCK classification		% of rejected ICs	No. of discordant ICs
				Artifact	Unlikely artifact		
10	3.6	10	22	9	13	41	0
10	3.6	11	22	12	10	55	0
10	3.6	12	24	11	13	46	0
10	3.6	13	21	12	9	57	0
10	3.6	14	21	10	11	48	0
10	3.6	15	26	15	11	58	0
10	3.6	16	19	6	13	32	0
10	3.6	17	21	8	13	38	0
10	3.6	18	22	11	11	50	0
10	3.6	19	22	12	10	55	0
10	3.6	20	18	8	10	44	0
10	3.6	21	17	6	11	35	0
10	3.6	22	19	5	14	26	0
10	3.6	23	16	9	7	56	0
10	3.6	24	19	11	8	58	0
10	3.6	25	14	6	8	43	0
10	3.6	26	18	7	11	39	0
10	3.6	27	14	7	7	50	0
10	3.6	28	18	11	7	61	0
10	3.6	29	16	6	10	38	0
10	3.6	30	21	11	10	52	0

SOCK classified between 26 and 61% of each subject's components as artifact (mean 47%). None of components identified as artifact by SOCK were discordant with the manual classification (last column).

Table A3 | ICA decomposition and the SOCK classification for 20 healthy controls who underwent a 9 min resting-state fMRI with TR of 2.0 s.

Length of study (min)	TR (s)	Subject	Number of ICA components	SOCK classification		% of rejected ICs	No. of discordant ICs
				Artifact	Unlikely artifact		
9	2.0	31	79	50	29	63	0
9	2.0	32	100	49	51	49	0
9	2.0	33	78	41	37	53	0
9	2.0	34	74	45	29	61	0
9	2.0	35	72	40	32	56	0
9	2.0	36	109	54	55	50	0
9	2.0	37	82	59	23	72	0
9	2.0	38	63	41	22	65	0
9	2.0	39	78	45	33	58	0
9	2.0	40	58	33	25	57	0
9	2.0	41	79	50	29	63	2
9	2.0	42	98	57	41	58	0
9	2.0	43	90	56	34	62	0
9	2.0	44	57	26	31	46	0
9	2.0	45	83	51	32	61	0
9	2.0	46	79	51	28	65	0
9	2.0	47	78	54	24	69	0
9	2.0	48	63	32	31	51	0
9	2.0	49	74	43	31	58	0
9	2.0	50	60	25	35	42	0

Data was obtained from the 1000 Functional Connectomes Project website. SOCK classified between 42 and 72% of each subject's components as artifact (mean 58%). Only 2 of the components identified as artifact by SOCK were discordant with the manual classification (last column); retrospective examination of these ICs suggested SOCK had correctly identified these as artifact.

APPENDIX B

This appendix describes how we arrived at the hard thresholds used to determine when a component could be safely classified as artifact solely on edge or solely on CSF criteria. Our subsequent validation of the algorithm on data substantially different from that used here indicates that this procedure does not need to be re-done by an end user of the SOCK algorithm.

SOCK uses a combination of measures with adaptively determined thresholds to assist classification. However when there is a very large amount of edge or CSF activity, this alone can be enough to definitively classify the component as artifact. Therefore we use additional fixed thresholds to classify components as artifact when extremes occur in the edge and CSF measures. We tested a combination of fixed edge and CSF thresholds from 5 subjects scanned on the same scanner as data sets 1 and 2 in Section 2.5, where a manual classification was known. This was done via a Receiver Operating Characteristic (ROC) (**Figure A1**), which illustrates the performance of SOCK on these subjects for a total of 525 combinations of edge and CSF thresholds ranging from 0 to 70%. Each combination represents an edge and CSF threshold, with combination 0 representing 0% edge and CSF threshold and combination 525 representing 70% edge and CSF threshold (**Figure A2**). We found the classification in the 5 subjects did not change significantly (within 10%) in the range of 40–50% for edge threshold and 20–30% for the CSF threshold (points in light gray). Lower values resulted in at least one neuronal component being misclassified as artifact (i.e., having a sensitivity of less than one which we regard as failure), whilst higher values resulted in fewer artifacts being identified (which we regard as a decrease in performance or smaller specificity). To minimize the chance of failure we chose the highest thresholds before a decrease in performance occurs (i.e., well away from the failure condition); 50 and 30% for the edge and CSF thresholds respectively.

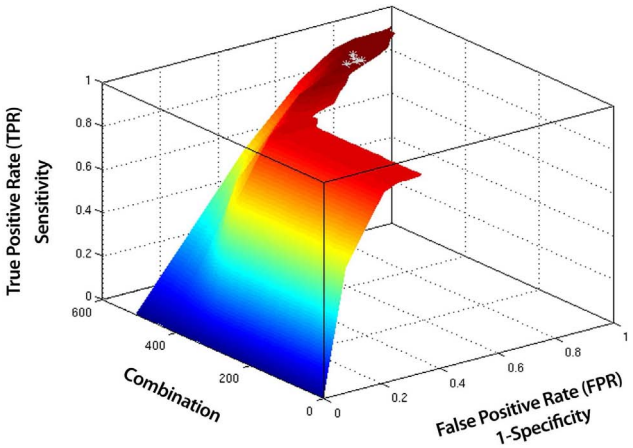

FIGURE A1 | Receiver Operating Characteristic (ROC) curve for edge and CSF thresholds for 5 test subjects. A total of 525 combinations of edge and CSF thresholds (ranging from 0 to 70%) were tested. Shown in light gray are combinations where the classification in the 5 subjects did not change significantly (within 10%). These represent the ranges, 40–50% for the edge threshold and 20–30% for the CSF threshold. Lower values resulted in at least one neuronal component being misclassified as artifact (i.e., having a sensitivity of less than one which we regard as failure), whilst higher values resulted in fewer artifacts being identified (which we regard as a decrease in performance or smaller specificity). To minimize the chance of failure we chose the highest thresholds before a decrease in performance occurs (i.e., well away from the failure condition); 50 and 30% for the edge and CSF thresholds respectively.

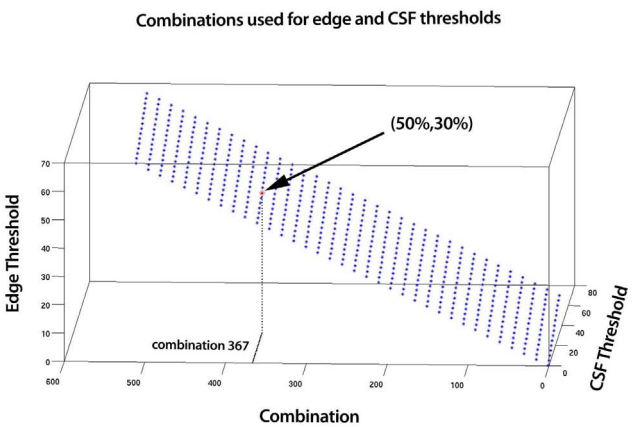

FIGURE A2 | A total of 525 combinations for edge and CSF thresholds ranging from 0 to 70% were tested. Each combination represents an edge and CSF threshold, with combination 0 representing 0% edge and CSF threshold and combination 525 representing 70% edge and CSF threshold. Shown on the graph is combination 367, which corresponds to 50% edge threshold and 30% CSF threshold.

frontiers in
HUMAN NEUROSCIENCE

ORIGINAL RESEARCH ARTICLE
published: 01 May 2013
doi: 10.3389/fnhum.2013.00168

Beyond noise: using temporal ICA to extract meaningful information from high-frequency fMRI signal fluctuations during rest

Roland N. Boubela[1,2,3]*†, Klaudius Kalcher[1,2,3†], Wolfgang Huf[1,2,3,4], Claudia Kronnerwetter[2,5], Peter Filzmoser[3] and Ewald Moser[1,2]

[1] Center for Medical Physics and Biomedical Engineering, Medical University of Vienna, Vienna, Austria
[2] MR Centre of Excellence, Medical University of Vienna, Vienna, Austria
[3] Department of Statistics and Probability Theory, Vienna University of Technology, Vienna, Austria
[4] Department of Psychiatry and Psychotherapy, Medical University of Vienna, Vienna, Austria
[5] Department of Radiodiagnostics and Nuclear Medicine, Medical University of Vienna, Vienna, Austria

Edited by:
Simon Daniel Robinson, Medical University of Vienna, Austria

Reviewed by:
Shanqing Cai, Boston University, USA
Erik Beall, Cleveland Clinic, USA

***Correspondence:**
Roland N. Boubela, MR Centre of Excellence, Centre of Medical Physics and Biomedical Engineering, Medical University of Vienna, Währinger Gürtel 18-20, 1090 Vienna, Austria.
e-mail: roland.boubela@meduniwien.ac.at

† Roland N. Boubela and Klaudius Kalcher have contributed equally to this work.

Analysis of resting-state networks using fMRI usually ignores high-frequency fluctuations in the BOLD signal – be it because of low TR prohibiting the analysis of fluctuations with frequencies higher than 0.25 Hz (for a typical TR of 2 s), or because of the application of a bandpass filter (commonly restricting the signal to frequencies lower than 0.1 Hz). While the standard model of convolving neuronal activity with a hemodynamic response function suggests that the signal of interest in fMRI is characterized by slow fluctuation, it is in fact unclear whether the high-frequency dynamics of the signal consists of noise only. In this study, 10 subjects were scanned at 3 T during 6 min of rest using a multiband EPI sequence with a TR of 354 ms to critically sample fluctuations of up to 1.4 Hz. Preprocessed data were high-pass filtered to include only frequencies above 0.25 Hz, and voxelwise whole-brain temporal ICA (tICA) was used to identify consistent high-frequency signals. The resulting components include physiological background signal sources, most notably pulsation and heart-beat components, that can be specifically identified and localized with the method presented here. Perhaps more surprisingly, common resting-state networks like the default-mode network also emerge as separate tICA components. This means that high-frequency oscillations sampled with a rather T1-weighted contrast still contain specific information on these resting-state networks to consistently identify them, not consistent with the commonly held view that these networks operate on low-frequency fluctuations alone. Consequently, the use of bandpass filters in resting-state data analysis should be reconsidered, since this step eliminates potentially relevant information. Instead, more specific methods for the elimination of physiological background signals, for example by regression of physiological noise components, might prove to be viable alternatives.

Keywords: resting-state fMRI, temporal ICA, heart rate variability, resting-state networks

1. INTRODUCTION

The investigation of BOLD fluctuations in the resting brain using fMRI has been a rapidly expanding field of research since the first identification of consistent patterns in these data (Biswal et al., 1995), and ICA in particular has gained great popularity in fMRI as a powerful tool for exploring these data (Biswal and Ulmer, 1999; Calhoun et al., 2001). The appeal of Independent Component Analysis (ICA) in the context of resting-state fMRI (rs-fMRI) lies to a great extent in the fact that, in contrast to task-fMRI, little *a priori* knowledge about the temporal dynamics of the fluctuations is available and ICA can be used to identify consistent patterns in an exploratory manner (Beckmann, 2012). Thus, using ICA on rs-fMRI data, several consistent resting-state networks have been identified in a multitude of different individual studies (Damoiseaux et al., 2006; Robinson et al., 2009; Allen et al., 2011; Yeo et al., 2011) as well as in collections of data pooled from multiple sites (Biswal et al., 2010; Kalcher et al., 2012).

A common feature to most rs-fMRI ICA studies thus far is the use of relatively long TRs (usually 2–3 s) in order to increase BOLD weighting (Kim and Ogawa, 2012), and scan durations of mostly between 5 and 10 min (Biswal et al., 2010), limiting the fluctuations that can be studied to those at frequencies between 0.001 and 0.25 Hz. Within this frequency range, the highest amplitudes of oscillations in resting-state networks in these studies have been observed in the lower part (<0.1 Hz), which lead to the general characterization of resting-state brain networks as networks of low-frequency fluctuations, typically between 0.01 and 0.1 Hz (Margulies et al., 2010; Yeo et al., 2011; Kalcher et al., 2012).

In recent years, simultaneous image readout (SIR) and multibanded (MB) EPI pulse sequences allowing simultaneous acquisition of multiple brain slices during a single EPI echo train have

opened new opportunities for accelerating fMRI scans without sacrificing spatial resolution (Feinberg et al., 2010; Feinberg and Yacoub, 2012). The increased temporal resolution can be put to use in different ways. First, the higher sampling rate allows to perform new kinds of analysis methods, leading to a new view on low-frequency fluctuations, as exemplified by the identification of temporal functional modes (TFM) by Smith et al. (2012). On the other hand, the increase in temporal resolution without the need to limit image acquisition to a few slices can be harnessed to investigate higher-frequency fluctuations at whole-brain level. Of course, this will change the specific contrast from mainly BOLD-based to flow/perfusion-based (Kim and Ogawa, 2012).

It should be noted at this point that the focus on low-frequency BOLD fluctuations is not only due to technical limitations, but also motivated by the temporal delays involved in the hemodynamic response to neuronal activity. Indeed, the peak of the hemodynamic response to a particular stimulus – and thus of the BOLD signal – occurs 3–10 s after the underlying neuronal response (Aguirre et al., 1998; Cunnington et al., 2002). Thus, the BOLD signal can be seen as temporally smoothed in comparison with the neuronal activity, motivating the neglect of signal fluctuations in higher frequencies. Nonetheless, the possibility to obtain this high-frequency signals opens the question to investigate what patterns can be found in these frequency domains.

Due to limited *a priori* knowledge on networks of high-frequency rs-fMRI BOLD oscillations, an exploratory approach seems most viable (Tukey, 1977) to get an unbiased estimation of the global structure of these oscillations. While different exploratory analysis techniques for fMRI data exist, e.g., principal components analysis (Baumgartner et al., 2000), canonical correlation analysis (Friman et al., 2001), fuzzy clustering (Baumgartner et al., 1998; Moser et al., 1999), as well as spatial or temporal ICA (Calhoun et al., 2001), our analysis specifically needs a method that can deal with overlapping spatial distributions of different signal sources. Temporal ICA (tICA) can achieve this in identifying temporally independent signal sources with potentially overlapping spatial distributions, and in this offers good interpretability, since its result is a solution to the blind source separation problem. In particular, the potential to better distinguish spatially overlapping signal sources might prove useful for the identification of cardiac and other physiological signal sources, a feature that spatial ICA cannot accomplish as shown by Beall and Lowe (2010).

Temporal ICA has rarely been used thus far in fMRI analyses, mostly due to two reasons. The first lies in originally unsurmountable computational difficulties in computing the necessary linear algebra operations, in particular computing the covariance matrix of dimension (number of voxels × number of voxels) (Calhoun et al., 2001), but new algorithms as well as the increased computational power available have greatly alleviated this limitation. The second reason is the limited number of time points (the data points for tICA) available in most fMRI scans, limited by common TRs of 2–3 s and scan durations under 10 min to about 300 time points. In contrast to spatial ICA, where the corresponding variable is the number of voxels instead of the number of time points, this limited amount of data points leads to computational issues regarding the stability of the ICA algorithm when applying it as temporal ICA. Multiplexed EPI sequences, with greatly reduced TRs, lead to larger amounts of data points without increasing scan duration, and thus allow for a reasonable application of tICA on the resulting datasets.

Beyond the increase in stability of tICA estimation, the high sampling rate also allows to see fluctuations of higher frequencies than before in whole-brain fMRI datasets. It is however unclear as of now what exactly is gained by critically sampling higher frequencies (at low TR). In this study, we set out to investigate the information gained in these high frequencies, and in particular the frequency domain above the highest frequency usually inspected in resting-state fMRI studies, about 0.25 Hz. *A priori*, two thoughts on these high-frequency fluctuations come to mind: first, they could be expected to contain pulsation-related artifacts, and second, due to the slow hemodynamic response usually expected for neuronal activity, one might be tempted not to expect to identify neuronal signals among the high-frequency BOLD oscillations. Indeed, early investigations by Cordes et al. (2001) on the relative contributions of different frequency ranges – Cordes et al. acquired signal from 4 slices with a TR of 400 ms – found that functional connectivity was almost exclusively dependent on the signal fluctuations below 0.1 Hz for neuronal signal sources, and only the correlation coefficients from signal in major arteries or veins as well as in the CSF were dependent upon higher frequencies.

However, there is some evidence in more recent studies that this latter expectation might not hold true. For once, studies on spectral characteristics of resting-state networks by Niazy et al. (2011) and Van Oort et al. (2012) have revealed that the spectral range of commonly identified resting-state networks is wider than the hypothesized 0.01–0.1 Hz and extend to at least 0.17 and 0.25 Hz, respectively. Moreover, there are studies on specific high-frequency behavior of BOLD oscillations, e.g., the co-occurrence of spikes in different regions of a particular network (Tagliazucchi et al., 2011, 2012) or variation in amplitude variance asymmetry (Davis et al., 2013), that can also be attributed to resting-state network activity, indicating consistent patterns of BOLD and/or perfusion variability beyond low-frequency fluctuations.

In this study, we investigated high-frequency signal fluctuations during rest by temporally filtering fMRI data with a low TR to frequencies above 0.25 Hz and analyzing the resulting time-courses using temporal ICA. In view of the hypotheses mentioned above, we examined the extent to which tICA is able to specifically separate physiological background signals, in particular heart-beat related signal fluctuations, from other signal sources in the brain, as this is seen as one of the "killer applications" of ICA in rs-fMRI (Beckmann, 2012). Moreover, we wanted to explore whether resting-state network related signals are still present in those high-frequency domains and could effectively be identified.

2. MATERIALS AND METHODS

2.1. SUBJECTS

Ten subjects (5 males/5 females, mean age 23.4, SD 3.1 years) were recruited at Medical University of Vienna. Exclusion criteria were prior psychiatric or neurologic illnesses, as well as the usual exclusion criteria for MR studies. All subjects gave written informed consent prior to the scan and the study was approved by the local institutional review board.

2.2. MEASUREMENTS

Subjects underwent a 6 min resting-state scan on a Siemens TIM Trio 3 T scanner using a 32-channel head coil with a multiplexed EPI sequence by Feinberg et al. (2010), acquiring in total 1024 volumes (flip angle = 30°, TE/TR = 32/354 ms, 2.4 mm × 1.9 mm × 3.5 mm, bandwidth = 1748 Hz/pixel, 20 axial slices, 2 mm slice gap, multiband acceleration factor 4, 6/8 partial Fourier). Subjects were instructed to keep their eyes closed, refrain from movement during the scan and avoid to fall asleep without concentrating on anything in particular. After the resting-state scan, a high-resolution anatomical image was acquired using MPRAGE with 1 mm × 1 mm × 1.1 mm resolution with 160 sagittal slices (TE/TR = 4.21/2300 ms, flip angle 9°, inversion time 900 ms).

2.3. PREPROCESSING

All data were preprocessed with a combination of AFNI (Cox, 1996) and FSL (Smith et al., 2004), using an analysis framework in R (Boubela et al., 2012; R Development Core Team, 2013) on Ubuntu Linux (Version 11.10 "Oneiric Ocelot"). Anatomical images were skullstripped and normalized to MNI152 standard space. Functional images were corrected for intensity inhomogeneity using a bias field estimation by FSL FAST, skullstripped and realigned to the 500th volume. Subsequently, functional images were aligned to the anatomical images in MNI152 standard space and resampled to 2 mm × 2 mm × 2 mm isotropic resolution, blurred with an isotropic Gaussian 6 mm FWHM kernel, and motion parameters (3 translations and 3 rotations) were regressed out using a generalized linear model (GLM).

2.4. INDEPENDENT COMPONENT ANALYSIS

After the preprocessing steps mentioned above, all further analyses were performed in R (Version Under Development (unstable) 2012-11-27 r61172 "Unsuffered Consequences"; this version was used to allow the allocation of objects with more than $2^{31} - 1$ elements, necessary for the processing of time concatenated group ICA). At single-subject level, the first 24 volumes of all subjects were discarded to account for transient effects, and all voxel time-series were scaled to mean 0 and standard deviation 1. To isolate high-frequency oscillations, a discrete Fourier transform was applied to each voxel's time course, all magnitudes in Fourier space corresponding to frequencies below 0.25 Hz (the highest frequency that can be sampled at a typical TR of 2 s) were set to 0, and the signal was then transformed back in the original space using the inverse discrete Fourier transform. Thus, the signal that was analyzed contained only fluctuations above 0.25 Hz. Single-subject data were analyzed individually as well as concatenated for group analysis, forming a 10,000 (i.e., 10 subjects × 1000 time points) × 239901 (number of voxels within the brain mask) matrix. Prewhitening and dimensionality reduction was performed by principal component analysis (PCA) using the R package irlba (Baglama and Reichel, 2005, 2012), which implements implicitly restarted Lanczos bidiagonalization singular value decomposition (SVD), and the 76 principal components with the largest eigenvalues were computed and used for the ICA analysis. All matrix multiplications on the data matrix necessary to compute the SVD and the principal components were performed using the library phiGEMM (Spiga and Girotto, 2012), which distributed computation on two NVidia Tesla C2070 graphics processing units. Finally, fastICA (Hyvärinen, 1999) was used to compute 75 temporally independent components for the time concatenated group dataset.

2.5. GROUP COMPONENTS

In the group analysis, components were discarded if they were driven by individual subjects only (as opposed to being present in all subjects; this can easily be identified in the component timecourses, see **Figure A1** in Appendix). As a formal criterion, components were discarded if the ratio of the sum of the squares of the time course of one subject divided by the sum of the squares of the time courses of all other subjects was larger than 1, i.e., if one subject contributed more variance to the component than all other subjects combined.

2.6. CHARACTERIZATION OF RESULTING COMPONENTS

Spatial maps of all resulting components were projected back from the principal component space into the original space. Temporal ICA time courses were Fourier transformed to compute power spectra, and the fraction of the power in each of the frequency ranges 0.25–0.5, 0.5–0.75, 0.75–1.0, 1.0–1.25, and 1.25–1.4 Hz was computed.

2.7. LOW-FREQUENCY REFERENCE NETWORKS

To get a sense of how resting-state networks obtained in the high-frequency range relate to low-frequency resting-state networks, the data preprocessed as above but without applying the high-pass filter were analyzed with temporal ICA directly and the resulting networks were used as reference for the high-frequency networks.

3. RESULTS

Of the 75 tICA components, 25 were found to be consistent across subjects using the definition above, i.e., no single subject contributed more to the component than all other subjects combined. Among these consistent group-level components, four distinct types of components can broadly be distinguished: pulsation or physiological components (8 components), components resembling known resting-state networks as described by previous low-frequency sICA studies (2), technical artifacts (2), and other signal sources (13).

Generally speaking, pulsation components were the most consistent across subjects using the measure described above. They were located primarily in the ventricles and in the vicinity of large blood vessels (see **Figure 1** left) and exhibited more amplitude in higher frequencies (mainly above 0.6 Hz, see **Figure 1** right). Specifically, the ventricular components had peak power between 0.6 and 0.8 Hz, while other pulsation components including mainly the insula had a broader frequency range between 0.6 and 1.4 Hz. Overall, though, it can be said that pulsation artifacts showed a flat, modulated power spectrum.

The resting-state components identified in the high-frequency range were the default-mode network and the fronto-parietal network, the corresponding maps are shown in **Figure 2**. In contrast to the pulsation artifacts, resting-state network timecourses tended to have higher amplitude in the lower frequencies (0.25–0.6 Hz). The

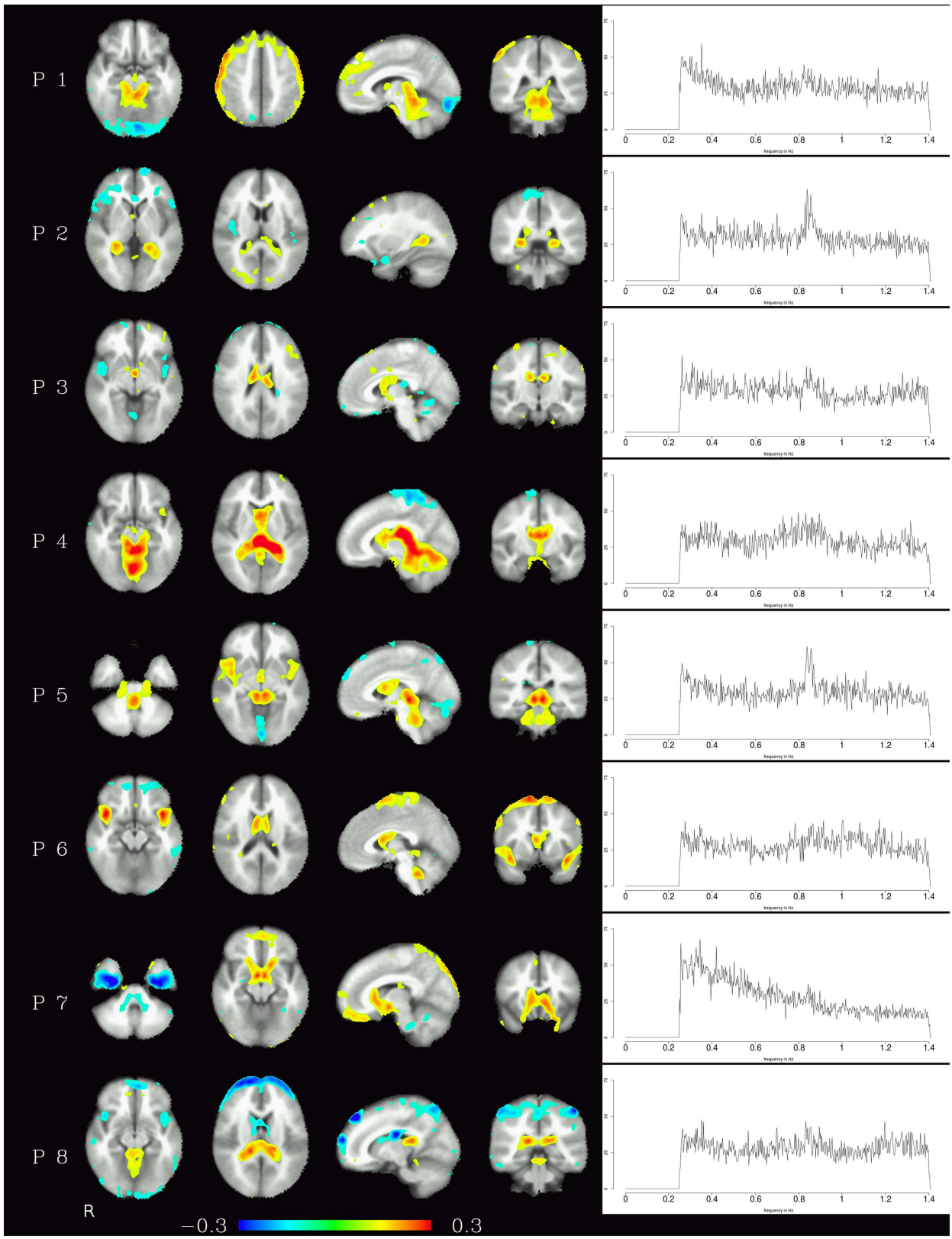

FIGURE 1 | Temporal ICA components attributed to pulsation in ventricles and large blood vessels. Left: maps thresholded at 0.1 (weights in the mixing matrix). Right: frequency spectra corresponding to the ICA components represented on the left.

most distinctive characteristic of the spectra of the resting-state networks as opposed to the pulsation and artifact components is their skewness – amplitude is highest for lower frequencies and decreases continually as the frequency increases, and converges to a minimum at about 0.6 Hz.

Corresponding resting-state networks could also be identified in the analysis of the non-bandpassed data (**Figure 3**). It can be seen that most of the power of the resting-state networks originates in the low-frequency range (below about 0.2 Hz), but the qualitatively very similar maps in the high-frequency data suggest that these same networks can also be identified by their distinctive high-frequency fluctuations, which indeed amount to about 50% of the total spectral power of these networks. **Table 1** summarizes the fraction of power of the fluctuations of these networks that fall in the frequency bands 0.01–0.1, 0.1–0.25, and 0.25–1.4 Hz. (For further reference, **Figure 4** shows the complete set of components identified by tICA on the unfiltered data.)

The third group of components were technical artifacts defined by two unique characteristics. The first emerges from the spatial maps of these components, which shows alternating bands of high and low loadings aligned in planes parallel to the acquisition slices (see **Figure 5** left). The second characteristic is the narrow peak of the frequency spectrum at about 0.8 Hz (see **Figure 5** right).

The relative power of each frequency range (0.25–0.5, 0.5–0.75, 0.75–1.0 Hz, 1.0–1.25 Hz, and 1.25–1.4 Hz) of the spectra is shown in **Figure 6**. The technical artifacts are easiest to distinguish due to their power being almost entirely in the range between 0.75 and 1.0 Hz, with much higher relative power in this range than all other components, and very low power in all other frequency bands. Resting-state networks can also be distinguished by their having highest relative power in the lowest of the frequency bands (0.25–0.5 Hz), while the pulsation components and other artifacts have lower power in this frequency range, but tend to have higher power in all other ranges. Overall, the distribution of relative spectral power is more similar between resting-state networks

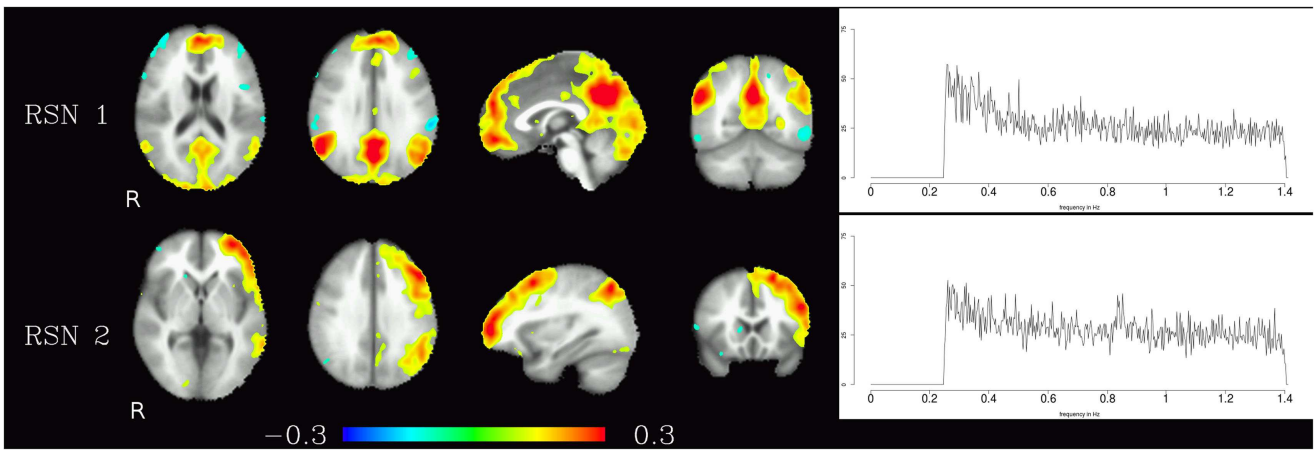

FIGURE 2 | Temporal ICA components representing high-frequency fluctuations in brain regions commonly associated with resting-state networks. Figure layout as in **Figure 1**.

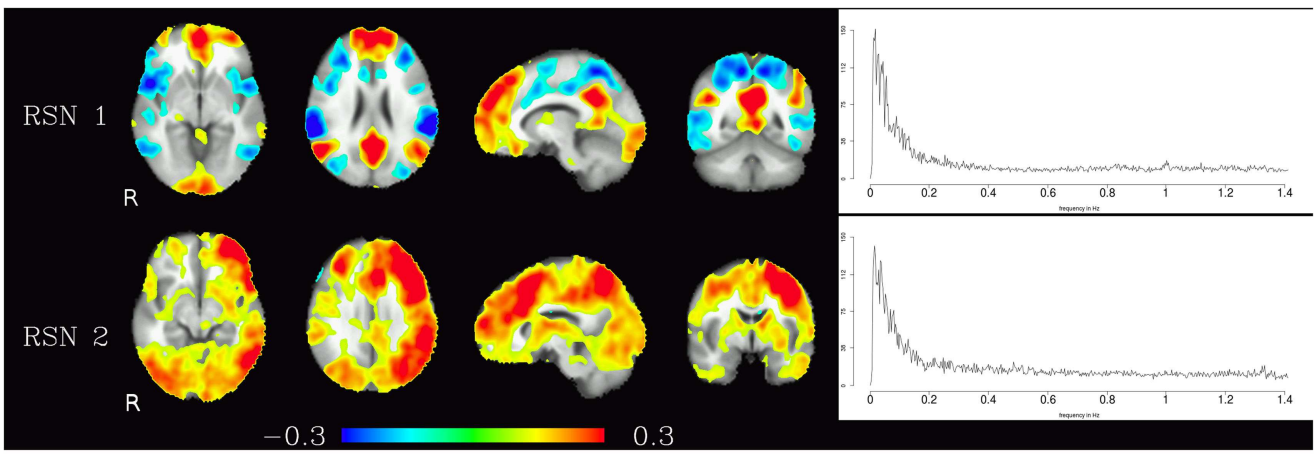

FIGURE 3 | Temporal ICA components from non-bandpassed data corresponding to the high-frequency resting-state networks in Figure 2. Figure layout, color scale, and threshold are identical to the ones in **Figure 2**.

Table 1 | Fractional amplitude of fluctuations in various frequency bands (0.01–0.25, 0.01–0.10, 0.10–0.25, 0.25–1.4 Hz) for RSN 1 and RSN 2 depicted in Figure 3.

	0.01–0.25 Hz (%)	0.01–0.10 Hz (%)	0.10–0.25 Hz (%)	0.25–1.4 Hz (%)
RSN 1	46.77	31.24	15.52	52.49
RSN 2	49.91	33.87	16.04	49.3

and pulsation components than between any one of these groups and technical artifacts.

Finally, components related to heart-beat could be found in the components discarded due to their inconsistency across subjects (this inconsistency presumably is due to heart rate differences between subjects). For each subject, the spectrum of the group component driven mainly by that subject that can be interpreted as heart-beat related signal is shown in **Figure 7**. The power spectra of these heart-beat components can be distinguished by their peak at frequencies around 1–1.3 Hz (the exact frequency of the peak varies, depending on the heart rate variability (HRV) of the individual subject). Thus, HRV would be a physiological parameter to be extracted from our data.

4. DISCUSSION

In this work, we have shown that consistent large-scale high-frequency signal oscillations in the brain exist and can be attributed to specific signal sources using temporal ICA. Potentially of most practical interest among these are the physiological or pulsation-related components and the resting-state networks, but other signal sources can be distinguished as well. We have concentrated on fluctuations of frequencies higher than 0.25 Hz to study consistent effects that cannot be identified in typical fMRI experiments with a TR of about 2–3 s, since they are beyond the Nyquist frequency of the measurements performed in these experiments. It should be noted that, even though they cannot be isolated when using TRs of 2–3 s, in the resulting data these high-frequency effects are nonetheless present in the form of aliased lower-frequency fluctuations, i.e., so-called physiological noise. The specific identification of pulsations and artifacts can be useful in disentangling them from neuronal signal sources, in order to isolate the latter more specifically, but also to study physiological effects by themselves.

Two innovations from different fields have been employed in this study in order to identify the high-frequency components of fMRI signal. First, the measurement of whole-brain time-series at the low TR required for a sufficiently high sampling rate has only become possible with the introduction of multiband EPI sequences (Feinberg et al., 2010; Moeller et al., 2010; Feinberg and Yacoub, 2012), allowing the simultaneous acquisition of multiple slices and leading to a reduction of the TR to 354 ms with the parameters used in this study. Second, new computational methods were needed to perform the analysis at hand. This included improvements in handling the large datasets generated by this sequence, with both high spatial and high temporal resolution, as well as fast iterative computation of SVD – and by consequence of PCA and ICA – on these datasets, both necessary to divide the signal acquired into temporally independent sources (Boubela et al., 2012).

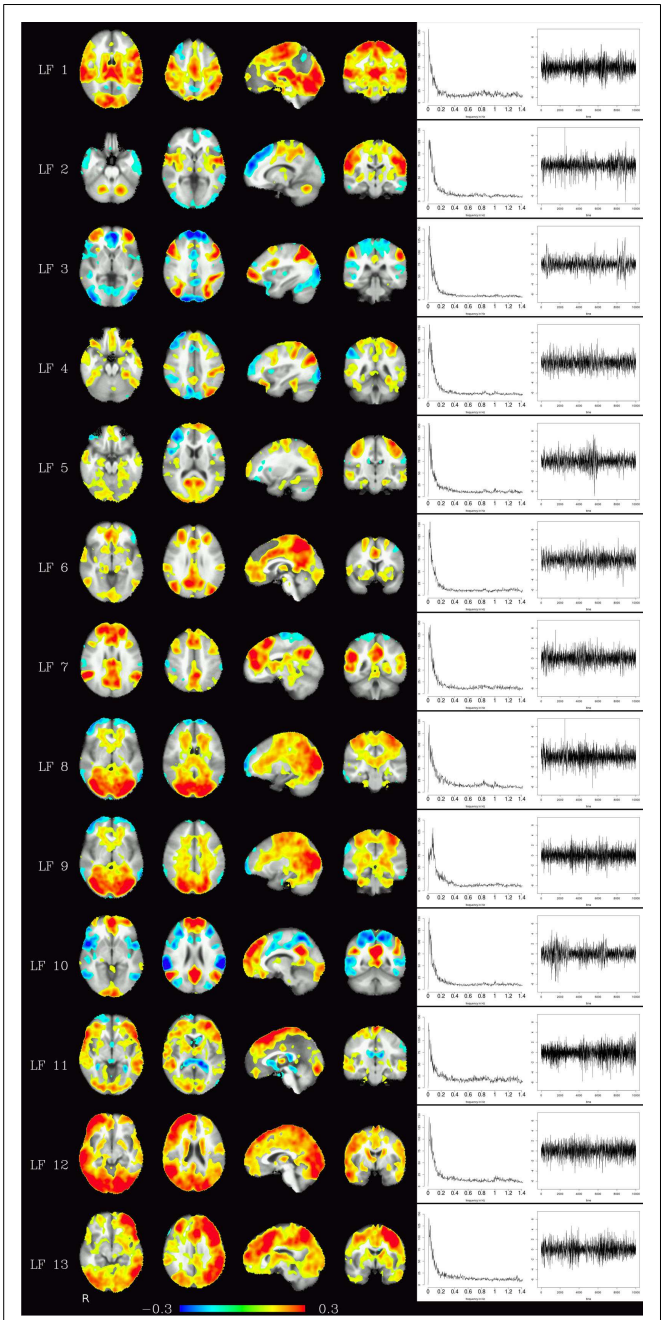

FIGURE 4 | Depending on the number of components chosen, various temporally independent low-frequency components (≤0.25 Hz) are separated by the algorithm (LF 1–LF 13, left row). Note that time courses and corresponding frequency spectra (right side) are not contaminated by any high-frequency components (e.g., respiration, heart-beat, etc.), increasing functional contrast-to-noise ratio. The interpretation whether a component is (predominantly) of vascular or brain tissue origin, however, is not obvious from the spectra alone.

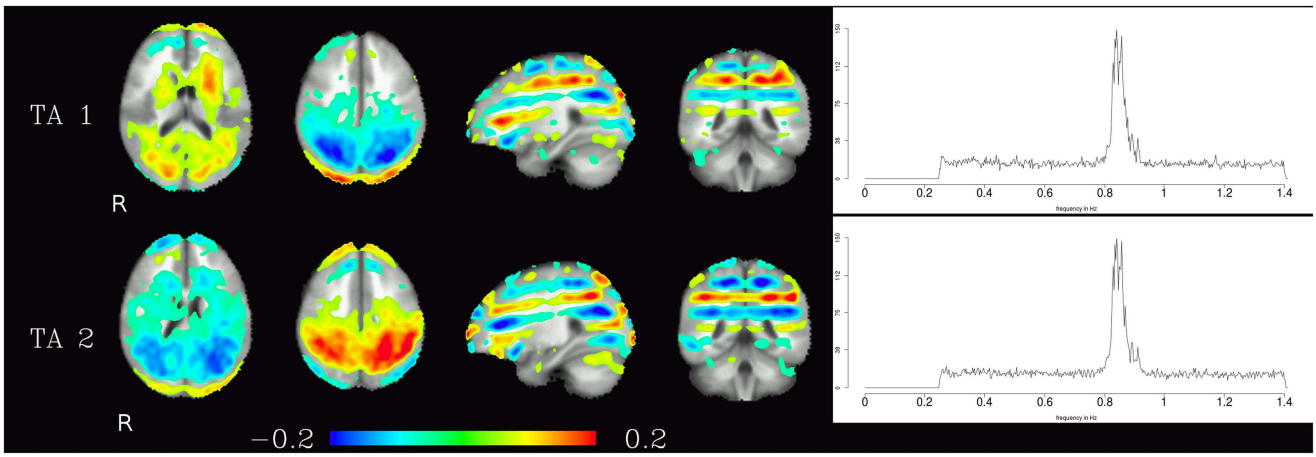

FIGURE 5 | Temporal ICA components attributed to technical artifacts. Figure layout as in **Figure 1**, spatial maps are thresholded at 0.05. Note that even though they cover almost the whole brain, and thus have at least some overlap with all other components, tICA is able to separate them from the other components due to the technical artifacts distinctive temporal characteristics (visible in their power spectra).

Perhaps the most surprising finding of this study was the identification of resting-state networks, and most notably the default-mode network, in the high-frequency data alone. While the traditional view of resting-state networks as low-frequency fluctuations below 0.1 Hz has been challenged, previous findings have related mostly to oscillations below 0.16 (Niazy et al., 2011) and 0.25 Hz (Van Oort et al., 2012). The present study adds to this the notion that even in frequencies beyond the frequency range critically sampled by usual fMRI acquisition sequences, oscillations attributable to resting-state networks can be recognized. Indeed, the amount of information contained in the high-frequency oscillations of these two networks is sufficient to produce a spatial delineation consistent with previously published spatial maps, even despite the small sample size. Consequently, further investigations into the fluctuation characteristics of resting-state networks embracing the recent developments in fast fMRI acquisition techniques appear to be worthwhile. Indeed, whether 'sources of resting-state BOLD responses are similar to those of stimulus-induced responses' is still an open question and part of ongoing research (Kim and Ogawa, 2012), and it is not yet clear if and to what extent the theory of hemodynamic coupling can be drawn upon to substantiate the widespread dismissal of high-frequency oscillations in resting-state fMRI.

The identification of resting-state networks in high-frequency data of course does not imply that they are primarily high-frequency phenomena, but rather that the frequency range of resting-state fluctuations is broader than previously assumed. Still, it must be noted that only two of the typically described resting-state networks were found in the high-pass-filtered data of this study. Both the default-mode network and the fronto-parietal network are characterized by high low-to-high-power ratio and high dynamic range (defined as the difference between the peak power of the spectrum minus the minimum of the power at higher frequencies compared to this peak) (Robinson et al., 2009; Kalcher et al., 2012), which seems paradoxical for networks that can be identified by their high-frequency oscillations. On the other hand, these two metrics are also associated with the robustness of the networks, i.e., networks with high power ratio and high dynamic range are identified more robustly across studies, and this robustness of the networks might be the reasons why only these two are identified here. High-frequency oscillations in other resting-state networks might exist, but in this case, their power must then be too low to be detected with the SNR level attained in this study.

The identification and separation of physiological signal sources made possible by the combination of a high sampling rate and temporal ICA of the resulting time courses can be seen as another way of using the high-frequency data and has multiple applications. First, the ability to disentangle physiological signal components from signals of neuronal origin could be used for the correction of the typical BOLD signal and thus for increasing the specificity not only of resting-state, but also of task-fMRI analyses (based on the assumption that physiological signals are the same during tasks and during rest). Correction of fMRI time-series for non-neuronal effects could then be performed using either the time course itself or a separately measured dataset (e.g., a resting-state dataset measured before or after a task-fMRI paradigm) (Kalcher et al., 2013). As another possible future application, measuring and separating physiological signals directly from fMRI data, as opposed to using separately acquired physiological respiratory and cardiac signals, would have the advantage that these signals could immediately be located in the brain using the spatial maps of the corresponding components, and would not require additional equipment for the acquisition of physiological signals. Indeed, the possibility of directly estimating cardiac and respiratory signal from the fMRI data has already been explored, e.g., by Beall and Lowe (2007) and Chuang and Chen (2001), and the methods presented here could be used to improve on these techniques. One potential advantage of avoiding the need for additional equipment is an increase in reliability of the complete system due to less individual parts that can possibly fail which might be critical for particular applications like real-time fMRI (Weiskopf, 2012). Furthermore, reducing the number of components separately introduced into the measuring systems

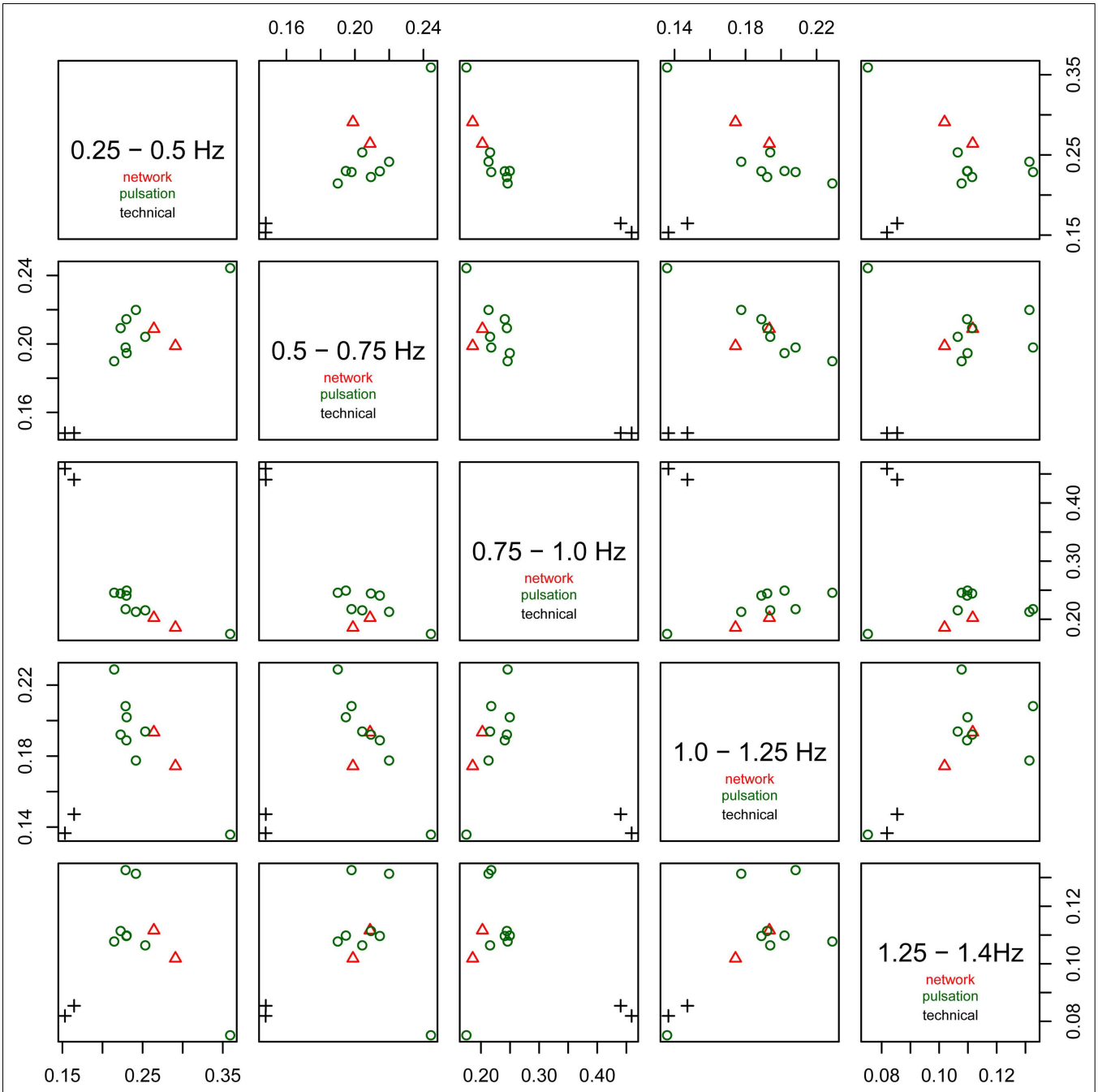

FIGURE 6 | Fractional amplitude of fluctuations in frequency bands 0.25–0.5, 0.5–0.75, 0.75–1.0, 1.0–1.25, and 1.25–1.4 Hz plotted against each other for all consistent tICA components. Note that technical artifacts can easily be separated from all other components in the frequency bands 0.25–0.5, 0.5–0.75, and 0.75–1.0 Hz. Components attributed to classical resting-state networks appear as mixed with pulsation components, though they tend to have higher power in the lowest frequency range, between 0.25 and 0.5 Hz, than most of the pulsation components.

means reducing the possible amount of operator bias – thus effectively increasing reproducibility of fMRI study results and comparability across studies in the face of possible future meta-analyses (Huf et al., 2011). Finally, direct measurement in the subject's brain could circumvent time-delay issues due to measurement of multiple physiological variables on different parts of the body, e.g., the acquisition of pulse-oximetry data on the finger. Of course, these suggestions would require further studies to demonstrate their suitability for routine application.

Previous approaches taken to eliminate physiological signal sources include bandpass-filtering to frequencies below 0.1 Hz, but the adequateness of this method has been questioned – one of the main reasons for this being that many physiological confounds (like heart-beat) occur beyond the Nyquist frequency of typical

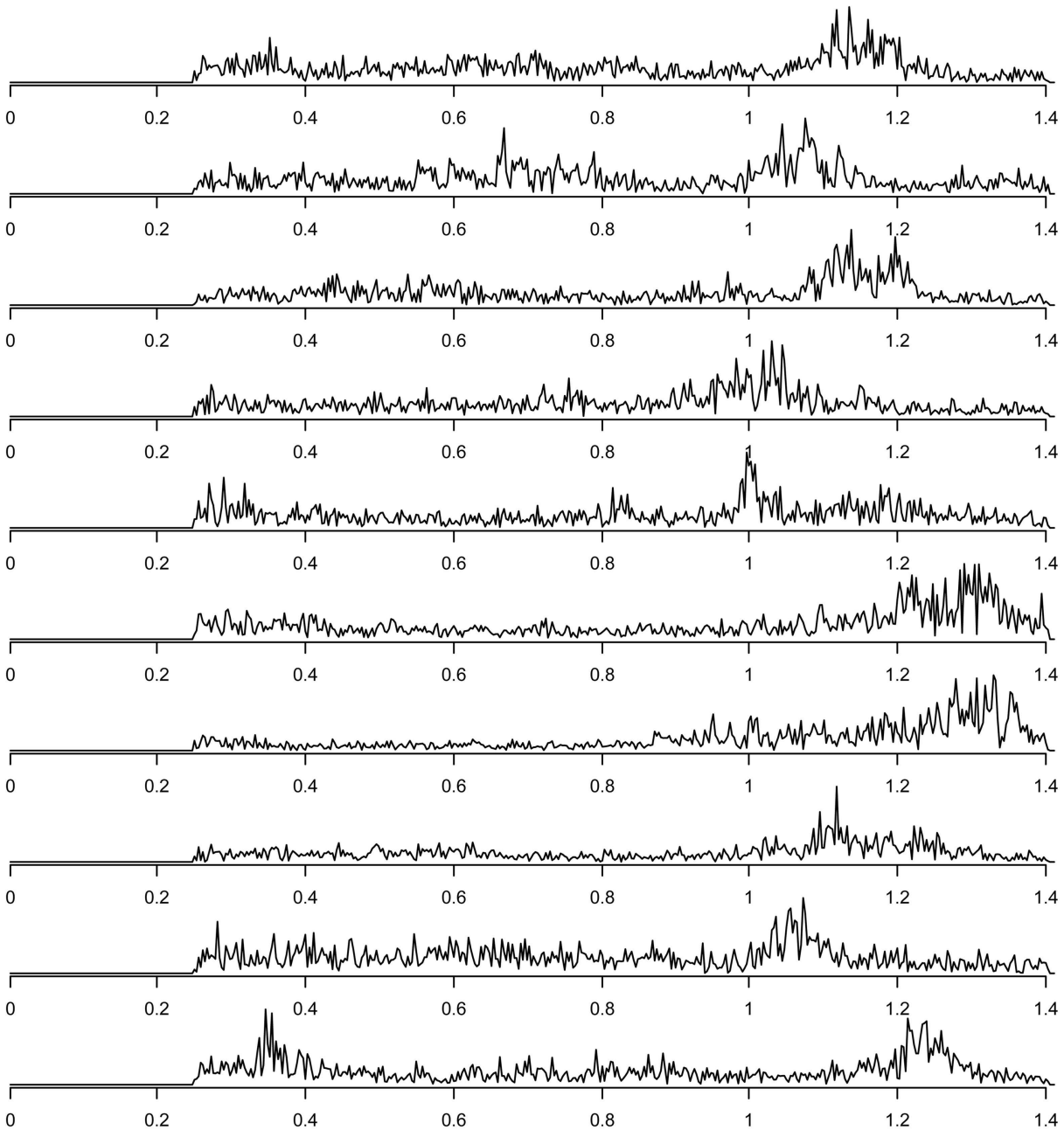

FIGURE 7 | Frequency spectra of components attributed to heart-beat (with peaks in the frequency range around 1–1.3 Hz), one component for each of the 10 subjects.

measurement sequences and are thus aliased into the lower frequency ranges. On one hand, the higher sampling rate as used in this study avoids aliasing of high-frequency signals into lower frequencies, thus making the bandpass approach potentially better able to separate low-frequency from higher-frequency signals than it has been the case for long-TR measurements. On the other hand, this study highlights that a considerable amount of information on resting-state network activity pattern is lost when only looking into low-frequency fluctuations. This corroborates existing findings by Tagliazucchi et al. (2011, 2012) that as much as 50% of correlation patterns are lost when eliminating the information in the BOLD spikes they investigated. Furthermore, there is evidence that blood-flow related BOLD signal sources originating in the vessels of the brain are important confounding factors that should be taken into account specifically (Strik et al., 2002). Thus, the use of a band-pass filter to frequencies below 0.1 Hz is only advisable if one is explicitly interested in low-frequency dynamics alone, as opposed to studies investigating resting-state networks more generally.

While the range of applications mentioned above see the physiological components as signal of no interest to be eliminated from the data, it is equally possible to treat them as the main target for analysis. The identification of disruptions in the normal pattern of physiological fluctuations in the brain can be useful for clinical applications, for example in the localization of lesions (Yating et al., 2013), an application where the high temporal resolution can be critical for the detection of signal delays. Indeed, pulsations in the arteries of the brain have already been studied as main focus of research by Strik et al. (2002), and HRV would be a valuable parameter when studying patients with cardiovascular diseases.

Scientific implications of the results shown here might be that high-frequency signal oscillations should not be ignored, they can and should be measured with current acquisition techniques and should not be eliminated from analyses by coarse-grained correction methods such as bandpassing the entire fMRI time-series. Future investigations might focus on the development of more specific correction for physiological effects, if one attempts to eliminate those from the dataset, for example by using their tICA component time courses as regressors.

The findings presented here further challenge the traditional view of resting-state networks as low-frequency oscillations alone and support the idea of them exhibiting more complex behavior. Additional work on the temporal dynamics of resting-state network activity patterns might help to understand the structure of the brain processes underlying the associated BOLD and perfusion related fluctuations. In this study, only two resting-state networks could be consistently identified across subjects by their high-frequency components. This could be interpreted in terms of differences in spectral characteristics between resting-state networks, but could also be due to the scan duration used here (6 min) being insufficient to detect other networks. Future studies might uncover similar high-frequency components in other resting-state networks using longer scan duration or higher sampling rate with lower TRs and higher sensitivity, e.g., at 7 T.

ACKNOWLEDGMENTS

This study was financially supported by the Austrian Science Fund (P22813, P23533). The authors are grateful to Lucie Bartova and Lukas Pezawas for managing the subject recruiting process, and to Georg Rath for technical support.

REFERENCES

Aguirre, G. K., Zarahn, E., and D'esposito, M. (1998). The variability of human, BOLD hemodynamic responses. *Neuroimage* 8, 360–369.

Allen, E. A., Erhardt, E. B., Damaraju, E., Gruner, W., Segall, J. M., Silva, R. F., et al. (2011). A baseline for the multivariate comparison of resting-state networks. *Front. Syst. Neurosci.* 5:2. doi:10.3389/fnsys.2011.00002

Baglama, J., and Reichel, L. (2005). Augmented implicitly restarted Lanczos bidiagonalization methods. *SIAM J. Sci. Comput.* 27, 19–42.

Baglama, J., and Reichel, L. (2012). *irlba: Fast Partial SVD by Implicitly-Restarted Lanczos Bidiagonalization. R Package Version 1.0.2.* Available at: http://CRAN.R-project.org/package=irlba

Baumgartner, R., Ryner, L., Richter, W., Summers, R., Jarmasz, M., and Somorjai, R. (2000). Comparison of two exploratory data analysis methods for fMRI: fuzzy clustering vs. principal component analysis. *Magn. Reson. Imaging* 18, 89–94.

Baumgartner, R., Windischberger, C., and Moser, E. (1998). Quantification in functional magnetic resonance imaging: fuzzy clustering vs. correlation analysis. *Magn. Reson. Imaging* 16, 115–125.

Beall, E. B., and Lowe, M. J. (2007). Isolating physiologic noise sources with independently determined spatial measures. *Neuroimage* 37, 1286–1300.

Beall, E. B., and Lowe, M. J. (2010). The non-separability of physiologic noise in functional connectivity MRI with spatial ICA at 3T. *J. Neurosci. Methods* 191, 263–276.

Beckmann, C. F. (2012). Modelling with independent components. *Neuroimage* 62, 891–901.

Biswal, B., Yetkin, F. Z., Haughton, V. M., and Hyde, J. S. (1995). Functional connectivity in the motor cortex of resting human brain using echo-planar MRI. *Magn. Reson. Med.* 34, 537–541.

Biswal, B. B., Mennes, M., Zuo, X.-N., Gohel, S., Kelly, C., Smith, S. M., et al. (2010). Toward discovery science of human brain function. *Proc. Natl. Acad. Sci. U.S.A.* 107, 4734–4739.

Biswal, B. B., and Ulmer, J. L. (1999). Blind source separation of multiple signal sources of fMRI data sets using independent component analysis. *J. Comput. Assist. Tomogr.* 23, 265–271.

Boubela, R. N., Huf, W., Kalcher, K., Sladky, R., Filzmoser, P., Pezawas, L., et al. (2012). A highly parallelized framework for computationally intensive MR data analysis. *MAGMA* 25, 313–320.

Calhoun, V. D., Adali, T., Pearlson, G. D., and Pekar, J. J. (2001). Spatial and temporal independent component analysis of functional MRI data containing a pair of task-related waveforms. *Hum. Brain Mapp.* 13, 43–53.

Chuang, K. H., and Chen, J. H. (2001). Impact: image-based physiological artifacts estimation and correction technique for functional MRI. *Magn. Reson. Med.* 46, 344–353.

Cordes, D., Haughton, V. M., Arfanakis, K., Carew, J. D., Turski, P. A., Moritz, C. H., et al. (2001). Frequencies contributing to functional connectivity in the cerebral cortex in "resting-state" data. *AJNR Am. J. Neuroradiol.* 22, 1326–1333.

Cox, R. W. (1996). AFNI: software for analysis and visualization of functional magnetic resonance neuroimages. *Comput. Biomed. Res.* 29, 162–173.

Cunnington, R., Windischberger, C., Deecke, L., and Moser, E. (2002). The preparation and execution of self-initiated and externally-triggered movement: a study of event-related fMRI. *Neuroimage* 15, 373–385.

Damoiseaux, J. S., Rombouts, S. A. R. B., Barkhof, F., Scheltens, P., Stam, C. J., Smith, S. M., et al. (2006). Consistent resting-state networks across healthy subjects. *Proc. Natl. Acad. Sci. U.S.A.* 103, 13848–13853.

Davis, B., Jovicich, J., Iacovella, V., and Hasson, U. (2013). Functional and developmental significance of amplitude variance asymmetry in the BOLD resting state signal. *Cereb. Cortex.* doi:10.1093/cercor/bhs416

Feinberg, D. A., Moeller, S., Smith, S. M., Auerbach, E., Ramanna, S., Gunther, M., et al. (2010). Multiplexed echo planar imaging for sub-second whole brain fMRI and fast diffusion imaging. *PLoS ONE* 5:e15710. doi:10.1371/journal.pone.0015710

Feinberg, D. A., and Yacoub, E. (2012). The rapid development of high speed, resolution and precision in fMRI. *Neuroimage* 62, 720–725.

Friman, O., Cedefamn, J., Lundberg, P., Borga, M., and Knutsson, H. (2001). Detection of neural activity in functional MRI using canonical correlation analysis. *Magn. Reson. Med.* 45, 323–330.

Huf, W., Kalcher, K., Pail, G., Friedrich, M.-E., Filzmoser, P., and Kasper, S. (2011). Meta-analysis: fact or fiction? How to interpret meta-analyses. *World J. Biol. Psychiatry* 12, 188–200.

Hyvärinen, A. (1999). Fast and robust fixed-point algorithms for independent component analysis. *IEEE Trans. Neural Netw.* 10, 626–634.

Kalcher, K., Boubela, R. N., Huf, W., Biswal, B. B., Baldinger, P., Sailer, U., et al. (2013). RESCALE: voxel-specific task-fMRI scaling using resting state fluctuation amplitude. *Neuroimage* 70, 80–88.

Kalcher, K., Huf, W., Boubela, R. N., Filzmoser, P., Pezawas, L., Biswal, B., et al. (2012). Fully exploratory network independent component analysis of the 1000 functional connectomes database. *Front. Hum. Neurosci.* 6:301. doi:10.3389/fnhum.2012.00301

Kim, S.-G., and Ogawa, S. (2012). Biophysical and physiological origins of blood oxygenation level-dependent fMRI signals. *J. Cereb. Blood Flow Metab.* 32, 1188–1206.

Margulies, D. S., Böttger, J., Long, X., Lv, Y., Kelly, C., Schäfer, A., et al. (2010). Resting developments: a review of fMRI post-processing methodologies for spontaneous brain activity. *MAGMA* 23, 289–307.

Moeller, S., Yacoub, E., Olman, C. A., Auerbach, E., Strupp, J., Harel, N., et al. (2010). Multiband multislice GE-EPI at 7 tesla, with 16-fold acceleration using partial parallel imaging with application to high spatial and temporal whole-brain fMRI. *Magn. Reson. Med.* 63, 1144–1153.

Moser, E., Baumgartner, R., Barth, M., and Windischberger, C. (1999). Explorative signal processing in functional MR imaging. *Int. J. Imaging Syst. Technol.* 10, 166–176.

Niazy, R. K., Xie, J., Miller, K., Beckmann, C. F., and Smith, S. M. (2011). Spectral characteristics of resting state networks. *Prog. Brain Res.* 193, 259–276.

R Development Core Team. (2013). *R: A Language and Environment for Statistical Computing.* Available at: http://www.R-project.org

Robinson, S., Basso, G., Soldati, N., Sailer, U., Jovicich, J., Bruzzone, L., et al. (2009). A resting state network in the motor control circuit of the basal ganglia. *BMC Neurosci.* 10:137. doi:10.1186/1471-2202-10-137

Smith, S. M., Jenkinson, M., Woolrich, M. W., Beckmann, C. F., Behrens, T. E. J., Johansen-Berg, H., et al. (2004). Advances in functional and structural MR image analysis and implementation as FSL. *Neuroimage* 23(Suppl. 1), S208–S219.

Smith, S. M., Miller, K. L., Moeller, S., Xu, J., Auerbach, E. J., Woolrich, M. W., et al. (2012). Temporally-independent functional modes of spontaneous brain activity. *Proc. Natl. Acad. Sci. U.S.A.* 109, 3131–3136.

Spiga, F., and Girotto, I. (2012). "phiGEMM: a CPU-GPU library for porting Quantum ESPRESSO on hybrid systems," in *Parallel, Distributed and Network-Based Processing (PDP), 2012 20th Euromicro International Conference on IEEE* (Los Alamitos: IEEE Computer Society), 368–375.

Strik, C., Klose, U., Kiefer, C., and Grodd, W. (2002). Slow rhythmic oscillations in intracranial CSF and blood flow: registered by MRI. *Acta Neurochir. Suppl.* 81, 139–142.

Tagliazucchi, E., Balenzuela, P., Fraiman, D., and Chialvo, D. R. (2012). Criticality in large-scale brain fMRI dynamics unveiled by a novel point process analysis. *Front. Physiol.* 3:15. doi:10.3389/fphys.2012.00015

Tagliazucchi, E., Balenzuela, P., Fraiman, D., Montoya, P., and Chialvo, D. R. (2011). Spontaneous BOLD event triggered averages for estimating functional connectivity at resting state. *Neurosci. Lett.* 488, 158–163.

Tukey, J. W. (1977). *Exploratory Data Analysis.* Reading: Addison-Wesley Publishing Company.

Van Oort, E., Norris, D., Smith, S. M., and Beckmann, C. (2012). "Resting state networks are characterized by high frequency BOLD fluctuations," in *OHBM*, Minneapolis. [Abstract Number 739].

Weiskopf, N. (2012). Real-time fMRI and its application to neurofeedback. *Neuroimage* 62, 682–692.

Yating, L., Margulies, D. S., Craddock, R. C., Long, X., Winter, B., Gierhake, D., et al. (2013). Identifying the perfusion deficit in acute stroke with resting-state fMRI. *Ann. Neurol.* 73, 136–140.

Yeo, B. T. T., Krienen, F. M., Sepulcre, J., Sabuncu, M. R., Lashkari, D., Hollinshead, M., et al. (2011). The organization of the human cerebral cortex estimated by intrinsic functional connectivity. *J. Neurophysiol.* 106, 1125–1165.

Conflict of Interest Statement: The authors declare that the research was conducted in the absence of any commercial or financial relationships that could be construed as a potential conflict of interest.

Received: 16 January 2013; accepted: 16 April 2013; published online: 01 May 2013.

Citation: Boubela RN, Kalcher K, Huf W, Kronnerwetter C, Filzmoser P and Moser E (2013) Beyond noise: using temporal ICA to extract meaningful information from high-frequency fMRI signal fluctuations during rest. Front. Hum. Neurosci. 7:168. doi: 10.3389/fnhum.2013.00168

APPENDIX

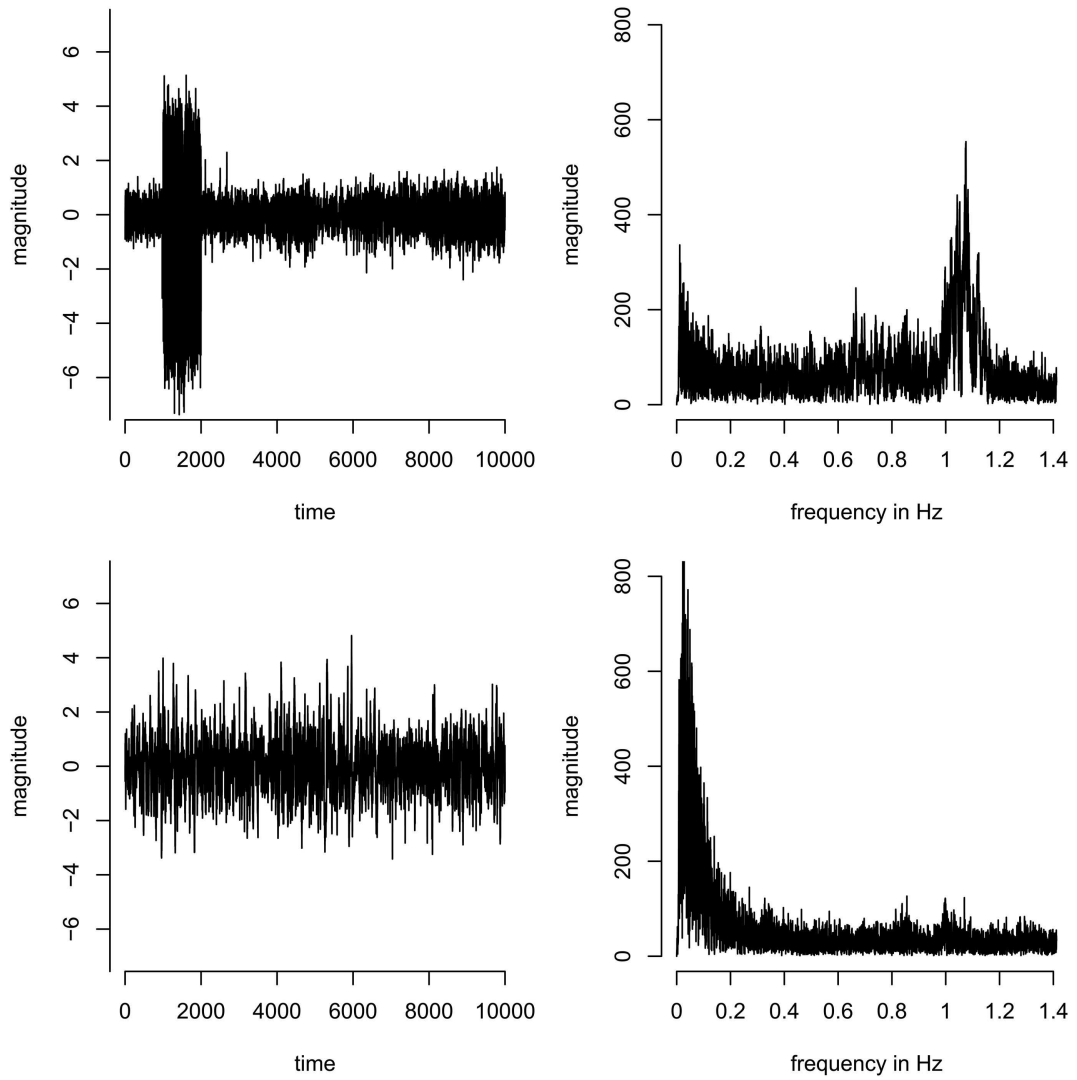

FIGURE A1 | Concatenated time-series (left) and corresponding spectra (right) of two example components. Top: a component dominated by a single subject – most of the variance of the time course originates from subject 2 (time points 1001–2000 in the concatenated time-series). Bottom: a component that is equally present in all subjects, i.e., the variance in the concatenated time course is more homogeneous across subjects.

frontiers in
HUMAN NEUROSCIENCE

ORIGINAL RESEARCH ARTICLE
published: 02 April 2013
doi: 10.3389/fnhum.2013.00118

The influence of the amplitude of low-frequency fluctuations on resting-state functional connectivity

*Xin Di[1], Eun H. Kim[1], Chu-Chung Huang[2], Shih-Jen Tsai[2], Ching-Po Lin[2] and Bharat B. Biswal[1]**

[1] Department of Biomedical Engineering, New Jersey Institute of Technology, Newark, NJ, USA
[2] Institute of Neuroscience, National Yang-Ming University, Taipei, Taiwan

Edited by:
Veronika Schöpf, Medical University Vienna, Austria

Reviewed by:
Ahmed Abou Elseoud, Oulu University Hospital, Finland
Martin Walter, Otto-von-Guericke-Universität Magdeburg, Germany

***Correspondence:**
Bharat B. Biswal, Department of Biomedical Engineering, New Jersey Institute of Technology, 607 Fenster hall, University Heights, Newark, NJ 07102, USA.
e-mail: bbiswal@yahoo.com

Studies of brain functional connectivity have provided a better understanding of organization and integration of large-scale brain networks. Functional connectivity using resting-state functional magnetic resonance imaging (fMRI) is typically based upon the correlations of the low-frequency fluctuation of fMRI signals. Reproducible spatial maps in the brain have also been observed using the amplitude of low-frequency fluctuations (ALFF) in resting-state. However, little is known about the influence of the ALFF on the functional connectivity measures. In the present study, we analyzed resting-state fMRI data on 79 healthy old individuals. Spatial independent component analysis and regions of interest (ROIs) based connectivity analysis were performed to obtain measures of functional connectivity. ALFF maps were also calculated. First, voxel-matched inter-subject correlations were computed between back-reconstructed IC and ALFF maps. For all the resting-state networks, there was a consistent correlation between ALFF variability and network strengths (within regions that had high IC strengths). Next, inter-subject variance of correlations across 160 functionally defined ROIs were correlated with the corresponding ALFF variance. The connectivity of several ROIs to other regions were more likely to correlate with its own regional ALFF. These regions were mainly located in the anterior cingulate cortex, medial prefrontal cortex, precuneus, insula, basal ganglia, and thalamus. These associations may suggest a functional significance of functional connectivity modulations. Alternatively, the fluctuation amplitudes may arise from physiological noises, and therefore, need to be controlled when studying resting-state functional connectivity.

Keywords: ALFF, basal ganglia, brain network, default mode network, independent component analysis, insula, thalamus

INTRODUCTION

Studies of brain networks and functional connectivity have provided a better understanding of organization and integration of large-scale brain networks. After the initial observation that the motor cortex exhibits highly synchronized intrinsic fluctuations during the absence of specific tasks (Biswal et al., 1995), the resting-state functional connectivity has emerged as a promising approach to investigate the functional integration of the brain. Studies using seed-based correlations have shown that the resting-state BOLD signal of functionally related regions generally demonstrate high correlation coefficients (e.g., Cordes et al., 2000). Seed-based correlation analysis has since been used to define brain networks such as the default mode network (DMN; Greicius et al., 2003), and to study the functional parcellation of specific brain structures, such as the cingulate cortex (Margulies et al., 2007), basal ganglia (Di Martino et al., 2008), and insula (Taylor et al., 2009).

As an alternative to seed-based analysis, where the region of interest is known, researchers have used independent component analysis (ICA), a data driven methodology to decompose the brain into spatially independent networks (McKeown et al., 1998). ICA simultaneously investigate multiple networks such as the DMN, salience, left/right executive, attention, motor, and visual networks (Greicius et al., 2004; Beckmann et al., 2005) and several successful applications have been reported in mental diseases (e.g., Greicius et al., 2004; Veer et al., 2010; Westlye et al., 2011).

The studies of functional connectivity and networks generally rely on the correlations and relative independence of low-frequency fluctuation signals of resting-state functional magnetic resonance imaging (fMRI). However, the influences of resting-state fMRI signal fluctuation amplitude on the measures of functional connectivity and networks have largely been ignored. Theoretically, the correlation coefficient should be independent of the scale of the signals. However, the reliability of fMRI signals might be associated with the level of noises as well as meaningful neuronal functions (e.g., Sirotin and Das, 2009). Therefore, the fluctuation amplitudes may indeed affect the functional connectivity and network measures.

The "noise" of the brain has been shown to characterize the developing (McIntosh et al., 2008) and the aging (Garrett et al., 2010, 2011) brain, and the variability of the noise has been shown to explain behavioral variability (for a review, see McIntosh et al., 2010). On the other hand, the resting-state fMRI is susceptible to many sources of noise such as head motion (Power et al., 2012; Van Dijk et al., 2012), respiration, and heartbeat (Birn et al., 2006, 2008; Chang et al., 2008). Data processing strategies were found to significantly affect connectivity measures (Weissenbacher

et al., 2009; Saad et al., 2012), which implies that the connectivity results are still largely influenced by different sources of noise even after following careful processing procedures. Taken together, a better understanding of how the resting-state fMRI fluctuation amplitude affect functional connectivity and networks is warranted.

The fluctuations of resting-state BOLD signals are generally observed to be present between 0.01 and 0.08 Hz frequency band (Biswal et al., 1995). The amplitude of resting-state BOLD fluctuations is usually calculated in this low-frequency band, which has been termed as the amplitude of low-frequency fluctuations (ALFF, Zang et al., 2007). Higher ALFF in resting-state have been shown in regions constituting the DMN (Zang et al., 2007), suggesting that ALFF to some extent reflects neural activity. In addition, recent studies have observed an overlap between changes in regional ALFF and functional connectivity in several brain regions in stuttering (Xuan et al., 2012) and seasonal affective disorder subjects (Abou Elseoud et al., 2012). These studies suggest a relationship between ALFF and functional connectivity; however, the extent and selectivity of this association has not been investigated.

In the present study, we aimed to systematically examine the relationships between ALFF and resting-state connectivity. A large dataset of healthy old subjects were analyzed so that the inter-subject variability of ALFF and connectivity was maximized. First, spatial ICA was performed on the resting-state fMRI data to identify resting-state networks. These networks were correlated with regional ALFFs in a voxel-wise manner to examine whether the inter-subject variability of the network strengths were correlated with ALFFs. Second, functional connectivity across 160 regions of interest (ROIs) were calculated. The functional connectivity was correlated with ALFF to examine whether the local amplitude fluctuations affect the strength of connectivity. We hypothesize that the strength of connectivity of ICA and ROI based analyses would be correlated to the local ALFF. In addition, the correlations were examined across different networks and connectivity pairs to determine whether these associations were across the entire brain or specific to selective networks.

MATERIALS AND METHODS

RESTING-STATE MRI DATA

Resting-state fMRI and anatomical MRI data were obtained on a sample of old male subjects. After removing data with large head motion, 79 subjects were included with a mean age of 80.3 years (range from 65 to 92) for further analysis. A 3.0-T Siemens Magnetom Tim Trio scanner equipped with a 12-channel head coil (Erlangen, Germany) was used to acquire the MR images. All the functional and anatomical images were scanned parallel to the anterior commissure-posterior commissure line. The resting-state data were scanned for 500 s with a TR of 2.5 s, resulting in 200 images for each subject. The scanning parameters were as follows: TE = 27; acquisition matrix = 64 × 64; flip angle = 77°; slices = 43; spatial resolution = 3.44 mm × 3.44 mm × 3.40 mm. High resolution MPRAGE anatomical images were also acquired with the scanning parameters as follows: TR = 2530 ms; TE = 3.5 ms; flip angle = 7°; resolution = 1 mm × 1 mm × 1 mm (no gap).

DATA ANALYSIS

Preprocessing

The functional and anatomical image preprocessing were performed using SPM8 toolbox[1] under MATLAB7.7 software[2]. The first two functional images were discarded. Then, the remaining functional images were motion corrected and coregistered to the subjects' own anatomical images. The anatomical images were segmented using the new segmentation routine in SPM8. The deformation field maps obtained in segmentation were used to normalize all the functional images into standard Montreal Neurological Institute (MNI) space. For each voxel, the six rigid body head motion parameters, the first five eigenvectors from white matter (WM) signals, and the first five eigenvectors from cerebrospinal fluid (CSF) signals were regressed out using linear regression. The WM and CSF masks were defined for each subject using the segmented WM and CSF images thresholded at $p > 0.99$. Finally, all the functional images were spatially smoothed using a Gaussian kernel of 8 mm full width at half maximum (FWHM).

Calculation of ALFF

Amplitude of low-frequency fluctuations maps were calculated between 0.01 and 0.08 Hz band using Resting-State fMRI Data Analysis Toolkit V1.6 (REST; Song et al., 2011). The ALFF maps were then divided by whole brain mean ALFF values to normalize the global effects.

Relationships between network strength and ALFF

Spatial ICA was conducted to define intrinsic networks using the Group ICA of fMRI Toolbox (GIFT)[3] (Calhoun et al., 2001). Twenty components were extracted. Resting-state networks were visually identified according to the literature (Biswal et al., 2010; Cole et al., 2010). These ICs were back-reconstructed to each subject using group ICA algorithm, resulting in 20 IC maps for each subject (Erhardt et al., 2011). To examine whether there was a consistent network effect across subjects, voxel-wise one-sample t tests was performed for each of the networks. The resulting t maps were thresholded at $|t| > 3.42$ ($p < 0.001$).

A voxel-matched correlation analysis was used to study the relationships between resting-state network strengths and ALFFs (similar to Mennes et al., 2010, 2011). For each voxel, network strengths of an IC were correlated with ALFFs across all subjects using Pearson's correlation coefficient. The correlation maps were calculated separately for each of the network maps. Some voxels within an IC had negative value which reflects a negative relationship between a given voxel to the corresponding IC. Therefore, negative correlation between ALFF and negative IC strength is equivalent to positive correlation between ALFF and positive IC strength.

The resulting r maps were thresholded at $|r| > 0.364$ ($p < 0.001$). Because the aim of the current analysis was to show the overall correlation patterns, we did not use multiple comparison correction. However, a Monte Carlo simulation using AlphaSim[4] indicated that a cluster exceeding 24 voxels were

[1] http://www.fil.ion.ucl.ac.uk/spm/
[2] http://www.mathworks.com/
[3] http://icatb.sourceforge.net/
[4] http://afni.nimh.nih.gov/pub/dist/doc/manual/AlphaSim.pdf

significant at $p < 0.05$ after a whole brain multiple comparison correction. This analysis shows that most of our large clusters reported in the results were still significant even after multiple comparison correction.

Relationships between functional connectivity and ALFF

Mean time series from 160 functionally defined ROIs were calculated within spherical ROIs with 8 mm radius (Dosenbach et al., 2010). These 160 ROIs were also assigned into six networks according to a modularity analysis of resting-state data (Dosenbach et al., 2010), including the cerebellar, cingulo-opercular, DMN, fronto-parietal, occipital, and sensorimotor networks (see **Table A1** in Appendix for details). Then, functional connectivity matrices were calculated for each subject using Pearson's correlation coefficient across 160 ROIs. The connectivity matrices were transformed into Fisher's *z*. For each of the ROI, the Fisher's *z* scores between a given ROI to other ROIs were correlated with ALFF value of the given ROI.

To identify which ROI's local ALFF were more likely to correlate with connectivity, the correlations were thresholded at $|r| > 0.364$ ($p < 0.001$). Then, we selected the ROIs with local ALFFs that were correlated with more than 30 significant connectivity between the given ROI and other ROIs. These ROIs and the corresponding connections with other ROIs were visualized using BrainNet Viewer[5].

RESULTS

RELATIONSHIPS BETWEEN NETWORK STRENGTH AND ALFF

Out of the 20 ICs, 8 ICs were identified which corresponded to the 8 networks described by Cole et al. (2010), including the DMN, left and right executive, attention, salience, motor, visual, and fronto-parietal opercular networks (the left column of **Figure 1**). The voxel-matched correlations between network strengths and ALFFs for the eight networks were shown in the right column.

[5]http://www.nitrc.org/projects/bnv/

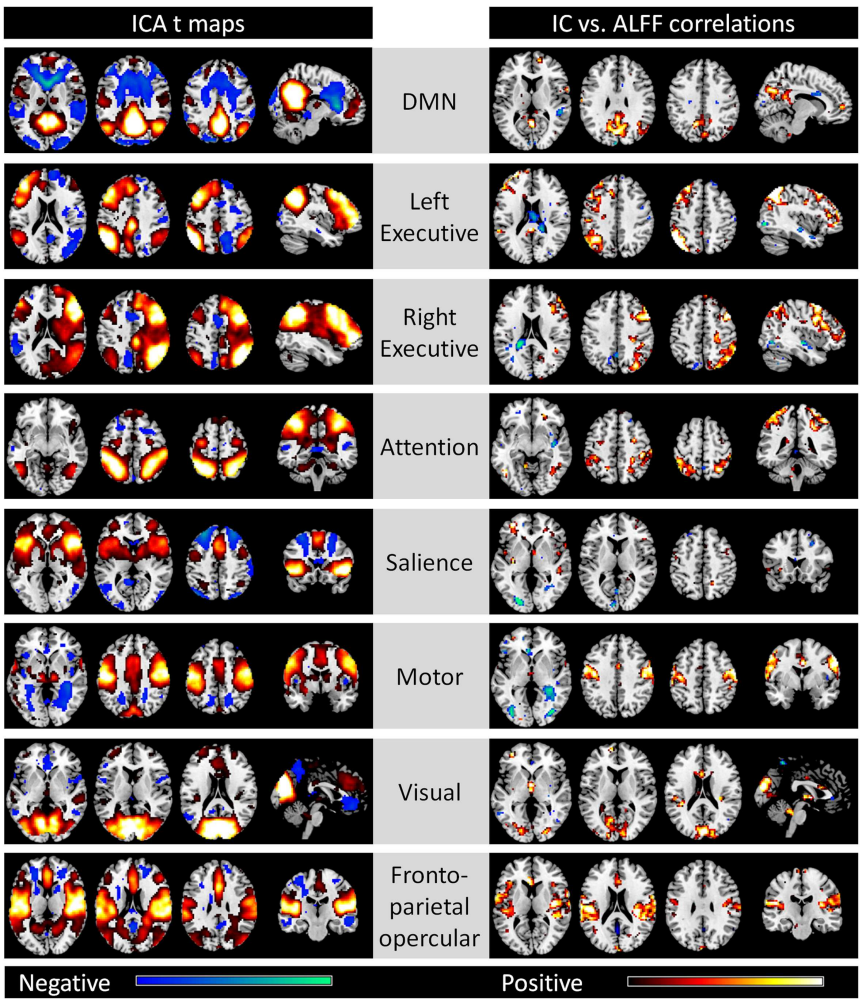

FIGURE 1 | Eight networks identified by spatial ICA that correspond to Cole et al. (2010) (left column) and voxel-wise correlations between network strengths and ALFFs (right column). All maps are thresholded at $p < 0.001$. For the ICA *t* maps, displayed range is absolute *t* value between 3.42 and 20, and for the correlation maps, display range is absolute *r* value between 0.364 and 0.6. Hot and cold colors encode positive and negative effects, respectively.

Strong correlations between network strengths and ALFFs were generally observed within each network with less spatial extent when using the compatible statistical threshold of $p < 0.001$. For the DMN network, correlations between network strengths and ALFFs were observed in the posterior cingulate cortex/precuneus, medial prefrontal cortex (MPFC), and the right inferior parietal lobule/superior temporal gyrus. Within the left and right executive network, correlations were identified in the left and right dorsolateral prefrontal cortex and superior parietal lobule, respectively. The attention network demonstrated correlations within the bilateral superior parietal lobule and middle temporal gyrus. In the salience network, although clusters of high correlations were unapparent, there were small clusters within the bilateral insula and inferior frontal gyrus. For the motor network, correlations were observed in the bilateral sensorimotor cortex and supplementary motor area. In the visual network, correlations were identified primarily in the visual cortex. Lastly, correlations were observed in the bilateral insula/inferior frontal gyrus, and cingulate cortex within the fronto-parietal opercular network.

In addition to the eight ICs, four other ICs were considered to be meaningful brain networks (the left column of **Figure 2**). IC 12 was mainly comprised of the bilateral insula, bilateral anterior temporal lobe, bilateral hippocampal gyrus, and bilateral amygdala. IC 14 included regions within the bilateral superior frontal gyrus, medial frontal gyrus, and bilateral inferior parietal lobe, whereas IC 15 was mostly within the bilateral temporal lobe. IC 18 was mainly located in the MPFC, anterior cingulate cortex, and posterior cingulate cortex. High correlation between IC strengths and regional ALFFs were also observed in these regions of each network, respectively (right column).

We classified the remaining eight ICs as components related to noise. Voxels with high values within these ICs were mainly located in the CSF, WM, or large vessels (see **Figure A1** in Appendix). We also observed high correlations between these IC strengths and ALFFs.

RELATIONSHIPS BETWEEN FUNCTIONAL CONNECTIVITY AND ALFF

The mean connectivity matrix across 160 ROIs is illustrated in the left panel of **Figure 3**. Even with strong connectivity coefficient values, we observed higher connectivity within each network compared with between networks. These ROIs were sorted by their six network affiliations (see **Table A1** in Appendix), and high correlation values within the networks are evident as subsquares along the mean connectivity matrix diagonal, for example the cerebellar network (ROI 1–18), DMN (ROI 51–84), fronto-parietal network (ROI 85–105), occipital network (ROI 106–127), and sensorimotor network (ROI 128–160). However, we did not observe strong within network connectivity of the cingulo-opercular network (ROI 19–50).

The correlation between the ALFF of a given ROI and the connectivity between the given ROI with other ROIs are illustrated in the middle panel of **Figure 3**. The matrix was thresholded ($|r| > 0.364$, i.e., $p < 0.001$) to determine which correlation between the ALFF of a given ROI and its connectivity were statistically significant. The right panel of **Figure 3** demonstrates that the matrix was asymmetrical with respect to the diagonal which suggests that ALFFs of both ROIs within a pair affect functional connectivity differently. It also demonstrates that ALFF of specific ROIs were more likely to influence the connectivity between these specific ROIs with other ROIs.

The number of positive and negative correlations correlated with the local ALFF was tabulated (**Figure 4**) to identify the regions where the local ALFF were more likely to affect connectivity. We set an arbitrary threshold of $n > 30$ to identify these regions (see

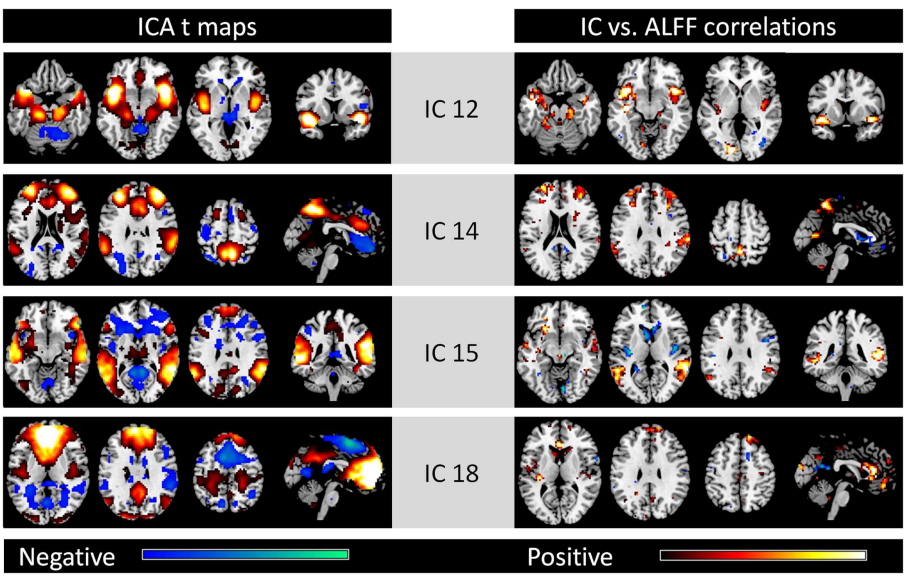

FIGURE 2 | Other four networks identified by spatial ICA (left column) and voxel-wise correlations between network strengths and ALFFs (right column). All maps are thresholded at $p < 0.001$. For the ICA t maps, display range is absolute t value between 3.42 and 20, and for the correlation maps, display range is absolute r value between 0.364 and 0.6. Hot and cold colors encode positive and negative effects, respectively.

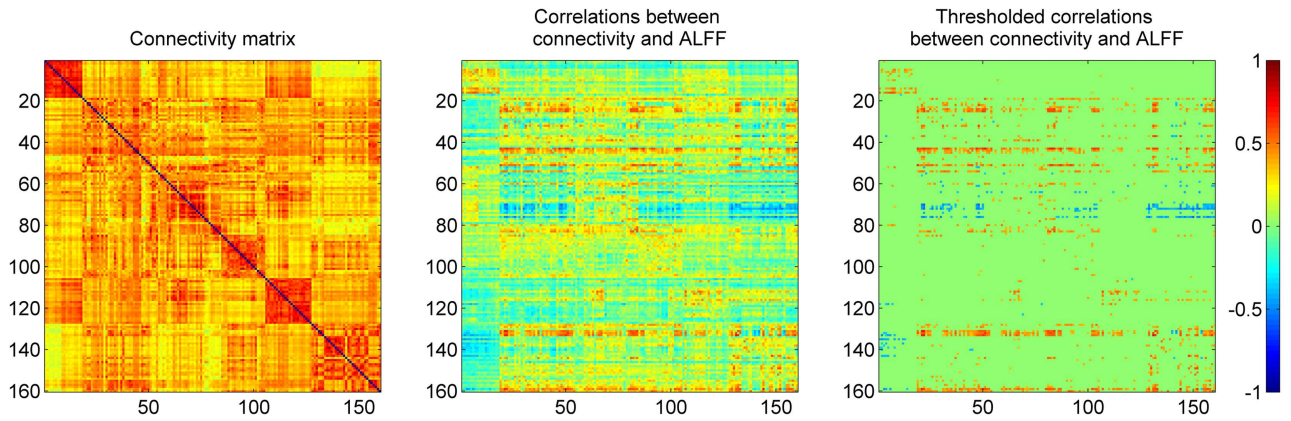

FIGURE 3 | Mean correlation matrix of resting-state connectivity across 160 ROIs (left), and their relationships to regional ALFF (middle and right). Each row of the middle panel revealed correlations between ALFF in one ROI and connectivity between this ROI to all the other ROIs. The thresholded correlations between ALFF and connectivity were shown in the right panel ($|r| > 0.364$, i.e., $p < 0.001$).

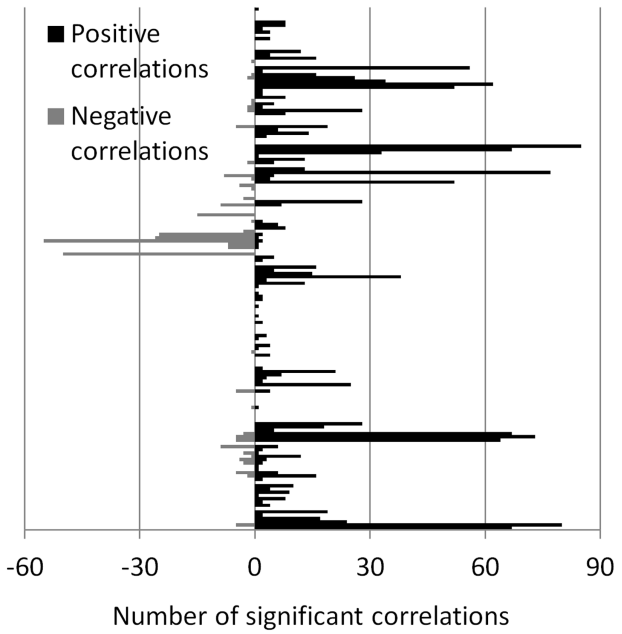

FIGURE 4 | Number of significant correlations between ALFF and connectivity for each ROI. The number of positive and negative correlations were shown separately, and displayed in positive and negative directions, respectively.

Table 1 | ROIs that have more than 30 connections that are correlated with the corresponding regional ALFF.

Label	ROI #	Network	MNI coordinates		
			x	*y*	*z*
POSITIVE EFFECTS					
ACC	19	Cingulo-opercular	−2	30	27
aPFC	23	Cingulo-opercular	27	49	26
Basal ganglia	24	Cingulo-opercular	14	6	7
Basal ganglia	25	Cingulo-opercular	−20	6	7
Thalamus	43	Cingulo-opercular	−12	−3	13
Thalamus	44	Cingulo-opercular	−12	−12	6
Thalamus	45	Cingulo-opercular	11	−12	6
ACC	51	Default	9	39	20
aPFC	54	Default	−25	51	27
vmPFC	83	Default	−11	45	17
Mid insula	131	Sensorimotor	−42	−3	11
Mid insula	132	Sensorimotor	−36	−12	15
Mid insula	133	Sensorimotor	33	−12	16
vFC	159	Sensorimotor	43	1	12
vFC	160	Sensorimotor	−55	7	23
NEGATIVE EFFECTS					
Precuneus	72	Default	5	−50	33
Precuneus	76	Default	−6	−56	29

Table 1). Fifteen ROIs revealed more than 30 connections that were positively correlated with ALFFs from the corresponding ROIs, while two ROIs revealed more than 30 connections that were negatively correlated with ALFFs from the corresponding ROIs.

These ROIs were categorized into four groups based on their spatial approximations and affiliated networks. The first group of ROIs were located in the MPFC and anterior cingulate cortex (ACC) (**Figure 5A**). These five ROIs were either a part of the DMN or the cingulo-opercular network as described by Dosenbach et al. (2010); however, these nearby ROIs exhibited similar correlation patterns. The connectivity between the five ROIs with other DMN, fronto-parietal, cingulo-opercular, sensorimotor, and occipital regions demonstrated positive correlations with local ALFF (**Figures 5E,I**). The second set of ROIs were located in the precuneus (**Figure 5B**), and the connectivity of these ROIs to cingulo-opercular, fronto-parietal, and sensorimotor regions were negatively correlated with local ALFF (**Figures 5F,J**). The third set was comprised of five ROIs in the bilateral putamen, caudate, and thalamus (**Figure 5C**), and their

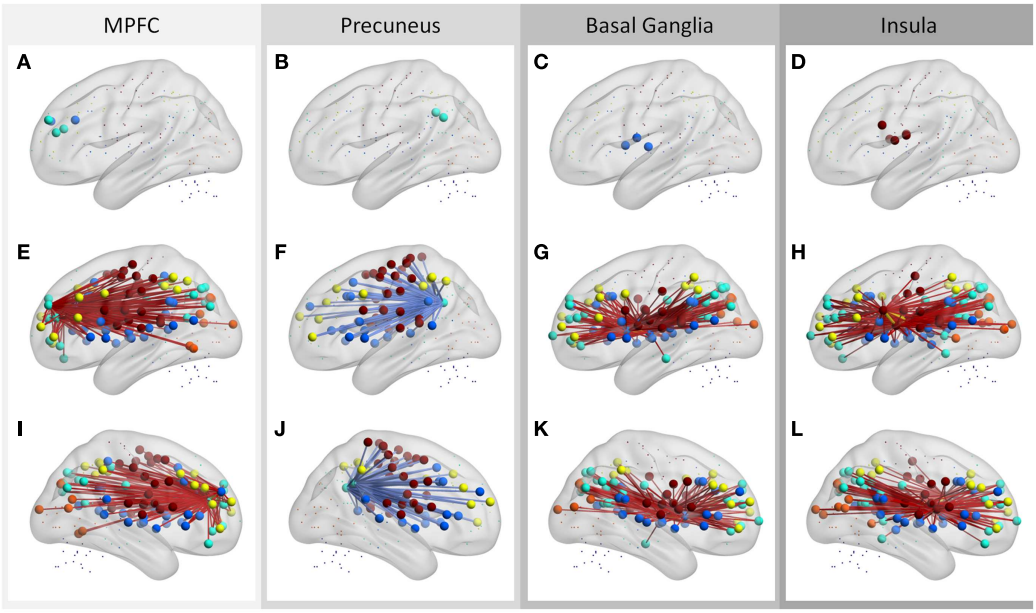

FIGURE 5 | Regions that have more than 30 connections correlated with regional ALFF (A–D), and their associated connections (E–L). The ROIs are stratified into four sets according to their affiliated networks and connectivity behavior (one for each column). Middle and bottom rows showed left and right lateral views, respectively. Hot and cold colors of connections indicate positive and negative correlations. Color codes of the ROIs: blue, cingulo-opercular network; cyan, DMN; yellow, fronto-parietal network; orange, occipital network; brown, sensorimotor network.

connectivity to the DMN, fronto-parietal, cingulo-opercular, and occipital regions revealed positive correlations with local ALFF (**Figures 5G,K**). The fourth group of ROIs were located at the bilateral insula and ventral fontal regions (**Figure 5D**), and their connectivity to the DMN, fronto-parietal, cingulo-opercular, and occipital regions revealed positive correlations with local ALFF (**Figures 5H,L**).

DISCUSSION

The current analysis demonstrates that the network strengths as measured by ICA were selectively correlated with ALFFs within the corresponding network. The network strength measured by ICA reflects the extent that a particular voxel correlates with the whole IC. Thus, the correlations between ALFFs and network strengths imply that the within network connectivity are correlated with the local fluctuation amplitudes. The relationship between ICA and ALFF were replicated by directly correlating ALFFs with connectivity measured via correlations. Within each network, ALFFs were positively correlated with the connectivity and were demonstrated as squares within each network nearby the diagonal of the matrix (see the right panel of **Figure 3**, e.g., cerebellar and sensorimotor networks). Interestingly, the correlation between ALFFs and connectivity were not restricted to within network but extends to between network connectivity. The functional connectivity of regions, particularly the MPFC, ACC, precuneus, basal ganglia, thalamus, and insula, with other regions were widely spread in the whole brain and suggest a special role of these regions in functional connectivity pattern.

The association between local fluctuations and connectivity may simply reflect that the BOLD signals are more reliable with less noise. However, given that the correlations are not uniform across the whole brain and that selective correlations are between specific regional ALFFs and connectivity, these associations may suggest functional significance. One possible explanation is that these selective regions may be involved in transmitting information to various brain regions, such that the greater the neural activity results in larger regional amplitude of fluctuations, and greater connectivity between these regions to other regions. In addition, the variances of ALFF may reflect different levels of neurotransmitters that give rise to functional connectivity variances. The later notion can be tested by combining resting-state fMRI with magnetic resonance spectroscopy (MRS) or positron emission tomography (PET) (Horn et al., 2010; Hahn et al., 2011; Cole et al., 2012; Kapogiannis et al., 2013).

Alternatively, it is also possible that these regions are more likely to be impacted by physiological noise. Even though ALFF is considered to be a measure of amplitude of neural activity, our recent studies have shown that ALFF is highly correlated with neurovascular response of breath holding task (Biswal et al., 2007; Di et al., 2013). In addition, the regions that demonstrate high correlations between ALFF and connectivity were also the regions that were more likely to be affected by physiological noise due to the adjacent large vessels, including the MPFC and precuneus, and insula (Di et al., 2013). These physiological noises may also influence functional connectivity (Birn et al., 2006, 2008; Chang et al., 2008), and therefore, reflect the common sources of physiological noise that affects both measures. Consistent with this notion, the ICs that reflected physiological noises exhibited high correlations in the regions located in the CSF, WM, and large vessels (see **Figure A1** in Appendix). However, for the ICs that reflect meaningful neural

networks, the correlations between ALFF and network strength may reflect both neural and noise contributions.

The first two sets of ROIs exhibiting correlations between connectivity and ALFF were within the DMN, including the MPFC/ACC regions, and precuneus. These regions are also defined as the structural core of the human brain that has the most anatomical connections to other brain regions (Hagmann et al., 2008). Most interestingly, the correlations between regional ALFF and connectivity showed reversed relationships between the prefrontal regions and precuneus. The connectivity between the two ROIs in precuneus with other regions was negatively correlated with the precuneus ALFF. These brain regions were task positive networks such as the sensorimotor, fronto-parietal, and cingulo-opercular networks. The connectivity between DMN and task positive networks is generally negative (Fox et al., 2005), which suggests that greater regional ALFF is associated with greater negative connectivity between DMN and task positive networks. In addition, we did not apply global scaling on the current dataset in order to prevent artificial negative correlations and no negative connectivity was observed. Thus, the negative relationship between connectivity (DMN and task positive networks) and ALFF is not due to preprocessing of the data. In contrast, the connectivity between MPFC/ACC ROIs and other regions revealed positive correlations with ALFF. MPFC/ACC ROIs were correlated with regions within other areas of the DMN, and with regions of the fronto-parietal, sensorimotor, cingulo-opercular, and occipital networks. These different correlation pattern suggests that the modulation of connectivity may involve different underlying mechanisms, e.g., via excitatory and inhibitory neurotransmitter modulations. Glutamate concentration, which reflects excitatory mechanisms in the ACC (Horn et al., 2010) and posteromedial cortex (Kapogiannis et al., 2013) has been shown to positively modulate the resting-state functional connectivity. In contrast, GABA concentration, which reflects inhibitory mechanisms, in the posteromedial cortex has been shown to negatively correlate with the resting-state functional connectivity. However, the links between the amplitude of fluctuations and neurotransmitter concentrations is still largely unknown, thus require further studies.

The other two sets of ROIs include the basal ganglia, thalamus, insula, and adjacent sensorimotor regions. Previous studies have demonstrated a widely spread functional connectivity of these regions to other brain regions (e.g., Di Martino et al., 2008; Taylor et al., 2009; Cauda et al., 2011; Tang et al., 2011). The positive correlations between connectivity and ALFF suggest a special role of these regions in functional connectivity pattern.

A practical implication of the present result is that when studying resting-state functional connectivity or networks, ALFF may be a potential confounding variable that needs to be taken into account. ALFF has been widely used to study the "baseline" activity of a wide spectrum of psychological states and mental diseases, for example aging (Biswal et al., 2010; Yan et al., 2011), schizophrenia (Hoptman et al., 2010; Huang et al., 2010), and attention deficit hyperactivity disorder (ADHD; Zang et al., 2007). Distributed differences of ALFF have been observed to be associated with different pathologies and mental states. On the other hand, increasingly studies have been conducted to investigate brain functional connectivity alterations in mental diseases using both seed-based correlation and spatial ICA (e.g., Greicius et al., 2004; Castellanos et al., 2008; Veer et al., 2010; Westlye et al., 2011). Although these differences are presumed to reflect the group differences in resting-state connectivity and networks, ALFF was not controlled by previous studies. Therefore, the underlying group differences in functional connectivity that have been reported by previous studies may be due to the unrestrained ALFF. By including ALFF as covariance, Abou Elseoud et al. (2012) demonstrated increased connectivity, but less number of voxels in the visual network. Thus, the current result and that of Abou Elseoud et al. (2012) raises a concern regarding ALFF as a potential confound when study functional connectivity and network. More specifically, our data suggests that one should be cautious when interpreting seed-based correlations of regions that are more likely to be affected by ALFF, such as the precuneus, MPFC, basal ganglia, thalamus, and insula.

The present study only analyzed a sample of old individuals because old subjects typically demonstrate larger variance of functional connectivity and the associations of functional connectivity with ALFF may be easier to identify. Even though we believe that the current results will also hold for younger individuals, further studies investigating younger individuals is needed to determine whether the relationship between local fluctuation amplitudes and functional connectivity generalizes to young population.

ACKNOWLEDGMENTS

This study was supported by a National Institute of Health grant 5R01AG032088.

REFERENCES

Abou Elseoud, A., Nissilä, J., Liettu, A., Remes, J., Jokelainen, J., Takala, T., et al. (2012). Altered resting-state activity in seasonal affective disorder. *Hum. Brain Mapp.* doi:10.1002/hbm.22164

Beckmann, C. F., DeLuca, M., Devlin, J. T., and Smith, S. M. (2005). Investigations into resting-state connectivity using independent component analysis. *Philos. Trans. R. Soc. Lond. B Biol. Sci.* 360, 1001–1013.

Birn, R. M., Diamond, J. B., Smith, M. A., and Bandettini, P. A. (2006). Separating respiratory-variation-related fluctuations from neuronal-activity-related fluctuations in fMRI. *Neuroimage* 31, 1536–1548.

Birn, R. M., Murphy, K., and Bandettini, P. A. (2008). The effect of respiration variations on independent component analysis results of resting state functional connectivity. *Hum. Brain Mapp.* 29, 740–750.

Biswal, B., Yetkin, F. Z., Haughton, V. M., and Hyde, J. S. (1995). Functional connectivity in the motor cortex of resting human brain using echo-planar MRI. *Magn. Reson. Med.* 34, 537–541.

Biswal, B. B., Kannurpatti, S. S., and Rypma, B. (2007). Hemodynamic scaling of fMRI-BOLD signal: validation of low-frequency spectral amplitude as a scalability factor. *Magn. Reson. Imaging* 25, 1358–1369.

Biswal, B. B., Mennes, M., Zuo, X. N., Gohel, S., Kelly, C., Smith, S. M., et al. (2010). Toward discovery science of human brain function. *Proc. Natl. Acad. Sci. U.S.A.* 107, 4734–4739.

Calhoun, V. D., Adali, T., Pearlson, G. D., and Pekar, J. J. (2001). A method for making group inferences from functional MRI data using independent component analysis. *Hum. Brain Mapp.* 14, 140–151.

Castellanos, F. X., Margulies, D. S., Kelly, C., Uddin, L. Q., Ghaffari, M., Kirsch, A., et al. (2008). Cingulate-precuneus interactions: a new locus of dysfunction in adult attention-deficit/hyperactivity disorder. *Biol Psychiatry.* 63, 332–337.

Cauda, F., D'Agata, F., Sacco, K., Duca, S., Geminiani, G., and Vercelli, A. (2011). Functional connectivity of the insula in the resting brain. *Neuroimage* 55, 8–23.

Chang, C., Thomason, M. E., and Glover, G. H. (2008). Mapping and correction of vascular hemodynamic latency in the BOLD signal. *Neuroimage* 43, 90–102.

Cole, D. M., Beckmann, C. F., Searle, G. E., Plisson, C., Tziortzi, A. C., Nichols, T. E., et al. (2012). Orbitofrontal connectivity with resting-state networks is associated with midbrain dopamine D3 receptor availability. *Cereb. Cortex* 22, 2784–2793.

Cole, D. M., Smith, S. M., and Beckmann, C. F. (2010). Advances and pitfalls in the analysis and interpretation of resting-state FMRI data. *Front. Syst. Neurosci.* 4:8. doi:10.3389/fnsys.2010.00008

Cordes, D., Haughton, V. M., Arfanakis, K., Wendt, G. J., Turski, P. A., Moritz, C. H., et al. (2000). Mapping functionally related regions of brain with functional connectivity MR imaging. *AJNR Am. J. Neuroradiol.* 21, 1636–1644.

Di, X., Kannurpatti, S. S., Rypma, B., and Biswal, B. B. (2013). Calibrating BOLD fMRI activations with neurovascular and anatomical constraints. *Cereb. Cortex* 23, 255–263.

Di Martino, A., Scheres, A., Margulies, D. S., Kelly, A. M., Uddin, L. Q., Shehzad, Z., et al. (2008). Functional connectivity of human striatum: a resting state fMRI study. *Cereb. Cortex* 18, 2735–2747.

Dosenbach, N. U., Nardos, B., Cohen, A. L., Fair, D. A., Power, J. D., Church, J. A., et al. (2010). Prediction of individual brain maturity using fMRI. *Science* 329, 1358–1361.

Erhardt, E. B., Rachakonda, S., Bedrick, E. J., Allen, E. A., Adali, T., and Calhoun, V. D. (2011). Comparison of multi-subject ICA methods for analysis of fMRI data. *Hum. Brain Mapp.* 32, 2075–2095.

Fox, M. D., Snyder, A. Z., Vincent, J. L., Corbetta, M., Van Essen, D. C., and Raichle, M. E. (2005). The human brain is intrinsically organized into dynamic, anticorrelated functional networks. *Proc. Natl. Acad. Sci. U S A.* 102, 9673–9678.

Garrett, D. D., Kovacevic, N., McIntosh, A. R., and Grady, C. L. (2010). Blood oxygen level-dependent signal variability is more than just noise. *J. Neurosci.* 30, 4914–4921.

Garrett, D. D., Kovacevic, N., McIntosh, A. R., and Grady, C. L. (2011). The importance of being variable. *J. Neurosci.* 31, 4496–4503.

Greicius, M. D., Krasnow, B., Reiss, A. L., and Menon, V. (2003). Functional connectivity in the resting brain: a network analysis of the default mode hypothesis. *Proc. Natl. Acad. Sci. U.S.A.* 100, 253–258.

Greicius, M. D., Srivastava, G., Reiss, A. L., and Menon, V. (2004). Default-mode network activity distinguishes Alzheimer's disease from healthy aging: evidence from functional MRI. *Proc. Natl. Acad. Sci. U.S.A.* 101, 4637–4642.

Hagmann, P., Cammoun, L., Gigandet, X., Meuli, R., Honey, C. J., Wedeen, V. J., et al. (2008). Mapping the structural core of human cerebral cortex. *PLoS Biol.* 6:e159. doi:10.1371/journal.pbio.0060159

Hahn, A., Wadsak, W., Windischberger, C., Baldinger, P., Hoflich, A. S., Losak, J., et al. (2011). Differential modulation of the default mode network via serotonin-1A receptors. *Proc. Natl. Acad. Sci. U.S.A.* 109, 2619–2624.

Hoptman, M. J., Zuo, X. N., Butler, P. D., Javitt, D. C., D'Angelo, D., Mauro, C. J., et al. (2010). Amplitude of low-frequency oscillations in schizophrenia: a resting state fMRI study. *Schizophr. Res.* 117, 13–20.

Horn, D. I., Yu, C., Steiner, J., Buchmann, J., Kaufmann, J., Osoba, A., et al. (2010). Glutamatergic and resting-state functional connectivity correlates of severity in major depression – the role of pregenual anterior cingulated cortex and anterior insula. *Front. Syst. Neurosci.* 4:33. doi:10.3389/fnsys.2010.00033

Huang, X. Q., Lui, S., Deng, W., Chan, R. C., Wu, Q. Z., Jiang, L. J., et al. (2010). Localization of cerebral functional deficits in treatment-naive, first-episode schizophrenia using resting-state fMRI. *Neuroimage* 49, 2901–2906.

Kapogiannis, D., Reiter, D. A., Willette, A. A., and Mattson, M. P. (2013). Posteromedial cortex glutamate and GABA predict intrinsic functional connectivity of the default mode network. *Neuroimage* 64, 112–119.

Margulies, D. S., Kelly, A. M., Uddin, L. Q., Biswal, B. B., Castellanos, F. X., and Milham, M. P. (2007). Mapping the functional connectivity of anterior cingulate cortex. *Neuroimage* 37, 579–588.

McIntosh, A. R., Kovacevic, N., and Itier, R. J. (2008). Increased brain signal variability accompanies lower behavioral variability in development. *PLoS Comput. Biol.* 4:e1000106. doi:10.1371/journal.pcbi.1000106

McIntosh, A. R., Kovacevic, N., Lippe, S., Garrett, D., Grady, C., and Jirsa, V. (2010). The development of a noisy brain. *Arch. Ital. Biol.* 148, 323–337.

McKeown, M. J., Jung, T. P., Makeig, S., Brown, G., Kindermann, S. S., Lee, T. W., et al. (1998). Spatially independent activity patterns in functional MRI data during the stroop color-naming task. *Proc. Natl. Acad. Sci. U.S.A.* 95, 803–810.

Mennes, M., Kelly, C., Zuo, X. N., Di Martino, A., Biswal, B. B., Castellanos, F. X., et al. (2010). Inter-individual differences in resting-state functional connectivity predict task-induced BOLD activity. *Neuroimage* 50, 1690–1701.

Mennes, M., Zuo, X. N., Kelly, C., Di Martino, A., Zang, Y. F., Biswal, B., et al. (2011). Linking inter-individual differences in neural activation and behavior to intrinsic brain dynamics. *Neuroimage* 54, 2950–2959.

Power, J. D., Barnes, K. A., Snyder, A. Z., Schlaggar, B. L., and Petersen, S. E. (2012). Spurious but systematic correlations in functional connectivity MRI networks arise from subject motion. *Neuroimage* 59, 2142–2154.

Saad, Z. S., Gotts, S. J., Murphy, K., Chen, G., Jo, H. J., Martin, A., et al. (2012). Trouble at rest: how correlation patterns and group differences become distorted after global signal regression. *Brain Connect.* 2, 25–32.

Sirotin, Y. B., and Das, A. (2009). Anticipatory haemodynamic signals in sensory cortex not predicted by local neuronal activity. *Nature* 457, 475–479.

Song, X. W., Dong, Z. Y., Long, X. Y., Li, S. F., Zuo, X. N., Zhu, C. Z., et al. (2011). REST: a toolkit for resting-state functional magnetic resonance imaging data processing. *PLoS ONE* 6:e25031. doi:10.1371/journal.pone.0025031

Tang, L., Ge, Y., Sodickson, D. K., Miles, L., Zhou, Y., Reaume, J., et al. (2011). Thalamic resting-state functional networks: disruption in patients with mild traumatic brain injury. *Radiology* 260, 831–840.

Taylor, K. S., Seminowicz, D. A., and Davis, K. D. (2009). Two systems of resting state connectivity between the insula and cingulate cortex. *Hum. Brain Mapp.* 30, 2731–2745.

Van Dijk, K. R., Sabuncu, M. R., and Buckner, R. L. (2012). The influence of head motion on intrinsic functional connectivity MRI. *Neuroimage* 59, 431–438.

Veer, I. M., Beckmann, C. F., van Tol, M. J., Ferrarini, L., Milles, J., Veltman, D. J., et al. (2010). Whole brain resting-state analysis reveals decreased functional connectivity in major depression. *Front. Syst. Neurosci.* 4:41. doi:10.3389/fnsys.2010.00041

Weissenbacher, A., Kasess, C., Gerstl, F., Lanzenberger, R., Moser, E., and Windischberger, C. (2009). Correlations and anticorrelations in resting-state functional connectivity MRI: a quantitative comparison of preprocessing strategies. *Neuroimage* 47, 1408–1416.

Westlye, E. T., Lundervold, A., Rootwelt, H., Lundervold, A. J., and Westlye, L. T. (2011). Increased hippocampal default mode synchronization during rest in middle-aged and elderly APOE ε4 carriers: relationships with memory performance. *J. Neurosci.* 31, 7775–7783.

Xuan, Y., Meng, C., Yang, Y., Zhu, C., Wang, L., Yan, Q., et al. (2012). Resting-state brain activity in adult males who stutter. *PLoS ONE* 7:e30570. doi:10.1371/journal.pone.0030570

Yan, L., Zhuo, Y., Wang, B., and Wang, D. J. (2011). Loss of coherence of low frequency fluctuations of BOLD fMRI in visual cortex of healthy aged subjects. *Open Neuroimag. J.* 5, 105–111.

Zang, Y. F., He, Y., Zhu, C. Z., Cao, Q. J., Sui, M. Q., Liang, M., et al. (2007). Altered baseline brain activity in children with ADHD revealed by resting-state functional MRI. *Brain Dev.* 29, 83–91.

Conflict of Interest Statement: The authors declare that the research was conducted in the absence of any commercial or financial relationships that could be construed as a potential conflict of interest.

Received: 14 December 2012; accepted: 18 March 2013; published online: 02 April 2013.

*Citation: Di X, Kim EH, Huang C-C, Tsai S-J, Lin C-P and Biswal BB (2013) The influence of the amplitude of low-frequency fluctuations on resting-state functional connectivity. Front. Hum. Neurosci. **7**:118. doi: 10.3389/fnhum.2013.00118*

APPENDIX

Table A1 | One hundred sixty functionally defined ROIs used in the current study.

ROI #	x	y	z	Label	Network
1	−34	−67	−29	Inf cerebellum	Cerebellum
2	32	−61	−31	Inf cerebellum	Cerebellum
3	−25	−60	−34	Inf cerebellum	Cerebellum
4	−37	−54	−37	Inf cerebellum	Cerebellum
5	18	−81	−33	Inf cerebellum	Cerebellum
6	−6	−79	−33	Inf cerebellum	Cerebellum
7	−21	−79	−33	Inf cerebellum	Cerebellum
8	33	−73	−30	Inf cerebellum	Cerebellum
9	−24	−54	−21	Lat cerebellum	Cerebellum
10	21	−64	−22	Lat cerebellum	Cerebellum
11	−28	−44	−25	Lat cerebellum	Cerebellum
12	−34	−57	−24	Lat cerebellum	Cerebellum
13	14	−75	−21	Med cerebellum	Cerebellum
14	1	−66	−24	Med cerebellum	Cerebellum
15	−6	−60	−15	Med cerebellum	Cerebellum
16	−16	−64	−21	Med cerebellum	Cerebellum
17	5	−75	−11	Med cerebellum	Cerebellum
18	−11	−72	−14	Med cerebellum	Cerebellum
19	−2	30	27	ACC	Cingulo-opercular
20	−41	−47	29	Angular gyrus	Cingulo-opercular
21	38	21	−1	Ant insula	Cingulo-opercular
22	−36	18	2	Ant insula	Cingulo-opercular
23	27	49	26	aPFC	Cingulo-opercular
24	14	6	7	Basal ganglia	Cingulo-opercular
25	−20	6	7	Basal ganglia	Cingulo-opercular
26	−6	17	34	Basal ganglia	Cingulo-opercular
27	11	−24	2	Basal ganglia	Cingulo-opercular
28	9	20	34	dACC	Cingulo-opercular
29	54	−31	−18	Fusiform	Cingulo-opercular
30	0	15	45	mFC	Cingulo-opercular
31	37	−2	−3	Mid insula	Cingulo-opercular
32	−30	−14	1	Mid insula	Cingulo-opercular
33	32	−12	2	Mid insula	Cingulo-opercular
34	−55	−44	30	Parietal	Cingulo-opercular
35	58	−41	20	Parietal	Cingulo-opercular
36	−4	−31	−4	Post cingulate	Cingulo-opercular
37	−30	−28	9	Post insula	Cingulo-opercular
38	8	−40	50	Precuneus	Cingulo-opercular
39	42	−46	21	Sup temporal	Cingulo-opercular
40	43	−43	8	Temporal	Cingulo-opercular
41	−59	−47	11	Temporal	Cingulo-opercular
42	51	−30	5	Temporal	Cingulo-opercular
43	−12	−3	13	Thalamus	Cingulo-opercular
44	−12	−12	6	Thalamus	Cingulo-opercular
45	11	−12	6	Thalamus	Cingulo-opercular
46	−52	−63	15	TPJ	Cingulo-opercular
47	−46	10	14	vFC	Cingulo-opercular
48	−48	6	1	vFC	Cingulo-opercular
49	51	23	8	vFC	Cingulo-opercular
50	34	32	7	vPFC	Cingulo-opercular
51	9	39	20	ACC	Default
52	−48	−63	35	Angular gyrus	Default
53	51	−59	34	Angular gyrus	Default
54	−25	51	27	aPFC	Default
55	28	−37	−15	Fusiform	Default
56	−59	−25	−15	Inf temporal	Default
57	−61	−41	−2	Inf temporal	Default
58	52	−15	−13	Inf temporal	Default
59	−36	−69	40	IPS	Default
60	0	51	32	mPFC	Default
61	45	−72	29	Occipital	Default
62	−9	−72	41	Occipital	Default
63	−42	−76	26	Occipital	Default
64	−28	−42	−11	Occipital	Default
65	−2	−75	32	Occipital	Default
66	10	−55	17	Post cingulate	Default
67	−11	−58	17	Post cingulate	Default
68	−8	−41	3	Post cingulate	Default
69	1	−26	31	Post cingulate	Default
70	−5	−52	17	Post cingulate	Default
71	−5	−43	25	Post cingulate	Default
72	5	−50	33	Precuneus	Default
73	11	−68	42	Precuneus	Default
74	9	−43	25	Precuneus	Default
75	−3	−38	45	Precuneus	Default
76	−6	−56	29	Precuneus	Default
77	23	33	47	Sup frontal	Default
78	−16	29	54	Sup frontal	Default
79	46	39	−15	vlPFC	Default
80	6	64	3	vmPFC	Default
81	−6	50	−1	vmPFC	Default
82	9	51	16	vmPFC	Default
83	−11	45	17	vmPFC	Default
84	8	42	−5	vmPFC	Default
85	−1	28	40	ACC	Fronto-parietal
86	29	57	18	aPFC	Fronto-parietal
87	−29	57	10	aPFC	Fronto-parietal
88	−42	7	36	dFC	Fronto-parietal
89	40	17	40	dFC	Fronto-parietal
90	44	8	34	dFC	Fronto-parietal
91	40	36	29	dlPFC	Fronto-parietal
92	46	28	31	dlPFC	Fronto-parietal
93	−44	27	33	dlPFC	Fronto-parietal
94	−48	−47	49	IPL	Fronto-parietal
95	−41	−40	42	IPL	Fronto-parietal
96	−53	−50	39	IPL	Fronto-parietal
97	44	−52	47	IPL	Fronto-parietal
98	54	−44	43	IPL	Fronto-parietal
99	−32	−58	46	IPS	Fronto-parietal
100	32	−59	41	IPS	Fronto-parietal

(Continued)

Table A1 | Continued

ROI #	x	y	z	Label	Network
101	−35	−46	48	Post parietal	Fronto-parietal
102	42	48	−3	Vent aPFC	Fronto-parietal
103	−43	47	2	Vent aPFC	Fronto-parietal
104	39	42	16	vlPFC	Fronto-parietal
105	−52	28	17	vPFC	Fronto-parietal
106	−44	−63	−7	Occipital	Occipital
107	17	−68	20	Occipital	Occipital
108	36	−60	−8	Occipital	Occipital
109	−34	−60	−5	Occipital	Occipital
110	39	−71	13	Occipital	Occipital
111	19	−66	−1	Occipital	Occipital
112	−16	−76	33	Occipital	Occipital
113	9	−76	14	Occipital	Occipital
114	15	−77	32	Occipital	Occipital
115	29	−73	29	Occipital	Occipital
116	−29	−75	28	Occipital	Occipital
117	20	−78	−2	Occipital	Occipital
118	−18	−50	1	Occipital	Occipital
119	−29	−88	8	Post occipital	Occipital
120	13	−91	2	Post occipital	Occipital
121	27	−91	2	Post occipital	Occipital
122	−4	−94	12	Post occipital	Occipital
123	−5	−80	9	Post occipital	Occipital
124	29	−81	14	Post occipital	Occipital
125	33	−81	−2	Post occipital	Occipital
126	−37	−83	−2	Post occipital	Occipital
127	46	−62	5	Temporal	Occipital
128	60	8	34	dFC	Sensorimotor
129	58	11	14	Frontal	Sensorimotor
130	53	−3	32	Frontal	Sensorimotor
131	−42	−3	11	Mid insula	Sensorimotor
132	−36	−12	15	Mid insula	Sensorimotor
133	33	−12	16	Mid insula	Sensorimotor
134	−26	−8	54	Parietal	Sensorimotor
135	−47	−18	50	Parietal	Sensorimotor
136	−38	−15	59	Parietal	Sensorimotor
137	46	−20	45	Parietal	Sensorimotor
138	−55	−22	38	Parietal	Sensorimotor
139	−38	−27	60	Parietal	Sensorimotor
140	−24	−30	64	Parietal	Sensorimotor
141	41	−23	55	Parietal	Sensorimotor
142	18	−27	62	Parietal	Sensorimotor
143	−47	−12	36	Parietal	Sensorimotor
144	42	−24	17	Post insula	Sensorimotor
145	−41	−31	48	Post parietal	Sensorimotor
146	10	5	51	Pre-SMA	Sensorimotor
147	−54	−22	22	Precentral gyrus	Sensorimotor
148	−54	−9	23	Precentral gyrus	Sensorimotor
149	44	−11	38	Precentral gyrus	Sensorimotor
150	−44	−6	49	Precentral gyrus	Sensorimotor
151	46	−8	24	Precentral gyrus	Sensorimotor
152	58	−3	17	Precentral gyrus	Sensorimotor
153	0	−1	52	SMA	Sensorimotor
154	34	−39	65	Sup parietal	Sensorimotor
155	−53	−37	13	Temporal	Sensorimotor
156	−41	−37	16	Temporal	Sensorimotor
157	59	−13	8	Temporal	Sensorimotor
158	−54	−22	9	Temporal	Sensorimotor
159	43	1	12	vFC	Sensorimotor
160	−55	7	23	vFC	Sensorimotor

The ROIs were obtained from Dosenbach et al. (2010), and sorted by their affiliating networks. The x, y, and z coordinates were given in MNI space.

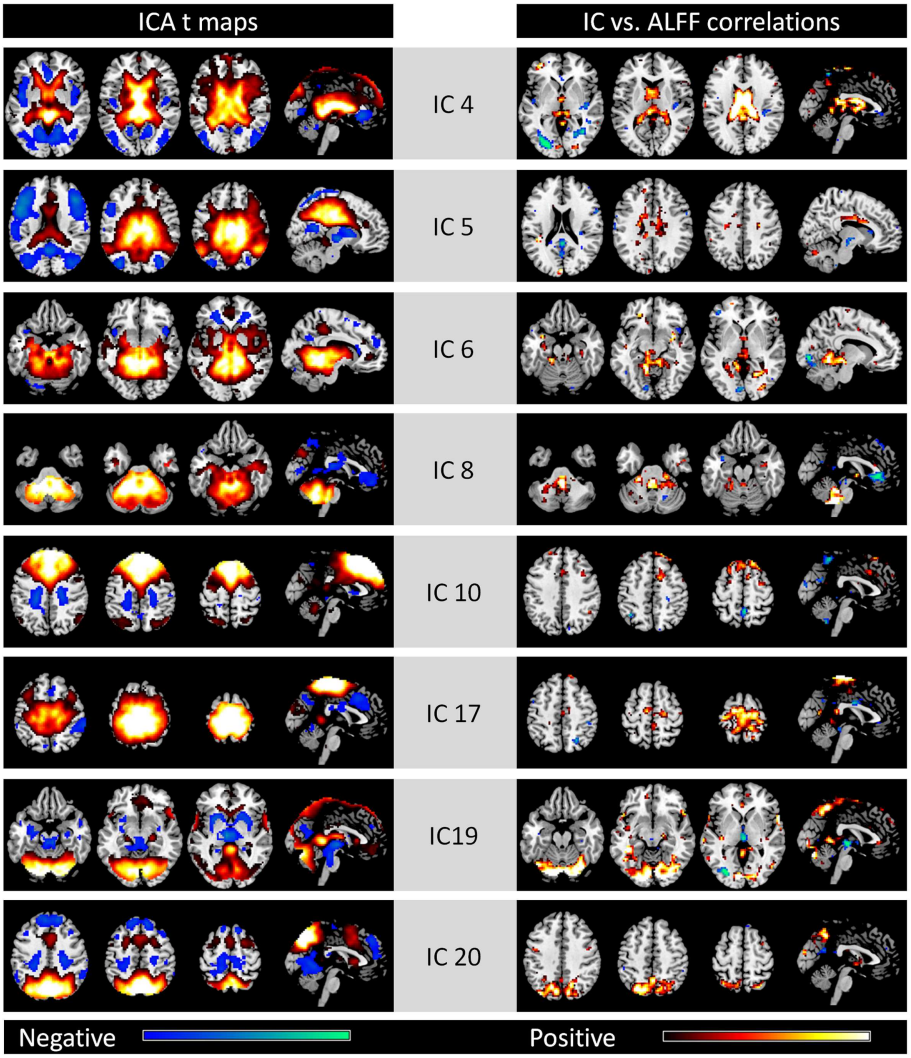

FIGURE A1 | Eight noise networks identified by spatial ICA (left column) and voxel-wise correlations between network strengths and ALFFs (right column). All maps are thresholded at $p < 0.001$. For the ICA t maps, display range is absolute t value between 3.42 and 20, and for the correlation maps, display range is absolute r value between 0.364 and 0.6. Hot and cold colors encode positive and negative effects, respectively.

frontiers in
HUMAN NEUROSCIENCE

ORIGINAL RESEARCH ARTICLE
published: 19 October 2012
doi: 10.3389/fnhum.2012.00288

Dual processing streams in chemosensory perception

Johannes Frasnelli[1,2]*, Johan N. Lundström[3,4], Veronika Schöpf[5], Simona Negoias[2], Thomas Hummel[2] and Franco Lepore[1]

[1] Centre de Recherche en Neuropsychologie et Cognition, Université de Montréal, Montréal, QC, Canada
[2] Department of ENT-Medicine, Technical University of Dresden, Dresden, Germany
[3] Cognitive Neuroimaging Laboratory, Monell Chemical Senses Center, Philadelphia, PA, USA
[4] Department of Clinical Neuroscience, Karolinska Institute, Stockholm, Sweden
[5] Department of Radiology, Division of Neuro- and Musculoskeletal Radiology, Medical University Vienna, Vienna, Austria

Edited by:
Simon D. Robinson, Medical University of Vienna, Austria

Reviewed by:
Hidenao Fukuyama, Kyoto University, Japan
Nicola Soldati, CIMeC-Center for Mind-Brain Sciences, Italy

***Correspondence:**
Johannes Frasnelli, Département de Psychologie, Université de Montréal, Salle F-475, Pavillon Marie-Victorin, 90, Ave. Vincent-d'Indy, Montréal, QC H2V 2S9, Canada.
e-mail: frasnelli@yahoo.com

Higher order sensory processing follows a general subdivision into a ventral and a dorsal stream for visual, auditory, and tactile information. Object identification is processed in temporal structures (ventral stream), whereas object localization leads to activation of parietal structures (dorsal stream). To examine whether the chemical senses demonstrate a similar dissociation, we investigated odor identification and odor localization in 16 healthy young subjects using functional MRI. We used two odors—(1) eucalyptol; (2) a mixture of phenylethanol and carbon dioxide)—which were delivered to only one nostril. During odor identification subjects had to recognize the odor; during odor localization they had to detect the stimulated nostril. We used general linear model (GLM) as a classical method as well as independent component analysis (ICA) in order to investigate a possible neuroanatomical dissociation between both tasks. Both methods showed differences between tasks—confirming a dual processing stream in the chemical senses—but revealed complementary results. Specifically, GLM identified the left intraparietal sulcus and the right superior frontal sulcus to be more activated when subjects were localizing the odorants. For the same task, ICA identified a significant cluster in the left parietal lobe (paracentral lobule) but also in the right hippocampus. While GLM did not find significant activations for odor identification, ICA revealed two clusters (in the left central fissure and the left superior frontal gyrus) for this task. These data demonstrate that higher order chemosensory processing shares the general subdivision into a ventral and a dorsal processing stream with other sensory systems and suggest that this is a global principle, independent of sensory channels.

Keywords: olfaction, trigeminal system, independent component analysis, general linear model, ventral, dorsal

INTRODUCTION

Over the last 20 years, neuroimaging methods such as positron emission tomography (PET) and functional magnetic resonance imaging (fMRI) have allowed for the investigation of brain regions involved in olfactory processing. Since Zatorre and colleague's seminal paper, in which they localized olfactory information processing to piriform and orbitofrontal cortex (Zatorre et al., 1992), researchers have investigated cerebral areas involved in different olfactory tasks. The olfactory system has been suggested to be dependent on concurrent parallel and hierarchial pathways. According to this model, olfactory stimulation always leads to activation of basic olfactory processing areas, such as the piriform cortex, amygdala, orbitofrontal cortex and insula, independent of the task. Higher order brain structures (e.g., prefrontal cortex) are thereafter activated dependent on the specific task (e.g., olfactory memory) (Savic et al., 2000). For example, by presenting two concentrations (low and high) of each a pleasant and an unpleasant odor, Anderson et al. investigated cortical representation of odor valence and intensity. They observed an intensity-dependent activation of the amygdala dissociated from odor valence. Regions of the orbitofrontal cortex, in contrast, were differentially activated by odor valence where odor intensity had no effect (Anderson et al., 2003). However, these results were later suggested to be paradigm rather than intensity-dependent (Winston et al., 2005). Later a study with a similarly elegant design investigated the effect of chemical structure and quality using cross adaptation. Here, anterior portions of the piriform cortex were demonstrated to encode information regarding chemical structure, whereas posterior parts of the same area responded independent of chemical structure, but differentially to odor quality (Gottfried et al., 2006). These studies provide evidence that the olfactory system is indeed organized both hierarchically and topographically. This is in analogy to the other sensory systems, such as tonotopy in audition, with high and low frequencies being represented in medial and lateral portions, respectively, of the Heschl gyrus (Schonwiesner et al., 2002) or retinotopy in vision, where neighboring retinal areas project to adjacent cortical areas in the occipital cortex (Grill-Spector and Malach, 2004).

Analogies between the senses may extend beyond hierarchical and topographical organization with dual processing streams being a possible candidate. Two separate processing streams, the

dorsal and ventral stream, were first described within the visual system of the monkey (Mishkin et al., 1983). The dorsal stream, extending from visual cortex to posterior parietal cortex, has a role in spatial perception (i.e., localization of an object in space, "where is the object?"), whereas the ventral stream to the temporal cortex processes object perception (i.e., identification of an object, "what is the object?"). This model of separation of processing according to stimulus characteristics has subsequently been confirmed also within the human visual (Haxby et al., 1991), auditory (Rauschecker and Tian, 2000), and somatosensory systems (Reed et al., 2005), as well as in multisensory integration (Renier et al., 2009).

Whether a dual processing stream also exists within the chemical senses is not known. Several lines of evidence do, however, indicate that a separation according to stimulus characteristics exists. The intranasal chemical systems are able to extract information related to both object localization, a ventral stream associated process, as well as object identification, a dorsal stream associated process. The main noticeable difference to our visual and auditory senses is that these abilities—especially object localization—are dependent on associative processing in two separate senses, the olfactory and trigeminal sense. While object identification is evident for olfaction (Doty et al., 1984), localization of odorous objects seems to be more difficult, if not impossible, for humans based on the sense of smell solely. When directional smelling, i.e., the ability to localize odors in space, is assessed in humans, researchers achieve a maximal concentration gradient between both nostrils by stimulating only one nostril with an odor; the other nostril receives only air. Even in this extreme case, subjects were not able to correctly localize the stimulated nostril unless the odor additionally stimulates the intranasal trigeminal system (von Skramlik, 1924; Schneider and Schmidt, 1967; Wysocki et al., 2003; Frasnelli et al., 2009, 2010; Kleemann et al., 2009; Wise et al., 2012); these odors are called mixed olfactory trigeminal stimuli as opposed to pure odors, which stimulate the sense of smell exclusively (Kobal et al., 1989). Nonetheless, studies have claimed that localization of pure odors is possible for humans (von Békésy, 1964; Porter et al., 2005), however, they used odors which under certain circumstances are known to stimulate the trigeminal nerve (Frasnelli et al., 2011). In fact, the vast majority, if not all, odors stimulate the trigeminal nerve, at least in higher concentrations (Doty et al., 1978; Frasnelli et al., 2011) rendering a pure odor sensation a very rare event (Wise et al., 2012).

Nasal stimulation with a pure odorant (phenyl ethanol), a pure trigeminal stimulus (carbon dioxide), and a mixture thereof were recently studied in more detail (Boyle et al., 2007). The pure odor activated brain areas classically considered to be olfactory (piriform cortex—PIR, and orbitofrontal cortex—OFC). The pure trigeminal stimulus, in turn, activated the somatosensory brain areas (thalamus, postcentral gyrus) as well as those aforementioned olfactory related areas. The mixture of both stimuli, however, activated additional brain areas than the sum of the activations to the individual components. Specifically, the mixture activated chemosensory processing areas (PIR, OFC) and multisensory integration areas located in the parietal lobe (such as the intraparietal sulcus—IPS) and the temporal lobe (such as the superior temporal sulcus—STS) more than the individual components (Boyle et al., 2007).

Mixed olfactory-trigeminal stimuli which are both identifiable (Doty et al., 1984; Laska et al., 1997) and localizable (Kobal et al., 1989; Frasnelli et al., 2009, 2011) are therefore good stimulus candidates if one aims to investigate whether a dual processing stream using a ventral and a dorsal pathway exists in the chemical senses, akin our other senses.

The literature provides us with several brain regions in which multisensory integration takes place on a cortical level. Some studies compared superadditive effects of multimodal compared to unimodal stimulation, e.g., for auditory and visual stimuli (Calvert et al., 2001) or for olfactory and trigeminal stimuli (Boyle et al., 2007). The resulting activation maps of both studies overlapped partially, and exhibited superadditive effects for the insula, IPS, STS, as well as frontal regions (middle and superior frontal gyrus). Some of these multisensory integration areas were activated in a task specific manner in another study which used auditory and vibrotactile multimodal stimuli. Here, the task of localizing the stimuli activated parietal cortex (left and right inferior parietal lobule—IPL, right precuneus, superior parietal lobule—SPL), whereas identifying the stimuli activated bilateral insula, and right inferior frontal gyrus (Renier et al., 2009). These multisensory integration areas are prime candidates to serve as nodes also within a chemosensory ventral and a dorsal stream.

The aim of this study was to determine the existence of a separation into a ventral and dorsal stream for chemosensory processing. In contrast to earlier studies, which showed dual streams for monomodal processing, we aimed to investigate this question by using stimuli which stimulated separate sensory systems, i.e., the olfactory system and the trigeminal system. Despite the fact that both sensory systems exhibit distinct peripheral pathways—the olfactory nerve and bulb as well as piriform cortex for the olfactory system, the trigeminal nerve and ganglion, thalamic rely for the trigeminal system—they share important central processing areas such as the orbitofrontal cortex and the insula (Boyle et al., 2007; Albrecht et al., 2010). These brain areas can therefore be considered chemosensory processing areas (Albrecht et al., 2010), in line with the notion of a unique flavor sense (Auvray and Spence, 2008) integrating inputs from different sensory channels to one single percept.

In this study we used both exploratory and model driven fMRI analyses. To this extent, we performed a standard regression based fMRI analysis based on the general linear model (GLM) and compared the results to the fully exploratory method based on independent component analysis (ICA). Chemosensory experiments are susceptible to factors such as movement due to the very nature of the stimulus. Although motion parameters of the subject can be included as nuisance regressors in the GLM analysis, this reduces motion effects particularly in event-related designs (Birn et al., 1999), but BOLD sensitivity is substantially reduced even if a moderate correlation between motion and task is present (Johnstone et al., 2006). These time-locked effects can lead to false positive results in a GLM (Hajnal et al., 1994). We

therefore additionally performed an analysis based on spatial ICA, which is able to isolate activation in data based on spatial independence rather than temporal similarity between stimulus and response adding a beneficial factor to the analysis in this study.

MATERIALS AND METHODS

SUBJECTS

We included 16 healthy, young participants (12 women, mean age: 24; 20–29 years) in this study. The study was conducted at the University of Dresden Medical School, according to the Declaration of Helsinki and all subjects gave written informed consent prior to the study. It was approved by the local Ethics Committee (EK number 185062009).

BEHAVIORAL TESTING

Before the fMRI session, we assessed subjects' olfactory abilities and trigeminal chemoreception. Subjects' ability to identify odors was determined by means of the Sniffin' Sticks identification test kit (Kobal et al., 2000). In this test, subjects are presented with 12 pen-like odor dispensing devices. Their task was to choose the right descriptor from a list of four for each odor. We counted the number of correct responses. Further, we assessed subjects' ability to localize odors by means of the odor lateralization test for eucalyptol (Hummel et al., 2003). We stimulated subjects with a device which allows the delivery of predefined volumes of air to both nostrils simultaneously. In this test, subjects were stimulated with odorized air to one nostril and odorless air to the other; their task was to detect the side of odor stimulation. We used neat eucalyptol as the odor stimulus. The task was repeated 40 times with each trial separated by 40 s. We counted the number of correct localizations. We only included participants with a normal ability to identify odors [i.e., who were able to identify more than 10 out of 12 sticks (Hummel et al., 2001)] and the ability to localize odors above chance [more than 25 out of 40 (Frasnelli et al., 2008)].

CHEMOSENSORY STIMULI

We used 20% of eucalyptol saturated air (eucalyptus odor) and a mix of 20% of phenyl ethyl alcohol saturated air (rose odor) with 60% carbon dioxide (CO_2) (Boyle et al., 2007) as bimodal odors; both are known to activate the olfactory and the intranasal trigeminal system (Hummel et al., 2003; Boyle et al., 2007). The reasons why we decided to use a mixture of phenyl ethanol and carbon dioxide instead of a monomolecular substance are twofold. First, phenyl ethanol is a pure odorant and therefore very difficult to be localized by humans (Frasnelli et al., 2009); carbon dioxide is virtually odorless and therefore very difficult to identify; the mixture of both, however, is both localizable and identifyable (Boyle et al., 2007). Second, it is difficult to match a monomolecular substance with regards to olfactory and trigeminal intensity. By using a mixture, we could adjust both trigeminal and olfactory intensity (by changing the concentrations of phenyl ethanol and CO_2 separately) to match eucalyptol's in pilote experiments. Stimuli were therefore isointense on both, the olfactory and the trigeminal dimensions. Subjects were familiarized with both odors and could easily distinguish them.

ODOR PRESENTATION

Odor stimuli were applied by means of a computer-controlled air-dilution olfactometer (OM6b; Burghart, Wedel, Germany). This stimulator allows application of rectangular-shaped chemical stimuli with controlled stimulus onset. Mechanical stimulation is avoided by embedding stimuli into a constant flow of odorless, humidified air of controlled temperature (80% relative humidity, total flow 8 L/min, 36°C) (Kobal, 1981). Thus, throughout the experiment, the subjects received humidified, warm air to their nostril. During stimulation an odor was embedded into this constant airflow. The olfactometer allows for stimulation of each nostril separately. Subjects were instructed to breathe through their mouth to avoid potential sniff-related activity.

TESTING PARADIGM

We used a block design for stimulation. During the entire fMRI session, subjects focussed on a black cross on a screen. Nine seconds before the "on-period", the cross switched to one of two questions [task; either "where?" (German: "wo?") or "what?" ("was?")]. The order of the questions was pseudo-randomized and counterbalanced. The text stayed on the screen for 5 s after which it switched back to the black cross. Four seconds later, the "on"-period begun during which odor stimuli were delivered five times, each 400 ms long, every 4 s. The chemosensory stimuli were either eucalyptol or the PEA/CO_2 mixture and delivered either to the left or the right nostril (all stimuli pseudorandomized and counterbalanced). After each stimulus, subjects responded to the task by pressing one of two buttons with the index of their right hand. Specifically, during the localization task they had to indicate whether their left or their right nostril was stimulated and during the identification task, they had to indicate whether they received eucalyptol or the PEA/CO_2 mix. The "on"-period was followed by a 30 s "off"-period, during which subjects received odorless air (AIR). During one run, we delivered 10 "on"- and 10 "off"-periods; subjects were tested in two runs. For data analysis we classified volumes during the "on"-periods as "where" or "what" conditions, whereas the "off"-periods were classified as "baseline" condition.

IMAGE ACQUISITION

The study was performed using a 1.5 MRI scanner (Sonata; Siemens, Erlangen, Germany). For anatomical overlays, a T1-weighted (turboflash sequence) axial scan with 224 slices, voxel size of 1.6 × 1.1 × 1.5 mm, a repetition time (TR) of 3000 ms, echo time (TE) of 3.93 ms, and 2 averages (2130/3.93/2) was acquired. Functional data acquisition was performed in the axial plane (oriented parallel to the planum sphenoidale to minimize artifacts) using a multislice spin-echo echo-planar imaging sequence. Scan parameters included a 64 × 64 matrix, voxel size of 3 × 3 × 3.75 mm, TR of 3000 ms, and a TE of 35 ms. A total of 207 images were acquired at each of 24 slice locations per run over the course of a total functional acquisition session of approximately 10 min in length. The three imaging conditions consisted of (1) subjects identifying a chemosensory stimulus ("what"), (2) subjects localizing a chemosensory stimulus ("where"), and (3) chemosensory-free low-level baseline.

DATA ANALYSIS

The functional MRI data was analyzed by means of SPM8 (Wellcome Trust, http://www.fil.ion.ucl.ac.uk/spm/software/spm8/) implemented in Matlab (Mathworks Inc., Natick, MS). Functional data were registered, motion-corrected, and resliced using SPM8 preprocessing procedures. Mean functional images were coregistered to the anatomical T1 volume. We then performed the analysis on spatially normalized stereotactically transformed into ICBM152-space and smoothed images (8 mm full width at half maximum Gaussian kernel).

General linear model—GLM

We calculated a second level analysis contrasting images using a paired sample *t*-test to highlight the difference between conditions (what and where vs. baseline; what vs. where; where vs. what). We corrected for whole brain family-wise error (FWE) thresholding at $p < 0.05$ If this analysis yielded no significant result, we lowered the criterion to $p < 0.001$ uncorrected (indicated as "uncorrected") and then only reported areas where we had a strong a-priori hypothesis of result based on the existing literature. Moreover, in order to minimize the potential for false positive findings, indeed a worry when reporting uncorrected results, we set the cluster criterion to 10 voxels to only detect areas of extended neural activity, thus lowering the possibly of results based on random fluctuations.

Independent component analysis—ICA

Functional data sets were post-processed using probabilistic independent component analysis (P-ICA) (Beckmann and Smith, 2004) as implemented in MELODIC (Multivariate Exploratory Linear Decomposition into Independent Components) version 3.10, a part of FSL (FMRIB's Software Library, www.fmrib.ox.ac.uk/fsl). The optimum number of components to be estimated was 29, determined using the implemented criterion Minimum Description Length (MDL) (Rissanen, 1978). Regression was used by utilizing the first two stages of the dual regression approach version v0.5, a part of FSL (Filippini et al., 2009) to obtain single-subject specific component maps and time courses. For each individual subject temporal correlations revealed the single-subject independent component (IC) with the best fit for both conditions (condition 1: "what," condition 2: "where") using Matlab (Matlab 7.8, Release 2009a). Corresponding spatial IC maps for every subject and both conditions were then exported to SPM8 for statistical testing and visualization. For second-level analysis, two separate *t*-tests were performed for both conditions ($p < 0.05$, FWE corrected). Again, the cluster threshold was set at 10 voxels.

RESULTS

GENERAL LINEAR MODEL (GLM)

In order to first verify that our imaging paradigm reliably activated chemosensory processing areas, we initially assessed the main effect of odor stimulation by comparing both odor conditions against no odor condition (where + what vs. no-odor baseline). We observed activations areas commonly associated with chemosensory processing, such as left and right insula, the right OFC, as well as multisensory integration centers such as the right inferior parietal lobule and the left supramarginal gyrus (see **Table 1**).

To verify task specific brain activations, we compared the two stimulation conditions to each other. When contrasting odor localization against odor identification (where vs. what), we observed activations of a cluster in the left intraparietal sulcus, and one in the right superior frontal sulcus (**Table 2**).

The opposite contrast (what vs. where) did not reveal any significant activation above threshold criteria.

INDEPENDENT COMPONENT ANALYSIS (ICA)

We used ICA to obtain specific component maps for individual subjects. We then extracted, for each subject, the component with the best fit to the time course of each condition. Information on correlation coefficients for individual components in both tasks is outlined in **Table 3**.

The resulting statistical maps were submitted to a subsequent second level analysis where the component for odor identification ("what") revealed two significant clusters within an area of the left central fissure and the left superior frontal gyrus (**Table 4**).

For odor localization ("where"), we detected two clusters above set criterion, one located in the right hippocampal region and another in left paracentral lobule (**Table 5**).

In **Figure 1** we provide an overview of activations in the parietal cortex obtained in different conditions (**Figure 1**).

DISCUSSION

In this study we examined whether processing of chemosensory information displays a subdivision into localization and identification following the notion of a dual stream demonstrated for other senses (Mishkin et al., 1983). We investigated localization and identification of mixed trigeminal-olfactory objects and observed that subjects activated distinct brain regions.

Table 1 | Brain activation due to stimulation with eucalyptus and a phenyl ethanol/ CO_2 mixture: comparison of both tasks vs. baseline [contrast (where & what) vs. baseline].

Area	*x*	*y*	*z*	*T*	Voxels
Right insula	54	14	4	10.1	260
Left insula	−42	14	1	6.8	42
Right lateral OFC	45	44	−5	8.5	38
Right inferior parietal lobule	51	−37	49	6.9	20
Right middle frontal G	42	41	19	7.1	23

$p < 0.05$, corrected, extent threshold 10 voxels.

Table 2 | Brain activation due to stimulation with eucalyptus and a phenyl ethanol/CO_2 mixture: comparison of between odor localization vs. odor identification (contrast where—what).

Area	*x*	*y*	*z*	*T*	Voxels
Left intraparietal sulcus	−36	−43	31	4.7	10
Right superior frontal sulcus	21	20	34	4.3	10

$p < 0.001$, uncorrected, extent threshold 10 voxels.

Table 3 | Correlation between independent component and task (left: "where"; right: "what") per subject.

Subject	"where"				"what"			
	max cc	IC#	mean abs cc	SD abs cc	max cc	IC#	mean abs cc	SD abs cc
1	0.03	4	0.06	0.04	0.02	4	0.06	0.06
2	0.21	14	0.07	0.06	0.21	16	0.09	0.05
3	0.09	5	0.09	0.05	0.13	2	0.07	0.05
4	0.07	11	0.05	0.03	0.13	10	0.08	0.07
5	0.05	16	0.03	0.02	0.16	16	0.04	0.04
6	0.05	7	0.04	0.03	0.11	2	0.06	0.03
7	0.13	2	0.11	0.08	0.10	13	0.08	0.06
8	0.06	4	0.05	0.03	0.09	4	0.05	0.03
9	0.20	1	0.10	0.07	0.31	9	0.14	0.08
10	0.10	14	0.07	0.04	0.23	14	0.09	0.06
11	0.11	14	0.04	0.04	0.12	16	0.05	0.04
12	0.08	7	0.05	0.03	0.16	6	0.05	0.04
13	0.08	7	0.07	0.05	0.16	16	0.06	0.05
14	0.21	4	0.10	0.08	0.13	13	0.07	0.06
15	0.09	7	0.05	0.05	0.17	16	0.07	0.05
16	0.03	16	0.10	0.08	0.08	14	0.11	0.08

Subject, consecutive subject ID; max cc, maximal correlation coefficients; IC#, number independent component corresponding to max cc; mean abs cc, mean of absolute values of correlation coefficients; SD abs cc, standard deviation of absolute values of correlation coefficients.

Table 4 | Brain activation due to stimulation with eucalyptus and a phenyl ethanol/CO_2 mixture: independent component analysis: component fitting best for odor identification [ICA (what)].

Area	*x*	*y*	*z*	*T*	Voxels
Left central fissure	−24	−31	52	15.9	19
Left superior frontal gyrus	−24	−16	40	5.92	20

$p < 0.05$, corrected, extent threshold 10 voxels.

Table 5 | Brain activation due to stimulation with eucalyptus and a phenyl ethanol/CO_2 mixture: independent component analysis: component fitting best for odor localization [ICA (where)].

Area	*x*	*y*	*z*	*T*	Voxels
Right hippocampus	30	−46	4	6.73	19
Left paracentral lobule	−3	−31	55	5.21	11

$p < 0.05$, corrected, extent threshold 10 voxels.

Specifically, when subjects localized unilaterally presented mixed olfactory-trigeminal stimuli, regions in the left intraparietal sulcus and the right superior frontal sulcus were activated to a higher degree than if they were identifiying the same stimuli. Further, an ICA allowed us to extract task specific networks for each odor localization and odor identification. For odor localization, the network revealed two clusters, one in the right hippocampus, and one in the left paracentral lobule. For odor identification, also two clusters could be observed, one located around the left central fissure, the other one in the left superior frontal gyrus.

DUAL CHEMOSENSORY PROCESSING STREAMS

When subjects were localizing the odorous objects, both means of analysing the neuroimaging data identified significant activation of the left posterior parietal lobe, in addition to its general activation independent of the task. These observations fit well with the literature where object localization consistently activates posterior parietal regions. For instance, in analogy to the findings in non-human primates (Mishkin et al., 1983) a visual spatial localization task led to activation in the lateral superior parietal cortex (Haxby et al., 1991). In the auditory system, object localization activated a dorsal stream from the caudal primary auditory cortex to the inferior parietal cortex (somewhat lower than for visual stimuli) to middle and inferior frontal gyri, whereas anterior primary auditory cortex to posterior frontal and orbitofrontal regions formed the ventral stream for object identification (Rauschecker and Tian, 2000; Maeder et al., 2001).

Different subregions of the parietal lobe play particular roles in the dual stream dichotomy. SPL and IPS, whose activation is often associated with activation of the dorsoloateral frontal lobe, are part of the dorsal frontoparietal system for directing spatial attention. IPL on the other hand, is activated, together with more ventral frontal regions when individuals perform non-spatial tasks. Thus, there is a gradient from more spatial tasks in SPL to less spatial tasks in IPL, with the IPL's suggested role to sustain attention over time (Husain and Nachev, 2007). The data obtained within the present study corresponds closely with these earlier reports, especially with regards the parietal lobe: unilateral chemosensory stimuli triggered activation of right IPL independent of the task subjects performed, indicating multisensory integration. Localization of these stimuli, however, led to a significantly stronger activation of the left IPS than what we observed for stimulus identification. Therefore, the cortex in and

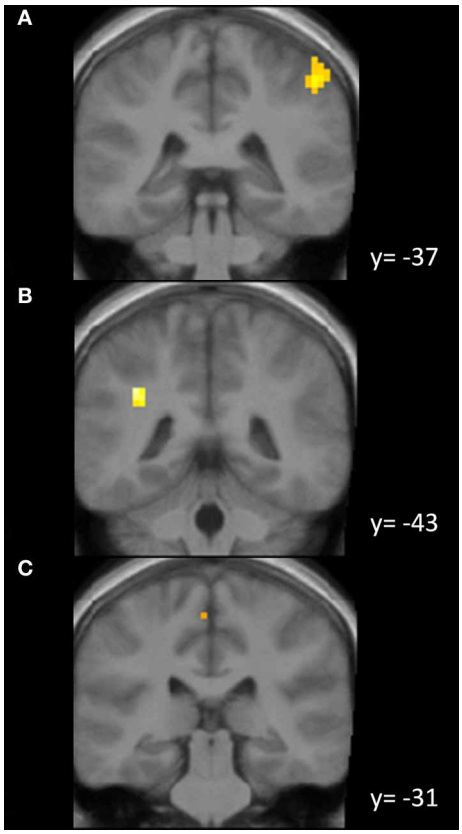

FIGURE 1 | Activations in the parietal lobe. (A) Activation in the right inferior parietal lobule due to odorant perception [GLM—contrast: (odor identification and odor localization) vs. baseline; $p < 0.05$ (corrected)]; **(B)** activation in the left intraparietal sulcus due to odor localization [GLM—contrast: odor localization vs. odor identification; $p < 0.001$ (uncorrected)]; **(C)** activation in the left paracentral lobule due to odor localization [ICA—component fitting best for odor localization; $p < 0.05$ (corrected)].

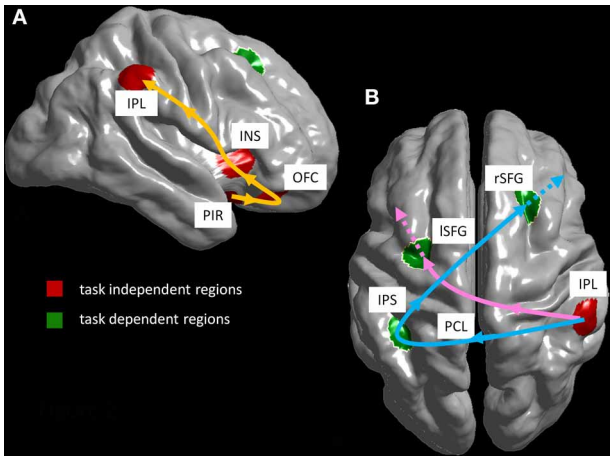

FIGURE 2 | Suggested pathways: (A) task-independent pathway (regions in red; orange arrow) from piriform cortex (PIR) via orbitofrontal cortex (OFC) and insula (INS) to right inferior parietal lobule (IPL). (B) Task-dependent pathway (regions in green): localization pathway (blue arrow) from right inferior parietal lobule (IPL) via left intraparietal sulcus (IPS) and left paracentral lobule (PCL) to right superior frontal gyrus (rSFG); odorant identification pathway (pink arrow) from IPL to left superior frontal gyrus (lSFG).

around the IPS is part of a dorsal stream responsible for object localization in different sensory systems, including the chemical senses. Activation of this particular brain region was observed when subject localized monomodal stimuli, such as visual (Haxby et al., 1991), auditory (Rauschecker and Tian, 2000; Maeder et al., 2001), and somatosensory (Reed et al., 2005) ones as well as multimodal stimuli such as audio-somatosensory (Renier et al., 2009) and olfactory-trigeminal ones (present study). It is commonly activated with mixed olfactory trigeminal stimuli (Boyle et al., 2007; Lombion et al., 2009).

Next to the parietal activations, we also observed activations in the frontal lobe. First, object localization led to a significant activation of the right superior frontal sulcus, as shown by the GLM contrast "where" vs. "what." Second, the ICA demonstrated odor object identification to be associated with the left superior frontal gyrus. In addition to these hemispheric differences, the latter activation was located more posteriorily than the former. It has been demonstrated that there are distinct working memory systems for spatial and verbal information predominantly located in the (dorsolateral) prefrontal cortex of both hemispheres. The right hemisphere stores and maintains information on spatial features, whereas the left hemispheres does the same for verbal and object identity information (Smith and Jonides, 1997; Belger et al., 1998). This appears to be modality independent, as both visual and tactile working memory evoked similar frontoparietal networks including the posterior parietal cortex and the dorsolateral prefrontal cortex, with a leftwards tendency for object discrimination (Ricciardi et al., 2006). In **Figure 2** we highlight how our results fit into the same framework. After activation of chemosensory regions common to both tasks, both tasks activated a parieto-frontal network, from the posterior parietal cortex to prefrontal areas, with activation of a left sided and a right sided frontal area for object identification and localization, respectively (**Figure 2**).

ICA revealed a puzzling finding in the activation of the right posterior hippocampus when subjects were localizing odors. Hippocampal activation is usually linked to spatial navigation and episodic memory (Igloi et al., 2010). Localizing odorants to the left or right nostril is clearly a spatial task; however, our paradigm did not explicitly involve a mnesic component. We know that hippocampus also stores serial working memory of spatial locations even in the encoding phase (Toepper et al., 2010). Importantly, this is true even in implicit conditions: hippocampal activation can be observed when subjects learn the temporal structure of sequences even without any conscious sequence knowledge (Schendan et al., 2003). In our paradigm, we presented our subjects with a series of spatial locations. Therefore, implicit spatial sequence learning may therefore explain the hippocampal activity we observed.

There has been a prior attempt to investigate the dissociation between object localization and identification in the chemical senses (Porter et al., 2005). Here, subjects smelled four odorants. Similarly to our study, odors were delivered monorhinally, and subjects were asked to either identify or localize the odors. Although the main focus of the study was to investigate nostril specific receptive fields within the piriform cortex, the authors also compared brain activations between both tasks. They did indeed observe dissociations between tasks which differentially activated three specific brain areas: odor identification activated the occipital gyrus and the paracentral lobule to a larger extent than odor localization; odor localization, in turn, activated the superior temporal gyrus more than odor identification. These findings contradict the existing literature where activation of different regions of the occipital cortex has been reported mainly for visual stimuli, during object identification [e.g., the occipitotemporal junction for face recognition (Haxby et al., 1991)] rather than for object localization. On the other hand, temporal areas have been associated with object identification rather than object localization (Mishkin et al., 1983), with the exception of sound localization (Maeder et al., 2001). Further, the existing literature, paired with the present results, suggest that activation of superior parietal areas, such as the paracentral lobule, appears to be more commonly linked to object localization (Haxby et al., 1991; Rauschecker and Tian, 2000; Maeder et al., 2001; Reed et al., 2005; Renier et al., 2009). The exact implications of Porter and colleagues (Porter et al., 2005) findings therefore remain unclear.

COMPARISON BETWEEN ICA AND GLM

An earlier study on chemosensory stimulation with CO_2 has compared regression-based analysis of fMRI based data using the GLM with that of group analysis using the ICA methods. Some activations were only detected by group ICA, but not by GLM; this could be explained by the fact that activity in these regions was shifted temporally and therefore delayed with respect to the expected response. Furthermore, it showed a variation of CO_2-stimulus-evoked responses which was different for the selected ROIs within one subject (Schopf et al., 2011). This finding of differing hemodynamic responses across subjects, brain regions and sessions is a known constraint of regression-based methods such as GLM (Aguirre et al., 1998; Cunnington et al., 2003; Neumann et al., 2003; Handwerker et al., 2004; Menz et al., 2006). Fully exploratory analysis methods such as ICA [introduced by (McKeown et al., 1998)] do not require the specification of a model or a hemodynamic response function. A number of approaches have been developed to extend ICA from the analysis of a single data set to the group level (Calhoun et al., 2009); the most widely adopted method is to concatenate single-subject data in time prior to performing ICA (Calhoun et al., 2001; Beckmann and Smith, 2005) [for a comparison of toolboxes using temporal concatenation ICA see (Schopf et al., 2010)].

A challenge in group ICA is the need to identify and evaluate group components. This can either be done by temporally correlating the model time course with the corresponding time courses of the group components or by template matching, which includes the spatial correlation of a predefined template with the group component maps. For the present data, we used temporal correlation to find spatial activity patterns across subjects. As hypothesized earlier (Schopf et al., 2011) our study showed that group ICA provides supplemental information—in our case regarding parallel pathways processing—in addition to a priori defined model-dependent regression-based analysis.

CONCLUSION

Earlier studies have demonstrated that cerebral architecture follows a subdivision into two parallel sensory processing pathways linking modality specific primary regions with amodal processing regions (posterior parietal cortex for the dorsal pathway, temporal, and inferior parietal regions for the ventral pathway) to frontal regions where both pathways terminate (Reed et al., 2005). Our study using both exploratory and model-driven methods of fMRI analysis revealed results which fit into this framework and extends it to the chemical senses. Taken together, these data suggests that, as for our sensory modalities, the neural processing of intranasal chemosensory stimuli appears to follow a dual pathway model.

ACKNOWLEDGMENTS

This work was supported by a pilote grant of the Bioimaging Network Québec (RBIQ-QBIN 8436) to Johannes Frasnelli and Franco Lepore, and by a grant from the Deutsche Forschungsgemeinschaft to Thomas Hummel (DFG HU 441/10-1). Johannes Frasnelli holds a postdoctoral fellowship by the Canadian Institutes of Health Research.

REFERENCES

Aguirre, G. K., Zarahn, E., and D'esposito, M. (1998). The variability of human, BOLD hemodynamic responses. *Neuroimage* 8, 360–369.

Albrecht, J., Kopietz, R., Frasnelli, J., Wiesmann, M., Hummel, T., and Lundstrom, J. N. (2010). The neuronal correlates of intranasal trigeminal function – an ALE meta-analysis of human functional brain imaging data. *Brain Res. Rev.* 62, 183–196.

Anderson, A. K., Christoff, K., Stappen, I., Panitz, D., Ghahremani, D. G., Glover, G., et al. (2003). Dissociated neural representations of intensity and valence in human olfaction. *Nat. Neurosci.* 6, 196–202.

Auvray, M., and Spence, C. (2008). The multisensory perception of flavor. *Conscious. Cogn.* 17, 1016–1031.

Beckmann, C. F., and Smith, S. M. (2004). Probabilistic independent component analysis for functional magnetic resonance imaging. *IEEE Trans. Med. Imaging* 23, 137–152.

Beckmann, C. F., and Smith, S. M. (2005). Tensorial extensions of independent component analysis for multisubject FMRI analysis. *Neuroimage* 25, 294–311.

Belger, A., Puce, A., Krystal, J. H., Gore, J. C., Goldman-Rakic, P., and McCarthy, G. (1998). Dissociation of mnemonic and perceptual processes during spatial and nonspatial working memory using fMRI. *Hum. Brain Mapp.* 6, 14–32.

Birn, R. M., Bandettini, P. A., Cox, R. W., and Shaker, R. (1999). Event-related fMRI of tasks involving brief motion. *Hum. Brain Mapp.* 7, 106–114.

Boyle, J. A., Frasnelli, J., Gerber, J., Heinke, M., and Hummel, T. (2007). Cross-modal integration of intranasal stimuli: a functional magnetic resonance imaging study. *Neuroscience* 149, 223–231.

Calhoun, V. D., Adali, T., Pearlson, G. D., and Pekar, J. J. (2001). A method for making group inferences from functional MRI data using independent component analysis. *Hum. Brain Mapp.* 14, 140–151.

Calhoun, V. D., Liu, J., and Adali, T. (2009). A review of group ICA

for fMRI data and ICA for joint inference of imaging, genetic, and ERP data. *Neuroimage* 45, S163–S172.

Calvert, G. A., Hansen, P. C., Iversen, S. D., and Brammer, M. J. (2001). Detection of audio-visual integration sites in humans by application of electrophysiological criteria to the BOLD effect. *Neuroimage* 14, 427–438.

Cunnington, R., Windischberger, C., Deecke, L., and Moser, E. (2003). The preparation and readiness for voluntary movement: a high-field event-related fMRI study of the Bereitschafts-BOLD response. *Neuroimage* 20, 404–412.

Doty, R. L., Brugger, W. P. E., Jurs, P. C., Orndorff, M. A., Snyder, P. J., and Lowry, L. D. (1978). Intranasal trigeminal stimulation from odorous volatiles: psychometric responses from anosmic and normal humans. *Physiol. Behav.* 20, 175–185.

Doty, R. L., Shaman, P., and Dann, M. (1984). Development of the University of Pennsylvania Smell Identification Test: a standardized microencapsulated test of olfactory function. *Physiol. Behav.* 32, 489–502.

Filippini, N., Macintosh, B. J., Hough, M. G., Goodwin, G. M., Frisoni, G. B., Smith, S. M., et al. (2009). Distinct patterns of brain activity in young carriers of the APOE-epsilon4 allele. *Proc. Natl. Acad. Sci. U.S.A.* 106, 7209–7214.

Frasnelli, J., Charbonneau, G., Collignon, O., and Lepore, F. (2009). Odor localization and sniffing. *Chem. Senses* 34, 139–144.

Frasnelli, J., Hummel, T., Berg, J., Huang, G., and Doty, R. L. (2011). Intranasal localizability of odorants: influence of stimulus volume. *Chem. Senses* 36, 405–410.

Frasnelli, J., La Buissonnière Ariza, V., Collignon, O., and Lepore, F. (2010). Localisation of unilateral nasal stimuli across sensory systems. *Neurosci. Lett.* 478, 102–106.

Frasnelli, J., Ungermann, M., and Hummel, T. (2008). Ortho- and retronasal presentation of olfactory stimuli modulates odor percepts. *Chemosens. Percept.* 1, 9–15.

Gottfried, J. A., Winston, J. S., and Dolan, R. J. (2006). Dissociable codes of odor quality and odorant structure in human piriform cortex. *Neuron* 49, 467–479.

Grill-Spector, K., and Malach, R. (2004). The human visual cortex. *Annu. Rev. Neurosci.* 27, 649–677.

Hajnal, J. V., Myers, R., Oatridge, A., Schwieso, J. E., Young, I. R., and Bydder, G. M. (1994). Artifacts due to stimulus correlated motion in functional imaging of the brain. *Magn. Reson. Med.* 31, 283–291.

Handwerker, D. A., Ollinger, J. M., and D'esposito, M. (2004). Variation of BOLD hemodynamic responses across subjects and brain regions and their effects on statistical analyses. *Neuroimage* 21, 1639–1651.

Haxby, J. V., Grady, C. L., Horwitz, B., Ungerleider, L. G., Mishkin, M., Carson, R. E., et al. (1991). Dissociation of object and spatial visual processing pathways in human extrastriate cortex. *Proc. Natl. Acad. Sci. U.S.A.* 88, 1621–1625.

Hummel, T., Futschik, T., Frasnelli, J., and Huttenbrink, K. B. (2003). Effects of olfactory function, age, and gender on trigeminally mediated sensations: a study based on the lateralization of chemosensory stimuli. *Toxicol. Lett.* 140–141, 273–280.

Hummel, T., Konnerth, C. G., Rosenheim, K., and Kobal, G. (2001). Screening of olfactory function with a four-minute odor identification test: reliability, normative data, and investigations in patients with olfactory loss. *Ann. Otol. Rhinol. Laryngol.* 110, 976–981.

Husain, M., and Nachev, P. (2007). Space and the parietal cortex. *Trends Cogn. Sci.* 11, 30–36.

Igloi, K., Doeller, C. F., Berthoz, A., Rondi-Reig, L., and Burgess, N. (2010). Lateralized human hippocampal activity predicts navigation based on sequence or place memory. *Proc. Natl. Acad. Sci. U.S.A.* 107, 14466–14471.

Johnstone, T., Walsh, K. S. O., Greischar, L. L., Alexander, A. L., Fox, A. S., Davidson, R. J., et al. (2006). Motion correction and the use of motion covariates in multiple-subject fMRI analysis. *Hum. Brain Mapp.* 27, 779–788.

Kleemann, A. M., Albrecht, J., Schopf, V., Haegler, K., Kopietz, R., Hempel, J. M., et al. (2009). Trigeminal perception is necessary to localize odors. *Physiol. Behav.* 97, 401–405.

Kobal, G. (1981). *Elektrophysiologische Untersuchungen des menschlichen Geruchssinns.* Stuttgart: Thieme Verlag.

Kobal, G., Klimek, L., Wolfensberger, M., Gudziol, H., Temmel, A., Owen, C. M., et al. (2000). Multicenter investigation of 1, 036 subjects using a standardized method for the assessment of olfactory function combining tests of odor identification, odor discrimination, and olfactory thresholds. *Eur. Arch. Otorhinolaryngol.* 257, 205–211.

Kobal, G., Van Toller, S., and Hummel, T. (1989). Is there directional smelling? *Experientia* 45, 130–132.

Laska, M., Distel, H., and Hudson, R. (1997). Trigeminal perception of odorant quality in congenitally anosmic subjects. *Chem. Senses* 22, 447–456.

Lombion, S., Comte, A., Tatu, L., Brand, G., Moulin, T., and Millot, J. L. (2009). Patterns of Cerebral activation during olfactory and trigeminal stimulations. *Hum. Brain Mapp.* 30, 821–828.

Maeder, P. P., Meuli, R. A., Adriani, M., Bellmann, A., Fornari, E., Thiran, J. P., et al. (2001). Distinct pathways involved in sound recognition and localization: a human fMRI study. *Neuroimage* 14, 802–816.

McKeown, M. J., Makeig, S., Brown, G. G., Jung, T. P., Kindermann, S. S., Bell, A. J., et al. (1998). Analysis of fMRI data by blind separation into independent spatial components. *Hum. Brain Mapp.* 6, 160–188.

Menz, M. M., Neumann, J., Muller, K., and Zysset, S. (2006). Variability of the BOLD response over time: an examination of within-session differences. *Neuroimage* 32, 1185–1194.

Mishkin, M., Ungerleider, L. G., and Macko, K. A. (1983). Object vision and spatial vision – 2 cortical pathways. *Trends Neurosci.* 6, 414–417.

Neumann, J., Lohmann, G., Zysset, S., and Von Cramon, D. Y. (2003). Within-subject variability of BOLD response dynamics. *Neuroimage* 19, 784–796.

Porter, J., Anand, T., Johnson, B., Khan, R. M., and Sobel, N. (2005). Brain mechanisms for extracting spatial information from smell. *Neuron* 47, 581–592.

Rauschecker, J. P., and Tian, B. (2000). Mechanisms and streams for processing of "what" and "where" in auditory cortex. *Proc. Natl. Acad. Sci. U.S.A.* 97, 11800–11806.

Reed, C. L., Klatzky, R. L., and Halgren, E. (2005). What vs. where in touch: an fMRI study. *Neuroimage* 25, 718–726.

Renier, L. A., Anurova, I., De Volder, A. G., Carlson, S., Vanmeter, J., and Rauschecker, J. P. (2009). Multisensory integration of sounds and vibrotactile stimuli in processing streams for "what" and "where". *J. Neurosci.* 29, 10950–10960.

Ricciardi, E., Bonino, D., Gentili, C., Sani, L., Pietrini, P., and Vecchi, T. (2006). Neural correlates of spatial working memory in humans: a functional magnetic resonance imaging study comparing visual and tactile processes. *Neuroscience* 139, 339–349.

Rissanen, J. (1978). Modelling by shortest data description. *Automatica* 14, 465–471.

Savic, I., Gulyas, B., Larsson, M., and Roland, P. (2000). Olfactory functions are mediated by parallel and hierarchical processing. *Neuron* 26, 735–745.

Schendan, H. E., Searl, M. M., Melrose, R. J., and Stern, C. E. (2003). An fMRI study of the role of the medial temporal lobe in implicit and explicit sequence learning. *Neuron* 37, 1013–1025.

Schneider, R. A., and Schmidt, C. E. (1967). Dependency of olfactory localization on non-olfactory cues. *Physiol. Behav.* 2, 305–309.

Schonwiesner, M., Von Cramon, D. Y., and Rubsamen, R. (2002). Is it tonotopy after all? *Neuroimage* 17, 1144–1161.

Schopf, V., Windischberger, C., Kasess, C. H., Lanzenberger, R., and Moser, E. (2010). Group ICA of resting-state data: a comparison. *MAGMA* 23, 317–325.

Schopf, V., Windischberger, C., Robinson, S., Kasess, C. H., Fischmeister, F. P., Lanzenberger, R., et al. (2011). Model-free fMRI group analysis using FENICA. *Neuroimage* 55, 185–193.

Smith, E. E., and Jonides, J. (1997). Working memory: a view from neuroimaging. *Cognit. Psychol.* 33, 5–42.

Toepper, M., Markowitsch, H. J., Gebhardt, H., Beblo, T., Thomas, C., Gallhofer, B., et al. (2010). Hippocampal involvement in working memory encoding of changing locations: an fMRI study. *Brain Res.* 1354, 91–99.

von Békésy, G. (1964). Olfactory analogue to directional hearing. *J. Appl. Physiol.* 19, 369–373.

von Skramlik, E. (1924). Über die Lokalisation der Empfindungen bei den niederen Sinnen. *Z. Sinnesphysiol.* 56, 69.

Winston, J. S., Gottfried, J. A., Kilner, J. M., and Dolan, R. J. (2005).

Integrated neural representations of odor intensity and affective valence in human amygdala. *J. Neurosci.* 25, 8903–8907.

Wise, P. M., Wysocki, C. J., and Lundstrom, J. N. (2012). Stimulus selection for intranasal sensory isolation: eugenol is an irritant. *Chem. Senses* 37, 509–514.

Wysocki, C. J., Cowart, B. J., and Radil, T. (2003). Nasal trigeminal chemosensitivity across the adult life span. *Percept. Psychophys.* 65, 115–122.

Zatorre, R. J., Jones-Gotman, M., Evans, A. C., and Meyer, E. (1992). Functional localization and lateralization of human olfactory cortex. *Nature* 360, 339–340.

Conflict of Interest Statement: The authors declare that the research was conducted in the absence of any commercial or financial relationships that could be construed as a potential conflict of interest.

Received: 28 August 2012; accepted: 01 October 2012; published online: 19 October 2012.

Citation: Frasnelli J, Lundström JN, Schöpf V, Negoias S, Hummel T and Lepore F (2012) Dual processing streams in chemosensory perception. Front. Hum. Neurosci. ***6****:288. doi: 10.3389/fnhum.2012.00288*

frontiers in
HUMAN NEUROSCIENCE

ORIGINAL RESEARCH ARTICLE
published: 16 May 2013
doi: 10.3389/fnhum.2013.00207

BOLD frequency power indexes working memory performance

Joshua Henk Balsters[1,2]*, Ian H. Robertson[1] and Vince D. Calhoun[3,4]

[1] *Trinity College Institute of Neuroscience, School of Psychology, Trinity College Dublin, Dublin, Ireland*
[2] *Neural Control of Movement Lab, Department of Health Sciences and Technology, ETH Zurich, Zurich, Switzerland*
[3] *The Mind Research Network, Albuquerque, NM, USA*
[4] *Department of Electrical and Computer Engineering, University of New Mexico, Albuquerque, NM, USA*

Edited by:
Veronika Schöpf, Medical University of Vienna, Austria

Reviewed by:
Handwerker A. Daniel, National Institutes of Health, USA
Roser Sala-Llonch, University of Barcelona, Spain

****Correspondence:***
Joshua Henk Balsters, Neural Control of Movement Lab, Y36 M 12, Winterthurerstrasse 190, 8057 Zürich, Switzerland.
e-mail: joshua.balsters@hest.ethz.ch

Electrophysiology studies routinely investigate the relationship between neural oscillations and task performance. However, the sluggish nature of the BOLD response means that few researchers have investigated the spectral properties of the BOLD signal in a similar manner. For the first time we have applied group ICA to fMRI data collected during a standard working memory task (delayed match-to-sample) and using a multivariate analysis, we investigate the relationship between working memory performance (accuracy and reaction time) and BOLD spectral power within functional networks. Our results indicate that BOLD spectral power within specific networks (visual, temporal-parietal, posterior default-mode network, salience network, basal ganglia) correlated with task accuracy. Multivariate analyses show that the relationship between task accuracy and BOLD spectral power is stronger than the relationship between BOLD spectral power and other variables (age, gender, head movement, and neuropsychological measures). A traditional General Linear Model (GLM) analysis found no significant group differences, or regions that covaried in signal intensity with task accuracy, suggesting that BOLD spectral power holds unique information that is lost in a standard GLM approach. We suggest that the combination of ICA and BOLD spectral power is a useful novel index of cognitive performance that may be more sensitive to brain-behavior relationships than traditional approaches.

Keywords: BOLD oscillations, ICA, fMRI, delayed match-to-sample, aging

INTRODUCTION

Studies of neural oscillations are pervasive in neuroscience, from single and multi-unit recordings through to non-invasive whole brain methods such as electroencephalography (EEG) and magnetoencephalography (MEG). Studies using these methods have repeatedly demonstrated that the synchronization of neural oscillations within specific frequency bands impact on cognitive and motor processes (Klimesch, 1999; Buzsaki and Draguhn, 2004). For example, a number of studies have highlighted the role of midfrontal theta in cognitive control (Cavanagh et al., 2009; Cohen and Cavanagh, 2011), whilst posterior alpha power has been linked to sustained and spatial attention (Thut et al., 2006; Dockree et al., 2007; O'Connell et al., 2009). Nearly 20 years ago Jezzard et al. (1993) and Biswal et al. (1995) demonstrated regional BOLD differences in low frequency oscillatory fluctuations (0.01–0.1 Hz). Since then a large number of studies have demonstrated that this $<$0.1 Hz BOLD signal relates to underlying neural processes (He et al., 2010; He, 2011; Honey et al., 2012) and can be used to detect differences in resting connectivity between clinical populations (Greicius et al., 2004; Jafri et al., 2008; Zhang and Raichle, 2010), as well as task-related changes in functional networks (Grady et al., 2010; Zhang and Li, 2012). However, these aforementioned studies have used spectral information as a filtering tool, typically removing signal $>$0.1 Hz in order to remove potential artifacts, rather than analyzing the relationship between BOLD oscillations and task performance as one might in an EEG or MEG study. To our knowledge no previous studies have investigated whether a direct correlation exists between task performance (i.e., accuracy) and BOLD spectral power at different frequencies.

To date it is mostly resting state studies that have investigated BOLD oscillations. Studies investigating BOLD oscillations at rest have demonstrated that multiple frequency bands within the 0.004–0.15 Hz range contribute to the RSN signal (Niazy et al., 2011). Niazy et al. (2011) also showed that phase synchrony differs within this spectral range, suggesting that RSNs likely contain multiple oscillatory components. Studies by Baria et al. (2011) and Zuo et al. (2010) have additionally shown that BOLD signals originating from different cytoarchitectonic and anatomical regions resonate at distinct frequency ranges. Baria et al. (2011) is one of the few studies to also investigate BOLD oscillations during task performance (visual-motor task). They found a global decrease in lower BOLD frequency oscillations (0.01–0.05 Hz) during task compared to rest along with a global increase in higher frequency BOLD oscillations (0.05–0.1 Hz). Compared to a standard general linear model (GLM) analysis there was less than 30% spatial overlap in regions showing task-related differences in BOLD oscillations, suggesting that BOLD spectral changes are not detected by standard fMRI analyses. Salvador et al. (2008) investigated connectivity within the frequency domain [differing from Baria et al. (2011) who investigated regional changes in BOLD

spectral power] and found increased low frequency connectivity (<0.08 Hz) between prefrontal, parietal, and thalamic regions during performance of an N-back task compared to rest. There was also decreased high frequency connectivity (0.08–0.25 Hz) during the N-back task within the anterior cingulate/paracingulate gyri and insula. Whilst both Salvador et al. (2008) and Baria et al. (2011) have shown that BOLD oscillations differ in task compared to rest conditions neither of these studies investigated the extent to which task performance was correlated with BOLD spectral activity.

Apart from Baria et al. (2011) and Salvador et al. (2008) no other studies to date have investigated the relationship between BOLD spectral power and task performance. However, a handful of fMRI studies have begun to investigate temporal variability within the BOLD signal and its relationship to task performance. In a series of studies by Garrett et al. (2010, 2011, 2013) they used a partial least squares approach to extract functional networks and subsequently analyzed the variability (standard deviation) within these circuits and their relationship to age and task performance. Garrett et al. (2010) showed that BOLD variability was a robust marker of chronological age, explaining more age-related variance than mean BOLD signal. BOLD variability was also an important indicator of task performance. Garrett et al. (2011) showed that young participants increased BOLD variability during task performance and decreased variability during fixation. However, elderly participants failed to modulate BOLD variability between task and fixation conditions, showing reduced variability during task and increased variability during fixation. Samanez-Larkin et al. (2010) used a similar analytical approach and demonstrated increased BOLD variability in elderly participants within the nucleus accumbens (NAcc), which was associated with increased financial risk taking. As with the work of Garrett et al. (2010, 2011, 2013), Samanez-Larkin et al. (2010) found that these results were specific to BOLD variability measures and that the average NAcc signal did not predict risk seeking behavior. It is clear from both of these studies that BOLD variability might be a more sensitive measure of functional changes with age than average BOLD signal. It is likely that these changes in BOLD variability have an oscillatory underpinning and could be better explained by investigating the BOLD spectrum.

The previously mentioned studies show that spectral properties of the BOLD signal are anatomically and functionally informative, although this approach has typically only been applied to resting state fMRI. Studies investigating BOLD variability during task performance suggest that this measure holds unique task dependent information that is lost in a standard GLM analysis. Using tools available in the GIFT toolbox, we aim to bridge the gap between studies of BOLD oscillations at rest and studies of BOLD variability during task by investigating the relationship between BOLD spectral power and task performance (delayed match-to-sample task) in young and older participants.

MATERIALS AND METHODS

PARTICIPANTS

Sixteen young (22.08 ± 3.31) and nineteen elderly (70.2 ± 3.96) neurologically normal, right-handed subjects participated in this study. The two participant groups were matched for gender, handedness, hospital anxiety and depression scale (HADS) score, and Mini Mental State Exam (MMSE) score. Participants gave written informed consent prior to the study that was approved by the Trinity College Dublin School of Psychology Ethics Committee.

PROCEDURE

Trial structure

Figure 1 illustrates the trial structure. Throughout the experiment participants were asked to fixate on a white cross hair presented in the center of a black screen. The same basic trial structure was applied in all conditions, with condition-specific variations (see "Conditions" below). After a variable inter-trial interval (1782–6881 ms) a sample cue was presented in the center of the screen for 750 ms. This was replaced by the crosshair for a variable period between 4299 and 9630 ms. A probe cue was then presented left or right of the cross hair for 1500 ms. At this point the participant made a judgment about the stimuli by pressing the left or right button on the keypad placed in their right hand. No feedback was given to the participant about their response. In all trials the probe stimulus was presented at a different angle/orientation to the sample stimulus so they were not perceptually identical. This forced participants to encode stimulus identity and not just perceptual features of the stimulus.

Conditions

Four trial types were embedded in a 2×2 factorial design (two factors each with two levels).

Factor 1: task (match, respond). Participants performed four blocks where they had to make a judgment about whether the sample and probe matched (Match) and four blocks where they had to make a judgment about the position of the probe (Respond). These blocks were pseudo-randomly intermixed. At the beginning of each block a cue was presented for 750 ms saying "MATCH" or "RESPOND." This informed the subject which task they had to perform for the block. In blocks of Respond trials participants responded by pressing the left button if the probe cue was on the left of the screen, or the right button if the probe cue was on the right side of the screen. During Respond trials participants did not need to encode or attend to the sample cue, as it held no information that could guide the subsequent response. During blocks of Match trials participants had to respond at the time of the probe by pressing the left button if the probe stimulus matched the sample stimulus or the right button if they did not match. Each block lasted 4.14 min.

Factor 2: stimulus type (line, face). During both Respond and Match blocks the stimulus type was pseudo-randomly intermixed and could be either a gray line or a greyscale face. The faces were obtained from the Max Planck Institute for Biological Cybernetics database (Blanz and Vetter, 1999). For Line stimuli the participant was first presented with a horizontal line as a sample. At the time of the probe the participant was presented with a vertical line that was either the same or a different length. For Face stimuli, the participant was presented with a frontward facing face as a sample. At the time of the probe the face stimuli was presented at a 30° orientation facing either leftward or rightward (the presentation of leftward facing and rightward facing faces on the left or

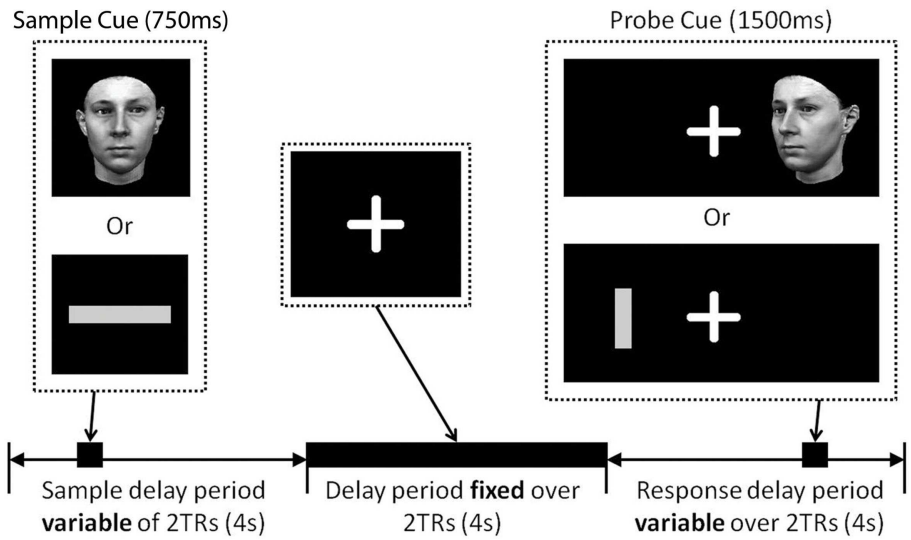

FIGURE 1 | Delay match-to-sample trial structure. A fixation cross was presented in the center of the screen for the duration of the study. Sample cues (either a face or a line) were presented in the center of the screen during the first 2TRs of a trial (stimulus onset jittered 0–3250 ms from the onset of the first TR), after a variable time delay (4299–9630 ms), a probe cue was presented left or right of the fixation cross (stimulus onset jittered 0–2500 ms from the onset of the fifth TR). Participants responded as quickly possible at the presentation of the probe cue making either a left/right judgment or a match/non-match judgment. Face and line probe cues were presented in a different orientation to the sample cue.

right of the screen was counterbalanced). This approach forced participants to encode stimulus identity and not just perceptual features of the stimulus.

The combination of these two factors with two levels each resulted in four conditions:

1. Line Respond: is the probe Line on the left or right of the screen? (40 trials)
2. Face Respond: is the probe Face on the left or right of the screen? (40 trials)
3. Line Match: is the length of the probe Line the same as the length of the sample Line? (40 trials)
4. Face Match: is the probe Face the same as the sample Face? (40 trials)

Participants practiced four to six shorter blocks of the task before entering the MRI scanner to make sure they understood the task. This typically lasted ∼7 min.

BEHAVIORAL ANALYSES

Behavioral measures were analyzed using a two way repeated measures ANOVA. Two factors of Task (Match, Respond) and Stimulus (Face, Line) were included with an additional between subject's factor of group (young, old). This was used to assess differences in error rate, reaction time (RT), and RT variability. RT variability (intra-individual coefficient of variation) was calculated by dividing the RT standard deviation of each individual by their mean RT (Stuss et al., 2003; Bellgrove et al., 2004).

APPARATUS

Subjects lay supine in an MRI scanner with the thumb of the right hand positioned on a two-button MRI-compatible response box. Stimuli were projected onto a screen behind the subject and viewed in a mirror positioned above the subjects face. Presentation software (Neurobehavioral Systems, Inc., USA) was used for stimulus presentation both inside and outside the scanner. TTL pulses were also used to drive the visual stimuli in Presentation. Event timings and RTs were calculated off-line using event timings acquired by a separate laptop running Brain Recorder (Brain Products, Munich, Germany) at a higher sampling frequency (5000 Hz).

fMRI DATA ACQUISITION

We first acquired a high-resolution T1-weighted anatomical MPRAGE image (FOV = 230 mm, thickness = 0.9 mm, voxel size = 0.9 mm × 0.9 mm × 0.9 mm), followed by phase and magnitude images at different echo times ($TE_1 = 1.46$ ms, $TE_2 = 7$ ms), which were used to generate a voxel displacement map. Each participant then performed a single EPI session containing 1024 volumes lasting ∼34 min. The field of view covered the whole brain, 224 mm × 224 mm (64 × 64 voxels), 34 axial slices were acquired (0.05 mm slice gap) with a voxel size of 3.5 mm × 3.5 mm × 4 mm; TR = 2 s, TE = 32, flip angle = 78°. This was a sparse-sampling sequence with the slices compressed to the first 1700 ms of the TR, leaving 300 ms without gradient switching to facilitate the simultaneously recorded EEG (Debener et al., 2005). The combined EEG/fMRI data will be presented in a separate manuscript. All MRI data was collected on a Philips 3T Achieva MRI Scanner (Trinity College Dublin).

fMRI PRE-PROCESSING

Scans were pre-processed using SPM8[1]. Images were realigned and unwarped using field maps to correct for motion artifacts,

[1]www.fil.ion.ucl.ac.uk/spm

susceptibility artifacts and motion-by-susceptibility interactions (Andersson et al., 2001; Hutton et al., 2002). Images were subsequently normalized to the ICBM EPI template using the unified segmentation approach (Ashburner and Friston, 2005). Lastly, a Gaussian kernel with a full-width at half-maximum (FWHM) of 8 mm was applied to spatially smooth the image.

fMRI ANALYSES

Group ICA analysis

A single group spatial ICA was run using the GIFT toolbox[2]. In this approach single-subject datasets were first compressed using principal component analysis (PCA, 123 components), single-subject data were then combined and PCA was performed for a second time on the whole group. Spatial ICA was then performed using the infomax algorithm (Bell and Sejnowski, 1995), with subsequent back reconstruction into single subjects (Calhoun et al., 2001; Erhardt et al., 2011). The resulting output is an independent component map and an associated timecourse for every component and subject. A modified minimum descriptive length (MDL) criteria (Li et al., 2007) determined that the optimal number of independent components was 82 and ICASSO was run with 100 re-runs and random initial conditions to ensure a robust decomposition (Himberg et al., 2004). Components with a quality (iQ; the difference between intra-cluster and extra-cluster similarity) below 0.9 were excluded from further analysis as were components that significantly correlated with regions of white matter or CSF. Head movement components (i.e., ringing around the edge of the brain) were also excluded from further analysis.

The Mancovan toolbox (Allen et al., 2011) was used to determine relationships between IC networks and descriptive variables such as age, gender, and task performance. This approach allowed us to investigate within component effects by analyzing IC spatial maps (SMs), and IC timecourse spectra as well as how descriptive variables modulate connectivity between networks using functional network connectivity (FNC; Jafri et al., 2008). For each component the BOLD spectrum were estimated on the detrended subject-specific timecourses (removing the mean, slope, and period π and 2π sines and cosines over each timecourse) using the multi-taper approach as implemented in Chronux[3], with the time-bandwidth product set to three and the number of tapers set to five (Mitra and Bokil, 2008). These are the default settings within the Mancovan toolbox.

Two mancovan models were run which both included age, gender, neuropsychological measures (NART, Logical memory subtest of the WMS, MMSE), and head movement (rotation and translation). Task performance (accuracy and RT) was also included in these models, but RT values for line match and face match performance were highly correlated ($r = 0.96$, $p = 2e{-}19$). In order to improve model estimation we ran two separate models; (1) face match performance orthogonalized with respect to line match performance (FM_r), and (2) line match performance orthogonalized with respect to face match (LM_r). Two linear regressions were used to calculate these residual values. As such one model included the aforementioned variables along with face match accuracy (FM_acc), face match RT (FM_RT), residual line match accuracy (LM_r_acc) and residual line match reaction time (LM_r_RT), and a second model was run with residual face match accuracy (FM_r_acc), residual face match RT (FM_r_RT), line match accuracy (LM_acc) and line match reaction time (LM_RT).

Multivariate analyses were first performed in order to assess the extent to which each of the independent variables explained variance in the data (**Figure 3**). At this stage redundant variables that do not explain significant variance in the data ($p > 0.05$) are removed from the model. This procedure determines how well the independent variables explain variance within the dependent variables once other independent variables are taken into account. For example, **Figure 3** shows that for component 58 BOLD spectral power is significantly modulated by FM accuracy, FM RT, gender, and rotation ($p < 0.05$, uncorrected). Importantly, we can see that rotation is the strongest predictor variable, explaining more variance in the BOLD spectrum then any other variables. Components will only be described as showing a significant relationship with task accuracy if they show the strongest relationship with BOLD spectral power based on these multivariate analyses.

In order to determine which spectral bins were associated with task performance we additionally performed univariate analyses. Partial correlation was used to measure the strength of the linear relationship between two variables [e.g., log(power) and face match accuracy] after adjusting for all other independent variables. Univariate tests were corrected for multiple comparisons at $p < 0.05$ using false discovery rate (FDR; Genovese et al., 2002).

Standard GLM analyses

Along with the ICA analyses we also conducted two standard GLM analyses implemented in SPM8 (Friston et al., 1995a,b). The first modeled events using the canonical hemodynamic response function (hrf), the second modeled events using Fourier basis functions (2 sine and 2 cosine functions of different frequencies with a 15-s Hanning window; Balsters and Ramnani, 2008). All first level models included nine event types. Sample and probe cues for each of the four conditions were modeled as eight separate event types. Trials in which responses were incorrect, too early (before the probe cue) or too late (responded after the presentation of the next sample cue) were modeled separately as a ninth event-type and differentiated from experimental conditions. This ninth event type included the onsets from both the sample and probe cues in error trials. Thus, activity time-locked to incorrect trials was excluded from regressors explaining instruction related activity. The residual effects of head motion were modeled as covariates of no interest in the analysis by including the six head motion parameters estimated during the realignment stage of the pre-processing. Prior to the study, a set of planned experimental timings were generated from two volunteers who performed the task outside of the scanner. These timings were carefully checked so that they resulted in an estimable GLM in which the statistical independence of the nine event types was preserved (piloting on volunteers allowed to generate a realistic error trial regressor).

To determine voxels significant at the group level, *t*-contrasts were incorporated into a random effects analysis using either one or two sample *t*-tests for the analyses using the canonical hrf or two way ANOVAs for analyses using the Fourier basis functions.

[2]http://mialab.mrn.org/software/gift
[3]http://chronux.org

ANOVAs had two factors; Group (two independent levels) and Basis functions (five non-independent levels). In all cases contrast images describing the main effect of stimulus (face vs. line), main effect of task (match vs. respond), and stimulus × task interactions at the single-subject level were calculated for both sample and probe cues. For analyses using the canonical HRF this was one contrast image per subject whereas analyses using the Fourier basis set used five contrast images per subject (one for each basis function).

Significant within group differences were established using a conjunction analysis (Price and Friston, 1997; Friston et al., 2005). This analysis confirms what is statistically similar across groups. Significant group differences were run on the same model. Beta values for the face match condition were also input into a one-sample *t*-test in order to see if beta values correlated with task accuracy in a similar manner to the ICA analyses. All results were corrected for multiple comparisons (FWE, $p < 0.05$).

RESULTS

BEHAVIOR

Error rates

For both young and old groups there was a significant main effect of task [$F(1, 28) = 170.99$, $p < 0.001$] as significantly more errors were made in the matching task (7.46 error trials ± 0.53) compared to the respond task (0.58 error trials ± 0.12). Both groups also made significantly more errors for faces (4.88 error trials ± 0.28) compared to lines [3.41 error trials ± 0.35; $F(1, 28) = 28.85$, $p < 0.001$]. There was also a significant stimulus by task interaction [$F(1, 28) = 34.42$, $p < 0.001$] as significantly more errors in face match condition than any other condition.

A number of group differences were also present. Although the main effect of group [$F(1, 28) = 3.77$, $p = 0.06$] did not reach significance, there were clear selective deficits in the performance of old participants compared to young. This was seen in the significant group × stimulus interaction [significantly more errors to faces than lines in the old participants; $F(1, 28) = 16.84$, $p < 0.001$], and a significant group × task × stimulus interaction [$F(1, 28) = 21.05$, $p < 0.001$], as elderly participants made significantly more errors in the face matching condition compared to any other condition [$T(1, 28) = 4.19$, $p < 0.001$]. This suggests that key difference in performance between the young and old participants was in the face match condition (see **Figure 2A**).

Reaction time

As with error rate, all participants showed a significant main effect of task on RT (slower RTs during match (1236.99 ± 43.33 ms) compared to respond conditions [718.2 ± 24.54 ms; $F(1, 28) = 159.85$, $p < 0.001$]. There was also a significant main effect of stimulus type [slower to respond to faces (1044.08 ± 30.92 ms) compared to lines (911.11 ± 26.99 ms); $F(1, 28) = 189.73$, $p < 0.001$], and a significant stimulus × task interaction [significantly slower on face matching compared to all other conditions; $F(1, 28) = 142.92$, $p < 0.001$].

Older participants showed significantly slower RTs compared to young participants (Old (1148.25 ± 41.8 ms); Young (806.93 ± 39.1 ms); significant main effect of group [$F(1, 28) = 35.564$, $p < 0.001$]). There were also significant group × stimulus interactions [$F(1, 28) = 22.14$, $p < 0.001$; old participants were significantly slower than young participants to respond to faces compared to lines] and significant group × task interactions [$F(1, 28) = 12.86$, $p < 0.005$; Older participants were significantly slower than young participants to match compared to respond]. Finally there was also a significant group × task × stimulus interaction illustrating the significant difference in face matching in young compared to old [$F(1, 28) = 34.56.2$, $p < 0.001$]. These results are illustrated in **Figure 2B**.

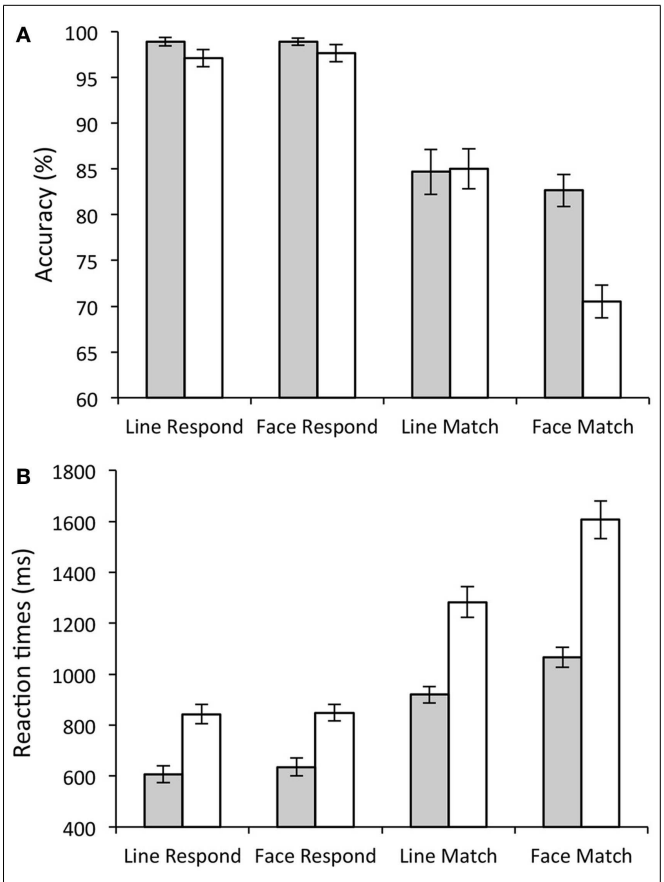

FIGURE 2 | Behavioral Results. Bar graphs showing task accuracy **(A)** and response times. **(B)** Gray bars show average scores for young participants; white bars show average scores for elderly participants. Error bars show the standard error.

Whilst there were no significant group effects on RT variability there was a significant main effect of stimulus type [$F(1, 28) = 8.49$, $p < 0.01$] on RT variability (greater variability for line stimuli compared to faces) and a significant task × stimulus interaction [$F(1, 28) = 4.3$, $p < 0.05$; greater variability in the line match condition compared to all other conditions].

fMRI ANALYSES

Group ICA analyses

Out of 82 ICs, 54 were included in the mancovan models. **Figure 3** shows the strength of the relationship between spectral power for each IC and each of the variables of interest and nuisance variables.

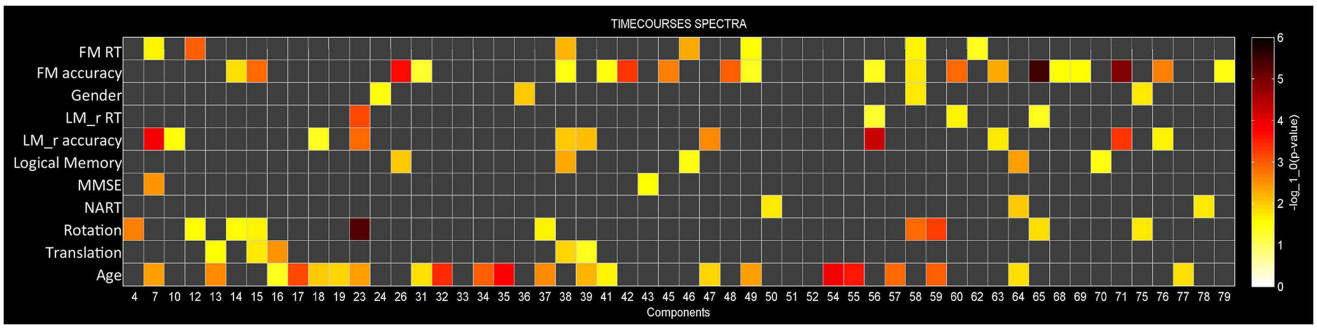

FIGURE 3 | Multivariate statistics. Results from the reduced mancova models, depicting the significance of covariates of interest and nuisance predictors for power spectra in $\log_{10}(p)$ units. Gray cells indicate terms that were removed from the full model during backward selection process.

ICs were ignored if they showed a stronger relationship with head movement than task performance.

Task performance. We first examined the relationship between IC features and accuracy. SMs and FNC showed no significant relationship to task accuracy, but for a number of ICs BOLD spectral power was significantly correlated with task performance (see **Figure 4**). In all cases there was a positive relationship between 0 and 0.1 Hz BOLD spectral power and task performance (greater spectral power = better performance) and a negative relationship between 0.1 and 0.25 Hz power and accuracy (greater spectral power = poorer performance). Spectral power within the anterior cingulate cortex (ACC) (area 24; IC 71) correlated to both LM and FM accuracy. Spectral power within the caudate nuclei (IC 47) was specific to LM accuracy. Spectral power within six networks related to FM accuracy including putamen (IC 14), visual (IC 15), right superior STG (IC 26), precuneus (posterior DMN; IC 48), insular (IC 63), and the salience network (SN) (ACC and bilateral anterior insular; IC 65) (see **Table 1** for details). All of these results were significant in the analysis of the residual values (FM_r_acc and LM_r_acc) as well as analysis of the original values. **Table 2** shows the results of linear multiple regression using single-subject IC timecourses as the dependent variable and the GLMs used for the hrf analysis as independent variables (see Standard GLM Analyses above for details). A one-sample t-test was performed on beta values to establish if there was a significant relationship between event timecourses and IC timecourses ($p < 0.05$, uncorrected). Two sample t-tests were also run on these same beta values to establish whether the relationship differed between groups ($p < 0.05$, uncorrected).

Figure 5 shows spectral profiles for both young and older participants and the correlations between spectral power and accuracy after variance associated with age had been removed from the data. Even after age-related variance was removed from the data there were still very strong correlations between task accuracy and spectral power below 0.1 Hz (r values between 0.64 and 0.79). However, removing age-related variance from higher frequencies (>0.1 Hz) typically removed the relationship between spectral power and accuracy for most ICs. Only the SN (IC 65) maintained significance at higher frequencies after removing age-related variance. All of the BOLD spectra presented in **Figure 5** show a clear peak at 0.08 Hz (every 12.5 s). This peak reflects the presentation of the stimuli and is not an artifact. Resting state data acquired immediately prior to the collection of this task was run through a similar analysis pipeline and the 0.08-Hz peak was not present (Balsters et al., 2013). **Table 3** shows partial correlation values for BOLD spectral power and task accuracy after age-related variance was regressed out of the data. Partial correlations were run across all subjects as well as young and old subjects only.

We also analyzed the extent to which RT related to IC features (see **Figure 6**). In this case only the original values explained IC features and there were no significant effects of residual values (FM_r_RT or LM_r_RT). Both FM_RT and LM_RT were significantly correlated to SM activity within motor lobules of the cerebellum [left lobule HVI (85%) (Diedrichsen et al., 2009)]. LM RT was correlated with 0.15–0.2 Hz spectral power in the thalamus [IC 12, Visual Thalamus (Behrens et al., 2003)], and FM RT was correlated with 0.15–0.2 Hz spectral power in fusiform gyrus (IC 46) and ACC (area 32; IC 62) (see **Table 1** for details). In all three cases 0.15–0.2 Hz spectral power was positively correlated with RT (greater spectral power = slower RT). The relationship between spectral power and RT was not present after variance associated with age had been removed from the data.

GLM analyses

Faces vs. lines. Within group analyses showed significant activations in predicted regions. For example, a comparison of stimulus type (faces vs. lines) showed greater activity in bilateral fusiform gyrus for faces compared to lines. This was present both at the time of the sample and probe cue. However, there were no significant group differences. The FDR thresholded main effect of faces vs. lines was compared spatially with all the ICs found to correlate with task performance by overlaying these images in MRIcron. There was no spatial overlap between any of these ICs and the main effect of stimulus type. These results were consistent for HRF and Fourier models.

Match vs. respond. Similarly, a comparison of task (match vs. respond) showed greater activation in right middle/inferior frontal gyrus, as well as ACC and bilateral insula for match compared to respond. Overlaying this FDR thresholded activation map with ICs found to correlate with task performance showed a clear spatial

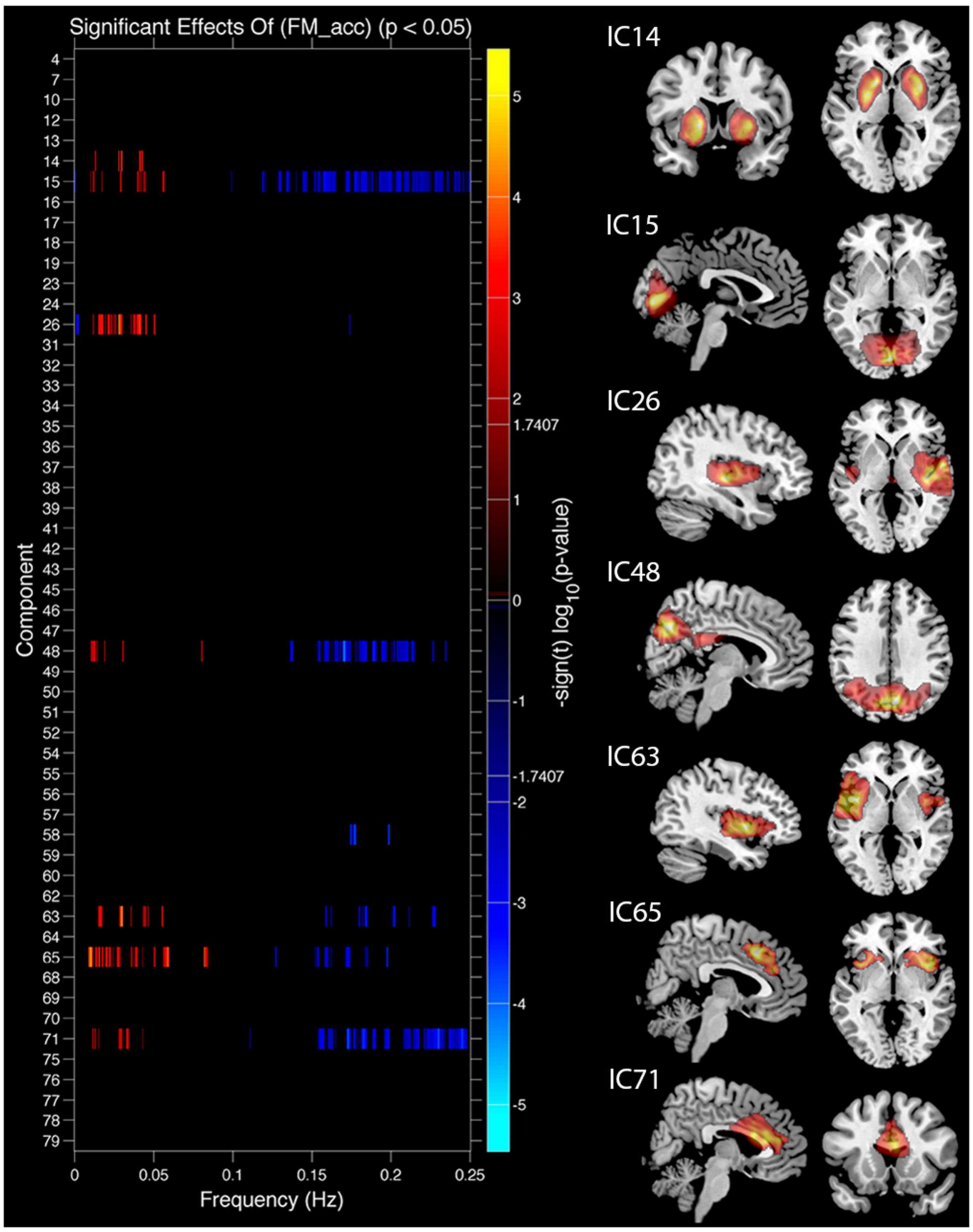

FIGURE 4 | Components showing a relationship between spectral power and face match accuracy. Left column shows components where spectral power significantly covaried with task accuracy. Red markers indicate a positive relationship with task accuracy (greater spectral power with higher accuracy), blue markers indicate a negative relationship (greater spectral power with lower accuracy), black indicates their was no significant difference after correcting for multiple comparisons. Right column shows spatial maps for components which showed a significant relationship with face match accuracy. All results are FDR thresholded ($p < 0.05$).

overlap with the previously identified SN (IC65; see **Figure 7**). There was no spatial overlap with any other of the ICs found to correlate with task performance. Despite significant behavioural differences (group × task interaction) there were no significant group differences for this comparison. These results were consistent for HRF and Fourier models.

Stimulus × task interaction. There were no significant within- or between group activations for the stimulus × task interaction, despite there being very significant behavioral differences. These results were consistent for HRF and Fourier models.

Face match and task performance. In order to more directly compare the ICA and GLM analyses, we performed a one-sample *t*-test looking for correlations between accuracy and beta values associated with Face match condition (both sample and probe). There were no significant correlations.

Table 1 | Peak activations of spatial maps showing a relationship with task performance.

Component # (Iq)	Brain region	Cluster size	*t*	Co-ordinates			Cytoarchitectonic BA (probability if available)
				x	*y*	*z*	
FACE AND LINE MATCH ACCURACY							
71 (0.93)	Left anterior cingulate cortex	3091	26.91	0	32	14	Area 24
FACE MATCH ACCURACY							
14 (0.98)	Left putamen	3277	31.42	−18	8	0	n/a
	Right putamen	3123	29.83	28	4	0	n/a
15 (0.98)	Left calcarine gyrus	6131	46.69	−2	−84	−2	Area 17 (90%)
26 (0.98)	Right insula lobe	4400	27.11	38	−20	0	Insula (Ig2) (90%)
	Left superior temporal gyrus	188	10.77	−46	−12	−2	Insula (Ig2) (10%)
48 (0.97)	Right precuneus	6738	32.23	6	−70	34	SPL (7M) (60%)
	Left angular gyrus	Same cluster	16.14	−38	−60	40	hIP2 (10%), hIP3 (10%)
	Right angular gyrus	Same cluster	10.86	36	−58	42	hIP1 (20%), hIP3 (10%)
63 (0.97)	Left insula lobe	3811	25.19	−40	4	0	Area 48
	Right insula lobe	1083	16.6	42	0	6	Area 48
	Right angular gyrus	319	11.41	52	−56	26	IPC (PGa) (50%)
	Left supramarginal gyrus	224	9.06	−58	−34	28	IPC (PF) (90%)
	Right anterior cingulate cortex	93	7.86	4	16	28	Area 24
65 (0.97)	Right superior medial gyrus	1495	24.05	4	20	42	Area 32
	Right insula lobe	1209	21.1	40	10	−2	Area 48
	Left insula lobe	563	17.9	−36	16	−10	Area 48
LINE MATCH ACCURACY							
47 (0.98)	Right caudate nucleus	3655	29.34	8	18	2	n/a
	Left caudate nucleus	Same cluster	27	−8	16	0	n/a
FACE MATCH RT							
46 (0.98)	Left inferior temporal gyrus	1121	18.89	−48	−62	−6	Area 37
	Right inferior temporal gyrus	862	16.13	46	−60	−14	Area 37
	Left cerebellum	445	17.29	−4	−78	−12	HVI (6%)
	Right superior parietal lobule	180	12.18	24	−72	48	SPL (7P) (40%)
	Left precuneus	152	11.11	−4	−52	18	Area 30
	Left middle cingulate cortex	90	9.8	−2	14	38	Area 24
62 (0.97)	Left anterior cingulate cortex	4681	30.48	−6	42	20	Area 32
	Left inferior frontal gyrus (p. orbitalis)	295	13.95	−48	24	−14	Area 47

The quality index (Iq) associated with each RSN is listed in parentheses adjacent to the component number. Cluster size refers to the number of voxels in each cluster, negative x co-ordinates refer to left hemisphere activations. Cytoarchitectonic probabilities were established where possible by using the Anatomy toolbox (Eickhoff et al., 2005, 2006, 2007).

DISCUSSION

It has been repeatedly shown that elements of executive function, such as working memory, degrade with age (Grady and Craik, 2000). As in other studies (Grady et al., 1995, 1998) we found that elderly participants performed significantly worse than young controls on a DMS task (both in terms of error rate and RT), with the group difference being largest when matching facial stimuli (see **Figure 2**). Whilst standard GLM-based approaches failed to distinguish between age groups or task performance, a combination of ICA and multi-taper spectral analyses illustrated a number of functional networks where BOLD spectral power tracked task performance. Multivariate statistics further demonstrated that task accuracy was the strongest predictor variable for BOLD spectral power within these networks, stronger than age, head movement, gender, or any neuropsychological variables (**Figure 3**).

AGE-RELATED CHANGES IN FUNCTIONAL NETWORKS DURING DMS PERFORMANCE

The functional networks identified as tracking task performance regardless of age included the primary visual network, temporal-parietal network, posterior default-mode network, SN, and basal ganglia. The visual, posterior DMN, and SNs also showed higher frequency BOLD oscillations that negatively correlated with both task accuracy and age. The differences between high and low

Table 2 | Linear regression between event-related task timecourses and IC timecourses.

IC	Sample line respond	Sample face respond	Sample line match	Sample face match	Probe line respond	Probe face respond	Probe line match	Probe face match
1 SAMPLE *t*-TEST								
14 (BG)		Y			Y	Y	Y	Y
15 (Visual)	Y	Y	Y		Y	Y	Y	Y
26 (Left STG)								Y
48 (Posterior DMN)					Y	Y	Y	Y
63 (Insula)					Y	Y	Y	Y
65 (Salience)	Y	Y	Y				Y	Y
71 (ACC)					Y	Y	Y	Y
46 (Fusiform)	Y	Y	Y	Y		Y	Y	Y
62 (ACC)	Y		Y	Y	Y	Y		Y
2 SAMPLE *t*-TEST								
14 (BG)					Y	Y		
15 (Visual)					Y	Y	Y	Y
26 (Left STG)	Y	Y				Y		
48 (Posterior DMN)			Y			Y		
63 (Insula)					Y			
65 (Salience)		Y					Y	
71 (ACC)							Y	
46 (Fusiform)	Y			Y		Y		
62 (ACC)	Y	Y					Y	Y

Y indicates a significant relationship (as measured by beta values) between task regressors and IC timecourses (1 Sample t-test) or a significant difference between groups (2 Sample t-test). Significance thresholded at $p < 0.05$ uncorrected.

frequency BOLD oscillations will be discussed below. Studies using the delayed match-to-sample task have typically found increased activity within the frontal-parietal network (FPN) and decreased activity within the DMN (Grady et al., 2010; Spreng et al., 2010; Salami et al., 2012). When investigating aging populations it has been further shown that the DMN decreases less during task performance with age whilst the FPN increases with age (Grady et al., 2010; Salami et al., 2012). There has been some indication that this increased FPN activity is compensatory, whilst others argue that this may indicate reduced neural efficiency (see Grady, 2012 for review). The results of this study move the focus away from prefrontal regions in working memory and place a greater emphasis on the DMN. It is well established that DMN connectivity decreases with age during rest (Damoiseaux et al., 2008; Allen et al., 2011; Balsters et al., 2013), however there is more debate surrounding DMN connectivity during task performance. Whilst some studies have shown increased DMN activity during task compared to young controls (Grady et al., 2010) others have shown a continued decrease in DMN functional connectivity (Andrews-Hanna et al., 2007; Sambataro et al., 2010). Sambataro et al. (2010) scanned young and old participants during a working memory task (1- and 2-back tasks) and showed reduced DMN connectivity with age, and that increased connectivity within this network was correlated with better performance. In line with the results of this study the Sambataro et al. (2010) also showed reduced low frequency BOLD spectral power (0.03–0.08 Hz) in the posterior DMN related to age and increased BOLD spectral power within the same band limits as task difficulty increased. Garrett et al. (2013) also found reduced BOLD variability with aging in regions of the posterior DMN during task performance (including DMS task) compared to rest. The precise role of the DMN in cognitive control is unclear, however these findings add to previous suggestions that the posterior nodes of the DMN are involved in memory retrieval (Menon, 2011; Vannini et al., 2011).

The SN was the only network which showed both low and high BOLD frequency correlates of task accuracy after accounting for age-related variance (**Figure 5F**). The SN comprises of bilateral anterior insula and ACC. The insula has been shown to be an important node in functional connectivity, linking multiple brain regions, and functional networks (see Menon and Uddin, 2010 for review). Two of the key roles proposed for the SN are: (1) detection of salient events and (2) switching between large-scale functional networks once a salient event has been detected (Menon and Uddin, 2010; Menon, 2011). Along with being the only IC to track accuracy at both high and low BOLD frequencies, this was also the only IC to overlap with GLM-based results (match > respond). As in our study, Sridharan et al. (2008) found a strong overlap between the SN found using ICA and GLM-based analyses. The behavioral results of our study showed a strong effect of task on RTs and accuracy (poorer performance on match trials compared to respond trials) indicating that the match task was more difficult. It is therefore likely that increased attentional demands were placed on the match blocks compared to the respond blocks, thus highlighting the SN in the GLM analyses for match > respond events. Control signals from the SN are believed to have a top-down influence on multiple networks including basic sensory networks and

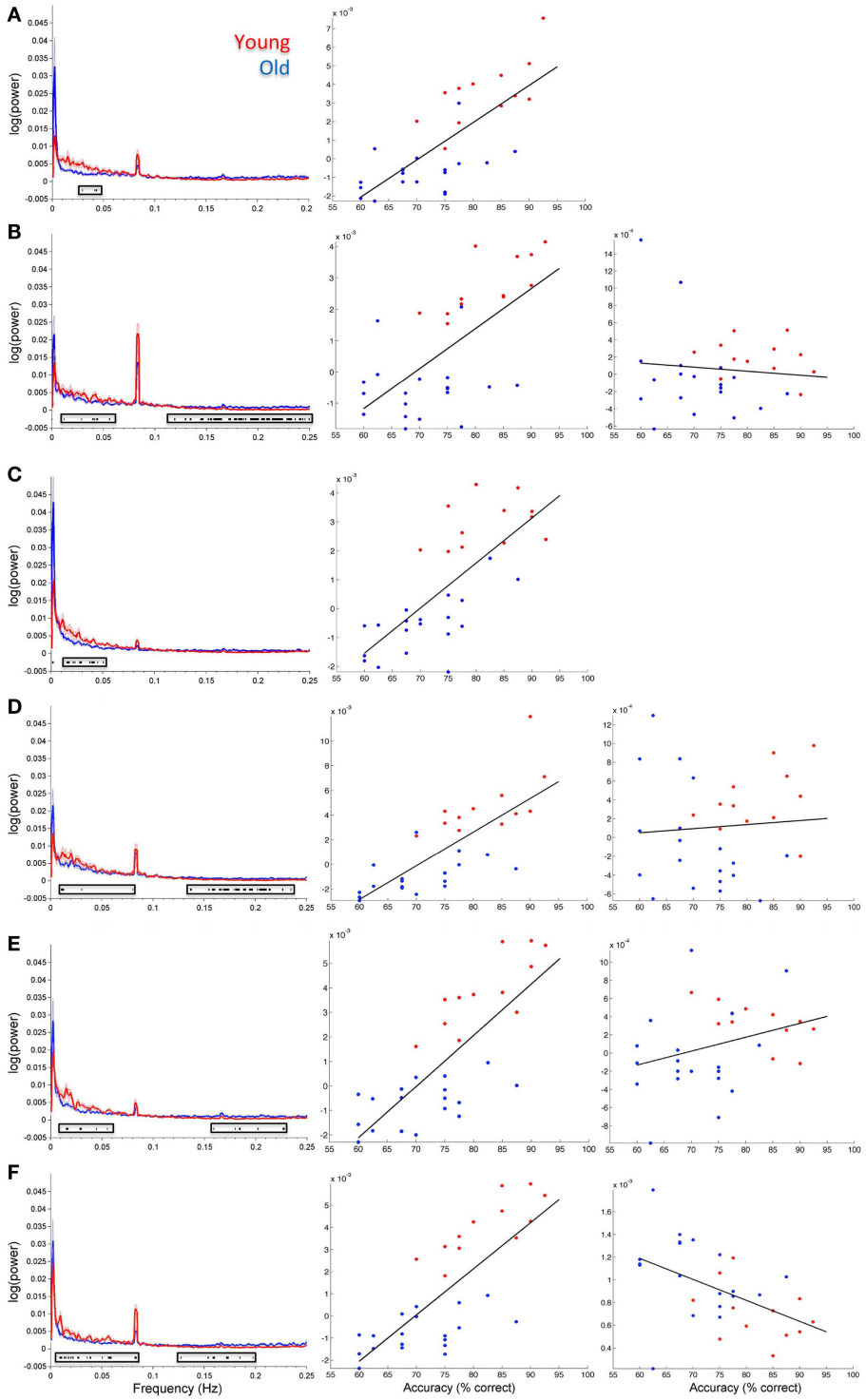

FIGURE 5 | Group spectral profiles and correlations with face match accuracy. Left column shows spectral power distributions for young and old participants. Shaded error bars show the standard error. Black markers underneath highlight where spectral power covaried with task accuracy (these are the same values shown in Figure 4). Middle and right columns show correlations with spectral power and accuracy after age was regressed out of the data. Middle column shows correlations for significant frequency points at lower frequencies (<0.1 Hz). The right column shows correlations for significant frequency points >0.1 Hz. **(A)** Putamen (IC 14), **(B)** Visual cortex (IC 15), **(C)** right STG (IC 26), **(D)** precuneus (posterior DMN; IC 48), **(E)** left insula (IC 63), **(F)** cingulo-insula network (salience network; IC 65). In all plots red refers to young participants and blue to elderly.

Table 3 | Partial Correlations between BOLD frequency power and task performance with age-related variance removed.

IC	Low frequency (0–0.1 Hz)						High frequency (0.1–0.25 Hz)					
	Group		Young		Old		Group		Young		Old	
	r	*p*	*r*	*p*	*r*	*p*	*r*	*p*	*r*	*p*	*r*	*p*
14 (BG)	0.7451	**<0.001**	0.6869	**0.0136**	0.4522	0.0519						
15 (Visual)	0.6414	**0.001**	0.6414	**0.001**	0.0655	0.79	−0.2419	0.1898	−0.2833	0.3722	−0.3849	0.1037
26 (Left STG)	0.8085	**<0.001**	0.0962	0.7662	−0.1585	0.5168						
48 (Posterior DMN)	0.7468	**<0.001**	0.627	**0.0291**	0.5326	**0.0189**	−0.293	0.1097	−0.219	0.4941	−0.5345	**0.0184**
63 (Insula)	0.7695	**<0.001**	0.7959	**0.002**	0.5348	**0.0183**	−0.3017	0.09	−0.6288	**0.0285**	−0.4624	**0.0462**
65 (Salience)	0.758	**<0.001**	0.7899	**0.022**	0.5322	**0.019**	**−0.4991**	**0.0042**	−0.6403	**0.0249**	−0.4347	0.0629

p-Values marked in bold were significant ($p < 0.05$, uncorrected).

functionally complex networks like the DMN and FPN. It is possible that control signals from the SN were impacting on BOLD oscillations within other identified networks such as the posterior DMN and visual cortex, however we did not find a significant correlation between these networks after correcting for multiple comparisons. One would also predict based on previous studies that the SN signal would elevate activity within the FPN rather than the DMN. This may suggest that an increase in FPN connectivity is not directly correlated with task accuracy in aging and may indeed index inefficient neural activity. As mentioned previously, there is still a great deal of debate about whether increased FPN connectivity is a positive or negative marker of executive function in aging (Grady, 2012).

MULTIPLE BOLD FREQUENCIES DIFFERENTIALLY CONTRIBUTE TO TASK PERFORMANCE

Our results suggest two broad relationships exist between task accuracy and BOLD oscillations; power at BOLD frequencies below 0.1 Hz were positively correlated with working memory performance and unrelated to the age of the subjects, whilst power at frequencies above 0.1 Hz were negatively associated with task performance and typically contained age-related variance (the SN being the only exception). Previous studies have also shown that multiple oscillatory dynamics are contributing to low frequency fluctuations in the BOLD signal and that these different oscillations may have distinct functional roles (Salvador et al., 2008; Baria et al., 2011; Niazy et al., 2011). Studies by Garrity et al. (2007), Malinen et al. (2010), and Calhoun et al. (2011) have shown that control groups had stronger BOLD fluctuations below 0.05 Hz whilst patient groups (schizophrenic, bipolar, and chronic pain patients) had stronger high frequency BOLD fluctuations (>0.1 Hz). Similarly, Allen et al. (2011) showed decreasing BOLD frequency power (<0.15 Hz) with age, whilst some RSNs showed increasing spectral power with age at frequencies greater than 0.2 Hz. All of these studies would suggest that increased higher frequency BOLD oscillations, present in schizophrenic patients, bipolar patients, chronic pain patients, and healthy aging, are a negative symptom (although none of these studies directly linked higher frequency oscillations to behavioral or neuropsychological measures). Our results are in keeping with the idea that high frequency BOLD fluctuations are a negative symptom given that we find a negative correlation with working memory performance and high frequency BOLD spectral power. One difference between this study and the studies of Garrity et al. (2007), Malinen et al. (2010), and Calhoun et al. (2011), is that our data was collected during task performance whilst the other studies report used resting data. Although it is likely that differences in the underlying causes of BOLD oscillations will differ between rest and task, Calhoun et al. (2008) showed that decreased low and increased high frequency BOLD spectral power was present in the same schizophrenic patients during both task performance (auditory oddball) and rest.

It has been proposed by Garrity et al. (2007) and Malinen et al. (2010) that increased higher frequency oscillations might be indicative of reduced connectivity within the functional network. It is well established that both structural and functional connectivity decreases with age (Andrews-Hanna et al., 2007; Damoiseaux et al., 2009; Allen et al., 2011), therefore an increase in BOLD spectral power at higher frequencies may represent reduced network synchronization. Cohen (2011) had participants perform a similar working memory task and investigated the delay period between the sample and probe using EEG. Cohen (2011) found a significant negative relationship between performance and peak oscillatory frequency (faster oscillations = poorer performance) during the delay period. Peak oscillatory frequency was also strongly negatively correlated with the structural connections between the hippocampus and ventrolateral PFC. These results add to the evidence that slower frequencies are necessary for encoding and maintaining complex information (Cohen, 2011; Honey et al., 2012), whilst changes in higher frequency oscillations might be indicative of reduced functional and structural connectivity.

A number of previous studies have suggested that resting state BOLD fluctuations >0.1 Hz are noise (Wise et al., 2004; Birn et al., 2006; Zou et al., 2008; Zuo et al., 2010), and might reflect cardiac or respiratory signals. One must therefore ask whether the >0.1 Hz effects seen in this study might be related to cardiac or respiratory signals. Unfortunately, we did not collect cardiac or respiratory recordings so we can not completely rule out this possibility, but we would argue based on previous resting state studies that BOLD fluctuations >0.1 Hz can contain meaningful information. First, it has been shown that ICA is capable of isolating physiological noise sources from functional networks (Birn et al., 2008; Beall and

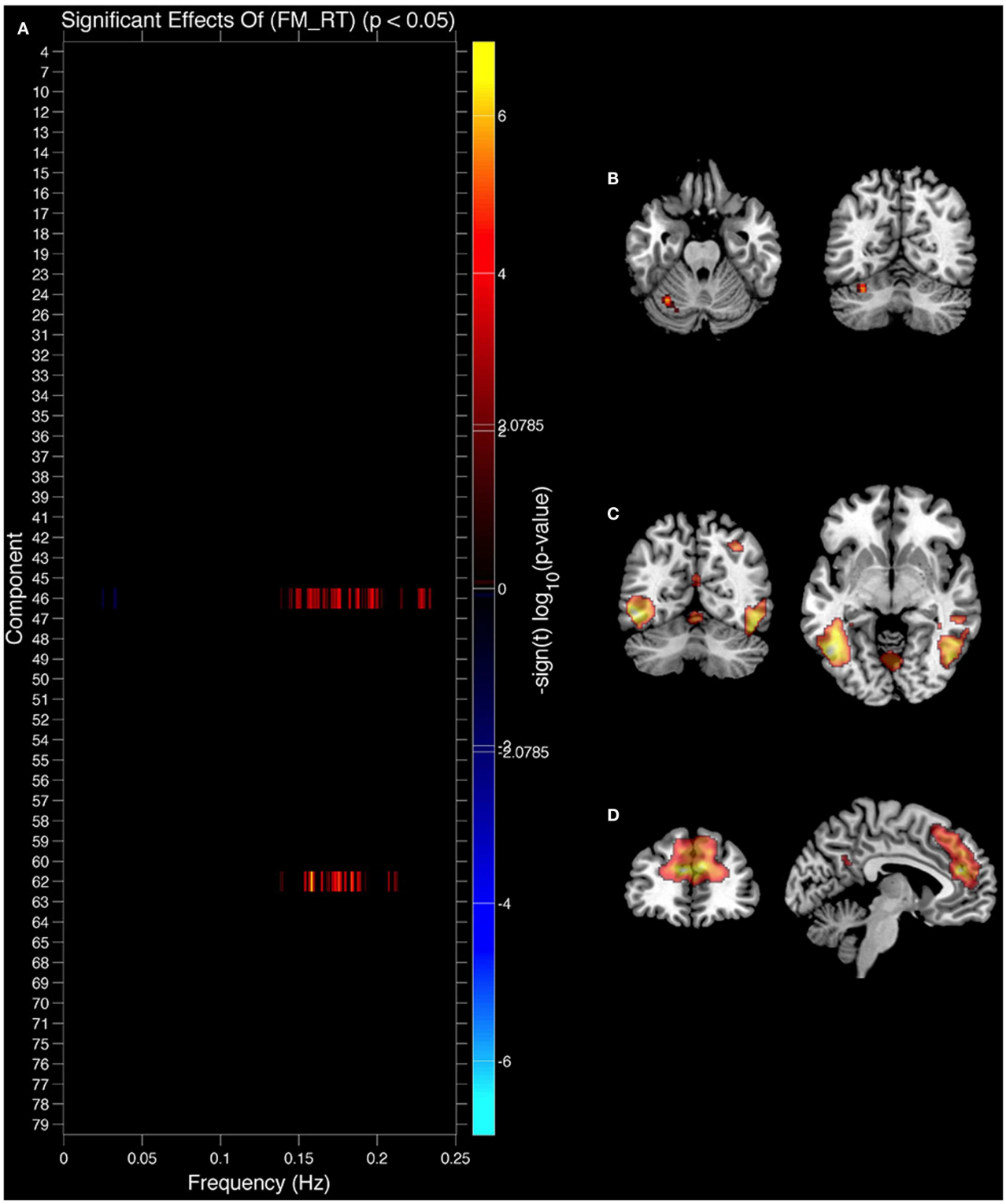

FIGURE 6 | Components showing a relationship between spectral power and face match reaction time (RT). **(A)** Components where spectral power significantly covaried with face match RT. Red markers indicate a positive relationship (greater spectral power = slower RT), black indicates their was no significant difference after correcting for multiple comparisons. **(B)** Significant covariation with voxel intensity and face match RT within left cerebellar lobule HVI. **(C)** IC 46 spatial map. **(D)** IC 62 spatial map. All results are FDR thresholded ($p < 0.05$).

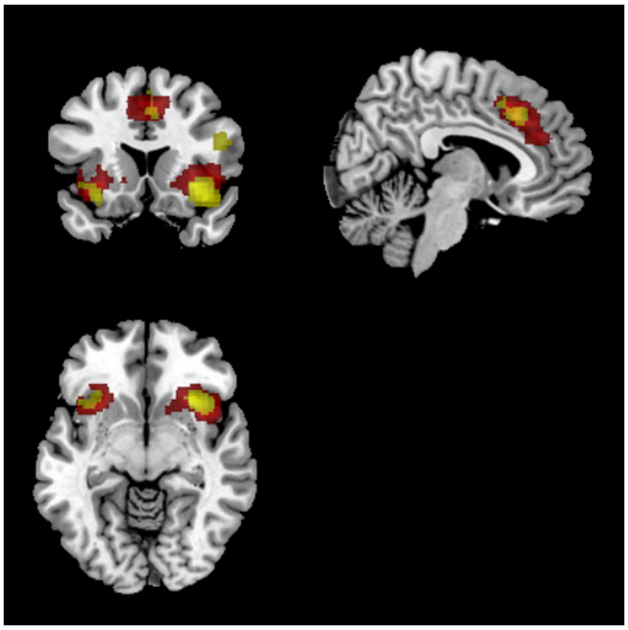

FIGURE 7 | Overlap between IC 65 (salience newtork) and SPM results. Red voxels show the spatial map for IC 65 which was identified to track task accuracy at both low (<0.1 Hz) and high (>0.1 Hz) frequencies. Activations in yellow were from the SPM analysis showing common activations between both groups for match compared to respond blocks. Both sets of activations were FDR corrected ($p < 0.05$).

Lowe, 2010; Allen et al., 2011). By excluding 28 components that correlated with white matter and CSF, displayed ringing around the edge of the brain, or had a variable decomposition, we believe we have managed to remove some physiological noise sources. Similar studies to ours were able to assess the impact of cardiac and respiration signals on BOLD oscillations at rest, and in both studies their results were not explained by these noise sources (Malinen et al., 2010; Baria et al., 2011). However, we would also reiterate that the strongest relationship between task accuracy and BOLD spectral power was at frequencies below 0.1 Hz that are widely acknowledged to reflect underlying neural fluctuations (He et al., 2010; He, 2011; Honey et al., 2012).

ADVANTAGES AND DISADVANTAGES OF ICA/SPECTRA APPROACH COMPARED TO GLM APPROACHES

A number of studies have previously demonstrated that BOLD signal correlates with task performance (Pessoa et al., 2002; Todd and Marois, 2004; Nagel et al., 2011). However, we believe there are a number of advantages to using BOLD frequency power instead of GLM-based values such as beta values or percent signal change. As mentioned previously, fluctuations in the BOLD signal are composed of a number of different oscillatory signals (Zuo et al., 2010; Baria et al., 2011; Niazy et al., 2011). As such, just investigating one oscillatory signal may not capture the underlying complexities that exist within BOLD data. Although BOLD variability has been shown to be more sensitive than mean BOLD signal, this approach still fails to take into account different BOLD frequency bands. For example, Garrett et al. (2013) found there was very little difference in BOLD variability within the elderly population between fixation and delayed match-to-sample performance. By investigating the entire BOLD spectrum we were able to find BOLD fluctuations that significantly correlate with delayed match-to-sample performance across young and old participants, as well as additional BOLD dynamics that are related to age. We therefore believe that this approach is more sensitive to brain-behavior relationships than other approaches such as GLM-based approaches and BOLD mean/variability measurements.

It may also be possible to integrate the spectral analyses conducted within this study with GLM approaches. For example, one could apply this spectral analysis to regions identified using a GLM approach instead of using ICA timecourses. However, GLM-based approaches require additional assumptions about the hrf. A number of studies have shown that BOLD response is far from canonical, changing across brain areas (Handwerker et al., 2004; Eichele et al., 2008; Wall et al., 2009), subjects (Aguirre et al., 1998), clinical populations (Rombouts et al., 2005), and in healthy aging (D'Esposito et al., 1999). In this study we used both the canonical HRF as well as more flexible Fourier basis functions to model events. The results were consistent across both GLM approaches, and neither of these highlighted the results established using ICA/spectral approaches. However, even if one uses multiple basis functions, or generates a custom HRF per subject, this still assumes that response functions are consistent from trial-to-trial. In event-related designs such as the one used in this study there is likely to be a great deal of trial-to-trial variability. By analyzing the spectral content of the whole time course we overcome this issue. However, this is also the main disadvantage of this approach. By analyzing the entire timecourse of the experiment we are not able to establish whether these BOLD spectral changes are time locked to specific cue types or task phases. Early investigations into working memory changes with age using the delayed match-to-sample task found that the deficit was specifically at the time of encoding rather than at the recognition/decision phase (Grady et al., 1995). Unfortunately, we are not able to address this question regarding the encoding and recognition phases of the experiment. It is possible to perform temporal regression on IC timecourses as we have done in this study (**Table 2**). However, this requires us to make assumptions about the shape of the hrf and trial-to-trial variability, which for reasons mentioned above may not be valid. Another alternative would be use a block design experiment where spectral content of encoding and recognition phases can be analyzed separately. Recent studies by Allen et al. (2012), Smith et al. (2012), and Sakoglu et al. (2010) are also investigating changes within and between functional networks over time. A modified version of these approaches may also allow us to investigate BOLD spectral changes in an event-related manner.

It is possible that the experimental design used in this study favored ICA/spectral analyses and biased against GLM approaches, however, we do not believe this to be the case. In this study we collected a long timeseries of data (∼34 min) which consisted of long 4.14 min blocks of task performance. Such a design is certainly amenable for Fourier transforms, however we do not believe that this unfairly biases against GLM approaches. Long, single session acquisitions such as the ones used in this study are recommended by a number of fMRI papers (Josephs and Henson, 1999; Smith

et al., 2005, 2007). In addition the results of our study are consistent with previous studies of BOLD oscillations/variability conducted by Salvador et al. (2008) and Garrett et al. (2011) who used much shorter task blocks of 48 and 36 s (DMS task) respectively for their analyses. It may still be the case that the experimental design used in this study is inefficient for GLM approaches, both to identify significance and accurately model response magnitude. Different filtering procedures were also used in the ICA analysis compared to the GLM-based analyses which could have impacted on the results. However, given the consistency with previous studies (Garrett et al., 2010, 2011, 2013; Samanez-Larkin et al., 2010; Baria et al., 2011), we believe that ICA/spectral analyses are tapping into brain-behavior relationships that are lost in GLM approaches.

CONCLUSION AND FUTURE DIRECTIONS

This study demonstrates for the first time that BOLD spectral power is a useful index of brain-behavior relationships that appears to be more sensitive than traditional GLM approaches. Unfortunately the sluggish nature of the BOLD response does not make it possible to directly compare BOLD spectral measures with similar EEG and MEG spectral measures. Simultaneous EEG/fMRI studies have begun to investigate the relationships between EEG frequency bands and fMRI SMs (Mantini et al., 2007; Balsters et al., 2011, 2013), however in order to understand the relationship between M/EEG oscillations and BOLD oscillations one must contend with the fact that M/EEG oscillations are significantly faster than events used in a task paradigm whereas BOLD oscillations are more likely to be directly influenced by the task paradigm. Further research is necessary to establish (a) the potential relationships between EEG and fMRI frequency bands and (b) the reliability of >0.1 Hz BOLD fluctuations in both task and rest.

ACKNOWLEDGMENTS

We would like to thank Dr. Redmond O'Connell for his helpful advice on this manuscript. We would also like to thank Dr. Kerskens and Mr. Josephs for their help in establishing the fMRI protocol and collecting data. This work was supported by funding from the GlaxoSmithKline/Trinity College Institute of Neuroscience Research Consortium on Neurodegeneration.

REFERENCES

Aguirre, G. K., Zarahn, E., and D'Esposito, M. (1998). The variability of human, BOLD hemodynamic responses. *Neuroimage* 8, 360–369.

Allen, E. A., Damaraju, E., Plis, S. M., Erhardt, E. B., Eichele, T., and Calhoun, V. D. (2012). Tracking whole-brain connectivity dynamics in the resting state. *Cereb. Cortex*. doi:10.1093/cercor/bhs352

Allen, E. A., Erhardt, E. B., Damaraju, E., Gruner, W., Segall, J. M., Silva, R. F., et al. (2011). A baseline for the multivariate comparison of resting-state networks. *Front. Syst. Neurosci.* 5:2. doi:10.3389/fnsys.2011.00002

Andersson, J. L., Hutton, C., Ashburner, J., Turner, R., and Friston, K. (2001). Modeling geometric deformations in EPI time series. *Neuroimage* 13, 903–919.

Andrews-Hanna, J. R., Snyder, A. Z., Vincent, J. L., Lustig, C., Head, D., Raichle, M. E., et al. (2007). Disruption of large-scale brain systems in advanced aging. *Neuron* 56, 924–935.

Ashburner, J., and Friston, K. J. (2005). Unified segmentation. *Neuroimage* 26, 839–851.

Balsters, J. H., O'Connell, R. G., Galli, A., Nolan, H., Greco, E., Kilcullen, S. M., et al. (2013). Changes in resting connectivity with age: a simultaneous electroencephalogram and functional magnetic resonance imaging investigation. *Neurobiol. Aging*. doi:10.1016/j.neurobiolaging.2013.03.004

Balsters, J. H., O'Connell, R. G., Martin, M. P., Galli, A., Cassidy, S. M., Kilcullen, S. M., et al. (2011). Donepezil impairs memory in healthy older subjects: behavioural, EEG and simultaneous EEG/fMRI biomarkers. *PLoS ONE* 6:e24126. doi:10.1371/journal.pone.0024126

Balsters, J. H., and Ramnani, N. (2008). Symbolic representations of action in the human cerebellum. *Neuroimage* 43, 388–398.

Baria, A. T., Baliki, M. N., Parrish, T., and Apkarian, A. V. (2011). Anatomical and functional assemblies of brain BOLD oscillations. *J. Neurosci.* 31, 7910–7919.

Beall, E. B., and Lowe, M. J. (2010). The non-separability of physiologic noise in functional connectivity MRI with spatial ICA at 3T. *J. Neurosci. Methods* 191, 263–276.

Behrens, T. E., Johansen-Berg, H., Woolrich, M. W., Smith, S. M., Wheeler-Kingshott, C. A., Boulby, P. A., et al. (2003). Non-invasive mapping of connections between human thalamus and cortex using diffusion imaging. *Nat. Neurosci.* 6, 750–757.

Bell, A. J., and Sejnowski, T. J. (1995). An information-maximization approach to blind separation and blind deconvolution. *Neural. Comput.* 7, 1129–1159.

Bellgrove, M. A., Hester, R., and Garavan, H. (2004). The functional neuroanatomical correlates of response variability: evidence from a response inhibition task. *Neuropsychologia* 42, 1910–1916.

Birn, R. M., Diamond, J. B., Smith, M. A., and Bandettini, P. A. (2006). Separating respiratory-variation-related fluctuations from neuronal-activity-related fluctuations in fMRI. *Neuroimage* 31, 1536–1548.

Birn, R. M., Murphy, K., and Bandettini, P. A. (2008). The effect of respiration variations on independent component analysis results of resting state functional connectivity. *Hum. Brain Mapp.* 29, 740–750.

Biswal, B., Yetkin, F. Z., Haughton, V. M., and Hyde, J. S. (1995). Functional connectivity in the motor cortex of resting human brain using echo-planar MRI. *Magn. Reson. Med.* 34, 537–541.

Blanz, V., and Vetter, T. (1999). "A morphable model for the synthesis of 3D faces," in *SIGGRAPH'99 Conference Proceedings* (Los Angeles: ACM Press/Addison-Wesley Publishing Co.), 187–194.

Buzsaki, G., and Draguhn, A. (2004). Neuronal oscillations in cortical networks. *Science* 304, 1926–1929.

Calhoun, V. D., Adali, T., Pearlson, G. D., and Pekar, J. J. (2001). A method for making group inferences from functional MRI data using independent component analysis. *Hum. Brain Mapp.* 14, 140–151.

Calhoun, V. D., Kiehl, K. A., and Pearlson, G. D. (2008). Modulation of temporally coherent brain networks estimated using ICA at rest and during cognitive tasks. *Hum. Brain Mapp.* 29, 828–838.

Calhoun, V. D., Sui, J., Kiehl, K., Turner, J., Allen, E., and Pearlson, G. (2011). Exploring the psychosis functional connectome: aberrant intrinsic networks in schizophrenia and bipolar disorder. *Front. Psychiatry* 2:75. doi:10.3389/fpsyt.2011.00075

Cavanagh, J. F., Cohen, M. X., and Allen, J. J. (2009). Prelude to and resolution of an error: EEG phase synchrony reveals cognitive control dynamics during action monitoring. *J. Neurosci.* 29, 98–105.

Cohen, M. X. (2011). Hippocampal-prefrontal connectivity predicts midfrontal oscillations and long-term memory performance. *Curr. Biol.* 21, 1900–1905.

Cohen, M. X., and Cavanagh, J. F. (2011). Single-trial regression elucidates the role of prefrontal theta oscillations in response conflict. *Front. Psychol.* 2:30. doi:10.3389/fpsyg.2011.00030

Damoiseaux, J. S., Beckmann, C. F., Arigita, E. J., Barkhof, F., Scheltens, P., Stam, C. J., et al. (2008). Reduced resting-state brain activity in the "default network" in normal aging. *Cereb. Cortex* 18, 1856–1864.

Damoiseaux, J. S., Smith, S. M., Witter, M. P., Sanz-Arigita, E. J., Barkhof, F., Scheltens, P., et al. (2009). White matter tract integrity in aging and Alzheimer's disease. *Hum. Brain Mapp.* 30, 1051–1059.

Debener, S., Ullsperger, M., Siegel, M., Fiehler, K., Von Cramon, D. Y., and Engel, A. K. (2005). Trial-by-trial coupling of concurrent electroencephalogram and functional magnetic resonance imaging identifies the dynamics of performance monitoring. *J. Neurosci.* 25, 11730–11737.

D'Esposito, M., Zarahn, E., Aguirre, G. K., and Rypma, B. (1999). The effect of normal aging on the coupling of neural activity to the bold hemodynamic response. *Neuroimage* 10, 6–14.

Diedrichsen, J., Balsters, J. H., Flavell, J., Cussans, E., and Ramnani, N. (2009). A probabilistic MR atlas of the human cerebellum. *Neuroimage* 46, 39–46.

Dockree, P. M., Kelly, S. P., Foxe, J. J., Reilly, R. B., and Robertson, I. H. (2007). Optimal sustained attention is linked to the spectral content of background EEG activity: greater ongoing tonic alpha (approximately 10 Hz) power supports successful phasic goal activation. *Eur. J. Neurosci.* 25, 900–907.

Eichele, T., Debener, S., Calhoun, V. D., Specht, K., Engel, A. K., Hugdahl, K., et al. (2008). Prediction of human errors by maladaptive changes in event-related brain networks. *Proc. Natl. Acad. Sci. U.S.A.* 105, 6173–6178.

Eickhoff, S. B., Paus, T., Caspers, S., Grosbras, M. H., Evans, A. C., Zilles, K., et al. (2007). Assignment of functional activations to probabilistic cytoarchitectonic areas revisited. *Neuroimage* 36, 511–521.

Eickhoff, S. B., Schleicher, A., Zilles, K., and Amunts, K. (2006). The human parietal operculum. I. Cytoarchitectonic mapping of subdivisions. *Cereb. Cortex* 16, 254–267.

Eickhoff, S. B., Stephan, K. E., Mohlberg, H., Grefkes, C., Fink, G. R., Amunts, K., et al. (2005). A new SPM toolbox for combining probabilistic cytoarchitectonic maps and functional imaging data. *Neuroimage* 25, 1325–1335.

Erhardt, E. B., Rachakonda, S., Bedrick, E. J., Allen, E. A., Adali, T., and Calhoun, V. D. (2011). Comparison of multi-subject ICA methods for analysis of fMRI data. *Hum. Brain Mapp.* 32, 2075–2095.

Friston, K. J., Frith, C. D., Frackowiak, R. S., and Turner, R. (1995a). Characterizing dynamic brain responses with fMRI: a multivariate approach. *Neuroimage* 2, 166–172.

Friston, K. J., Frith, C. D., Turner, R., and Frackowiak, R. S. (1995b). Characterizing evoked hemodynamics with fMRI. *Neuroimage* 2, 157–165.

Friston, K. J., Penny, W. D., and Glaser, D. E. (2005). Conjunction revisited. *Neuroimage* 25, 661–667.

Garrett, D. D., Kovacevic, N., McIntosh, A. R., and Grady, C. L. (2010). Blood oxygen level-dependent signal variability is more than just noise. *J. Neurosci.* 30, 4914–4921.

Garrett, D. D., Kovacevic, N., McIntosh, A. R., and Grady, C. L. (2011). The importance of being variable. *J. Neurosci.* 31, 4496–4503.

Garrett, D. D., Kovacevic, N., McIntosh, A. R., and Grady, C. L. (2013). The modulation of BOLD variability between cognitive states varies by age and processing speed. *Cereb. Cortex* 23, 684–693.

Garrity, A. G., Pearlson, G. D., McKiernan, K., Lloyd, D., Kiehl, K. A., and Calhoun, V. D. (2007). Aberrant "default mode" functional connectivity in schizophrenia. *Am. J. Psychiatry* 164, 450–457.

Genovese, C. R., Lazar, N. A., and Nichols, T. (2002). Thresholding of statistical maps in functional neuroimaging using the false discovery rate. *Neuroimage* 15, 870–878.

Grady, C. (2012). The cognitive neuroscience of ageing. *Nat. Rev. Neurosci.* 13, 491–505.

Grady, C. L., and Craik, F. I. (2000). Changes in memory processing with age. *Curr. Opin. Neurobiol.* 10, 224–231.

Grady, C. L., McIntosh, A. R., Bookstein, F., Horwitz, B., Rapoport, S. I., and Haxby, J. V. (1998). Age-related changes in regional cerebral blood flow during working memory for faces. *Neuroimage* 8, 409–425.

Grady, C. L., McIntosh, A. R., Horwitz, B., Maisog, J. M., Ungerleider, L. G., Mentis, M. J., et al. (1995). Age-related reductions in human recognition memory due to impaired encoding. *Science* 269, 218–221.

Grady, C. L., Protzner, A. B., Kovacevic, N., Strother, S. C., Afshin-Pour, B., Wojtowicz, M., et al. (2010). A multivariate analysis of age-related differences in default mode and task-positive networks across multiple cognitive domains. *Cereb. Cortex* 20, 1432–1447.

Greicius, M. D., Srivastava, G., Reiss, A. L., and Menon, V. (2004). Default-mode network activity distinguishes Alzheimer's disease from healthy aging: evidence from functional MRI. *Proc. Natl. Acad. Sci. U.S.A.* 101, 4637–4642.

Handwerker, D. A., Ollinger, J. M., and D'Esposito, M. (2004). Variation of BOLD hemodynamic responses across subjects and brain regions and their effects on statistical analyses. *Neuroimage* 21, 1639–1651.

He, B. J. (2011). Scale-free properties of the functional magnetic resonance imaging signal during rest and task. *J. Neurosci.* 31, 13786–13795.

He, B. J., Zempel, J. M., Snyder, A. Z., and Raichle, M. E. (2010). The temporal structures and functional significance of scale-free brain activity. *Neuron* 66, 353–369.

Himberg, J., Hyvarinen, A., and Esposito, F. (2004). Validating the independent components of neuroimaging time series via clustering and visualization. *Neuroimage* 22, 1214–1222.

Honey, C. J., Thesen, T., Donner, T. H., Silbert, L. J., Carlson, C. E., Devinsky, O., et al. (2012). Slow cortical dynamics and the accumulation of information over long timescales. *Neuron* 76, 423–434.

Hutton, C., Bork, A., Josephs, O., Deichmann, R., Ashburner, J., and Turner, R. (2002). Image distortion correction in fMRI: a quantitative evaluation. *Neuroimage* 16, 217–240.

Jafri, M. J., Pearlson, G. D., Stevens, M., and Calhoun, V. D. (2008). A method for functional network connectivity among spatially independent resting-state components in schizophrenia. *Neuroimage* 39, 1666–1681.

Jezzard, P., Lebihan, D., Cuenod, C., Pannier, L., Prinster, A., and Turner, R. (1993). "An investigation of the contribution of physiological noise in human functional MRI studies at 1.5 Tesla and 4 Tesla," in *Proceedings of the 12th Annual Meeting of SMRM* (New York: Society for Magnetic Resonance in Medicine), 1392.

Josephs, O., and Henson, R. N. (1999). Event-related functional magnetic resonance imaging: modelling, inference and optimization. *Philos. Trans. R. Soc. Lond. B Biol. Sci.* 354, 1215–1228.

Klimesch, W. (1999). EEG alpha and theta oscillations reflect cognitive and memory performance: a review and analysis. *Brain Res. Brain Res. Rev.* 29, 169–195.

Li, Y. O., Adali, T., and Calhoun, V. D. (2007). Estimating the number of independent components for functional magnetic resonance imaging data. *Hum. Brain Mapp.* 28, 1251–1266.

Malinen, S., Vartiainen, N., Hlushchuk, Y., Koskinen, M., Ramkumar, P., Forss, N., et al. (2010). Aberrant temporal and spatial brain activity during rest in patients with chronic pain. *Proc. Natl. Acad. Sci. U.S.A.* 107, 6493–6497.

Mantini, D., Perrucci, M. G., Del Gratta, C., Romani, G. L., and Corbetta, M. (2007). Electrophysiological signatures of resting state networks in the human brain. *Proc. Natl. Acad. Sci. U.S.A.* 104, 13170–13175.

Menon, V. (2011). Large-scale brain networks and psychopathology: a unifying triple network model. *Trends Cogn. Sci. (Regul. Ed.)* 15, 483–506.

Menon, V., and Uddin, L. Q. (2010). Saliency, switching, attention and control: a network model of insula function. *Brain Struct. Funct.* 214, 655–667.

Mitra, P., and Bokil, H. (2008). *Observed Brain Dynamics.* New York: Oxford University Press.

Nagel, I. E., Preuschhof, C., Li, S. C., Nyberg, L., Backman, L., Lindenberger, U., et al. (2011). Load modulation of BOLD response and connectivity predicts working memory performance in younger and older adults. *J. Cogn. Neurosci.* 23, 2030–2045.

Niazy, R. K., Xie, J., Miller, K., Beckmann, C. F., and Smith, S. M. (2011). Spectral characteristics of resting state networks. *Prog. Brain Res.* 193, 259–276.

O'Connell, R. G., Dockree, P. M., Robertson, I. H., Bellgrove, M. A., Foxe, J. J., and Kelly, S. P. (2009). Uncovering the neural signature of lapsing attention: electrophysiological signals predict errors up to 20 s before they occur. *J. Neurosci.* 29, 8604–8611.

Pessoa, L., Gutierrez, E., Bandettini, P., and Ungerleider, L. (2002). Neural correlates of visual working memory: fMRI amplitude predicts task performance. *Neuron* 35, 975–987.

Price, C. J., and Friston, K. J. (1997). Cognitive conjunction: a new approach to brain activation experiments. *Neuroimage* 5, 261–270.

Rombouts, S. A., Goekoop, R., Stam, C. J., Barkhof, F., and Scheltens, P. (2005). Delayed rather than decreased BOLD response as a marker for early Alzheimer's disease. *Neuroimage* 26, 1078–1085.

Sakoglu, U., Pearlson, G. D., Kiehl, K. A., Wang, Y. M., Michael, A. M., and Calhoun, V. D. (2010). A method for evaluating dynamic functional network connectivity and task-modulation: application to schizophrenia. *MAGMA* 23, 351–366.

Salami, A., Eriksson, J., and Nyberg, L. (2012). Opposing effects of aging on large-scale brain systems for memory encoding and cognitive control. *J. Neurosci.* 32, 10749–10757.

Salvador, R., Martinez, A., Pomarol-Clotet, E., Gomar, J., Vila, F., Sarro, S., et al. (2008). A simple view of the brain through a frequency-specific functional connectivity measure. *Neuroimage* 39, 279–289.

Samanez-Larkin, G. R., Kuhnen, C. M., Yoo, D. J., and Knutson, B. (2010). Variability in nucleus accumbens activity mediates age-related suboptimal financial risk taking. *J. Neurosci.* 30, 1426–1434.

Sambataro, F., Murty, V. P., Callicott, J. H., Tan, H. Y., Das, S., Weinberger, D. R., et al. (2010). Age-related alterations in default mode network: impact on working memory performance. *Neurobiol. Aging* 31, 839–852.

Smith, A. T., Singh, K. D., and Balsters, J. H. (2007). A comment on the severity of the effects of non-white noise in fMRI time-series. *Neuroimage* 36, 282–288.

Smith, S. M., Beckmann, C. F., Ramnani, N., Woolrich, M. W., Bannister, P. R., Jenkinson, M., et al. (2005). Variability in fMRI: a re-examination of inter-session differences. *Hum. Brain Mapp.* 24, 248–257.

Smith, S. M., Miller, K. L., Moeller, S., Xu, J., Auerbach, E. J., Woolrich, M. W., et al. (2012). Temporally-independent functional modes of spontaneous brain activity. *Proc. Natl. Acad. Sci. U.S.A.* 109, 3131–3136.

Spreng, R. N., Wojtowicz, M., and Grady, C. L. (2010). Reliable differences in brain activity between young and old adults: a quantitative meta-analysis across multiple cognitive domains. *Neurosci. Biobehav. Rev.* 34, 1178–1194.

Sridharan, D., Levitin, D. J., and Menon, V. (2008). A critical role for the right fronto-insular cortex in switching between central-executive and default-mode networks. *Proc. Natl. Acad. Sci. U.S.A.* 105, 12569–12574.

Stuss, D. T., Murphy, K. J., Binns, M. A., and Alexander, M. P. (2003). Staying on the job: the frontal lobes control individual performance variability. *Brain* 126, 2363–2380.

Thut, G., Nietzel, A., Brandt, S. A., and Pascual-Leone, A. (2006). Alpha-band electroencephalographic activity over occipital cortex indexes visuospatial attention bias and predicts visual target detection. *J. Neurosci.* 26, 9494–9502.

Todd, J. J., and Marois, R. (2004). Capacity limit of visual short-term memory in human posterior parietal cortex. *Nature* 428, 751–754.

Vannini, P., O'Brien, J., O'Keefe, K., Pihlajamaki, M., Laviolette, P., and Sperling, R. A. (2011). What goes down must come up: role of the posteromedial cortices in encoding and retrieval. *Cereb. Cortex* 21, 22–34.

Wall, M. B., Walker, R., and Smith, A. T. (2009). Functional imaging of the human superior colliculus: an optimised approach. *Neuroimage* 47, 1620–1627.

Wise, R. G., Ide, K., Poulin, M. J., and Tracey, I. (2004). Resting fluctuations in arterial carbon dioxide induce significant low frequency variations in BOLD signal. *Neuroimage* 21, 1652–1664.

Zhang, D., and Raichle, M. E. (2010). Disease and the brain's dark energy. *Nat. Rev. Neurol.* 6, 15–28.

Zhang, S., and Li, C. S. (2012). Task-related, low-frequency task-residual, and resting state activity in the default mode network brain regions. *Front. Psychol.* 3:172. doi:10.3389/fpsyg.2012.00172

Zou, Q. H., Zhu, C. Z., Yang, Y., Zuo, X. N., Long, X. Y., Cao, Q. J., et al. (2008). An improved approach to detection of amplitude of low-frequency fluctuation (ALFF) for resting-state fMRI: fractional ALFF. *J. Neurosci. Methods* 172, 137–141.

Zuo, X. N., Di Martino, A., Kelly, C., Shehzad, Z. E., Gee, D. G., Klein, D. F., et al. (2010). The oscillating brain: complex and reliable. *Neuroimage* 49, 1432–1445.

Conflict of Interest Statement: The authors declare that the research was conducted in the absence of any commercial or financial relationships that could be construed as a potential conflict of interest.

Received: 23 November 2012; accepted: 02 May 2013; published online: 16 May 2013.

Citation: Balsters JH, Robertson IH and Calhoun VD (2013) BOLD frequency power indexes working memory performance. Front. Hum. Neurosci. 7:207. doi: 10.3389/fnhum.2013.00207

frontiers in
HUMAN NEUROSCIENCE

ORIGINAL RESEARCH ARTICLE
published: 23 April 2013
doi: 10.3389/fnhum.2013.00156

An investigation of RSN frequency spectra using ultra-fast generalized inverse imaging

***Rasim Boyacioglu*[1]*, Christian F. Beckmann*[1,2] *and Markus Barth*[1,3]**

[1] *Radboud University Nijmegen, Donders Institute for Brain, Cognition and Behaviour, Nijmegen, Netherlands*
[2] *MIRA Institute for Biomedical Technology and Technical Medicine, University of Twente, Enschede, Netherlands*
[3] *Erwin L. Hahn Institute for Magnetic Resonance Imaging, University Duisburg-Essen, Essen, Germany*

Edited by:
Simon Daniel Robinson, Medical University of Vienna, Austria

Reviewed by:
Wolfgang Huf, Medical University of Vienna, Austria
Pierre LeVan, University Medical Center Freiburg, Germany

***Correspondence:**
Rasim Boyacioglu, Radboud University Nijmegen, Donders Institute for Brain, Cognition and Behaviour, Kapittelweg 29, 6525 EN, Nijmegen, Netherlands.
e-mail: rasim.boyacioglu@donders.ru.nl

With the advancements in MRI hardware, pulse sequences and reconstruction techniques, many low TR sequences are becoming more and more popular within the functional MRI (fMRI) community. In this study, we have investigated the spectral characteristics of resting state networks (RSNs) with a newly introduced ultra fast fMRI technique, called generalized inverse imaging (GIN). The high temporal resolution of GIN (TR = 50 ms) enables to sample cardiac signals without aliasing into a separate frequency band from the BOLD fluctuations. Respiration related signal changes are, on the other hand, removed from the data without the need for external physiological recordings. We have observed that the variance over the subjects is higher than the variance over RSNs.

Keywords: GIN, resting state, respiration, dual regression, ICA, frequency analysis, fMRI BOLD, physiological noise

INTRODUCTION

Functional MRI (fMRI) studies related to "resting" brain has been one of the constantly growing fields in cognitive neuroscience (Biswal et al., 1995; Beckmann et al., 2005; Damoiseaux et al., 2006; De Luca et al., 2006; Smith et al., 2009; Laird et al., 2011). For the interpretation of resting state networks (RSNs) a clean mapping of relevant frequencies is of relevance to prevent the conclusion that RSNs are a mere artifact of physiological signals. Moreover, it has also recently been shown that RSNs are detectable for frequencies well above 0.1 Hz (Niazy et al., 2011; Smith et al., 2012; van Oort et al., 2012). It is therefore important that the main physiological fluctuations are sampled without aliasing into functionally relevant frequency bands. The breathing frequency is particularly problematic as the related frequency band is close to the main frequencies commonly associated with RSNs and as breathing leads to a more global effect than cardiac noise. For example, the default mode network, a commonly observed RSN, has been linked to respiration depth (Birn, 2012). The cardiac noise, however, is spatially localized to big vessels and arteries and introduces variance especially into the auditory network (Beall and Lowe, 2007).

Recent developments in MR acquisition techniques in 2D which are called simultaneous multislice imaging (SMS) enable sufficiently fast sampling of the MR signal to separate and remove the respiration related fluctuations (Moeller et al., 2009; Feinberg and Yacoub, 2012; Setsompop et al., 2012). However, if one aims to discern the cardiac noise, then ultra-fast MRI techniques, such as MR-encephalography (MREG) (Hennig, 2012; Zahneisen et al., 2012) or inverse imaging based methods (Boyacioglu and Barth, 2012b; Lin et al., 2012) should be the method of choice. Among these methods resting state analysis has been carried out with MREG by using a seed based correlation analysis (Lee et al., 2012) and with SMS by applying ICA (Feinberg et al., 2010). Both of these studies are proof of principle studies showing the benefits of increased time points and investigate the spatial characteristics of RSNs. Another study that used SMS dissected the RSNs into temporal functional modes (TFMs) by using temporal ICA (Smith et al., 2012). In this study we investigated the frequency spectra of RSNs by largely avoiding physiological contamination which could obscure functional interpretation. Therefore, we used a recently developed ultra-fast acquisition technique, generalized inverse imaging (GIN) (Boyacioglu and Barth, 2012b), with implicit acquisition of a phase regressor that resembles physiological fluctuations.

MATERIALS AND METHODS

DATA ACQUISITION

The data were acquired with a 3-T MRI scanner (TIM Trio; Siemens Healthcare, Erlangen, Germany) and a 32-channel head coil. Six healthy subjects (one female, five male; aged 28–37) were recruited for the study and written informed consent was obtained according to the guidelines of the local IRB. Ultra-fast fMRI was performed using the GIN method (Boyacioglu and Barth, 2012b): the reference scan for the GIN reconstruction was carried out with a 3D EPI scan with the following parameters: in plane resolution 3.5 mm × 3.5 mm, slice thickness 3.5 mm, flip angle = 15°, TE/TR = 28/50 ms, 44 partition phase encoding steps, sagittal slices, FOV = 224 mm × 224 mm × 156 mm. The GIN data were acquired with the same parameters but with a 2D EPI scan with a slice thickness of 156 mm which resulted in a single collapsed slice in the left-right direction. Then, this slice was unaliased into a 3D volume using the GIN reconstruction framework. GIN uses the phase as a constraint to improve the solution of the highly undersampled regularized reconstruction and only needs a single 3D EPI prescan to obtain the necessary coil sensitivity information

and reference images that are used to reconstruct standard images, so that standard analysis methods such as ICA and general linear model (GLM) are applicable. 5 min of resting state data (eyes open) were collected from each subject.

ANALYSIS

The data was preprocessed with FSL's FEAT (v4.1.7)[1] by removing the temporal drift and spatially smoothing with an 8-mm kernel. We have used DRIFTER (Särkkä et al., 2012) for physiological noise correction. It was shown that the phase drift time course, a by-product obtained during the GIN reconstruction, fluctuates with the respiration (Boyacioglu and Barth, 2012a) and was therefore used as the reference signal for DRIFTER to estimate the frequencies which were removed from the data. We have registered the eight template RSNs from Beckmann et al. (2005)[2], to the individual subjects' native space. Dual regression of the subjects' functional data against these eight maps then gave rise to subject-dependent versions of these RSNs (Filippini et al., 2009). Dual regression analysis simply consists of two GLMs where the first one extracts the associated time course from the single subject data by using one of the RSNs as a spatial regressor and the second one uses that time course as a regressor to map the RSN onto the single subject level. The DICE overlap score (for subject $m = 1, 2 \ldots 6$ and RSN $k = 1, 2 \ldots 8$) was calculated to depict the similarity between a template (rsn_k) and an individual subject (sub_{mk}) map as follows,

$$\text{dice}_{mk} = \frac{2\,|\text{rsn}_k \cap \text{sub}_{mk}|}{|\text{rsn}_k| + |\text{sub}_{mk}|} \quad (1)$$

where $|\,|$ represents the number of voxels of a map and $\cap$ represents the intersection of two maps. Each RSN map on the single subject level was masked with a gray matter (GM) mask. The frequency spectra were normalized by their total power.

[1]http://www.fmrib.ox.ac.uk/fsl/

[2]http://www.fmrib.ox.ac.uk/analysis/royalsoc8/

RESULTS

Figure 1 shows the average time course (a) and frequency spectra (b) for eight RSNs for a single subject before and after physiological noise removal. When the phase drift is used as the reference signal for physiological noise estimation/removal with DRIFTER, the data shows clear power reduction in the frequency range of breathing (see red line shown in **Figure 1B**), but the power at other frequencies is preserved and is free from respiratory fluctuations. Note that the phase drift time course carries little information about the cardiac signal (for this specific run around the principal cardiac frequency at 1.2 Hz) and thus does not reduce the power in that specific frequency band (see red line).

Eight typical RSNs and the corresponding dual regression maps are shown in **Figure 2** for a single subject. The spatial patterns of the prototypical RSNs are matched by their GIN counterparts.

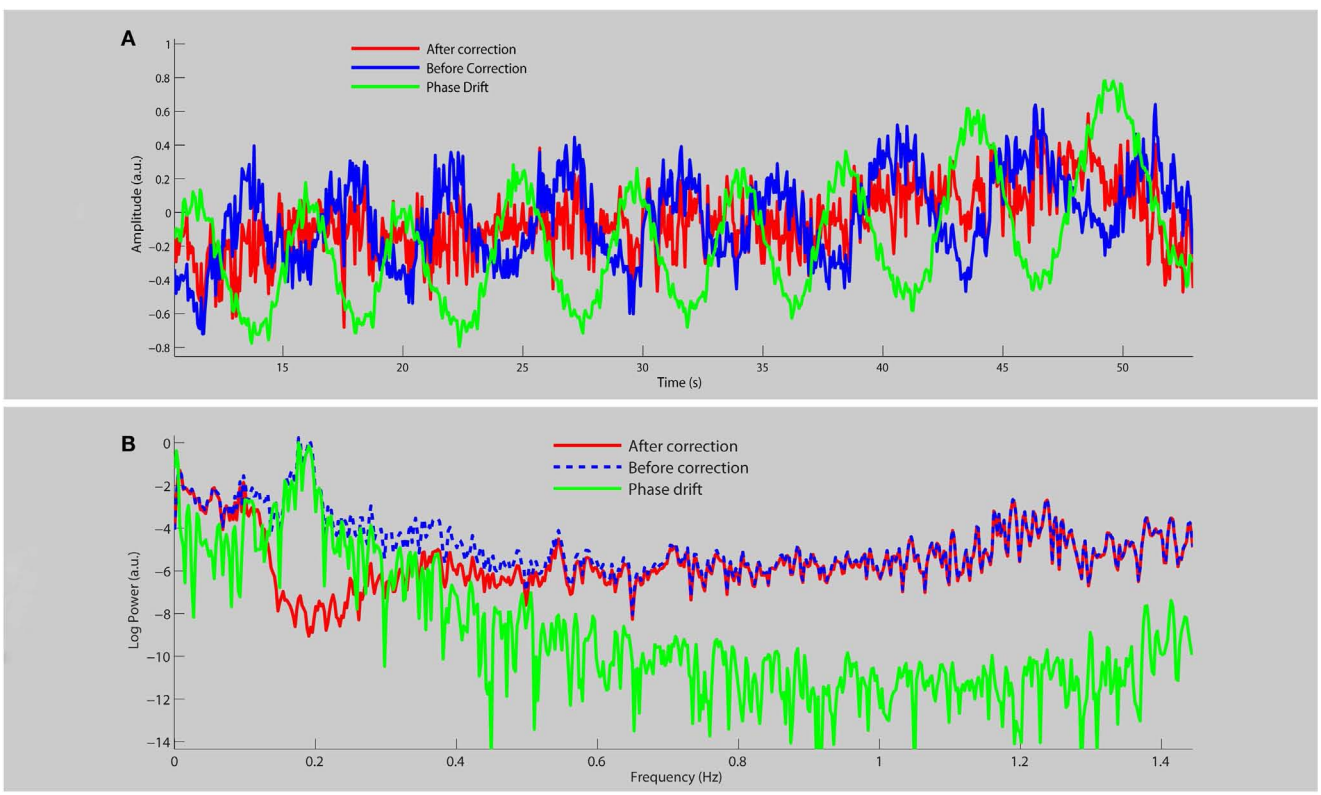

FIGURE 1 | A section of the average time course (A) and frequency spectrum on a log-linear scale (B) of RSNs for a single subject before (blue line) and after (red line) physiological noise removal, as well as the corresponding phase drift regressor (green line).

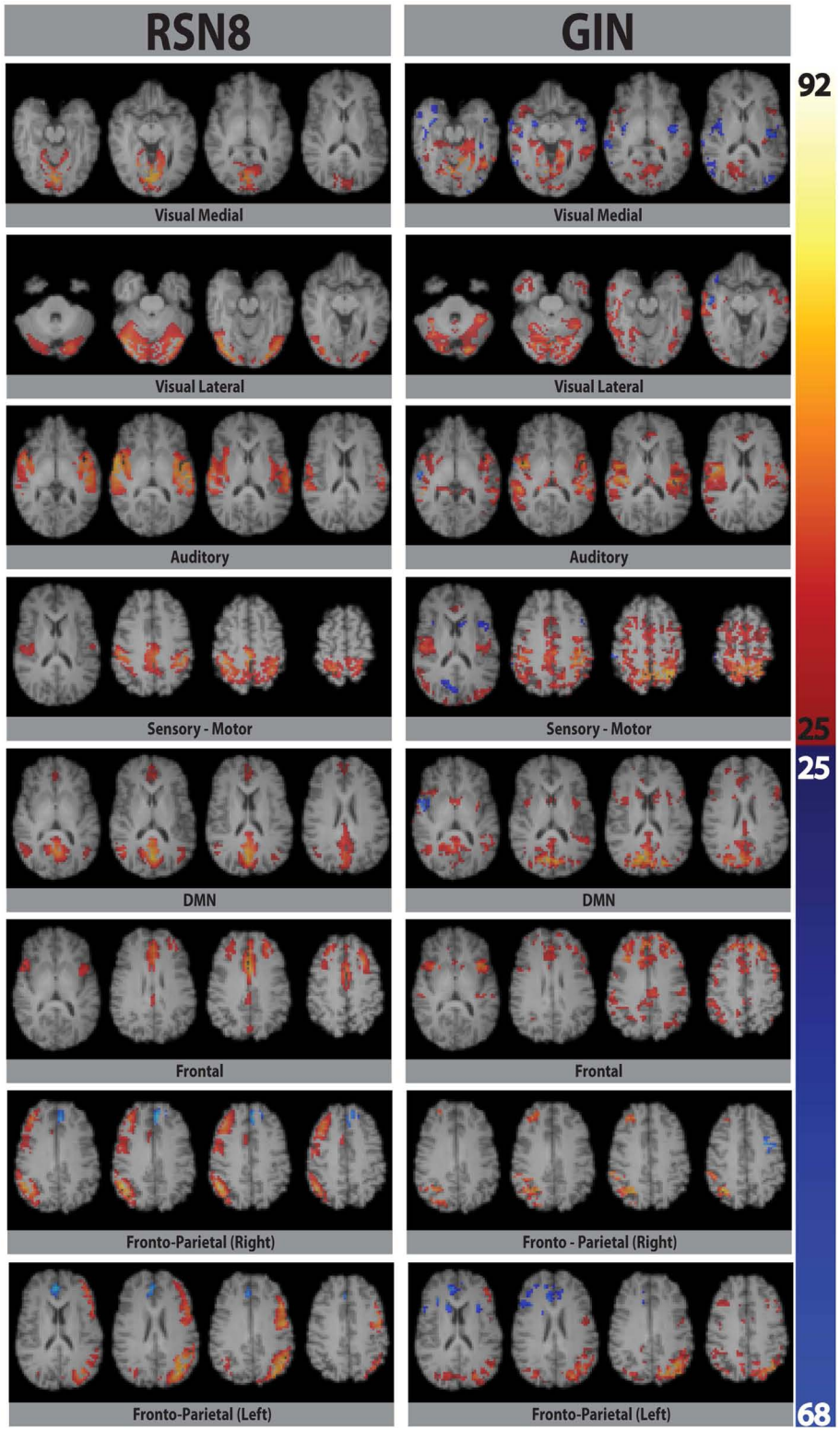

FIGURE 2 | Eight prototypical RSNs (Beckmann et al., 2005) and the corresponding dual regression maps (in *z*-scores) overlaid on the four most representative slices for a single subject.

Table 1 | DICE overlap scores for all the subjects and RSNs.

	Visual medial	Visual lateral	Auditory	Sensory motor	DMN	Frontal	Fronto parietal (right)	Fronto parietal (left)	Mean ± SD
S1	0.25	0.44	0.40	0.36	0.44	0.52	0.33	0.43	0.39 ± 0.08
S2	0.34	0.39	0.49	0.14	0.39	0.33	0.30	0.29	0.33 ± 0.10
S3	0.30	0.37	0.42	0.37	0.36	0.52	0.43	0.44	0.40 ± 0.07
S4	0.29	0.33	0.40	0.34	0.42	0.54	0.45	0.43	0.40 ± 0.08
S5	0.29	0.36	0.47	0.43	0.39	0.53	0.44	0.43	0.42 ± 0.07
S6	0.28	0.33	0.46	0.39	0.33	0.55	0.38	0.38	0.39 ± 0.08

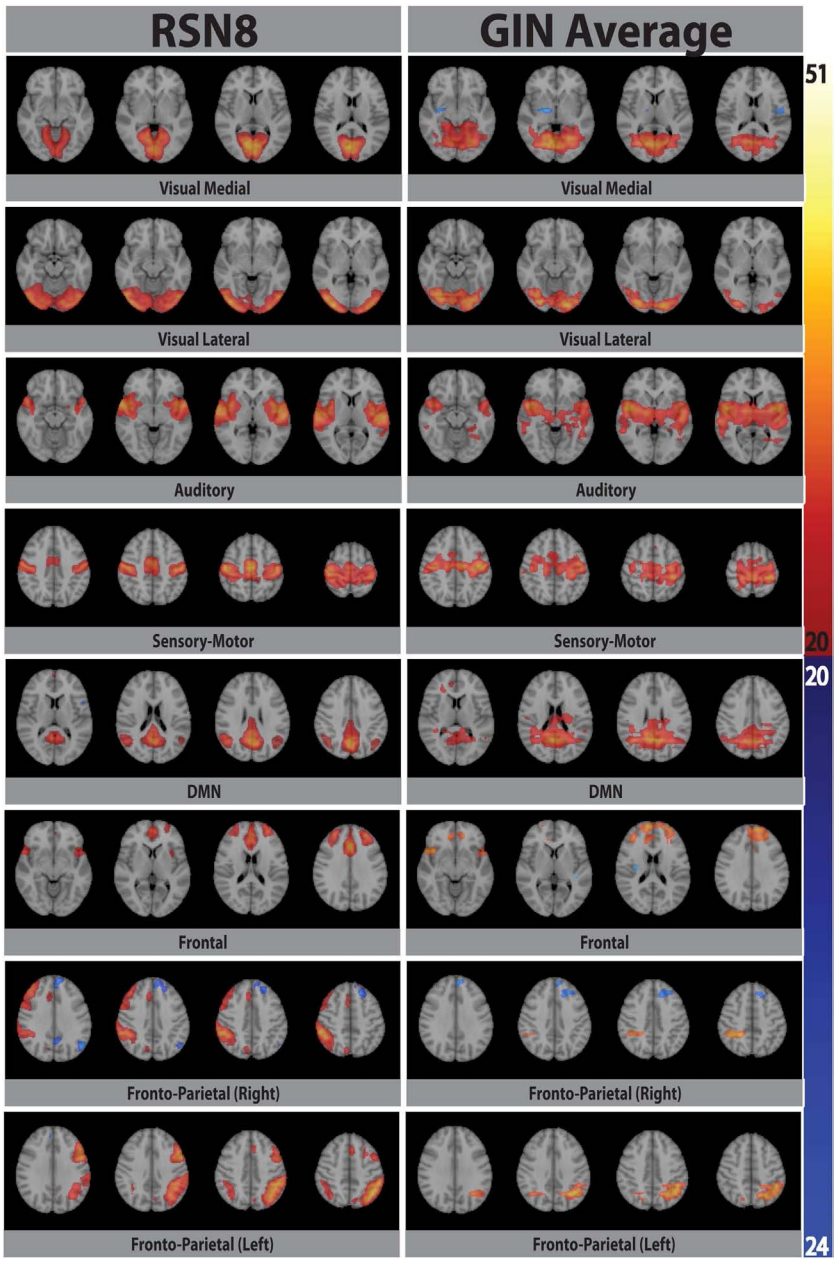

FIGURE 3 | Eight prototypical RSNs (Beckmann et al., 2005) and the corresponding dual regression maps (in *z*-scores) averaged over all subjects and overlaid on the four most representative slices in MNI space.

The similarity and spatial overlap between the dual regression maps and the typical RSNs is quantified with the DICE overlap score for all the subjects and RSNs in **Table 1**. The group level average of dual regression maps is shown in **Figure 3**. As the effective spatial resolution of GIN in the left-right direction is considerably reduced as a tribute to the high temporal resolution compared to fully encoded acquisitions the RSN maps are typically larger.

Figure 4 shows the normalized frequency spectra of all RSNs (in green) and their averages (in black) for all the subjects below 0.2 Hz. Most of the RSNs' power reduces significantly above 0.1 Hz and the RSNs have similar frequency spectra within subjects. However, there's considerable variation between the subjects' average frequency spectra. **Figure 5**, on the other hand, shows each RSNs' frequency spectra plotted for each subject (in green) and averaged over subjects (in black).

DISCUSSION

One very important point for using fast sampling in fMRI is that the main physiological fluctuations are sampled without aliasing into functional relevant frequency bands. For the interpretation of RSNs the breathing frequency is particularly problematic as the related frequency band is close to those frequencies commonly associated with RSNs. This has stirred some discussion to whether RSNs are an artifact of physiological signals (Birn et al., 2008; Birn, 2012). By using GIN, we are not only able to acquire the data fast enough but we can also correct for respiratory fluctuations, mostly due to bulk susceptibility changes, by using the information derived from the data itself. This can be seen from the blue curve in **Figure 1B** where respiration related signal changes are located in the frequency band of 0.15–0.25 Hz and are not only not aliased into lower frequencies, but also corrected for (red line). Since the phase drift time course is dominated by the global respiration signal, it matches the data within the same frequency band.

The phase drift time course does not carry much information about the cardiac signal (so very little variation around the principal cardiac frequency is removed), but this is of less concern as the frequency band is far from the typical RSN frequencies. Cardiac signals are much smaller in magnitude compared to respiration since they are localized to specific regions whereas respiration is a more global effect.

Within each subject we found very similar frequency characteristics for all RSNs, and that the variation over subjects was much higher than the variation over RSNs. Similar results have been reported in the literature (Niazy et al., 2011). These results could very likely be due to the result of differences of the hemodynamic response function (HRF) which is known to have high power in these frequencies (<0.1 Hz).

While the spatial fidelity of RSNs was not the specific focus of this study due to the inherent lower spatial resolution of GIN, all RSNs were spatially matched by their dual regression GIN counterparts, some (DMN, frontal) better than the others (fronto-parietal right, visual), however both the fronto-parietal networks – including their associated anti-correlated clusters – are recovered with GIN resting state data. As GIN does not have any gradient encoding in the left-right direction but uses the coil sensitivity information

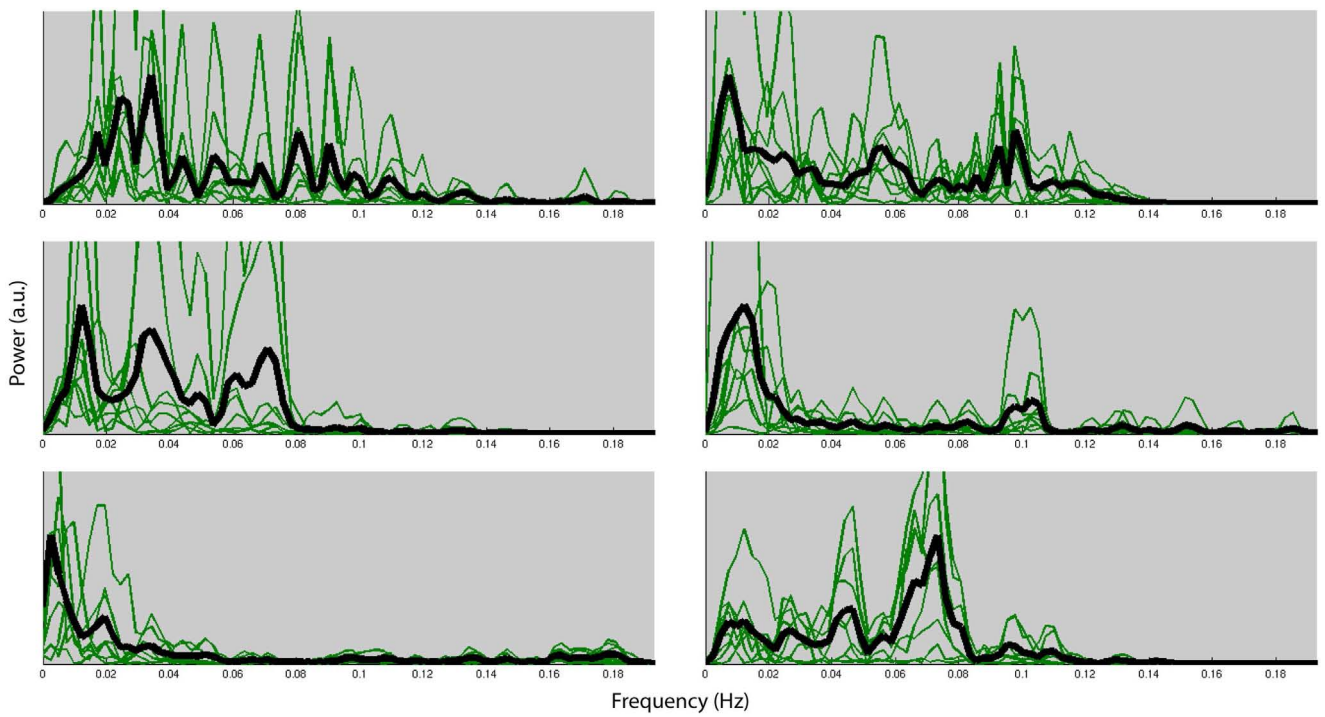

FIGURE 4 | Normalized frequency spectra of all RSNs (in green) and their average (in black) for each of the six subjects up to 0.2 Hz. Variation over subjects is much higher than the variation over RSNs.

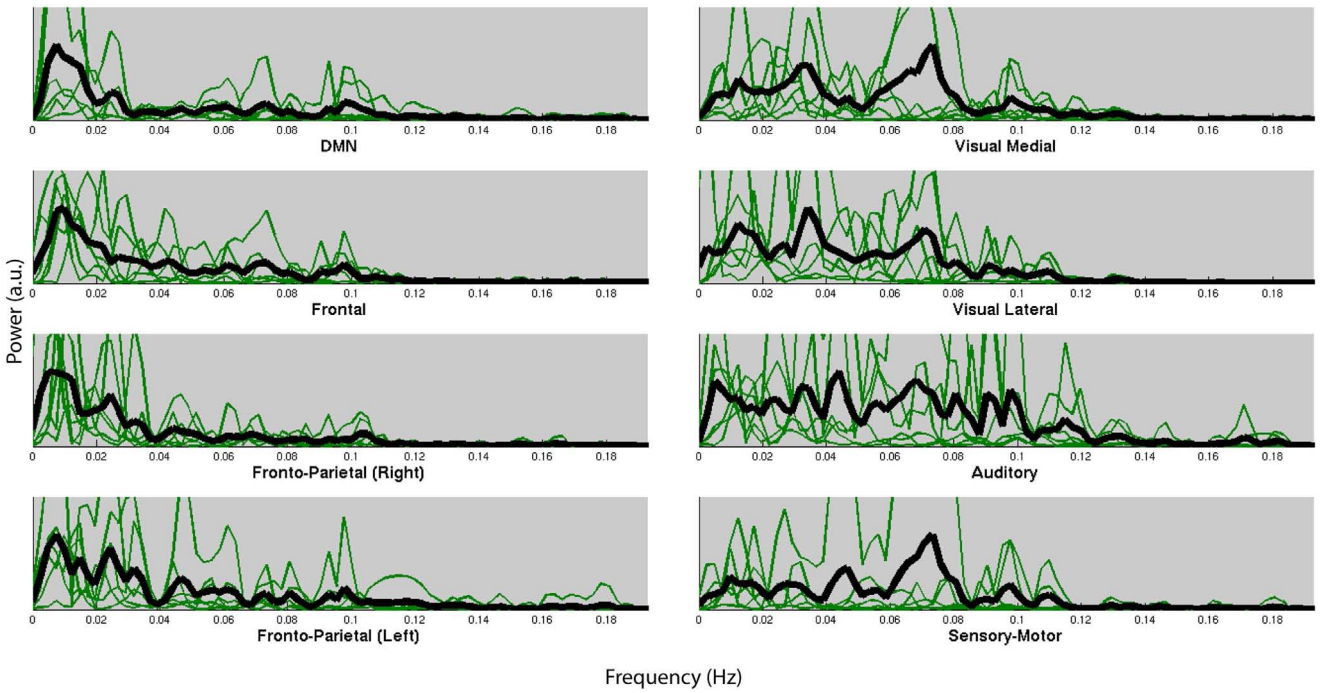

FIGURE 5 | Normalized frequency spectra of all RSNs (in green) and their average over subjects (in black) for each of the 8 RSNs up to 0.2 Hz. RSNs do not have specific frequencies associated with all the subjects.

to separate the aliased voxels, this inevitably results in the trade off spatial resolution for increased temporal resolution. The effective resolution depends on the independent and uncoupled information available from the coil channels. In general, the effective resolution is higher for GM than white matter and poses fewer problems for fMRI. Naturally, the lower spatial resolution of GIN leads to a larger spatial extent especially in the left-right direction for some of the networks, leading to some of the relatively low DICE scores in **Table 1**. Another drawback of low TR acquisitions and GIN is the abundance of physiological noise related components obtained with regular ICA as they dominate the total variance in the data. The dual regression approach used in the study enabled to directly obtain network specific frequency spectra and overcome the disadvantages of GIN and low TR acquisitions.

Studies related to temporal ICA (Smith et al., 2012) and the high frequency content of RSNs (Niazy et al., 2011; van Oort et al., 2012) would certainly benefit from the large number of time points obtained with GIN in relatively short scan times.

REFERENCES

Beall, E. B., and Lowe, M. J. (2007). Isolating physiologic noise sources with independently determined spatial measures. *Neuroimage* 37, 1286–1300.

Beckmann, C. F., DeLuca, M., Devlin, J. T., and Smith, S. M. (2005). Investigations into resting-state connectivity using independent component analysis. *Philos. Trans. R. Soc. Lond. B Biol. Sci.* 360, 1001–1013.

Birn, R. M. (2012). The role of physiological noise in resting-state functional connectivity. *Neuroimage* 62, 1–7.

Birn, R. M., Murphy, K., and Bandettini, P. (2008). The effect of respiration variations on independent component analysis results of resting state functional connectivity. *Hum. Brain Mapp.* 29, 740–750.

Biswal, B., Yetkin, F. Z., Haughton, V. M., and Hyde, J. S. (1995). Functional connectivity in the motor cortex of resting human brain using echo-planar MRI. *Magn. Reson. Med.* 34, 537–541.

Boyacioglu, R., and Barth, M. (2012a). "Filtering of physiological signals for high temporal resolution (50 ms) generalized inverse imaging (GIN) fMRI data," in *ESMRMB*, Lisbon. [Abstract #375].

Boyacioglu, R., and Barth, M. (2012b). Generalized inverse imaging (GIN): ultrafast fMRI with physiological noise correction. *Magn. Reson. Med.* doi:10.1002/mrm.24528

Damoiseaux, J. S., Rombouts, S. A. R. B., Barkhof, F., Scheltens, P., Stam, C. J., Smith, S. M., et al. (2006). Consistent resting-state networks. *Proc. Natl. Acad. Sci. U.S.A.* 103, 13848–13853.

De Luca, M., Beckmann, C. F., De Stefano, N., Matthews, P. M., and Smith, S. M. (2006). fMRI resting state networks define distinct modes of long-distance interactions in the human brain. *Neuroimage* 29, 1359–1367.

Feinberg, D. A., Moeller, S., Smith, S. M., Auerbach, E., Ramanna, S., Glasser, M. F., et al. (2010). Multiplexed echo planar imaging for sub-second whole brain fMRI and fast diffusion imaging. *PloS ONE* 5:e15710. doi:10.1371/journal.pone.0015710

Feinberg, D. A., and Yacoub, E. (2012). The rapid development of high speed, resolution and precision in fMRI. *Neuroimage* 62, 720–725.

Filippini, N., MacIntosh, B. J., Hough, M. G., Goodwin, G. M., Frisoni, G. B., Smith, S. M., et al. (2009). Distinct patterns of brain activity in young carriers of the APOE-epsilon4 allele. *Proc. Natl. Acad. Sci. U.S.A.* 106, 7209–7214.

Hennig, J. (2012). Functional spectroscopy to no-gradient fMRI. *Neuroimage* 62, 693–698.

Laird, A. R., Fox, P. M., Eickhoff, S. B., Turner, J. A., Ray, K. L., McKay, D. R., et al. (2011). Behavioral interpretations of intrinsic connectivity networks. *J. Cogn. Neurosci.* 23, 4022–4037.

Lee, H.-L., Zahneisen, B., Hugger, T., Levan, P., and Hennig, J. (2012). Tracking dynamic resting-state networks at higher frequencies using MR-encephalography. *Neuroimage* 65, 216–222.

Lin, F.-H., Tsai, K. W. K., Chu, Y.-H., Witzel, T., Nummenmaa, A., Raij,

T., et al. (2012). Ultrafast inverse imaging techniques for fMRI. *Neuroimage* 62, 699–705.

Moeller, S., Yacoub, E., Olman, C. A., Auerbach, E., Strupp, J., Harel, N., et al. (2009). Multiband multislice GE-EPI at 7 tesla, with 16-fold acceleration using partial parallel imaging with application to high spatial and temporal whole-brain fMRI. *Magn. Reson. Med.* 63, 1144–1153.

Niazy, R. K., Xie, J., Miller, K., Beckmann, C. F., and Smith, S. M. (2011). Spectral characteristics of resting state networks. *Prog. Brain Res.* 193, 259–276.

Särkkä, S., Solin, A., Nummenmaa, A., Vehtari, A., Auranen, T., Vanni, S., et al. (2012). Dynamic retrospective filtering of physiological noise in BOLD fMRI: DRIFTER. *Neuroimage* 60, 1517–1527.

Setsompop, K., Gagoski, B. A., Polimeni, J. R., Witzel, T., Wedeen, V. J., and Wald, L. L. (2012). Blipped-controlled aliasing in parallel imaging for simultaneous multislice echo planer imaging with reduced g-factor penalty. *Magn. Reson. Med.* 67, 1210–1224.

Smith, S. M., Fox, P. T., Miller, K. L., Glahn, D. C., Fox, P. M., Mackay, C. E., et al. (2009). Correspondence of the brain's functional architecture during activation and rest. *Proc. Natl. Acad. Sci. U.S.A.* 106, 13040–13045.

Smith, S. M., Miller, K. L., Moeller, S., Xu, J., Auerbach, E. J., Woolrich, M. W., et al. (2012). Temporally-independent functional modes of spontaneous brain activity. *Proc. Natl. Acad. Sci. U.S.A.* 109, 3131–3136.

van Oort, E., Norris, D., Smith, S. M., and Beckmann, C. F. (2012). "Resting state networks are characterized by high frequency BOLD fluctuations," in *OHBM*, Beijing. [Abstract #739].

Zahneisen, B., Hugger, T., Lee, K. J., Levan, P., Reisert, M., Lee, H.-L., et al. (2012). Single shot concentric shells trajectories for ultra fast fMRI. *Magn. Reson. Med.* 68, 484–494.

Conflict of Interest Statement: The authors declare that the research was conducted in the absence of any commercial or financial relationships that could be construed as a potential conflict of interest.

Received: 13 December 2012; accepted: 09 April 2013; published online: 23 April 2013.

Citation: Boyacioglu R, Beckmann CF and Barth M (2013) An investigation of RSN frequency spectra using ultra-fast generalized inverse imaging. Front. Hum. Neurosci. ***7****:156. doi: 10.3389/fnhum.2013.00156*

frontiers in
HUMAN NEUROSCIENCE

ORIGINAL RESEARCH ARTICLE
published: 29 May 2013
doi: 10.3389/fnhum.2013.00235

Combination of resting state fMRI, DTI, and sMRI data to discriminate schizophrenia by *N*-way MCCA + jICA

Jing Sui [1,2*†], ***Hao He*** [1,3†], ***Qingbao Yu*** [1], ***Jiayu Chen*** [1,3], ***Jack Rogers*** [4], ***Godfrey D. Pearlson*** [5,6,7], ***Andrew Mayer*** [1,8,9], ***Juan Bustillo*** [8,9], ***Jose Canive*** [8,9,10] ***and Vince D. Calhoun*** [1,3,5]

[1] *The Mind Research Network, Lovelace Biomedical and Environmental Research Institute, Albuquerque, NM, USA*
[2] *LIAMA Center for Computational Medicine, National Laboratory of Pattern Recognition, Institute of Automation, Chinese Academy of Sciences, Beijing, China*
[3] *Department of ECE, University of New Mexico, Albuquerque, NM, USA*
[4] *Division of Natural Science, New College of Florida, Sarasota, FL, USA*
[5] *Olin Neuropsychiatry Research Center, Hartford, CT, USA*
[6] *Department of Psychiatry, Yale University, New Haven, CT, USA*
[7] *Department of Neurobiology, Yale University, New Haven, CT, USA*
[8] *Department of Psychiatry, University of New Mexico, Albuquerque, NM, USA*
[9] *Department of Neuroscience, University of New Mexico, Albuquerque, NM, USA*
[10] *Psychiatry Research Program, New Mexico VA Health Care System, Albuquerque, NM, USA*

Edited by:
Veronika Schöpf, Medical University Vienna, Austria

Reviewed by:
Robert C. Welsh, University of Michigan, USA
Georg Langs, Medical University of Vienna, Austria

****Correspondence:***
Jing Sui, The Mind Research Network, 1101 Yale Blvd, NE, Albuquerque, NM 87106, USA
e-mail: kittysj@gmail.com

†Jing Sui and Hao He are co-first authors for this paper.

Multimodal brain imaging data have shown increasing utility in answering both scientifically interesting and clinically relevant questions. Each brain imaging technique provides a different view of brain function or structure, while multimodal fusion capitalizes on the strength of each and may uncover hidden relationships that can merge findings from separate neuroimaging studies. However, most current approaches have focused on pair-wise fusion and there is still relatively little work on *N*-way data fusion and examination of the relationships among multiple data types. We recently developed an approach called "mCCA + jICA" as a novel multi-way fusion method which is able to investigate the disease risk factors that are either shared or distinct across multiple modalities as well as the full correspondence across modalities. In this paper, we applied this model to combine resting state fMRI (amplitude of low-frequency fluctuation, ALFF), gray matter (GM) density, and DTI (fractional anisotropy, FA) data, in order to elucidate the abnormalities underlying schizophrenia patients (SZs, $n = 35$) relative to healthy controls (HCs, $n = 28$). Both modality-common and modality-unique abnormal regions were identified in SZs, which were then used for successful classification for seven modality-combinations, showing the potential for a broad applicability of the mCCA + jICA model and its results. In addition, a pair of GM-DTI components showed significant correlation with the positive symptom subscale of Positive and Negative Syndrome Scale (PANSS), suggesting that GM density changes in default model network along with white-matter disruption in anterior thalamic radiation are associated with increased positive PANSS. Findings suggest the DTI anisotropy changes in frontal lobe may relate to the corresponding functional/structural changes in prefrontal cortex and superior temporal gyrus that are thought to play a role in the clinical expression of SZ.

Keywords: multimodal fusion, mCCA + jICA, resting state fMRI, DTI, sMRI, schizophrenia, ALFF, GM

INTRODUCTION

Multimodal brain imaging techniques are playing increasingly important roles in elucidating structural and functional properties in normal and diseased brains, as well as providing the conceptual glue to bind together data from multiple types or levels of analysis. The related computational methods are also valuable for clinical research on the mechanisms of disease progression. The goal of multimodal fusion is to capitalize on the strength of each imaging modality as well as their inter-relationships in a joint analysis, rather than to analyze separately.

Each imaging modality provides a different view of brain function or structure, and data fusion capitalizes on the strengths of each imaging modality/task and their inter-relationships in a joint analysis, creating an important tool to help unravel the black box of psychotic disorders, such as schizophrenia (SZ) (Calhoun et al., 2006; Sui et al., 2012a). Recent advances in data fusion include integrating multiple (task) fMRI data sets (Sui et al., 2009b, 2010; Kim et al., 2010) from the same participant to specify common versus specific sources of activity to a greater degree than traditional general linear model-based approaches. This can increase confidence when making conclusions about the functional significance of brain regions and activation changes in brain diseases. In addition, the combination of function and structure may provide more informative insights into both altered brain patterns and connectivity (McCarley et al., 2008; Michael et al., 2010; Sui et al., 2011). For example, a lower and different function–structure connection is often found in patients with SZs compared with healthy controls (HCs) (Zhou et al., 2008; Venkataraman et al., 2010; Camchong

et al., 2011; Michael et al., 2011), while varied brain patterns are also identified frequently (Calhoun et al., 2008; Xu et al., 2009; Brown et al., 2012; Lu et al., 2012).

WHY GO BEYOND TWO MODALITIES?

However, most current approaches have focused on pair-wise fusion and there is still relatively little work on *N*-way data fusion and examination of the full relationships among multiple data types. Given the availability of more powerful MR scanners, there are typically more than two imaging modalities available for one participant. Hence, we believe the joint multivariate analysis of multiple data types (e.g., resting state fMRI, task-related fMRI, DTI, and sMRI) will improve our ability to understand brain diseases. We have proposed an *N*-way fusion model, "multi-set canonical correlation analysis (mCCA) + joint independent component analysis," i.e., "mCCA + jICA," which successfully identified both modal-common and modal-unique group-discriminative patterns for HCs and SZs via combination of task-related fMRI, DTI, and sMRI data (Sui et al., 2013). Considering the importance of the interpretation of multi-way features, the method and tool we propose will enable examination of full correspondence across *N* modalities by achieving reliable inter-modality associations and high decomposition accuracy together, thus making discoveries of changes in one modality causing related alterations in distant, but connected regions in other modalities possible.

To our knowledge, there have been only a few reports combining three or more types of brain imaging data to investigate brain disorders (e.g., Correa et al., 2009) examined changes that are related across fMRI, sMRI, and EEG data for SZ (Groves et al., 2011) compared Alzheimer's patients and age-matched controls by combining gray matter (GM) density and three diffusion data measures [fractional anisotropy (FA), mean diffusivity, and tensor mode]. For resting state fMRI data, several pair-wise fusion applications have been reported (Teipel et al., 2010; Long et al., 2012; Segall et al., 2012); however, there has been no report that combine resting state fMRI with other two or more different types of brain imaging data to study SZ.

In this project, we applied the *N*-way fusion model, "mCCA + jICA" (Sui et al., 2013), to compare not only modality-common but also modality-unique abnormalities among resting state fMRI, sMRI, and DTI data, which is the first attempt to combine such three types of data to discriminate SZ patients ($n = 35$) from HCs ($n = 28$). *N*-way fusion of brain imaging data is more challenging than pair-wise combination, since many fusion applications rely on studying correlations between highly distilled measures (e.g., small regions of interest), while there is still relatively little examination of the full relationships among data types. The method and tools we propose will enable such an examination and can be potentially useful for identification of unique biomarkers of brain disorders. Furthermore, the high-dimensional neuroimaging data is typically very noisy and massive redundancy reduction is usually necessary to facilitate the identification of relationships among modalities. For this purpose, each modality is first reduced to a "feature" for each subject, which tends to be more tractable than working with the large-scale original data (Calhoun and Adali, 2009) and provides a simpler space to link the data (Smith et al., 2009), e.g., an fMRI contrast map from the general linear model, a GM segmentation image from the sMRI scan and voxel-wise DTI measures such as FA. For resting state fMRI data, we used the amplitude of low-frequency fluctuation (ALFF) as fusion input (Zang et al., 2007; Zou et al., 2008; Calhoun and Allen, 2013), which has been used previously for default mode or other applications in multiple papers (Calhoun et al., 2012; Turner et al., 2012; Yu et al., 2012b, 2013).

MATERIALS AND METHODS

THEORY DEVELOPMENT

Existing multivariate fusion methods have different optimization priorities and limitations: some enable common as well as distinct levels of connection among modalities, such as mCCA (Correa et al., 2009) and partial least squares (PLS) (Lin et al., 2003; Chen et al., 2009), but their separated sources may not be sufficiently spatially sparse. For example, mCCA maximizes the inter-subject covariation across two sets of features and generates two linked variables, one from each dataset, i.e., canonical variants (CVs); which correlate with each other only on the same indices (rows) and their corresponding correlation values are called canonical correlation coefficients (CCC). This strategy allows for both common and distinct aspects of two features, but the brain maps of several components may look similar when the CCCs are not sufficiently distinct. Some approaches perform well in spatial decomposition, such as jICA (Calhoun et al., 2006) and linked ICA (Groves et al., 2012), which aim at maximizing the independence among estimated sources combining more than two modalities, but only allow a common mixing matrix. These two methods enable detection of features common to all modalities at the expense of features which may be distinct to one or more of them (a situation which becomes more likely when combining more than two modalities). Multiple previous studies that combined function and structure (Olesen et al., 2003; Rykhlevskaia et al., 2008; Camara et al., 2010; Sui et al., 2012b) provide support for the assumption that components decomposed from each modality have some degree of correlation between their mixing profiles among subjects. This motivates our data-driven model that is optimized for both flexibility in inter-modal associations and high capability on source separation.

The basic strategy of mCCA + jICA is shown in **Figure 1**. MCCA is first adopted to project the data in a space so that the correlations among mixing profiles ($\mathbf{D}_k, k = 1, 2, \ldots, n$) of n ($n = 3$ in this study) modalities are jointly maximized (in their sum of squared correlations). The resulting CVs $\mathbf{D}_k$ are sorted by correlation which provides a closer initial match to the potential highly or weakly correlated mixing profiles between components, which will make the subsequent application of jICA more reliable. At this time, the associated maps $\mathbf{C}_k$ may not be completely separated by mCCA. We then apply jICA on the concatenated maps ($\mathbf{C}_1$, $\mathbf{C}_{2,\ldots,}$ $\mathbf{C}_n$) to obtain the final maximally independent source $\mathbf{S}_k$. In other words, mCCA first relates multiple datasets with flexible linkages (correlation) in their mixing matrices, which matches well with the assumptions of jICA that is subsequently applied to the joint spatial maps. Hence, mCCA and jICA are complementary to one another, and can relax the limitations of each listed above if

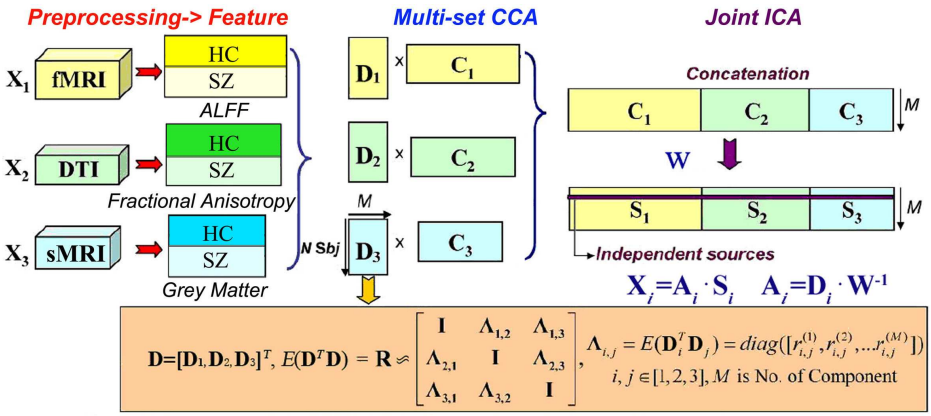

FIGURE 1 | *N*-way mCCA + jICA fusion strategy of for real human data ($n = 3$ in this study).

used together, generating both highly and weakly correlated joint components that are independent.

We assume that the multimodal dataset $\mathbf{X}_k$, is a linear mixture of M_k sources given by $\mathbf{S}_k$, mixed with a non-singular mixing matrix (or loading parameters) $\mathbf{A}_k$ for each, k denotes modality.

$$\mathbf{X}_k = \mathbf{A}_k\mathbf{S}_k \; k = 1, 2, \ldots, n \tag{1}$$

where $\mathbf{X}_k$ is a subjects-by-voxels feature matrix (we use voxels for our description but it could also be, e.g., time points or genes). The sources $\mathbf{S}_k$, are distinct within each dataset, while the columns of $\mathbf{A}_i$ and $\mathbf{A}_j$ have higher correlation only on their corresponding indices, $i, j \in \{1, 2, \ldots, n\}$ $i \neq j$ are modality number. Given that there are N subjects, typically, the number of voxels L in $\mathbf{X}_k$ is much larger than N. Due to the high dimensionality and high noise levels in the brain imaging data, order selection is critical to avoid over fitting the data. Using the improved minimum description length (MDL) criterion (Li et al., 2007), the number of independent components M_k are estimated for each modality and we set the final component number for jICA as $M = \max(M_1, M_2, \ldots, M_n)$. Dimension reduction is then performed on $\mathbf{X}_k$ using singular value decomposition to determine the signal subspace given by

$$\mathbf{Y}_k = \mathbf{X}_k\mathbf{E}_k \; k = 1, 2, \ldots, n \tag{2}$$

where $\mathbf{Y}_k$ is in size of $N \times M$ and $\mathbf{E}_k$ contains eigenvectors corresponding to significant (the top M highest) singular values. Multi-set CCA (Li et al., 2009) is thus performed on $\mathbf{Y}_k$, generating the CVs $\mathbf{D}_k = \mathbf{Y}_k\mathbf{w}_k$ by maximizing the sum-of-squares of all correlation values in the corresponding columns of $\mathbf{D}_k$ so that

$$E\{\mathbf{D}_k^T\mathbf{D}_k\} = \mathbf{I};\; E\{\mathbf{D}_k^T\mathbf{D}_j\} \approx diag(r_{k,j}^{(1)}, r_{k,j}^{(2)} \ldots r_{k,j}^{(M)}) \tag{3}$$

where $k, j \in \{1, 2, \ldots, n\}$, $k \neq j$. Based on the linear mixture model, we simultaneously obtain the associated components $\mathbf{C}_k$ via $\mathbf{X}_k = \mathbf{D}_k \cdot \mathbf{C}_k$, $\mathbf{C}_k = \text{pinv}(\mathbf{D}_k) \cdot \mathbf{X}_k$. However, the performance of mCCA for blind source separation (BSS) may suffer when $r_{k,j}^{(1)}, r_{k,j}^{(2)} \ldots r_{k,j}^{(M)}$ are very close in values, which might occur in applications using real brain data, since the multimodal connection among components usually are not very high and could be similar in value (Sui et al., 2011). Therefore, $\mathbf{C}_k$ will typically be a set of sources that are not completely independent. Joint ICA is then implemented on the concatenated maps ($\mathbf{C}_1, \mathbf{C}_2, \ldots, \mathbf{C}_n$), to maximize the independence among joint components by reducing their second and higher order statistical dependencies, as in Eq. 4. ICA as a central tool for BSS has been studied extensively and we utilized Infomax (Bell and Sejnowski, 1995) in our work due to its good stability.

$$[\mathbf{S}_1, \mathbf{S}_2 \ldots \mathbf{S}_n] = \mathbf{W} \cdot [\mathbf{C}_1, \mathbf{C}_2 \ldots \mathbf{C}_n] \tag{4}$$

Finally, n sets of independent components $\mathbf{S}_k$ are achieved, with their corresponding mixing matrices $\mathbf{A}_k$ linked via correlation. The proposed scheme "mCCA + jICA" can be summarized as shown in **Figure 1**.

$$\mathbf{X}_k = (\mathbf{D}_k \cdot \mathbf{W}^{-1}) \cdot \mathbf{S}_k,\; \mathbf{A}_k = \mathbf{D}_k \cdot \mathbf{W}^{-1} \tag{5}$$

Multi-set canonical correlation analysis + jICA was compared with its alternatives in simulation in Sui et al. (2013), where results show that combination of mCCA and jICA mitigates the performance deficits of each and achieves more reliable and better separation on both sources and mixing matrices. Interestingly, when the estimated component number is higher than the ground truth, the source estimation performance continues to be high, while the estimation of mixing coefficients achieves best performance when M equals to true values.

HUMAN BRAIN DATA

Participants

Multi-set canonical correlation analysis + jICA was applied to DTI, resting state fMRI, and sMRI data of 63 subjects recruited as part of a multimodal SZ center for biomedical research excellence (COBRE) study at the Mind Research Network[1]. Informed consent

[1]http://cobre.mrn.org

was obtained from all subjects according to institutional guidelines required by the Institutional Review Board at the University of New Mexico (UNM). **Table 1** lists the demographic information. All subjects were screened and excluded if they had history of neurological disorder, history of mental retardation, history of severe head trauma with more than 5 min loss of consciousness, or history of substance abuse, or dependence within the last 12 months (except for nicotine). HCs were free from any Axis I disorder, as assessed with the SCID-NP (Structured Clinical Interview for DSM-IV-TR, Non-patient version). Patients met criteria for SZ defined by the DSM-IV-TR based on the SCID-P interview (First et al., 1995). All patients were on stable medication prior to the fMRI scan session. The two groups did not differ with regard to age, gender, and ethnicity, see **Table 1**. Symptom scores were determined based on the positive and negative syndrome scale (PANSS) (Kay et al., 1987).

Imaging parameters

All the data were collected on a 3-T Siemens Trio scanner with a 12-channel radio frequency coil at the Mind Research Network. The imaging parameters were as follows: *fMRI*: resting state data were collected with single-shot full *k*-space echo-planar imaging (EPI) with ramp sampling correction using the inter commissural line (AC/PC) (anterior commissure/posterior commissure) as a reference (TR = 2 s, TE = 29 ms, matrix size = 64 × 64, flip angle = 75 °, slice thickness = 3.5 mm, slice gap = 1.05 mm, field of view (FOV) 240 mm, matrix size = 64 × 64, voxel size = 3.75 mm × 3.75 mm × 4.55 mm. *sMRI*: a multi-echo MPRAGE sequence was used with the following parameters: TR/TE/TI = 2530/(1.64, 3.5, 5.36, 7.22, 9.08)/900 ms, flip angle = 7 °, FOV = 256 × 256 mm, slab thickness = 176 mm, matrix size = 256 × 256 × 176, Voxel size = 1 mm × 1 mm × 1 mm, Pixel bandwidth = 650 Hz, Total scan time = 6 min. *DTI*: data was collected along the AC/PC line, throughout the whole brain, FOV = 256 × 256 mm, slice thickness = 2 mm, NEX (number of excitations) = 1, TE = 84 ms, TR = 9,000 ms. A multiple channel radio frequency coil was used, with GRAPPA (generalized autocalibrating partially parallel acquisition) (×2), 30 gradient directions with a diffusion sensitivity, $b = 800$ s/mm^2. The $b = 0$ experiment was repeated five times, and equally inter-spread between the 30 gradient directions. All $b = 0$ images were registered to the first $b = 0$ image with a six degrees-of-freedom transformation. This was followed by registering the $b = 800$ s/mm^2 image to the $b = 0$ image immediately before it by an affine 12 degrees-of-freedom transformation. The two transformations were multiplied and then one transformation applied to the $b = 800$ s/mm^2 image to align it to the first $b = 0$ image. This resulted in all images being registered to the first $b = 0$ image. FLIRT (FMRIB's Linear Image Registration Tool) was used for all registration steps.

Table 1 | Demographic information of the subjects.

	Num	Age	Gender	Ethnicity
HC	28	39 ± 15	21M/7F	21 Whites
SZ	35	36 ± 12	26M/9F	22 Whites
p Value		0.36	0.99	0.58

Resting state fMRI

Resting-state scans were a minimum of 5 min, 4 s in duration (152 volumes). Subjects were instructed to keep their eyes open during the scan and stare passively at a foveally presented fixation cross, as this is suggested to facilitate network delineation compared to eyes-closed conditions and helps ensure that subjects are awake.

fMRI preprocessing

SPM8 software package[2] was employed to perform fMRI preprocessing. Slice timing was performed with the middle slice as the reference frame. Images were realigned using INRIalign, a motion correction algorithm that is unbiased by local signal changes (Freire et al., 2002). Data were then spatially normalized into the standard Montreal Neurological Institute (MNI) space (Friston et al., 1995) with affine transformation followed by a nonlinear approach with 4 × 5 × 4 basis functions. Images (originally collected at 3.75 mm × 3.75 mm × 4.55 mm) were then slightly upsampled to 3 mm × 3 mm × 3 mm, resulting in a data cube of 53 × 63 × 46 voxels. Before smoothing, we further regress out the six motion parameters for each slice to remove the motion effect. Finally, data were spatially smoothed with a Gaussian kernel of full-width half maximum (FWHM) of 10 mm × 10 mm × 10 mm. For the rest fMRI, we extracted the voxel-wise ALFF to generate a map for each subject. The ALFF calculation consisted of computing the fast Fourier transform (FFT) of each voxel time series, taking the square root of the power spectrum to obtain amplitude, and averaging amplitude in (0.01, 0.1) Hz. Prior to computing ALFF, the original 4D fMRI data sets were divided by their global mean (over time and space) to normalize differences in scan intensity units. ALFF maps computed in this manner were used previously in a comparative classification analysis (Erhardt et al., 2011) and the use of ALFF maps in a "second-level" ICA has been previously studied (Calhoun and Allen, 2013).

DTI preprocessing

DTI data were preprocessed by FMRIB Software Library (FSL)[3] and consisted of the following steps: (a) quality check, any gradient directions with excessive motion or vibration artifacts were identified and removed; (b) motion and eddy current correction; (c) correction of gradient directions for any image rotation done during the previous motion correction step; (d) calculation of diffusion tensor and scalar measures such as FA, which were then smoothed and resized to a final 53 × 63 × 46 matrix for each subject, see more details in Sui et al. (2011).

sMRI preprocessing

sMRI data were also preprocessed using the SPM8 software package which was used to segment the brain into white-matter (WM), GM, and cerebral spinal fluid with unmodulated normalized parameters via the unified segmentation method (Ashburner and Friston, 2005). After segmentation, the GM images were smoothed to a FWHM Gaussian kernel of 10 mm (White et al., 2001) and

[2]http://www.fil.ion.ucl.ac.uk/spm/software/spm8
[3]www.fmrib.ox.ac.uk/fsl

re-sliced to a matrix of 53 × 63 × 46 voxels. Subject outlier detection was further performed using a spatial Pearson correlation with the template image, to ensure that all subjects were properly segmented (for details, see Segall et al., 2009).

Normalization

After feature extraction (preprocessing), the 3D brain images of each subject were reshaped into a one-dimensional vector and stacked, forming a matrix with dimensions of 63 × number of voxels for each of the three modalities. These three feature matrices were then normalized to have the same average sum-of-squares (computed across all subjects and all voxels/locus for each modality) to ensure all modalities had the same ranges. Following normalization, the relative scaling (a normalization factor) within a given data type was preserved (i.e., 1.08, 0.24, 0.39 for ALFF, FA, GM respectively), but the normalized input units have the same voxel-wise mean square variance for all modalities. Next, the data was processed via the pipeline shown in **Figure 1**, i.e., dimension reduction → multi-set CCA → jICA → component analysis. The component number was estimated using modified MDL (Li et al., 2007) to be 10, 5, 8 for fMRI, DTI, and sMRI respectively. We thus choose $M = 10$ for the following analysis since we have found that a slight overestimation of the component number does not adversely affect the results in simulation (Sui et al., 2011). Note that the estimated IC number is lower than that used for 4D fMRI data typically, since mCCA + jICA works on extracted features of interests, instead of the original imaging data. However, a considerable amount of variance is retained for the $M = 10$ case, i.e., 95, 96, 99% for fMRI, DTI, and sMRI respectively.

ANALYZING GENERATED COMPONENTS AND MIXING COEFFICIENTS

After applying the mCCA + jICA to the human brain data, independent component $\mathbf{S}_k$ and the mixing matrices $\mathbf{A}_k$ for each modality ($k = 3$ in this study) were generated, providing a variety of ways to analyze the inter-correlation between modalities as well as the group differences, as in Sui et al. (2011). In this paper, we are most interested in:

Shared/distinct abnormalities

Two-sample t-tests were performed on mixing coefficients of each IC for each modality (i.e., first 28 elements corresponding HC versus last 35 elements corresponding SZ from mth column of $\mathbf{A}_k$ for the mth IC of modality k), the results tell us which components are significantly abnormal in SZ. If the components of the same index show group differences in more than one modality, they are called modality-common (or joint) group-discriminative ICs. By contrast, if the component shows significant group difference only in a single modality, it is called a modality-unique group-discriminative IC. That are what we call shared or distinct abnormalities.

Inter-modality correlation

We also looked into the column-wise correlations between A_1, A_2, and A_3 pair wisely. It is likely that the joint group-discriminative components have a strong inter-modality correlation between their mixing coefficents, which indicates the interaction and correspondence among modalities.

Impact of clinical measures

The derived mixing coefficients also provide a way to investigate the relationships between the identified components and subjects' clinical data, e.g., the correlation between mixing coefficients of patients for each component and antipsychotic medication doses [standardized as olanzapine equivalents (Gardner et al., 2010)] or PANSS scores. In this paper, we computed the correlation with PANSS (Kay et al., 1987), which rate the scale of severity of positive, negative, and general symptoms in SZ.

Potential use for classification

To test the potential use of the identified group-discriminative components (i.e., corresponding rows of $\mathbf{S}_k$ of modality k), we next used them to generate features (e.g., the Z map above certain threshold) and train a classifier, to see whether they are able to predict diagnosis or serve as potential biomarkers, which may prove the great significance for multimodal analysis.

For each modality, we transferred the group-discriminating components (for ALFF and GM, we use only two ICs with minimum p values) into Z values and thresholded at $|Z| > 3.5$, generating a mask from each component. The masks of the same modality were then combined and applied to the raw input matrix of each modality, which served as the input to the further classification based on uni-modal and multimodal features. Each individual was assigned one of two class memberships (SZ versus HC). We trained four different classification algorithms: linear support vector machine (LSVM) (Cortes and Vapnik, 1995), radial basis function support vector machine (RSVM) (Amari and Wu, 1999), k-nearest neighbor algorithm (KNN) (Geva and Sitte, 1991), and Gaussian naïve bayes (GNB) (McCallum and Nigam, 1998). Each algorithm was trained on 50% of the data (randomly chosen samples) with 10-fold cross validation, and tested on the other half for 1000 times, with the mean and maximal success rate recorded. Because this paper is not mainly focused on classification, we will not address the details of each algorithm. One limitation of this experiment is that the data set used to identify group-discriminating components is the same as the one which we did classification with, since we don't have other similar resting fMRI-DTI-sMRI data at hand for cross validation and our main aim is to test whether mCCA + jICA is able to serve as an effective feature selection method for group prediction.

RESULTS

GROUP DIFFERENCES IN HUMAN BRAIN DATA

Two-sample t-tests found both modality-common group-discriminative ICs (e.g., IC6 and IC7 in green frames, as shown in **Figure 2**) as well as modality-unique group-discriminative ICs, e.g., GM_IC5, ALFF_IC3 in our case. Interestingly, the modal-connection between joint-discriminative ICs indicate significant correlations (GM-ALFF IC6: $r = 0.28$, $p = 0.025$; FA-GM IC7: $r = 0.38$, $p = 0.002$; FA-ALFF IC7: $r = 0.31$, $p = 0.015$) between their mixing profiles.

CORRELATION WITH PANSS SCORES

There was no significant correlation regarding the antipsychotic medication doses. However, two ICs: FA_IC4 (anterior thalamic radiation, ATR and superior longitudinal fasciculus, SLF) and

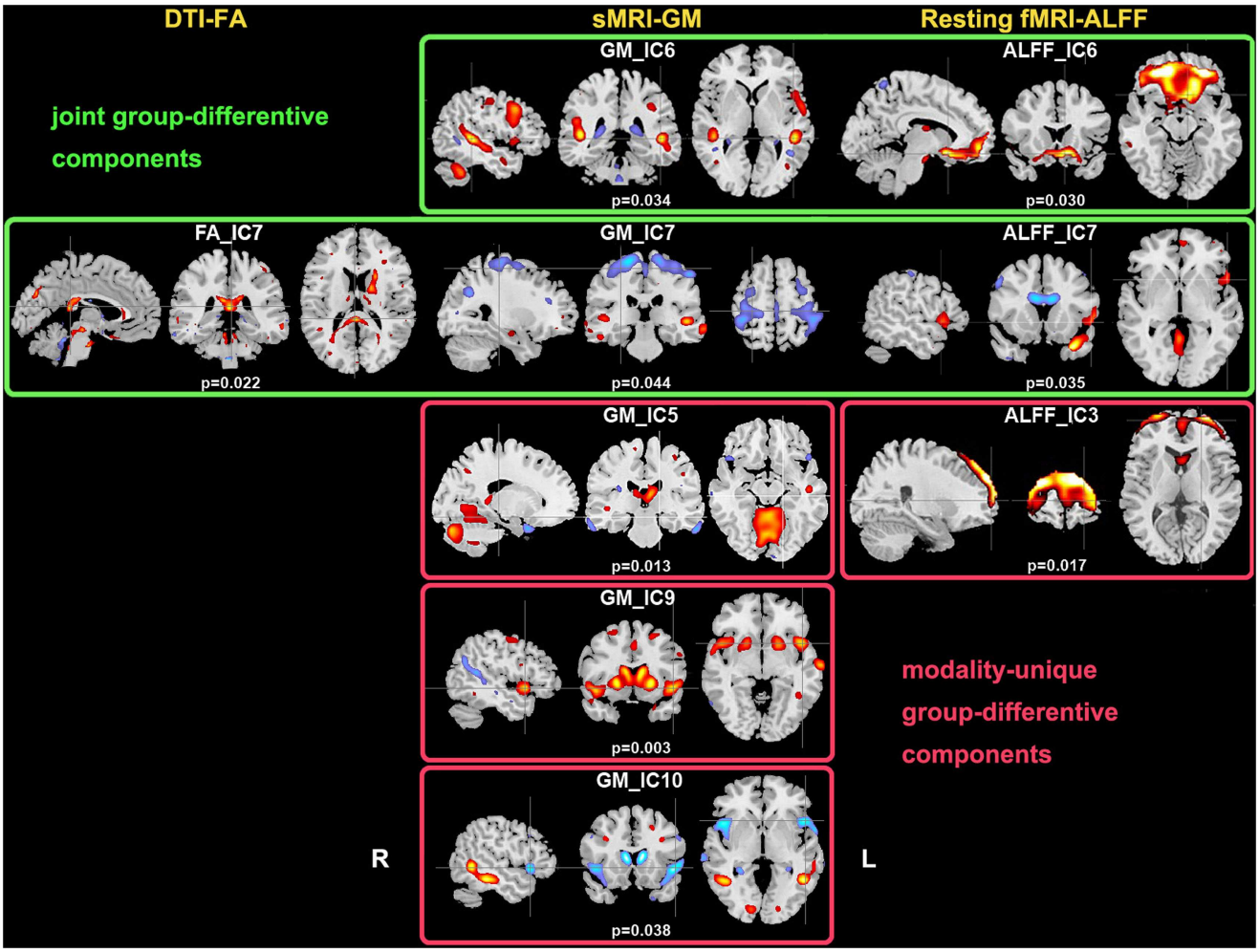

FIGURE 2 | Group-discriminating regions across three modalities, with a threshold of $|Z| > 2.5$. Two-sample *t*-tests were performed on mixing coefficients of each IC for each modality. If the components of the same index show group differences in more than one modality, they are called modality-common (or joint) group-discriminative ICs in green frames; otherwise, it is called a modality-unique group-discriminative IC, e.g., GM_IC5, ALFF_IC3 in red frames.

GM_IC4 (subregions of the default mode) were significantly correlated with positive PANSS scores, while there was no significant correlation with negative PANSS score. The scatter plots and linear trends are shown in **Figure 3**.

The specific identified regions of the components of interest and their abbreviations are summarized in **Table 2** for resting state fMRI components (Talairach labels), **Table 3** for DTI (WM tracts), and **Table 4** for sMRI (MNI labels) respectively. For fMRI and sMRI, each IC is transformed into a *Z* map by dividing its standard deviation across all voxels, and the voxels above the threshold ($|Z| > 2.5$) were converted from MNI coordinates to Talairach coordinates and entered into a database to provide anatomic and functional labels for the right (R) and left (L) hemispheres. The volume of identified voxels in each area is provided in cubic centimeters (cm^3). Within each area, the maximum *Z* value and its MNI coordinates are provided for all three tables. To summarize the WM results, we used the Johns Hopkins WM tractography atlas (from FSL) (Hua et al., 2008), from which 20 structures were identified; mostly large bundles. In **Table 3**, the WM tract labels, the identified volume (cc), and the percentage that indicates the overlap of the identified voxels with each WM tract are listed in detail.

CLASSIFICATION BASED ON SELECTED COMPONENTS

After transferring the group-discriminating components into *Z* values and thresholded at $|Z| > 3.5$, the mask from each component were generated and applied to the raw input matrix of each modality, resulting in three feature matrices in dimension of subject by voxels, i.e., FA: 63 × 312, ALFF 63 × 566, GM 63 × 1035, which served as the input to the further classification based on uni-modal and multimodal features.

Each individual was assigned one of two class memberships (SZ versus HC) and we have seven modal combinations (three single, three pair-wise, one three-way) as shown in **Figure 4**.

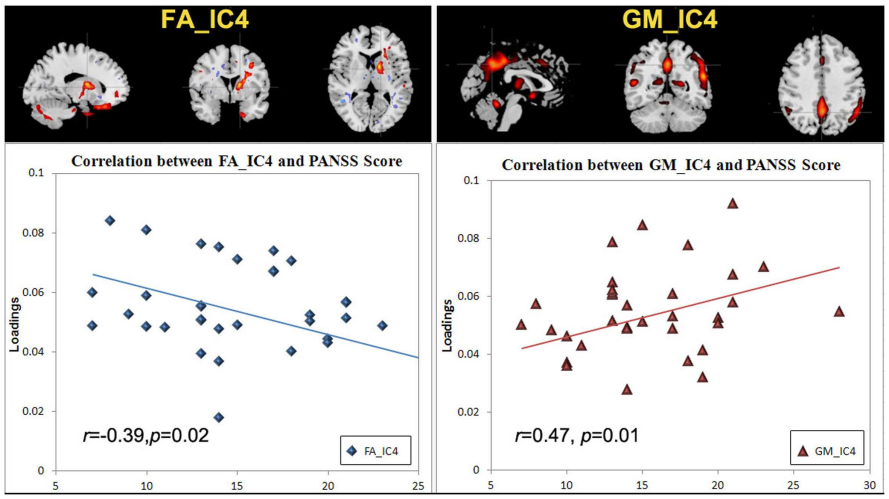

FIGURE 3 | The scatter plots and linear trends of components with significant correlation between positive PANSS score and its loadings.

After comparison, RSVM achieved the best classification accuracy among the four algorithms we trained with each of seven modal combinations; its mean, and maximum rates were summarized in **Figure 4**, where GM features obtained the highest accuracy in single modality, while FA + GM predict best among all seven modal combinations (mean 0.79, max 0.96).

DISCUSSION

In this paper we applied the mCCA + jICA model to three-way fusion of resting state fMRI, sMRI, and DTI data. The aim of the method is to identify precise correspondence among *n* data types and make possible the investigation of both shared and distinct abnormalities spanning multiple modalities for a specified brain disorder. Some abnormalities may occur in specific modalities, while others may be found in more than one modality simultaneously. Also, hidden linkages between components from different modalities may underlie in the data.

GROUP DIFFERENCES

IC 7 significantly differentiated SZ from HC in all three modalities, suggesting the following abnormalities in SZ: (a) prefrontal cortex and left superior temporal gyrus (STG) (rest fMRI); (b) ATR, corticospinal tract (CSF), and forceps major (FMAJ; WM, DTI); and (c) regions of the motor cortex, medial/superior frontal cortex, and temporal gyrus (GM density). Furthermore, these identified affected regions may share some underlying relationship in SZ. The FA changes in ATR, CST, and FMAJ were previously associated with disconnectivity of brain networks in SZ in separate studies (Schlosser et al., 2007; Friedman et al., 2008; Sussmann et al., 2009). In particular, ATR projects from the anterior and medial regions of the thalamus to the frontal lobe, while CST subserves motor control. Accordingly, GM_IC7 shows strong alterations in motor cortex and, corresponding nicely to findings in Douaud et al. (2007) where the abnormalities in the primary sensorimotor and premotor cortices and in WM CST tracts were detected. Moreover, ALFF_IC7 implicates prefrontal cortex as abnormal, which plays an important role in the sensory integration and has been frequently reported dysfunction in SZ (Badcock et al., 2005; Hamilton et al., 2009; Yu et al., 2012a). These two pairs of components (FA-ALFF IC7, FA-GM IC7) depict a set of functional-anatomical "connected" regions. Note that both pairs have significant correlations (0.31/0.38) between their subject-mixing profiles as mentioned before, suggesting that disrupted WM connectivity may contribute to coordinated brain dysfunction, especially in the frontal and motor cortex, which is frequently hypothesized to be "disconnected" from other brain regions in SZ (Williams et al., 2004). Our results suggest that the anisotropy changes may relate to functional/structural changes in brain connectivity that are thought to play a central role in the clinical expression of SZ (Douaud et al., 2007).

Furthermore, GM-ALFF IC6 is another joint group-discriminative component, with middle/medial frontal cortex and thalamus (Woodward et al., 2012) indicated in ALFF map and temporal/frontal cortex shown in GM changes. The abnormality in each component have been previously found associated with the SZ deficits separately (Onitsuka et al., 2004; Zhou et al., 2007a; Edgar et al., 2012). Specifically, the result in Jayakumar et al. (2005) was in well accordance with our findings that SZ patients have significantly smaller global and regional GM volumes in inferior frontal, superior temporal, and parahippocampal gyri etc. Our results also suggest that functional disconnectivity associated with frontal lobe (also shown in ALFF_IC3) is present in SZ during rest (Hoptman et al., 2009). This is consistent with the notion that deregulation of medial frontal regions is associated with self-directed thoughts. This may lead to confusion between the source of internal and external stimuli, and may provide a neurophysiological basis for hallucinations (Whitfield-Gabrieli et al., 2009). This would have to be verified in future work.

We also identified ICs of interest showing significance only in one modality, such as GM_IC 5, 9, 10 and ALFF_IC3 (pink frame). The three structural components indicated regions including STG, precuneus, prefrontal cortex, insula, and thalamus, Hence, GM

Table 2 | Anatomic regions of the GM components of interest.

Area	Brodmann area	Vol. (cm^3)	*Z* max value (L/R) (*x, y, z*)
GM IC6 (JOINT)			
Positive			
Superior temporal gyrus	13, 22, 38, 39, 41	4.4/3.4	3.6 (−48, −40, 8)/4.6 (48, −38, 7)
Middle temporal gyrus	21, 22, 37, 39	5.4/1.3	4.5 (−48, −35, 2)/3.5 (48, −32, 2)
Middle frontal gyrus	6, 8, 9, 46	3.4/1.5	3.7 (−50, 16, 32)/3.0 (50, 19, 32)
Inferior frontal gyrus	9, 44, 45, 47	3.8/0.1	3.1 (−50, 10, 33)/2.1 (42, 30, 12)
Negative			
Middle temporal gyrus	21	0.7/0.3	3.1 (−45, −55, 6)/2.6 (42, −52, 8)
Parahippocampal gyrus	30	0.3/0.2	3.0 (−24, −46, 5)/2.6 (27, −46, 5)
GM IC7 (JOINT)			
Positive			
Superior temporal gyrus	21, 22, 39	1.0/2.0	2.9 (−48, −40, 8)/3.6 (50, −26, −1)
Middle temporal gyrus	19, 20, 21, 22, 39	1.8/2.9	3.2 (−48, −32, 2)/3.5 (48, −26, −4)
Inferior frontal gyrus	13, 46	1.2/1.6	2.7 (−39, 30, 12)/3.1 (39, 35, 9)
Parahippocampal gyrus	28, 36	1.3/1.0	2.8 (−27, −12, −15)/2.4 (30, −7, −17)
Fusiform gyrus	37	0.8/0.4	2.8 (−48, −47, −13)/2.5 (48, −47, −13)
Negative			
Precentral gyrus	4, 6	6.1/6.0	4.3 (−24, −23, 65)/3.3 (15, −23, 67)
Lingual gyrus	18	0.6/1.0	4.0 (3, −73, −6)/4.2 (12, −82, −14)
Paracentral lobule	4, 5, 6, 31	2.6/2.5	4.2 (0, −29, 51)/3.9 (3, −32, 51)
Postcentral gyrus	1, 2, 3, 5, 7, 40	4.3/3.3	4.1 (−21, −26, 65)/3.0 (50, −29, 51)
Medial frontal gyrus	6, 8, 32	3.0/4.2	4.1 (0, −23, 56)/3.6 (3, −20, 56)
Posterior cingulate	29	0.3/0.4	3.2 (−3, −58, 6)/3.6 (3, −58, 6)
Superior frontal gyrus	6, 8	3.4/3.2	3.3 (0, 5, 49)/3.2 (21, −8, 67)
Precuneus	7, 39	1.4/4.9	3.3 (−30, −62, 34)/3.2 (9, −74, 42)
Inferior parietal lobule	40	1.6/2.0	3.3 (−42, −35, 54)/3.3 (48, −32, 54)
GM IC4			
Positive			
Middle temporal gyrus	19, 21, 22, 37, 39	6.2/2.2	3.7 (−42, −69, 15)/2.9 (53, −58, 11)
Superior temporal gyrus	13, 22, 38, 39, 41, 42	5.2/2.6	3.5 (−53, −57, 19)/3.0 (50, −52, 14)
Supramarginal gyrus	40	2.9/2.4	3.4 (−53, −54, 22)/2.8 (53, −45, 30)
Precuneus	7, 19, 23, 31, 39	3.2/6.0	3.2 (0, −51, 36)/3.3 (3, −36, 43)
Parahippocampal gyrus	19, 28, 34	2.3/0.9	3.2 (−24, −38, 5)/2.7 (24, −41, 5)
Cingulate gyrus	24, 31, 32	2.0/2.1	3.1 (0, −42, 35)/3.2 (3, −33, 40)
Anterior cingulate	25	0.6/0.3	3.1 (0, 5, −8)/2.7 (3, 5, −10)
Postcentral gyrus	2, 40	2.0/0.2	3.1 (−50, −33, 49)/2.1 (50, −32, 51)
GM IC5			
Positive			
Precuneus	7, 19, 39	2.9/1.5	4.0 (−24, −65, 36)/4.6 (30, −59, 36)
Cerebellum		8.8/7.8	3.7 (0, −47, −8)/3.5 (3, −50, −8)
Middle frontal gyrus	6, 10	1.0/0.7	3.6 (−33, 39, 20)/2.9 (33, 47, 6)
Thalamus		1.8/1.0	3.5 (−6, −23, 12)/2.7 (3, −14, 12)
Middle temporal gyrus	19, 21, 22, 37, 39	1.8/0.9	3.1 (−48, −38, 5)/2.9 (48, −35, 2)
Negative			
Superior temporal gyrus	21, 38	1.5/0.6	3.1 (−30, 16, −24)/2.4 (45, 20, −16)
GM IC9			
Positive			
Superior temporal gyrus	22, 38	1.4/2.5	3.1 (−45, 11, −11)/3.7 (48, 11, −6)
Cuneus	7, 17, 18, 23, 30	2.6/0.7	3.5 (−12, −93, 5)/2.4 (18, −96, 8)
Superior frontal gyrus	6, 8, 9, 10	4.0/3.1	3.3 (−24, 48, 31)/3.1 (21, 11, 49)
Middle frontal gyrus	6, 8, 9, 10	5.3/2.6	3.1 (−33, 58, 3)/2.7 (27, 3, 52)
Precuneus	7, 19, 31	1.5/0.6	3.1 (−27, −62, 34)/2.9 (30, −62, 36)
Medial frontal gyrus	6, 8, 10, 32	1.3/1.1	3.1 (0, 11, 44)/3.0 (21, 5, 49)

(Continued)

Table 2 | Continued

Area	Brodmann area	Vol. (cm^3)	*Z* max value (L/R) (*x, y, z*)
Negative			
Middle temporal gyrus	19, 22, 39	1.8/1.5	3.9 (−48, −43, 5)/5.0 (42, −57, 22)
GM IC10			
Positive			
Angular gyrus	39	0.6/0.4	3.7 (−33, −54, 36)/3.8 (36, −56, 36)
Precuneus	7, 19, 39	1.5/0.6	3.7 (−30, −62, 36)/3.1 (36, −62, 36)
Supramarginal gyrus	40	0.4/0.4	3.1 (−36, −51, 36)/3.2 (36, −51, 36)
Middle frontal gyrus	6, 8, 9, 10	1.0/2.6	3.0 (−33, 16, 27)/2.9 (33, 19, 27)
Lingual gyrus	17	1.7/0.5	3.0 (−12, −87, 2)/2.6 (18, −87, 4)
Negative			
Inferior frontal gyrus	9, 44, 45, 47	2.7/2.1	3.7 (−48, 14, −3)/3.7 (48, 17, −6)
Superior temporal gyrus	22, 38, 42	4.2/1.7	3.7 (−48, 11, −6)/3.2 (50, 14, −6)
Insula	13	1.6/0.1	3.5 (−45, 8, −5)/2.2 (45, 8, −5)

Table 3 | White-matter tract labels of the FA components of interest.

Abbreviation	WM tracts	Vol. (cm^3)	%	*Z* max (R/L)
FA IC7 (JOINT)				
Positive				
ATR	Anterior thalamic radiation	2.3/7.2	5/14	4.7 (26, 31, 13)/5.2 (28, 25, 6)
CST	Corticospinal tract	2.1/2.3	6/7	5(25, 33, 7)/5.1(31, 34, 14)
CG	Cingulum	0.5/0.7	2/2	2.9(18, 21, 18)/3.1(28, 14, 31)
FM	Forceps minor/Forceps major	1.7/3.4	3/7	3.9(27, 47, 21)/5(27, 26, 22)
IFO	Inferior fronto-occipital fasciculus	1.1/2	2/5	3.9(16, 11, 22)/3.7(35, 45, 21)
ILF	Inferior longitudinal fasciculus	1.7/3.1	4/7	3.9(12, 19, 17)/5.3(41, 31, 15)
SLF	Superior longitudinal fasciculus	5.6/4.6	5/4	4.8(6, 25, 15)/5.4(44, 27, 15)
UF	Uncinate fasciculus	0.3/0.5	3/4	3.8(22, 51, 13)/2.9(40, 37, 10)
Negative				
ATR	Anterior thalamic radiation	1.1/0.9	2/2	3.3(20, 38, 27)/3.4(27, 27, 4)
CST	Corticospinal tract	1.9/1.4	5/4	3.5(25, 27, 7)/4.6(29, 31, 8)
SLF	Superior longitudinal fasciculus	3.2/4.1	3/4	5.2(12, 39, 29)/6(46, 30, 11)
FA IC4				
Positive				
ATR	Anterior thalamic radiation	0.8/4.2	2/8	7.8(27, 26, 2)/7.4(28, 24, 1)
CST	Corticospinal tract	2.7/1.9	7/6	8.5(26, 26, 1)/9.3(27, 26, 1)
ILF	Inferior longitudinal fasciculus	0.7/2.2	2/5	2.9(11, 32, 12)/4.2(44, 30, 12)
SLF	Superior longitudinal fasciculus	1.6/3.0	2/3	5.6(4, 26, 17)/5.3(48, 29, 10)
Negative				
ATR	Anterior thalamic radiation	2.3/1.2	6/4	4.2(24, 24, 8)/4.3(28, 31, 11)
IFO	Inferior fronto-occipital fasciculus	2.1/1.7	4/4	3.6(19, 9,23)/3.7(40, 15, 25)
ILF	Inferior longitudinal fasciculus	2.1/1.4	5/3	3.4(13, 15, 18)/3.3(45, 32, 13)
SLF	Superior longitudinal fasciculus	4.4/6.3	5/6	5(7, 27, 15)/5.1(48, 29, 14)

concentrations were significantly reduced in the above regions in the SZ group, consistent with other findings (Ha et al., 2004; Chua et al., 2007; Segall et al., 2009). Since structurally segregated and functionally specialized regions of the human cerebral cortex are interconnected by a dense network of cortico-cortical pathways (Hagmann et al., 2008; Segall et al., 2012), supporting the hypothesis that the SZ deficit may lie in aberrant structural changes and disconnectivity among different cortical areas.

CORRELATION WITH POSITIVE SYMPTOMS

Positive symptoms refer to an excess or distortion of normal psychological functions, e.g., hallucinations and delusions. In **Figure 3**, the higher positive symptoms were correlated with identified voxels in the middle/STG, precuneus, anterior cingulate, and the parahippocampal gyrus in GM_IC4. This is consistent with similar findings in fMRI (Garrity et al., 2007) where PANSS positive scores were associated with abnormal activation of STG,

Table 4 | Anatomic regions of the group-discriminating fMRI components.

Area	Brodmann area	Vol. (cm^3)	*Z* max value (L/R) (*x*, *y*, *z*)
ALFF – IC 6 (JOINT)			
Positive			
Superior frontal gyrus	8, 9, 10, 11	3.8/4.8	9.5 (−30, 43, −15)/9.5 (21, 43, −17)
Middle frontal gyrus	6, 10, 11, 46, 47	6.5/5.8	7.9 (−30, 40, −17)/7.8 (30, 40, −17)
Inferior frontal gyrus	11, 46, 47	2.4/3.3	7.4 (−24, 31, −19)/6.0 (15, 31, −17)
Medial frontal gyrus	10, 11, 25	5.8/6.8	6.0 (−12, 28, −17)/6.1 (9, 43, −17)
Superior temporal gyrus	22, 38	0.4/0.4	3.5 (−56, 11, −6)/2.8 (59, 11, −6)
Anterior cingulate	10, 25, 32	1.0/0.3	3.5 (−12, 49, −5)/2.3 (15, 46, −5)
Thalamus		0.3/0.2	3.0 (−6, −11, 14)/3.0 (6, −5, 11)
ALFF – IC 7 (JOINT)			
Positive			
Superior frontal gyrus	6, 10, 11	0.8/0.3	5.4 (−18, 64, 8)/3.4 (9, 67, 8)
Superior temporal gyrus	22, 38	5.4/0.1	4.9 (−33, 13, −28)/2.3 (30, 10, −31)
Medial frontal gyrus	10	0.9/0.0	4.3 (−6, 64, 5)/−999.0 (0, 0, 0)
Inferior frontal gyrus	44, 45, 46, 47	2.0/0.0	4.0 (−53, 20, −9)/−999.0 (0, 0, 0)
Middle frontal gyrus	10, 11	1.3/0.3	3.4 (−42, 52, −10)/3.7 (30, 62, 19)
Negative			
Cingulate gyrus	23, 24, 32	2.2/2.8	3.5 (−9, 4, 27)/4.1 (9, 4, 27)
Anterior cingulate	24, 33	0.5/0.8	3.5 (−6, 10, 24)/4.0 (12, 13, 24)
Superior frontal gyrus	8, 10, 11	1.1/1.7	3.7 (−30, 32, 51)/3.9 (18, 43, −15)
Middle temporal gyrus	21, 38, 39	0.1/0.8	3.0 (−56, −66, 28)/2.6 (62, −35, −8)
ALFF – IC 3			
Positive			
Superior frontal gyrus	6, 8, 9, 10, 11	14.3/14.1	6.6 (−21, 57, 28)/6.5 (18, 65, 16)
Middle frontal gyrus	6, 8, 9, 10, 11, 46	12.5/11.6	5.0 (−27, 59, 19)/5.6 (24, 62, 19)
Medial frontal gyrus	6, 8, 9, 10	4.9/4.5	4.7 (−3, 49, 42)/4.7 (3, 49, 42)
Inferior frontal gyrus	9, 10, 45, 46, 47	2.6/2.0	3.9 (−42, 55, 0)/2.9 (56, 10, 33)
Superior temporal gyrus	38	0.6/0.1	3.1 (−42, 19, −26)/2.2 (39, 22, −26)

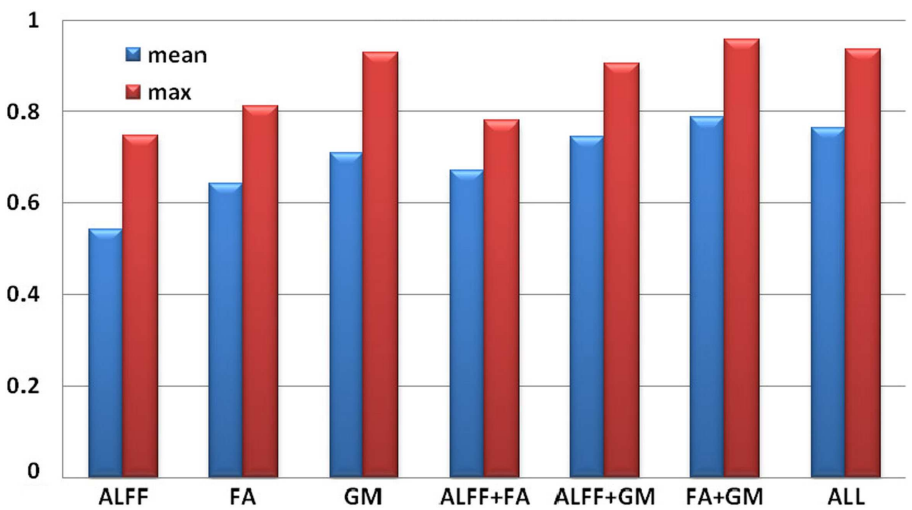

FIGURE 4 | Classification accuracy based on selected group-discriminative components from mCCA + jICA for seven modal combinations.

precuneus. Similarly GM volumes in anterior and posterior cingulate regions were correlated with positive symptoms (Choi et al., 2005; Yan et al., 2012). Additionally, in Meda et al. (2012), similar regions were also reported in resting state fMRI data, in which anterior default mode and frontal-occipital regions have significant correlation with the PANSS positive subscale in SZ. All these

findings suggest a general hypothesis that psychotic symptoms derive from functionally disconnected brain circuits, e.g., the disintegrated brain connectivity between medial frontal/prefrontal and parietal networks in SZ (Zhou et al., 2007b). For FA_IC4, the FA values in left ATR and SLF showed a significant negative correlation with positive PANSS, consistent with (Caprihan et al., 2008; Cui et al., 2011), suggesting that deficits of WM integrity in left frontal-parietal lobe may also be involved in the pathophysiology of positive symptoms. Finally, this data also supports the hypothesis that the failure of left-hemisphere lateralization might be involved in the pathophysiology of SZ (Szeszko et al., 2005).

CLASSIFICATION BASED ON SELECTED ICs

The classification in **Figure 4** shows that GM feature achieves the best classification among three single modalities, consistent with the fact that the selected GM components have much smaller *p* values than ALFF or FA. The most powerful prediction can be accomplished by using features from FA + GM, which is able to detail the multifaceted pathology that is likely to be present in SZ compared with single modality. Our results suggest that multimodal fusion of the selected group-discriminative components can improve the potential diagnosis prediction, in accordance with Sui et al. (2009a) and Yang et al. (2010), however, fusing as many modalities as possible in the training sample does not guarantee best classification rates, as we showed here and reported in Zhang et al. (2012); thus it would be helpful to compare a combination of uni-modal and multimodal results, as we did in Kim et al. (2010), to detect the potential biomarkers. We plan to pursue this possibility in future work by using larger data sets and various modalities, which aims to have bigger effect size and achieve higher accuracy.

FUTURE WORK

In this paper we develop and evaluate a novel multivariate method that can explore cross-information in multiple (more than two) data types and applied it to compare SZ patients to controls using an fMRI-DTI-sMRI combination. This is a novel attempt to perform a fusion of three different imaging modalities. The method described here could be applied straightforwardly to study other brain diseases (or subsets of a particular illness, such as psychotic or non-psychotic bipolar disorder). In addition, the choice of which multimodal data type to utilize is flexible, i.e., EEG, MEG, or genetic data, different features like fractional ALFF (fALFF) from fMRI (Kalcher et al., 2013) are also applicable. In a recent study, we found both ALFF and fALFF to be interesting and decided to start with ALFF (Turner et al., 2012), and will consider fALFF in future work. Finally the proposed method is very computationally efficient.

A limitation to the current study is that the subject number is not very high. Several statistical tests did not survive from the multiple comparisons, which may be complemented in future studies by including more subject samples or by multi-site recruitment. Additionally, mCCA + jICA operates on extracted features, rather than the original imaging data (e.g., using FA values instead of raw DTI data). Although some of the information is lost using this method, a "feature" tends to be more tractable than working with the large-scale original data due to the reduced number of dimensions (Calhoun and Adali, 2009) and provides a simpler space to link the data (Smith et al., 2009). Note that in our study we did not perform WM tractography but provided a type of summary statistic. A major strength of mCCA + jICA is that it can discover changes in one modality, e.g., which are related to alterations in distant, but connected regions in other modalities, without requiring a direct link.

Another point worth noting is that we did not collect physiologic data during the rest fMRI session as studies of patients tend to make this more difficult to collect. However it would be worth evaluating this in future work. With the advent of more rapid scanning (e.g., multiband sequences) which can adequately sample the cardiac noise, it is becoming much more feasible to characterize physiologic noise in large patient studies. We did not collect information on nicotine use either in these subjects, which may have potential effects on the imaging results, and would better be taken into account in the future. For example, recent studies indicated evidences of smoking effect in resting-state networks (Janes et al., 2012) and more prevalence in subjects with psychiatric disorder like SZ (Dickerson et al., 2013).

Multimodal fusion is an effective approach for analyzing biomedical imaging data that combines multiple data types in a joint analysis. It helps to identify the unique and shared variance associated with each imaging modality that underlies cognitive functioning in HCs and impairment in mental illness. In this real-world fusion application, we highlighted data from rest fMRI, WM tract, and GM concentration from SZ and healthy control subjects. We identified both modality-common and modality-unique group-discriminating aspects that verified the abnormalities in SZ, as well as replicated and extended previous findings. Such observations add to our understanding of the neural correlates of SZ. The proposed model promises a widespread utilization in the neuroimaging community and may be used to identify potential brain illness biomarkers.

ACKNOWLEDGMENTS

This work was supported by the National Institutes of Health grants R01EB 006841, R01EB 005846, and 5P20RR021938 (to Vince D. Calhoun), and R01MH43775, R01MH074797, and R01MH077945 (to Godfrey D. Pearlson).

REFERENCES

Amari, S., and Wu, S. (1999). Improving support vector machine classifiers by modifying kernel functions. *Neural Netw.* 12, 783–789. doi:10.1016/S0893-6080(99)00032-5

Ashburner, J., and Friston, K. J. (2005). Unified segmentation. *Neuroimage* 26, 839–851. doi:10.1016/j.neuroimage.2005.02.018

Badcock, J. C., Michiel, P. T., and Rock, D. (2005). Spatial working memory and planning ability: contrasts between schizophrenia and bipolar I disorder. *Cortex* 41, 753–763. doi:10.1016/S0010-9452(08)70294-6

Bell, A. J., and Sejnowski, T. J. (1995). An information-maximization approach to blind separation and blind deconvolution. *Neural Comput.* 7, 1129–1159. doi:10.1162/neco.1995.7.6.1129

Brown, P. L., Shepard, P. D., Elmer, G. I., Stockman, S., McFarland, R., Mayo, C. L., et al. (2012). Altered spatial learning, cortical plasticity and hippocampal anatomy

in a neurodevelopmental model of schizophrenia-related endophenotypes. *Eur. J. Neurosci.* 36, 2773–2781. doi:10.1111/j.1460-9568.2012.08204.x

Calhoun, V. D., and Adali, T. (2009). Feature-based fusion of medical imaging data. *IEEE Trans. Inf. Technol. Biomed.* 13, 711–720. doi:10.1109/TITB.2008.923773

Calhoun, V. D., Adali, T., Giuliani, N. R., Pekar, J. J., Kiehl, K. A., and Pearlson, G. D. (2006). Method for multimodal analysis of independent source differences in schizophrenia: combining gray matter structural and auditory oddball functional data. *Hum. Brain Mapp.* 27, 47–62. doi:10.1002/hbm.20166

Calhoun, V. D., and Allen, E. (2013). Extracting intrinsic functional networks with feature-based group independent component analysis. *Psychometrika*, 78, 243–259. doi:10.1007/s11336-012-9291-3

Calhoun, V. D., Eichele, T., Adali, T., and Allen, E. A. (2012). Decomposing the brain: components and modes, networks and nodes. *Trends Cogn. Sci. (Regul. Ed.)* 16, 255–256. doi:10.1016/j.tics.2012.03.008

Calhoun, V. D., MacIejewski, P. K., Pearlson, G. D., and Kiehl, K. A. (2008). Temporal lobe and "default" hemodynamic brain modes discriminate between schizophrenia and bipolar disorder. *Hum. Brain Mapp.* 29, 1265–1275. doi:10.1002/hbm.20463

Camara, E., Rodriguez-Fornells, A., and Munte, T. F. (2010). Microstructural brain differences predict functional hemodynamic responses in a reward processing task. *J. Neurosci.* 30, 11398–11402. doi:10.1523/JNEUROSCI.0111-10.2010

Camchong, J., MacDonald, A. W. III, Bell, C., Mueller, B. A., and Lim, K. O. (2011). Altered functional and anatomical connectivity in schizophrenia. *Schizophr. Bull.* 37, 640–650. doi:10.1093/schbul/sbp131

Caprihan, A., Pearlson, G. D., and Calhoun, V. D. (2008). Application of principal component analysis to distinguish patients with schizophrenia from healthy controls based on fractional anisotropy measurements. *Neuroimage* 42, 675–682. doi:10.1016/j.neuroimage.2008.04.255

Chen, K., Reiman, E. M., Huan, Z., Caselli, R. J., Bandy, D., Ayutyanont, N., et al. (2009). Linking functional and structural brain images with multivariate network analyses: a novel application of the partial least square method. *Neuroimage* 47, 602–610. doi:10.1016/j.neuroimage.2009.04.053

Choi, J. S., Kang, D. H., Kim, J. J., Ha, T. H., Roh, K. S., Youn, T., et al. (2005). Decreased caudal anterior cingulate gyrus volume and positive symptoms in schizophrenia. *Psychiatry Res.* 139, 239–247. doi:10.1016/j.pscychresns.2004.05.008

Chua, S. E., Cheung, C., Cheung, V., Tsang, J. T., Chen, E. Y., Wong, J. C., et al. (2007). Cerebral grey, white matter and csf in never-medicated, first-episode schizophrenia. *Schizophr. Res.* 89, 12–21. doi:10.1016/j.schres.2006.09.009

Correa, N. M., Li, Y. O., Adali, T., and Calhoun, V. D. (2009). "Fusion of fMRI, sMRI, and EEG data using canonical correlation analysis," in *ICASSP 2009* (Taipei: IEEE), 385–388.

Cortes, C., and Vapnik, V. (1995). "Support-vector networks," in *Machine Learning* (Boston: Kluwer Academic Publishers), 273–297.

Cui, L., Chen, Z., Deng, W., Huang, X., Li, M., Ma, X., et al. (2011). Assessment of white matter abnormalities in paranoid schizophrenia and bipolar mania patients. *Psychiatry Res.* 194, 347–353. doi:10.1016/j.pscychresns.2011.03.010

Dickerson, F., Stallings, C. R., Origoni, A. E., Vaughan, C., Khushalani, S., Schroeder, J., et al. (2013). Cigarette smoking among persons with schizophrenia or bipolar disorder in routine clinical settings, 1999-2011. *Psychiatr. Serv.* 64, 44–50. doi:10.1176/appi.ps.201200143

Douaud, G., Smith, S., Jenkinson, M., Behrens, T., Johansen-Berg, H., Vickers, J., et al. (2007). Anatomically related grey and white matter abnormalities in adolescent-onset schizophrenia. *Brain* 130, 2375–2386. doi:10.1093/brain/awm184

Edgar, J. C., Hunter, M. A., Huang, M., Smith, A. K., Chen, Y., Sadek, J., et al. (2012). Temporal and frontal cortical thickness associations with M100 auditory activity and attention in healthy controls and individuals with schizophrenia. *Schizophr. Res.* 140, 250–257. doi:10.1016/j.schres.2012.06.009

Erhardt, E. B., Allen, E. A., Damaraju, E., and Calhoun, V. D. (2011). On network derivation, classification, and visualization: a response to Habeck and Moeller. *Brain Connect.* 1, 1–19. doi:10.1089/brain.2011.0022

First, M. B., Spitzer, R. L., Gibbon, M., and Williams, J. B. (1995). *Structured Clinical Interview for DSM-IV axis I disorders*. New York: New York State Psychiatric Institute.

Freire, L., Roche, A., and Mangin, J. F. (2002). What is the best similarity measure for motion correction in fMRI time series? *IEEE Trans. Med. Imaging* 21, 470–484. doi:10.1109/TMI.2002.1009383

Friedman, J. I., Tang, C., Carpenter, D., Buchsbaum, M., Schmeidler, J., Flanagan, L., et al. (2008). Diffusion tensor imaging findings in first-episode and chronic schizophrenia patients. *Am. J. Psychiatry* 165, 1024–1032. doi:10.1176/appi.ajp.2008.07101640

Friston, K. J., Ashburner, J., Frith, C. D., Poline, J. P., Heather, J. D., and Frackowiak, R. S. (1995). Spatial registration and normalization of images. *Hum. Brain Mapp.* 2, 165–189. doi:10.1002/hbm.460030303

Gardner, D. M., Murphy, A. L., O'Donnell, H., Centorrino, F., and Baldessarini, R. J. (2010). International consensus study of antipsychotic dosing. *Am. J. Psychiatry* 167, 686–693. doi:10.1176/appi.ajp.2009.09060802

Garrity, A. G., Pearlson, G. D., McKiernan, K., Lloyd, D., Kiehl, K. A., and Calhoun, V. D. (2007). Aberrant "default mode" functional connectivity in schizophrenia. *Am. J. Psychiatry* 164, 450–457. doi:10.1176/appi.ajp.164.3.450

Geva, S., and Sitte, J. (1991). Adaptive nearest neighbor pattern classification. *IEEE Trans. Neural Netw.* 2, 318–322. doi:10.1109/72.80344

Groves, A. R., Beckmann, C. F., Smith, S. M., and Woolrich, M. W. (2011). Linked independent component analysis for multimodal data fusion. *Neuroimage* 54, 2198–2217. doi:10.1016/j.neuroimage.2010.09.073

Groves, A. R., Smith, S. M., Fjell, A. M., Tamnes, C. K., Walhovd, K. B., Douaud, G., et al. (2012). Benefits of multi-modal fusion analysis on a large-scale dataset: life-span patterns of inter-subject variability in cortical morphometry and white matter microstructure. *Neuroimage* 63, 365–380. doi:10.1016/j.neuroimage.2012.06.038

Ha, T. H., Youn, T., Ha, K. S., Rho, K. S., Lee, J. M., Kim, I. Y., et al. (2004). Gray matter abnormalities in paranoid schizophrenia and their clinical correlations. *Psychiatry Res.* 132, 251–260. doi:10.1016/j.pscychresns.2004.05.001

Hagmann, P., Cammoun, L., Gigandet, X., Meuli, R., Honey, C. J., Wedeen, V. J., et al. (2008). Mapping the structural core of human cerebral cortex. *PLoS Biol.* 6:e159. doi:10.1371/journal.pbio.0060159

Hamilton, L. S., Altshuler, L. L., Townsend, J., Bookheimer, S. Y., Phillips, O. R., Fischer, J., et al. (2009). Alterations in functional activation in euthymic bipolar disorder and schizophrenia during a working memory task. *Hum. Brain Mapp.* 30, 3958–3969. doi:10.1002/hbm.20820

Hoptman, M. J., Zuo, X. N., Butler, P. D., Javitt, D. C., D'Angelo, D., Mauro, C. J., et al. (2009). Amplitude of low-frequency oscillations in schizophrenia: a resting state fMRI study. *Schizophr. Res.* 117, 13–20. doi:10.1016/j.schres.2009.09.030

Hua, K., Zhang, J., Wakana, S., Jiang, H., Li, X., Reich, D. S., et al. (2008). Tract probability maps in stereotaxic spaces: analyses of white matter anatomy and tract-specific quantification. *Neuroimage* 39, 336–347. doi:10.1016/j.neuroimage.2007.07.053

Janes, A. C., Nickerson, L. D., Frederick Bde, B., and Kaufman, M. J. (2012). Prefrontal and limbic resting state brain network functional connectivity differs between nicotine-dependent smokers and non-smoking controls. *Drug Alcohol Depend.* 125, 252–259. doi:10.1016/j.drugalcdep.2012.02.020

Jayakumar, P. N., Venkatasubramanian, G., Gangadhar, B. N., Janakiramaiah, N., and Keshavan, M. S. (2005). Optimized voxel-based morphometry of gray matter volume in first-episode, antipsychotic-naive schizophrenia. *Prog. Neuropsychopharmacol. Biol. Psychiatry* 29, 587–591. doi:10.1016/j.pnpbp.2005.01.020

Kalcher, K., Boubela, R. N., Huf, W., Biswal, B. B., Baldinger, P., Sailer, U., et al. (2013). RESCALE: voxel-specific task-fMRI scaling using resting state fluctuation amplitude. *Neuroimage* 70, 80–88. doi:10.1016/j.neuroimage.2012.12.019

Kay, S. R., Fiszbein, A., and Opler, L. A. (1987). The positive and negative syndrome scale (PANSS) for schizophrenia. *Schizophr. Bull.* 13, 261–276. doi:10.1093/schbul/13.2.261

Kim, D. I., Sui, J., Rachakonda, S., White, T., Manoach, D. S., Clark, V. P., et al. (2010). Identification of imaging biomarkers in schizophrenia: a coefficient-constrained independent component analysis of the mind multi-site schizophrenia study. *Neuroinformatics* 8, 213–229. doi:10.1007/s12021-010-9077-7

Li, Y. O., Adali, T., and Calhoun, V. D. (2007). Estimating the number of independent components for functional magnetic resonance imaging data. *Hum. Brain Mapp.* 28, 1251–1266. doi:10.1002/hbm.20359

Li, Y. O., Adali, T., Wang, W., and Calhoun, V. D. (2009). Joint blind source separation by multi-set canonical correlation analysis. *IEEE Trans. Signal Process.* 57, 3918–3929. doi:10.1109/TSP.2009.2021636

Lin, F. H., McIntosh, A. R., Agnew, J. A., Eden, G. F., Zeffiro, T. A., and Belliveau, J. W. (2003). Multivariate analysis of neuronal interactions in the generalized partial least squares framework: simulations and empirical studies. *Neuroimage* 20, 625–642. doi:10.1016/S1053-8119(03)00333-1

Long, D., Wang, J., Xuan, M., Gu, Q., Xu, X., Kong, D., et al. (2012). Automatic classification of early Parkinson's disease with multi-modal MR imaging. *PLoS ONE* 7:e47714. doi:10.1371/journal.pone.0047714

Lu, L. H., Zhou, X. J., Keedy, S. K., Reilly, J. L., and Sweeney, J. A. (2012). White matter microstructure in untreated first episode bipolar disorder with psychosis: comparison with schizophrenia. *Bipolar Disord.* 13, 604–613. doi:10.1111/j.1399-5618.2011.00958.x

McCallum, A. and Nigam, K. (1998). "A comparison of event models for naive bayes text classification," in *AAAI/ICML-98 Workshop on Learning for Text Categorization*, Technical Report WS-98-05. Madison: AAAI Press, 41–48.

McCarley, R. W., Nakamura, M., Shenton, M. E., and Salisbury, D. F. (2008). Combining ERP and structural MRI information in first episode schizophrenia and bipolar disorder. *Clin. EEG Neurosci.* 39, 57–60. doi:10.1177/155005940803900206

Meda, S. A., Gill, A., Stevens, M. C., Lorenzoni, R. P., Glahn, D. C., Calhoun, V. D., et al. (2012). Differences in resting-state functional magnetic resonance imaging functional network connectivity between schizophrenia and psychotic bipolar probands and their unaffected first-degree relatives. *Biol. Psychiatry* 71, 881–889. doi:10.1016/j.biopsych.2012.01.025

Michael, A. M., Baum, S. A., White, T., Demirci, O., Andreasen, N. C., Segall, J. M., et al. (2010). Does function follow form? Methods to fuse structural and functional brain images show decreased linkage in schizophrenia. *Neuroimage* 49, 2626–2637. doi:10.1016/j.neuroimage.2009.08.056

Michael, A. M., King, M. D., Ehrlich, S., Pearlson, G., White, T., Holt, D. J., et al. (2011). A data-driven investigation of gray matter-function correlations in schizophrenia during a working memory task. *Front. Hum. Neurosci.* 5:71. doi:10.3389/fnhum.2011.00071

Olesen, P. J., Nagy, Z., Westerberg, H., and Klingberg, T. (2003). Combined analysis of DTI and fMRI data reveals a joint maturation of white and grey matter in a fronto-parietal network. *Brain Res. Cogn. Brain Res.* 18, 48–57. doi:10.1016/j.cogbrainres.2003.09.003

Onitsuka, T., Shenton, M. E., Salisbury, D. F., Dickey, C. C., Kasai, K., Toner, S. K., et al. (2004). Middle and inferior temporal gyrus gray matter volume abnormalities in chronic schizophrenia: an MRI study. *Am. J. Psychiatry* 161, 1603–1611. doi:10.1176/appi.ajp.161.9.1603

Rykhlevskaia, E., Gratton, G., and Fabiani, M. (2008). Combining structural and functional neuroimaging data for studying brain connectivity: a review. *Psychophysiology* 45, 173–187. doi:10.1111/j.1469-8986.2007.00621.x

Schlosser, R. G., Nenadic, I., Wagner, G., Gullmar, D., Von Consbruch, K., Kohler, S., et al. (2007). White matter abnormalities and brain activation in schizophrenia: a combined DTI and fMRI study. *Schizophr. Res.* 89, 1–11. doi:10.1016/j.schres.2006.09.007

Segall, J. M., Allen, E. A., Jung, R. E., Erhardt, E. B., Arja, S. K., Kiehl, K., et al. (2012). Correspondence between structure and function in the human brain at rest. *Front. Neuroinform.* 6:10. doi:10.3389/fninf.2012.00010

Segall, J. M., Turner, J. A., Van Erp, T. G., White, T., Bockholt, H. J., Gollub, R. L., et al. (2009). Voxel-based morphometric multisite collaborative study on schizophrenia. *Schizophr. Bull.* 35, 82–95. doi:10.1093/schbul/sbn150

Smith, S. M., Fox, P. T., Miller, K. L., Glahn, D. C., Fox, P. M., Mackay, C. E., et al. (2009). Correspondence of the brain's functional architecture during activation and rest. *Proc. Natl. Acad. Sci. U.S.A.* 106, 13040–13045. doi:10.1073/pnas.0905267106

Sui, J., Adali, T., Pearlson, G., Yang, H., Sponheim, S. R., White, T., et al. (2010). A CCA+ICA based model for multi-task brain imaging data fusion and its application to schizophrenia. *Neuroimage* 51, 123–134. doi:10.1016/j.neuroimage.2010.01.069

Sui, J., Adali, T., Pearlson, G. D., and Calhoun, V. D. (2009a). An ICA-based method for the identification of optimal FMRI features and components using combined group-discriminative techniques. *Neuroimage* 46, 73–86. doi:10.1016/j.neuroimage.2009.01.026

Sui, J., Adali, T., Pearlson, G. D., Clark, V. P., and Calhoun, V. D. (2009b). A method for accurate group difference detection by constraining the mixing coefficients in an ICA framework. *Hum. Brain Mapp.* 30, 2953–2970. doi:10.1002/hbm.20721

Sui, J., Adali, T., Yu, Q., Chen, J., and Calhoun, V. D. (2012a). A review of multivariate methods for multimodal fusion of brain imaging data. *J. Neurosci. Methods* 204, 68–81. doi:10.1016/j.jneumeth.2011.10.031

Sui, J., Yu, Q., He, H., Pearlson, G. D., and Calhoun, V. D. (2012b). A selective review of multimodal fusion methods in schizophrenia. *Front. Hum. Neurosci.* 6:27. doi:10.3389/fnhum.2012.00027

Sui, J., He, H., Pearlson, G. D., Adali, T., Kiehl, K. A., Yu, Q., et al. (2013). Three-way (N-way) fusion of brain imaging data based on mCCA+jICA and its application to discriminating schizophrenia. *Neuroimage* 2, 119–132. doi:10.1016/j.neuroimage.2012.10.051

Sui, J., Pearlson, G., Caprihan, A., Adali, T., Kiehl, K. A., Liu, J., et al. (2011). Discriminating schizophrenia and bipolar disorder by fusing fMRI and DTI in a multimodal CCA+ joint ICA model. *Neuroimage* 57, 839–855. doi:10.1016/j.neuroimage.2011.05.055

Sussmann, J. E., Lymer, G. K., McKirdy, J., Moorhead, T. W., Munoz Maniega, S., Job, D., et al. (2009). White matter abnormalities in bipolar disorder and schizophrenia detected using diffusion tensor magnetic resonance imaging. *Bipolar Disord.* 11, 11–18. doi:10.1111/j.1399-5618.2008.00646.x

Szeszko, P. R., Ardekani, B. A., Ashtari, M., Kumra, S., Robinson, D. G., Sevy, S., et al. (2005). White matter abnormalities in first-episode schizophrenia or schizoaffective disorder: a diffusion tensor imaging study. *Am. J. Psychiatry* 162, 602–605. doi:10.1176/appi.ajp.162.3.602

Teipel, S. J., Bokde, A. L., Meindl, T., Amaro, E. Jr., Soldner, J., Reiser, M. F., et al. (2010). White matter microstructure underlying default mode network connectivity in the human brain. *Neuroimage* 49, 2021–2032. doi:10.1016/j.neuroimage.2009.10.067

Turner, J. A., Chen, H., Mathalon, D. H., Allen, E. A., Mayer, A. R., Abbott, C. C., et al. (2012). Reliability of the amplitude of low-frequency fluctuations in resting state fMRI in chronic schizophrenia. *Psychiatry Res.* 201, 253–255. doi:10.1016/j.pscychresns.2011.09.012

Venkataraman, A., Rathi, Y., Kubicki, M., Westin, C. F., and Golland, P. (2010). Joint generative model for fMRI/DWI and its application to population studies. *Med. Image Comput. Comput. Assist. Interv.* 13, 191–199.

White, T., O'Leary, D., Magnotta, V., Arndt, S., Flaum, M., and Andreasen, N. C. (2001). Anatomic and functional variability: the effects of filter size in group fMRI data analysis. *Neuroimage* 13, 577–588. doi:10.1006/nimg.2000.0716

Whitfield-Gabrieli, S., Thermenos, H. W., Milanovic, S., Tsuang, M. T., Faraone, S. V., McCarley, R. W., et al. (2009). Hyperactivity and hyperconnectivity of the default network in schizophrenia and in first-degree relatives of persons with schizophrenia. *Proc. Natl. Acad. Sci. U.S.A.* 106, 1279–1284. doi:10.1073/pnas.0809141106

Williams, L. M., Das, P., Harris, A. W., Liddell, B. B., Brammer, M. J., Olivieri, G., et al. (2004). Dysregulation of arousal and amygdala-prefrontal systems in paranoid schizophrenia. *Am. J. Psychiatry* 161, 480–489. doi:10.1176/appi.ajp.161.3.480

Woodward, N. D., Karbasforoushan, H., and Heckers, S. (2012). Thalamocortical dysconnectivity in schizophrenia. *Am. J. Psychiatry* 169, 1092–1099. doi:10.1176/appi.ajp.2012.12010056

Xu, L., Pearlson, G., and Calhoun, V. D. (2009). Joint source based morphometry identifies linked gray and white matter group differences. *Neuroimage* 44, 777–789. doi:10.1016/j.neuroimage.2008.09.051

Yan, H., Tian, L., Yan, J., Sun, W., Liu, Q., Zhang, Y. B., et al. (2012). Functional and anatomical connectivity abnormalities in cognitive division of anterior cingulate cortex in schizophrenia. *PLoS One* 7:e45659. doi:10.1371/journal.pone.0045659

Yang, H., Liu, J., Sui, J., Pearlson, G. D., and Calhoun, V. D. (2010). A hybrid machine learning method for fusing fMRI and genetic

data: combining both improves classification of schizophrenia. *Front. Hum. Neurosci.* 4:192. doi:10.3389/fnhum.2010.00192

Yu, Q., Allen, E. A., Sui, J., Arbabshirani, M. R., Pearlson, G., and Calhoun, V. D. (2012a). Brain connectivity network in schizophrenia underlying resting state functional magnetic resonance imaging. *Curr. Top. Med. Chem.* 12, 2415–2425. doi:10.2174/156802612805289890

Yu, R., Chien, Y. L., Wang, H. L., Liu, C. M., Liu, C. C., Hwang, T. J., et al. (2012b). Frequency-specific alternations in the amplitude of low-frequency fluctuations in schizophrenia. *Hum. Brain Mapp.* (in press) doi:10.1002/hbm.22203

Yu, Q., Sui, J., Liu, J., Plis, S. M., Kiehl, K. A., Pearlson, G., et al. (2013). Disrupted correlation between low frequency power and connectivity strength of resting state brain networks in schizophrenia. *Schizophr. Res.* 143, 165–171. doi:10.1016/j.schres.2012.11.001

Zang, Y. F., He, Y., Zhu, C. Z., Cao, Q. J., Sui, M. Q., Liang, M., et al. (2007). Altered baseline brain activity in children with ADHD revealed by resting-state functional MRI. *Brain Dev.* 29, 83–91. doi:10.1016/j.braindev.2006.07.002

Zhang, H., Liu, L., Wu, H., and Fan, Y. (2012). "Feature selection and SVM classification of multiple modality images for predicting MCI," in *OHBM*, Beijing.

Zhou, Y., Liang, M., Jiang, T., Tian, L., Liu, Y., Liu, Z., et al. (2007a). Functional dysconnectivity of the dorsolateral prefrontal cortex in first-episode schizophrenia using resting-state fMRI. *Neurosci. Lett.* 417, 297–302. doi:10.1016/j.neulet.2007.02.081

Zhou, Y., Liang, M., Tian, L., Wang, K., Hao, Y., Liu, H., et al. (2007b). Functional disintegration in paranoid schizophrenia using resting-state fMRI. *Schizophr. Res.* 97, 194–205. doi:10.1016/j.schres.2007.05.029

Zhou, Y., Shu, N., Liu, Y., Song, M., Hao, Y., Liu, H., et al. (2008). Altered resting-state functional connectivity and anatomical connectivity of hippocampus in schizophrenia. *Schizophr. Res.* 100, 120–132. doi:10.1016/j.schres.2007.11.039

Zou, Q. H., Zhu, C. Z., Yang, Y., Zuo, X. N., Long, X. Y., Cao, Q. J., et al. (2008). An improved approach to detection of amplitude of low-frequency fluctuation (ALFF) for resting-state fMRI: fractional ALFF. *J. Neurosci. Methods* 172, 137–141. doi:10.1016/j.jneumeth

Conflict of Interest Statement: The authors declare that the research was conducted in the absence of any commercial or financial relationships that could be construed as a potential conflict of interest.

Received: 14 January 2013; accepted: 15 May 2013; published online: 29 May 2013.

Citation: Sui J, He H, Yu Q, Chen J, Rogers J, Pearlson GD, Mayer A, Bustillo J, Canive J and Calhoun VD (2013) Combination of resting state fMRI, DTI, and sMRI data to discriminate schizophrenia by N-way MCCA + jICA. Front. Hum. Neurosci. 7:235. doi: 10.3389/fnhum.2013.00235

frontiers in
HUMAN NEUROSCIENCE

ORIGINAL RESEARCH ARTICLE
published: 02 September 2013
doi: 10.3389/fnhum.2013.00496

Applying independent component analysis to clinical fMRI at 7T

***Simon Daniel Robinson*[1,2]*, *Veronika Schöpf*[1,2], *Pedro Cardoso*[1,2], *Alexander Geissler*[1,3], *Florian Ph. S. Fischmeister*[1,3], *Moritz Wurnig*[1,3], *Siegfried Trattnig*[1,2] and *Roland Beisteiner*[1,3]**

[1] *High Field Magnetic Resonance Imaging Centre of Excellence, Medical University of Vienna, Vienna, Austria*
[2] *Department of Radiology, Medical University of Vienna, Vienna, Austria*
[3] *Study Group Clinical fMRI, Department of Neurology, Medical University of Vienna, Vienna, Austria*

Edited by:
Hauke R. Heekeren, Freie Universität Berlin, Germany

Reviewed by:
David J. McGonigle, Cardiff University, UK
Erick Joseph Paul, University of Illinois Urbana Champaign, USA

***Correspondence:**
Simon Daniel Robinson, High Field Magnetic Resonance Center of Excellence, Department of Radiology, Lazarettgasse 14, A-1090 Vienna, Austria
e-mail: simon.robinson@meduniwien.ac.at

Increased BOLD sensitivity at 7T offers the possibility to increase the reliability of fMRI, but ultra-high field is also associated with an increase in artifacts related to head motion, Nyquist ghosting, and parallel imaging reconstruction errors. In this study, the ability of independent component analysis (ICA) to separate activation from these artifacts was assessed in a 7T study of neurological patients performing chin and hand motor tasks. ICA was able to isolate primary motor activation with negligible contamination by motion effects. The results of General Linear Model (GLM) analysis of these data were, in contrast, heavily contaminated by motion. Secondary motor areas, basal ganglia, and thalamus involvement were apparent in ICA results, but there was low capability to isolate activation in the same brain regions in the GLM analysis, indicating that ICA was more sensitive as well as more specific. A method was developed to simplify the assessment of the large number of independent components. Task-related activation components could be automatically identified via these intuitive and effective features. These findings demonstrate that ICA is a practical and sensitive analysis approach in high field fMRI studies, particularly where motion is evoked. Promising applications of ICA in clinical fMRI include presurgical planning and the study of pathologies affecting subcortical brain areas.

Keywords: independent component analysis, ultra-high field fMRI, presurgical planning, motor, neurology, motion, artifacts

INTRODUCTION

Time-series SNR and BOLD sensitivity (BS) increase with field strength (Triantafyllou et al., 2005; van der Zwaag et al., 2009; Beisteiner et al., 2011; Duchin et al., 2012), motivating the use of very high field for fMRI (Barth and Poser, 2011; De Martino et al., 2011; Ugurbil, 2012). In clinical fMRI applications such as presurgical planning (Roessler et al., 2005; Stippich, 2007) with a patient cohort that may have limited tolerance in an fMRI session, increased BS may allow the measurement time to be reduced, or the reliability of fMRI findings to be increased for a particular measurement time. Against this prospect of increased sensitivity at ultra-high field stand a number of methodical challenges. In clinical practice, the most significant of these is increased head motion artifacts. Motion artifacts are the most frequent reason for the failure of presurgical fMRI even at 1.5 T (Krings et al., 2001). This study addresses the question of whether activation may be isolated from motion and other artifacts in ultra-high field fMRI using independent component analysis (ICA), and assesses the specificity of activation maps derived with ICA compared with those generated with the general linear model (GLM) approach.

Head motion between image volumes generates signal changes at contrast boundaries such as the ventricles and edge of the brain, while displacement in the slice select direction during one TR leads to spin history effects (Friston et al., 1996). Motion also introduces dynamic non-linear distortions in regions of high susceptibility gradients (Hutton et al., 2002; Robinson and Jovicich, 2011; Visser et al., 2012) and increases Nyquist ghosting and parallel imaging reconstruction artifacts (Poser et al., 2013). Head motion artifacts are particularly severe in patient studies (Bullmore et al., 1999; Seto et al., 2001) and at very high field, as parallel imaging reconstruction artifacts, eddy currents, and B0 changes due to motion increase (Beisteiner et al., 2011).

Head motion can be reduced to some extent using molded cushions (Kearfott et al., 1984) or restraining masks or helmets (Greitz et al., 1980; Fox et al., 1985; Edward et al., 2000). Some residual motion will be present, however, particularly if jaw movement is inherent to the task. While motion can be corrected for prospectively by tracking the head position (Zaitsev et al., 2006; Ooi et al., 2009; Qin et al., 2009), this cannot eliminate effects relating to motion during acquisition of a volume or changes to the shim brought about by a modified head, jaw, or tongue position. Motion-correction algorithms can improve the quality of fMRI results (Oakes et al., 2005) but cannot correct for changing distortions or spin history effects, and can also lead to false positive fMRI results (Wu et al., 1997; Freire and Mangin, 2001). Motion parameters can be included in a GLM as nuisance variables. This reduces motion contamination, particularly in event-related designs (Birn et al., 1999), but substantially reduces BS when even moderate correlation exists between motion and task (Johnstone et al., 2006).

In short, while a range of strategies exist to minimize and correct for motion, some level of motion artifacts will remain, particularly in ultra-high field fMRI with tasks which necessitate some motion, such as overt speech (Foki et al., 2008) and motor tasks, particularly of the jaw or feet. If motion is uncorrelated with the stimulus these effects lead to increased residuals after fitting with a GLM, which reduces BS (Friston et al., 1996). If they are time-locked to the stimulus they can lead to false positive results in a GLM (Hajnal et al., 1994).

Spatial ICA is a promising alternative analysis approach to isolating activation in data containing motion effects since it identifies signal sources on the basis of spatial independence rather than the temporal similarity between stimulus and response. As well as proving effective in identifying activation in conventional fMRI experiments (McKeown et al., 1998), ICA can detect BOLD signal changes resulting from epileptic events (LeVan and Gotman, 2009) and multiple neuronal networks to be separated in such challenging contexts as natural stimulation (Malinen et al., 2007) and the resting state (Beckmann et al., 2005).

Independent component analysis has proved capable of separating activation from computer-simulated motion (McKeown et al., 1998). In the context of real motion, however, ICA has, to date, been used as a filtering tool (Kochiyama et al., 2005; Tohka et al., 2008; Kundu et al., 2012) or to motion-correction data (Liao et al., 2006). In this study, we test ICA as the primary means to identify activation in data containing real motion effects. Our study hypotheses were:

1. that ICA would allow a near complete separation of stimulus-correlated motion and activation, even where there are deviations from task timing or modified HRF in the region of pathology and
2. that it would be possible to identify one or more components reflecting task-relevant activation automatically on the basis of temporal and/or spatial characteristics, or "features."

These hypotheses were tested in a clinical study involving chin and hand motion tasks at very high field.

MATERIALS AND METHODS

PATIENTS

All patients participated in the study, which was approved by the Ethics Committee of the Medical University of Vienna, with written informed consent. In the case of minors this was provided by legal guardians. Patients were referred for functional localization of essential motor cortex (primary hand representation – typically localized in the precentral "knob" (Yousry et al., 1997) and primary chin representation – typically the most lateral and inferior part of primary motor cortex) by physicians who were not involved in this study. Most referrals were for surgical planning prior to excision of a tumor. All patients were in a good general state of health at the time of measurement and were able to perform the tasks. Those patients undergoing chin localizations showed normal masticatory function and those undergoing hand localizations could move the relevant hand against resistance. One patient from the Chin group was excluded due to poor performance (difficulty following task timing). Ten patients remained in the Chin study (age range 8–55 years old, mean age 30 ± 16 years old, 5 females); see **Table 1** for demographic and clinical details. The Hand study consisted of 12 patients (age range 11–61 years old, mean age 31 ± 17 years old, 5 females); see **Table 1**.

TASKS

The functional chin paradigm was repetitive opening and closing of the mouth with a target of one open and close cycle per second.

Table 1 | Patient demographics.

Patient ID		Head coil (# elements)	Age	Gender	Number of runs completed		Pathology
Chin	Hand				Chin	Hand	
C1	H1	24	55	F	12	7	Left precentral tumor, unknown origin
C2	H2	24	32	F	12	8	Temporal lobe resection left (status post glioblastoma)
C3	H3	24	11	M	10	5	Fronto-central focal cortical dysplasia right
C4	H4	24	21	M	12	8	Right central tumor, unknown origin
C5	H5	8	36	M	12	8	Right frontal tumor, unknown origin
C6	H6	24	28	M	11	8	Oligodendroglioma II., frontal lobe right
C7	H7	32	54	F	10	8	Left parietal tumor, unknown origin
C8	H8	32	14	M	10	8	Extra-temporal epilepsy
C9	H9	32	21	F	12	8	Temporal lobe epilepsy right, status post partial temporal lobe resection right
	H10	24	61	F		4	Suspected precentral glioma right
	H11	24	14	M		10	Cryptogenic epilepsy of the right parietal lobe
	H12	24	21	M		7	Fibrillary astrocytoma (grade 2), temporal lobe epilepsy right
C10		32	8	F	8		Focal cortical dysplasia frontal and occipital

Patients who performed the chin task have patient IDs beginning with "C" and those who performed the hand task "H." These IDs are used in other images and descriptions in the text.

The movement was self-paced and symmetrically performed in a blocked design. The hand task was a repetitive opening and closing of the affected hand with the eyes open. For both tasks, each run consisted of four rest and three movement phases of 20 s (eight volumes). Patients were asked to perform 20 runs in total if they were able. If a number of tasks were performed in the same scan session (e.g., chin, hand, foot localizations), the task for each run was communicated prior to the beginning of the run. Commands to begin and stop movement were communicated via headphones during image acquisition.

fMRI ACQUISITION

Images were acquired with a 7 T Siemens MAGNETOM scanner (Siemens, Erlangen, Germany). Three different head RF coils were used, as hardware upgrades were undertaken during the study. These were an 8-channel coil (Rapid Biomedical, Würzburg, Germany), a 24-channel coil (Nova Medical, Wilmington, MA, USA) and a 32-channel coil (Nova Medical). **Table 1** lists which coil was used for each patient measurement. To minimize head movement, plaster helmets were individually constructed for each patient (Edward et al., 2000). Functional MRI data were acquired with a 2D single-shot gradient echo (GE) EPI sequence, with 34 slices acquired parallel to the AC-PC plane, with a matrix size of 128×128, FOV = 230 mm × 230 mm (nominal 1.8 mm × 1.8 mm in-plane resolution), 3 mm thick slices with 0.3 mm gap. This EPI protocol has been used in a number of prior studies with neurological patients at 3 T (e.g., Foki et al., 2007; Beisteiner et al., 2010), and has been validated in clinical application at 7 T (Beisteiner et al., 2011). The resolution is in the higher resolution regime in which physiological noise is minimized and the highest BS gains are expected with field strength (Triantafyllou et al., 2005). Three dummy excitations were performed before acquisition of 56 volumes per run. TE/TR were 22/2500 ms, and partial Fourier encoding was used, with omission of the first 25% of phase-encoding steps, receiver bandwidth was 1445 Hz/pixel, and parallel imaging with GRAPPA (Griswold et al., 2002) was used with a factor of 2.

High-resolution T1-weighted MR images were acquired using a 3D MPRAGE sequence with a matrix size of $320 \times 320 \times 224$, with 0.7 mm isotropic resolution, flip angle of 9°, and GRAPPA acceleration factor 2; acquisition time 7 min 57 s.

fMRI PREPROCESSING

Acquisition, preprocessing, and analysis steps are schematically illustrated in **Figure 1**.

Image preprocessing was carried out in general accordance with the approach used by the Clinical fMRI Study Group at the Department of Neurology of the Medical University of Vienna for presurgical mapping (e.g., Foki et al., 2007; Beisteiner et al., 2010, 2011). For the single-subject analysis, the following preprocessing steps were carried out, with FSL (Smith et al., 2004), in the native space of the high-resolution EPI of each patient. Each run was registered to the first volume of the middle run using FLIRT (Jenkinson et al., 2002), with 12 degrees of freedom, after which runs were concatenated. In the GLM, temporal concatenation equates to a fixed effects analysis in which run is treated as a fixed effect, a valid approach if there is signal stability between runs

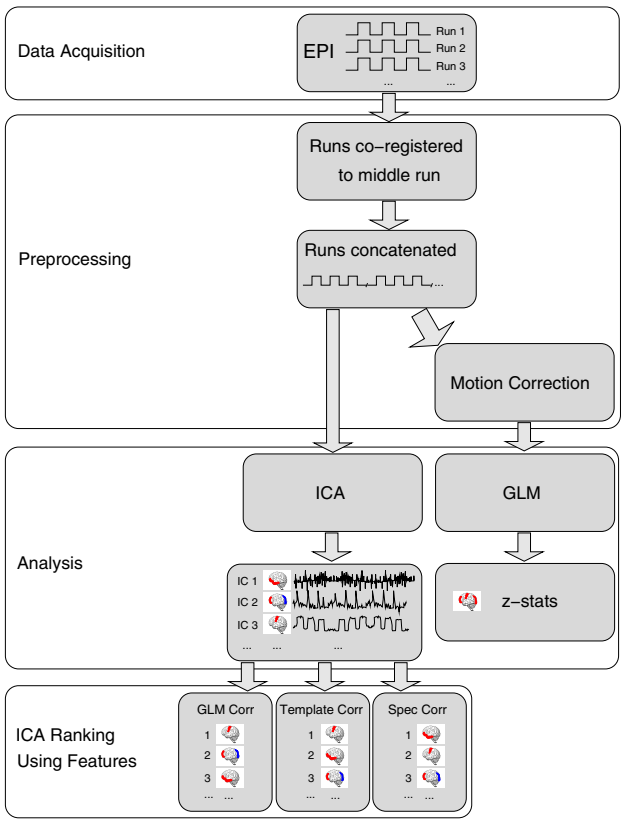

FIGURE 1 | A schematic representation of data processing steps for each patient in the main analysis.

and no inferences are to be drawn about a group. No slice timing, normalization, or spatial smoothing was performed. These data were analyzed with MELODIC ICA (Beckmann and Smith, 2004). For GLM analysis, the concatenated time-series was additionally motion-corrected using MCFLIRT (Jenkinson et al., 2002). Non-brain tissue was also removed using BET (Smith, 2002), the grand-mean intensity of the entire 4D dataset was normalized using a single multiplicative factor and high-pass temporal filtering was applied (Gaussian-weighted least-squares straight line fitting, with sigma = 20.0 s).

GLM ANALYSIS

Analysis was carried out using FSL's FEAT (Smith et al., 2004). The six parameter rigid-body transformations determined in motion correction were included in the analysis model as confounds. Time-series statistical analysis was carried out using FILM with local autocorrelation correction (Woolrich et al., 2001). Resulting statistical z-images were first thresholded at $Z > 2.3$ to determine continuous clusters. Each resulting cluster was then compared against a (corrected) cluster significance threshold of $P < 0.05$ using Gaussian random field theory (Worsley, 2001).

The possibility the GLM may be able to provide an improved separation of activation and motion-related artifacts at higher statistical thresholds was investigated by closely examining results

over a range of thresholds. In supplementary analyses, the possibility of reducing motion-related artifacts in GLM results via cluster size was evaluated by using larger cluster extent thresholds. The possibility that using no cluster thresholding might reveal activation in the basal ganglia and thalamus in GLM results was assessed by applying no cluster extent threshold.

To explore additional possibilities for reducing motion artifacts, GLM analysis was also repeated (i) with the inclusion of the temporal derivatives of motion parameters (in addition to the motion parameters themselves), (ii) on data which were smoothed with a Gaussian kernel with FWHM of 5 mm, and (iii) in a subject-level analysis, rather than a temporal concatenation analysis.

INDEPENDENT COMPONENT ANALYSIS

Probabilistic ICA was carried out with FSL's MELODIC (Beckmann and Smith, 2004). No temporal filtering was performed on the assumption that the signal was stable and that ICA would prove capable of isolating minor drifts, if present, in separate components. Non-brain voxels were masked before voxel-wise de-meaning of the data and a normalization of voxel-wise variance. Pre-processed data were whitened and projected into an n-dimensional subspace using probabilistic principal component analysis. The number of components into which the data was decomposed (the model order) was estimated for each patient using the Laplace approximation to the Bayesian evidence of the model order (Beckmann and Smith, 2004).

AUTOMATED IDENTIFICATION OF SALIENT ICs

Several hundred components may be generated in the analysis of data from each patient. From these, the single component or small number of components which reflect task activation must be identified. In MELODIC, components are ordered by the percentage of the total signal variance in the data for which they account. In the presence of motion and other artifacts, task-related activation often appears low in the list, meaning that a large number of components need to be assessed.

One or more ICs related to task activation were identified by a clinical fMRI expert (RB), who assessed all components for all patients. The identification was based on the presence of clear activation in primary and secondary motor areas, with consideration of the effects of the brain pathology (e.g., cluster divisions), supported by time courses which approximately accorded with that expected from the paradigm, and with reference to the clinical report (the local gold standard) (Beisteiner et al., 2000, 2008).

Automatic identification of task-activation components was implemented via ranking of components on the basis of spatial and temporal features. Three features were implemented. The first was the value of the correlation between each IC spatial map and the GLM t-map ("GLMcorr"). The second was the correlation between each IC spatial map and a mask for the precentral gyrus ("TEMPLATEcorr"). The third feature was the correlation between the frequency distribution of ICs and the frequency distribution of the model regressor ("SPECcorr"). For the third feature, correlation between frequency spectra rather than time courses was used to ensure sensitivity to responses which could be delayed due to modified HRF or late task performance (Moritz et al., 2003), and to reduce sensitivity to low frequency behavior such as drift. All features were programed in MATLAB (Mathworks Inc, Natick, MA, USA).

GLMcorr was calculated as the correlation between in-brain voxels in the unthresholded IC maps and the unthresholded Z-statistic map for the sole contrast of interest in the GLM, using MATLAB's "corrcoef" function.

The Harvard-Oxford template (Desikan et al., 2006)[1] was used for the calculation of the *TEMPLATEcorr* feature. This probabilistic atlas assigns unique numerical labels to 48 cortical and 21 subcortical regions. For the *TEMPLATEcorr* feature, the Harvard–Oxford template was converted to a precentral gyrus mask by converting atlas values of 7 (the template value for the precentral gyrus) to 1, and setting all other values to 0. This mask was registered to the space of each patient's EPI using a transformation derived as follows. First, the MNI T1 brain (i.e., skull-stripped) template, which is in the same space as the Harvard-Oxford template, was coregistered, using FLIRT (Jenkinson et al., 2002), to patients' MPRAGE structural scans, which had been bias-field corrected with FAST (Zhang et al., 2001), and skull-stripped using BET (Smith, 2002). This defined the first transformation matrix. Secondly, each patient's skull-stripped, bias-field corrected MPRAGE was coregistered to the middle EPI of the concatenated time-series. This defined the second transformation matrix. The two transformations were combined to define the transformations from the template space to the space of each patient's EPI. The correlation between the precentral gyrus of this template and each IC map was calculated.

For the *SPECcorr* feature, the frequency distribution of each IC, calculated using MELODIC, was correlated with the frequency distribution associated with the predicted responses. This latter was calculated as the Fourier transform of the convolution of a regressor for the ON and OFF task periods convolved with a HRF. The HRF was generated with the statistical parametric mapping (SPM) software (Friston et al., 1995) using the function spm_hrf.m, in the SPM8 version[2], using default values for the parameters (p) of the response. The convolution and Fourier Transform were carried out in MATLAB.

TIME-COURSE ANALYSIS

To assess the signal behavior in activated areas virtually free from bias of analysis approach (ICA or GLM), the mean time courses (over runs) of voxels in the left and right primary motor areas (PMA) were calculated for each patient, and averaged over runs. VOIs were coboids sized $9 \times 9 \times 9$ voxels centered on the peak voxel in the ICA results in the left and right motor cortex. The ICA results were chosen because they were cleaner, but selection of the GLM peak voxels would not significantly affect results, as these were close to ICA peak voxels, and VOIs were large.

INDEPENDENT ASSESSMENT OF ACTIVATION

To provide an additional means to assess the validity of GLM and ICA results, activation maps were also generated with the "risk map" approach (Beisteiner et al., 2000, 2008); a correlation

[1] http://www.cma.mgh.harvard.edu/fsl_atlas.html
[2] http://www.fil.ion.ucl.ac.uk/spm/software/spm8/

analysis over a range of thresholds and with shifted regressors to generate a map of a small number of highly reliably activated voxels. This method has been validated via reference to Direct Electrocortical Stimulation (Roessler et al., 2005), and is used locally as a clinical gold standard to generate clinical reports.

RESULTS

EXTENT OF HEAD MOTION

Patients in the Chin group completed between 8 and 12 runs (average 11.0 ± 1.4), and those in the Hand group between 4 and 10 runs (average 7.4 ± 1.6). Rigid-body motion correction yielded three translation vectors (x, y, z) and three rotation vectors (roll, pitch, yaw). These were reduced to two representative metric vectors, one for translation – the root-mean-square (RMS) translation and one for rotation – the sum of the magnitudes of the individual angles (i.e., disregarding sign). Over all patients and all runs in the Chin group, the mean RMS displacement was 0.43 ± 0.45 mm, and the mean rotation 0.0078 ± 0.0083 rad. Corresponding values for the Hand group were a mean RMS displacement of 0.107 ± 0.058 mm and a mean rotation of 0.0035 ± 0.0030 rad.

CHIN TASK

General linear model

There were no significant signal discontinuities between runs. Motion artifacts were identified as suprathreshold voxels either on the edge of the brain or at high contrast boundaries or in areas affected by Nyquist ghosts (Hajnal et al., 1994; Robinson and Moser, 2004; Beckmann, 2012). This attribution was supported by an assessment of the independent components whose time courses correlated best with motion parameters (not shown). Motion artifacts were present in all GLM results at a cluster-corrected threshold of $P < 0.05$ (**Figure 2**, left). Partial volume motion artifacts manifested as suprathreshold voxels either on the edge of the brain or at high contrast boundaries. These were apparent in the GLM results of patients C2, C4, C5, C7, and C8 (**Figure 2**, left, at yellow arrows). Broad areas of false positive results, tentatively ascribed to reconstruction artifacts, were present in GLM results of patients C1, C2, C4, C5, C6, and C10 (**Figure 2**, left, at cyan arrows). Typically these artifacts were reduced at higher thresholds but did not disappear. Increasing the cluster extent threshold did not help to reduce motion artifacts, as they were large and distributed. Inclusion of the temporal derivatives of

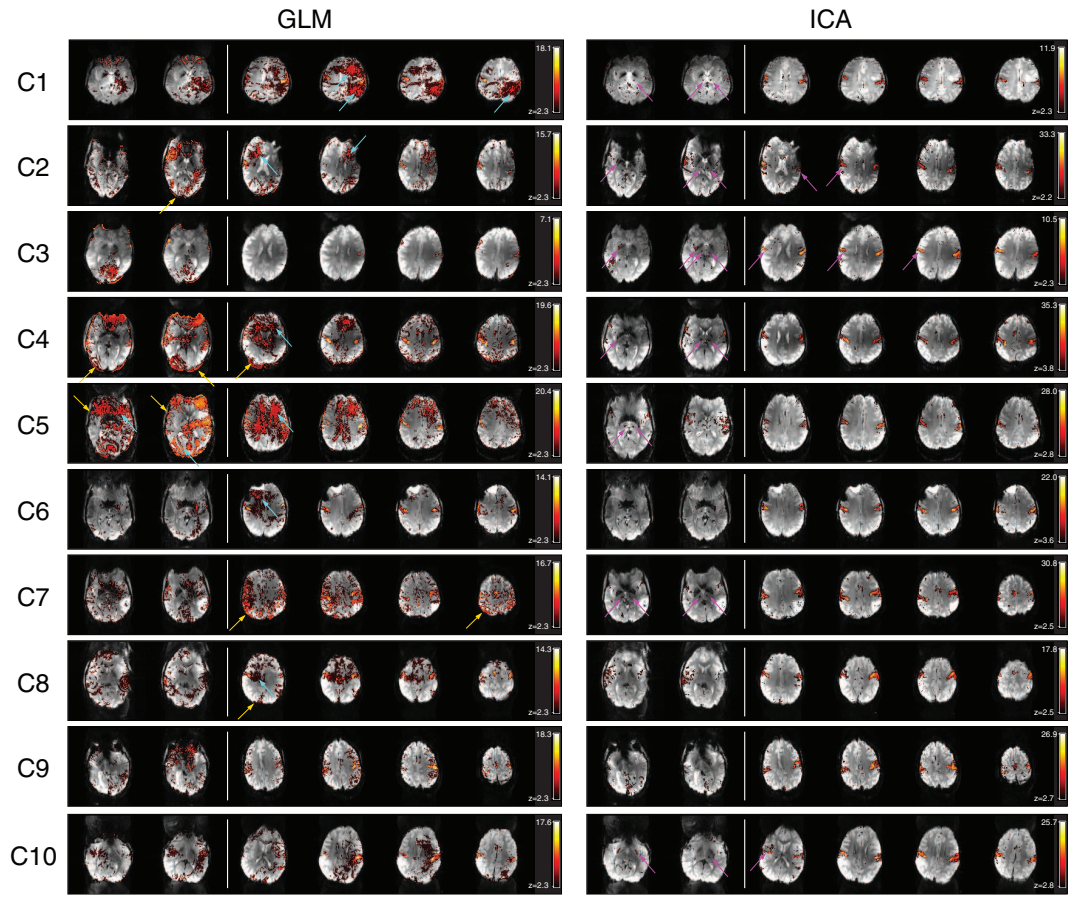

FIGURE 2 | A comparison of GLM and ICA analyses of 7T fMRI data with a chin task. GLM results are contaminated by motion artifacts (yellow and cyan arrows). ICA components show no motion contamination and bilateral activation throughout primary motor areas. Activated areas not present in corresponding GLM results, or not distinguishable from artifacts, are indicated by magenta arrows. White vertical lines separate sample slices covering the basal ganglia from those showing primary motor regions. All brain images are displayed in radiological convention.

motion parameters in the analysis (in addition to the motion parameters themselves) led to a moderate reduction in the artifact level in two patients (C7 and C9, not shown) but not in other patients. Smoothing data prior to GLM analysis increased significance values in both artifacts and activation clusters, leaving the overall pattern of suprathreshold voxels smoother, but broadly unchanged. The contamination of GLM results by artifacts was no lower in subject-level analysis than in the temporal concatenation analysis reported here throughout. Basal ganglia activation present in ICA results but not GLM is indicated in **Figure 2** by magenta arrows in lower slices.

Despite artifacts, it was possible to identify the perirolandic area via detection of central sulcus activation in all patients. Activation was not apparent in some known motor regions, however (**Figure 2**, magenta arrows). In many patients there was no clearly segregable activation in the basal ganglia and thalamus. The extent to which motion artifacts and low sensitivity to basal ganglia activation may be threshold effects is investigated in **Figure 3**, and reported in Section "Additional Task-related Components."

Independent component analysis

A task-activation component was identified for all patients. Bilateral precentral gyrus activation was identified in these, with no contamination by motion artifacts (**Figure 2**, right column). Activation was confirmed to correspond to the clinical report and also to the GLM results (**Table 2**). Subcortical motor activation, in the basal ganglia, was also present in all patient's results other than C9 (**Figure 2**). This was evaluated and judged, on a neuroanatomical and neurophysiological basis, to be plausible task-related activation.

Separate resting-state networks in motor regions (Biswal et al., 1995) and the basal ganglia (Robinson et al., 2009), which are known from other studies to persist during task execution (Fox et al., 2007; Calhoun et al., 2008) could also be identified in the ICA results of a number of patients (not shown).

Comparison of GLM and ICA

Primary motor activation in ICA generally extended into more inferior parts of the motor strip and was more concordant with known motor regions than GLM results, and motion artifacts were dramatically reduced (**Figure 2**). Basal ganglia activation associated with the motor task was apparent in most patients' ICA results, but not GLM results. GLM results in the basal ganglia were not substantially changed when no cluster extent size was imposed, regardless of the statistical threshold at which these results were assessed. This demonstrates that the low sensitivity of GLM in subcortical regions was not a cluster extent or a thresholding effect. Thalamic activation was present in all patients' ICA results other than those of C9, and in the putamen in the results of all patients other than C1 and C9 (**Figure 2**). Artifacts were also lower in ICA results than in high-threshold GLM images (**Figure 3**).

For patients C1, C2, C5, C6, C7, C8, and C10, the most inferior and lateral extent of primary motor activation merged with motion artifacts in the GLM analyses, so that their detection was much more difficult, regardless of the statistical threshold. **Table 2** lists the extent to which activation could be detected with GLM and ICA in cortical and subcortical regions. GLM and ICA results are compared over a range of GLM thresholds in **Figure 3** in slices which indicate increased ICA sensitivity.

HAND TASK

General linear model

General linear model results for patients H1, H2, H4, H5, H8, H9, H10, H11, and H12 were subject to significant contamination by motion artifacts at a cluster-corrected threshold of $P < 0.05$. These artifacts appeared as areas of false positive results on the edge of the brain and/or at boundaries between high contrast areas (**Figure 4**, at yellow arrows). Wide areas of false positives were also present in H1, H8, and H9 (cyan arrows), originating from reconstruction errors for these GRAPPA-accelerated acquisitions.

Despite contamination by false positive voxels, activation in the contralateral primary motor area, responsible for hand motion, was detected in all the patients. However, activation in the supplementary motor area was difficult to identify due to motion artifacts in H1 and could not be identified in H3 with the GLM at this threshold (magenta arrows). Thalamic activation was present bilaterally in patient H7 and unilaterally in patients H2, H3, H4, H5, H6, H8, H11, and H12. No thalamic activation was evident in patients H1, H9, and H10.

Basal ganglia activation was present in H3, H4, H5, H6, H7, H8, H11, and H12, depicting the putamen either bilaterally (H4, H5, H6, H7, H11, H12) or unilaterally (H3, H8). The posterior part of the left putamen was apparent in H1, but not the right, due to the presence of GRAPPA artifacts. No basal ganglia activation was detected with the GLM in H2, H9, and H10.

Independent component analysis

Clear and well-defined activation of the contralateral primary motor area was evident in one or more components in the ICA results for each of the 12 patients. There was little or no motion-related artifact contamination at a canonical Gaussian mixture model threshold of 0.5. Activation in the supplementary motor area was clearly depicted in all the patients.

Activation of subcortical structures, such as the thalamus and the putamen, was evident in the ICA results for all patients except for H9 and H10. A small number of voxels corresponding to activation in the right putamen and in the right thalamus were visible in H3.

Motion artifact level was higher in ICA results in H7 than in other patients, though activation in the primary and supplementary motor regions and in the basal ganglia (putamen and thalamus) was still clearly visible.

Comparison of GLM and ICA

There was a high level of consistency in all the patients between PMA identified as being activated using GLM and ICA. Motion-related false positive results were more prominent in GLM results, in which detected activation was in many cases highly contaminated. Motion-related false positives were strongly reduced in both cortical and subcortical regions in ICA results for all patients except for H7, in which the quality of the results was similar in GLM and ICA.

Independent component analysis results for patient H1 show a clear advantage over the GLM results in the depiction of

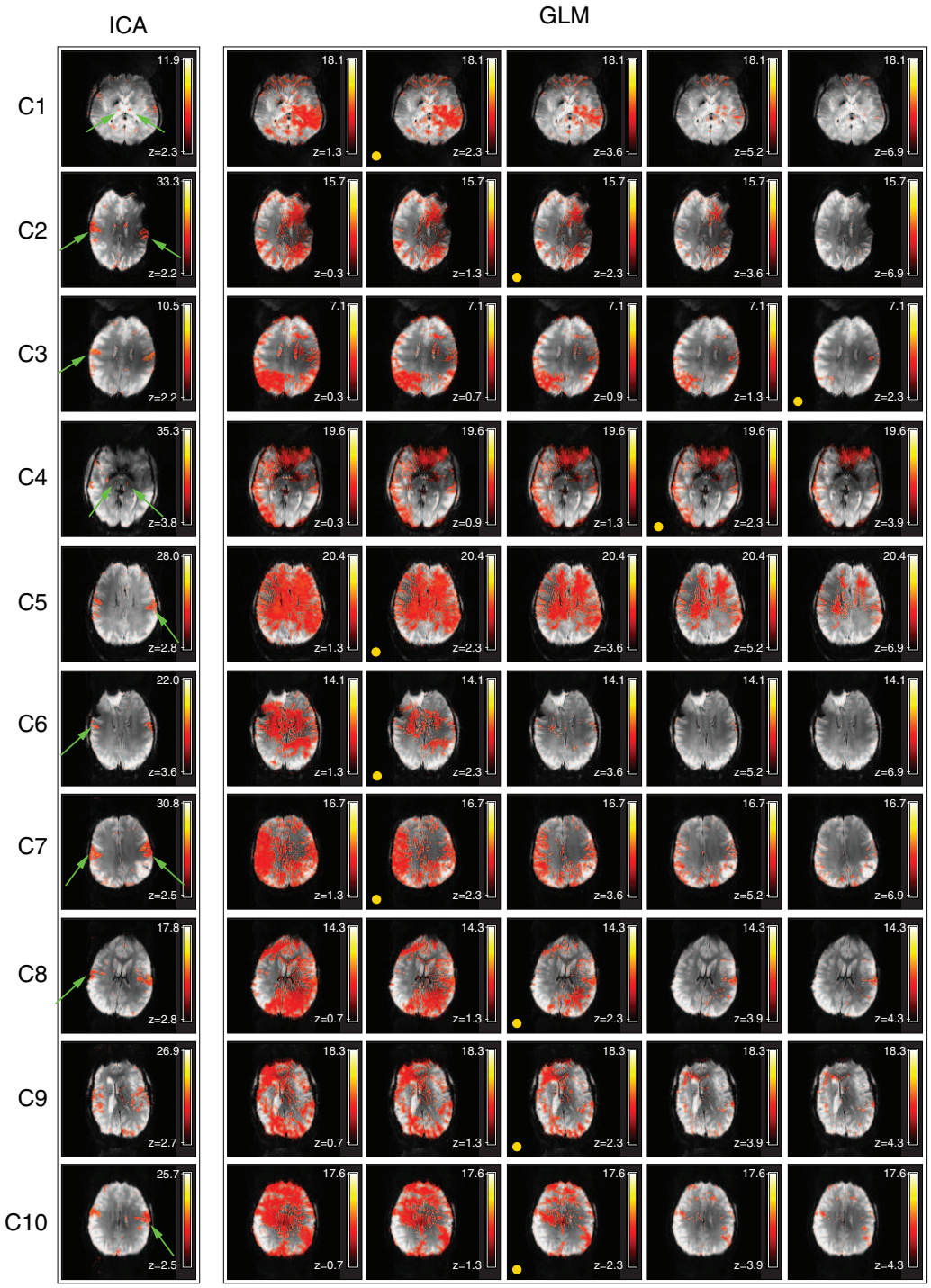

FIGURE 3 | Examination of the activation visible in GLM results over a range of thresholds (chin task). Activation visible in independent components and GLM results is compared in a single slice. The threshold corresponding to a GLM cluster-corrected $P = 0.05$ is indicated by a yellow spot. Activation maps are illustrated at higher and lower thresholds than this to allow the ability to separate activation and motion in GLM results to be assessed. Clusters which are substantially better defined in ICA are indicated by green arrows.

activation in the putamen. The anterior part of the right putamen and the left putamen are easily identified in ICA results, with no surrounding false positives, whereas in the GLM results the anterior part of the right putamen is not visible, even at higher thresholds, and only the posterior part of the left putamen is clearly depicted.

Table 2 | A comparison of the ability of the GLM and ICA to detect activation in cortical and subcortical sensorimotor areas in the chin task.

Patient	Cortical sensorimotor activity (perirolandic cortex)		Subcortical sensorimotor activity (basal ganglia/thalamus)	
	GLM	ICA	GLM	ICA
C1	y	y	(y)	y
C2	y	y	n	y
C3	y	y	(y)	y
C4	y	y	n	(y)
C5	y	y	(y)	y
C6	y	y	y	y
C7	y	y	n	y
C8	y	y	(y)	y
C9	y	y	n	n
C10	y	y	(y)	y

GLM results were assessed at a number of statistical thresholds. Activation was marked as unequivocally present "y," arguable "(y)," or not detectable "n." A clear benefit for detection of subcortical activation was evident with ICA, with better depiction of the basal ganglia in 8 out of 10 patients.

Table 3 details the extent to which activation could be detected with GLM and ICA in cortical and subcortical regions.

ADDITIONAL TASK-RELATED COMPONENTS

For patients C4, C5, C7, and C8, only one component was related to task-related motor activation. For C1, C2, C3, C6, C9, and C10, some task-related activation was present in additional components. In most cases this was secondary motor and basal ganglia activation. These components are illustrated in **Figure 5**. For C1, a component was identified which showed activation mainly on the side of the pathology, in face-M1. The time course of this second component suggests that it was dominated by activation in a single run. A component for C2 detected secondary motor regions, including the precentral sulcus and SMA, indicating the capacity for ICA to separate subnetworks of motor function. This component was associated with a more rapidly fluctuating time course than the primary component. A component for C3 contained both pre-SMA, SMA, precentral sulcus, and posterior parietal activation, again demonstrating ICA's ability to separate PMA from secondary areas responsible for motor planning and sensorimotor integration. Neither this nor the primary motor IC showed a time course which correlated well with the stimulus (see **Figure 6**). An additional component of interest for C6 included participation of the basal ganglia, particularly the thalamus, with activation also in the SMA and right perirolandic area on the pathological side. The time-course of this IC was similar to that of the main component but was dominated by later runs. A secondary component for C9 showed activation in the precentral sulcus and inferior parietal regions, language-related areas, including Wernicke's area arising from the response to auditory command and possible vocalization. An additional component for C10 showed activation in primary motor area (left hemisphere) and the postcentral sulcus (right hemisphere), reflecting sensorimotor integration (**Figure 5**).

In H4, the main component shows the predicted activation in the right hemisphere (see **Figure 4**, which uses radiological convention). An additional task-related motor component was found for patient H4 (see **Figure 5**), which represents bilateral integrative parietal activity and additional M1 activation in the left hemisphere, in response to motion of the left hand. This could be interpreted as auxiliary M1 activation due to paresis elicited by motion of the contralateral arm. The time course associated with this activation is delayed, so was not detected in the GLM analysis.

An additional bilateral component was also found for patient H9. This was interpreted as representing activation in the face area. The time course of this component is counter to that of the task, indicating that it could be associated with facial movements during the rest phases or with systematic reduction in perfusion in the face area.

TIME COURSES

With the exception of patients C2 and C3, time-courses in the PMA in the chin task accorded well with the prescribed timing; four rest periods (A) and three task periods (B) of equal duration, presented in an ABABABA design (**Figure 6**). Time courses in PMA in C2 and C3 are non-model-conform (see graphs outlined red in **Figure 6**), and GLM results show high levels of noise as well as activation in the PMA. Clean activation is detected in the ICA results, however, indicating that characteristic signal changes take place in the PMA, despite a lack of conformity with the model.

Time courses for the hand task were in good agreement with the prescribed timing, which was identical to that in chin task (**Figure 7**).

MOTION ARTIFACTS

Independent component analysis allows contributions to the motion artifacts in GLM to be separated into contributing sources and assessed in more detail. We examine these here as an aside from the central aim of this study. Examples of the most prominent artifacts are illustrated in **Figure 8**, for a single patient, C5, along with tentative attribution of their origin. Artifacts labeled "A" and "B" in **Figure 8** arise from motion in the anterior-posterior direction, and manifest at contrast boundaries; the edge of the brain and the borders of gyri. Artifact "C" reflects motion in the through-plane direction, and presents as an outline of the ventricles. One component indicates rapid intensity fluctuations in the Nyquist ghost of a single slice ("D"). Component "E" likewise occurs in a Nyquist ghost region but occurs in every second slice of the volume (which was acquired interleaved), and shows interference with the signal in the main image. These components were identified by their similarity with those reported in Beckmann (2012).

AUTOMATIC IDENTIFICATION OF SALIENT ICs

In MELODIC, independent components are ranked by the percentage of total variance in the data that they explain. Primary task components in the Chin group (which had been identified by an expert) were ranked by variance on average in position 145 ± 48 out of a total of 194 ± 73 components (with quoted errors being one standard deviation). In the single-patient analysis of the hand

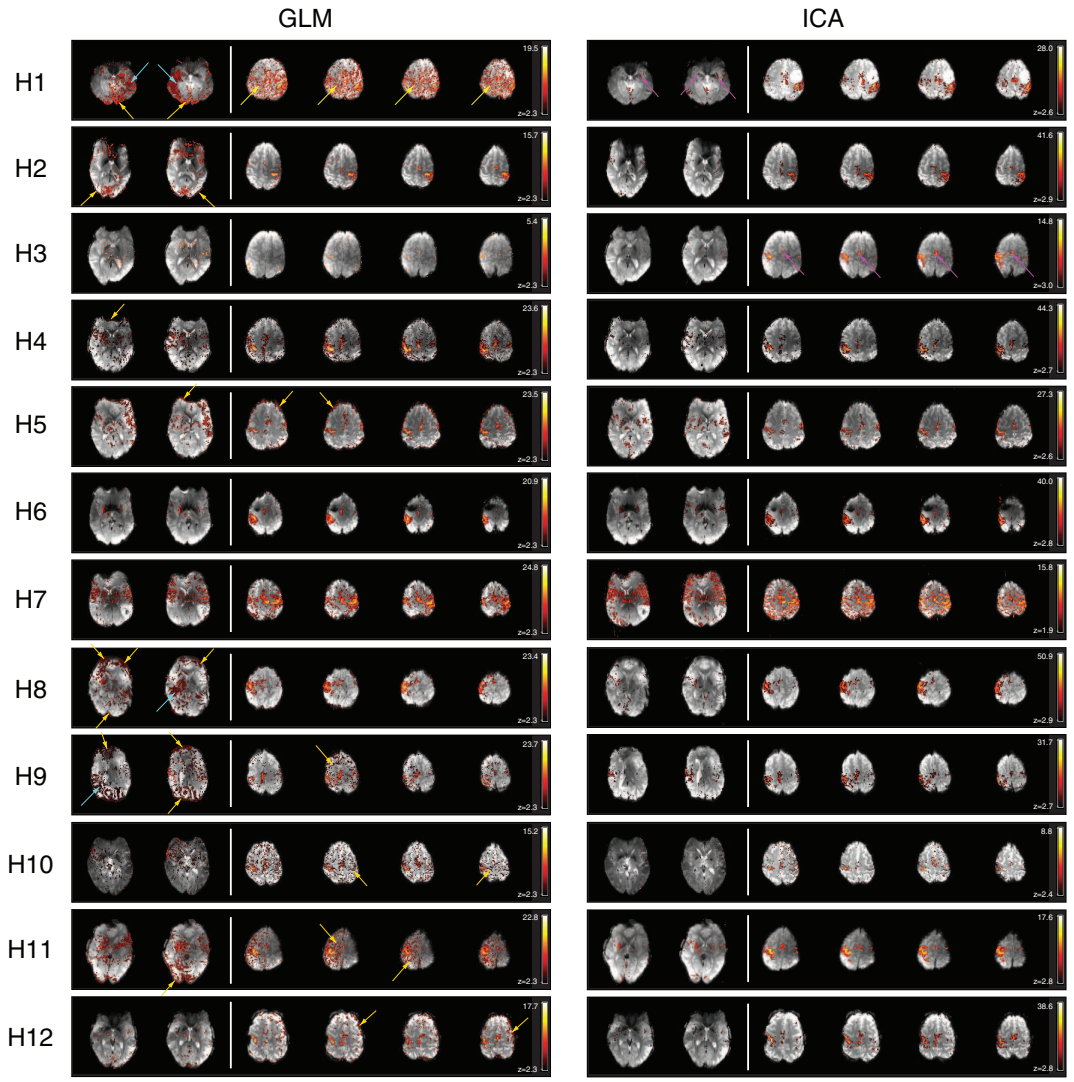

FIGURE 4 | A comparison of GLM and ICA analyses of 7T fMRI data with a hand task. The same thresholds were applied as in **Figure 2**. Activation in the basal ganglia and thalamus is indicated by arrows in ICA. Activated areas not present in corresponding GLM results, or not distinguishable from artifacts, are indicated by magenta arrows.

task, they were ranked in position 92 ± 36 out of 126 ± 43. Primary motor components were ranked more highly using the features tested; GLMcorr, TEMPLATEcorr, and SPECcorr. Of these, both GLMcorr and TEMPLATEcorr were highly effective. Over the Chin and Hand tasks, the primary activation component was ranked in position 1.8 ± 1.0 using TEMPLATEcorr, in position 2.6 ± 6.6 using GLMcorr and 17 ± 47 using SPECcorr. A full list of component rankings by feature is given in **Tables 4** and **5** for the Chin and Hand groups, respectively. The potential of the GLMcorr and TEMPLATEcorr features to discriminate from other components is demonstrated in **Figure 9**.

DISCUSSION

Independent component analysis of 7 T fMRI data acquired from neurological patients performing chin and hand tasks cleanly separated primary motor activation from motion artifacts. Secondary motor areas and the basal ganglia and thalamus could also be distinguished in most patients. A single (default) ICA threshold was appropriate to be able to visualize PMA bilaterally in all patients. GLM analysis of the same data was, in contrast, contaminated by severe motion artifacts arising from partial volume and spin history effects, increased Nyquist ghosting and parallel imaging reconstruction noise. This was despite the use of effective head fixation, motion correction, and the inclusion of motion parameters in the analysis model. Because of these artifacts, GLM results had to be assessed over a range of statistical thresholds in order to be able to identify primary motor activation. The participation of some secondary motor regions and subcortical regions could, in many patients, not be distinguished from artifacts in GLM results. The advantages of ICA were particularly evident in patients whose responses deviated – either because of locally modified hemodynamics or because

Table 3 | A comparison of the ability of the GLM and ICA to detect activation in cortical and subcortical sensorimotor areas in the hand task.

Patient	Cortical sensorimotor activity (perirolandic cortex)		Subcortical sensorimotor activity (basal ganglia/thalamus)	
	GLM	ICA	GLM	ICA
H1	y	y	(y)	y
H2	y	y	(y)	(y)
H3	y	y	(y)	(y)
H4	y	y	y	y
H5	y	y	y	y
H6	y	y	y	y
H7	y	y	y	y
H8	y	y	y	y
H9	(y)	y	n	n
H10	y	y	n	n
H11	y	y	y	y
H12	y	y	y	y

GLM results were assessed at a number of statistical thresholds. Activation was marked as unequivocally present "y," arguable "(y)," or not detectable "n." ICA detected cortical sensorimotor activation in one patient in which it was not clearly visible in GLM (H9), and in the basal ganglia in one patient in which it was not detectable in GLM (H1).

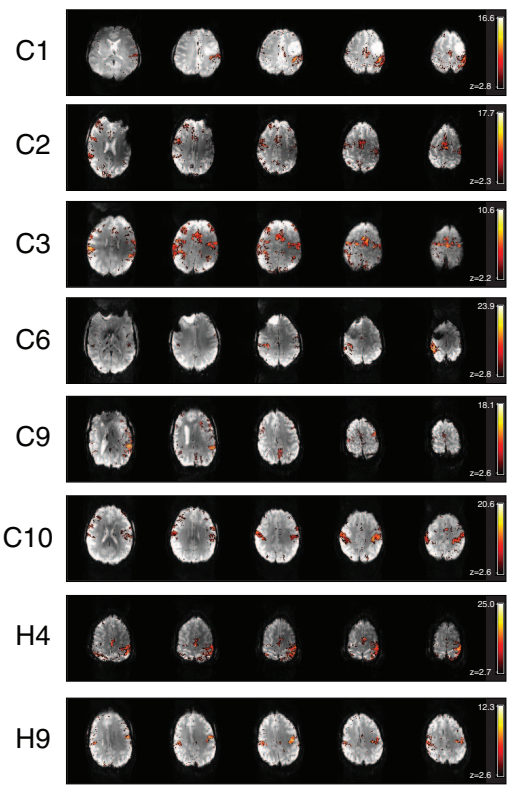

FIGURE 5 | Additional motor components identified in the ICA results of chin patients C1, C2, C3, C6, C9, C10, H4, and H9.

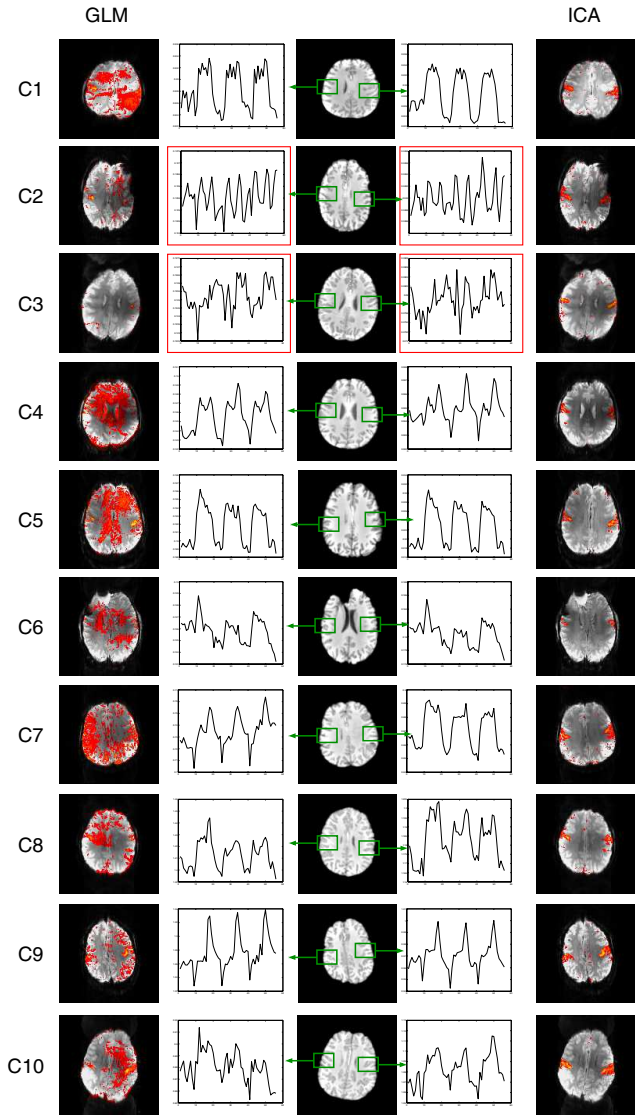

FIGURE 6 | Mean responses in voxels in primary motor areas in the chin task. Time courses in PMA in C2 and C3 (outlined in red) are non-model-conform, and correspond with low sensitivity in GLM results (left) but not ICA (right).

task execution strayed from the intended task timing – from the model.

Previous studies have used ICA to identify and remove non-activation components (Kochiyama et al., 2005; Tohka et al., 2008). The features implemented included slice-to-slice signal variation, brain boundary signal, and time-course heteroscedasticity, which are very different from the features we applied here, which were targeted at identifying activation rather than artifacts. While artifact removal using ICA was successful in those prior studies at 1.5 and 3 T, it would be substantially more challenging to correctly identify only artifacts in the data acquired in this study, particularly in the chin task. At 7 T, signals resulting from motion – partial volume effects, spin history effects, parallel imaging artifacts, and

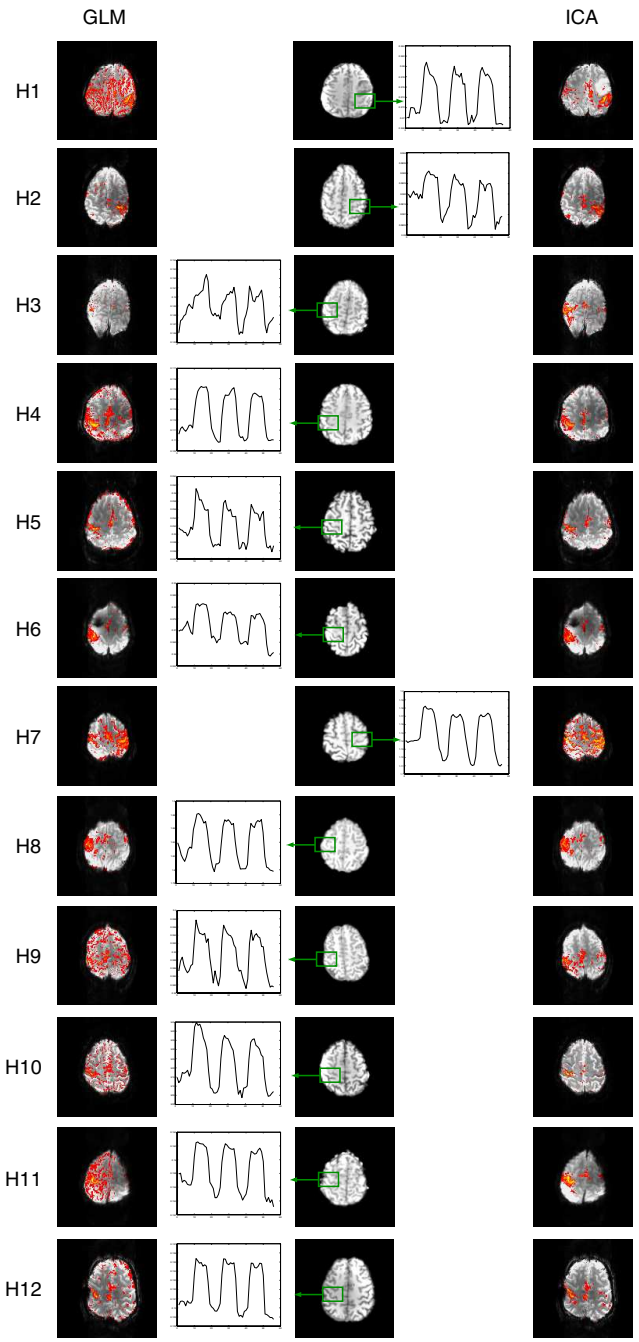

FIGURE 7 | Mean responses in voxels in primary motor areas in the hand task. Time courses in PMA in C2 and C3 (outlined in red) are non-model-conform, and correspond with low sensitivity in GLM results (left) but not ICA (right).

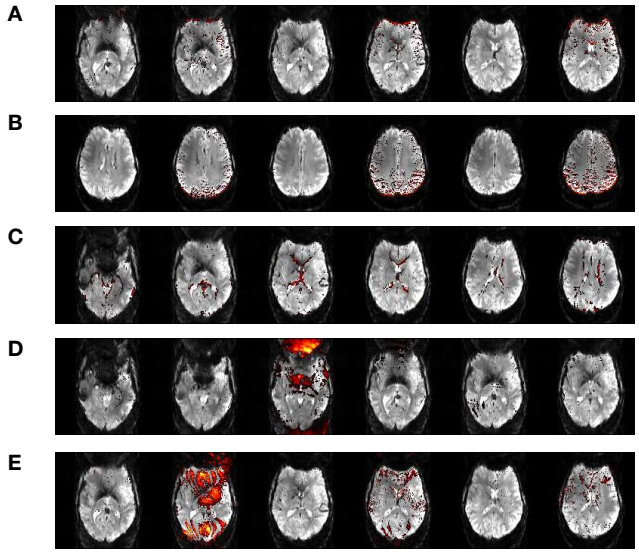

FIGURE 8 | Motion artifact components isolated in data from Chin patient C5. These artefacts are attributed to motion in the anterior-posterior direction **(A, B)**, through-plane motion **(C)**, fluctuating Nyquist ghost **(D, E)**.

B0 changes – account for a larger proportion of the total variance than at lower field strength, and motion effects manifest with very different spatial signatures. As such, there is increased likelihood that some motion-related components would not be identified by the algorithms proposed (false negatives), or that activation-related components be erroneously removed (false positives). For that reason, a direct analysis with ICA, with ranking/classification of components, would seem to be a more promising option than filtering with ICA prior to GLM analysis.

The model orders estimated in this study (mean $\pm$ SD over patients: 194 ± 73) were much higher than those reported by Tohka et al. (2008). This is likely to be because our concatenated runs were longer and the data itself more complex, due to the artifacts induced by the task combined with higher resolution, the use of GRAPPA, and very high field. In a study into model order, Abou-Elseoud et al. (2010) found that 70 ± 10 components were appropriate for PICA of the 1.5-T data they considered, but that "Different model orders may be found more optimal when higher field strengths and higher resolutions are used." Our findings support those authors' conclusions.

Resting-state networks in motor regions (Biswal et al., 1995) and the basal ganglia (Robinson et al., 2009), which are known from other studies to persist during task execution (Fox et al., 2007; Calhoun et al., 2008) (and which are also known as "Temporally Coherent Brain Networks" in this context) could also be identified using ICA in this study. This is of particular relevance for patients who may have difficulty performing motor tasks, as others studies have shown that the sensorimotor area can be localized with resting-state measurements in presurgical populations (Kokkonen et al., 2009).

Recent implementations of ICA (Calhoun et al., 2001; Beckmann et al., 2005) make it a simple analysis to perform. The identification of relevant, activation-related component(s) can, however, be time-consuming, given a large number of independent components. The use of ranking according to one of a number of simple features greatly simplifies this problem. When components were correlated with a precentral gyrus mask, the primary motor component was ranked in position 1 for most patients, and within

Table 4 | Summary of the total number of components identified in the Chin group (No. ICs) and ranking of the primary motor component in the list by (i) percentage of variance explained (MELODIC default) (ii) GLMcorr: the correlation between IC spatial map and GLM t-map (iii) TEMPLATEcorr: the correlation between IC spatial map and a precentral gyrus template (iv) SPECcorr: the correlation between the frequency spectra of model time courses and frequency spectra of IC.

Patient ID	No. ICs	Primary motor IC position in ranking by			
		Variance (i)	GLMcorr (ii)	TEMPLATEcorr (iii)	SPECcorr (iv)
C1	234	132	1	2	4
C2	205	191	2	2	18
C3	138	129	32	1	223
C4	200	155	1	1	15
C5	250	159	5	2	16
C6	118	110	1	1	10
C7	209	167	1	1	19
C8	163	162	1	1	5
C9	256	113	1	1	16
C10	165	138	1	1	1
Median	**203**	**147**	**1.0**	**1.0**	**15.5**
Mean	**194**	**145**	**4.6**	**1.3**	**32.7**
SD	**73**	**48**	**9.7**	**0.5**	**67.2**

Table 5 | Summary of the total number of components identified in the Hand group (No. ICs) and ranking of the primary motor component in the list by (i) percentage of variance explained (MELODIC default) (ii) correlation between IC spatial map and GLM t-map (iii) correlation between IC spatial map and a precentral gyrus template (iv) correlation between frequency spectrum of model time course and frequency spectrum of IC.

Patient ID	No. ICs	Primary motor IC position in ranking by			
		Variance (i)	GLMcorr (ii)	TEMPLATEcorr (iii)	SPECcorr (iv)
H1	161	99	1	1	1
H2	138	130	1	3	1
H3	120	80	1	2	44
H4	126	58	1	3	1
H5	169	93	1	6	1
H6	100	70	1	2	2
H7	24	16	1	1	1
H8	158	122	1	3	1
H9	163	108	1	1	1
H10	84	79	1	1	1
H11	159	157	1	1	1
H12	108	102	1	2	1
Median	**132**	**96**	**1.0**	**2.0**	**1.0**
Mean	**126**	**93**	**1.0**	**2.2**	**4.7**
SD	**43**	**37**	**0**	**1.5**	**12.4**

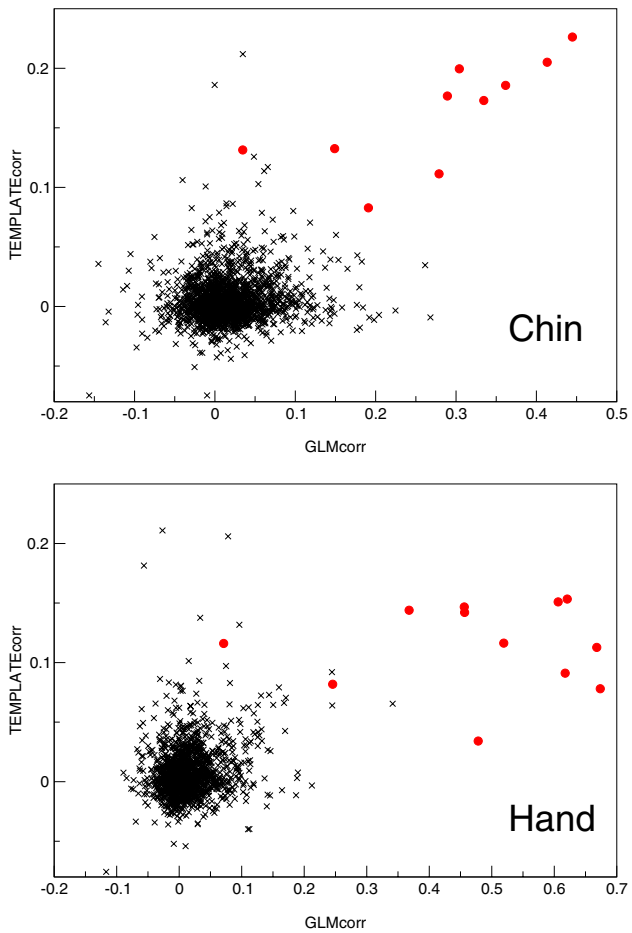

FIGURE 9 | A plot of the two most successful features used to automatically identify primary motor activation components (red circles) amongst other components (black crosses) in the Chin and Hand groups.

the first six positions for all others. This reduces the time required for an interpretation of the ICA results by the clinician. A similar approach might also work for other clinical tasks such as presurgical language mapping with neuroanatomical predefinition of Brocas and Wernicke areas. Limitations concern the possibility of missing components related to neuroplastically shifted brain activations or difficulties in defining neuroanatomical regions of interest in largely distorted brains. In these cases, individual screening of all components would probably still be necessary. In an extension of the ranking we have demonstrated, fully automatic identification of the primary motor component might be achieved with a combination of the "GLMcorr" and "TEMPLATEcorr" features using a trained classifier (Tohka et al., 2008; e.g., Soldati et al., 2009), although this would need to be developed with a larger number of data sets for training and testing. The performance of the *SPECcorr* feature, which has shown to be an effective ranking feature in a previous motor task study at 1.5 T (Moritz et al., 2003) was relatively poor in this context. This is due to the similarity between the frequency spectra of activation

and stimulus-correlated motion. The poor performance of the *SPECcorr* feature also suggests that the Hybrid ICA approach of McKeown (2000), which combines components with time courses similar to a hypothesized reference function, would be likely to incorporate motion components if applied to these data.

In contrast to Tohka et al. (2008), no motion correction was carried out prior to analysis with ICA in this study. Given effective head restraint, it was expected that ICA would be able to cleanly separate activation from motion-related signal sources without using prior motion correction. This proved to be the case, probably because the dominant motion artifacts in these data were not related to voxel shifts, but rather to changes in B0 and GRAPPA reconstruction errors, which are more pronounced at very high field. At lower field and with less effective head restraint voxel shifts may constitute the dominant source of signal change, and a prior motion correction may be necessary to ensure the effective performance of ICA.

We consider the potential implications of our findings for ultra-high field presurgical planning with motor tasks. In the resection of tumors close to motor regions, the primary aim is to reliably identify the perirolandic area via detection of central sulcus activation. If reliable definition of the course of the central sulcus is possible, the primary motor cortex may be spared in its entirety. In this study, central sulcus activation could be identified in all patients using the GLM approach, despite substantial motion-related artifacts. Depending on the degree of malformations present in the perirolandic area, precentral gyrus regions can be rendered dysfunctional by a tumor, however, and neoplastic reorganization may take place. This leads to function being subsumed by other portions of the precentral gyrus or the contralateral precentral gyrus. In this case it may be necessary to map the primary motor homunculus with a variety of motor tasks. In such cases sensitivity may be required in more inferior regions, where motion artifacts are more pronounced, as observed in this study. ICA results have been shown to be more sensitive and specific in these regions.

The presence of pathology can lead to modification of the hemodynamic response. In presurgical planning it may be necessary to include the temporal derivative of the HRF, use a Finite Impulse Response or Fourier Basis set approach, or estimate the HRF for each patient (Carter et al., 2008; Casanova et al., 2008) and assess the consistency of response over a range of thresholds and runs (Beisteiner et al., 2000, 2010). The results achieved here suggest that the same end – robust results in the case of atypical temporal dynamics – may be achieved using ICA with a much reduced clinical analysis and assessment overhead. "Killer applications" of ICA are those in which task timing cannot be monitored, such as studies of the resting state (Beckmann, 2012). While performance can be recorded for many tasks, such as the simple motor tasks described here, there may be an absence of compatible monitoring devices for ultra-high field systems, and some stages of processing may be hard to monitor for other tasks relevant to presurgical planning, such as the "home town walking" task used to map memory (Beisteiner et al., 2008).

For specific clinical questions targeting responses of all parts of a motor network (e.g., movement disorders) and for research purposes, it is desirable to have the sensitivity to be able to detect the participation of motor regions which may show smaller BOLD signal changes, such as subcortical sensorimotor areas predominantly involved in extrapyramidal motor disease. Our results indicate the most prominent benefit of ICA for such tasks.

Although not directly assessed in this study, the artifacts observed here are expected to be similar to those encountered with overt speech paradigms used in presurgical localization of language (Gartus et al., 2009). Language tasks lead to smaller BOLD signal changes which are localized more inferiorly, where artifacts are more pronounced. Another promising area of application is basic neuroscience studies involving painful or emotionally evocative stimuli, which may likewise elicit substantial motion (Moser et al., 2007). The effectiveness of ICA in isolating the weaker and more variable responses in emotion and language tasks needs to be established in dedicated studies, however.

We have shown that ICA, combined with feature-based ranking of components, constitutes a fast and practical approach to the analysis of 7 T fMRI motor task data containing stimulus-correlated motion. Assessment of the first few ranked components at a single statistical threshold is sufficient to identify motor activation without contamination by motion artifacts, offering additional information and clarity compared to a GLM analysis. ICA allows advantage to be taken of the increased SNR and BS promised by ultra-high field for clinical studies (Beisteiner et al., 2011) even for challenging tasks involving head motion. This paves the way for increased reliability of results and the use of higher resolution in such applications as presurgical mapping at 7 T.

CONCLUSION

Independent component analysis was found to be capable of cleanly separating activation from motion artifacts in ultra-high field fMRI data which contained stimulus-correlated motion. Some activated regions were evident in ICA results but not GLM results, indicating not only higher specificity to activation but also higher sensitivity in the analysis of motion-contaminated data. The features presented here allowed task-relevant activation components to be easily identified from the large number of contributing signals, making ICA a feasible approach to the routine analysis of presurgical planning fMRI data with motor tasks in the lab and clinic. The fact the correlation between GLM results and ICA spatial maps allowed the primary motor components to be identified in most patients adds weight to the argument that both methods should be applied to the analysis of such patient data.

ACKNOWLEDGMENTS

This study was carried out as part of the "Vienna Advanced Clinical Imaging Center" (VIACLIC) project, funded by the Vienna Spots of Excellence Program of the Center of Innovation and Technology, City of Vienna (ZIT), Austria and the Austrian Science Fund (FWF) project KLI264. Additional support was provided by the Austrian Science Fund (FWF) project P18057 and a research cluster grant of the Medical University of Vienna and the University of Vienna. We would like to thank Prof. Christine Marosi from the Department for Internal Medicine 1 for patient recruitment.

REFERENCES

Abou-Elseoud, A., Starck, T., Remes, J., Nikkinen, J., Tervonen, O., and Kiviniemi, V. (2010). The effect of model order selection in group PICA. *Hum. Brain Mapp.* 31, 1207–1216. doi:10.1002/hbm.20929

Barth, M., and Poser, B. A. (2011). Advances in high-field BOLD fMRI. *Materials* 4, 1941–1955. doi:10.3390/ma4111941

Beckmann, C. F. (2012). Modelling with independent components. *Neuroimage* 62, 891–901. doi:10.1016/j.neuroimage.2012.02.020

Beckmann, C. F., Deluca, M., Devlin, J. T., and Smith, S. M. (2005). Investigations into resting-state connectivity using independent component analysis. *Philos. Trans. R. Soc. Lond. B Biol. Sci.* 360, 1001–1013. doi:10.1098/rstb.2005.1634

Beckmann, C. F., and Smith, S. M. (2004). Probabilistic independent component analysis for functional magnetic resonance imaging. *IEEE Trans. Med. Imaging* 23, 137–152. doi:10.1109/TMI.2003.822821

Beisteiner, R., Drabeck, K., Foki, T., Geissler, A., Gartus, A., Lehner-Baumgartner, E., et al. (2008). Does clinical memory fMRI provide a comprehensive map of medial temporal lobe structures? *Exp. Neurol.* 213, 154–162. doi:10.1016/j.expneurol.2008.05.019

Beisteiner, R., Klinger, N., Hollinger, I., Rath, J., Gruber, S., Steinkellner, T., et al. (2010). How much are clinical fMRI reports influenced by standard postprocessing methods? An investigation of normalization and region of interest effects in the medial temporal lobe. *Hum. Brain Mapp.* 31, 1951–1966. doi:10.1002/hbm.20990

Beisteiner, R., Lanzenberger, R., Novak, K., Edward, V., Windischberger, C., Erdler, M., et al. (2000). Improvement of presurgical patient evaluation by generation of functional magnetic resonance risk maps. *Neurosci. Lett.* 290, 13–16. doi:10.1016/S0304-3940(00)01303-3

Beisteiner, R., Robinson, S., Wurnig, M., Hilbert, M., Merksa, K., Rath, J., et al. (2011). Clinical fMRI: evidence for a 7T benefit over 3T. *Neuroimage* 57, 1015–1021. doi:10.1016/j.neuroimage.2011.05.010

Birn, R. M., Bandettini, P. A., Cox, R. W., and Shaker, R. (1999). Event-related fMRI of tasks involving brief motion. *Hum. Brain Mapp.* 7, 106–114. doi:10.1002/(SICI)1097-0193(1999)7:2<106::AID-HBM4>3.0.CO;2-O

Biswal, B., Yetkin, F. Z., Haughton, V. M., and Hyde, J. S. (1995). Functional connectivity in the motor cortex of resting human brain using echo-planar MRI. *Magn. Reson. Med.* 34, 537–541. doi:10.1002/mrm.1910340409

Bullmore, E. T., Brammer, M. J., Rabe-Hesketh, S., Curtis, V. A., Morris, R. G., Williams, S. C., et al. (1999). Methods for diagnosis and treatment of stimulus-correlated motion in generic brain activation studies using fMRI. *Hum. Brain Mapp.* 7, 38–48. doi:10.1002/(SICI)1097-0193(1999)7:1<38::AID-HBM4>3.3.CO;2-H

Calhoun, V. D., Adali, T., Pearlson, G. D., and Pekar, J. J. (2001). A method for making group inferences from functional MRI data using independent component analysis. *Hum. Brain Mapp.* 14, 140–151. doi:10.1002/hbm.1048

Calhoun, V. D., Kiehl, K. A., and Pearlson, G. D. (2008). Modulation of temporally coherent brain networks estimated using ICA at rest and during cognitive tasks. *Hum. Brain Mapp.* 29, 828–838. doi:10.1002/hbm.20581

Carter, C. S., Heckers, S., Nichols, T., Pine, D. S., and Strother, S. (2008). Optimizing the design and analysis of clinical functional magnetic resonance imaging research studies. *Biol. Psychiatry* 64, 842–849. doi:10.1016/j.biopsych.2008.06.014

Casanova, R., Ryali, S., Serences, J., Yang, L., Kraft, R., Laurienti, P. J., et al. (2008). The impact of temporal regularization on estimates of the BOLD hemodynamic response function: a comparative analysis. *Neuroimage* 40, 1606–1618. doi:10.1016/j.neuroimage.2008.01.011

De Martino, F., Esposito, F., Van De Moortele, P. F., Harel, N., Formisano, E., Goebel, R., et al. (2011). Whole brain high-resolution functional imaging at ultra high magnetic fields: an application to the analysis of resting state networks. *Neuroimage* 57, 1031–1044. doi:10.1016/j.neuroimage.2011.05.008

Desikan, R. S., Segonne, F., Fischl, B., Quinn, B. T., Dickerson, B. C., Blacker, D., et al. (2006). An automated labeling system for subdividing the human cerebral cortex on MRI scans into gyral based regions of interest. *Neuroimage* 31, 968–980. doi:10.1016/j.neuroimage.2006.01.021

Duchin, Y., Abosch, A., Yacoub, E., Sapiro, G., and Harel, N. (2012). Feasibility of using ultra-high field (7 T) MRI for clinical surgical targeting. *PLoS ONE* 7:e37328. doi:10.1371/journal.pone.0037328

Edward, V., Windischberger, C., Cunnington, R., Erdler, M., Lanzenberger, R., Mayer, D., et al. (2000). Quantification of fMRI artifact reduction by a novel plaster cast head holder. *Hum. Brain Mapp.* 11, 207–213. doi:10.1002/1097-0193(200011)11:3<207::AID-HBM60>3.0.CO;2-J

Foki, T., Gartus, A., Geissler, A., and Beisteiner, R. (2008). Probing overtly spoken language at sentential level: a comprehensive high-field BOLD-fMRI protocol reflecting everyday language demands. *Neuroimage* 39, 1613–1624. doi:10.1016/j.neuroimage.2007.10.020

Foki, T., Geissler, A., Gartus, A., Pahs, G., Deecke, L., and Beisteiner, R. (2007). Cortical lateralization of bilateral symmetric chin movements and clinical relevance in tumor patients – a high field BOLD-fMRI study. *Neuroimage* 37, 26–39. doi:10.1016/j.neuroimage.2007.02.059

Fox, M. D., Snyder, A. Z., Vincent, J. L., and Raichle, M. E. (2007). Intrinsic fluctuations within cortical systems account for intertrial variability in human behavior. *Neuron* 56, 171–184. doi:10.1016/j.neuron.2007.08.023

Fox, P. T., Perlmutter, J. S., and Raichle, M. E. (1985). A stereotactic method of anatomical localization for positron emission tomography. *J. Comput. Assist. Tomogr.* 9, 141–153. doi:10.1097/00004728-198501000-00025

Freire, L., and Mangin, J. F. (2001). Motion correction algorithms may create spurious brain activations in the absence of subject motion. *Neuroimage* 14, 709–722. doi:10.1006/nimg.2001.0869

Friston, K., Holmes, A., Worsley, K., Poline, J.-B., Frith, C., and Frackowiak, R. (1995). Statistical parametric maps in functional imaging: a general linear approach. *Hum Brain Mapp* 2, 189–210. doi:10.1002/hbm.460020402

Friston, K. J., Williams, S., Howard, R., Frackowiak, R. S., and Turner, R. (1996). Movement-related effects in fMRI time-series. *Magn. Reson. Med.* 35, 346–355. doi:10.1002/mrm.1910350312

Gartus, A., Foki, T., Geissler, A., and Beisteiner, R. (2009). Improvement of clinical language localization with an overt semantic and syntactic language functional MR imaging paradigm. *AJNR Am. J. Neuroradiol.* 30, 1977–1985. doi:10.3174/ajnr.A1725

Greitz, T., Bergstrom, M., Boethius, J., Kingsley, D., and Ribbe, T. (1980). Head fixation system for integration of radiodiagnostic and therapeutic procedures. *Neuroradiology* 19, 1–6.

Griswold, M. A., Jakob, P. M., Heidemann, R. M., Nittka, M., Jellus, V., Wang, J., et al. (2002). Generalized autocalibrating partially parallel acquisitions (GRAPPA). *Magn. Reson. Med.* 47, 1202–1210. doi:10.1002/mrm.10171

Hajnal, J., Myers, R., Oatridge, A., Schwieso, J., Young, I., and Bydder, G. (1994). Artifacts due to stimulus correlated motion in functional imaging of the brain. *Magn. Reson. Med.* 31, 283–291. doi:10.1002/mrm.1910310307

Hutton, C., Bork, A., Josephs, O., Deichmann, R., Ashburner, J., and Turner, R. (2002). Image distortion correction in fMRI: a quantitative evaluation. *Neuroimage* 16, 217–240. doi:10.1006/nimg.2001.1054

Jenkinson, M., Bannister, P., Brady, M., and Smith, S. (2002). Improved optimization for the robust and accurate linear registration and motion correction of brain images. *Neuroimage* 17, 825–841. doi:10.1006/nimg.2002.1132

Johnstone, T., Ores Walsh, K. S., Greischar, L. L., Alexander, A. L., Fox, A. S., Davidson, R. J., et al. (2006). Motion correction and the use of motion covariates in multiple-subject fMRI analysis. *Hum. Brain Mapp.* 27, 779–788. doi:10.1002/hbm.20219

Kearfott, K. J., Rottenberg, D. A., and Knowles, R. J. (1984). A new headholder for PET, CT, and NMR imaging. *J. Comput. Assist. Tomogr.* 8, 1217–1220. doi:10.1097/00004728-198412000-00042

Kochiyama, T., Morita, T., Okada, T., Yonekura, Y., Matsumura, M., and Sadato, N. (2005). Removing the effects of task-related motion using independent-component analysis. *Neuroimage* 25, 802–814. doi:10.1016/j.neuroimage.2004.12.027

Kokkonen, S. M., Nikkinen, J., Remes, J., Kantola, J., Starck, T., Haapea, M., et al. (2009). Preoperative localization of the sensorimotor area using independent component analysis of resting-state fMRI. *Magn. Reson. Imaging* 27, 733–740. doi:10.1016/j.mri.2008.11.002

Krings, T., Reinges, M. H., Erberich, S., Kemeny, S., Rohde, V., Spetzger, U., et al. (2001). Functional MRI for presurgical planning: problems, artefacts, and solution strategies. *J. Neurol. Neurosurg. Psychiatr.* 70, 749–760. doi:10.1136/jnnp.70.6.749

Kundu, P., Inati, S. J., Evans, J. W., Luh, W. M., and Bandettini, P. A. (2012). Differentiating BOLD and non-BOLD signals in fMRI time series using multi-echo EPI. *Neuroimage* 60, 1759–1770. doi:10.1016/j.neuroimage.2011.12.028

LeVan, P., and Gotman, J. (2009). Independent component analysis as a model-free approach for the detection of BOLD changes related to epileptic spikes: a simulation study. *Hum. Brain Mapp.* 30, 2021–2031. doi:10.1002/hbm.20647

Liao, R., McKeown, M. J., and Krolik, J. L. (2006). Isolation and minimization of head motion-induced signal variations in fMRI data using independent component analysis. *Magn. Reson. Med.* 55, 1396–1413. doi:10.1002/mrm.20893

Malinen, S., Hlushchuk, Y., and Hari, R. (2007). Towards natural stimulation in fMRI – issues of data analysis. *Neuroimage* 35, 131–139. doi:10.1016/j.neuroimage.2006.11.015

McKeown, M. J. (2000). Detection of consistently task-related activations in fMRI data with hybrid independent component analysis. *Neuroimage* 11, 24–35. doi:10.1006/nimg.1999.0518

McKeown, M. J., Makeig, S., Brown, G. G., Jung, T. P., Kindermann, S. S., Bell, A. J., et al. (1998). Analysis of fMRI data by blind separation into independent spatial components. *Hum. Brain Mapp.* 6, 160–188. doi:10.1002/(SICI)1097-0193(1998)6:5/6<368::AID-HBM7>3.3.CO;2-5

Moritz, C. H., Rogers, B. P., and Meyerand, M. E. (2003). Power spectrum ranked independent component analysis of a periodic fMRI complex motor paradigm. *Hum. Brain Mapp.* 18, 111–122. doi:10.1002/hbm.10081

Moser, E., Derntl, B., Robinson, S., Fink, B., Gur, R. C., and Grammer, K. (2007). Amygdala activation at 3T in response to human and avatar facial expressions of emotions. *J. Neurosci. Methods* 161, 126–133. doi:10.1016/j.jneumeth.2006.10.016

Oakes, T. R., Johnstone, T., Ores Walsh, K. S., Greischar, L. L., Alexander, A. L., Fox, A. S., et al. (2005). Comparison of fMRI motion correction software tools. *Neuroimage* 28, 529–543. doi:10.1016/j.neuroimage.2005.05.058

Ooi, M. B., Krueger, S., Thomas, W. J., Swaminathan, S. V., and Brown, T. R. (2009). Prospective real-time correction for arbitrary head motion using active markers. *Magn. Reson. Med.* 62, 943–954. doi:10.1002/mrm.22082

Poser, B. A., Barth, M., Goa, P. E., Deng, W., and Stenger, V. A. (2013). Single-shot echo-planar imaging with Nyquist ghost compensation: interleaved dual echo with acceleration (IDEA) echo-planar imaging (EPI). *Magn. Reson. Med.* 69, 37–47. doi:10.1002/mrm.24222

Qin, L., Van Gelderen, P., Derbyshire, J. A., Jin, F., Lee, J., De Zwart, J. A., et al. (2009). Prospective head-movement correction for high-resolution MRI using an in-bore optical tracking system. *Magn. Reson. Med.* 62, 924–934. doi:10.1002/mrm.22076

Robinson, S., Basso, G., Soldati, N., Sailer, U., Jovicich, J., Bruzzone, L., et al. (2009). A resting state network in the motor control circuit of the basal ganglia. *BMC Neurosci.* 10:137. doi:10.1186/1471-2202-10-137

Robinson, S., and Jovicich, J. (2011). B0 mapping with multi-channel RF coils at high field. *Magn. Reson. Med.* 66, 976–988. doi:10.1002/mrm.22879

Robinson, S., and Moser, E. (2004). Positive results in amygdala fMRI: emotion or head motion? *NeuroImage* 22(Suppl. 1), 294.

Roessler, K., Donat, M., Lanzenberger, R., Novak, K., Geissler, A., Gartus, A., et al. (2005). Evaluation of preoperative high magnetic field motor functional MRI (3 Tesla) in glioma patients by navigated electrocortical stimulation and postoperative outcome. *J. Neurol. Neurosurg. Psychiatr.* 76, 1152–1157. doi:10.1136/jnnp.2004.050286

Seto, E., Sela, G., McIlroy, W. E., Black, S. E., Staines, W. R., Bronskill, M. J., et al. (2001). Quantifying head motion associated with motor tasks used in fMRI. *Neuroimage* 14, 284–297. doi:10.1006/nimg.2001.0829

Smith, S. M. (2002). Fast robust automated brain extraction. *Hum. Brain Mapp.* 17, 143–155. doi:10.1002/hbm.10062

Smith, S. M., Jenkinson, M., Woolrich, M. W., Beckmann, C. F., Behrens, T. E., Johansen-Berg, H., et al. (2004). Advances in functional and structural MR image analysis and implementation as FSL. *Neuroimage* 23, S208–S219. doi:10.1016/j.neuroimage.2004.07.051

Soldati, N., Robinson, S., Persello, C., Jovicich, J., and Bruzzone, L. (2009). Automatic classification of brain resting states using fMRI temporal signals. *Electron. Lett.* 45, 19–21. doi:10.1049/el:20092178

Stippich, C. (2007). *Clinical Functional MRI*. Berlin: Springer.

Tohka, J., Foerde, K., Aron, A. R., Tom, S. M., Toga, A. W., and Poldrack, R. A. (2008). Automatic independent component labeling for artifact removal in fMRI. *Neuroimage* 39, 1227–1245. doi:10.1016/j.neuroimage.2007.10.013

Triantafyllou, C., Hoge, R. D., Krueger, G., Wiggins, C. J., Potthast, A., Wiggins, G. C., et al. (2005). Comparison of physiological noise at 1.5 T, 3 T and 7 T and optimization of fMRI acquisition parameters. *Neuroimage* 26, 243–250. doi:10.1016/j.neuroimage.2005.01.007

Ugurbil, K. (2012). The road to functional imaging and ultrahigh fields. *Neuroimage* 62, 726–735. doi:10.1016/j.neuroimage.2012.01.134

van der Zwaag, W., Francis, S., Head, K., Peters, A., Gowland, P., Morris, P., et al. (2009). fMRI at 1.5, 3 and 7 T: characterising BOLD signal changes. *Neuroimage* 47, 1425–1434. doi:10.1016/j.neuroimage.2009.05.015

Visser, E., Poser, B. A., Barth, M., and Zweirs, M. P. (2012). Reference-free unwarping of EPI data using dynamic off-resonance correction with multiecho acquisition (DOCMA). *Magn. Reson. Med.* 68, 1247–1254. doi:10.1002/mrm.24119

Woolrich, M. W., Ripley, B. D., Brady, M., and Smith, S. M. (2001). Temporal autocorrelation in univariate linear modeling of fMRI data. *Neuroimage* 14, 1370–1386. doi:10.1006/nimg.2001.0931

Worsley, K. J. (2001). "Statistical analysis of activation images," in *Functional MRI: An Introduction to Methods*, eds P. Jezzard, P. M. Matthews, and S. M. Smith (Oxford: Oxford University Press).

Wu, D. H., Lewin, J. S., and Duerk, J. L. (1997). Inadequacy of motion correction algorithms in functional MRI: role of susceptibility-induced artifacts. *J. Magn. Reson. Imaging* 7, 365–370. doi:10.1002/jmri.1880070219

Yousry, T. A., Schmid, U. D., Alkadhi, H., Schmidt, D., Peraud, A., Buettner, A., et al. (1997). Localization of the motor hand area to a knob on the precentral gyrus. A new landmark. *Brain* 120(Pt 1), 141–157. doi:10.1093/brain/120.1.141

Zaitsev, M., Dold, C., Sakas, G., Hennig, J., and Speck, O. (2006). Magnetic resonance imaging of freely moving objects: prospective real-time motion correction using an external optical motion tracking system. *Neuroimage* 31, 1038–1050. doi:10.1016/j.neuroimage.2006.01.039

Zhang, Y., Brady, M., and Smith, S. (2001). Segmentation of brain MR images through a hidden Markov random field model and the expectation-maximization algorithm. *IEEE Trans. Med. Imaging* 20, 45–57. doi:10.1109/42.906424

Conflict of Interest Statement: The authors declare that the research was conducted in the absence of any commercial or financial relationships that could be construed as a potential conflict of interest.

Received: 30 January 2013; accepted: 05 August 2013; published online: 02 September 2013.

Citation: Robinson SD, Schöpf V, Cardoso P, Geissler A, Fischmeister FPhS, Wurnig M, Trattnig S and Beisteiner R (2013) Applying independent component analysis to clinical fMRI at 7 T. Front. Hum. Neurosci. ***7****:496. doi: 10.3389/fnhum.2013.00496*

This article was submitted to the journal Frontiers in Human Neuroscience.

frontiers in
HUMAN NEUROSCIENCE

ORIGINAL RESEARCH ARTICLE
published: 09 August 2013
doi: 10.3389/fnhum.2013.00474

Comparing the microvascular specificity of the 3- and 7-T BOLD response using ICA and susceptibility-weighted imaging

Alexander Geißler[1,2], Florian Ph. S. Fischmeister[1,2], Günther Grabner[2,3], Moritz Wurnig[1,2], Jakob Rath[1,2], Thomas Foki[1,2], Eva Matt[1,2], Siegfried Trattnig[2,3], Roland Beisteiner[1,2] and Simon Daniel Robinson[2,3]*

[1] *Study Group Clinical fMRI, Department of Neurology, Medical University of Vienna, Vienna, Austria*
[2] *High Field Magnetic Resonance Imaging Center of Excellence, Medical University of Vienna, Vienna, Austria*
[3] *Department of Biomedical Imaging and Image-guided Therapy, High Field Magnetic Resonance Imaging Center of Excellence, Medical University of Vienna, Vienna, Austria*

Edited by:
Veronika Schöpf, Medical University of Vienna, Austria

Reviewed by:
Mark Haacke, Wayne State University, USA
Andreas Deistung, Friedrich Schiller University Jena, Germany

****Correspondence:***
Simon Daniel Robinson, Department of Biomedical Imaging and Image-guided Therapy, High Field Magnetic Resonance Center of Excellence, Medical University of Vienna, Lazarettgasse 14, A-1090 Vienna, Austria
e-mail: simon.robinson@meduniwien.ac.at

In functional MRI it is desirable for the blood-oxygenation level dependent (BOLD) signal to be localized to the tissue containing activated neurons rather than the veins draining that tissue. This study addresses the dependence of the specificity of the BOLD signal – the relative contribution of the BOLD signal arising from tissue compared to venous vessels – on magnetic field strength. To date, studies of specificity have been based on models or indirect measures of BOLD sensitivity such as signal to noise ratio and relaxation rates, and assessment has been made in isolated vein and tissue voxels. The consensus has been that ultra-high field systems not only significantly increase BOLD sensitivity but also specificity, that is, there is a proportionately reduced signal contribution from draining veins. Specificity was not quantified in prior studies, however, due to the difficulty of establishing a reliable network of veins in the activated volume. In this study we use a map of venous vessel networks extracted from 7T high resolution Susceptibility-Weighted Images to quantify the relative contributions of micro- and macro-vasculature to functional MRI results obtained at 3 and 7T. High resolution measurements made here minimize the contribution of physiological noise and Independent Component Analysis (ICA) is used to separate activation from technical, physiological, and motion artifacts. ICA also avoids the possibility of timing-dependent bias from different micro- and macro-vasculature responses. We find a significant increase in the number of activated voxels at 7T in both the veins and the microvasculature – a BOLD sensitivity increase – with the increase in the microvasculature being higher. However, the small increase in sensitivity at 7T was not significant. For the experimental conditions of this study, our findings do not support the hypothesis of an increased specificity of the BOLD response at ultra-high field.

Keywords: fMRI, specificity, BOLD, susceptibility-weighted imaging, independent component analysis

INTRODUCTION

In functional MRI it is desirable for the blood-oxygenation level dependent (BOLD) signal to be localized, as closely as possible, to the site of neurons activated by a task. Veins draining the capillary bed also give rise to BOLD signal changes, however, leading to a shift in the detected signal away from its origins (Yacoub et al., 2001; Shmuel et al., 2007). The proportion of the BOLD response (quantified either by the number of activated voxels, or mean Z value) that arises in tissue to that which comes from the draining veins defines the specificity of the BOLD response. A body of evidence suggests that the relative contribution of draining veins (Menon, 2012) decreases with field strength, leading to the expectation that in ultra-high field functional MRI (fMRI) the measured BOLD signal is better localized to its origin in gray matter (Gati et al., 1997; Ogawa et al., 1998; Yacoub et al., 2001; Duong et al., 2003). These studies are based on numeric models, and measurements examining signal changes and relaxation rate changes in isolated veins and tissue voxels. To date, however, specificity has not been measured with activation statistics or quantified over the whole activated volume, due to difficulty in establishing a reliable network of veins.

Questions as to the exact vascular origin of BOLD signal changes began to be raised soon after the first human fMRI experiments (Bandettini et al., 1992; Kwong et al., 1992; Ogawa et al., 1992). In 1993, Gomiscek et al. indicated that inflow effects originating in large vessels might be a relevant source of the fMRI signal (Gomiscek et al., 1993). Haacke et al. (1994) proceeded to demonstrate that the high signal changes observed in FLASH-based fMRI at 1.5 T were due to large vessels rather than the parenchyma. This finding was supported by experiments in which Stejskal–Tanner gradients, which suppress signal from flowing blood, were included in measurement sequences (Boxerman et al., 1995). The BOLD fMRI signal was reduced by 70–100%, demonstrating that the 1.5-T BOLD fMRI signal originates predominantly from blood in vessels rather than tissue.

Later experiments across the field strengths 0.5, 1.5, and 4.0 T demonstrated that the percentage signal change between rest and activated conditions increases more than linearly with field strength in tissue but less than linearly in vessels (Gati et al., 1997). These findings were extended to 7.0 T, and it was established that the short T2 of blood at high magnetic field was the origin of the reduced vessel contribution at very high field given the relatively long echo time used in fMRI (Yacoub et al., 2001). These studies provided evidence of and an explanation for an increase in the relative specificity of the BOLD signal to gray matter with field strength. The effect has only been measured in isolated vessels identified in T1 and T2 scans, however. The extent to which any changes in the relative contribution of the tissue and vessel signal affects the localization of BOLD signal in a bulk volume of activated tissue is clearly dependent on the distribution of veins in the imaged volume, however. In this study we define maps of venous vessel networks from 7 T Susceptibility-Weighted Images (SWI) (Reichenbach et al., 1997, 1998) to allow the relative contributions of vessel and tissue signal to fMRI results obtained at 3 and 7 T to be quantified. Applying independent component analysis (ICA), rather than a General Linear Model analysis, allows a clean separation of activation from technical, physiological, and motion artifacts, and avoids the possibility of bias to draining vein or microvasculature responses which could have different timing and thereby influence the assessment of specificity.

MATERIALS AND METHODS

HEALTHY SUBJECTS

Twelve healthy, right handed volunteers (eight male, four female, mean age 31.6 years, age range from 23 to 45) participated in the study, which was approved by the Ethics Committee of the Medical University of Vienna, with written informed consent.

TASK DESIGN AND PROCEDURE

A hand motor task was chosen because it elicits a strong and reproducible BOLD response which is localized in a well circumscribed region. Volunteers were instructed to perform repetitive opening and closing of the right hand at 1 Hz. Auditory start and stop commands were computer-generated and communicated via the scanner intercom system. The sequence of timed commands was executed with the software Presentation (Neurobehavioral Systems, Albany, CA, USA) and was triggered by the MRI scanner. All subjects performed a simple blocked design consisting of four movement and five rest periods of 20 s each, with two runs at each field strength.

DATA ACQUISITION

All subjects were examined with both a 3-T Siemens MAGNETOM TIM TRIO scanner and a 7-T Siemens MAGNETOM scanner (Siemens Medical, Erlangen, Germany). A 32 channel head coil was used on both systems (on 3 T, manufactured by Siemens Medical, on 7 T, manufactured by Nova Medical, Wilmington, MA, USA).

Functional data were acquired on both systems with high resolution 2D single shot gradient-echo (GE) EPI, with slices aligned parallel to the AC-PC plane and whole brain coverage. To ensure that results obtained here are relevant to fMRI in general practice, we chose to assess specificity using the echo time which, for each field strength, provides the maximum BOLD sensitivity (approximately equal to T2* in gray matter; Deichmann et al., 2002). Protocols used at 3 and 7 T were also independently optimized according to specific absorption rate (SAR) constraints, the requirement of whole brain coverage and other recommendations in the literature (Triantafyllou et al., 2005; Robinson et al., 2008; Speck et al., 2008; van der Zwaag et al., 2009).

At both field strengths, GE-EPI was acquired with a square field of view (FOV) of 220 mm, in-plane matrix size 220 × 220, with slice thickness of 2 mm and 20% gap (i.e., 1 mm × 1 mm × 2.4 mm voxels), with 73 repetitions, a repetition time (TR) of 3000 ms, fat suppression with a chemical shift selective saturation pulse prior to every slice, 6/8 partial Fourier factor (omitting the first 25% of k-space phase-encoding lines), and parallel imaging with a GRAPPA-iPAT factor of 4. This relatively high GRAPPA factor was required to achieve the desired echo times with these high resolution acquisitions. At 3 T, 37 slices were acquired with TE = 35 ms, a receiver bandwidth per pixel (BW) of 1082 Hz, flip angle (FA) of 90°. At 7 T, 44 slices were acquired with TE = 22 ms, BW = 990 Hz, FA = 75°. As these echo times are different between the two field strengths (35 ms for 3 T, 22 ms for 7 T) we also performed an additional comparison of specificity with a single subject (subject 8) using runs with both echo times – 35 and 22 ms – at both field strengths, to assess to what extent specificity findings are echo-time dependent. A total of four additional motor runs – two with 35 ms and two with 22 ms – were measured at each field strength for subject 8 only.

High resolution, fully flow compensated T2*-weighted 3D GE images were acquired at 7 T for SWI. The acquisition matrix size was 704 × 704 × 96 voxel, with a FOV of 220 mm, leading to 0.3125 mm × 0.3125 mm × 1.2 mm, TE/TR = 11.9/28 ms, FA = 15°, with BW = 163 Hz/px, and an acquisition time of 13 min 20 s.

DATA PROCESSING

Functional data analysis

Echo planar images were motion corrected using MCFLIRT (Jenkinson et al., 2002) from Version 5.0.1 of the FSL software package (Smith et al., 2004), with all volumes registered to the first volume of the first functional experiment (3 and 7 T separately). ICA was performed in this native EPI space with "MELODIC" (Beckmann and Smith, 2004) for each subject with no smoothing applied. MELODIC was run in multi-session tensorial mode (TICA) without skull stripping but with the brain volumes of interest (VOI) as a confinement. The mean bias-corrected EPI was used as a background image for functional overlays. The threshold for the mixture model-based inference was 0.5 (the default) and the model order, or number of components into which the data is split – was determined automatically using Laplacian estimation.

To identify which voxels overlay veins and which tissue, functional data were registered to SWI space in a number of linear registration steps, with increasing number of degrees of freedom as the quality of the result improved, followed by non-linear

registration. Registration was performed using the mean EPI and magnitude SWI image, both of which were skull stripped with BET2 (Jenkinson et al., 2002), with subject-specific fractional intensity thresholds and bias-corrected with FSL's "FAST" package. Magnitude SWI were additionally denoised with FSL's non-linear noise reduction tool "SUSAN" and intensity-normalized to a value of 1000. A binary brain mask was generated from this image (by setting all non-zero values to 1). This was for used with FNIRT and for the generation of venous vessel maps (see "Generation of Venous Vessel Maps").

For 7 T EPI, the first step was linear registration of mean skull stripped, bias-corrected EPI to 7 T SWI using FSL's "FLIRT" (Jenkinson et al., 2002) with correlation ratio as the cost function and 7 degrees of freedom (three translational, three rotational, and global rescaling). The output matrix of this transformation was used as a starting point for a second execution of FLIRT (again to SWI), using mutual information as the cost function and 12 degrees of freedom. The final registration step was a non-linear transformation of the output of the linear transformations to SWI using "FNIRT." In the light of the sequence-dependent intensity disparity between EPI and SWI, the local non-linear intensity model was used for FNIRT.

For 3 T EPI, registration steps were as described for 7 T above, other than that they were preceded by the addition step of linear registration to the 7-T EPI using FLIRT with 7 degrees of freedom. The normalized correlation ratio was used as the cost function for all linear registration stages of 3 T data. Normalized correlation ratio is usually used for intermodal registration, but provided the best results in this application due to the contrast differences between 3 and 7 T data. The global non-linear intensity model was used for FNIRT.

This multi-step registration procedure was found to provide accurate registration for all subjects. For both 3 and 7 T fMRI data all transformation steps, both linear and non-linear, were combined to define the transformation from EPI to 7 T SWI. The merged transformations were finally applied to ICA maps. This approach ensured the equal treatment of 3 and 7 T functional data – of a single transformation with one resampling step, vital because every applied transformation causes some smoothing of the data.

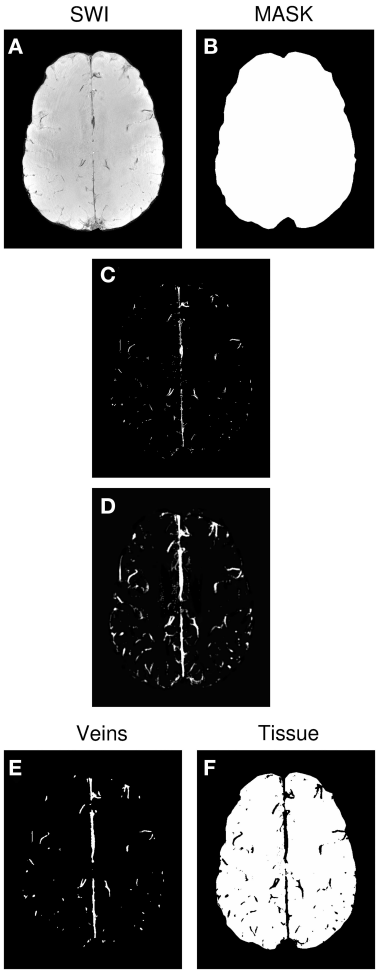

FIGURE 1 | Generation of the venous vessel maps. **(A)** SWI. **(B)** Brain mask. **(C)** Preliminary vein mask, achieved by applying threshold "T" to SWI. **(D)** Smoothed version of preliminary vein mask. **(E)** Final vein mask derived from **(D)**. **(F)** Tissue mask derived from **(D)**.

Generation of venous vessel maps

Vessel maps were generated semi-automatically from SWI magnitude images using MATLAB (MathWorks, Inc., Natick, MA, USA). Steps are illustrated in **Figure 1**, and were as follows. For each subject's magnitude SWI (**Figure 1A**), a threshold "T" was determined for the whole volume by hand, below which images were classified as consisting of veins or background signal. Voxels whose value was below T and which were inside a BET mask of the brain (**Figure 1B**) were set to 1, and all other voxels were set to 0 (**Figure 1C**). This preliminary vein mask was smoothed using the "smoothn" MATLAB function with the smoothing parameter S of 1 (Garcia, 2009) (**Figure 1D**). A binary vein map was created by assigning the value of 1 to voxels in the smoothed preliminary mask (**Figure 1D**) which exceeded a value of 0.3 (yielding **Figure 1E**). The vein mask was compared by visual inspection with the SWI for the verisimilitude of the vessels identified, and the threshold "T" modified, if necessary. A "tissue" mask was assigned the value of one where values in the smoothed preliminary mask (**Figure 1D**) were below 0.15 (yielding **Figure 1F**).

The process of thresholding, smoothing, and thresholding a second time removed isolated voxels and bridged gaps in vessels (compare **Figures 1C,E**). Using different thresholds for the vein and tissue masks (0.15 and 0.3 respectively) led to a cleaner allocation of voxels to the vein and tissue categories. fMRI activation was classified as being in a vein if it coincided with the vein mask and being in the microvasculature if it was in the tissue mask. Voxels in the zone between the two were not considered in further analysis.

Statistical analysis

To assess effects related to the two field strengths under controlled conditions, anatomical VOIs were located within the primary hand motor area. VOI's were manually defined for each subject by an experienced fMRI expert (RB) and comprised the

neurophysiological representation of the human hand area, i.e., the knob structure. The individual VOI was the same for both field strengths. The following values were calculated for both veins and microvasculature: (1) number of activated voxels (alternative hypothesis test at a Gaussian mixture modeling threshold of $p > 0.5$; Beckmann and Smith, 2004), (2) percent activated voxels, (3) mean Z value, and (4) ratio of the mean Z values in the microvasculature/veins for all voxels within the anatomical VOI. Both the number of activated voxels as well as the mean t-values of those voxels was assessed with a Student's paired two-tailed t-test carried out in Microsoft Excel 2007 (Redmond, Washington, MA, USA). A decreased vascular contribution to the BOLD signal is to be expected at 7 T due to the short T2 of blood. As specificity effects can be expected to be echo-time dependent, data at the same echo times (22 and 35 ms) were likewise compared.

RESULTS

Figure 2 illustrates, for a single subject, both the accuracy of the image registration and the appearance of the vein maps, the outline of which are overlaid (in cyan) on sample 3 and 7 T EPI volumes, and SWI. Some identified veins appear to lie outside the brain. A proportion of these are genuine veins on the surface of the brain, beyond the cortical surface, which appear further outside the brain due to partial volume effect over slices. In EPI there is also strong T2* dephasing of signal from the periosteal and meningeal dural layers, which makes the brain appears slightly smaller than the skull-stripped SWI, enhancing the impression that these veins lie further outside the brain. Any errors in the vein maps outside the anatomically defined VOIs in the primary motor cortex do not affect our results, as analysis was constrained to those VOIs.

Figure 3 illustrates typical functional results within the predefined anatomical VOI (green) for a single subject. Row A shows voxels above threshold (determined via the Gaussian mixture modeling approach described in the see "Statistical Analysis"), row B all functional voxels. The zoomed depiction clarifies the situation inside the target area. Both the number of voxels above threshold as well as the mean Z values of all voxels in the VOI were assessed for each subject (see **Table 1**).

On average, 21% more voxels were above threshold in veins at 7 T than at 3 T and 42% more voxels were above threshold in the microvasculature at 7 T than at 3 T (see **Table 2**). These increases in BOLD sensitivity with field strength in both veins and the microvasculature were statistically significant in student's two-tailed t-tests assessed at $p < 0.05$. The proportion of activated voxels in the microvasculature to the total did not differ significantly between the two field strengths, however, indicating no increase in specificity.

Mean Z values were significantly higher in the 7-T results in both the vessels and the microvasculature. In veins, the increase was 41%, in the microvasculature it was 48%. The increase in the ratio of mean Z values in the microvasculature to veins with field strength was small and not statistically significant, indicating no increase in specificity. The same finding, of no substantial increase in specificity, held when the assessment was carried out at the same echo time (**Table 3**).

DISCUSSION

The field strength dependence of the specificity of the BOLD response has been studied using high resolution fMRI at 3 and 7 T with a hand task. ICA was used to identify task-related activation in order to obviate possible bias of a model-based analysis to either the vascular or microvascular response, as these could be subject to different latencies. Activation maps were meticulously normalized to the space of vessel maps derived from high resolution 7 T SWI scans using state-of-the-art non-linear image registration. The results of this analysis allowed both the relative sensitivity and the relative specificity of the BOLD response at 3 and 7 T to be assessed.

There was significant increase in the number of activated voxels at 7 T in both the veins and the microvasculature, with the increase in the microvasculature being higher. The increase in

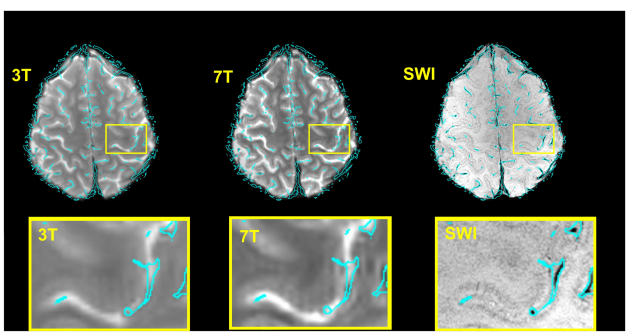

FIGURE 2 | Verification of the accuracy of the normalization 7T → SWI space and 3 → 7T (SWI) space for a typical subject and illustration of the corresponding vein map. For the illustration only, the boundaries of the veins (rather than the vein masks themselves) are shown, overlaid in cyan. These were generated with the contour function of CorelDraw (Corel Corporation, Ottawa, ON, Canada). Bottom row: zoomed depiction of the hand area.

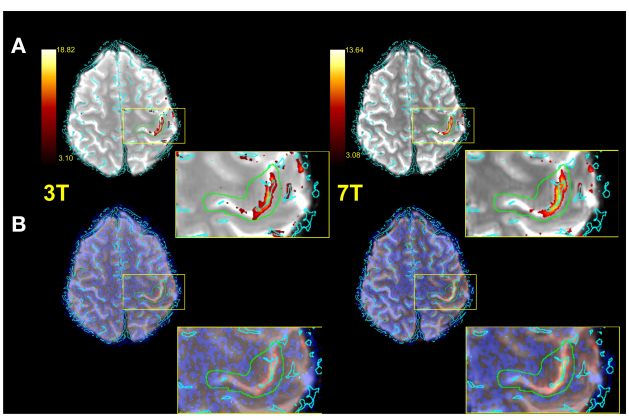

FIGURE 3 | Exemplified single subject illustration (radiological convention). **(A)** Functional image with vessels (cyan) thresholded IC map and anatomical VOI (green) overlaid. **(B)** As in **(A)**, but with no thresholding applied to IC map. A zoomed representation of the target area is also illustrated.

Table 1 | Individual subject results showing the number of activated voxels and mean *Z* values in regions identified as vessels and microvasculature.

3T	Subject	Number of activated voxels in VOI			Mean *Z* over all voxel in VOI		
		Vessels	μvasc	% In μvasc	Vessel	μvasc	*Z* μv/*Z* vessel
	1	1521	17,367	91.9	2.1	1.3	0.61
	2	1323	6982	84.1	2.6	1.1	0.41
	3	1345	8058	85.7	2.2	1.0	0.48
	4	1209	5056	80.7	1.9	1.0	0.53
	5	1926	4720	71.0	2.1	0.7	0.33
	6	2339	8856	79.1	2.8	1.4	0.50
	7	1314	6746	83.7	1.9	0.8	0.44
	8	2083	8097	79.5	3.3	1.2	0.37
	9	1655	7075	81.0	1.8	0.8	0.44
	10	2124	13,940	86.8	3.6	1.5	0.41
	11	1026	7732	88.3	1.8	1.0	0.54
	12	2094	14,617	87.5	2.2	1.0	0.45
	Mean	**1670**	**9100**	**82.9**	**2.4**	**1.1**	**0.45**
	SD	**430**	**4000**	**7.5**	**0.6**	**0.2**	**0.08**
7T	1	1986	25,895	68.0	2.8	1.8	0.64
	2	1366	9849	92.9	3.3	1.8	0.53
	3	1840	10,869	87.8	3.4	1.7	0.50
	4	1269	5598	85.5	2.3	1.4	0.59
	5	2422	11,218	81.5	3.0	1.5	0.49
	6	2392	11,206	82.2	2.9	1.6	0.56
	7	1664	9019	82.4	2.3	1.0	0.45
	8	2343	8490	84.4	3.4	1.3	0.38
	9	1804	5316	78.4	2.3	0.9	0.41
	10	2339	20,568	74.7	4.9	2.0	0.40
	11	2213	16,217	89.8	3.9	1.8	0.45
	12	2780	19,780	88.0	4.5	1.8	0.40
	Mean	**2030**	**12,800**	**84.3**	**3.2**	**1.5**	**0.47**
	SD	**460**	**6400**	**5.6**	**0.8**	**0.3**	**0.08**
3/7T stats	***t*-Test**	**0.0025***	**0.0025***	**n.s.**	**0.0017***	**7.33E−05***	**n.s.**

*All values are investigated within neuroanatomically defined VOIs. *Indicate statistically significant differences between 3 and 7T, and "n.s.," indicates a non-significant result.*

Table 2 | Summary sensitivity and specificity results extracted from Table 1.

7/3T SENSITIVITY	
N vessels	1.21 (0.31)
N μvasc	1.42 (0.44)
Z vessels	1.41 (0.35)
Z μvasc	1.48 (0.32)
7/3T SPECIFICITY	
% In μvasc	1.01 (0.13)
Z μv/*Z* vessel	1.07 (0.17)

Values in brackets are standard deviations on the mean.

both tissue classes confirms the increase in BOLD sensitivity of 7 T fMRI observed in other studies (Triantafyllou et al., 2005; van der Zwaag et al., 2009; Beisteiner et al., 2011). While the fact that there was a larger increase in the number of voxels activated in the microvasculature might suggest an increase in microvascular specificity at 7 T, this tendency was non-significant due to high variance over subjects. Findings were the same for mean *Z* values. There were significant increases, of ∼40%, in *Z* values in both the veins and tissue in 7 T results compared to 3 T results. Again, the increase was consistently higher in tissue, but not significantly so. The obvious conclusion, that BOLD specificity is not significantly higher at 7 T than at 3 T could be affected by our choice of echo times, which was different (and near optimum) for each field strength (35 ms for 3 T and 22 ms for 7 T) (Yacoub et al., 2001; Robinson et al., 2004). We tested the generality of our conclusion, however, by performing additional measurements at both 22 and 35 ms at each field strength. Although there was a small difference in all Z values between echo times the ratio *Z* μvasc/*Z* vessel did not differ substantially. We therefore conclude that while changing echo-time

Table 3 | A comparison of functional specificities measured at two the same echo times at 3 and 7T in one subject (subject 8; mean over two runs).

3T	Echo time (ms)	Number of activated voxels in VOI			Mean *Z* over all voxel in VOI		
		Vessels	μvasc		Vessel	μvasc	Ratio
			μvasc	% In μvasc	*Z* mean	*Z* mean	*Z* μv/*Z* vessel
	22	1735	10,608	85.94	2.55	1.41	0.55
	35	2028	13,004	86.51	2.88	1.63	0.57
7T	22	3561	28,622	88.94	8.15	3.38	0.41
	35	3630	31,608	89.70	7.81	3.71	0.48

All values are investigated within neuroanatomically defined VOIs. There is no substantial increase in specificity, measured via percentage of activated voxels in the microvasculature, or the ratio of mean Z values in the microvasculature to that in vessels, with field strength, even if the same echo times are used at 3 and 7T.

(unsurprisingly) influences BOLD sensitivity, it did not, to a measurable degree, affect specificity.

Our primary hypothesis in this study was that the increase in sensitivity would be larger in tissue than veins, demonstrating an increase in specificity and indicating that improved localization of the BOLD signal is to be expected at ultra-high field. This could not be confirmed, in apparent contradiction of prior work. For instances, Gati et al. (1997) predicted larger signal increases in tissue than veins in the visual cortex at 0.5, 1.5, and 4.0 T on the basis of measurement of SNR, $\Delta R2^*$, and $R2^*$ at these field strengths. Yacoub et al. (2001) extended Gati et al.'s findings relating to $\Delta R2^*$ and $R2^*$ from 4 to 7 T, but likewise based their predictions on increasing signal changes compared to relatively constant noise. The authors assumed that thermal noise "will ultimately dominate the noise term" – i.e., that when physiological noise is better understood and imaging systems are more developed, physiological noise will be reduced to below the level of thermal noise. Despite progress on this front (e.g., Boyacioglu and Barth, 2012), this point has not yet been reached. One source of physiological noise is pulsatory blood flow. In conventional EPI at least, the signal changes related to pulsatory flow (which typically have a frequency of 1–1.5 Hz) are undersampled with TRs of ∼0.5 Hz, and other physiological noise sources cannot be comprehensively removed, meaning that physiological noise is still at least as large as thermal noise at 7 T (Triantafyllou et al., 2005). The relatively high resolution measurements we made here with full brain coverage and accelerated imaging go as far as possible to reducing the relative contribution of physiological noise to the total (physiological plus thermal noise), and thereby yield the best specificity possible. A relatively high GRAPPA factor of 4 was used to achieve the desired echo times with these high resolution acquisitions. While the use of high parallel imaging factors increases g-factor noise and reduces BOLD sensitivity, the BOLD sensitivity in this study was sufficient to detect activation in the primary motor cortices of all subject. This GRAPPA factor is not expected to have any influence on specificity.

Fully automatic identification of vessels from SWI scans is a complex process and the subject of considerable research effort as a separate field (see, e.g., Frangi et al., 1998). Our attempts to apply a leading existing approach (Kroon, 2009) in this study led to imperfect detection of vessels and false positive vessel detection and enlarged vessels, and motivated the development of our own method. While our simple magnitude threshold-based approach performed much better than existing methods with this data it is also subject to shortcomings. Firstly, a threshold needs to be set to determine where veins end (how broad a vein mask is for a given appearance in SWI) and where tissue begins. Our vein maps were defined quite conservatively and a margin was left before defining voxels as belonging to tissue. In this way, we minimized the influence of this border zone between vein and tissue on our specificity results. Veins have low signal in SWI, but so does CSF and the interhemispheric fissure, so these regions are erroneously included in the vein mask. These errors did not influence results obtained here, as all analysis was performed within a VOI for the primary motor cortex which excluded these problems, but would lead to errors if applied uncritically in other studies.

It should be noted that our finding of no demonstrable increase in specificity at 7 T compared to 3 T are constrained to the motor system. A motor paradigm was chosen due to its robustness and our group's interest in precise localization of motor function in the context of presurgical planning (Beisteiner et al., 1995, 2001). Future work could involve extending this examination to the visual system, which would afford more direct comparison with prior studies, although specificity findings should be independent of the region studied. Finally, these findings are constrained to the measurement sequence and methods applied at both field strengths. Future developments in fast imaging may allow both the sensitivity and specificity of ultra-high field fMRI to be increased (Poser et al., 2013).

In summary, this study, comparing high resolution fMRI of the motor system at 3 and 7 T, does not confirm a significant increase in the specificity of the BOLD response at ultra-high field.

ACKNOWLEDGMENTS

This study was carried out as part of the "Vienna Advanced Clinical Imaging Center" (VIACLIC) project, funded by the Vienna Spots of Excellence Program of the Center of Innovation and Technology, City of Vienna (ZIT), Austria. Additional support was provided by the Austrian Science Fund (FWF) project KLI264.

REFERENCES

Bandettini, P. A., Wong, E. C., Hinks, R. S., Tikofsky, R. S., and Hyde, J. S. (1992). Time course EPI of human brain function during task activation. *Magn. Reson. Med.* 25, 390–397. doi:10.1002/mrm.1910250220

Beckmann, C. F., and Smith, S. M. (2004). Probabilistic independent component analysis for functional magnetic resonance imaging. *IEEE Trans. Med. Imaging* 23, 137–152. doi:10.1109/TMI.2003.822821

Beisteiner, R., Gomiscek, G., Erdler, M., Teichtmeister, C., Moser, E., and Deecke, L. (1995). Comparing localization of conventional functional magnetic resonance imaging and magnetoencephalography. *Eur. J. Neurosci.* 7, 1121–1124. doi:10.1111/j.1460-9568.1995.tb01101.x

Beisteiner, R., Robinson, S., Wurnig, M., Hilbert, M., Merksa, K., Rath, J., et al. (2011). Clinical fMRI: evidence for a 7T benefit over 3T. *Neuroimage* 57, 1015–1021. doi:10.1016/j.neuroimage.2011.05.010

Beisteiner, R., Windischberger, C., Lanzenberger, R., Edward, V., Cunnington, R., Erdler, M., et al. (2001). Finger somatotopy in human motor cortex. *Neuroimage* 13, 1016–1026. doi:10.1006/nimg.2000.0737

Boxerman, J. L., Bandettini, P. A., Kwong, K. K., Baker, J. R., Davis, T. L., Rosen, B. R., et al. (1995). The intravascular contribution to fMRI signal change: Monte Carlo modeling and diffusion-weighted studies in vivo. *Magn. Reson. Med.* 34, 4–10. doi:10.1002/mrm.1910340103

Boyacioglu, R., and Barth, M. (2012). Generalized iNverse imaging (GIN): ultrafast fMRI with physiological noise correction. *Magn. Reson. Med.* doi:10.1002/mrm.24528

Deichmann, R., Josephs, O., Hutton, C., Corfield, D. R., and Turner, R. (2002). Compensation of susceptibility-induced BOLD sensitivity losses in echo-planar fMRI imaging. *Neuroimage* 15, 120–135. doi:10.1006/nimg.2001.0985

Duong, T. Q., Yacoub, E., Adriany, G., Hu, X., Ugurbil, K., and Kim, S. G. (2003). Microvascular BOLD contribution at 4 and 7 T in the human brain: gradient-echo and spin-echo fMRI with suppression of blood effects. *Magn. Reson. Med.* 49, 1019–1027. doi:10.1002/mrm.10472

Frangi, A. F., Niessen, W. J., Vincken, K. L., and Viergever, M. A. (1998). "Multiscale vessel enhancement filtering," in *Medical Image Computing and Computer-Assisted Medical Intervention – MICCAI'98*, Vol. 1496 in Lecture Notes in Computer Science, eds W. M. Wells, A. Colchester, and S. Delp (Berlin: Springer), 130–137.

Garcia, D. (2009). *Robust Spline Smoothing for 1-D to N-D Data*. MATLAB Central. Available at: http://www.mathworks.com/matlabcentral/fileexchange/25634-robust-spline-smoothing-for-1-d-to-n-d-data [accessed].

Gati, J. S., Menon, R. S., Ugurbil, K., and Rutt, B. K. (1997). Experimental determination of the BOLD field strength dependence in vessels and tissue. *Magn. Reson. Med.* 38, 296–302. doi:10.1002/mrm.1910380220

Gomiscek, G., Beisteiner, R., Hittmair, K., Müller, E., and Moser, E. (1993). A possible role of in-flow effects in functional MR-imaging. *MAGMA* 1, 109–113. doi:10.1007/BF01769410

Haacke, E. M., Hopkins, A., Lai, S., Buckley, P., Friedman, L., Meltzer, H., et al. (1994). 2D and 3D high resolution gradient echo functional imaging of the brain: venous contributions to signal in motor cortex studies. *NMR Biomed.* 7, 54–62. doi:10.1002/nbm.1940070109

Jenkinson, M., Bannister, P., Brady, M., and Smith, S. (2002). Improved optimization for the robust and accurate linear registration and motion correction of brain images. *Neuroimage* 17, 825–841. doi:10.1006/nimg.2002.1132

Kroon, D. J. (2009). *Hessian Based Frangi Vesselness Filter*. MATLAB Central. Available at: http://www.mathworks.com/matlabcentral/fileexchange/24409-hessian-based-frangi-vesselness-filter [accessed].

Kwong, K. K., Belliveau, J. W., Chesler, D. A., Goldberg, I. E., Weisskoff, R. M., Poncelet, B. P., et al. (1992). Dynamic magnetic resonance imaging of human brain activity during primary sensory stimulation. *Proc. Natl. Acad. Sci. U.S.A.* 89, 5675–5679. doi:10.1073/pnas.89.12.5675

Menon, R. S. (2012). The great brain versus vein debate. *Neuroimage* 62, 970–974. doi:10.1016/j.neuroimage.2011.09.005

Ogawa, S., Menon, R. S., Kim, S. G., and Ugurbil, K. (1998). On the characteristics of functional magnetic resonance imaging of the brain. *Annu. Rev. Biophys. Biomol. Struct.* 27, 447–474. doi:10.1146/annurev.biophys.27.1.447

Ogawa, S., Tank, D. W., Menon, R., Ellermann, J. M., Kim, S. G., Merkle, H., et al. (1992). Intrinsic signal changes accompanying sensory stimulation: functional brain mapping with magnetic resonance imaging. *Proc. Natl. Acad. Sci. U.S.A.* 89, 5951–5955. doi:10.1073/pnas.89.13.5951

Poser, B. A., Barth, M., Goa, P. E., Deng, W., and Stenger, V. A. (2013). Single-shot echo-planar imaging with Nyquist ghost compensation: interleaved dual echo with acceleration (IDEA) echo-planar imaging (EPI). *Magn. Reson. Med.* 69, 37–47. doi:10.1002/mrm.24222

Reichenbach, J., Venkatesan, R., Schillinger, D., and Haacke, E. (1997). Small vessels in the human brain: MR-venography with deoxyhemoglobin as an intrinsic contrast agent. *Radiology* 204, 272–277.

Reichenbach, J. R., Essig, M., Haacke, E. M., Lee, B. C., Przetak, C., Kaiser, W. A., et al. (1998). High-resolution venography of the brain using magnetic resonance imaging. *MAGMA* 6, 62–69. doi:10.1016/S1352-8661(98)00011-8

Robinson, S., Pripfl, J., Bauer, H., and Moser, E. (2008). The impact of EPI voxel size on SNR and BOLD sensitivity in the anterior medio-temporal lobe: a comparative group study of deactivation of the default mode. *MAGMA* 21, 279–290. doi:10.1007/s10334-008-0128-0

Robinson, S., Windischberger, C., Rauscher, A., and Moser, E. (2004). Optimized 3T EPI of the amygdalae. *Neuroimage* 22, 203–210. doi:10.1016/j.neuroimage.2003.12.048

Shmuel, A., Yacoub, E., Chaimow, D., Logothetis, N. K., and Ugurbil, K. (2007). Spatio-temporal point-spread function of fMRI signal in human gray matter at 7 Tesla. *Neuroimage* 35, 539–552. doi:10.1016/j.neuroimage.2006.12.030

Smith, S. M., Jenkinson, M., Woolrich, M. W., Beckmann, C. F., Behrens, T. E., Johansen-Berg, H., et al. (2004). Advances in functional and structural MR image analysis and implementation as FSL. *Neuroimage* 23, S208–S219. doi:10.1016/j.neuroimage.2004.07.051

Speck, O., Stadler, J., and Zaitsev, M. (2008). High resolution single-shot EPI at 7T. *MAGMA* 21, 73–86. doi:10.1007/s10334-007-0087-x

Triantafyllou, C., Hoge, R. D., Krueger, G., Wiggins, C. J., Potthast, A., Wiggins, G. C., et al. (2005). Comparison of physiological noise at 1.5 T, 3 T and 7 T and optimization of fMRI acquisition parameters. *Neuroimage* 26, 243–250. doi:10.1016/j.neuroimage.2005.01.007

van der Zwaag, W., Francis, S., Head, K., Peters, A., Gowland, P., Morris, P., et al. (2009). fMRI at 1.5, 3 and 7 T: characterising BOLD signal changes. *Neuroimage* 47, 1425–1434. doi:10.1016/j.neuroimage.2009.05.015

Yacoub, E., Shmuel, A., Pfeuffer, J., Van De Moortele, P. F., Adriany, G., Andersen, P., et al. (2001). Imaging brain function in humans at 7 Tesla. *Magn. Reson. Med.* 45, 588–594. doi:10.1002/mrm.1080

Conflict of Interest Statement: The authors declare that the research was conducted in the absence of any commercial or financial relationships that could be construed as a potential conflict of interest.

Received: 17 February 2013; accepted: 29 July 2013; published online: 09 August 2013.

Citation: Geißler A, Fischmeister FPhS, Grabner G, Wurnig M, Rath J, Foki T, Matt E, Trattnig S, Beisteiner R and Robinson SD (2013) Comparing the microvascular specificity of the 3- and 7-T BOLD response using ICA and susceptibility-weighted imaging. Front. Hum. Neurosci. ***7****:474. doi: 10.3389/fnhum.2013.00474*

frontiers in
HUMAN NEUROSCIENCE

ORIGINAL RESEARCH ARTICLE
published: 20 May 2013
doi: 10.3389/fnhum.2013.00216

Insular dysfunction reflects altered between-network connectivity and severity of negative symptoms in schizophrenia during psychotic remission

Andrei Manoliu[1,2,3]*, Valentin Riedl[2,3,4,5,6], Anselm Doll[2,3], Josef Georg Bäuml[2,3], Mark Mühlau[3,5], Dirk Schwerthöffer[1], Martin Scherr[1,7], Claus Zimmer[2], Hans Förstl[1], Josef Bäuml[1], Afra M. Wohlschläger[2,3,5], Kathrin Koch[2,3] and Christian Sorg[1,2,3,4]

[1] Department of Psychiatry, Klinikum Rechts der Isar, Technische Universität München, Munich, Germany
[2] Department of Neuroradiology, Klinikum Rechts der Isar, Technische Universität München, Munich, Germany
[3] TUM-Neuroimaging Center, Technische Universität München, Munich, Germany
[4] Department of Nuclear Medicine, Klinikum Rechts der Isar, Technische Universität München, Munich, Germany
[5] Department of Neurology, Klinikum Rechts der Isar, Technische Universität München, Munich, Germany
[6] Munich Center for Neurosciences Brain & Mind, Ludwig-Maximilians-Universität München, Munich, Germany
[7] Department of Neurology, Christian Doppler Klinik, Paracelsus Medical University Salzburg, Salzburg, Austria

Edited by:
Veronika Schöpf, Medical University Vienna, Austria

Reviewed by:
Ayna Baladi Nejad, Brain and Spine Institute, France
Lena Palaniyappan, University of Nottingham, UK

***Correspondence:**
Andrei Manoliu, Department of Psychiatry and Neuroradiology, Klinikum rechts der Isar, Technische Universität München, Ismaningerstrasse 22, 81675 München, Germany.
e-mail: a.manoliu@googlemail.com

Schizophrenia is characterized by aberrant intrinsic functional connectivity (iFC) within and between intrinsic connectivity networks (ICNs), including the Default Mode- (DMN), Salience- (SN), and Central Executive Network (CEN). The anterior insula (AI) of the SN has been demonstrated to modulate DMN/CEN interactions. Recently, we found that the dependence of DMN/CEN interactions on SN's right AI activity is altered in patients with schizophrenia in acute psychosis and related to psychotic symptoms, indicating a link between aberrant AI, DMN, CEN, and psychosis. However, since structural alterations of the insula are also present during psychotic remission and associated with negative symptoms, impaired AI interaction might be relevant even for psychotic remission and corresponding symptoms. Twelve patients with schizophrenia during psychotic remission (SR) and 12 healthy controls were assessed using resting-state fMRI and psychometric examination. High-model-order independent component analysis of fMRI data revealed ICNs including DMN, SN, and CEN. Scores of iFC within (intra-iFC) and between (inter-iFC) distinct subsystems of the DMN, SN, and CEN were calculated, compared between groups and correlated with the severity of symptoms. Intra-iFC was altered in patients' SN, DMN, and CEN, including decreased intra-iFC in the left AI within the SN. Patients' inter-iFC between SN and CEN was increased and correlated with the severity of negative symptoms. Furthermore, decreased intra-iFC of the left AI correlated with both severity of negative symptoms and increased inter-iFC between SN and CEN. Our result provides first evidence for a relationship between AI dysfunction and altered between-network interactions in schizophrenia during psychotic remission, which is related to the severity of negative symptoms. Together with our previous results, data suggest specific SN/DMN/CEN reorganization in schizophrenia with distinct insular pathways for distinct symptom dimensions.

Keywords: schizophrenia, remission, anterior insula, salience network, default mode network, central executive network

INTRODUCTION

Schizophrenia is a severe mental disorder associated with aberrant functional and structural connectivity within and between intrinsic connectivity networks (ICNs), including the Default Mode- (DMN), Salience- (SN), and Central Executive Network (CEN) (Menon, 2011; Palaniyappan and Liddle, 2012). ICNs are characterized by spatially consistent functional connectivity (FC) of intrinsic brain activity (Fox and Raichle, 2007; Allen et al., 2011). Since DMN, SN and CEN play a critical role in high-level cognition [and are therefore considered as core neurocognitive networks (Uddin et al., 2011)], they have been suggested to be involved in different symptom dimensions of schizophrenia (Williamson, 2007).

More specifically, the DMN includes primarily the ventromedial prefrontal cortex, the posterior cingulate cortex, bilateral inferior parietal cortex, and the middle temporal lobe and is involved in self-related/internally oriented processes (Buckner et al., 2008). The CEN includes mainly the dorsolateral prefrontal cortex and posterior parietal cortex and is involved in goal-directed/externally oriented tasks (Fox and Raichle, 2007). In schizophrenia, alterations in FC have been reported for DMN as well as CEN during both rest (Whitfield-Gabrieli et al., 2009; Rotarska-Jagiela et al.,

2010; Skudlarski et al., 2010), and task (Garrity et al., 2007; Minzenberg et al., 2009; Whitfield-Gabrieli et al., 2009). Furthermore, the interaction between these networks has been reported to be disrupted in patients (Hasenkamp et al., 2011), suggesting that altered between-network interactions and thus impaired coordination of self-related processes and goal-directed tasks might underlie both positive and negative symptoms in schizophrenia (Williamson, 2007).

The SN includes primarily the anterior insular cortex and dorsal anterior cingulate cortex and is involved in detecting and orienting to salient external stimuli and internal events, including emotional, autonomic, and interoceptive informations (Seeley et al., 2007). Within the SN, the anterior insular cortex plays a crucial role in maintaining representations and updating of current and predictive salience (Singer et al., 2009; Palaniyappan and Liddle, 2012). Functional and structural alterations within the insular cortex are among the most frequently reported anomalies in schizophrenia (Palaniyappan and Liddle, 2012), including altered functional activity during tasks (Murray et al., 2008), reduced gray matter (GM) (Ellison-Wright et al., 2008), and decreased white matter (WM) fractional anisotropy (Ellison-Wright and Bullmore, 2009). Therefore, it has been suggested that functional and/or structural alterations within the insular cortex might contribute to aberrant salience processing, leading to the emergence of symptoms in schizophrenia (Palaniyappan and Liddle, 2012).

But how are anomalies in the anterior insula (AI) within the SN linked to aberrant DMN/CEN interactions in schizophrenia? Recently, it has been demonstrated that the anterior insula within the SN is crucial for modulating interactions between DMN-mediated self-related and CEN-mediated external-task directed processes in response to cognitive demands (Sridharan et al., 2008; Uddin et al., 2011). Recent models of insular dysfunction in schizophrenia hypothesized a relationship between impaired activity of the AI within the SN, disrupted DMN/CEN interaction, and different symptoms in schizophrenia (Menon, 2011; Palaniyappan and Liddle, 2012). Corresponding with these models, we demonstrated in a previous study (Manoliu et al., 2013) that the dependence of DMN/CEN interactions on SN's right AI activity was aberrant in patients with schizophrenia during state of acute psychosis and related to psychotic symptoms. More specifically, we found that the decreased connectivity within the SN's right AI correlated with both increased connectivity between DMN and CEN and the severity of hallucinations. These data demonstrate a specific link between right anterior insular dysfunction, aberrant inter-network connectivity, and positive symptoms in schizophrenia during psychosis. However, these data provide no information about insula's role in psychotic remission and for negative symptoms particularly in the context of network interactions. This might be of relevance because insular alterations such as structural reorganization or aberrant reward-related activity have been demonstrated to be present during psychotic remission and to be associated with negative symptoms (Palaniyappan et al., 2011; Gradin et al., 2013). Based on these data, we suggested that insular network interactions might be aberrant also during psychotic remission and associated with negative symptoms.

To test this hypothesis, we followed the approach previously reported (Manoliu et al., 2013) and performed resting-state functional magnetic resonance imaging (rs-fMRI), which measures ongoing blood-oxygenation-level-dependent (BOLD) fluctuations, and structural magnetic resonance imaging as well as psychometric assessment in 12 patients with schizophrenia during state of psychotic remission and 12 matched healthy controls (HCs). Rs-fMRI data were decomposed by high-model-order independent component analysis (ICA) into spatially independent z-maps of functionally coherent brain areas and corresponding time courses (TCs) of component activity (Calhoun et al., 2001). From these spatial maps, we selected those representing the SN, DMN, and CEN. Main outcome measures were Pearson's correlation between-network time series, reflecting inter-network intrinsic functional connectivity (inter-iFC), and components' z-maps, reflecting the intra-network intrinsic functional connectivity (intra-iFC). We controlled our analyses for effects of age, sex, medication, and structural anomalies.

MATERIALS AND METHODS

PARTICIPANTS

Twelve patients with schizophrenia during state of remission and 12 age and sex-matched HCs participated in the study (**Table 1**). Participants' data have been used in a previous study, which focused on intrinsic striatal activity in patients with schizophrenia during psychosis and psychotic remission (Sorg et al., 2013). In particular, data from patients in psychotic remission were reanalyzed in the current study focusing on the relationship between insular dysfunction, aberrant inter-network interactions and negative symptoms in schizophrenia. All patients provided informed consent in accordance with the Human Research Committee guidelines of the Klinikum Rechts der Isar, Technische Universität München. Patients were recruited from the Department of Psychiatry, controls by word-of-mouth advertising. Participants' examination included medical history, psychiatric interview,

Table 1 | Demographic and clinical characteristics.

Measure	SR ($n = 12$)	HC ($n = 12$)	SR vs. HC[1]	
	Mean (SD)	Mean (SD)	*T*-score	*p*-Value
Age	32.50 (10.04)	34.67 (12,25)	−0.474	0.640
Sex (m/f)	4/8	4/8		
PANSS				
Total	53.09 (14.56)	30.41 (1.44)	5.379	<0.001*
Positive	12.09 (3.75)	7.08 (0.29)	4.824	<0.001*
Negative	13.08 (5.95)	7.17 (0.58)	3.431	0.002*
General	27.36 (8.69)	16.17 (0.58)	4.458	<0.001*
GAF	59.09 (15.14)	99.17 (2.89)	−9.013	<0.001*
CPZ	207.42 (198.12)			
Duration of illness (years)	4.11 (3.29)			

[1]*Two-sample t-test; *significant for $p < 0.05$, Bonferroni-corrected for multiple comparisons.*

SR, patients with schizophrenia during state of remission; HC, healthy control group; PANSS, Positive and Negative Syndrome Scale; GAF, Global Assessment of Functioning Scale; CPZ, chlorpromazine equivalent dose.

psychometric assessment, and blood tests for patients. Psychiatric diagnoses were based on DSM-IV (American Psychiatric Association, 2000). The Structured Clinical Interview for DSM-IV [SCID-I (Spitzer et al., 1992)] was used to assess the presence of psychiatric diagnoses. Severity of clinical symptoms was measured with the Positive and Negative Syndrome Scale (PANSS) (Kay et al., 1987) on the day of scanning. Psychiatrists Dirk Schwerthöffer and Martin Scherr, who performed clinical-psychometric assessment, have been professionally trained for SCID and PANSS-based interviews with inter-rater reliability for diagnoses and scores of more than 95%. The global level of social, occupational, and psychological functioning was measured with the Global Assessment of Functioning Scale (GAF) (Spitzer et al., 1992).

All patients were diagnosed with schizophrenia and were ambulatory during state of remission at the time-point of scanning. Further inclusion criteria were age between 18 and 60 years and remission of psychotic symptoms [as indicated by significantly decreased PANSS scores compared to the admission during state of acute psychosis, see (Sorg et al., 2013) for detailed presentation of clinical characteristics at time-point of admission]. On average about 10 months after psychosis ($t_{\text{mean}} = 306.08$ days, $t_{\text{SD}} = 278.72$ days), patients approved an investigation during state of remission. Patients were free of any current or past neurological or internal systemic disorder, current or past depressive or manic episode, substance abuse (except nicotine), and cerebral pathology in MRI. The mean duration of illness was 4.11 years (SD = 3.29 years), the mean number of hospital stays was 4.00 (SD = 1.07). Four out of 12 patients were free of antipsychotic medication. All other patients received mono- or dual therapy with atypical antipsychotic medication, including Amisulpride ($n = 1$ case), Olanzapine ($n = 1$), Clozapine ($n = 3$), Quetiapine ($n = 3$), Risperidone ($n = 2$), and Aripiprazole ($n = 1$) (see **Table 2** for individual medication protocols and dosage and **Table 1** for mean chlorpromazine (CPZ) equivalent dose (Woods, 2003). All controls were free of any current or past psychiatric, neurological or systemic disorder or psychotropic medication.

All participants underwent 10 min of rs-fMRI with the instruction to keep their eyes closed and not to fall asleep. We verified that subjects stayed awake by interrogating via intercom immediately after the rs-fMRI scan. Before and after scanning, a medical examination of patients validated their stable condition and investigated whether they had feelings of odd situations during the scanning. No patient dropped out during the scanning session.

MRI DATA ACQUISITION

MRI was performed on a three T MR scanner (Achieva, Philips, Netherlands) using an eight-channel phased-array head coil. For co-registration and volumetric analysis, T1-weighted anatomical data were obtained by using a magnetization-prepared rapid acquisition gradient echo sequence (TE = 4 ms, TR = 9 ms, TI = 100 ms, flip angle = 5°, FoV = 240 mm^2 × 240 mm^2, matrix = 240 × 240, 170 slices, voxel size = 1 mm^3 × 1 mm^3 × 1 mm^3). fMRI data were obtained by using a gradient echo EPI sequence (TE = 35 ms, TR = 2000 ms, flip angle = 82°, FoV = 220 mm^2 × 220 mm^2, matrix = 80 × 80, 32 slices, slice thickness = 4 mm, and 0 mm interslice gap; 300 volumes).

Table 2 | Individual subject medication protocol and dosage.

Participants	Scan during state of remission
1	400 mg Clozapine
2	NO medication
3	2 mg Risperidone
4	NO medication
5	12.5 mg Olanzapine
6	NO medication
7	NO medication
8	300 mg Clozapine
9	600 mg Quetiapine
10	600 mg Amisulpride, 400 mg Quetiapine
11	600 mg Quetiapine, 5 mg Risperidone
12	450 mg Clozapine, 15 mg Aripiprazole

fMRI DATA ANALYSIS

Preprocessing

For each participant, first three functional scans of fMRI were discarded due to magnetization effects. SPM8 (Wellcome Department of Cognitive Neurology, London) was used for motion correction, spatial normalization into the stereotactic space of the Montreal Neurological Institute (MNI) and spatial smoothing with an 8 mm × 8 mm × 8 mm Gaussian kernel. To control for differences in motion between groups, excessive head motion (linear shift > 3 mm across run and on a frame-to-frame basis, rotation > 1.5°) was applied as exclusion criteria (Sorg et al., 2013). None of the participants had to be excluded. Two-sample t-tests between patients with schizophrenia during psychotic remission (SR) and HC yielded no significant results regarding translational (SR vs. HC: x-axis: $T = -0.035$, $p = 0.972$; y-axis: $T = 0.478$, $p = 0.639$; z-axis: $T = -0.082$, $p = 0.936$) and rotational movements of any direction (SR vs. HC: pitch: $T = 0.594$, $p = 0.560$; roll: $T = 1.013$, $p = 0.325$; yaw: $T = -0.107$, $p = 0.298$). Signal-to-noise ratio of fMRI data was not different between patients with schizophrenia during state of remission (mean = 46.16, SD = 11.46) and HCs (mean = 45.79, SD = 11.58)(two-sample t-test, $p = 0.94$).

Independent component analysis

Following a recently proposed approach (Allen et al., 2011), preprocessed data were decomposed into 75 spatial independent components within a group-ICA framework (Calhoun et al., 2001), based on the infomax-algorithm and implemented in the GIFT-software[1]. High-model-order ICA approaches yield independent components, which are in accordance with known anatomical and functional segmentations (Damoiseaux et al., 2006; Kiviniemi et al., 2009; Smith et al., 2009; Abou-Elseoud et al., 2010; Allen et al., 2011). fMRI data were concatenated and reduced by two-step principal component analysis, followed by independent component estimation with the infomax-algorithm. We subsequently ran 20 ICA (ICASSO) to ensure stability of the estimated components. This results in a set of average group components, which

[1] http://icatb.sourceforge.net

are then back-reconstructed into single-subject space. Each back-reconstructed component consists of a spatial z-map reflecting component's FC pattern across space (intra-iFC) and an associated time course reflecting component's activity across time.

Selection of model-order and networks-of-interest

The selection of the optimal ICA model-order to analyze rs-fMRI data is still a subject of ongoing debate (see Manoliu et al., 2013 for extensive discussion). However, it has been demonstrated that a model-order around 70 components may represent an optimal level to detect between-group differences and to avoid false positive results (Abou-Elseoud et al., 2010). Bearing this in mind and exactly following a recently proposed approach of Allen et al. (2011), we decomposed our data into 75 independent components. The congruence with Allen's approach enables greater comparability of results across studies and reduced subjective bias for ICN selection. In more detail, Allen and colleagues used an ICA model-order of 75 to decompose rs-fMRI data of 603 subjects within a group-ICA framework based on the infomax-algorithm and implemented in the GIFT-software[2] (Calhoun et al., 2001). Authors provided T-maps of 28 components, which reflect canonical ICNs online[3] (Allen et al., 2011). To select components, which reflect networks-of-interest, in an automated and objective way, we chose from these T-maps those representing subsystems of the SN, DMN, and CEN (7 of 28 maps, see **Figure 1**), and performed multiple spatial regression analyses of our 75 independent components' spatial maps on these templates. We selected components of highest correlation coefficient with the templates, resulting in seven ICNs of interest: one component reflecting the SN, three reflecting subsystems of the DMN or CEN, respectively. In the end, this approach yielded for each subject and ICN a component's z-map and time course, which reflect network's coherent activity.

Outcome measures and statistical analysis

Intra-iFC. To statistically evaluate intra-iFC of selected ICs, we calculated voxel-wise one-sample t-tests on participants' reconstructed spatial maps for each group, using SPM8 [$p < 0.05$, family-wise-error (FWE)-corrected for multiple comparisons]. To analyze group differences, participants' spatial maps were entered into two-sample t-tests with age, sex and total GM volumes [see Voxel-based Morphometry Analysis. for detailed presentation of calculation of total GM] as covariates-of-no-interest ($p < 0.05$ FWE-corrected).

Inter-iFC. To statistically evaluate inter-iFC between selected ICs, subject specific ICN TCs were detrended, despiked, filtered using a fifth-order Butterworth low-pass filter with a high frequency cutoff of 0.15 Hz, and pairwise correlated by Pearson's correlation, following the approach of Jafri et al. (2008). To assess group differences, correlation coefficients were transformed to z-scores using Fisher's z-transformation and entered into two-sample t-tests with age, sex, and total GM volumes (see Voxel-Bases Morphometry Analysis. for details regarding the calculation of total GM) as covariate-of-no-interest ($p < 0.05$, Bonferroni-corrected for multiple comparisons).

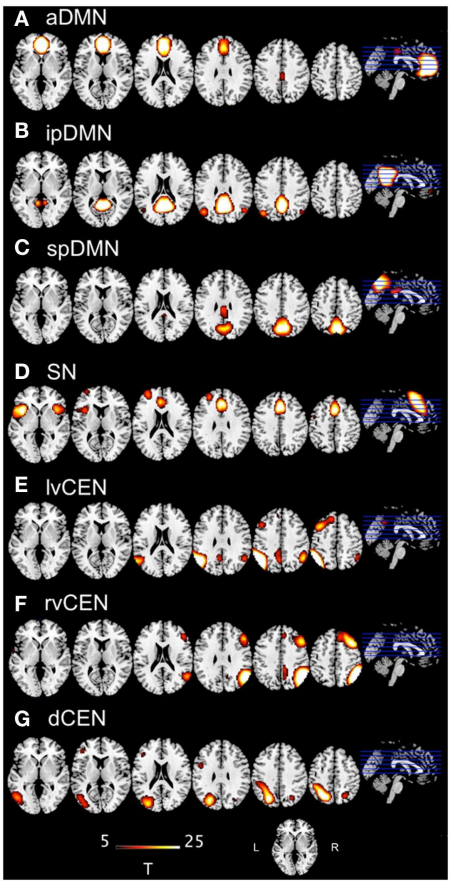

FIGURE 1 | T-maps of intrinsic connectivity networks of interest as described and provided online by Allen et al. (2011). Allen and colleagues used an ICA model-order of 75 to decompose rs-fMRI data of 603 subjects, obtaining 28 components. T-maps of components were provided online (http://mialab.mrn.org/data/hcp/RSN_HC_unthresholded_tmaps.nii). In the present study, we chose the T-maps of ICs representing the default mode network, salience network and central executive network, and performed multiple spatial regression analyses of our 75 independent components' spatial maps on these templates to select the networks-of-interest in an automated and objective way. Here, provided T-maps were superimposed on a single-subject high resolution T1 image (color scale representing t-values from 5 to 25). **(A)** Anterior default mode network (aDMN), corresponding to Allen-IC 25. **(B)** Inferior-posterior default mode network (ipDMN), corresponding to Allen-IC 53. **(C)** Superior-posterior default-mode network, corresponding to Allen-IC 50. **(D)** Salience network (SN), corresponding to Allen-IC 55. **(E)** Left-ventral central executive network (lvCEN), corresponding to Allen-IC 34. **(F)** Right-ventral central executive network (rvCEN), corresponding to Allen-IC 60. **(G)** Dorsal central executive network (dCEN), corresponding to Allen-IC 52.

Correlation analyses. Insular dysfunction has been suggested to be associated with various symptom dimensions, including both positive and negative symptoms in schizophrenia (Menon, 2011; Palaniyappan and Liddle, 2012). Accordingly, PANSS scores for total positive and negative symptoms were selected for further

[2]http://icatb.sourceforge.net
[3]http://mialab.mrn.org/data/hcp/RSN_HC_unthresholded_tmaps.nii

correlation analyses. To evaluate potential relationships between AI's aberrant intra-iFC within the SN and both altered between-network interactions (inter-iFCs) and severity of symptoms in patients with schizophrenia during state of psychotic remission, we followed a recently reported analysis approach (Manoliu et al., 2013). By applying the same analysis procedures as previously reported, we were able to ensure a broad comparability between our recently reported findings in patients with schizophrenia during state of acute psychosis and the current study's results in patients with schizophrenia during state of psychotic remission, thus providing the possibility to potentially infer on disease-state specific alterations in FC in schizophrenia. First, we calculated voxel-wise one-sample t-tests on patients' reconstructed intra-iFC maps for the SN and masked the result with a mask derived from the two-sample-t-test contrasting patients from HCs. Subsequently, we extracted principle eigenvariates of the clusters representing intra-iFC of the left and right AI within the SN. Then we used eigenvariate-scores for partial correlation analyses of Fisher-z-transformed inter-iFC scores and PANSS scores of total positive and negative PANSS scores, respectively, including age, sex, total GM, and CPZ as covariates of no interest (see Voxel-Bases Morphometry Analysis. for detailed description of the calculation of total GM). To study the relationship between inter-iFCs and severity of symptoms in patients, we used Fisher-z-transformed inter-iFC scores for partial correlation analyses of total positive and negative PANSS scores, respectively, including age, sex, total GM, and CPZ as covariates of no interest. Results of partial correlation analyses were thresholded at $p < 0.05$, Bonferroni-corrected for multiple comparisons.

VOXEL-BASED MORPHOMETRY ANALYSIS

The VBM analysis followed the description provided in Manoliu et al. (2013). The FC of intrinsic brain networks depends on widespread structural integrity of polysynaptic pathways (Lu et al., 2011). Since we focus on alterations of functional interactions among networks, we included total GM scores as covariate-of-no-interest in above-mentioned FC analyses to control for this influence of structural variations. As described recently (Sorg et al., 2013), we used the VBM8 toolbox[4] to analyze brain structure. T1-weighted images were corrected for bias-field in homogeneity, registered using linear (12-parameter affine) and non-linear transformations, and tissue-classified into GM, WM, and cerebrospinal fluid (CSF) within the same generative model (Ashburner and Friston, 2005). The resulting GM images were modulated to account for volume changes resulting from the normalization process. Here, we only considered non-linear volume changes so that further analyses did not have to account for differences in head size. Finally images were smoothed with a Gaussian kernel of 8 mm (FWHM). For group comparisons, voxel-wise t-tests were performed. We applied a height threshold (voxel level) of 0.05, family-wise error (FWE) corrected. Global volumes of GM and WM were derived from the first segmentation process. Groups were compared by two-sample t-tests. Finally, we included total GM scores as covariate-of-no-interest in the functional analyses of ICNs.

[4]http://dbm.neuro.uni-jena.de/vbm.html

RESULTS

INTRINSIC CONNECTIVITY NETWORKS: INTRA- AND INTER-iFC

In general, both intra-iFC and inter-iFC were almost perfectly in line with findings of Allen et al. (2011), indicating that the basic functional architecture of SN, DMN, and CEN was present in both groups (see **Figure 1** for presentation of spatial templates, **Figure 2** and **Table 3** for detailed presentation of intra-iFC within ICNs of interest and **Figure 3** and **Table 5** for detailed presentation of inter-iFC between ICNs of interest).

Intra-iFC

Automated component selection, which was based on spatial templates representing subsystems of the DMN, SN, and CEN (see **Figure 1** for presentation of spatial templates), revealed seven components of interest for each individual: the SN was represented in one component. The DMN was represented in three components [anterior DMN (aDMN), inferior-posterior DMN (ipDMN), superior-posterior DMN (spDMN)]. The CEN was represented in three components [left-ventral CEN (lvCEN), right-ventral CEN (rvCEN), dorsal CEN (dCEN)]. Selected components were spatially consistent across groups and matched previous results of SN, DMN, and CEN (Allen et al., 2011) (see **Figure 2**; **Table 3** for detailed description of intra-iFC within selected ICNs, $p < 0.05$, FWE-corrected).

Inter-iFC

Inter-iFC between intrinsic networks matched results of Allen et al. (2011) (see **Figure 3**; **Table 5** for detailed description of inter-iFC between all network-pairs). Noteworthy, we found positive correlations between distinct subsystems of the DMN and CEN in both groups. Although this is inconsistent with previously described patterns of anti-correlation between these two networks (Fox and Raichle, 2007), it is well in line with recent findings using high-model-order ICA (Allen et al., 2011). Furthermore, Smith et al. (2012) identified several sub-networks within the DMN, each associated with characteristic patterns of inter-network connectivity by using high temporal resolution resting-state fMRI.

INTRA-iFC OF THE SN IS DISRUPTED IN BILATERAL ANTERIOR INSULA IN PATIENTS WITH SCHIZOPHRENIA DURING REMISSION

Compared to HCs, patients demonstrated altered intra-iFC within the DMN, SN, and CEN. (**Figure 2**; **Table 4**; $p < 0.05$ FWE-corrected with age, sex, and total GM as covariates-of-no-interest). Regarding the SN, patients showed decreased intra-iFC within the bilateral AI. Furthermore, intra-iFC was increased in bilateral ACC within the SN (see **Figure 2D**). Regarding the DMN, patients showed decreased intra-iFC in bilateral ACC within the aDMN (see **Figure 2A**) and decreased intra-iFC in bilateral precuneus within the ipDMN (see **Figure 2B**). No between-group differences were observed within the spDMN. Regarding the CEN, patients showed increased intra-iFC in the left inferior temporal gyrus within the dCEN (see **Figure 1G**). No between-group differences were observed within both lvCEN and rvCEN.

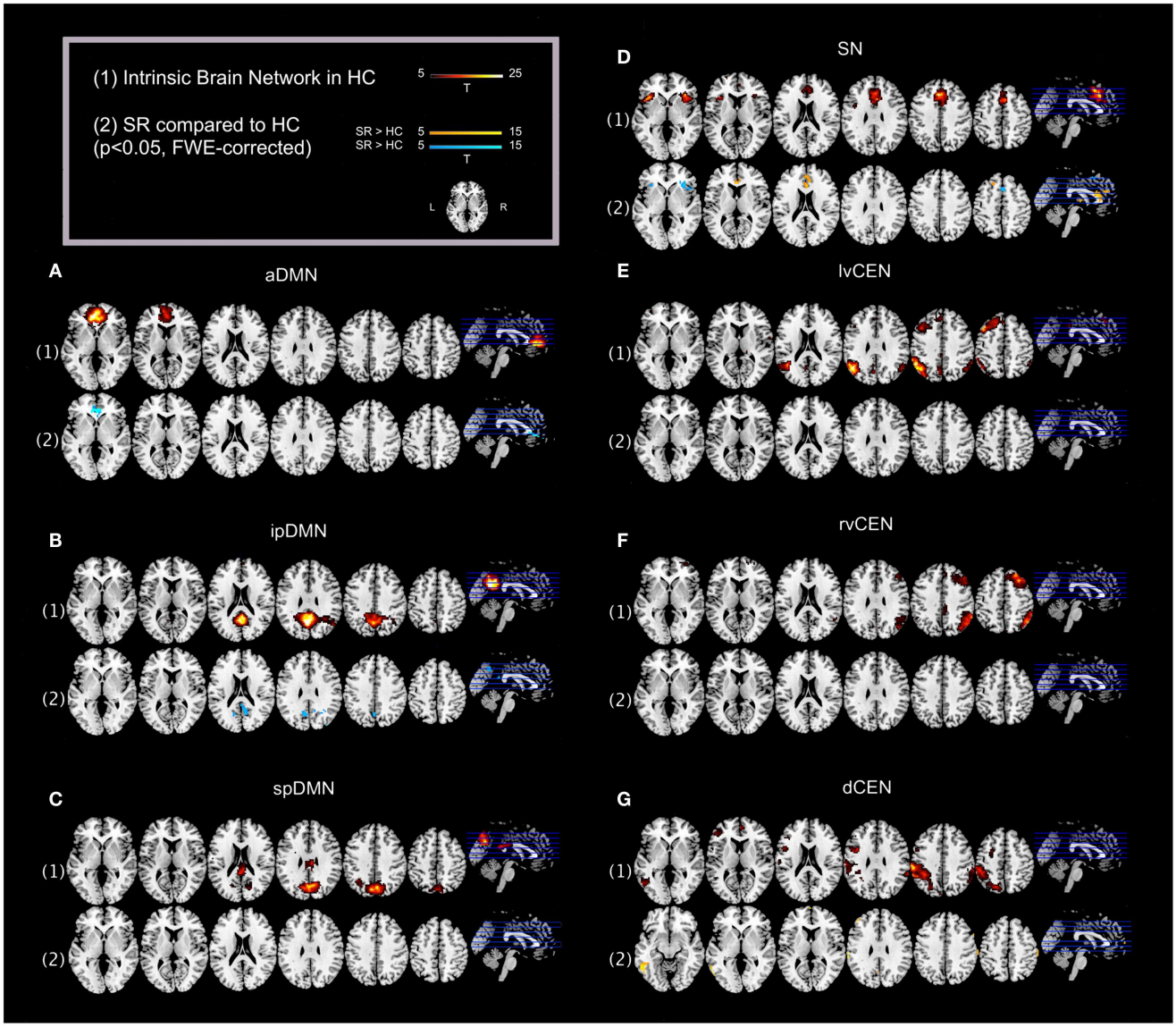

FIGURE 2 | Default mode network, salience network, and central executive network in healthy controls (HCs) and corresponding group differences for patients with schizophrenia in state of remission. (1) Spatial maps of selected ICs representing the default mode, salience, and central executive network (DMN, SN, CEN) in HCs were entered into voxel-wise one-sample *t*-tests and thresholded at $p < 0.05$, corrected for family-wise error (FWE). Statistical parametric maps (SPMs) representing brain areas with significantly co-varying activity were superimposed on a single-subject high resolution T1 image (color scale representing *t*-values from 5 to 25; only maps of HCs are shown). (2) To analyze between-group differences, patients' and controls' ICs of the DMN, SN, and CEN were entered into voxel-wise two-sample-*t*-test with age, sex, and total GM volume as covariates of no interest and thresholded at $p < 0.05$, FWE-corrected. SPMs were superimposed on a single-subject high resolution T1 image (color scale representing *t*-values from 5 to 15; yellow ("hot") color maps indicate regions displaying higher intra-iFC in SR compared to HC; blue ("cold") color maps indicate regions displaying less intra-iFC in SR compared to HC). Results for each network of interest are presented panel-wise: **(A)** anterior default mode network (aDMN); **(B)** inferior-posterior default mode network (ipDMN); **(C)** superior-posterior default-mode network; **(D)** salience network (SN); **(E)** left-ventral central executive network (lvCEN); **(F)** right-ventral central executive network (rvCEN); **(G)** dorsal central executive network (dCEN). SR, group of patients with schizophrenia during remission; HC, healthy control group (see also **Tables 3** and **4**).

INTER-iFC BETWEEN SN AND CEN IS INCREASED IN PATIENTS WITH SCHIZOPHRENIA DURING REMISSION

Compared to HCs, patients during psychotic remission showed both increased and decreased inter-iFC (**Figure 4**; **Table 5**; $p < 0.05$, corrected for age, sex, and total GM, Bonferroni-corrected for multiple comparisons). Patients showed decreased inter-iFC between ipDMN and rvCEN, suggesting a decreased FC between the DMN and CEN. Furthermore, patients showed increased inter-iFC between SN and rvCEN, indicating increased FC between the SN and CEN.

Table 3 | Intrinsic connectivity networks in healthy controls.

Anatomical region	L/R/Bi	cluster	*z*-Score	*p*-Value*	MNI (*x,y,z*)[1]
(A) ANTERIOR DEFAULT MODE NETWORK (aDMN)					
Medial prefrontal cortex	L	451	6.88	<0.001	−6, 45, 0
Medial prefrontal cortex	R	″	6.73	<0.001	6, 39, −3
(B) INFERIOR-POSTERIOR DEFAULT MODE NETWORK (ipDMN)					
Medial posterior parietal cortex	L	579	>8.00	<0.001	−3, −60, 30
Medial posterior parietal cortex	R	″	6.80	<0.001	6, −51, 24
Angular gyrus	R	″	6.55		48, −57, 27
(C) SUPERIOR-POSTERIOR DEFAULT MODE NETWORK (spDMN)					
Precuneus	Bi	344	6.53	<0.001	−9, −75, 36
Inferior parietal lobule	L	″	4.77	<0.001	−33, −37, 39
Posterior cingulate cortex	Bi	57	5.90	<0.001	−3, −36, 24
(D) SALIENCE NETWORK (SN)					
Anterior cingulate cortex	Bi	255	6.19	<0.001	−3, 27, 39
Insula lobe	L	77	5.91	<0.001	−39, 18, −3
Insula lobe	R	66	5.90	<0.001	36, 27, 0
(E) LEFT-VENTRAL CENTRAL EXECUTIVE NETWORK (lvCEN)					
Inferior parietal lobule	L	412	6.87	<0.001	−48, −63, 33
Superior frontal gyrus	L	137	6.16	<0.001	−39, 21, 51
Middle frontal gyrus	L	″	5.65	<0.001	−33, 9, 42
Inferior parietal lobule	R	42	5.00	<0.001	60, −51, 39
Precuneus	L	33	4.86	<0.001	−6, −69, 39
(F) RIGHT-VENTRAL CENTRAL EXECUTIVE NETWORK (rvCEN)					
Inferior parietal lobule	R	229	6.00	<0.001	42, −69, 45
Middle frontal gyrus	R	167	6.54	<0.001	30, 24, 45
Middle cingulate cortex	R	70	5.25	<0.001	9, −27, 36
Middle orbital gyrus	R	22	4.81	<0.001	30, 57, −6
(G) DORSAL CENTRAL EXECUTIVE NETWORK (dCEN)					
Supramarginal gyrus	L	300	6.35	<0.001	−60, −30, 39
Inferior temporal gyrus	L	24	5.96	<0.001	−51, −57, −6
Inferior frontal gyrus	L	12	5.20	<0.001	−48, 3, 33
Supramarginal gyrus	R	7	5.19	<0.001	63, −42, 30

One-sample-t-test, significant for p < 0.05, FWE-corrected for multiple comparisons, cluster-threshold > 10 voxel. [1]MNI, Montreal Neurological Institute; L, left hemisphere; R, right hemisphere; Bi, bilateral (see also **Figure 2).*

LEFT ANTERIOR INSULA'S ABERRANT SN CONNECTIVITY IS ASSOCIATED WITH ALTERED SN-CEN INTERACTION IN PATIENTS WITH SCHIZOPHRENIA DURING REMISSION

To study the influence of insular SN activity on altered inter-network connectivity in patients, we correlated eigenvariates of SN's left and right AI group difference clusters with Fisher-z-transformed correlation coefficients of each pair of network TCs (**Figure 5**; **Table 6**, $p < 0.05$, partial correlations with age, sex, total GM, and CPZ as covariates of no-interest, Bonferroni-corrected for multiple comparisons). In patients, SN's left AI intra-iFC correlated negatively with inter-iFC between SN and rvCEN ($r = -0.96$). There was no further significant correlation of SN's right or left AI intra-iFC with inter-iFC scores.

LEFT ANTERIOR INSULA'S ABERRANT SN CONNECTIVITY IS ASSOCIATED WITH SEVERITY OF NEGATIVE SYMPTOMS IN PATIENTS WITH SCHIZOPHRENIA DURING REMISSION

To study the influence of insular SN activity on the severity of positive and negative symptoms in patients, we correlated eigenvariates of SN's left and right AI group difference clusters with PANSS scores for total positive symptoms and total negative symptoms, respectively (**Figure 5**; **Table 7**; $p < 0.05$, partial correlations with age, sex, total GM, and CPZ as covariates of no-interest, Bonferroni-corrected for multiple comparisons). In patients, SN's left AI's intra-iFC correlated negatively with the severity of total negative symptoms ($r = -0.97$) but not with the severity of total positive symptoms. Furthermore, SNs right AI's intra-iFC correlated positively with the severity of total positive symptoms ($r = 0.886$). However, this result was not significant when corrected for multiple comparisons. There was no further significant correlation of SN's right or left AI intra-iFC with behavioral scores.

IMPAIRED SN-CEN INTERACTION IS SELECTIVELY ASSOCIATED WITH SEVERITY OF NEGATIVE SYMPTOMS

To study the relationship of between-network interactions with severity of positive and negative symptoms, we correlated inter-iFC scores with PANSS scores for both total positive symptoms and total negative symptoms, respectively (**Figure 5**; **Table 8**; $p < 0.05$,

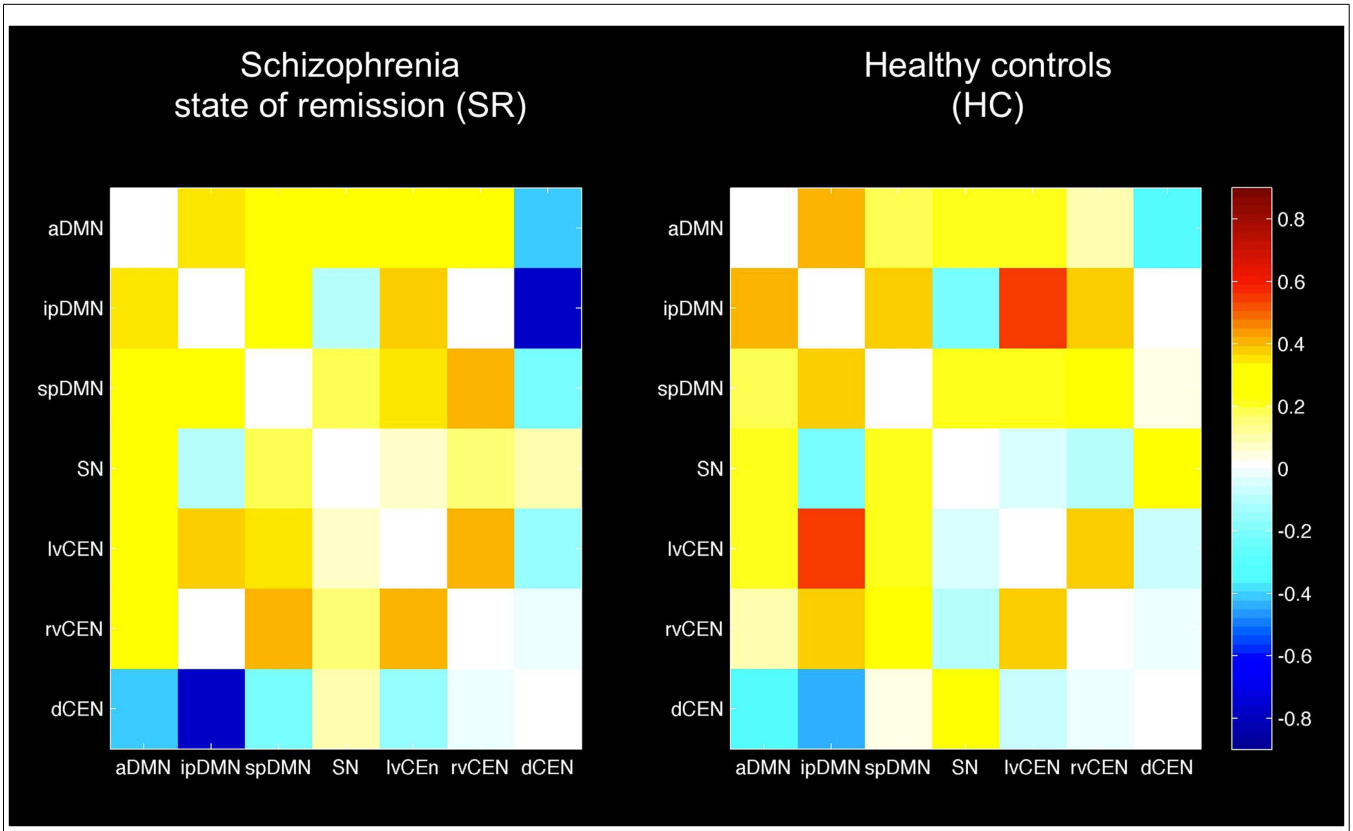

FIGURE 3 | Inter-network intrinsic functional connectivity matrix for patients with schizophrenia in state of remission and healthy controls (HCs). Pairwise Pearson's correlations between time courses of the default mode, salience, and central executive network (DMN, SN, CEN) were Fisher-z-transformed, averaged across subjects for each group of patients with schizophrenia and HCs, and presented in a correlation matrix. Colors represent intensity of averaged *z*-scores. a/ip/spDMN: anterior/inferior-posterior/superior-posterior DMN; lv/rv/dCEN: left-ventral/right-ventral/dorsal CEN (see also **Table 5**).

partial correlations with age, sex, total GM, and CPZ as covariates of no-interest, Bonferroni-corrected for multiple comparisons). Inter-iFC between SN and rvCEN correlated positively with the severity of total negative symptoms ($r = 0.969$) but not with the severity of positive symptoms. There was no further significant correlation of inter-iFC across network-pairs with behavioral scores.

ALTERATIONS IN INTRA-iFC AND INTER-iFC ARE NOT EXPLAINED BY BRAIN STRUCTURE OR MEDICATION

Regarding potential alterations in brain structure, voxel-wise tests yielded no regional GM or WM differences between groups. Although slightly decreased, total GM was not significantly changed in patients ($T = -0.16$, $p = 0.98$). Regarding potential effects of medication, we correlated CPZ with both intra-iFC of each ICN and inter-iFC for each pair of ICNs. CPZ showed no significant effect on both intra- ($p < 0.05$, FWE-corrected) and inter-iFC ($p < 0.05$, corrected for multiple comparisons), respectively. In addition, we included total GM and CPZ-scores as covariate-of-no-interest in the functional analyses of ICNs to account for these measures as potential confounders.

DISCUSSION

To test our hypothesis that insular dysfunction, altered between-network interactions, and negative symptoms are related in schizophrenia during psychotic remission, we investigated the intrinsic FC within- and between the SN, DMN, and CEN in patients with schizophrenia during psychotic remission and HCs. We found decreased intra-iFC in the left anterior insular cortex within the SN as well as increased inter-iFC between the SN and CEN. Furthermore, these alterations were related to each other and associated with the severity of negative symptoms. In addition, we found a strong trend for the association between decreased intra-iFC within the right AI and patients' positive symptoms, corresponding to our previous finding in psychotic patients. This result extends our knowledge about insular dysfunction in schizophrenia by demonstrating a link between left anterior insular dysfunction, altered inter-network connectivity and negative symptoms, which is present during psychotic remission. Together with our previous result of impaired right anterior insula dysfunction in psychosis, data suggest specific SN/DMN/CEN reorganization in schizophrenia with distinct insular pathways for distinct symptom dimensions.

Table 4 | Altered intra-iFC in patients with schizophrenia in state of remission compared to healthy controls.

Anatomical Region	L/R/Bi	cluster	*z*-Score	*p*-Value*	MNI (*x,y,z*)[1]
(A) ANTERIOR DEFAULT MODE NETWORK (aDMN)					
(a) SR > HC					
–	–	–	–	–	–
(b) SR < HC					
Anterior cingulate cortex	Bi	179	>8.00	<0.001	9, 42, −3
(B) INFERIOR-POSTERIOR DEFAULT MODE NETWORK (ipDMN)					
(a) SR > HC					
–	–	–	–	–	–
(b) SR < HC					
Precuneus	R	21	5.71	<0.001	12, −60, 24
	L	23	5.37	0.001	−9, −60, 30
(C) SUPERIOR-POSTERIOR DEFAULT MODE NETWORK (spDMN)					
(a) SR > HC					
–	–	–	–	–	–
(b) SR < HC					
–	–	–	–	–	–
(D) SALIENCE NETWORK (SN)					
(a) SR > HC					
Anterior cingulate cortex	Bi	33	5.83	<0.001	0, 27, 12
(b) SR < HC					
Insula lobe	R	18	5.68	<0.001	36, 27, 0
Insula lobe	L	8	5.08	<0.001	−27, 27, 9
(E) LEFT-VENTRAL CENTRAL EXECUTIVE NETWORK (lvCEN)					
(a) SR > HC					
–	–	–	–	–	–
(b) SR < HC					
–	–	–	–	–	–
(F) RIGHT-VENTRAL CENTRAL EXECUTIVE NETWORK (rvCEN)					
(a) SR > HC					
–	–	–	–	–	–
(b) SR < HC					
–	–	–	–	–	–
(G) DORSAL CENTRAL EXECUTIVE NETWORK (dCEN)					
(a) SR > HC					
Inferior temporal gyurs	L	111	7.52	<0.001	−54, −52, −21
(b) SR < HC					
–	–	–	–	–	–

Two-sample-t-test with age, sex, and total GM volume as covariates of no-interest, significant for $p < 0.05$, FWE-corrected for multiple comparisons. cluster-threshold > 5 voxel. [1]MNI, Montreal Neurological institute; L, left hemisphere; R, right hemisphere, Bi, bilateral (see also **Figure 2).*

THE SALIENCE NETWORK IN PSYCHOTIC REMISSION

The link between insular dysfunction within the SN, aberrant inter-network connectivity, and severity of symptoms in psychotic remission

In accordance to our hypothesis (Menon, 2011; Palaniyappan and Liddle, 2012), we found both altered intra-iFC in the left AI within the SN and altered inter-iFC between the SN and CEN. We demonstrated that both findings are related to each other (**Figure 5**; **Table 6**) and to the severity of negative symptoms in patients (**Figure 5**; **Tables 7** and **8**), indicating an association between insular dysfunction and aberrant inter-network connectivity in patients with schizophrenia during psychotic remission. Noteworthy, the right anterior insula, which showed also decreased intra-iFC within the SN, yielded a trend for a correlation with the severity of positive symptoms ($r = 0.89$, $p = 0.02$). Although this result is well in line with previous findings (Palaniyappan et al., 2012; Manoliu et al., 2013), and current models of insular dysfunction in psychosis (Menon, 2011; Palaniyappan and Liddle, 2012), it did not survive correction for multiple comparisons. This missing significance might be explained by small statistical power due to the limited size of our patient sample and low levels of variance of positive symptoms in patients (see also Limitations). All tests were performed including age, sex, total GM and CPZ as covariates-of-no-interest. Therefore, it is unlikely

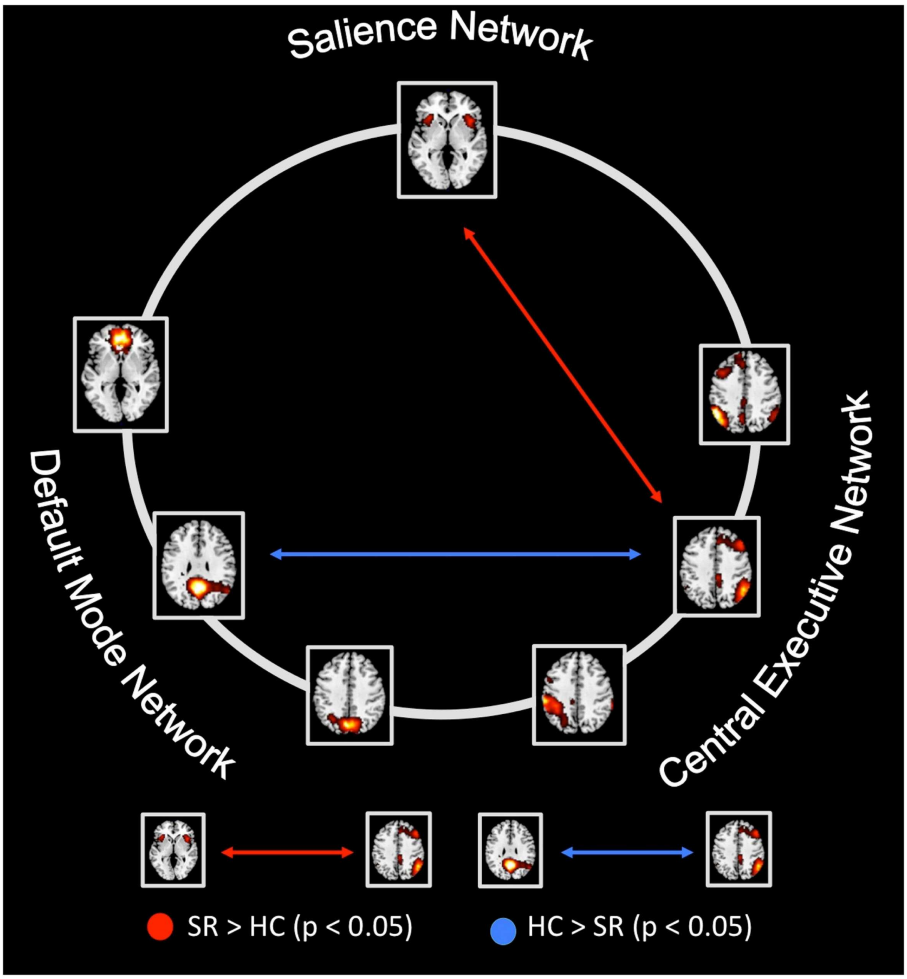

FIGURE 4 | Between-group differences of inter-network intrinsic functional connectivity. Based on network time courses (TCs), inter-network intrinsic functional connectivity (inter-iFC) were calculated by the use of Pearson's correlation between subject specific ICN TCs. The red arrows indicates increased inter-iFC in patients compared to healthy controls (HCs) (two-sample *t*-test, $p < 0.05$, Bonferroni-corrected for multiple comparisons); The blue arrows indicates decreased inter-iFC in patients compared to HCs (two-sample *t*-test, $p < 0.05$, Bonferroni-corrected for multiple comparisons). Spatial maps indicate the anterior/inferior-posterior/superior-posterior default mode network (a/ip/spDMN), left-ventral/right-ventral/dorsal central executive network (lv/rv/dCEN), and salience network (SN). All tests were corrected for age, sex and total GM volume. Abbreviations: SR, group of patients with schizophrenia during remission; HC, healthy control group (see also **Table 5**).

that present results are explained by these factors. Taken together, data demonstrate that dysfunction of the left AI within the SN in schizophrenia is present during psychotic remission and related to both altered inter-network connectivity and severity of patients' negative symptoms.

These results are in line within the suggested disruption of the AI's control function for between-network interactions in schizophrenia, which may persist even during psychotic remission and may be related to distinct symptom dimensions (Palaniyappan and Liddle, 2012). Several findings support this idea: Firstly, the AI has been demonstrated to play a critical role regarding the modulation of between-network interactions (Sridharan et al., 2008; Menon and Uddin, 2010). Secondly, alterations within the AI such as structural reorganization or aberrant reward-related activity have been shown in patients with schizophrenia during psychotic remission and to be linked with negative symptoms (Palaniyappan et al., 2011; Gradin et al., 2013). Thirdly, the current findings correspond with previous findings demonstrating that an impaired dependence of aberrant between-network interactions on right insular dysfunction is related with positive symptoms (Manoliu et al., 2013). Fourthly, recently formulated models providing a link between aberrant engagement and disengagement of large-scale intrinsic connectivity networks and psychopathology suggest an impaired control function of the AI in patients with schizophrenia, giving rise to both positive and negative symptoms (Menon, 2011; Palaniyappan and Liddle, 2012). Therefore, the present results suggest that anterior insular dysfunction may contribute to symptoms of schizophrenia via aberrant inter-network interaction.

Our findings suggest an asymmetric involvement of the AI in patients with schizophrenia as a function of state of disease. While

Table 5 | Inter-network intrinsic functional connectivity in patients with schizophrenia in state of remission and healthy controls.

Inter-iFC	SR ($n = 12$)		HC ($n = 12$)		SR vs. HC[1]	
	Mean	SD	Mean	SD	Direction	*p*-Value
aDMN – ipDMN	0.351	0.188	0.424	0.200	HC > SR	0.266
aDMN – spDMN	0.328	0.195	0.138	0.141	SR > HC	*0.034*
aDMN – SN	0.274	0.148	0.152	0.188	SR > HC	0.141
aDMN – lvCEN	0.261	0.168	0.157	0.124	SR > HC	0.078
aDMN – rvCEN	0.312	0.131	0.105	0.173	SR > HC	*0.011*
aDMN – dCEN	−0.411	0.223	−0.318	0.121	HC > SR	0.473
ipDMN – spDMN	0.268	0.123	0.317	0.295	HC > SR	0.563
ipDMN – SN	−0.094	0.178	−0.301	0.194	SR > HC	0.052
ipDMN – lvCEN	0.387	0.195	0.545	0.195	HC > SR	0.14
ipDMN – rvCEN	0.003	0.143	0.371	0.107	*HC > SR*	*<0.001**
ipDMN – dCEN	−0.782	0.195	−0.523	0.126	HC > SR	*0.008*
spDMN – SN	0.171	0.193	0.149	0.148	SR > HC	0.988
spDMN – lvCEN	0.343	0.176	0.162	0.267	SR > HC	0.076
spDMN – rvCEN	0.418	0.197	0.190	0.192	SR > HC	*0.021*
spDMN – dCEN	−0.222	0.216	0.032	0.229	HC > SR	0.066
SN – lvCEN	0.071	0.134	−0.140	0.240	SR > HC	0.066
SN – rvCEN	0.166	0.157	−0.177	0.237	*SR > HC*	*0.002**
SN – dCEN	0.109	0.176	0.260	0.147	HC > SR	0.088
lvCEN – rvCEN	0.410	0.166	0.359	0.223	SR > HC	0.609
lvCEN – dCEN	−0.150	0.230	−0.119	0.159	HC > SR	0.678
rvCEN – dCEN	−0.025	0.195	−0.088	0.168	SR > HC	0.289

*[1]Two-sample t-test, controlled for age, sex, and total GM volume. Italics indicate $p < 0.05$; *significant for $p < 0.05$, Bonferroni-corrected for multiple comparisons ($n = 21$).*

*SR, group of patients with schizophrenia during remission; HC, healthy control group; inter-iFC, inter-network intrinsic functional connectivity; a/ip/spDMN: anterior/inferior-posterior/superior-posterior DMN; lv/rv/dCEN: left-ventral/right-ventral/dorsal CEN; SN: salience network (see also **Figures 3** and **4**).*

the intra-iFC within the left AI was associated with both altered interactions between SN and CEN and severity of negative symptoms in patients during state of remission (**Figure 5**, **Tables 6** and **7**), the intra-iFC within the right AI was associated with both altered interactions between the DMN and CEN and severity of positive symptoms in patients during state of psychosis [(Manoliu et al., 2013), see also **Table 7**]. This observation corresponds to the asymmetric representation of body-related interoceptive information in the AI, which has been suggested to originate from the asymmetry of the peripheral autonomic nervous system; the left AI is more associated with the parasympathetic system, the right AI more with the sympathetic system (Craig, 2002). It has been suggested that this asymmetric autonomous representation in the AI might underlie asymmetric representations of emotions and interoceptive awareness (Craig, 2009). For example, the right AI is more involved in "sympathetic" emotions induced by stimuli that increase arousal and energy costs of behavioral responses such as pain or aversive pictures (Craig, 2009), while the left AI is more related to positive emotions such as maternal and romantic love, joy, or positive reactions induced by pleasant stimuli, and relaxation (Craig, 2009). Considering the left AI's role in processing positive and affiliative emotional feelings (Craig, 2009), deficits within the left AI might be associated with negative symptoms in schizophrenia (Palaniyappan and Liddle, 2012). For example, negative symptoms such as anhedonia and diminished social interactions might be associated with anomalies within the left anterior insula via impaired responses on pleasant stimuli. Accordingly, structural deficits within the anterior insular cortex have been demonstrated to be highly related to the severity of negative symptoms in patients with schizophrenia (Koutsouleris et al., 2008) while Horn et al. (2010) demonstrated a relationship between altered connectivity between AI and ACC and the severity of affective symptoms in patients with major depressive disorder. Bearing these findings in mind, our results might represent a first hint toward a relationship between asymmetric interoceptive-emotional representation in the left and right AI and the AI's asymmetric association with positive and negative symptoms in schizophrenia as a function of state of disease. However, it is to note that we did not explicitly test for asymmetry in the present study. Future studies investigating the potential link between aberrant intrinsic FC within the left and right AI and positive and negative symptoms in patients with schizophrenia during both psychosis and psychotic remission are necessary to improve our understanding of the left and right AI's relevance for distinct symptom dimensions in schizophrenia.

Further observations

In the following we want to make three further comments that may help to better evaluate and contextualize our findings centered on the SN.

Potential inconsistency with previous findings. In contrast to the current study, Woodward et al. (2011) found no significant findings regarding the intra-iFC of the SN in patients with schizophrenia. More specifically, the authors observed a non-significant trend to decreased network connectivity within the SN by applying a seed-based region-of-interest correlation analysis to calculate SN's iFC in a combined group of patients with schizophrenia and schizoaffective disorder. According to the evaluation of the reported coordinates for the seeds using the "SPM Anatomy toolbox" (Eickhoff et al., 2005), the seeds were placed in the left and right inferior frontal gyrus pars orbitalis, near to the AI. In contrast, we investigated selectively patients with schizophrenia, once during state of acute psychosis in a previous study (Manoliu et al., 2013) and once during state of psychotic remission in the current study by the use of an ICA-approach. Our analyses yielded consistently aberrant intra-iFC in both AI and ACC within the SN in patients with schizophrenia during both state of acute psychosis and state of remission. Although Woodward and colleagues also found a trend for reduced intra-iFC within the SN, these contradictory results might be explained by different methodological approaches, including the exact position of the seed as reported in Woodward et al. (2011) and, maybe more important, by the highly different composition of the patient samples.

Findings beyond altered interactions within and between the SN, DMN, and CEN in schizophrenia. Although increasing evidence for functional (White et al., 2010; Gradin et al., 2013; Manoliu

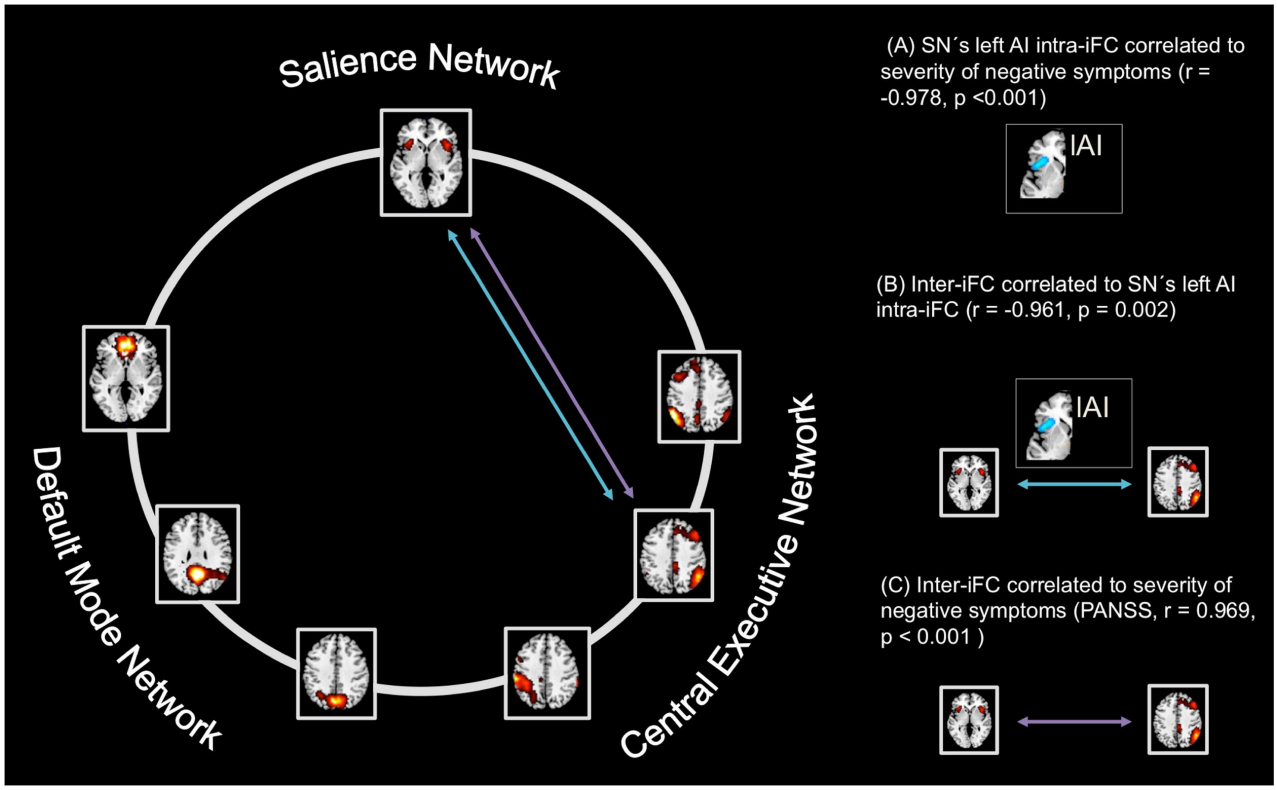

FIGURE 5 | Intra-iFC in the left anterior insula within the salience network is associated with increased SN-CEN interaction and severity of negative symptoms. Intrinsic functional connectivity (inter-iFC) between ICNs of interest was calculated by the use of Pearson's correlation between-networks' time courses. **(A)** Intra-iFC in the left anterior insula within the SN (turquoise spatial map) was significantly correlated with severity of negative symptoms in patients (partial correlation, $r = -0.978$, $p < 0.001$). **(B)** Furthermore, intra-iFC in the left anterior insula within the SN was significantly correlated with the inter-iFC between SN and CEN in patients (turquoise arrow, partial correlation, $r = -0.961$, $p = 0.002$). **(C)** Finally, the inter-iFC between SN and CEN was significantly correlated with the severity of negative symptoms (purple arrow, partial correlation, $r = 0.969$, $p < 0.001$). All partial correlations were corrected for age, sex, total GM volume, and medication (CPZ). Spatial maps indicate the anterior/inferior-posterior/superior-posterior default mode network (a/ip/spDMN), left-ventral/right-ventral/dorsal central executive network (lv/rv/dCEN), and salience network (SN) (see also **Tables 6–8**).

et al., 2013) and structural alterations (Palaniyappan et al., 2012) within the salience network of patients with schizophrenia points at the important role of aberrant SN-centered triple network interactions in schizophrenia (Menon, 2011), it is unclear whether and how findings beyond the SN, DMN, and CEN link with such altered triple network properties. For example Williamson and colleagues argue that models considering only the connectivity within and between SN, DMN, and CEN miss to account for both known alterations within auditory networks in patients with schizophrenia and differences between schizophrenia and other neuropsychiatric disorders demonstrating also altered FC within the SN (Williamson and Allman, 2012). Furthermore, it is unknown how aberrant iFC within subcortical regions such as the striatum (Sorg et al., 2013) or neurochemical anomalies such as increased dopaminergic activity during psychosis (Howes et al., 2009; Howes et al., 2012) are related with altered interactions between these three networks. Future studies are necessary to investigate the relationship between altered connectivity within and between the SN, DMN, and CEN and anomalies the triple network model (Menon, 2011) does not account for. It is an important research question whether the integrative potential of the SN-centered triple network model can be extended to allow also for further reported findings such as alterations in auditory networks, subcortical structures, and neurochemical activity.

Proximal and motivational salience in schizophrenia. Current results are well in line with the aberrant proximal salience model of Palaniyappan and Liddle (2012). Proximal salience refers to a momentary interoceptive state, which results from the evaluation of internal/external stimuli; it is represented by the SN activity particularly the AI, and it modulates both subsequent choices of actions/cognitions and learning processes to optimize evaluation; this modulation includes the control of DMN/CEN interactions via AI signals. Palaniyappan and colleagues suggest that AI/SN-related proximal salience is impaired in patients with schizophrenia contributing to distinct symptom dimensions. It is obvious that our findings support this model. Noteworthy, the concept of proximal salience is distinct from the more popular idea of motivational salience and its relevance for psychotic symptoms via aberrant prediction error processing (Kapur, 2003). Motivational salience refers to the assignment of motivational value to an external/internal stimulus after the stimulus has been evaluated;

Table 6 | Partial correlations between intra-iFC in the right/left AI within the SN and inter-iFC in patients with schizophrenia in state of remission.

Inter-iFC	right AI		left AI	
	r-score	*p*-Value	*r*-score	*p*-Value
aDMN – ipDMN	0,056	0,916	−0,603	0,205
aDMN – spDMN	−0,015	0,977	0,507	0,305
aDMN – SN	−0,671	0,145	−0,009	0,987
aDMN – lvCEN	0,232	0,658	0,392	0,442
aDMN – rvCEN	0,101	0,849	0,793	0,06
aDMN – dCEN	−0,604	0,204	0,605	0,204
ipDMN – spDMN	0,306	0,555	−0,698	0,123
ipDMN – SN	−0,05	0,925	0,038	0,943
ipDMN – lvCEN	0,672	0,144	−0,132	0,803
ipDMN – rvCEN	0,819	*0,046*	−0,24	0,646
ipDMN – dCEN	−0,374	0,466	0,293	0,572
spDMN – SN	−0,034	0,949	0,84	*0,036*
spDMN – lvCEN	0,049	0,926	−0,236	0,653
spDMN – rvCEN	−0,407	0,423	−0,597	0,21
spDMN – dCEN	−0,28	0,591	0,493	0,321
SN – lvCEN	−0,602	0,206	0,238	0,65
SN – rvCEN	0,207	0,695	−0,961	*0,002**
SN – dCEN	−0,528	0,281	0,956	*0,003*
lvCEN – rvCEN	0,356	0,488	−0,491	0,322
lvCEN – dCEN	−0,779	0,068	−0,037	0,945
rvCEN – dCEN	−0,362	0,481	0,319	0,538

*Italics indicate $p < 0.05$; *significant for $p < 0.05$, Bonferroni-corrected for multiple comparisons ($n = 21$). Partial correlation, corrected for age, sex, total GM volume and chlorpromazine equivalent dose (CPZ).*

*a/ip/spDMN: anterior/inferior-posterior/superior-posterior DMN; lv/rv/dCEN: left-ventral/right-ventral/dorsal CEN; SN: salience network; AI: anterior insula (see also **Figure 5**).*

Table 7 | Partial correlations between intra-iFC in the right/left AI within the SN and severity of positive and negative symptoms in patients with schizophrenia in state of remission.

PANSS scores	right AI		left AI	
	r-Score	*p*-Value	*r*-Score	*p*-Value
(A) TOTAL SCORES				
Total positive symptoms	0,886	*0,019*	−0,553	0,255
Total negative symptoms	0,141	0,789	−0,978	*0,001**

*Italics indicate $p < 0.05$; *significant for $p < 0.05$, Bonferroni-corrected for multiple comparisons ($n = 4$). Partial correlation, corrected for age, sex, total GM volume and chlorpromazine equivalent dose (CPZ).*

*AI: anterior Insula; PANSS: Positive and Negative Syndrome Scale (see also **Figure 5**).*

Table 8 | Partial correlations between inter-iFC and severity of positive and negative symptoms in patients with schizophrenia in state of remission.

Inter-iFC	Total Positive Symptoms		Total Negative Symptoms	
	r-score	*p*-Value	*r*-score	*p*-Value
aDMN – ipDMN	0.443	0.379	0.595	0.213
aDMN – spDMN	−0.254	0.627	−0.574	0.233
aDMN – SN	−0.717	0.109	0.135	0.799
aDMN – lvCEN	−0.152	0.774	−0.402	0.429
aDMN – rvCEN	−0.243	0.643	−0.869	*0.025*
aDMN – dCEN	−0.764	0.077	−0.463	0.355
ipDMN – spDMN	0.361	0.482	0.597	0.211
ipDMN – SN	−0.184	0.727	−0.016	0.977
ipDMN – lvCEN	0.807	0.052	0.071	0.893
ipDMN – rvCEN	0.844	*0.034*	0.105	0.844
ipDMN – dCEN	−0.166	0.753	−0.129	0.808
spDMN – SN	−0.256	0.624	−0.865	0.026
spDMN – lvCEN	−0.03	0.955	0.188	0.722
spDMN – rvCEN	−0.115	0.828	0.643	0.169
spDMN – dCEN	−0.327	0.526	−0.362	0.481
SN – lvCEN	−0.615	0.194	−0.073	0.89
SN – rvCEN	0.555	0.253	0.969	*<0.001**
SN – dCEN	−0.686	0.133	−0.9	*0.014*
lvCEN – rvCEN	0.396	0.437	0.486	0.329
lvCEN – dCEN	−0.728	0.101	0.179	0.735
rvCEN – dCEN	−0.509	0.302	−0.228	0.663

*Italics indicate $p < 0.05$; *significant for $p < 0.05$, Bonferroni-corrected for multiple comparisons ($n = 21$). Partial correlation, corrected for age, sex, total GM volume and chlorpromazine equivalent dose (CPZ).*

*a/ip/spDMN: anterior/inferior-posterior/superior-posterior DMN; lv/rv/dCEN: left-ventral/right-ventral/dorsal CEN; SN: salience network (see also **Figure 5**).*

this process depends on the reward prediction error, which in turn is associated with aberrant dopamine activity in the striatum of psychotic patients. This model is in line with broader models of schizophrenia, which suggest aberrant prediction error processing as critical element underlying patients' positive symptoms, taking the huge body of evidence for aberrant striatal dopamine in psychotic patients into account (Murray et al., 2008; Fletcher and Frith, 2009). As mentioned above, it seems to be important to study how these two concepts of aberrant salience link in schizophrenia, i.e., in terms of our finding: how do aberrant AI interactions relate with aberrant striatal prediction error activity?

DMN/CEN INTERACTIONS IN PSYCHOTIC REMISSION

Intra-iFC within the DMN in psychotic remission

Compared to HCs, patients showed decreased intra-iFC in both ACC and PCC within the DMN, while inter-iFC between DMN's subsystems was not altered. Although alterations in FC within the DMN in patients with schizophrenia are frequently reported during both task (Garrity et al., 2007) and rest (Whitfield-Gabrieli and Ford, 2012), the nature of this alterations remains still unclear. For instance, recent fMRI studies investigating the FC within the DMN demonstrated both decreased (Camchong et al., 2011) and increased (Whitfield-Gabrieli et al., 2009) intra-iFC in patients with schizophrenia. Among other things, inhomogeneous patient samples, often including patients during both state of psychosis

and state of remission, and the application of not-standardized methodological approaches might account for this contradictory results (Whitfield-Gabrieli and Ford, 2012).

In the present study, we adopted a recently proposed pipeline for ICA of resting-state fMRI data (Allen et al., 2011) to obtain canonical ICNs in a robust and reproducible way, thus allowing for better comparability with studies using the same approach. Previously, we found decreased intra-iFC within as well as increased inter-iFC between distinct subsystems of the DMN in patients with schizophrenia during psychosis using the same methodological approach (Manoliu et al., 2013). Furthermore, the absence of increased FC between distinct subsystems of the DMN in psychotic remission is well in line with current literature, suggesting a relationship between increased FC within the DMN, severity of positive symptoms and psychosis (Garrity et al., 2007). Taken these findings together, our data suggest an aberrant intrinsic FC within the DMN as a function of state of disease.

Intra-iFC within the CEN in psychotic remission

Compared to HCs, patients showed increased intra-iFC in the left inferior temporal gyrus, while inter-iFC between CEN's subsystems was not altered. Heterogeneous alterations within the CEN have been reported in schizophrenia, including both increased and decreased intra-iFC within the CEN during rest (Woodward et al., 2011). Following the above-mentioned argument for the DMN, inconsistent findings of aberrant intra-iFC within the CEN in schizophrenia might be due to both heterogeneous patient samples and distinct methodological approaches (Whitfield-Gabrieli and Ford, 2012). Previously, we found both increased and reduced intra-iFC within the CEN in psychotic patients (Manoliu et al., 2013). Due to the identical methodological approaches applied in the previous and current study, the present data suggest that the aberrant intrinsic FC within the CEN may depend on the state of disease.

Inter-iFC between DMN and CEN in psychotic remission

Compared to HCs, patients showed decreased inter-iFC between ipDMN and rvCEN, suggesting an aberrant inter-network connectivity between DMN and CEN. It has been suggested that schizophrenia is characterized by a disrupted relationship between the task-negative DMN and task-positive CEN (Williamson, 2007), which might underlie both positive and negative symptoms (Menon, 2011; Palaniyappan and Liddle, 2012). In particular, aberrant recruitment of anti-correlated networks has been demonstrated in schizophrenia (Hasenkamp et al., 2011). Furthermore, we demonstrated aberrant connectivity within DMN and CEN in patients with schizophrenia during acute psychosis (Manoliu et al., 2013). Our current result extends this finding by demonstrating that impaired between-network interactions in schizophrenia are also present during psychotic remission.

LIMITATIONS

We acknowledge several limitations, which have to be considered in the present study. Firstly, antipsychotic drugs have been shown to have an impact on FC in patients with schizophrenia (Sambataro et al., 2010). However, only 4 out of 12 patients were free of antipsychotic medication, while all other patients received mono- or dual therapy with atypical antipsychotic medication. To account for this potential confounder, the total current CPZ equivalent dose was calculated and entered as covariate of no interest in all corresponding analyses. Furthermore, CPZ-scores had no significant effect on both intra-iFC and inter-iFC. Nevertheless, CPZ was entered as a linear covariate, thus not ruling out non-linear effects of antipsychotic medication. Moreover, the possible effects of different antipsychotic drugs on BOLD activity are currently not completely understood. In addition to these observations, antipsychotic drugs have in most cases an effect on positive symptoms but not on negative symptoms, potentially being reflected in a higher standard deviation of negative symptoms compared to positive symptoms in our patient sample and thus complicating the investigation of the relation between SN dysfunction and psychotic symptoms. Therefore, the present results should be interpreted with care until replicated in an unmedicated patient sample.

Secondly, limitations of the ICA have to be taken into consideration, including the arbitrary model-order selection and subjective bias in selection of the components of interest (Cole et al., 2010). Bearing this in mind, we adopted a recently proposed analysis pipeline (Allen et al., 2011) to provide a better comparability with current and future studies using the same approach. A detailed discussion of this methodological limitation can be found in Manoliu et al. (2013). Finally, only 12 patients with schizophrenia during state of remission were included in this study. It has been shown that analyses of rather small patient samples can yield very robust and interpretable results (Dovern et al., 2012; Sorg et al., 2013). However, small study samples increase the risk of obtaining false-negative statistical results, possibly explaining our negative finding regarding a relationship between intra-iFC within the right AI and the severity of positive symptoms. Therefore, a replication of our results in a larger patient sample might contribute to our current understanding of insular dysfunction in schizophrenia.

CONCLUSION

Results provide evidence that left anterior insular dysfunction within the SN is selectively associated with both aberrant between-network interactions and severity of negative symptoms in patients with schizophrenia during psychotic remission. Together with correspondent findings concerning the right anterior insula in patients during psychosis, these findings suggest that the relationship between insular dysfunction and altered between-network interactions is a characteristic feature of schizophrenia, with possibly distinct insular pathways for distinct symptom dimensions.

ACKNOWLEDGMENTS

This work was supported by the German Federal Ministry of Education and Research (BMBF 01EV0710 to Afra M. Wohlschläger, BMBF 01ER0803 to Christian Sorg) and the Kommission für Klinische Forschung, Technischen Universität München (KKF 8765162 to Christian Sorg). We are grateful to the participants of the study and the staff of the Department of Psychiatry and Neuroradiology for their help in recruitment and data collection. The authors have declared that there are no conflicts of interest in relation to the subject of this study.

REFERENCES

Abou-Elseoud, A., Starck, T., Remes, J., Nikkinen, J., Tervonen, O., and Kiviniemi, V. (2010). The effect of model order selection in group Pica. *Hum. Brain Mapp.* 31, 1207–1216.

Allen, E. A., Erhardt, E. B., Damaraju, E., Gruner, W., Segall, J. M., Silva, R. F., et al. (2011). A baseline for the multivariate comparison of resting-state networks. *Front. Syst. Neurosci.* 5:2. doi:10.3389/fnsys.2011.00002

Ashburner, J., and Friston, K. J. (2005). Unified segmentation. *Neuroimage* 26, 839–851.

American Psychiatric Association. (2000). *American Psychiatric Association: Diagnostic and Statistical Manual of Mental Disorders – Dsm Iv – Tr.* Washington: American Psychiatric Association.

Buckner, R. L., Andrews-Hanna, J. R., and Schacter, D. L. (2008). The brain's default network: anatomy, function, and relevance to disease. *Ann. N. Y. Acad. Sci.* 1124, 1–38.

Calhoun, V. D., Adali, T., Pearlson, G. D., and Pekar, J. J. (2001). A method for making group inferences from functional Mri data using independent component analysis. *Hum. Brain Mapp.* 14, 140–151.

Camchong, J., MacDonald, A. W. 3rd, Bell, C., Mueller, B. A., and Lim, K. O. (2011). Altered functional and anatomical connectivity in schizophrenia. *Schizophr. Bull.* 37, 640–650.

Cole, D. M., Smith, S. M., and Beckmann, C. F. (2010). Advances and pitfalls in the analysis and interpretation of resting-state fMRI data. *Front. Syst. Neurosci.* 4:8. doi:10.3389/fnsys.2010.00008

Craig, A. D. (2002). How do you feel? Interoception: the sense of the physiological condition of the body. *Nat. Rev. Neurosci.* 3, 655–666.

Craig, A. D. (2009). How do you feel – now? The anterior insula and human awareness. *Nat. Rev. Neurosci.* 10, 59–70.

Damoiseaux, J. S., Rombouts, S. A., Barkhof, F., Scheltens, P., Stam, C. J., Smith, S. M., et al. (2006). Consistent resting-state networks across healthy subjects. *Proc. Natl. Acad. Sci. U.S.A.* 103, 13848–13853.

Dovern, A., Fink, G. R., Fromme, A. C., Wohlschlager, A. M., Weiss, P. H., and Riedl, V. (2012). Intrinsic network connectivity reflects consistency of synesthetic experiences. *J. Neurosci.* 32, 7614–7621.

Eickhoff, S. B., Stephan, K. E., Mohlberg, H., Grefkes, C., Fink, G. R., Amunts, K., et al. (2005). A new Spm toolbox for combining probabilistic cytoarchitectonic maps and functional imaging data. *Neuroimage* 25, 1325–1335.

Ellison-Wright, I., and Bullmore, E. (2009). Meta-analysis of diffusion tensor imaging studies in schizophrenia. *Schizophr. Res.* 108, 3–10.

Ellison-Wright, I., Glahn, D. C., Laird, A. R., Thelen, S. M., and Bullmore, E. (2008). The anatomy of first-episode and chronic schizophrenia: an anatomical likelihood estimation meta-analysis. *Am. J. Psychiatry* 165, 1015–1023.

Fletcher, P. C., and Frith, C. D. (2009). Perceiving is believing: a bayesian approach to explaining the positive symptoms of schizophrenia. *Nat. Rev. Neurosci.* 10, 48–58.

Fox, M. D., and Raichle, M. E. (2007). Spontaneous fluctuations in brain activity observed with functional magnetic resonance imaging. *Nat. Rev. Neurosci.* 8, 700–711.

Garrity, A. G., Pearlson, G. D., McKiernan, K., Lloyd, D., Kiehl, K. A., and Calhoun, V. D. (2007). Aberrant "default mode" functional connectivity in schizophrenia. *Am. J. Psychiatry* 164, 450–457.

Gradin, V. B., Waiter, G., O'Connor, A., Romaniuk, L., Stickle, C., Matthews, K., et al. (2013). Salience network-midbrain dysconnectivity and blunted reward signals in schizophrenia. *Psychiatry Res.* 211, 104–111.

Hasenkamp, W., James, G. A., Boshoven, W., and Duncan, E. (2011). Altered engagement of attention and default networks during target detection in schizophrenia. *Schizophr. Res.* 125, 169–173.

Horn, D. I., Yu, C., Steiner, J., Buchmann, J., Kaufmann, J., Osoba, A., et al. (2010). Glutamatergic and resting-state functional connectivity correlates of severity in major depression – the role of pregenual anterior cingulate cortex and anterior insula. *Front. Syst. Neurosci.* 4:33. doi:10.3389/fnsys.2010.00033

Howes, O. D., Kambeitz, J., Kim, E., Stahl, D., Slifstein, M., Abi-Dargham, A., et al. (2012). The nature of dopamine dysfunction in schizophrenia and what this means for treatment. *Arch. Gen. Psychiatry* 69, 776–786.

Howes, O. D., Montgomery, A. J., Asselin, M. C., Murray, R. M., Valli, I., Tabraham, P., et al. (2009). Elevated striatal dopamine function linked to prodromal signs of schizophrenia. *Arch. Gen. Psychiatry* 66, 13–20.

Jafri, M. J., Pearlson, G. D., Stevens, M., and Calhoun, V. D. (2008). A method for functional network connectivity among spatially independent resting-state components in schizophrenia. *Neuroimage* 39, 1666–1681.

Kapur, S. (2003). Psychosis as a state of aberrant salience: a framework linking biology, phenomenology, and pharmacology in schizophrenia. *Am. J. Psychiatry* 160, 13–23.

Kay, S. R., Fiszbein, A., and Opler, L. A. (1987). The positive and negative syndrome scale (Panss) for schizophrenia. *Schizophr. Bull.* 13, 261–276.

Kiviniemi, V., Starck, T., Remes, J., Long, X., Nikkinen, J., Haapea, M., et al. (2009). Functional segmentation of the brain cortex using high model order group Pica. *Hum. Brain Mapp.* 30, 3865–3886.

Koutsouleris, N., Gaser, C., Jager, M., Bottlender, R., Frodl, T., Holzinger, S., et al. (2008). Structural correlates of psychopathological symptom dimensions in schizophrenia: a voxel-based morphometric study. *Neuroimage* 39, 1600–1612.

Lu, J., Liu, H., Zhang, M., Wang, D., Cao, Y., Ma, Q., et al. (2011). Focal pontine lesions provide evidence that intrinsic functional connectivity reflects polysynaptic anatomical pathways. *J. Neurosci.* 31, 15065–15071.

Manoliu, A., Riedl, V., Zherdin, A., Muhlau, M., Schwerthoffer, D., Scherr, M., et al. (2013). Aberrant dependence of default mode/central executive network interactions on anterior insular salience network activity in schizophrenia. *Schizophr. Bull.* doi:10.1093/schbul/sbt037. [Epub ahead of print].

Menon, V. (2011). Large-scale brain networks and psychopathology: a unifying triple network model. *Trends Cogn. Sci. (Regul. Ed.)* 15, 483–506.

Menon, V., and Uddin, L. Q. (2010). Saliency, switching, attention and control: a network model of insula function. *Brain Struct. Funct.* 214, 655–667.

Minzenberg, M. J., Laird, A. R., Thelen, S., Carter, C. S., and Glahn, D. C. (2009). Meta-analysis of 41 functional neuroimaging studies of executive function in schizophrenia. *Arch. Gen. Psychiatry* 66, 811–822.

Murray, G. K., Corlett, P. R., Clark, L., Pessiglione, M., Blackwell, A. D., Honey, G., et al. (2008). Substantia nigra/ventral tegmental reward prediction error disruption in psychosis. *Mol. Psychiatry* 13, 267–276.

Palaniyappan, L., Balain, V., Radua, J., and Liddle, P. F. (2012). Structural correlates of auditory hallucinations in schizophrenia: a meta-analysis. *Schizophr. Res.* 137, 169–173.

Palaniyappan, L., and Liddle, P. F. (2012). Does the salience network play a cardinal role in psychosis? an emerging hypothesis of insular dysfunction. *J. Psychiatry Neurosci.* 37, 17–27.

Palaniyappan, L., Mallikarjun, P., Joseph, V., White, T. P., and Liddle, P. F. (2011). Regional contraction of brain surface area involves three large-scale networks in schizophrenia. *Schizophr. Res.* 129, 163–168.

Rotarska-Jagiela, A., van de Ven, V., Oertel-Knochel, V., Uhlhaas, P. J., Vogeley, K., and Linden, D. E. (2010). Resting-state functional network correlates of psychotic symptoms in schizophrenia. *Schizophr. Res.* 117, 21–30.

Sambataro, F., Blasi, G., Fazio, L., Caforio, G., Taurisano, P., Romano, R., et al. (2010). Treatment with olanzapine is associated with modulation of the default mode network in patients with schizophrenia. *Neuropsychopharmacology* 35, 904–912.

Seeley, W. W., Menon, V., Schatzberg, A. F., Keller, J., Glover, G. H., Kenna, H., et al. (2007). Dissociable intrinsic connectivity networks for salience processing and executive control. *J. Neurosci.* 27, 2349–2356.

Singer, T., Critchley, H. D., and Preuschoff, K. (2009). A common role of insula in feelings, empathy and uncertainty. *Trends Cogn. Sci. (Regul. Ed.)* 13, 334–340.

Skudlarski, P., Jagannathan, K., Anderson, K., Stevens, M. C., Calhoun, V. D., Skudlarska, B. A., et al. (2010). Brain connectivity is not only lower but different in schizophrenia: a combined anatomical and functional approach. *Biol. Psychiatry* 68, 61–69.

Smith, S. M., Fox, P. T., Miller, K. L., Glahn, D. C., Fox, P. M., Mackay, C. E., et al. (2009). Correspondence of the brain's functional architecture during activation and rest. *Proc. Natl. Acad. Sci. U.S.A.* 106, 13040–13045.

Smith, S. M., Miller, K. L., Moeller, S., Xu, J., Auerbach, E. J., Woolrich, M. W., et al. (2012). Temporally-independent functional modes of spontaneous brain activity. *Proc. Natl. Acad. Sci. U.S.A.* 109, 3131–3136.

Sorg, C., Manoliu, A., Neufang, S., Myers, N., Peters, H., Schwerthoffer,

D., et al. (2013). Increased intrinsic brain activity in the striatum reflects symptom dimensions in schizophrenia. *Schizophr. Bull.* 39, 387–395.

Spitzer, R. L., Williams, J. B., Gibbon, M., and First, M. B. (1992). The structured clinical interview for Dsm-Iii-R (Scid). I: history, rationale, and description. *Arch. Gen. Psychiatry* 49, 624–629.

Sridharan, D., Levitin, D. J., and Menon, V. (2008). A critical role for the right fronto-insular cortex in switching between central-executive and default-mode networks. *Proc. Natl. Acad. Sci. U.S.A.* 105, 12569–12574.

Uddin, L. Q., Supekar, K. S., Ryali, S., and Menon, V. (2011). Dynamic reconfiguration of structural and functional connectivity across core neurocognitive brain networks with development. *J. Neurosci.* 31, 18578–18589.

White, T. P., Joseph, V., Francis, S. T., and Liddle, P. F. (2010). Aberrant salience network (bilateral insula and anterior cingulate cortex) connectivity during information processing in schizophrenia. *Schizophr. Res.* 123, 105–115.

Whitfield-Gabrieli, S., and Ford, J. M. (2012). Default mode network activity and connectivity in psychopathology. *Annu. Rev. Clin. Psychol.* 8, 49–76.

Whitfield-Gabrieli, S., Thermenos, H. W., Milanovic, S., Tsuang, M. T., Faraone, S. V., McCarley, R. W., et al. (2009). Hyperactivity and hyperconnectivity of the default network in schizophrenia and in first-degree relatives of persons with schizophrenia. *Proc. Natl. Acad. Sci. U.S.A.* 106, 1279–1284.

Williamson, P. (2007). Are anticorrelated networks in the brain relevant to schizophrenia? *Schizophr. Bull.* 33, 994–1003.

Williamson, P. C., and Allman, J. M. (2012). A framework for interpreting functional networks in schizophrenia. *Front. Hum. Neurosci.* 6:184. doi:10.3389/fnhum.2012.00184

Woods, S. W. (2003). Chlorpromazine equivalent doses for the newer atypical antipsychotics. *J. Clin. Psychiatry* 64, 663–667.

Woodward, N. D., Rogers, B., and Heckers, S. (2011). Functional resting-state networks are differentially affected in schizophrenia. *Schizophr. Res.* 130, 86–93.

Conflict of Interest Statement: The authors declare that the research was conducted in the absence of any commercial or financial relationships that could be construed as a potential conflict of interest.

Received: 28 February 2013; accepted: 06 May 2013; published online: 20 May 2013.

Citation: Manoliu A, Riedl V, Doll A, Bäuml JG, Mühlau M, Schwerthöffer D, Scherr M, Zimmer C, Förstl H, Bäuml J, Wohlschläger AM, Koch K and Sorg C (2013) Insular dysfunction reflects altered between-network connectivity and severity of negative symptoms in schizophrenia during psychotic remission. Front. Hum. Neurosci. 7:216. doi: 10.3389/fnhum.2013.00216

frontiers in
HUMAN NEUROSCIENCE

ORIGINAL RESEARCH ARTICLE
published: 31 July 2013
doi: 10.3389/fnhum.2013.00392

Single trial decoding of belief decision making from EEG and fMRI data using independent components features

Pamela K. Douglas[1]*, Edward Lau[1], Ariana Anderson[1,2], Austin Head[1], Wesley Kerr[1], Margalit Wollner[1], Daniel Moyer[1], Wei Li[3], Mike Durnhofer[1], Jennifer Bramen[1] and Mark S. Cohen[1,4]

[1] *LINT Laboratory, University of California, Los Angeles, Los Angeles, CA, USA*
[2] *Department of Neurology, University of California, Los Angeles, Los Angeles, CA, USA*
[3] *Interdepartmental Program in Neuroscience, University of California, Los Angeles, Los Angeles, CA, USA*
[4] *California Nanosystems Institute, University of California, Los Angeles, Los Angeles, CA, USA*

Edited by:
Srikantan S. Nagarajan, University of California, San Francisco, USA

Reviewed by:
Martin P. Paulus, University of California, San Diego, USA
Tamer Demiralp, Istanbul University, Turkey

***Correspondence:**
Pamela K. Douglas, Semel Institute for Neuroscience and Human Behavior, University of California, Los Angeles, 760 Westwood Plaza, B8-169, Los Angeles, CA 90095, USA
e-mail: pdouglas@mednet.ucla.edu

The complex task of assessing the veracity of a statement is thought to activate uniquely distributed brain regions based on whether a subject believes or disbelieves a given assertion. In the current work, we present parallel machine learning methods for predicting a subject's decision response to a given propositional statement based on independent component (IC) features derived from EEG and fMRI data. Our results demonstrate that IC features outperformed features derived from event related spectral perturbations derived from any single spectral band, yet were similar to accuracy across all spectral bands combined. We compared our diagnostic IC spatial maps with our conventional general linear model (GLM) results, and found that informative ICs had significant spatial overlap with our GLM results, yet also revealed unique regions like amygdala that were not statistically significant in GLM analyses. Overall, these results suggest that ICs may yield a parsimonious feature set that can be used along with a decision tree structure for interpretation of features used in classifying complex cognitive processes such as belief and disbelief across both fMRI and EEG neuroimaging modalities.

Keywords: machine learning, decoding, EEG, fMRI, ICA, decision making, decision tree, interpretation

INTRODUCTION

The complex process of decision-making appears to engage distinct cortical regions whose spatio-temporal evolution occurs over multiple stages of directed processing. While this processing likely varies according to the specific task and its difficulty, its framework is thought proceed by internal representation of variables, valuation of these internal states, and eventual action selection (Rangel et al., 2008). EEG and fMRI have each been used according to their individual strengths in temporal and spatial precision to measure both serial and parallel aspects of neural computation involved in decision-making in humans (Heekeren et al., 2008).

Neuroimaging studies using fMRI have demonstrated that decision tasks involving perceptual stimuli discrimination consistently activate fronto-parietal networks (White et al., 2012) including the dorsolateral prefrontal cortex (dlPFC). Similar functional activation patterns also emerge in humans during the process of consciously assessing the truth content of a statement, as revealed by fMRI (Harris et al., 2008). Nonetheless, the specific brain loci and patterns of activation appear to vary uniquely according to both the eventual decision outcome, and the categorical decision being made (Heekeren et al., 2003).

Machine learning (ML) methods are now commonly applied to neuroimaging data and have been used predicatively to decode decision responses based on blood oxygenation level dependent (BOLD) signals in selected brain regions (Calvert and Brammer, 2012). However, the volume of data in fMRI is vast—far beyond what can be interpreted readily from a simple localization perspective, and a more parsimonious representation of the data can ease the interpretation process. When applied in a "transparent" fashion, ML methods can also be leveraged for their explanatory power to gain insight into the underpinnings of neural circuitry (O'Toole et al., 2007; Ecker et al., 2010; Hanke et al., 2010).

On the one hand, whole brain voxel data has been used effectively for fMRI decoding (e.g., LaConte et al., 2007), particularly when a classifier such as a support vector machine (SVM) is well tuned on these data (Chu et al., 2012). However, with too many inputs, a classifier may begin to fit the noise, and this overfitting may lead to poor generalization capability (Yamashita et al., 2008). Physiologically-driven approaches such as selecting functional regions of interest (ROIs) diminish input size substantially (Cox and Savoy, 2003; Chu et al., 2012), but require *a priori* knowledge of brain morphology associated with a given task (Mourão-Miranda et al., 2006). While tools like multivoxel pattern analysis (Norman et al., 2006) provide methods for determining voxel subsets with high signal-to-noise ratio, these subsets may differ across individual scans, and spatially adjacent voxels may provide redundant information.

The challenge or extracting class specific signal features from EEG data is similarly challenging. EEG are inherently noisy and non-stationary, varying significantly from trial-to-trial (Müller

et al., 2008). Nonetheless, decoding brain states at the single trial level has been made possible by developing analysis tools that explain the high dimensional data with a well-defined underlying structure. While event related potential features derived from the EEG signal itself (e.g., P300) have been used to drive ML based brain computer interfaces (Krusienski et al., 2008), it is often useful to apply a dimension reduction technique first. Common spatial patterns (e.g., Dornhege et al., 2006) that seek to find filters that maximize variance in one condition, principle component analysis (Subasi and Ismail Gursoy, 2010) and analytic signal reconstruction of event related spectral perturbations (D'Zmura et al., 2009) have all been useful for feature extraction in decoding EEG signals. Ideally, the dimension reduction step is both interpretable and capable of being used in the absence of a class specific signature hypothesis (Lal et al., 2004), particularly if the goal is identification of novel EEG components related to a cognitive process.

Using a method such as independent component analysis (ICA) allows basis images to cover the entire brain, and is an *unsupervised* blind source separation technique (Bell and Sejnowski, 1995; Calhoun and Adali, 2006) that does not require a priori physiologic knowledge about a certain brain process. ICA has found numerous applications in fMRI and EEG (Lan et al., 2005) to include: data exploration (Beckmann et al., 2006), noise component elimination (Tohka et al., 2008), and as a basis for decoding analysis (De Martino et al., 2007; Anderson et al., 2009; Douglas et al., 2011). A key advantage is that ICs are nominated by the data themselves. Furthermore, IC spatio-temporal signatures across individuals appear both stable and consistent within functional neural subsystems (Damoiseaux et al., 2006; Smith et al., 2012).

In the present paper, we describe an ICA based ML approach to classify fMRI and EEG data of persons engaged in a bivariate task, asserting their belief or disbelief of a variety of propositional statements. We extend previous work (Douglas et al., 2011) by developing a quantitative metric for comparing IC features with traditional general linear model (GLM) analysis results for interpretation purposes. We then create a parallel ML approach for single trial classification of belief versus disbelief using high-density electrode EEG data, and compare the classification accuracy achieved using ICs derived from each functional modality.

METHODS

OVERVIEW

Our method involved application of parallel IC processing to both EEG and fMRI data for the purpose of classification of belief decision making. In brief, we collected EEG and fMRI from subjects who were prompted to decide whether they believed or disbelieved a particular statement presented to them on a screen. Decision responses were recorded and used for training and testing a ML classifier. ICA was run on training sets for both fMRI and EEG data. ICs were sampled at time points that were determined to be informative for discrimination. We then projected our ICs forward onto test data and applied our ML classifier to test data. We then calculated accuracy by comparing the subject's keypad response to our ML predicted response. A schematic illustrating the parallel ICA ML processing pipelines for fMRI and EEG is shown in **Figure 1**.

SUBJECTS

A total of 37 healthy participants volunteered for this experiment. Written informed consent was obtained from each participant prior to the experiment, which was approved by the UCLA Institutional Review Board. Fourteen subjects participated in the fMRI portion of the study, while 23 participants participated in the EEG portion of the experiment. All subjects were healthy volunteers aged 18–45 years old, with 15 of the participants being female.

EXPERIMENTAL DESIGN

During the experiment, subjects were asked to evaluate truth content from a given statement, and indicate their assessment with a keypad response. Statements were chosen at random from the following categories: mathematical, geographical, semantic factual, autobiographical, religious, and ethical. For the fMRI task, statements were presented via MR-compatible goggles. For additional details about the fMRI stimulus paradigm, and categorical statements see (Harris et al., 2008). For the purposes of our ML analysis here, we collapse all belief and disbelief events across statement category.

The stimuli task paradigm was implemented in MATLAB (Mathworks, Inc.) using the Psychophysics Toolbox, Version 3.0 (Brainard, 1997). Each subject trial began with a brief instructional statement following by a crosshair fixation. Statements were presented in random order as black text against a gray background. For the subjects who participated in the EEG portion of the experiment, a subset of subjects ($n = 10$) viewed each statement using a rapid serial visual presentation (RSVP) protocol with inter-word and inter-stimulus intervals of 500 ms. However, in the present work, we focus on EEG data from subjects that viewed the statements using the same protocol as for the fMRI portion of the experiment. In this design, the entire statement was presented on the screen at once. Each statement was centered on the screen with new lines beginning after each set of four words to minimize saccade artifact. Progression to the following statement was self-paced, and a central crosshair was presented on the screen during the interval between successive statements. Presentation of each new stimulus occurred 500 ms after subject key press response.

The correspondence of the keyboard keys to belief or disbelief was also randomized and the statements themselves were excluded from the MATLAB report to protect subject privacy and as a double-blind measure. The statements were also counterbalanced across each category with the goal of approximately half of the statements yielding a "belief" response. For example, the total number of mathematical statements that were true such as, "$2 + 2 = 4$," was equal to the number of mathematical statements that were false. The aim of this is to derive activation related to belief and disbelief in a content-independent manner, with approximately equal numbers of data exemplars in each response category. Each session consisted of ∼180 trials, which were subsequently used for training and testing of machine learning classifiers.

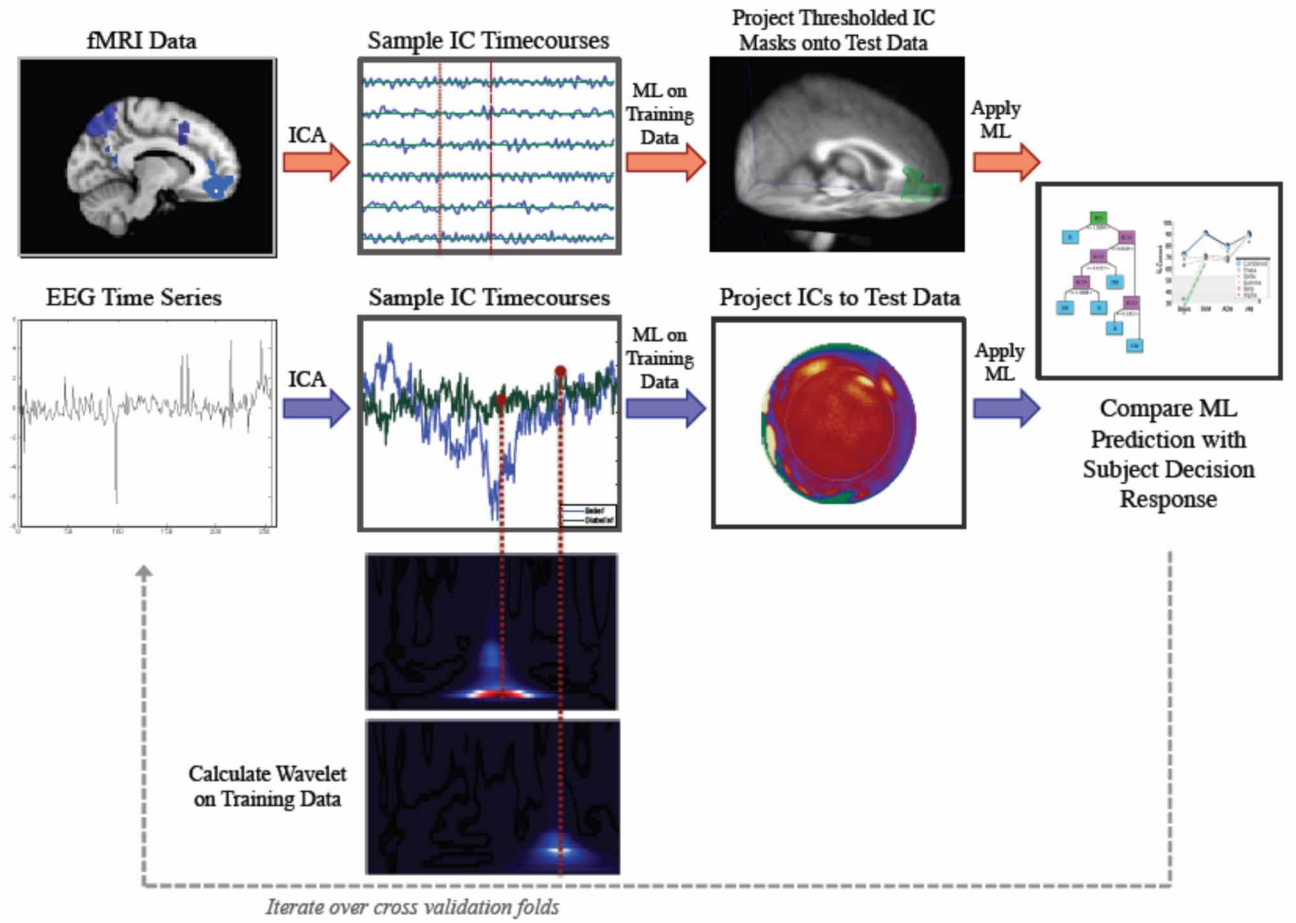

FIGURE 1 | Parallel Method for Independent Component Analysis (ICA) based discrimination of belief and disbelief using machine learning techniques. Following ICA decomposition on data exemplars randomly parsed into the training set, FMRI ICs (top, red arrows) are thresholded and binarized. These spatial masks are then multiplied by testing data. Mean activation values are then extracted for each IC, and sampled timecourses are used as features for decoding. EEG IC activations (bottom, blue arrows) are projected onto testing data, and IC activation timecourses are sampled at time points determined by wavelet data, and used as inputs for classification.

DATA ACQUISITION AND PREPROCESSING

fMRI

All structural and functional MRI scans were acquired using a Siemens Allegra 3T scanner (Siemens, Milwaukee, WI). High-resolution structural images were acquired using a magnetization-prepared rapid gradient-echo sequence. Additional scanning parameter details can be found in Harris et al. (2008). Standard preprocessing of data including brain extraction, slice timing correction, motion correction, spatial smoothing using a 5 mm kernel, high-pass filtering, and registration were carried using tools available in FSL (FMRIB Image Analysis Group, http://www.fmrib.ox.ac.uk/fsl) (Woolrich et al., 2001; Jenkinson et al., 2002)

EEG

EEG data were recorded using a high density 256-channel GES 300 Geodesic Sensor Net (Electrical Geodesics Inc.) with a sampling rate of 250 Hz in a copper shielded room that was dimly lit. Initial data preprocessing steps were carried out using NetStation 4.4.2 software. These steps included: bandpass filtering from 0.1 to 100 Hz, and a 60 Hz notch filter with a passband gain of –0.1 dB (99%) and stopband gain –40dB (1.0%). We then segmented data 500 ms before and 2500 ms after the stimulus presentation for each event.

Artifact detection for removal of eye movement was accomplished using a moving average of 80 samples with a window size 160 samples to correct for eye movement. Channels that contained >20% error and segments with >10 bad channels were excluded from analysis. Ocular artifact removal was then performed to exclude eye blinks from the analysis, using a blink threshold of 10 μV/ms for eyeblink detection. Identification and subsequent removal of these artifacts from all channels was accomplished using methods described here (Gratton et al., 1983; Miller et al., 1988). Segments were then averaged across each stimuli condition, and baseline corrected using a 100 ms baseline prior to the stimulus onset for correction.

For our analysis of ERSPs, we bandpass filtered the EEG data into each of the following respective subands: delta (0.1–4 Hz),

theta (4–8 Hz), alpha (8–12 Hz), beta (12–20 Hz), and gamma (20–45 Hz). Following preprocessing, the power envelope of each characteristic frequency band was calculated using software developed for this purpose in Matlab (Mathworks, Inc.), and sampled at time points as described below.

INDEPENDENT COMPONENT ANALYSIS AND FEATURE EXTRACTION

fMRI

We performed a global ICA computation on each subject's data set. ICA is a powerful tool for finding hidden factors that underlie multivariate data. Known input data, D, is decomposed into a linear combination of statistically independent latent variables, or components, in an unknown mixing system, M. Classic ICA proceeds by the following decomposition:

$$\mathrm{D} = \mathrm{MA}. \tag{1}$$

The matrix A is optimized to obtain statistically independent spatial maps that correspond to various regions of the brain with corresponding temporal aspects. Probabilistic ICA was performed here, using the methodology described above, which forms the basis for the computational program FSL MELODIC, (Beckmann and Smith, 2004).

IC timecourses calculated on training data were sampled at time points corresponding to the maximum predicted BOLD response value. Due to the rapid, self-paced experimental paradigm, multiple belief and disbelief events sometimes occurred within a single repetition time (TR). To avoid overlap in these cases, we included only those data instances whose class label was identical for two or more consecutive trials, effectively reducing the number of exemplars by approximately one third.

In order to extract corresponding IC timecourses from data parsed into the test set for ML purposes, IC spatial masks were binarized and multiplied by the fMRI test data over time. In our previous work, we found that approximately six ICs were effective for classification and describing the data (Anderson et al., 2011). We therefore extracted mean values from each of these IC spatial masks multiplied by the test data, and sampled at time points corresponding to the maximal BOLD activity for each keypad response for subsequent predictive labeling.

EEG

Following preprocessing, ICA decomposition was performed on each set of training data for all subjects using the Infomax algorithm (Bell and Sejnowski, 1995) as implemented in the logistic infomax algorithm "binICA" call within EEGLab (Delorme and Makeig, 2004). ICA decomposition of EEG channel data is decomposed into a mixing matrix of weights and IC activations, analogous to equation 1. Segmented data epochs were randomly parsed into ten approximately equal bins. As explained further in the machine learning section, nine of the ten bins were used for training on each cross validation fold. In order to project ICs derived from the training data onto the test data, we calculate the inverse of the mixing matrix and multiply it by the new data as follows:

$$\mathrm{A}_{\mathrm{Test}} = \mathrm{D}_{\mathrm{Training}}\mathrm{M}^{-1}_{\mathrm{Training}} \tag{2}$$

In each case, our mixing matrix was square and invertible, where the number of ICs was equal to the number of channels. IC data was demeaned for each channel prior to ML analysis. We compared classification of ICs to accuracy using data from each spectral band. In order to accomplish this, we similarly demeaned and squared each spectral time course, and sampled each spectral band along with ICs at time points described below.

Wavelet Informed EEG IC Sampling. In order to determine time points for feature extraction, we utilized time-frequency information contained in the wavelet spectrogram, whose transform is described by equation 3 (Sanei, 2007):

$$W(s,t) = \int x(t)\frac{1}{s}y^*\left(\frac{t-t}{s}\right)dt \tag{3}$$

where, ψ is the equation of the mother wavelet, σ is the scaling factor used to dilate and contract the mother wavelet and achieve different pseudofrequencies, τ is the position parameter, and x(t) is the signal being analyzed. Wavelet decomposition was performed on all electrode channels, using the wavelet toolbox within NetStation (v 4.4.2). We used a Morlet wavelet which has a Gaussian shape in both time and frequency domains, with a width of 6 (Tallon-Baudry et al., 1996) and a frequency step of 1 Hz. Power spectrograms in the training data were then averaged across conditions, as has been done by many (e.g., Tallon-Baudry et al., 1997). We baseline corrected and calculated the power by squaring the magnitude of the complex wavelet coefficient and dividing the mean power across the entire segment for each frequency step.

A between-condition difference was then calculated for each channel by averaging the power for each condition at all time points and subtracting the mean power from the opposite condition. The time point that maximized the sum of the power across frequency bands in these differences across all channels was selected for feature extraction as follows:

$$\begin{aligned} &\mathrm{argmax}\left[f_B, \{t, n\}\right] \quad f_B = \sum_{jw}\left(E_B^2 - E_{DB}^2\right) \\ &\mathrm{argmax}\left[f_{DB}, \{t, n\}\right] \quad f_{DB} = \sum_{jw}\left(E_{DB}^2 - E_B^2\right) \end{aligned} \tag{4}$$

where, E_B is the power for belief at time point t in channel n averaged across the frequencies contained within the band jω, and $\mathrm{E_{DB}}$ is the corresponding measure for disbelief. Feature extraction time points were averaged across all subjects using a leave one out cross validation approach, so wavelet information from the current subject undergoing classification was not used to inform the time point selection. Feature extraction proceeded by sampling power envelopes of either IC time courses or spectral band signatures for each electrode channel at these key discriminatory time points.

MACHINE LEARNING CLASSIFICATION

Within subject classification of EEG and fMRI data was accomplished using a nested 10-fold cross validation procedure. Events are first parsed randomly into ten bins. Nine bins are then used for training and parameter tuning via an inner cross

validation procedure, and the tenth held out data is used as the test set. We tested four machine learning classifiers over a range of complexity: Bayes Net, Support vector machine (SVM) (Burges, 1998; Vapnik, 2000), Adaboost (Viola and Jones, 2001), and J48 decision tree based on the C4.5 decision tree algorithm (Quinlan, 1993). Classification accuracy for each algorithm was assessed via 10-fold cross validation. Hyperparameters were optimized using a 10-fold nested cross validation procedure and ranked features were sequentially added to the training set using a forward feature subset approach, as described in Douglas et al. (2011). For the J48 decision tree, we set the minimum number of instances per leaf to 40. We used implementations of each ML algorithm available in the open source Weka (Waikato Environment for Knowledge Analysis) software.

Interpretation of classification

In order to visualize the classification structure for interpretation purposes, we used the WEKA Knowledge Flow tool to illustrate the underlying classifier structure for the J48 decision tree. FMRI IC features that were assigned to either the root node or a decision node further along in the partitioning structure were compared to the GLM data quantitatively by thresholding ($z \geq 2.3$) and then binarizing each spatial map.

RESULTS

EEG BELIEF DECISION DATA

We averaged the number of responses in each category across subjects to compare the number of data exemplars in each category. Overall, we found that subjects responded "belief" to 45.6% of questions, thus making "disbelief" a slightly more frequent response. The feature extraction time averaged across the group was 578 ± 19 ms earlier than the average time for disbelief. Wavelet spectrograms from an illustrative individual are shown in **Figure 2** for channels that mutually maximized belief and disbelief contrasts, along with selected channels location with respect to the electrode channel configuration.

CLASSIFICATION ACCURACY INTERPRETING CLASSIFIER STRUCTURE

Comparing IC spatial maps with GLM results

Mean 10-fold cross validation accuracy for IC based classification of FMRI was 80.8, 91, 84, and 80% for support vector machine, naïve Bayes, J48 decision tree and k-star classifiers. We generated decision trees for each cross validation fold using reduced error pruning. Based on our nested cross validation, we selected a minimum number of 10 data instances per leaf. The structure of an IC based decision tree classifier using fMRI data from a representative subject's data is shown in **Figure 3**, with final labels of belief (B) and (DB) indicating the final predicted response.

The root IC and subsequent nodal ICs used in partitioning the data are shown in the inset. IC voxels that also survived threshold in GLM contrasts for belief-disbelief, and disbelief-belief are shown in left and right columns respectively. The root node, IC 5, and ICs 15 and 19 colocalized with belief GLM areas in left middle frontal gyrus and precuneus. ICs 13, 19 and GLM disbelief-belief contrast revealed significant voxels in lateral occipital cortex, whereas paracingulate gyrus was unique to IC 13. Areas that were unique to IC maps included right medial frontal gyrus, right precentral gyrus, right amygdala, and bilateral cingulate cortex.

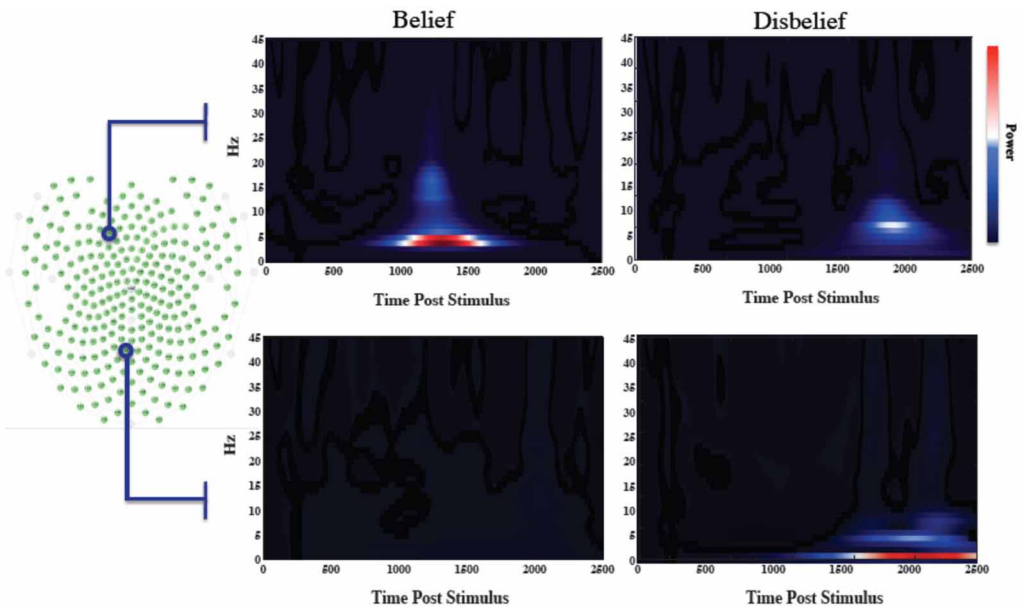

FIGURE 2 | Wavelet informed sampling of EEG data. Stimulus-locked wavelet data are shown for a specific individual for illustrative purposes. (Left) Electrode array configuration. (Right) In the top panel, wavelet power data are shown for each category for a particular frontal channel that was used to determine the belief extraction time point. The lower panel similarly shows data from the channel used to determine the disbelief extraction time. Power increases occurred earlier for belief events than for disbelief events.

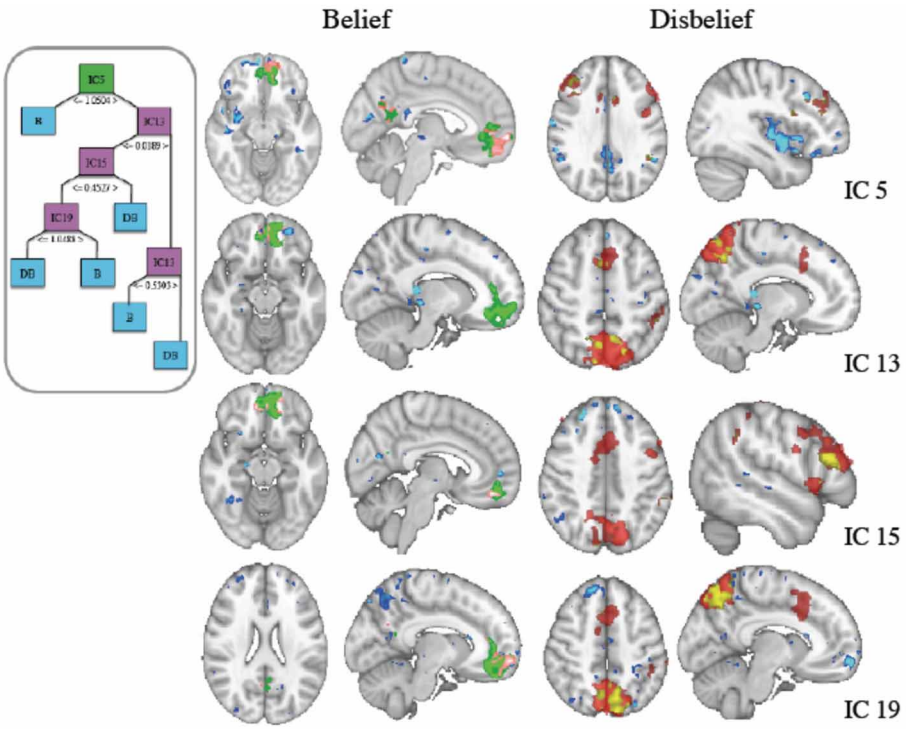

FIGURE 3 | (Inset) J48 Decision tree structure using independent component (IC) features derived from fMRI data. The green box at top is the root node, pink boxes are used for subsequent nodes for splitting of the data, and blue boxes indicate terminal decisions or leaf nodes. These IC spatial maps along with general linear model (GLM) contrasts are shown at right. (Left Column) Belief (Green) thresholded z-stat masks generated from a GLM analysis with the contrast of belief-disbelief are overlaid with IC masks (blue) and the voxels that are common to both (pink). (Right Column) Disbelief (red) shown similarly with blue for IC and coregistered voxels in yellow.

EEG classification accuracy

Similar to our fMRI analysis, we calculated classification accuracy with respect to the four classifiers tested. IC and power envelopes from spectral timecourses were sampled at points determined from wavelets, as described previously. **Figure 4** shows the pruned J48 decision tree hierarchical structure for a specific subject's EEG data. Average classification across all four algorithms was 78.8, 77.1, 73.5, 72.2, and 66.1% for gamma, theta, beta, alpha, and delta, respectively. We also stacked all of the spectral features into a "combined" classifier. Mean accuracy for the combined spectral classifier was 82.3%. Overall, the mean of each of these spectral bans as well as the combined spectral classifier were less than 88.6%, the average accuracy achieved using ICs across the four algorithms. Accuracy obtained from using IC features was 85.9, 87.7, 92.6, 88.7%, for support vector machine, BayesNet, AdaBoost, and the J48 Decision tree. Classification accuracy using power envelopes from spectral bands and ICs as features is summarized in **Figure 4**.

DISCUSSION

In the current study, we described a method for bivariate classification of belief and disbelief brain states using ICA for both dimension reduction and subsequent feature extraction. We previously developed a method for training a ML classifier on mean time courses extracted from thresholded IC spatial maps (Douglas et al., 2011). In this analysis, we tested the performance of six different ML classifiers in their utility for shattering belief and disbelief data. In this previous analysis, our goal was to develop a classifier that was interpretable by trading off model complexity with error. In this analysis we modeled our classifier output using a sum of exponentials and terminated the addition of more features to the model using the Akaike Information Criterion. While the addition of more features would often diminish the error on the training set marginally, we argued that the sparse classifier would be easier to interpret from a neuroscientific point of view. In the current work, we extended this analysis in two ways. First, we interpreted the classifiers that resulted from our initial analysis by visualizing the extent to which our sparse remaining IC features correlated spatially with the voxel set of significant BOLD activations that resulted from a conventional GLM analysis. Second, we collected EEG data on the same belief decision making paradigm, and applied an analogous ML approach to determine how well IC timecourses could be used to classify EEG belief data.

We first presented the structure of example decision trees classifiers based on fMRI ICs. We found that the spatial patterns of certain IC decision tree nodes were quite similar to conventional GLM results. However, certain IC nodes mapped to regions with unknown relevance to belief decision making. Given the sparsity with which these classifiers were operating, it is possible that

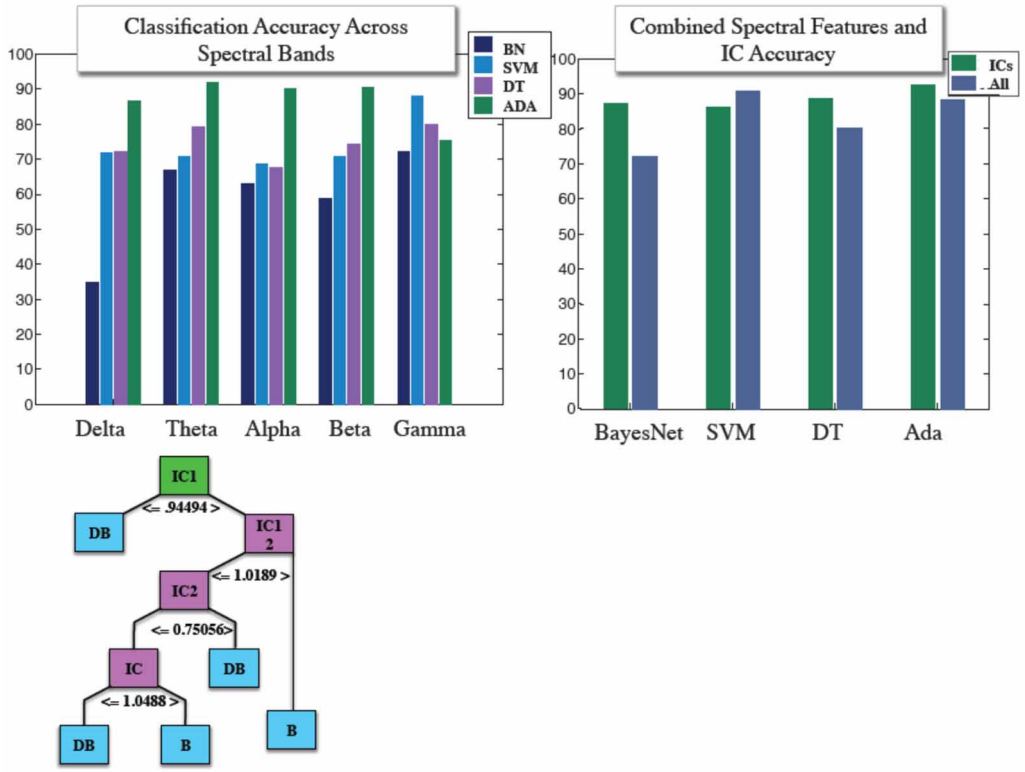

FIGURE 4 | (Top) Mean classification accuracy achieved using features derived from power envelopes for each spectral band for four classifier algorithms shown in left panel, and IC accuracy with compared with accuracy achieved when combining all spectral features into a single classifier for the same four machine learning algorithms. (Bottom) Structure of an individual subject example J48 decision tree used in IC based classification.

these additional areas are involved in some stage of the complex directed processing that occurs in decision making. These regions may only be involved in certain categorical decisions or for certain individuals, and therefore did not survive thresholding in conventional analyses. It is possible that this process may be one mechanism for using IC for exploratory purposes.

We also presented EEG based IC classification results on this same task. The J48 decision tree structure for partitioning data into classes is somewhat similar to decision flow diagrams used for triage in the clinical setting. Decision trees may therefore represent an intuitive structure for interpreting ML features and their output. Overall, we found that ICs proved useful as features for discriminating between the cognitive states of "belief" and "disbelief" at the single trial level in both fMRI and EEG data collected from a high density 256 electrode net. Our IC based classification process can be easily mapped back to the data for interpretive purposes.

INTERPRETING DIAGNOSTIC FEATURES: fMRI BOLD ACTIVATIONS AND ICs

It is often the case in fMRI decoding studies that the ML process is abstract and can involve thousands of features. While a large vector of features often outperforms a reduced feature set, the margin of improved accuracy may only be slight (e.g., Brodersen et al., 2011; Chu et al., 2012). Selecting relevant features while concurrently minimizing extraneous and redundant features is a key challenges in machine learning (ML) applications, as the performance of certain classifiers degrades with abundant or extraneous information (Kohavi and John, 1997). A parsimonious attribute subset may not only improve the generalization capability of a classifier (Yamashita et al., 2008), but also all for scientific gain when the process is readily intelligible.

Depending on the objective, IC features may be advantageous for ML, as they offer a concise functional representation of the data, which can be easily interpreted and does not require a priori information. It is not surprising that our analysis revealed that certain highly discriminatory ICs coregistered to a large extent with the group level contrasts for Belief-Disbelief and Disbelief-Belief. It is perhaps more interesting to consider regions unique to IC maps.

IC activity not related to the GLM spatial maps that remained in the decision tree after pruning may be meaningful. For example, reading phrases that contain negative emotional associations have been shown to activate amygdala (Osaka et al., 2013), and the amygdala also appears to play a key role in autobiographical memory encoding, consolidation, and retrieval (Markowitsch and Staniloiu, 2011). Others have shown that basolateral amygdala is part of a circuit involved in effort based decision making

in rodents (Floresco and Ghods-Sharifi, 2007). Our observation here could therefore relate to emotional or autobiographical memory processing or even the amount of effort required for a particular decision. Activation that did not coregister with GLM regions might also reflect neural activity that non-linearly discriminates between disbelief and belief in a way that t-statistics do not capture. It is also important to note that in our analysis here as well as in (Douglas et al., 2011), we collapsed our analysis across all belief and disbelief categories. Previous work by our group demonstrated that there were no statistically significant differences between these categorical decisions using fMRI GLM analysis (Harris et al., 2008). It is therefore possible that differential regions that we observed, here, reflect categorical differences that did not survive statistical thresholding.

Given the highly complex and distributed nature of the cognitive processing of belief, it is highly likely that the independent multivariate normal assumption of the GLM is violated. However, the nature of this activity is difficult to interpret using simple concepts of up or down regulation of networks. It is also possible that discriminatory information revealed by ICA may not be present in all subjects or all belief/disbelief data exemplars, and therefore a GLM analysis may be underpowered to detect these changes.

FEATURE SELECTION AND SPECTRAL CLASSIFICATION IN EEG

We used power envelopes derived from spectral bands as features in classification of belief decision-making. Overall, these results demonstrated that the gamma frequency band was most the most discriminatory spectral band for belief/disbelief labeling. Compared to these results, IC features outperformed power envelope in other spectral bands, but was overall similar to the performance of the gamma band features across each of the four classification algorithms discussed here.

A number of studies have found that EEG classification accuracy can vary across frequency subands (e.g., D'Zmura et al., 2009). The functional significance of different neural oscillations are thought to be reflect with different cognitive or neuronal states (Engell et al., 2012). However, interactions across frequencies provide the rich potential for computational encoding of higher order representations. Gamma frequencies, for example, are often modulated by lower frequencies (Buzsáki and Wang, 2012). In terms of decision-making, cross frequency entrainment has been shown to be important in rodent navigation and decision-making (Tort et al., 2008). A number of papers have suggested cross-frequency coupling as a potential mechanism for hierarchical integration of network-level activity (Canolty and Knight, 2010) for higher cognitive processing such as sensory binding. Our wavelet informed feature selection method is consistent with the idea that belief and disbelief would require synchronous activity across frequency bands. However future work is needed to fully understand cross frequency interactions and how they are related to decision processing and whether or not ICs reflect aspects of this coupling.

fMRI vs. EEG

Overall, IC features derived from EEG data outperformed fMRI data. It is interesting to note that in many of the EEG channels, there were observable event-locked changes in spectral power for both belief and disbelief that were separated in time. Given that these categorical time-frequency changes were separated by ∼500 ms, it is unlikely that these temporal changes would be reflected in the BOLD signal. Nonetheless, it is possible that signal changes measured at different times at the same loci on the scalp were actually generated by spatially distinct brain regions, resolvable by fMRI. Future work may involve analyzing EEG in the source domain.

DECISION TREES AS HIERARCHICAL INTERPRETABLE CLASSIFIERS

In the present work, we used decision trees for not only classification but also for interpretation of features used in the multistage learning process. Decision trees, which are directed trees with edges and nodes that provide a unique mapping from the root node to a class label. While the overall process is indeed non-linear, decision tree classifiers break down complexity learning problems into the union of a series of simple decisions. Decision trees are perhaps intuitive because provide a quantitative process not all that unlike a decision flow diagrams used commonly in medical triage. When decision tress are used in combination with IC features, decision trees may allow for combining statistical knowledge of activations and deactivations in an interpretable way.

CONCLUSIONS AND FUTURE WORK

Overall, these results suggest that ICs may yield an important basis set for classifying complex cognitive processes such as belief and disbelief across both fMRI and EEG neuroimaging modalities. Future work may focus on studying belief and disbelief decision making using concurrently collected EEG-fMRI data. A joint analysis of simultaneous data using methods like joint ICA (e.g., Franco et al., 2008; Edwards et al., 2012) may yield a more in-depth understanding of the neural comparators involved in belief decision-making.

There are strong motivations for understanding the mechanisms underlying veracity assessment, and subsequent decision making about truth content in particular, since a number of potential applications exist given this understanding. When used in combination with machine learning (ML) pattern classification techniques, such knowledge could be used in biomedical applications to drive brain computer interface based communication devices or improved consumer product testing (Calvert and Brammer, 2012). While the ICA computation may be time consuming, in the present work ICs were calculated on training data, and then applied to testing data. Given that the application of ICs to testing data is computationally rapid, real-time application of this methodology may be possible.

ACKNOWLEDGMENTS

The authors would like to thank Sam Harris for useful discussions on the nature of belief. This work was supported by the following organizations: National Institute on Drug Abuse (NIDA; R33 DA01609), the Klingenstein Foundation, and the Keck Foundation.

REFERENCES

Anderson, A., Bramen, J., Douglas, P. K., Lenartowicz, A., Cho, A., Culbertson, C., et al. (2011). Large sample group independent component analysis of functional magnetic resonance imaging using anatomical atlas-based reduction and bootstrapped clustering. *Int. J. Imaging Syst. Technol.* 21, 223–231. doi: 10.1002/ima.20286

Anderson, A., Dinov, I. D., Sherin, J. E., Quintana, J., Yuille, A. L., and Cohen, M. S. (2009). Classification of spatially unaligned fMRI scans. *Neuroimage* 49, 2509–2519. doi: 10.1016/j.neuroimage.2009.08.036

Beckmann, C. F., Jenkinson, M., Woolrich, M. W., Behrens, T. E. J., Flitney, D. E., Devlin, J. T., et al. (2006). Applying FSL to the FIAC data: model-based and model-free analysis of voice and sentence repetition priming. *Hum. Brain Mapp.* 27, 380–391. doi: 10.1002/hbm.20246

Beckmann, C. F., and Smith, S. M. (2004). Probabilistic independent component analysis for functional magnetic resonance imaging. *IEEE Trans. Med. Imaging* 23, 137–152. doi: 10.1109/TMI.2003.822821

Bell, A. J., and Sejnowski, T. J. (1995). An information-maximization approach to blind separation and blind deconvolution. *Neural Comput.* 7, 1129–1159.

Brainard, D. H. (1997). The psychophysics toolbox. *Spat. Vis.* 10, 433–436.

Brodersen, K. H., Schofield, T. M., Leff, A. P., Ong, C. S., Lomakina, E. I., Buhmann, J. M., et al. (2011). Generative embedding for model-based classification of fMRI data. *PLoS Comput. Biol.* 7:e1002079. doi: 10.1371/journal.pcbi.1002079

Burges, C. (1998). A tutorial on support vector machines for pattern recognition. *Data Min. Knowl. Discov.* 2, 121–167. doi: 10.1023/A:1009715923555

Buzsáki, G., and Wang, X.-J. (2012). Mechanisms of gamma oscillations. *Annu. Rev. Neurosci.* 35, 203–225. doi: 10.1146/annurev-neuro-062111-150444

Calhoun, V. D., and Adali, T. (2006). Unmixing fMRI with independent component analysis. *IEEE Eng. Med. Biol. Mag.* 25, 79–90. doi: 10.1109/MEMB.2006.1607672

Calvert, G. A., and Brammer, M. J. (2012). Predicting consumer behavior: using novel mind-reading approaches. *IEEE Pulse* 3, 38–41. doi: 10.1109/MPUL.2012.2189167

Canolty, R. T., and Knight, R. T. (2010). The functional role of cross-frequency coupling. *Trends cogn. Sci.* 14, 506–515. doi: 10.1016/j.tics.2010.09.001

Chu, C., Hsu, A.-L., Chou, K.-H., Bandettini, P., and Lin, C. (2012). Does feature selection improve classification accuracy? Impact of sample size and feature selection on classification using anatomical magnetic resonance images. *Neuroimage* 60, 59–70. doi: 10.1016/j.neuroimage.2011.11.066

Cox, D. D., and Savoy, R. L. (2003). Functional magnetic resonance imaging (fMRI) "brain reading": detecting and classifying distributed patterns of fMRI activity in human visual cortex. *Neuroimage* 19, 261–270.

Damoiseaux, J. S., Rombouts, S. A. R. B., Barkhof, F., Scheltens, P., Stam, C. J., Smith, S. M., et al. (2006). Consistent resting-state networks across healthy subjects. *Proc. Natl. Acad. Sci. U.S.A.* 103, 13848–13853. doi: 10.1073/pnas.0601417103

Delorme, A., and Makeig, S. (2004). EEGLAB: an open source toolbox for analysis of single-trial EEG dynamics including independent component analysis. *J. Neurosci. Methods* 134, 9–21. doi: 10.1016/j.jneumeth.2003.10.009

De Martino, F., Gentile, F., Esposito, F., Balsi, M., Di Salle, F., Goebel, R., et al. (2007). Classification of fMRI independent components using IC-fingerprints and support vector machine classifiers. *Neuroimage* 34, 177–194. doi: 10.1016/j.neuroimage.2006.08.041

Dornhege, G., Blankertz, B., Krauledat, M., Losch, F., Curio, G., and Müller, K.-R. (2006). Combined optimization of spatial and temporal filters for improving brain-computer interfacing. *IEEE Trans. Bio. Med. Eng.* 53, 2274–2281. doi: 10.1109/TBME.2006.883649

Douglas, P. K., Harris, S., Yuille, A., and Cohen, M. S. (2011). Performance comparison of machine learning algorithms and number of independent components used in fMRI decoding of belief vs. disbelief. *Neuroimage* 56, 544–553. doi: 10.1016/j.neuroimage.2010.11.002

D'Zmura, M., Deng, S., Lappas, T., Thorpe, S., and Srinivasan, R. (2009). Toward EEG sensing of imagined speech. *Hum. Comput. Interact.* 5610, *Part I* 40–49. doi: 10.1007/978-3-642-02574-7_5

Ecker, C., Marquand, A., Mourão-Miranda, J., Johnston, P., Daly, E. M., Brammer, M. J., et al. (2010). Describing the brain in autism in five dimensions–magnetic resonance imaging-assisted diagnosis of autism spectrum disorder using a multiparameter classification approach. *J. Neurosci.* 30, 10612–10623. doi: 10.1523/JNEUROSCI.5413-09.2010

Edwards, B. G., Calhoun, V. D., and Kiehl, K. A. (2012). Joint ICA of ERP and fMRI during error-monitoring. *Neuroimage* 59, 1896–1903. doi: 10.1016/j.neuroimage.2011.08.088

Engell, A. D., Huettel, S., and McCarthy, G. (2012). The fMRI BOLD signal tracks electrophysiological spectral perturbations, not event-related potentials. *Neuroimage* 59, 2600–2606. doi: 10.1016/j.neuroimage.2011.08.079

Floresco, S. B., and Ghods-Sharifi, S. (2007). Amygdala-prefrontal cortical circuitry regulates effort-based decision making. *Cereb. Cortex* 17, 251–260. doi: 10.1093/cercor/bhj143

Franco, A. R., Ling, J., Caprihan, A., Calhoun, V. D., Jung, R. E., Heileman, G. L., et al. (2008). Multimodal and multi-tissue measures of connectivity revealed by joint independent component analysis. *IEEE J. Sel. Top. Signal Process.* 2, 986–997. doi: 10.1109/JSTSP.2008.2006718

Gratton, G., Coles, M. G., and Donchin, E. (1983). A new method for off-li … *Electroencephalogr. Clin. Neurophysiol.* Available Online at: http://www.ncbi.nlm.nih.gov/pubmed/6187540

Hanke, M., Halchenko, Y. O., Haxby, J. V., and Pollmann, S. (2010). Statistical learning analysis in neuroscience: aiming for transparency. *Front. Neurosci.* 4:38. doi: 10.3389/neuro.01.007.2010

Harris, S., Sheth, S. A., and Cohen, M. S. (2008). Functional neuroimaging of belief, disbelief, and uncertainty. *Ann. Neurol.* 63, 141–147. doi: 10.1002/ana.21301

Heekeren, H. R., Marrett, S., and Ungerleider, L. G. (2008). The neural systems that mediate human perceptual decision making. *Nat. Rev. Neurosci.* 9, 467–479. doi: 10.1038/nrn2374

Heekeren, H. R., Wartenburger, I., Schmidt, H., Schwintowski, H.-P., and Villringer, A. (2003). An fMRI study of simple ethical decision-making. *Neuroreport* 14, 1215–1219. doi: 10.1097/01.wnr.0000081878.45938.a7

Jenkinson, M., Bannister, P., Brady, M., and Smith, S. (2002). Improved optimization for the robust and accurate linear registration and motion correction of brain images. *Neuroimage* 17, 825–841.

Kohavi, R., and John, G. H. (1997). Wrappers for feature subset selection. *Artif. Intell.* 97, 273–324. doi: 10.1016/S0004-3702(97)00043-X

Krusienski, D. J., Sellers, E. W., McFarland, D. J., Vaughan, T. M., and Wolpaw, J. R. (2008). Toward enhanced P300 speller performance. *J. Neurosci. Method* 167, 15–21. doi: 10.1016/j.jneumeth.2007.07.017

LaConte, S. M., Peltier, S. J., and Hu, X. P. (2007). Real-time fMRI using brain-state classification. *Hum. Brain Mapp.* 28, 1033–1044. doi: 10.1002/hbm.20326

Lal, T. N., Schroder, M., Hinterberger, T., Weston, J., Bogdan, M., Birbaumer, N., et al. (2004). Support vector channel selection in BCI. *IEEE Trans. Biomed. Eng.* 51, 1003–1010. doi: 10.1109/TBME.2004.827827

Lan, T., Erdogmus, D., Adami, A., and Pavel, M. (2005). Feature selection by independent component analysis and mutual information maximizaiton in EEG signal classification. *IEEE Int. Joint Conf. Neural Netw.* 5, 3011–3016. doi: 10.1109/IJCNN.2005.1556405

Markowitsch, H. J., and Staniloiu, A. (2011). Amygdala in action: relaying biological and social significance to autobiographical memory. *Neuropsychologia* 49, 718–733. doi: 10.1016/j.neuropsychologia.2010.10.007

Miller, G. A., Gration, G., and Yee, C. M. (1988). Generalized implementation of an eye movement correction procedure. *Psychophysiology* 25, 241–243. doi: 10.1111/j.1469-8986.1988.tb00999.x

Mourão-Miranda, J., Reynaud, E., McGlone, F., Calvert, G., and Brammer, M. (2006). The impact of temporal compression and space selection on SVM analysis of single-subject and multi-subject fMRI data. *Neuroimage* 33, 1055–1065. doi: 10.1016/j.neuroimage.2006.08.016

Müller, K.-R., Tangermann, M., Dornhege, G., Krauledat, M., Curio, G., and Blankertz, B. (2008). Machine learning for real-time single-trial EEG-analysis: from brain–computer interfacing to mental state monitoring. *J. Neurosci. Methods* 167, 82–90. doi: 10.1016/j.jneumeth.2007.09.022

Norman, K. A., Polyn, S. M., Detre, G. J., and Haxby, J. V. (2006). Beyond mind-reading: multi-voxel pattern analysis of fMRI data. *Trends Cogn. Sci.* 10, 424–430. doi: 10.1016/j.tics.2006.07.005

Osaka, M., Yaoi, K., Minamoto, T., and Osaka, N. (2013). When do negative

and positive emotions modulate working memory performance? *Sci. Rep.* 3:1375. doi: 10.1038/srep01375

O'Toole, A. J., Jiang, F., Abdi, H., Pénard, N., Dunlop, J. P., and Parent, M. A. (2007). Theoretical, statistical, and practical perspectives on pattern-based classification approaches to the analysis of functional neuroimaging data. *J. Cogn. Neurosci.* 19, 1735–1752. doi: 10.1162/jocn.2007.19.11.1735

Quinlan, J. R. (1993). *Programs for Machine Learning*, San Francisco, CA: Morgan Kaufmann Publishers Inc.

Rangel, A., Camerer, C., and Montague, P. R. (2008). A framework for studying the neurobiology of value-based decision making. *Nat. Rev. Neurosci.* 9, 545–556. doi: 10.1038/nrn2357

Sanei, S. (2007). *EEG Signal Processing*. Chichester; Hoboken, NJ: John Wiley and Sons.

Smith, S. M., Miller, K. L., Moeller, S., Xu, J., Auerbach, E. J., Woolrich, M. W., et al. (2012). Temporally-independent functional modes of spontaneous brain activity. *Proc. Natl. Acad. Sci. U.S.A.* 109, 3131–3136. doi: 10.1073/pnas.1121329109

Subasi, A., and Ismail Gursoy, M. (2010). EEG signal classification using PCA, ICA, LDA and support vector machines. *Expert Syst. Appl.* 37, 8659–8666. doi: 10.1016/j.eswa.2010.06.065

Tallon-Baudry, C., Bertrand, O., Delpuech, C., and Pernier, J. (1996). Stimulus specificity of phase-locked and non-phase-locked 40 Hz visual responses in human. *J. Neurosci.* 16, 4240–4249.

Tallon-Baudry, C., Bertrand, O., Delpuech, C., and Permier, J. (1997). Oscillatory gamma-band (30–70 Hz) activity induced by a visual search task in humans. *J. Neurosci.* 17, 722–734.

Tohka, J., Foerde, K., Aron, A. R., Tom, S. M., Toga, A. W., and Poldrack, R. A. (2008). Automatic independent component labeling for artifact removal in fMRI. *Neuroimage* 39, 1227–1245. doi: 10.1016/j.neuroimage.2007.10.013

Tort, A. B. L., Kramer, M. A., Thorn, C., Gibson, D. J., Kubota, Y., Graybiel, A. M., et al. (2008). Dynamic cross-frequency couplings of local field potential oscillations in rat striatum and hippocampus during performance of a T-maze task. *Proc. Natl. Acad. Sci. U.S.A.* 105, 20517–20522. doi: 10.1073/pnas.0810524105

Vapnik, V. (2000). *The Nature of Statistical Learning Theory, 2nd Edn.* New York, NY: Springer.

Viola, P., and Jones, M. (2001). Rapid object detection using a boosted cascade of simple features. *Int. Conf. Comput. Vis. Pattern Recognit.* 511–518. doi: 10.1109/CVPR.2001.990517

White, C. N., Mumford, J. A., and Poldrack, R. A. (2012). Perceptual criteria in the human brain. *J. Neurosci.* 32, 16716–16724. doi: 10.1523/JNEUROSCI.1744-12.2012

Woolrich, M. W., Ripley, B. D., Brady, M., and Smith, S. M. (2001). Temporal autocorrelation in univariate linear modeling of FMRI data. *Neuroimage* 14, 1370–1386. doi: 10.1006/nimg.2001.0931

Yamashita, O., Sato, M., Yoshioka, T., Tong, F., and Kamitani, Y. (2008). Sparse estimation automatically selects voxels relevant for the decoding of fMRI activity patterns. *Neuroimage* 42, 1414–1429. doi: 10.1016/j.neuroimage.2008.05.050

Conflict of Interest Statement: The authors declare that the research was conducted in the absence of any commercial or financial relationships that could be construed as a potential conflict of interest.

Received: 26 December 2012; accepted: 04 July 2013; published online: 31 July 2013.

Citation: Douglas PK, Lau E, Anderson A, Head A, Kerr W, Wollner M, Moyer D, Li W, Durnhofer M, Bramen J and Cohen MS (2013) Single trial decoding of belief decision making from EEG and fMRI data using independent components features. Front. Hum. Neurosci. 7:392. doi: 10.3389/fnhum.2013.00392